SCHOLARLY PUBLICATIONS

A CURRENT AWARENESS BULLETIN
OF RESEARCH OUTPUT

@DTU

(22nd Edition)

OCTOBER 2014

BY: CENTRAL LIBRARY

DELHI TECHNOLOGICAL UNIVERSITY
(FORMERLY *DELHI COLLEGE OF ENGINEERING)*
GOVT. OF N.C.T. OF DELHI
SHAHBAD DAULATPUR, MAIN BAWANA ROAD
DELHI 110042

PREFACE

This is the Twenty second Issue of Current Awareness Bulletin started by Delhi Technological University, Central Library. The aim of the bulletin is to compile, preserve and disseminate information published by the faculty, students and alumni for mutual benefits. The bulletin also aims to propagate the intellectual contribution of Delhi Technological University (DTU) as a whole to the academia.

The bulletin contains information resources available in the internet in the form of articles, reports, presentations published in international journals, websites, etc. by the faculty and students of DTU. The publications of faculty and student which are not covered in this bulletin may be because of the reason that the full text either was not accessible or could not be searched by the search engine used by the library for this purpose.

The learned faculty and students are requested to provide their uncovered publications to the library either through email or in CD, etc to make the bulletin more comprehensive.

This issue contains the information published during October 2014. The arrangement of the contents is alphabetical. The full text of the article which is either subscribed by the university or available in the web is provided in this bulletin.

Central Library

CONTENTS

1. A Review of High-Speed Coherent Transmission Technologies for Long-Haul DWDM Transmission at 100G and Beyond, Geoff Bennett, Kuang-Tsan Wu, ***£Anuj Malik***, Soumya Roy, and Ahmed Awadalla, ECE, DCE

2. A Review on Maximum Power Point Tracking Techniques for Photovoltaic Power Generating Systems, ***£Aseem Sayal @P.C. Sekhar *Dr. Sukumar Mishra***, Electrical Engineering, DTU

3. A Secure and Efficient Authentication Protocol in Wireless Sensor Network, Kakali Chatterjee, Asok De and ****Daya Gupta***, Computer Engineering Department, DTU

4. A Survey on LTE Downlink Packet Scheduling, $Vallari Sharma1***, £Prof. P.K Chopra***, Electronics, DTU

5. Agile vs waterfall: A Comparative Analysis, ***Vaishnavi Kannan *Smita Jhajharia*** and DR. Seema Verma

6. An Adaptive Mesh Strategy for Singularly Perturbed Convection Diffusion Problems, ****Vivek Kumar*** and Balaji Srinivasan, Applied Mathematics, DTU

7. Analysis of Software Project Reports for Defect Prediction Using KNN, Rajni Jindal, ****Ruchika Malhotra*** and ****Abha Jain***

8. Assessment of water quality and suitability analysis of River Ganga in Rishikesh, India, ****A. K. Haritash, *Shalini Gaur*** and ****Sakshi Garg***, Environmental Engineering, DTU

9. Chaos based Joint Compression and Encryption Framework for End-to-End Communication Systems, ****Nidhi Goel***, Balasubramanian Raman, Indra Gupta, ECE, DTU

10. Closure to "Fastest Rapid Loading Methods of Vertical and Radial Consolidations" by S. K. Tewatia, ***~Pratima Rani Bose*** and Asuri Sridharan, Civil Engineering, DTU

11. Comparison study of Vector Control of Induction Motor Using Rotor Flux Estimation by Two Different Methods, ***Ashish Chourasia, *Vishal Srivastava, *Abhishek Choudhary*** and ***Sakshi Praliya***, Electrical Engineering Department, DTU

12. Curcumin-based IKKb inhibiting anticancer lead design using novel fragment-based group QSAR modeling, ***Kunal Patel***, Chetna Tyagi, Sukriti Goyal, Jaspreet Kaur Dhanjal, ***Navneeta Bharadvaja*** and Abhinav Grover, Biotechnology, DTU

13. Design and Implementation of PID Controller for Second Order Plant and Comparison of its Performance with Fuzzy Logic based Controller, ***Ashok Kumar Kumawat***, ***Sandeep Rana*** and Ashish Sharma, EE Department, DTU

14. Energy Exergy Analysis of a high pressure Claude Haylentsystem for liquefaction of Gases, ***Devender Kumar*** and ***R. S. Mishra***, Mechanical Engineering, DTU

15. ENHANCED BACK-CONTACT BACK-JUNCTION CRYSTALLINE SILICON SOLAR CELL PERFORMANCE WITH A SILICON-CARBIDE (SIC) BASED FRONT SURFACE PASSIVATION, ***Rahul Pandey*** and Rishu Chaujar, Engineering Physics, DTU

16. Examining the Effectiveness of Machine Learning Algorithms for Prediction of Change Prone Classes, ***Ruchika Malhotra*** and Megha Khanna, Software Engineering, DTU

17. Experimental Investigations on Friction Stir Processed Copper and Enhancement of Mechanical Properties of the Composite Material, ***V. Jeganathan Arulmoni*** and ***R. S. Mishra***, Department of Mechanical Engineering, DTU

18. Failure of Piston in IC Engines: A Review, ***R. C. Singh, *Roop. Lal, *Ranganath M S*** and ***Rajiv Chaudhary***, Department of Mechanical Engineering, DTU

19. Feasibility Study of a Solar Crematorium in India, ***@Akhilesh Chandra Kashyap*** and ***Janardan Prasad Kesari***, Department of Mechanical Engineering, DTU

20. INFLUENCE OF HETEROGENEOUS GATE DIELECTRIC ON HETERO-DIELECTRIC-DMG-GAATFET FOR IMPROVED TUNNELING CURRENT, ***Jaya Madan***, R.S. Gupta and ***Rishu Chaujar***, Engineering physics, DTU

21. INVESTIGATION OF FREQUENCY DEPENDENT PARAMETER OF GEWE-SiNW MOSFET FOR MICROWAVE AND RF APPLICATIONS, ***Neha Gupta,** ***Ajay Kumar** and ***Rishu Chaujar**, Engineering physics, DTU

22. Leachate characterization and evaluating its impact on groundwater quality in vicinity of landfill site area, ***Lovleen Gupta** and ***Swati Rani**, Environmental Engineering Department, DTU

23. Modelling of Contaminant Transport from Landfills, ***@Archana Chawla**, ***Dr. S.K. Singh,** HOD Department of Environmental Engineering, DTU

24. Investigation on Multi-Response Parameter Optimization of Cold Spray Coating Process, Tarun Goyal, ***R.S. Walia** and T.S. Sidhu, DTU

25. On Petri Net Generating all the Standard Basis for n-Dimensional Euclidean Space, ***<Gajendra Pratap Singh***, Applied Mathematics, DTU in 3rd International Conference On "Innovative Approach in Applied Physical, Mathematical/Statistical, Chemical Sciences and Emerging Energy Technology for Sustainable Development

26. On the performance of Tamm-plasmon and surface-plasmonhybrid-mode refractive-index sensor in metallo-dielectricheterostructure configuration, Ritwick Dasa, ***~Triranjita Srivastava***, Rajan Jhaca School, DTU

27. Optimization of Proces Parameters in Turning Operation Using Response Surface Methodology: A Review, ***Ranganath M S,** ***Vipin,** and ***£Harshit***, Mechanical Engineering, DTU

28. Performance Analysis of A Novel Scheduling Algorithm for Different Traffics in LTE Networks, Vallari Sharma and ***#Prof. P.K Chopra,** Electronics, DTU

29. Performance Analysis of Brushless DC Motor Using Intelligent Controllers and Minimization of Torque Ripples, ***Vishal Srivastava,** ***Ashish Chourasia** and ***Shaba Anjum***, Electrical Engineering Department, DTU

30. Performance Analysis of Three Phase Induction Motor Controlled Via Indirect Vector Control Using D Space 1104 R&D Controller Board, ***Abhishek Choudhary, *Ashish Chourasia*** and ***Vishal Srivastava***, Electrical Engineering Department, DTU

31. Realization of DVCCTA Based Versatile Modulator, ***Neeta Pandey,*Rajeshwari Pandey, Aseem Sayal,*B** and ***Manan Tripathi***, Electronics & Communication Engineering and Dept. of Electrical Engineering, DTU

32. Reconfigurable Inverted Circular Patch Antenna for Wireless Applications, Preet Kaur, ***$S. K. aggarwal*** and Asok De, DTU

33. Red light emitting BaNb2O6: Eu3+ phosphor for solid state lighting applications, ***Amit K. Vishwakarma, *Kaushal Jha, *M. Jayasimhadri, *A.S. Rao, *Kiwan Jang, *B. Sivaiah*** and D. Haranath, Department of Applied Physics, DTU

34. Study of Designing a Solar Concentrator for Crematorium using Solar Energy, ***A. C. Kashyap, *J. P. Kesari, *A. K. Rai*** and ***Hukam Singh***, Mechanical Engineering, DTU

35. Synthesis of Nano-structured p-type Higher Manganese Silicide, Govind Ram Gurjar, Purnima Swarup Khare,, ***Saravanan Muthiah***, ***B.D. Pathak*** and Ajay Dhar, Mechanical Engineering, DTU

36. Thermodynamic analysis of a Solar Thermal Syphon Pump, ***Kaushalendra K. Dubey, *R. S. Mishra*** and Gopal P. Sinha, Industrial & Automobile Engineering, DTU

37. WIRELESS CONTROL OF DC GEARED MOTOR AND HOME APPLIANCES FROM COMPUTER USING MICROCONTROLLER, ***J.N.Rai, *Rohit Devdhar*** and ***Utkarsh Sareen***, Department Of Electrical Engineering, DTU

***Faculty**	**@Research Scholar**	**$PG Scholar**
#Alumni	**£Undergraduate Student**	**~ Ex Faculty**
! Teaching-cum-Research Fellow	**<Ex Research Scholar**	**>Ex PG Scholar**

BENNETT_LAYOUT.qxp_Layout 9/25/14 1:31 PM Page 102

A Review of High-Speed Coherent Transmission Technologies for Long-Haul DWDM Transmission at 100G and Beyond

Geoff Bennett, Kuang-Tsan Wu, Anuj Malik, Soumya Roy, and Ahmed Awadalla

ABSTRACT

Over the past five years, coherent transmission technologies have delivered more than an order of magnitude improvement in the capacity-reach product for long-haul DWDM transmission systems. This article provides a working definition of "coherent transmission" based on current market realities; provides a functional model for beyond 100G coherent systems, and then examines five key technologies that will deliver beyond 100G: evolving transmitter technologies, including Nyquist pulse shaping and nonlinear compensation of transmitter devices; nonlinear compensation for the propagation effect; further advances in FEC technology; flexible grid DWDM and coherent super-channels. In each case we explain the factors in terms of optical or electronic component performance that are most likely to result in system performance limitations, and discuss engineering strategies to mitigate those limitations.

OVERVIEW: THE SUCCESS OF COHERENT TRANSMISSION

There is no doubt that 100G coherent transponders and 500G coherent super-channels have transformed the way in which service providers deploy long-haul transmission capacity. This article offers a brief overview of how coherent detection works, and examines the technology that will appear in the next generation of coherent transmission systems for transmission at 100 Gb/s and beyond.

HOW DOES COHERENT DETECTION WORK?

Figure 1 shows a simple direct detection transmitter and receiver. The modulation technique is chosen so that decoding in the receiver can be done directly, with a minimum of signal processing. Intensity modulation with direct detection (IM-DD) works effectively up to data rates of 10 Gb/s (note that there is no "hard limit" because of trade-offs that can be made). Note that this type of direct detection receiver is nonlinear — its output responds to a square law relationship with respect to the received signal. This means that it is very difficult to implement signal processing techniques to compensate for linear impairments, such as chromatic dispersion (CD) and polarization mode dispersion (PMD).

In a coherent detector, an amplitude/phase modulation technique is used in the transmitter, and a local oscillator (LO) laser source in the receiver. The LO (and baseband filtering) effectively acts as a low-noise amplifier with very good rejection of neighboring channel interference. Combining the incoming signal and the LO signal in a coherent receiver creates a coherent beat signal that represents the original digital signal (plus noise from various sources), which can then be extracted via opto-electronics [1].

A coherent detector has a number of advantages compared to IM-DD. First, coherent detection enables the use of polarization multiplex, and both in-phase and quadrature modulation to achieve a much better capacity-reach product. Second, the LO provides low-noise amplification and adjacent channel rejection. Third, this is a linear detection technique, which means that linear impairments, such as CD and PMD, can be effectively compensated for using powerful digital signal processing (DSP) components and algorithms [2].

In effect, coherent transmission is a synergy of high-performance optical and electronic components, and both are essential to achieving the end result. The "state of the market" in coherent transmission today is 100 Gb/s per wavelength, and often a number of 100G channels are logically bundled on a single line card to create a "super-channel" of, for example, 500 Gb/s or higher.

A MARKET DEFINITION OF COHERENT DETECTION

Referring to Fig. 2, a typical commercial 100 Gb/s transponder will contain the transmitter (Tx), which makes use of a narrow line width and a tunable laser with a super-Mach-Zehnder amplitude/phase modulator (shown as MZM_X and MZM_Y).

The authors are with Infinera Corporation.

 0163-6804/14/$25.00 © 2014 IEEE

BENNETT_LAYOUT.qxp_Layout 9/25/14 1:31 PM Page 103

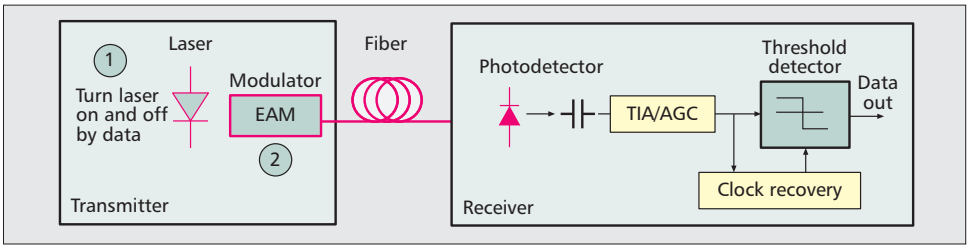


Figure 1. Transmitter and receiver circuit for intensity modulation with direct detection (IM-DD). Modulation can be achieved (1) directly (turning laser on and off) or (2) using an external modulator. Note the very small number of optical components (in red).

The most common coherent modulation type is polarization multiplexed quadrature phase shift keying (PM-QPSK), which carries 4 b/modulation symbol (including both polarizations). Typical real-world reach for this modulation type is between 3000 and 4500 km.

The spectral width of the 100 Gb/s PM-QPSK carrier is designed to fit into a 50 GHz fixed G.694.1 frequency slot. The variation of the carrier width for a given vendor implementation is predominantly the size of the forward error correction (FEC) field for that implementation, which varies from 15 to 35 percent overhead (OH).

PM-binary phase shift keying (PM-BPSK), carrying 2 b/modulation symbol (including both polarizations), may be used as an alternative to PM-QPSK for extended reach of 10,000 km or more.

The coherent receiver (Rx) comprises:

1. A tunable LO laser. The ideal LO should have very narrow line width and very stable frequency locking. Note that some degree of tolerance is acceptable, and can be compensated for in the DSP, but the better the laser, the less work is needed from the DSP.
2. Elements (polarization beam splitter, PBS; and beam splitter, BS) that split the polarizations of the incoming signal, and split the power of the LO.
3. An array of 90° hybrid (amplitude/phase) optical demodulators. These are effectively extracting the coherent beat signal (i.e., the original baseband signal in the transmitter). Successful 90° hybrids, for example, have been fabricated using InP or silicon photonics.
4. An array of balanced photodetectors. Balanced photodetectors are preferred in order to reduce the common-mode noise, and for more efficient use of the combination of LO and signal power.
5. An array of transimpedence amplifiers (TIAs). These must be designed with low noise and sufficient bandwidth to amplify the signals coming out of the photodetectors.
6. High-speed analog-to-digital converters (ADCs). These are the most demanding components in today's 100G implementation as their bandwidth and sample rate typically limit the transmission Baud rate of the system. The "state of the market" for these devices today allows symbol rates of around 35 GBaud, but faster devices are available for use in hero experiments.
7. DSP, typically implemented as an application-specific integrated circuit (ASIC), which includes ADCs. A modern DSP ASIC performs at least four key functions: clock recovery, CD compensation, PMD compensation, and carrier recovery.

Coherent processing is so effective that many people have wondered why the industry has not implemented it sooner. The answer lies in the combination of very high sampling rate ADCs and high-performance ASICs to implement the electronic compensation function. For example, a 100 Gb/s coherent implementation requires around 3×10^{13} operations/s — the equivalent of around 7000 laptop computers. In terms of a functional split, about 65 percent of the ASIC would be used for coherent modem functions, and 35 percent for soft-decision FEC (SD-FEC) processing.

Using a 40 nm complementary metal oxide semiconductor (CMOS) process, the ASIC would have about 50 million gates. To a first order approximation, one can assume a 0.8 improvement factor (i.e., reduction of power consumption) moving from 40 to 28 nm and 0.65 moving from 28 to 16 nm, assuming the circuit functionality does not change. This assumption does not usually hold true for any technology area, and in terms of coherent processing we will see that emerging functions such as pulse shaping and nonlinear compensation are already planned for integration into the next generation of ASICs.

Figure 2 shows the details of the DSP functional block." CD compensation is the same for Xpol and Ypol, and does not involve Xpol and Ypol coupling, whereas PMD compensation (shown as PMD EQ) requires both Xpol and Ypol signals to unravel the channel response. Both CD and PMD compensation blocks use finite impulse response (FIR) filters. As an example, at 28 Gbaud, compensation of 50,000 ps/nm requires on the order of 512 taps (at 2 samples/symbol), whereas for equalizing 100 ps of PMD requires 7 or 9 taps. Since CD compensation on each polarization is independent, it is more computationally efficient to separate CD compensation from PMD compensation in order to avoid building a very long PMD compensating filter. This separation allows CD compensation to be implemented in the frequency domain (using fast Fourier transform, FFT) and PMD compensation in the time domain. Tap adaptation algorithms exist, such as the well-known least mean square (LMS)

Coherent processing is so effective that many people have wondered why the industry has not implemented it sooner. The answer lies in the combination of very high sampling rate ADCs and high-performance ASICs to implement the electronic compensation function.

BENNETT_LAYOUT.qxp_Layout 9/25/14 1:31 PM Page 104

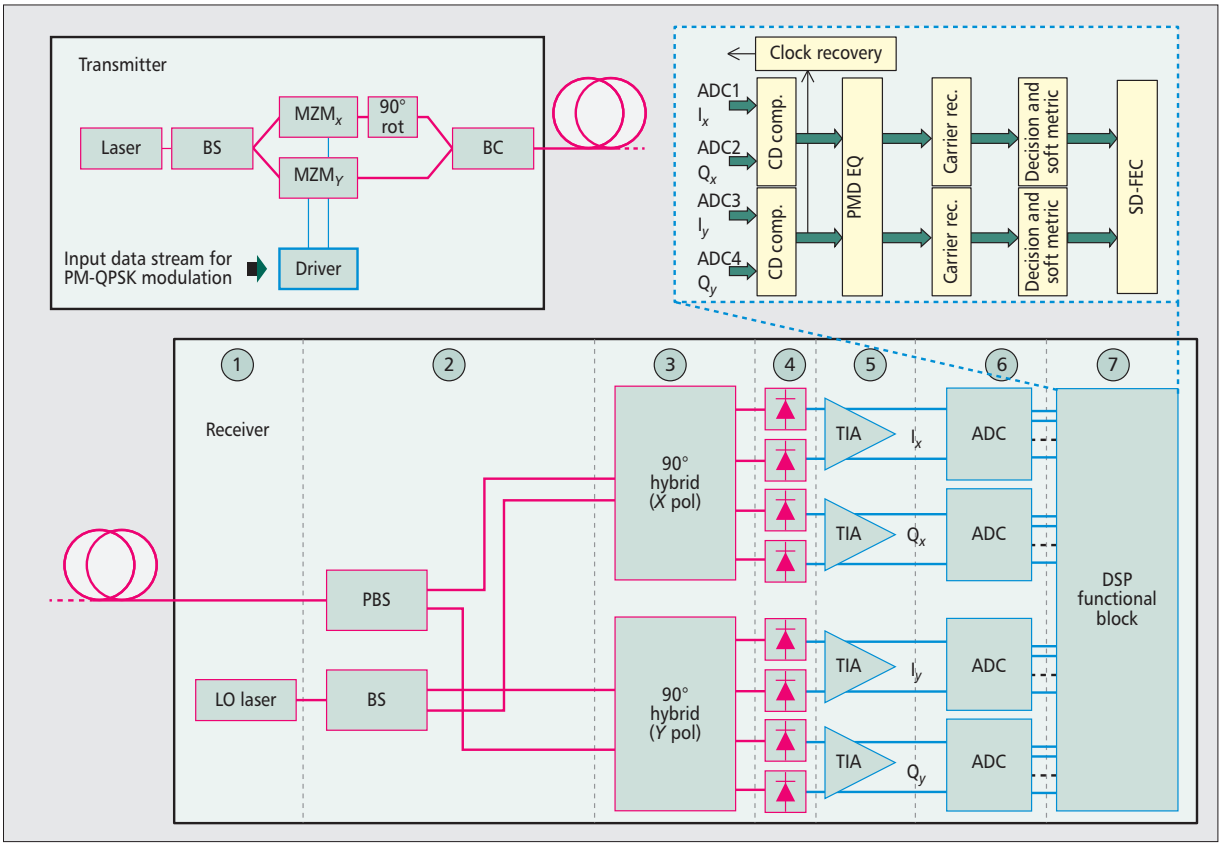


Figure 2. Coherent transmitter and receiver indicating optical (red) and electronic (blue) component blocks.

algorithm. Both data-aided and blind adaptation methods can be used [6].

After PMD equalization, carrier recovery is needed to track the frequency and phase difference between Tx and Rx lasers. Known algorithms such as the Viterbi-Viterbi algorithm [5] can be used. Depending on lasers used, line width can be 100 kHz for external cavity lasers and 1 to 6 MHz for distributed feedback (DFB) lasers, which could result in different design and loop bandwidth required. For the detection of PM-QPSK (which has 90° symmetry in constellation), if the combined effect of line width and noise (ASE and self/cross phase modulation, SPM/XPM) causes the instantaneous phase error to exceed 45°, the carrier recovery will slip into the next lock point, which is 90° away from the present phase, causing incorrect data. This is known as a cycle slip, which, if not handled properly in the design, can cause severe impact on system operation, such as uncorrectable burst errors. This problem can be alleviated by differential encoding, but this can cause a > 1 dB penalty when SD-FEC is used. Thus, other methods may be desired to reduce this penalty.

The SD-FEC block following carrier recovery in Fig. 2 offering 11 dB or more of net coding gain (NCG) would typically be implemented as a part of the receiver ASIC, and is covered later in this article.

Beyond 100 Gb/s

Moving beyond 100G requires a number of component technologies to scale to higher performance levels and for new techniques to be developed. We describe four different areas in which technology is evolving: transmitter-based techniques, nonlinear compensation, advances in forward error correction, and flexible grid operation. Finally, we consider a design strategy intended to mitigate component performance bottlenecks; that is, the coherent super-channel.

Transmitter-Based Techniques

High Order Modulation

Today the Rx ADC performance limits per wavelength transmission rates to around 35 GBaud, and, like CPU core clock speed, this performance is not expected to scale linearly in the near future.

We expect the performance bottleneck for transmission symbol rate to shift to the emerging transmitter technologies that will be introduced to facilitate higher order modulation (i.e., carrying more bits in each modulation symbol). This bottleneck would most likely be in the digital-to-analog converter (DAC), and nonlinear compensation DSP in the next generation of higher order modulation coherent transmitters.

Thus, in concert with higher order modulation [3], it is necessary to develop pulse-shaping

BENNETT_LAYOUT.qxp_Layout 9/25/14 1:31 PM Page 105

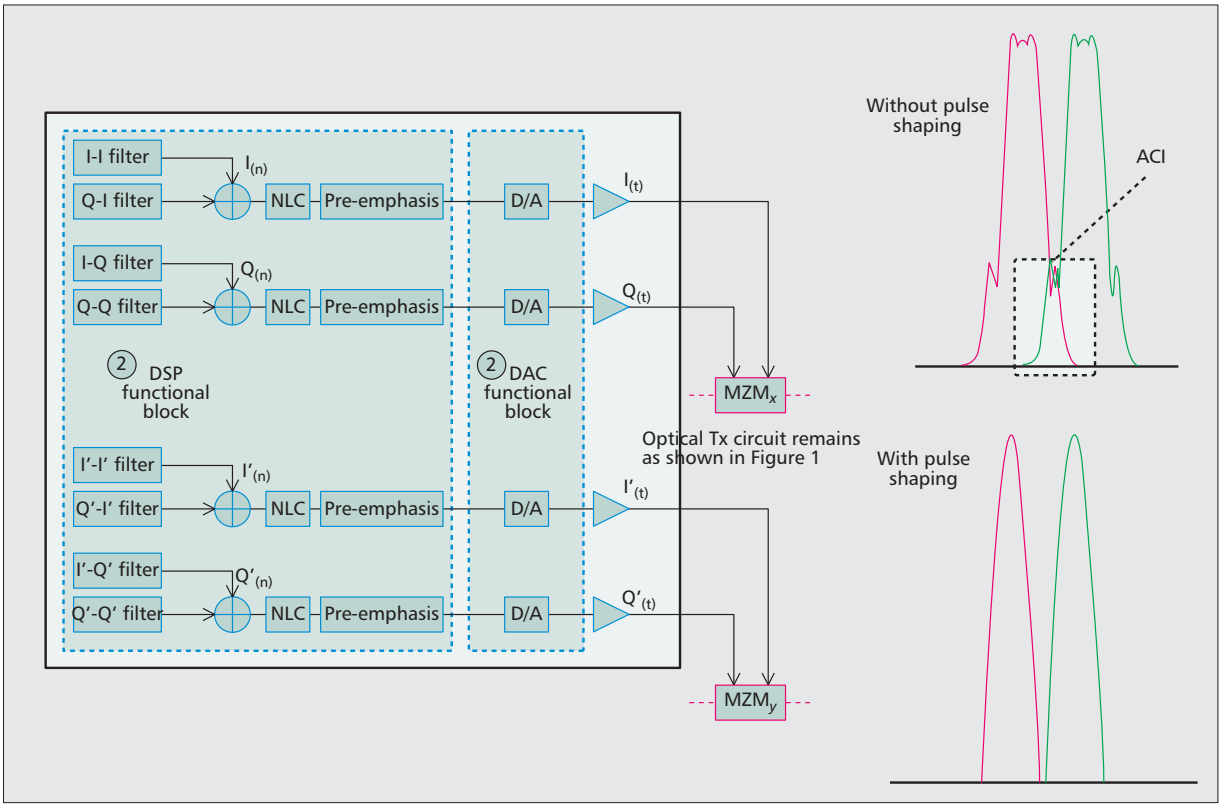


Figure 3. Transmit DSP and DAC functional blocks for pulse shaping and pre-compensation.

techniques that optimize spectral efficiency, and nonlinear compensation techniques to mitigate the impact from device nonlinearity and propagation through fiber. Both of these techniques require leading edge opto-electronic components for a successful implementation.

Pulse Shaping Techniques

A typical unfiltered amplitude/phase modulated signal spectrum will appear as a large central peak, with *n*-order lobes on either side (see the red and green spectra in the upper right of Fig. 3). Improper filtering of the side lobes in order to "shape" the pulse will result in a loss of real information from each symbol, creating undesired intersymbol interference (ISI).

"Intelligent" pulse shaping on the signal involves more complex electronic driver circuit, shown in Fig. 4. This basic objective serves as an interesting example of how one compensation methodology may require a second or even a third compensation approach.

Stage 1: The DSP creates a complex digital signal, which drives the DAC. Referring to Fig. 2, you can consider that the "Driver" box is now replaced by the more advanced electronic circuit shown in Fig. 3. In the upper right diagram, the illustrative two adjacent channel signals are not well shaped, and if channel spacing is too tight, the result is higher adjacent channel interference (ACI) in addition to ISI. The well shaped signals in the lower right part of the diagram minimize both ISI and ACI, and allow higher spectral efficiency.

So what is the impact on component complexity? For Mach-Zehnder modulator (MZM), if the drive voltage amplitude is kept under half Vπ, the output optical field can be shown to be modulated linearly by the drive voltage. The output electric field on one polarization is completely controlled by the two drive voltages I(t) and Q(t). By using a pair of DACs, the electrical field can be controlled by the DSP engine; and using four DACs and four MZMs, the entire optical field in both polarizations (x and y) and all dimensions (I and Q) can be controlled by the DSP.

Stage 2: Increasing the signal power out of the MZM implies increasing the drive voltage, and beyond a certain point the MZM will become nonlinear.

Fortunately, the nonlinearity of the MZM is instantaneous; thus, a simple lookup table can be used to compensate for the MZM nonlinearity as shown by the NLC block in Fig. 3. In contrast, a real-time computation of the MZM nonlinearity (as shown by the NLC block) could be a complex task, especially for high baud rate and high-order modulation format such as 16-QAM and beyond.

Stage 3: To compensate for the analog distortion arising from the electric path and DAC, some pre-emphasis filtering is needed to reduce the penalty from the electric path. This can also be performed in the DSP section shown in Fig. 3 as "Pre-emphasis."

Thus, the resulting transmitter component

BENNETT_LAYOUT.qxp_Layout 9/25/14 1:31 PM Page 106

The resulting increase in reach and performance of the system is critical for extending the life of (in particular) submarine links and for reducing the number of regenerators in long terrestrial links, and leads to considerable savings in both CAPEX and OPEX.

architecture has the capability of generating complex high order modulation formats such as multi-level quadrature amplitude modulation (QAM) and orthogonal frequency-division multiplexing (OFDM), including pulse shaping and pre-emphasis [4]. Using these techniques, it is possible to approach the point where individual dense wavelength-division multiplexing (DWDM) carriers can be spaced at close to the symbol rate, a situation called Nyquist DWDM. A critical consequence of Nyquist DWDM is that it is now spectrally efficient to divide a given DWDN channel into multiple subcarriers without losing spectral efficiency. This "super-channel" approach is described in more detail below.

Another important capability with Tx DSP is for linear dispersion pre-compensation [9], which can be useful in some fiber links to gain some performance by distributing the CD compensation at the Tx and Rx (e.g., a 50/50 split). This is also good from the circuit implementation point of view in reducing the size of FFT/inverse FFT (IFFT) to compensation large CD for the new fiber links with large CD coefficient fibers. A set of cross-coupled digital filters (shown in Fig. 3) generates the distorted voltages on I and Q channels in order to compensate for CD. Digital filtering can be done either in the time domain as linear tap delay line filters, or using FFT/IFFT for more computational efficiency.

Nonlinear Compensation for the Propagation Effect

Fiber nonlinearity can be classified into single channel effects such as SPM, and WDM effects such as XPM and four wave mixing (FWM). Techniques that are effective for compensating SPM may not be as effective for XPM, and vice versa; and in almost all applications, WDM effects (particularly XPM) prevail. There has been extensive research on NLC algorithms [10–12], which are summarized in order. We describe three techniques: digital back propagation (DBP), nonlinear polarization crosstalk cancellation (NPCC), and time varying ISI.

DBP [9] solves the propagation equation for the link in hand and uses the inverse of the solution to cancel the nonlinear distortion. This method can be used in several different implementation combinations.

First, it can be implemented in the Tx or Rx. Implementing the method in the Tx [10] has the advantage of using the signal with no noise but the disadvantage of needing feedback from the Rx, and vice versa for the Rx side implementation. Both implementations also suffer from needing to know the exact link launch power and fiber parameters.

Second, the technique can include the whole WDM spectrum or use the channel under test only. The former is not computationally practical today, while the latter compensates for SPM only, which is not a dominant noise source for WDM links.

In all cases available ASIC performance is a key limit for DBP, and although simplifications of the above algorithms have been tried, no commercial coherent ASICs have been shown to incorporate these techniques.

Referring to the NPCC approach, for dual pol systems XPM is manifested in two components, distortion from a polarization onto itself and distortion from the cross polarization onto the polarization observed. In a first order approximation, the nonlinear distortion can be modeled as shown in Eq. 1.

$$R_x = S_x + f_x S_x + g_y S_y \quad (1)$$

In Eq. 1, S_x, S_y are transmitted symbols for X and Y polarizations, and R_x is the received symbol for polarization X. The second term on the RHS represents the same polarization component, and the third term represents the cross polarization component. The processes f_x and g_y are a function in the symbols of the observed channel neighbors, launch powers, and fiber parameters. Obviously, the neighbor symbols are unknown, but due to dispersion, the rate of change of these processes is much slower than the symbol rate. This is key as it enables tracking, while if they were changing rapidly there would be no way of tracking and canceling them, and they would have to be treated as white noise.

Several methods were proposed to track these impairment components [11]. The idea can be explained as follows. With the assumption that all linear distortions together with carrier phase noise have been compensated, with the knowledge of R_x and R_y in Eq. 1, hard decisions are made to get an approximate estimation of S_x and S_y, and then Eq. 1 is used for both polarizations to solve for f_x and g_y using a Weiner filter. The estimate is then used to cancel the distortion. This method has significant benefit in dispersion-managed links and is modestly useful for non-dispersion-managed links.

Another promising development called "Time varying ISI model for nonlinear interference noise" has recently been reported [12], it basically shows that in the presence of dispersion, Eq. 1 needs to be expanded to include neighboring symbols of both polarizations X and Y, making the XPM model look like an ISI, but with ISI factors that are time varying. The temporal variance of the ISI is significantly slower than the symbol rate, and thus it is possible to track and cancel the full XPM contribution, which shows in theory significant dB can be obtained if the transmit symbols are known. The challenge is what gain can be achieved given more and more systems are using soft FEC and the operational BER is above 0.01, making the estimates of Sx and Sy more noisy.

Today all of the NLC techniques are open to ongoing development in terms of improving their effectiveness for a given level of compute power.

Advances in FEC Technology

In FEC, additional bits are added to the data that will allow processors in the receiver to identify, and more importantly recover errors that occurred during transmission. FEC evolution is a direct consequence of increasing availability of digital processing power [13].

BENNETT_LAYOUT.qxp_Layout 9/25/14 1:31 PM Page 107

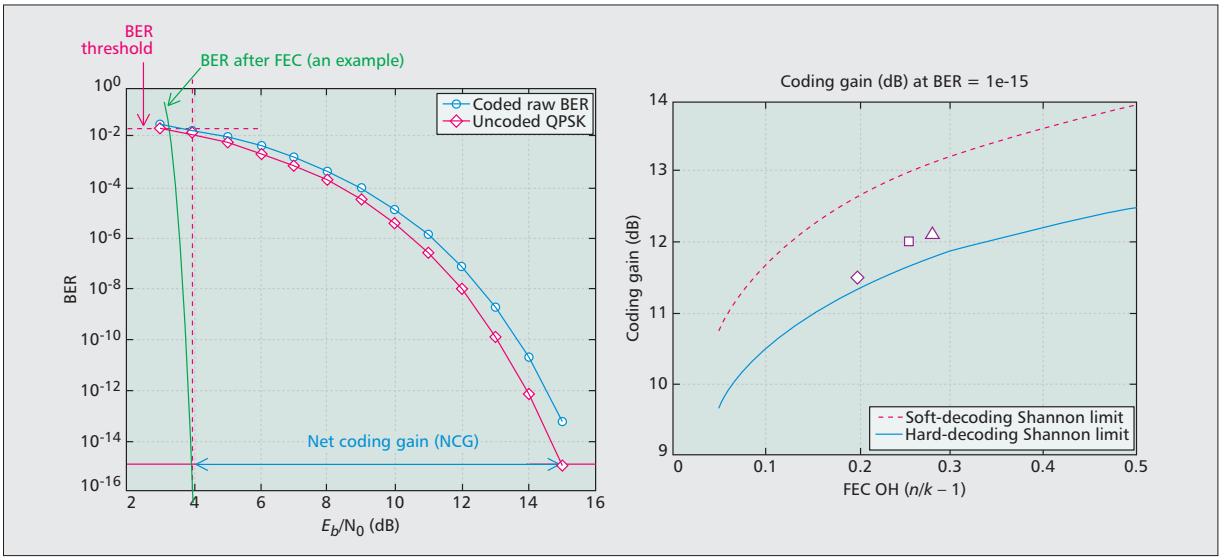


Figure 4. a) Illustrative NCG calculation; b) Shannon limit and recently reported examples of SD-FEC.

Evolution of FEC

FEC evolution is generally regarded as having three distinct generations. In First and Second Generation HD-FEC (Hard Decision) algorithms, the FEC Decoder would detect bit errors using a binary decision — anything above the hard decision threshold is interpreted as a 1, and anything below is interpreted as a 0. First generation FEC was single-iteration, hard decision; while second generation was multi-iteration, hard decision.

With SD-FEC (Soft Decision), the Decoder uses multiple bits (e.g., 4 bits) to represent the received signal sample to provide a "soft," or more granular, indication that not only produces a 1 or 0 as the output, but also a confidence level in the decision. By combining the confidence level with the additional bits in the FEC overhead, the SD-FEC algorithm can deliver about 2dB increase in Net Coding Gain (NCG) compared to a second generation "hard decision" FEC. The resulting increase in reach and performance of the system is critical for extending the life of (in particular) submarine links and for reducing the number of regenerators in long terrestrial links, and leads to considerable savings in both CapEx and OpEx.

NCG, Overhead (OH), Implementation Challenges and Shannon Limit

The definition of NCG is illustrated in Fig. 4a For BPSK/QPSK using FEC with a code rate $R = k/n$ (k = number of information bits and n = total number of channel bits), it can be shown that:

$$BER = \frac{1}{2} erfc\left(\sqrt{R \cdot \frac{E_b}{N_0}}\right) \quad (2)$$

where E_b is the energy per information bit and N_0 is the noise density per Hz. Note that $R = 1$ means "uncoded," and $R = 0.87$ is for FEC OH $= 1/R - 1 = \sim 15$ percent as an example. Reading from Fig. 4a, for BER = 1e-15, it requires $E_b/N_0 = 15$ dB for the uncoded case. When 15 percent OH is added, the coded raw BER is worse, but FEC can correct the raw BER at around 1.7e-2 to 1e-15, or at $E_b/N_0 = 4$ dB.

$$NCG = \left(\frac{E_b}{N_0}\right)_{Uncoded} - \left(\frac{E_b}{N_0}\right)_{Coded} = 15 - 4 = 11dB \quad (3)$$

The OH used in optical transport systems today range from 7 percent to 35 percent. In terms of coding schemes for SD-FEC, there are mainly two: product turbo code (PTC) and low density parity check (LDPC) code. Both use iterative decoding with about 4 to 12 iterations depending on the tradeoff between NCG and power consumption. In a coherent modem ASIC, the proportion in gate count is approximately 35 percent for SD-FEC and 65 percent for modem DSP functions, and a typical clock rate for SD-FEC decoding is around 500MHz. The key challenges for SD-FEC circuit implementation are proper use of fixed-point bits for decoding to ensure no error floor, minimizing the gate count with little reduction on NCG, routing/floor planning and closing timing in certain critical parts of the circuit.

As to further gain possible with FEC, it is insightful to reviewthe Shannon limit. Figure 4b summarizes the soft decision Shannon limit and hard decision Shannon limit versus FEC OH, together with 3 examples of reported FEC coders. Some observations are highlighted below.

- Soft-decision Shannon limit is about 2 dB better than Hard-decision limit. Practical SD-FECs have been demonstrated to perform slightly better than Hard-decision Shannon limit. One example: NCG = 12 dB for OH = 25.5 percent [14].
- There is a diminishing return on NCG for further increase of FEC OH.

BENNETT_LAYOUT.qxp_Layout 9/25/14 1:31 PM Page 108

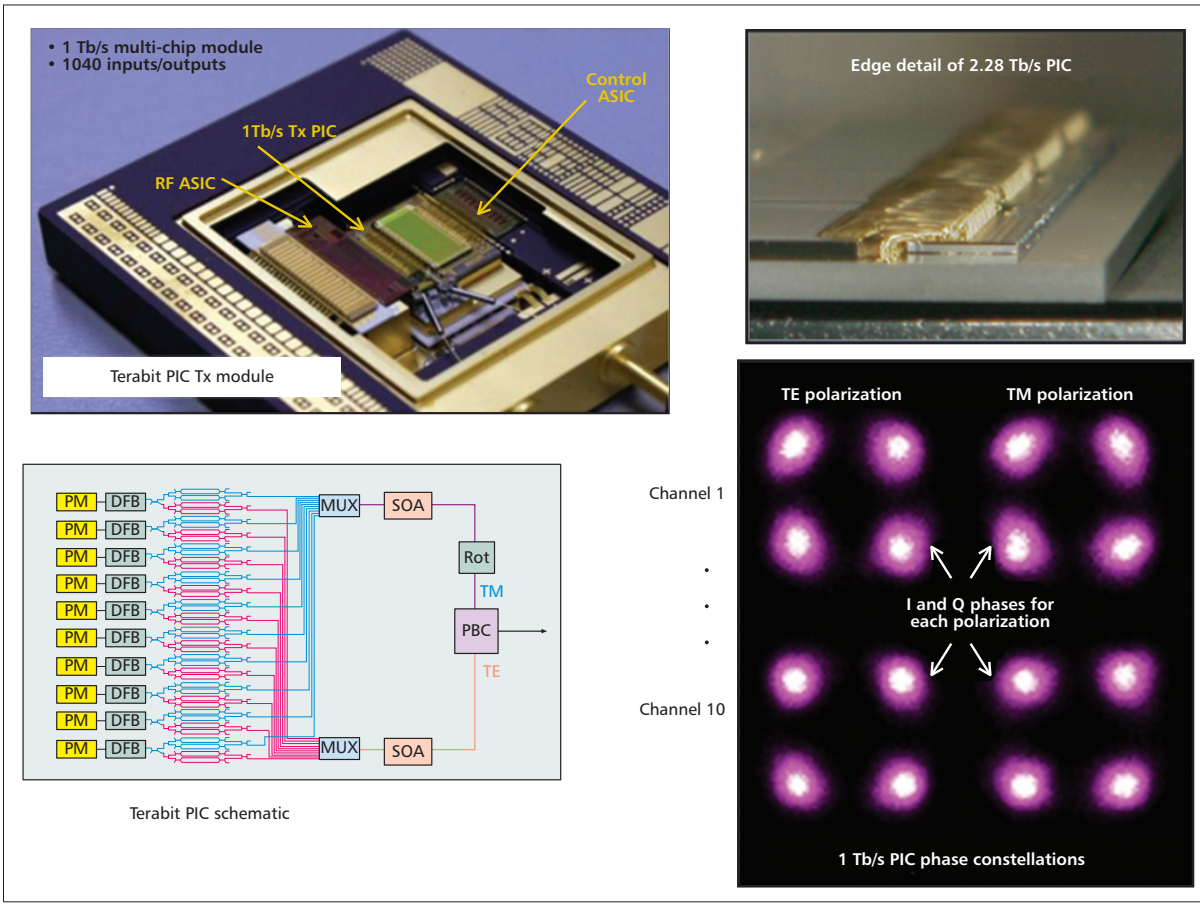


Figure 5. Advanced Terabit PIC and 2.28Tb/s PIC designs.

- Increase in FEC OH results in higher baud rate, and further increase in FEC OH is a tradeoff between capacity and reach.

Generally speaking, the FEC technology has been advanced to approach within 2 dB of the Shannon soft-decision limit. Even a gain of fractions of a dB would need significant increase in gate count and power for a CMOS ASIC. A more practical approach is to use processing power for pulse shaping or NLC instead of more powerful FEC.

Flexible Grid

Nyquist DWDM and super-channels are placing stress on the existing fixed grid DWDM model described in ITU-T G.694.1. A more flexible approach to spectrum allocations was recognized, and ITU-T has defined a flexible grid in the latest version of this standard [8]. Flexible grid defines flexible frequency slots with spectral width of $m \times 12.5$ GHz, to accommodate any combination of optical carriers, modulations, and data rate. In addition, the $m \times 12.5$-GHz spectral width of a flex-grid super-channel can be tuned, enabling rapid changes when the operating specifications of the super-channel are varied. While not directly related to electronic or optical component performance, flexible grid operation allows DWDM network designers to take full advantage of the spectral efficiency of variable width DWDM super-channels that are enabled using advanced opto-electronic processing.

Coherent Super-Channels

The term *super-channel* refers to an evolution in DWDM transmission in which multiple coherent optical carriers are implemented on a single line card, are brought into service in a single operational cycle, and are seen as a single unit of digital capacity by the services that use it [15].

Thanks to advances in pulse shaping technology, there is little or no spectral efficiency penalty in using a super-channel approach compared to a single high data rate carrier. For example, a single-carrier 1.2 Tb/s solution using PM-QPSK modulation would occupy around 460 GHz of spectrum and would need to transmit symbols at 384 GBaud. As mentioned above, the limiting components would include the DAC performance in the pulse-shaping transmitter, the Rx ADC performance, and Tx and Rx component bandwidth. In contrast, a 12-carrier 1.2 Tb/s super-channel line card would only require 32 GBaud symbol rates and associated electronics. It is worth noting that for the same line rate,

BENNETT_LAYOUT.qxp_Layout 9/25/14 1:31 PM Page 109

Function	Current commercial performance limit	Performance bottleneck	Solution(s)	Refs
Coherent receiver ADC	~64 GSamples/s for (40 nm and 28 nm) ~20 GHz 3 dB analog BW ENOB: 5.5 to 6.5	Suitable for 32 GBaud Not sufficient for 64 GBaud and beyond	Drive development of higher conversion rate DACs and 3 dB BW. Alternative: Use of multiple subcarriers with 32 GBaud in a super-channel.	
Coherent receiver DSP engine	Example: 40 nm, ~34 Mgates	Not currently a performance bottleneck. Able to deliver ample CD and PMD compensation capability.	Development is focused on reducing electrical power consumption. Strategy will be to move to 16 nm process.	[7]
Coherent Receiver SD-FEC processor	Example: 40 nm, ~18 Mgates	Current SD-FEC performance delivers 11 to 12 dB NCG, depending on FEC OH and coding scheme.	Goal of developing "application-specific" FEC that balances overhead and reach. Goal of reducing electrical power consumption.	[7]
Coherent transmitter DSP	Example: 28 nm, TBD Mgates	Not an issue for CD precompensation and pulse shaping. Compensation of MZM, especially for high order QAM, is needed, and is being investigated.	Continue to find ways for nonlinear compensation of MZM, especially with CD precompensation and small rolloff Nyquist filtering	
Coherent transmitter DAC	~64 Gsamples/s for (40 nm and 28 nm) ~20 GHz 3 dB analog BW ENOB: 5.5 to 6.5	Suitable for 32 GBaud. Not sufficient for 64 GBaud and beyond	Drive development of higher conversion rate DACs and 3 dB BW. Alternative: use of multiple subcarriers with 32 GBaud in a super-channel.	
Nonlinear compensation (NLC) for propagation effect	NPCC is implementable with 0.5 to 1 dB gain depending on link scenarios	Digital back propagation (DBP) is elegant, but beyond the DSP capability. For various NLC methods, need to quantify the realistic gain in DWDM.	Simplified DBP is actively being researched. Time-varying ISI model based NLC is promising, but also needs to quantify gain vs. circuit complexity.	[9–12]

Table 1. A summary of components required in next generation coherent transmission, including likely performance limitations and strategies for overcoming these limits.

using multiple subcarriers with lower baud rate also has slightly more tolerance to nonlinear propagation compared to the single-carrier approach [1].

It would be impractical to implement super-channels with large numbers of subcarriers using discrete optical components, so large-scale photonic integrated circuits (PICs) formed the foundation of the first commercial super-channel implementations that began shipping in mid-2012. These are 500 Gb/s super-channels, and a key question is whether PIC technology can scale to higher aggregate rates. Figure 5 shows a schematic of a terabit PIC, consisting of 10 channels of 100 Gb/s PM-QPSK. The component transmitter module for this device is also shown in Fig. 5, measuring only a few centimeters across.

Scaling the number of components on a PIC can be taken even further, and the upper right part of Fig. 5 shows a 2.28 Tb/s prototype chip, which integrates 40 channels of 57 Gb/s PM-QPSK.

By delivering a highly parallel implementation for terabit scale data rates, PIC-based super-channels can offload opto-electronics, and more rapid product development is enabled.

SUMMARY

Coherent transmission has delivered an order of magnitude increase in capacity-reach product compared to 10 Gb/s direct detection transmission, and today's coherent technology easily takes us to 100 Gb/s transmission with ultra-long-haul reach. The next steps in DWDM evolution take existing super-channel principles and apply ever more powerful signal processing, in

BENNETT_LAYOUT.qxp_Layout 9/25/14 1:31 PM Page 110

As a system design strategy, multi-carrier super-channels provide an elegant way to spread the processing load without sacrificing optical performance or spectral efficiency, and thus provide an alternative to higher data rate, single wavelength operation.

both the receiver and the transmitter. At the same time, DWDM architecture will evolve toward flexible grid solutions in order to take advantage of more spectrally efficient transmission techniques.

Table 1 summarizes the discussion presented earlier in this article, and for each technology aspect it identifies the coherent function (column 1), the current commercial performance limit of that function (column 2), the performance bottleneck (column 3), and the most promising strategy to overcome these limitations (column 4). Where possible we have provided references, but some of the detailed information is not available in the published literature.

As a system design strategy, multi-carrier super-channels provide an elegant way to spread the processing load without sacrificing optical performance or spectral efficiency, and thus provide an alternative to higher data rate single-wavelength operation.

References

[1] M. Mitchell *et al*, "Optical Integration and Multi-Carrier Solutions for 100G and Beyond," *Optical Fiber Tech.*, vol. 17, 2011, pp. 412–20.
[2] C.R.S. Fludger *et al*, "Digital Signal Processing — From Simulation to Silicon," Tu.5.A.1, ECOC 2010.
[3] G. Bosco *et al.*, "On the Performance of Nyquist-WDM Terabit Superchannels Based on PM-BPSK, PM-QPSK, PM-8QAM or PM-16QAM Subcarriers," *J. Lightwave Tech.*, vol. 29, no. 1, Jan., 2011, pp. 53–61.
[4] R. Schmogrow *et al.*, "Real-Time Nyquist-WDM and OFDM Signal Generation: Spectral Efficiency vs. DSP Complexity," Mo.2.A.4, ECOC 2012.
[5] A. J. Viterbi and A. M. Viterbi, "Nonlinear Estimation of PSK-Modulated Carrier Phase with Application to Burst Digital Transmission," *IEEE Trans. Info. Theory*, vol. 29, no. 4, July 1983, pp. 543–51.
[6] M. Kuschnerov *et al.*, "Data-Aided vs. Blind Single-Carrier Coherent Receivers," OMR5, OFC 2010.
[7] Y. Wu *et al.*, "Free Razor: A Novel Adaptive Voltage Scaling Low Power Technique for Data Path SoC Designs," *IEEE SOCC 2012*, pp. 33–38.
[8] ITU-T Rec. G.694.1, "Spectral Grids for WDM Applications: DWDM Frequency Grid."
[9] E. Ip and J. Kahn, "Fiber Impairment Compensation Using Coherent Detection and Digital Signal Processing," *J. Lightwave Tech.*, 2010, pp. 502–19.
[10] Z. Tao *et al.*, "Multiplier-Free Intrachannel Nonlinearity Compensating Algorithm Operating at Symbol Rate," *J. Lightwave Tech.*, vol. 29, no. 17, Sept. 1, 2011, pp. 2570–76.
[11] L. Li *et al.*, "Nonlinear Polarization Crosstalk Canceller for Dual-Polarization Digital Coherent Receivers," OWE3, OFC 2010.
[12] R. Dar *et al.*, "Time Varying ISI Model for Nonlinear Interference Noise," W2A.62, OFC 2014.
[13] A. Malik *et al.*, "Network Economics of Optical Transport Networks with Soft Decision Forward Error Correction (SD-FEC) Technology," *Photonic Network Commun.*, July 2014.
[14] K. Sugihara *et al.*, "A Spatially-Coupled Type LDPC Code with an NCG of 12 dB for Optical Transmission beyond 100Gb/s," OM2B.4, OFC 2013.
[15] X. Liu and S. Chandrasekhar, "Superchannel for Next Generation Optical Networks," W1H.5, OFC 2014.

Biographies

GEOFF BENNETT received a B.Sc. in polymer engineering from Loughborough University, United Kingdom, in 1983, and worked as a materials research scientist before moving into the networking area in 1986 with router pioneer, Proteon. He has worked in technical roles in the telecommunications industry for over 25 years at companies such as Wellfleet, FORE Systems, and Marconi, where he held the position of Distinguished Engineer. He has been with Infinera for eight years and is a director of solutions and technology, responsible for technology evangelism and technical sales support. He has been the author or co-author of numerous papers, and the author of *Designing TCP/IP Internetworks* (VNR).

KUANG-TSAN WU [M'81, SM'12] received his B.S. and M.A.Sc. degrees from National Taiwan University (NTU), Taipei, in 1975 and 1979, respectively, and his Ph.D. degree from the University of Ottawa, Ontario, Canada, in 1986, all in electrical engineering. He was an instructor at the National Taiwan Institute of Technology and NTU from 1979 to 1982. He was involved in research on satellite modems at Microtel Pacific Research, Burnaby, British Columbia, Canada, during 1986–1987. He moved back to Ottawa in 1987 to join BNR and was the key system designer for the world's first 512-QAM digital radio. From 1994 to 1995, he was with the Wireless R&D Group, CCL/ITRI, Taiwan, developing a digital-enhanced cordless telecommunication system. At Nortel, he was involved in research on GSM and fixed broadband wireless systems, where he later joined the Metro Ethernet Networks Division in 1999 and led the system design of the 40G coherent optical modem in which the receiver ASIC worked without any respin. Since May 2009, he has been with Infinera Canada, Ottawa, where he leads the Ottawa Design Center. He is applying coherent technologies in conjunction with photonic integrated circuits for current and future optical transport systems. He has been granted 33 U.S. patents and one Canadian patent. He is an Infinera Fellow.

ANUJ MALIK is senior manager, product marketing at Infinera. Currently, he is working in the product strategy group at Infinera, and is responsible for market development, network achitecture strategy, and business development. He has an experience of over 14 years in the telecommunications industry focusing on optical transport and ROADM technologies. Prior to Infinera, he held leadership roles in architecture, product management, and development at Ciena and Hughes. He has several publications in reputed journals and conferences, and holds a B.E. in electronics and communications engineering from Delhi College of Engineering (2000).

SOUMYA ROY is senior manager, product marketing at Infinera. Currently, he is responsible for tactical and strategic delivery of competitive content, analysis, and network modeling. His interests are in the field of network design, optimization, and control. Over the last 15 years, he has held leadership roles in research, architecture, and marketing in multiple domains of telecommunications: optical, wireless, routers, and CDNs. He has published over 16 articles in reputed journals and conferences and has a granted patent. He holds a Ph.D. in computer engineering from University of California (UC), Santa Cruz (2003) and a B.Tech. in electrical and electronic communications engineering from the Indian Institute of Technology, Kharagpur (1998). He also teaches networking at UC Santa Cruz-Silicon Valley division.

AHMED AWADALLA received his B.S. degree from the Faculty of Engineering, Ain Shams University, in 2003, and his M.Sc. degree in physics from the University of Waterloo, Ontario, Canada, in 2007. He joined Nortel Networks in 2007 to work in the system design group for coherent optical communication products. His work experience also includes working at BTI on systems model based design for optical amplifiers control. Since December 2011, he has been with Infinera Canada, Ottawa, working on DSP design, modeling/testing of coherent optical communication systems, and product field support. He is currently working part time toward a Ph.D. degree in physics from the University of Waterloo.

A Review on Maximum Power Point Tracking Techniques for Photovoltaic Power Generating Systems

Aseem Sayal
3rd year B.Tech Student
Department of Electrical Engineering
Delhi Technological University
E-mail:aseem.sayal@gmail.com

P.C. Sekhar
Ph.D Scholar
Department of Electrical Engineering
Indian Institute of Technology Delhi
E-mail: psekhar.chandra@gmail.com

Dr. Sukumar Mishra
Associate Professor
Department of Electrical Engineering
Indian Institute of Technology Delhi
E-mail: sukumar@ee.iitd.ac.in

Abstract: The photovoltaic energy is one of the renewable energies that attracts the attention of researchers in the recent decades. The photovoltaic generators exhibit nonlinear I-V and P-V characteristics and maximum power that it can produce varies with solar insolation and temperature. It requires maximum power point tracking (MPPT) control techniques to extract the maximum available power from PV arrays. In this paper, various MPPT algorithms are reviewed and their merits, demerits are discussed.

Keywords: Photovoltaic cell/generator, Maximum Power Point Tracking, Perturb & Observe, Incremental Conductance, Fuzzy Logic Controller.

I. INTRODUCTION

IN recent decades, the continuous growth of energy demand from all around the world has urged the society to seek for alternative energies due to the depletion of conventional energy resources and their undesirable impact on environment. Among the available alternative energies, photovoltaic (PV) energy is one of the most promising renewable energies. PV energy is clean, inexhaustible and free to harvest [1]. However, there are two main drawbacks of PV system, namely the high installation cost and the low conversion efficiency of PV modules which is only in the range of 9-17% [1]. Besides that, PV characteristics are non linear and weather dependent. Fig.1, 2 show the I-V and P-V characteristics of a typical PV module for a series of temperatures and solar irradiance levels [2,3]. It can be seen from the P-V characteristic curve that there is only one operating point at which the power output is maximum, which is named as the maximum power point (MPP), say operating voltage. The MPPT control techniques are essential to extract the maximum available power from PV array in order to maximize the utilization efficiency of a PV array. As such, many MPP tracking (MPPT) methods have been developed and implemented in the literature. The methods vary in complexity, number of sensors required, convergence speed, cost, and range of effectiveness, implementation hardware and in other respects. They range from the almost obvious (but not necessarily ineffective) to the most creative (not necessarily most effective). In this paper, 7 MPPT techniques taken from the literature are discussed and analyzed in terms of their merits and demerits. In addition to this, 3 MPPT techniques are proposed. The proposed methods are more efficient than existing ones. This paper steps through a wide variety of methods with a brief discussion and categorization of each.

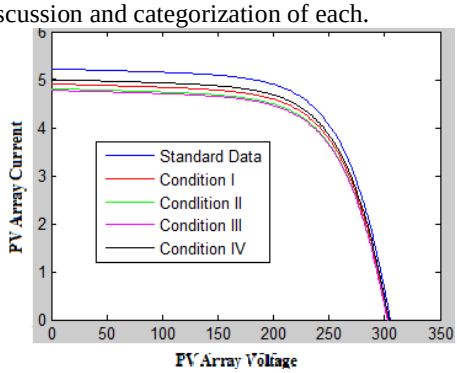


Figure 1: I-V Characteristics

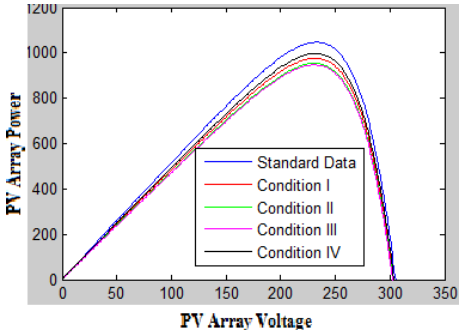


Figure 2: P-V Characteristics

II. MATHEMATICAL MODEL OF PV GENERATOR

The building block of PV arrays is the solar cell, which is basically a p-n junction semiconductor, shown in Fig.3. The V-I characteristics of a solar array is given by (1) [4], which considers the effect of shunt resistance R_{sh}.

$$I = I_{SC} - I_o \left\{ \exp\left[\frac{q(V + R_s I)}{nkT_c} \right] - 1 \right\} - \frac{(V + R_s I)}{R_{sh}} \quad (1)$$

where V and I represent the output voltage and current of the PV array, respectively; R_s and R_{sh} are the series and shunt resistance of the cell; q is the charge of electron; I_{sc} is

the short circuit current; I_o is the reverse saturation current; n is number of cells connected in parallel ; k is the Boltzmann constant and T_c is the temperature in K^0.
The *I-V* and *P-V* curves for five different operating conditions (mentioned in table 3) are shown:

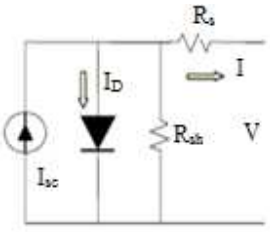


Figure3: Equivalent circuit of PV array.

Thermal voltage for standard temperature *Tc*:[3]

$$V_T = \frac{nkT_c}{q} \tag{2}$$

Open circuit voltage, [2]:

$$V_{OC} = \left\{ \ln\left(1 + \frac{I_{SC}}{I_o}\right) \right\} V_T \tag{3}$$

Temperature dependence of open circuit voltage, [3]:

$$V_{OCT} = V_{OC} + k_v \left(T_x - T_c\right) \tag{4}$$

where k_v is the temperature coefficient of $V_{OC.}$ The value of k_v taken is : -0.16V/^{o}C
The variation of short circuit current with temperature is,[3]:

$$C_{TI} = \frac{I_{SCT}}{I_{SC}} = k_1 \left(T_x - T_c\right) \tag{5}$$

The value of k_I used is:0.0006A/^{o}C.
The variation of reverse saturation current (I_o) with temperature is[2] where A_D is diode ideality factor:

$$I_{oT} = I_o \left(\frac{T_x}{T_c}\right)^3 \exp\left\{ \frac{qE_g}{A_D k} \left(\frac{1}{T_c} - \frac{1}{T_x} \right) \right\} \tag{6}$$

The variation of short circuit current with insolation(S) is,[3]:

$$C_{SI} = \frac{I_{SCG}}{I_{SC}} = \frac{S_x}{S_c} \tag{7}$$

where, S_x is variable insolation and S_c is insolation at reference conditions. The variation of the short circuit current with temperature and insolation is,[3]:

$$I_{SC(TG)} = C_{TI} C_{SI} I_{SC} \tag{8}$$

Using these equations (2-8), substituting in equation (1), different P-V and I-V curves are obtained for different operating conditions.

III.MPPT ALGORITHMS

In this section, various MPPT algorithms are discussed along with their merits and demerits.

A. Perturb and Observe (P&O) Method

The P&O method is the most widely used MPPT technique because of its simple structure and implementation. It involves a perturbation in the operating voltage of the PV array. Fig. 4 shows the flow chart of P&O method. It perturbs the PV array's terminal voltage periodically and then it compares the PV output power with that of the power in the previous cycle of perturbation [5-9].

From Fig.2, it can be seen that incrementing (decrementing) the voltage increases (decreases) the power when operating on the left of the MPP and decreases (increases) the power when on the right of the MPP. Therefore, if there is an increase in power, the subsequent perturbation should be kept in the same direction to reach the MPP and if there is a decrease in power, the perturbation direction should be reversed. Based on Fig. 4, when PV power and PV voltage increase at the same time and vice versa, a perturbation step size, *C* will be added to the operating voltage to generate the next cycle of perturbation in order to force the operating point moving towards the MPP. This process will be carried on continuously until MPP is reached. However, the system will oscillate around the MPP in steady state and this will result in loss of energy. These oscillations can be minimized by reducing the perturbation step size but it slows down the MPP tracking system [10,11].

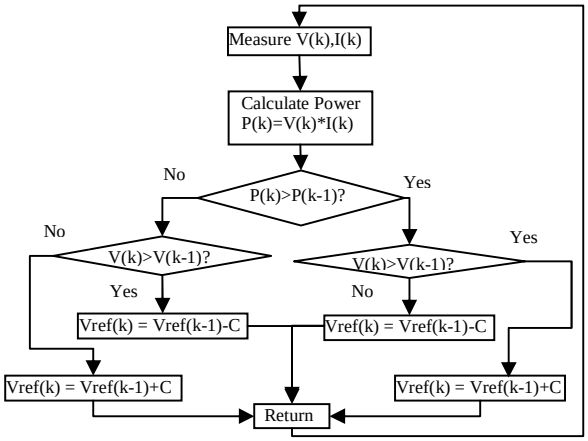


Figure 4: Flow chart of P&O algorithm.

B. Incremental Conductance Method

The incremental conductance method is based on (9) with the derivative of PV output power with respect to the PV voltage.

$$\frac{dP}{dV} = I + V\left(\frac{dI}{dV}\right) = I + V\left(\frac{\Delta I}{\Delta V}\right) \tag{9}$$

$$\frac{\Delta I}{\Delta V} = -\frac{I}{V} \quad \left(\frac{dP}{dV} = 0\right) \text{ at MPP} \tag{10}$$

$$\frac{\Delta I}{\Delta V} > -\frac{I}{V} \quad \left(\frac{dP}{dV} > 0\right) \text{ left side of MPP} \tag{11}$$

$$\frac{\Delta I}{\Delta V} < -\frac{I}{V} \quad \left(\frac{dP}{dV} < 0\right) \text{ right side of MPP} \qquad (12)$$

The MPP is tracked by comparing the instantaneous conductance (*I/V*) to the incremental conductance (*ΔI/ΔV*). Based on the flow chart in Fig.5, *V(k)* and *I(k)* are the PV array output voltage and current at time *k*. When the PV output voltage is constant but the output current increases, the perturbation should be kept in the same direction. If the current decreases with the constant voltage, the perturbation direction is reversed. The function of the algorithm is to search a suitable value of perturb at which the incremental conductance equals to instantaneous conductance so that the PV system always operates at the MPP.

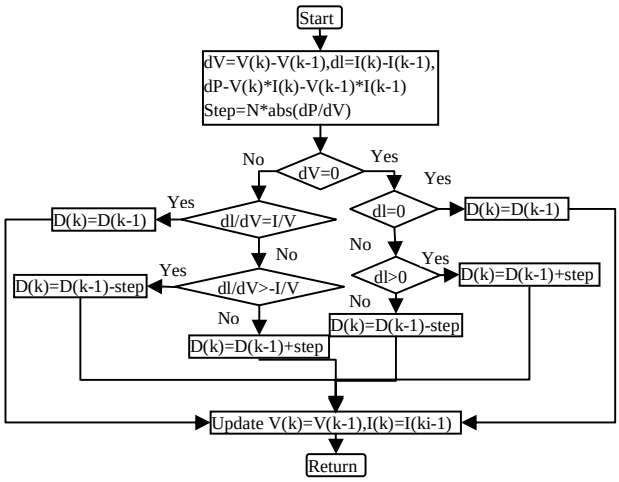


Figure 5: Flow chart of INCond. algorithm

The incremental size, *ΔD*, determines how fast the MPP is being tracked. Fast tracking can be reached by greater incremental size, but it will make the system oscillates about its MPP. The main advantage of INCond method is that it can produce good results under rapidly changing environment. INCond. algorithm is able to achieve lower oscillation around MPP than P&O method. However, high cost, large amount of power loss and more computational load due to complex calculations are main demerits of this method.

C. Three Weighted Comparison Method

The P&O algorithm compares only two points, which are the current operation point and the subsequent perturbation point, to observe their changes in power and accordingly increase or decrease the solar array voltage. The P&O algorithm oscillates around the MPP, resulting in a loss of PV power. In case of rapidly changing solar radiation, P&O algorithm fails in tracking MPP correctly [7,9]. Therefore, the three point weight comparison method is proposed to avoid having to move rapidly the operation point, when the solar radiation is varying quickly or when a disturbance or data reading error occur. Restated, the MPPT can be traced accurately when the solar radiation is stable and power loss is low. Fig.6 presents a flow chart of the three-point weight comparison algorithm. In this flowchart, *M* is a variable.

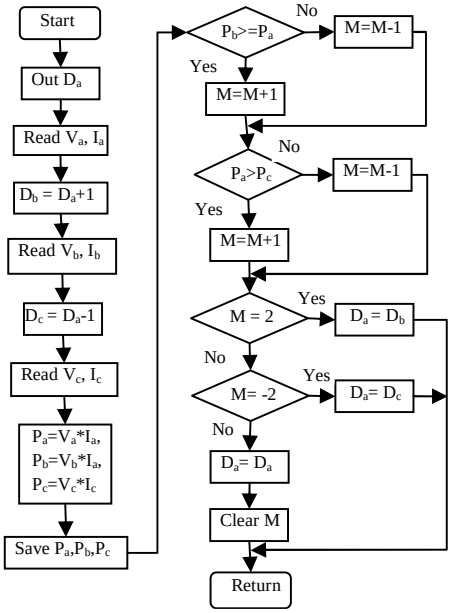


Figure 6: Flowchart of three-point weight comparison method

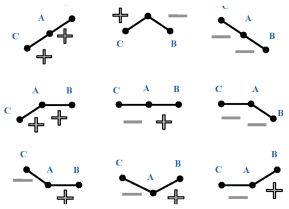


Figure 7: Possible states of the three perturbation points.

The algorithm of the three-point weight comparison is run periodically by perturbing the PV array terminal voltage and comparing its output power on three points of the P-V curve. The three points are the current operation point (A), a point, B, perturbed from point A, and a point, C, with doubly perturbed in the opposite direction from point B. Fig.7 depicts the nine possible cases. In these cases, for the point A and B, if the power of point B is greater than or equal to that of point A, the status is assigned a positive weighting. Otherwise, the status is assigned a negative weighting. And, for the point A and C, when the power of point C is smaller than that of point A, the status is assigned a positive weighting. Otherwise, the status is assigned a negative weighting. Of the three measured points, if two are positively weighted, the perturb direction should be kept same. On the contrary, when two are negatively weighted, the perturb direction should be reversed. In the other cases with one positive and one negative weighting, the MPP is reached and the voltage is not to be changed.

D. Open-Circuit Voltage & Modified Open-Circuit Voltage Method (Proposed)

This is a method based on the linear relationship between

output voltage of the PV array at the MPP, V_{MPP} and the PV array's open circuit voltage, V_{OC} as in (13) under varying temperature and solar irradiance [8,9].

$$V_{MPP} \approx k1 * V_{OC} \quad (13)$$

Constant value of *k1* is dependent on the characteristics of PV array. Generally, it has to be computed empirically in order to determine the V_{MPP} and V_{OC} for varied temperatures and solar irradiances. The value of *k1* ranges from 0.73 to 0.80 for polycrystalline PV module over a temperature range of 0 to 60° C and solar irradiance range of 200 to 1000W/m2 [8,9].In the open circuit voltage method, V_{OC} is measured periodically by shutting down the power converter momentarily. The MPPT calculates V_{MPP} from the pre-set value of *k1* and the calculated value of V_{OC}. Then, the array's voltage is set at V_{MPP} by choosing suitable value of *k1*[13]. The shutdown of power converter periodically will incur temporary loss of power which results in power extracted will not be the maxima. Since (13) is an approximation, the PV array will not operate at the MPP. Even though this technique is very easy and cost effective for implementation, yet the constant value of *k1* is not valid for all operating conditions. [8,11]

To overcome the above limitations, modified open circuit voltage method is proposed. In this method, the PV array is not temporarily isolated from MPPT, the open circuit voltage, V_{OC} is calculated for different values of insolation and temperature by making use of (14-16).

$$C_{TV} = \left(\frac{V_{OCT}}{V_{OC}}\right) = 1 + \left(\frac{k_v}{V_{OC}}\right)\left(T_x - T_c\right) \quad (14)$$

where k_v is the temperature coefficient of $V_{OC.}$ The value of k_v taken is : -0.16V/°C

$$C_{SV} = 1 + \beta\alpha_s\left(S_x - S_c\right) \quad (15)$$

where $\alpha_s = \frac{dT_c}{S_x - S_c}$, dT_C is temperature change due to change in irradiation. The values of β_T and α_S taken are 0.0042 and 0.0061 respectively. So overall effect of temperature and insolation on open circuit voltage is:

$$V_{OC(TG)} = C_{TV} C_{SV} V_{OC} \quad (16)$$

There is no shutdown of power converter periodically, hence will not incur any temporary loss of power.

E. Short-Circuit Current Modified Short-Circuit Current Method (Proposed)

This method is quite similar to the open circuit voltage method. It is based on the linear relationship between PV array output current at MPP, I_{MPP} and PV array short-circuit current, I_{SC} as shown (17) [12,13].

$$I_{MPP} \approx k2 * I_{SC} \quad (17)$$

where *k2* is a proportionality constant. The constant value of *k2* also depends on characteristics of PV array. Generally, it ranges from 0.78 to 0.92 for polycrystalline PV modules under the same conditions like the one mentioned previously [12,13]. After *k2* is obtained, the PV system remains with the approximation in (17), until the next calculation of *k2*. The procedure of short-circuit current method is the same as that of open-circuit voltage method. An additional switch is added to the power converter and it is switched on momentarily to measure the short-circuit current, I_{SC} by using a current sensor, then the MPP current is calculated [13]. The output current of PV array is adjusted until the MPP current is reached. This process is repeated periodically. Like open-circuit voltage method, the PV array will not be operated at MPP since (17) is an approximation.

To overcome the above limitations, modified short circuit method is proposed. The short circuit current varies due to temperature and insolation both. The combined effect is taken into account to calculate short circuit current for different conditions of temperature and insolation by using (17-19).

The variation of short circuit current with temperature is,[3]:

$$C_{TI} = \frac{I_{SCT}}{I_{SC}} = k_I\left(T_x - T_c\right) \quad (18)$$

where value of k_I is 0.0006A/°C.

The variation of short circuit current with insolation(*S*) is, [3]:

$$C_{SI} = \frac{I_{SCG}}{I_{SC}} = \frac{S_X}{S_C} \quad (19)$$

where S_x is variable insolation and S_c is insolation at reference conditions

The variation of short circuit current with temperature and insolation is,[3]:

$$I_{SC(TG)} = C_{TI} C_{SI} I_{SC} \quad (20)$$

The output current of PV array is set at I_{MPP} by choosing suitable value of k_2. This process is repeated periodically. There is no shutdown of power converter periodically, hence will not incur any temporary loss of power. But MPP is never reached since (17) is an approximation, hence the output power produced will not be the maximum for all operating conditions.

F. PI-P&O Method (Adaptive Perturb)

The main idea behind this technique is that at the start of any hill climbing technique, large perturb steps are needed to quickly reach the maximum power point and as the maximum power point is approached, the perturb value needs to be decreased to avoid large oscillations around this maximum output power operating point. The P&O techniques are not capable of achieving this target if the perturb value is fixed [13-17]. Therefore adaptive techniques are better solutions. The adaptive technique utilizes the error between two successive array power signals calculated from the measured array voltage and current signals to create an adaptive perturb. Basically, when the operating point is far away from MPP, this error is large and decreases as the maximum power operating

point is approached and in steady state. Therefore, this error can be treated like an error signal in a closed loop system that needs to be minimized at steady state, prevented from overshoot at startup, and free from steady state oscillations. The simplest clue to achieve all these targets is to process this error signal using a conventional PI controller, therefore named as PI-P&O technique. This PI controller is utilized as the adaptive perturb value generator for the reference array voltage. Another PI controller is used to force the PV array output voltage to track the reference voltage. The system requires two signals to be measured, PV array voltage and current. Therefore, by tuning both PI controllers, good performance is achieved with less computational load and no pre-defined constants.

G. Adaptive Perturb with Sampling Method (Proposed) Method)

The main idea behind the proposed technique is same as that of PI-PPO technique. The proposed adaptive technique utilizes the error between array power signal and next sampled signal calculated from the measured array voltage and current signals to create an adaptive perturb. Therefore, this error can be treated like an error signal in a closed loop system that needs to be minimized at steady state, prevented from overshoot at startup, and free from steady state oscillations.

The advantages of this proposed method over the PI-PPO method is that it is more efficient than PI-PPO method, there are less oscillations about MPPT and MPP is tracked quickly. But there are drawbacks of this method also. The first drawback is that it requires additional memory to store array power of next sampled signal. The second drawback is that the perturb step depends on power difference of the present and next sampled signal which further depends on fixed perturb given to system. If value of fixed perturb is more, then results may not be so accurate.

H. Fuzzy Logic Controller (FLC)

Fuzzy Logic controller (FLC) works with imprecise inputs, it does not need an accurate mathematical model and it can handle nonlinearity as well. It relies on the human knowledge and experience rather than the technical understanding of the system. FLC constitutes four parts, which include fuzzification, inference, rule base and defuzzification as shown in Fig.8 [17-18].

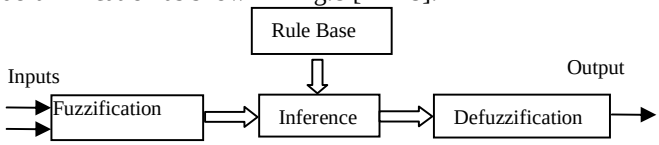


Figure 8: Block diagram of fuzzy logic controller.

In this study, the inputs of FLC are error, E and change in error, CE at sample time *k*, while the output of FLC is the output voltage(*V*).

$$E(k)=\frac{P(k)-P(k-1)}{V(k)-V(k-1)} \quad (21)$$

$$CE(k)=E(k)-E(k-1) \quad (22)$$

During fuzzification, the numerical input variables are converted into linguistic variables based on the membership functions as shown in Fig.9,10 [19]. Five fuzzy levels are used for all the inputs and outputs variables: NB (negative big), NS (negative small), ZE (zero), PS (positive small), and PB (positive big).

Once *E* and *CE* are calculated, they are converted into linguistic variables and then the output is generated by after defuzzification. Rule base consisting of 25 rules is considered in this paper, as shown in Table I. Usually, weights are added to the rules to improve reasoning accuracy and to reduce undesirable consequent. The most commonly used Mamdani's inference method is used to determine the output of fuzzy logic controller [20, 21]. The centroid method is used as defuzzification method because of its good averaging properties .

Table 1: A Fuzzy Rule Base Table for MPPT

CE(k) / E(k)	NB	NS	ZE	PS	PB
NB	PB	PB	PS	PS	PS
NS	ZE	ZE	PS	PS	PS
ZE	NS	NS	ZE	PS	PS
PS	NS	NS	NS	ZE	ZE
PB	NB	NB	NS	NS	NS

FLC exhibits a better behavior than P&O method, which provides faster tracking of MPP and it presents smoother signal with less fluctuation in steady-state. It achieves very fast transient response and reduces the oscillations around MPP in steady state.

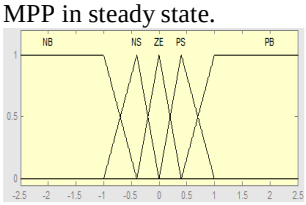


Figure9: Membership function of E(n) &CE(n)

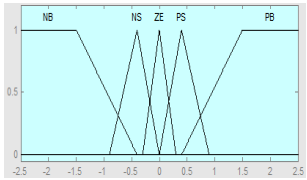


Figure10: Membership function of V(n)

IV. SIMULATION RESULTS

The results of different MPPT algoritms are compared by programming in MATLAB environment. They showed that the tracker is able to maintain the operating point of the photovoltaic module at the maximum power point thereby improving the amount of energy successfully extracted from the module.The Standard Test Condition Data is mentioned in Table 2.

Table 2: Standard Test Condition Data.

Electrical Parameters	**Value**
Series Resistance (R_S)	1Ω
Shunt Resistance (R_{SH})	100 Ω
Short Circuit Current (I_{sc})	5.23 A

Reverse Saturation Current (I_o)	0.0002A
No. of cells in parallel (n)	72
No. of cells in series (n_c)	16
Temperature Coefficient of Voc (k_v)	-.16V/^oC
Band Gap Energy (E_g)	1.1 eV
Ideality factor of Diode (B)	1.0
Reference Temperature (T_c)	28^oC
Reference Insolation (S_c)	693W/m^2

The Variable operating Conditions Data is mentioned in Table 3. Various MPPT algorithms are compared at standard test conditions on the basis of oscillations at MPP, maximum power extracted and tracking time. Table 5 shows this comparison.

Table 3: Variable Conditions Data

Condition	**Temperature**	**Insolation**
Condition I	26.6^o C	652 W/m^2
Condition II	25.7^o C	639 W/m^2
Condition III	25.2^o C	635 W/m^2
Condition IV	27.0^o C	664 W/m^2

Table 4: Comparison of various MPPT Algorithms

Method	Voltage Ripples around MPP	Maximum Power Output P_m	Tracking Time
P&O	0.2V	1046.9 W	More
IncCond.	0.2V	1046.9 W	More
PI-PPO	0.02V	1049.2 W	Less
Adaptive Perturb & Sampling	0.004 V	1048.3 W	Very Less
FLC	0.3V	1049.2 W	Less

In conventional methods like P&O, IncCond, Three Weight Comparison, Open Circuit and Short Circuit methods, the perturb step is set as 0.1V. In PI-PPO method, value of perturb when operating point is far away from MPP is about 1.4 V and decreases to 0.01V at steady state. In FLC, voltage ripples of about 0.3 V around MPP in steady state.

V. CONCLUSION

The purpose of the MPPT is to adjust the solar operating voltage close to the MPP under changing atmospheric conditions. In this paper, mathematical model is proposed to simulate the PV array in the in Matlab environment for evaluation of the algorithms performances under randomly varying atmospheric conditions. Total 7 MPPT techniques taken from the literature are discussed and analyzed with their merits and demerits. Also, 3 new techniques are proposed. The proposed methods are more efficient than existing ones and have been verified from smulation results. Conventional methods like P&O, IncCond., three weight comparison,open circuit voltage and short circuit current methods are easy to implement but they suffer from oscillations at MPP and tracking speed is less due to fixed perturb step. Intelligent methods like PI-PPO, Adaptive Perturb with Sampling and FLC are efficient, oscillations are lesser at MPP in steady state and tracked quickly in comparison to conventional methods.

VI. ACKNOWLEDGEMENT

This work was supported by Indian Institute of Technology under Summer Research Fellowship Programme 2011.

REFERENCES

[1] Roberto Faranda, S.L., Energy Comparison of MPPT Techniques for PV Systems. WSEAS Trans. On POWER SYSTEMS, vol. 3, No.6.

[2] S. Yuvarajan, Juline Shoeb, A Fast and Accurate Maximum Power Point Tracker for PV Systems, Applied Power Electronics Conference, 2008.

[3] Krisztina Leban, Ewen RitchieAalborg, Selecting the Accurate Solar Panel Simulation Model, Nordic Workshop on Power and Industrial Electronics, 2008.

[4] Wang NianCHun,Wu MeiYue, China,SHi GuoSHeng, Study on characteristics of photovoltaic cells based on MATLAB simulation, Power and Energy Engineering Conference (APPEEC) Asia-Pacific,2011 .

[5] A.Yafaoui., B.Wu, R.Cheung, Implementation Of Maximum Power Point Tracking Algorithm For Residential Photovoltaic Systems, 2nd Canadian Solar Buildings Conference Calgary, 2007

[6] A. Durgadevi,S. Arulselvi and S.P.Natarajan, Study and Implementation of Maximum Power Point Tracking (MPPT) Algorithm for Photovoltaic Systems, Electrical Energy Systems (ICEES),1st International Conference,2011.

[7] Mei Shan Ngan, Chee Wei Tan ,A Study of Maximum Power Point Tracking Algorithms for Stand-alone Photovoltaic Systems, IEEE Applied Power Electronics Colloquium (IAPEC), 2011

[8] Koutroulis, E., Kalaitzakis, K. and Voulgaris, N. C.,"Development of a Microcontroller-Based Photovoltaic Maximum Power Point Tracking Control System," IEEE Transactions on Power Electronics, Vol. 16, pp. 46_54 ,2001.

[9] Ying-Tung Hsiao, China-Hong Chen, Maximum Power Tracking for Photovoltaic Power System, Industry Applications Conference, 2002

[10] Joe-Air Jiang, Tsong-Liang Huang, Ying-Tung Hsiao, Chia-Hong Chen, Maximum Power Tracking for Photovoltaic Power Systems, Tamkang Journal of Science and Engineering, Vol. 8, No 2, pp. 147_153 ,2005

[11] Ahmed K. Abdelsalam, Ahmed M. Massoud, Shehab Ahmed, Prasad Enjeti, High Performance Adaptive Perturb and Observe MPPT Technique for Photovoltaic Based Microgrids,Power Electronics,IEEE Transactions,vol.26, 2011.

[12] Trishan Esram, J.W.K., Philip T. Krein, Patrick L. Chapman, and Pallab Midya., Dynamic Maximum Power Point Tracking of Photovoltaic Arrays Using Ripple Correlation Control. IEEE Trans. on Power Electronics,Vol.21,No.5, 2006.

[13] Kalantari, A., et al., A Faster Maximum Power Point Tracker Using Peak Current Control, IEEE Symposium on Industrial Electronics and Applications, 2009.

[14] N. Femia, D. Granozio, G. Petrone, G. Spagnuolo, M. Vitelli, Predictive & Adaptive MPPT Perturb and Observe Method, IEEE Transactions on Aerospace and Electronic systems vol. 43, no.3, 2007.

[15] Weidong Xiao, William G. Dunford, A Modified Adaptive Hill Climbing MPPT Method for Photovoltaic Power Systems, 35th Annual IEEE Power Electronics Specialists Conference Aachen, Germany,2004.

[16] M.S. Aït Cheikh, C.L., G.F. Tchoketch Kebir and A. Zerguerras, Maximum power point tracking using a fuzzy logic control scheme, Revue des Energies, Renouvelables, Vol. 10, No.3, p.p. 387 – 395, 2007.

[17] Chih-Chiang Hua and Jong-Rong Lin, Fully Digital Control of Distributed Photovoltaic Power Systems, ISIE 2001.

[18] F.Bouchafaa, D.B., M.S.Boucherit, Modeling and Simulation of A Gird Connected PV Generation System With MPPT Fuzzy Logic Control,7th International Multi-Conference on Systems, Signals and Devices, 2010.

[19] Subiyanto, A.M., M A Hannan, Maximum Power Point Tracking in Grid Connected PV System Using A Novel Fuzzy Logic Controller, IEEE Student Conference on Research and Development, 2009.

[20] Neil S. D'Souza, L.A.C.L.a.X.L., An Intelligent Maximum Power Point Tracker Using Peak Current Control, Power Electronics Specialist Conference, 2005, IEEE.

[21] Chian-Song Chiu, Ya-Lun Ouyang, Robust Maximum Power Tracking Control of Uncertain Photovoltaic Systems: A Unified T-S Fuzzy Model-Based Approach, IEEE Transactions on Control Systems technology, vol 19

Wireless Pers Commun
DOI 10.1007/s11277-014-2115-2

A Secure and Efficient Authentication Protocol in Wireless Sensor Network

Kakali Chatterjee · Asok De · Daya Gupta

© Springer Science+Business Media New York 2014

Abstract With increasing popularity of wireless sensor networks (WSN), the security issues related to such networks have become crucial. Most of the networks use shared key among all the nodes to make communicational overhead minimal. But it is vulnerable to many attacks like replay attack, node-compromise attack, impersonation attack etc. Further many traditional security mechanisms cannot be suitably implemented in WSN as resources are constrained in terms of power, energy and speed. In this paper, we propose a mutual authentication protocol based on timestamp in WSN which generates a new session key for each session. The proposed authentication approach requires light computational and communicational load and resist the major vulnerable attacks in WSN.

Keywords Mutual authentication · Wireless sensor networks (WSN) · Elliptic curve Diffie–Hellman (ECDH) · Timestamp

1 Introduction

As wireless sensor networks (WSN) are now extensively used to transmit critical data relating to area monitoring (e.g. military), infrastructure monitoring (e.g. airport) etc, the security mechanisms are essential to ensure integrity, confidentiality and authenticity of the data. These networks consist of many tiny and smart devices, referred to as nodes, which typically combine an 8-bit processor with memory (program + data) between 128 and 1,024 KB RAM. The data gathered by these sensor nodes relay to a central server which processes the data according to the application. Implementation of suitable authentication protocol in this environment is challenging as these devices are constrained in terms of memory, computing

K. Chatterjee (✉) · A. De
National Institute of Technology, Patna, India
e-mail: kakali2008@gmail.com

D. Gupta
Computer Engineering Department, Delhi Technological University, Delhi, India

Published online: 21 October 2014

power and energy supply. Thus we identify two major issues in this area is key management and access control.

Key management plays an important role in WSN as the data collected by sensor nodes need to be encrypted before transmitting to neighbouring nodes and base stations for further processing. While considering the different security threats involved in such wireless sensor networks, different key management schemes are proposed in [1–3]. In general these approaches either need pre-distributed keys which means a higher configuration effort before deployment or they produce much traffic which results in higher energy consumption [4]. Further most of the secure protocols in sensor networks, such as secure routing, secure key agreement [6,7,10] and secure group communication protocols [8,9] etc. assume that all nodes must have pre-shared a secret or pre-obtained public-key certificates before joining the network [5]. However, this assumption has a practical weakness for some emergency applications as the nodes without pre-obtained certificates will not be able to join the network.

Access control is an old problem which has not received much attention in the context of WSNs. If the data collected within a sensor network is valuable or should be kept confidential then we need to control the access to this data in convenient ways. For access control, we focus on user authentication, a central problem when trying to build access control mechanisms for sensor networks. Considering the different attacks many researchers proposed different user authentication scheme in wireless sensor network. Benenson et al. [11] proposed an user authentication protocol in the presence of node capture attacks. Wong et al. [12] pointed out some major weaknesses on Benenson et al. scheme such as impersonation attack, denial-of-service (DoS) attacks could be mounted by sending many false signatures in authentication phase and proposed a dynamic user authentication scheme based on password. This scheme imposes on very light computational cost but vulnerable to many attacks such as replay attacks, forgery attacks, stolen-verifier attacks and password guessing attacks.

Tseng et al. [13] removed the weaknesses of Wong et al. scheme and proposed an improved dynamic user authentication scheme to improve security features with better efficiency such as resistance to replay attack, forgery attack, reduction of user password leakage risk etc. In addition, it also allowed users to change their password freely whenever demanded.

Ko [14] pointed out some weaknesses of Tseng et al. scheme that might cause user authentication mechanism insecure and proposed a novel dynamic user authentication scheme for WSN, which provides better security features than Tseng et al.'s scheme.

Lee [15] proposed a simple dynamic user authentication scheme for WSN, which is the variant of strong password-based solution. The scheme is more simplified in term of authentication process by reducing the computational load, communication cost and further an intruder cannot impersonate the gateway node.

Das [16] mentioned some security flaw in Wong et al. such as the scheme vulnerable to many logged in user with the same login-id threat and also susceptible to stolen-verifier attacks. Das proposed a two-factor user authentication for WSNs, where the legitimate users must prove the possession of both a password and smart card.

Nyang and Lee [17] identified that Das's scheme is still vulnerable and proposed a enhanced two factor user authentication protocol for WSNs, which overcome the security flaws with some additional security services such as, confidentiality and authenticity of user's query response. Subsequently Kumar et al. [18] also proposed an efficient two-factor user authentication framework for WSN.

Recently Yeh et al. [19] proposed a user authentication protocol using the elliptic curve cryptography (ECC). This protocol has certain weakness like no mutual authentication between the user & the sensor node and no perfect forward secrecy.

Keeping in view of these two major issues as described above, we propose an authentication scheme based on ECC which imposes access control (user authentication) and solve key management problem. Our scheme also resists the major vulnerable attacks in wireless sensor networks such as man-in-the-middle attack, dictionary attack, impersonation attack, stolen-verifier attack, node-compromise attack, perfect forward secrecy, replay attack as detailed in security analysis section.

Our proposed scheme based on Elliptic Curve Diffie–Hellman (ECDH) in wireless sensor network which gives authentication and confidentiality and includes the following aspects:

- Our proposed scheme efficiently covers two major issues like key management and access control in WSN.
- Due to the lack of a prior knowledge of post-deployment configuration as topology can change after deployment, secure communication is not possible in sensor networks. Thus we divide the authentication process in four different phases. After registration to the BS, node validity is checked by the cluster heads (CH) in login phase. In mutual authentication phase two nodes will mutually authenticate themselves and in key generation phase they will generate the secret key.
- Any registered node in the same cluster can authenticate each other to exchange information in a secure way. Registered nodes of different clusters can also communicate using this process after getting valid login by CH.
- Authentication approach imposes very light computational load as it requires simple operations such as one-way hash function and exclusive-OR operations.
- Secret key is generated independently by two nodes and is not transmitted.
- New session key is established for each particular session to protect data which resists replay attack in wireless network.
- It requires low communicational load as message is transmitted using symmetric encryption process to save energy and storage (which is critical for constrained devices).

The rest of the Paper is organized as follows:

Section 2 presents Background, Sect. 3 provides Elliptic Curve Cryptosystem, Sect. 4 provides Proposed Mutual Authentication Protocol; Sect. 5 discusses Security Analysis; Sect. 6 presents Performance Analysis; Finally, we conclude the paper in Sect. 7.

2 Background

In this section we will discuss challenges, classification and common threats in wireless sensor networks.

2.1 Security Challenges in WSN

Wireless network is broadly categorized in two classes: wireless ad hoc networks and cellular networks. Cellular network requires fixed infrastructure to support communication between mobile devices whereas wireless ad hoc networks do not requires fixed infrastructure. Wireless sensor network is a special type of wireless ad hoc network where the network topology may be static or dynamic. A typical sensor node is a small, inexpensive device where resources such as computational power, communication capability and storage space are very limited [10]. The following issues make secure communication between sensor networks different from traditional networks:

- Life-time of sensor nodes is limited as each sensor node is battery-powered. Once the deployed sensor nodes expire, it is necessary to deploy some fresh nodes for continuing the data collection operation.
- Public key cryptosystems is partially impractical as it has more complex mathematical operations which require more storage and processing speed.
- Nodes are vulnerable to physical capture as a part of the network may be captured by the adversary. The resilience measurement against node capture is computed by comparing the number of nodes captured, with the fraction of total network communications that are exposed to the adversary not including the communications in which the compromised nodes are directly involved.
- There is lack of a prior knowledge of post-deployment configuration as topology can change after deployment because of irregularities in the sensor field like obstacles or due to jamming, noise, etc., or due to the mobile sensor nodes in the network.
- Computation power is limited. Each sensor node contains a primitive processor featuring very low computing speed and only small amount of programmable memory.
- Bandwidth and transmission power are limited. Sensor nodes have ability to communicate each other and the base stations by the short range wireless radio transmission at low bandwidth and over small communication ranges.
- Sensor nodes may be mobile or static. If sensor nodes are mobile, they can change the network configuration at any time.

2.2 Network Classification

According to different application scenarios such as habitat and environment monitoring, surveillance, smart homes and offices, industrial process control etc. sensor networks are classified in two categories as discussed below:

High/Low Density Static Sensor Network This type of sensor networks has a large number of low cost nodes scattered around the target area with a high node density per unit area [5]. In habitat and environment monitoring applications required large no of nodes, but the nodes in such networks are normally static. In smart home applications small number of nodes is required. In most cases of indoor applications, sensor nodes are static.

High/Low Density Dynamic Sensor Network This type of sensor networks has a large number of low cost nodes moving around the target area with a high node density per unit area [5]. For example in ocean monitoring applications, sensor nodes can be moved from one place to another. Low density dynamic network is found in large offices with a sensor identity card on every person.

Broadly speaking, a WSN may have a flat or a hierarchical architecture.

In *flat WSNs* [10], all nodes play similar roles in sensing, data processing, and routing. In particular, to lower energy consumption, nodes operate with limited radio transmission range, and are unable to communicate with everyone in the network directly. Communication node-to-BS is thus multi-hop, with ordinary nodes working as routers for each other.

In *hierarchical WSNs* [10], on the other hand, the network is typically organized into clusters, with ordinary cluster members and the CHs playing different roles. While ordinary cluster members are responsible for sensing, the CHs are responsible for additional tasks such as collecting and processing the sensing data from their cluster members, and forwarding the results towards the BS.

2.3 Threats in WSN

An attacker can launch different types of attack on multiple layers of the sensor network protocol stack. Most popular attacks [5] in a sensor network are discussed below:

Jamming Attack This is a type of Denial of Service (DoS) attack occurs in the physical layer. This type of attack is carried out with the help of outsider node. Interference with the radio frequencies a network's nodes are using disrupts the communication channel between the communicating sensor nodes.

Node Tampering In this attack, an adversary gets hold of a sensor node physically and gains access to all data, information and important cryptographic material. It can be used to listen to communication, intercept, modify and fabricate messages.

Selective Forwarding In this type of attack, malicious nodes refuse to forward certain messages and simply drop data packets to disrupt network operations. This type of attack occurs in the network layer.

Sinkhole Attack This attack is similar to selective forwarding except that it is not passive attack. In this case, the adversary attracts the surrounding nodes with unfaithful routing information.

Sybil Attack In this case, a single node presents multiple identities to other nodes either by creating them or by stealing the identities of other nodes.

Wormhole Attack In this case, two distant malicious nodes are used to create a wormhole in the target sensor network. Both malicious nodes have an out of band communication channel.

HELLO Flood Attack An attacker broadcasts information with enough transmission power convincing every node in the network that he is his neighbor. Also, other sensor nodes lose their energy in replying to the hello packet.

Flooding Attack This type of attack occurs in the transport layer. In this case, the adversary sends many connection establishment requests to the victim (memory and resource exhaustion).

3 Elliptic Curve Cryptosystems

Elliptic curve cryptosystems are widely found in literature [20–27]. For implementing ECC, the hierarchical structure for operations is as follows:

In the highest level different protocols such as ECDH/ECDSA are used based on curve arithmetic. Scalar Multiplication (i.e. addition and doubling) is at the next lower level. It is based on the choice of curves and coordinates. The lowest level is based on finite field arithmetic to perform field operations such as addition, subtraction, multiplication and inversion. In this section we discuss the authentication schemes of ECC.

3.1 ECC Authentication Schemes

ECC based authenticated key agreement protocol in wireless media are discussed in [28,29]. We proposed a secure access of smart cards using ECC in [30,31]. Three-Pass Authenticated Key Agreement Protocol based on elliptic curves is found in [32].

In our ECC based scheme, ECDH is used for the shared secret key generation and ECDSA is used for entity authentications respectively. ECDH protocol establishes a shared key between two parties. The original Diffie–Hellman algorithm is based on the multiplicative group modulo p, while the ECDH protocol is based on the additive elliptic curve group.

- *Elliptic Curve Diffie–Hellman (ECDH) protocol*

Party A (trusted party) chooses ECC system parameters over F_q is given below:
$(\mathbb{F}, C, G, p, q, n)$ where

q prime power, that is $q = p$ or $q = 2^m$, where p is a prime and m is a positive integer.
$\mathbb{F}$ field representation for representing field elements $\in F_q$
C The elliptic curve containing the value of a, b
G A base point represented on E (F_q)
n Order of point G

After publishing system parameters A selects an integer n_A less than n. This is A's private key. The secret key generation is explained by the following steps:

1. A then generates a public key $P_A = n_A \times G$.
2. A sends public key to B.
3. B similarly selects a private key n_B and computes a public key P_B
4. B sends public key to A.
5. Now A generates the secret key $K = n_A \times P_B$.
6. Party B generates the secret key $K = n_B \times P_A$

The two calculations in this step will produce the same result because $n_A \times P_B = n_A \times (n_B \times G) = n_B \times (n_A \times G) = n_B \times P_A$

- *Elliptic Curve Digital Signature Algorithm (ECDSA)*

Party A, with system parameters $(\mathbb{F}, C, G, p, q, n)$, public key P_A and private key n_A, does the following steps to sign the message m

ECDSA Signature Generation User A signs the message m using these steps:

1. Select a random integer $k \in [2, n-2]$.
2. Compute $k \times P = (x_1, y_1)$ and $r = x_1 \bmod n$.
3. Compute $k^{-1} \bmod n$.
4. Compute $s = k^{-1}(H(m) + dr) \bmod n$.

Here H is secure hash algorithm.
The signature for the message m is the pair of integers (r, s).
To verify A's signature, B does the following steps:

5. Compute $c = s^{-1} \bmod n$ and H (m).
6. Compute $u_1 = H(m)c \bmod n$ and
7. $u_2 = rc \bmod n$.
8. Compute $u_1 \times P + u_2 \times Q = (x_0, y_0)$ and $v = x_0 \bmod n$
9. Accept the signature if $v = r$.

4 Proposed Authentication Protocol

In this section we propose an authentication protocol based on elliptic curves.

4.1 System Network Model

Suppose in a hierarchical wireless sensor network (HWSN), there is L no. of nodes which are divided into M no. of clusters. There are l no. of nodes in each cluster which consists of

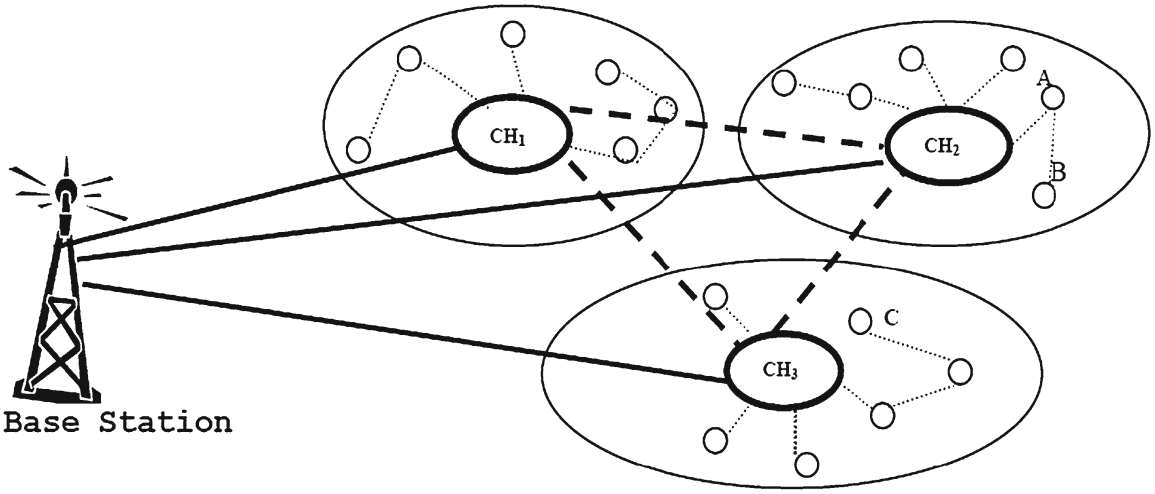


Fig. 1 System model of HWSN. *Dotted line* Communication between nodes in a cluster, *dashed line* Communication between CH, *solid line* Communication between BS and CH

Cluster Head (CH) node and member nodes. We assume that after deployment of the sensor nodes, they become static. Sensor nodes form a cluster, can communicate with each other in that cluster and also can communicate with CH. This CH can communicate with each other directly and relay data between its cluster members and the Base Station (BS). A BS is typically a gateway to another network.

A system model of HWSN is shown in Fig. 1.

Description In our model large no of low cost sensor nodes are scattered around the target area with a high node density per unit area. After deployment of the sensor nodes, they become static. After deployment, nodes do not move but can become unavailable (by energy exhaustion or any other reason). After deployment, each node is preloaded with two keys: a master key to communicate with cluster head and a key that it shares with the BS only. BS also load a one-way keyed hash function F to all node. For mutual authentication nodes also maintain a list for pair wise secret key. The security of the secret key is based on elliptic curve discrete logarithm problem. This secret key will not transferred through the network. It only compromised by node tampering. We assume that an intruder will succeed only after a time t, and the network can be considered secure for t units of time after deployment. After each session, all the keys are regularly updated and maintained in a table.

To protect the anonymity of sensor nodes in a sensor network, our model used to store the hashed value of ID and PIN in the sensor node [33]. We use a one-way keyed hash function for producing a sequence of hash values of ID of the node. This keyed hash function that can change IDs such that an adversary cannot link with the input and output values of keyed hash function without knowing the key.

For congestion control in the network, we use the concept of Hop-by-hop flow control method [34]. In our protocol, each sensor sets a congestion bit in the header of every outgoing packet. At regular interval the sensor samples the state of the channel. Then it calculates a utilization factor, based on the number of times the channel is busy. If utilization is above a certain level, the congestion bit is set. Otherwise, the congestion bit is cleared. When a sensor receives a packet from its parent with the congestion bit set, it stops forwarding data. So the parent node can release its queues. This method is helpful to minimize transmission delay.

The network lifetime of a sensor node basically depends on energy it consumes over time and energy is available for its use. We reduce the no of complex operations so that minimum energy is consume over time. We use only public key cryptography in session key generation phase, rest of the phases use symmetric encryption to save the energy.

4.2 Notations Used in this Protocol

Consider Elliptic Curve $E_q(a, b)$ over a prime field ($\mathbb{F}_p$).

G	Point on elliptic curve whose order is *n*
Q	Point generated after multiplying large prime p with G.
$H(\cdot)$	One-way hash function with fixed length output.
$E_k(\cdot)$	Symmetric encryption algorithm with key K
$D_k(\cdot)$	Symmetric decryption algorithm with key K
T_A, T_B	Timestamp of node A and B respectively
ΔT	Expected transmission delay
T_s	Regular time interval for new session key
$\oplus$	Logic exclusive OR (XOR) operation
$\|\|$	A bitwise concatenation operation
UID_A	Identity of A on a session
UID_B	Identity of B on a session
CID	Cluster ID
PIN	Personal identification number
PIN_A	PIN of node A
PIN_B	PIN of node B
RC	Unique Request code.
P_A, n_A	Public and Private key of A respectively.
P_B, n_B	Public and Private key of B respectively.
K:	Common secret key.
K_s:	Session key

Assumptions
Following assumptions are made

- Cluster heads have more resources than sensor nodes. They are equipped with high power batteries, large memory storage, powerful antenna and data processing capabilities.
- After valid registration sensor nodes are called user node.
- CH node is considered as trusted node.
- Clock of the nodes in all clusters are synchronized.
- Each user node in a cluster can communicate with each other after mutual authentication.
- Each user node must login once with the concerned CH.
- After registration, each node in a cluster gets a secret value from BS.
- BS is trusted authority which keeps the details of all sensor nodes and CHs.
- Signal intensity of all nodes does not exceeds the threshold value.

4.3 Description of the Proposed Authentication Protocol

Proposed mutual authentication protocol between two nodes in the same cluster is shown in Fig. 2. The proposed scheme is divided into six phases as described below:

(i) *Registration phase* In this phase all nodes under a BS gets registered following the steps as shown in Table 1. Initially each sensor node contains a user identity (UID) and a private key. Before deployment, each sensor node (UN) submits their user identity (UID) by sending Sub_id() to BS over a secure channel. Then BS will assign a CID which is a unique no. for each node under a particular cluster. Now each node is preloaded with two keys: a master key to communicate with CH and a key that it shares with the BS only. BS also load

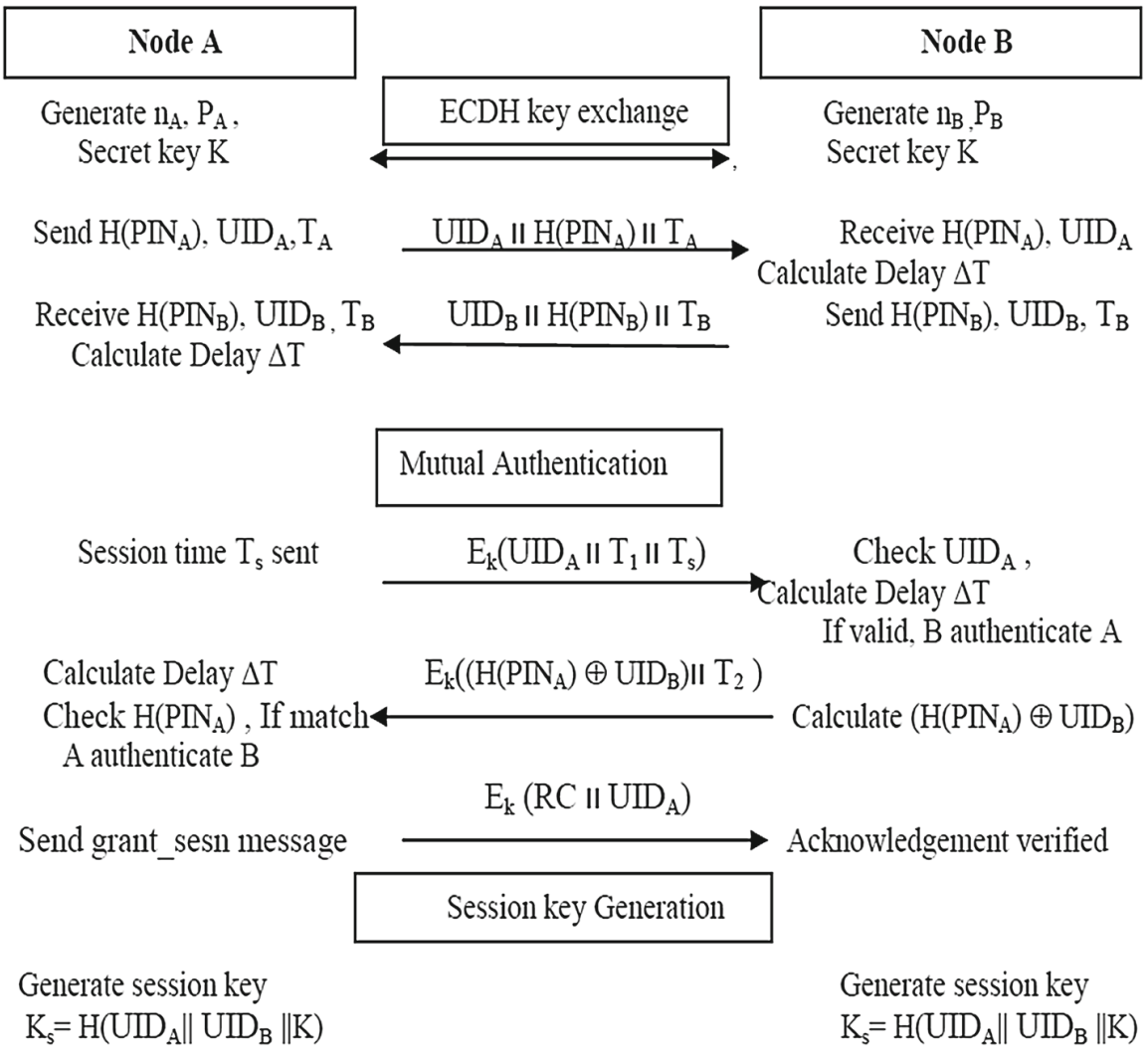


Fig. 2 Proposed time stamp based mutual authentication scheme

Table 1 Flow of registration phase

Steps	Flow	Message	Description
1.	UN → BS	Sub_id()	UID
2.	BS → UN	Reg_no()	E_n [H(PIN) ‖ RC]
3.	BS → CH	Nod_list()	E_k [UID ‖ PIN ‖ RC]

a one-way keyed hash function F to all node. After deployment BS will send a message Reg_no () containing H(PIN) and RC to a sensor node where PIN = UID ⊕ CID. BS will take the UID of each node and use encryption key E_n = H(UID) for communication. After the deployment of the sensor nodes, BS will send Nod_list() message which is a list containing the UID, RC, PIN of all nodes of the clusters, to all CH in a confidential way. BS will take the CID of each CH and use encryption key E_k = H(CID) for communication. CH is also send information to BS using this key. After each valid time interval, BS will send an updated list of records to CH including changed PIN, RC and CH will inform it to its member nodes in a encrypted form. The generator is always renewed by BS.

(ii) *Login phase* User login request is granted after performing the following steps as shown in Table 2:

Table 2 Flow of login phase

Steps	Flow	Message	Description
1.	UN → CH	Req_login()	E_{Km} [UID ‖ H(PIN)]
2.	CH → UN		Check UID,PIN
		Val_login()	If valid, send E_{Km}(UID), (p, q, Q, G, E)
		Inval_login()	Else Reject
3.	UN → CH	Grant_login()	H(RC ⊕ UID)

Table 3 Flow of key exchange phase

Steps	Flow	Message	Description
1.	CH → A,B	Session ID	USID
2.	A ↔ B	Public Key	P_A, P_B
3.	A → B	set_id_A()	$E_{PB}[UID_A \| \| H(PIN_A) \| \| T_A]$
4.	B → A	set_id_B()	$E_{PA}[UID_B \| \| H(PIN_B) \| \| T_B]$

Step 1 First User Node (UN) sends request message Req_login to CH with his H(PIN) and UID. It will use master key K_m = H(RC) for encryption and decryption.

Step 2 CH will check the received UID and H(PIN) with the values stored in the list. If it is valid, then it sends the Val_login message which contains the UID (in a encrypted form) and the public parameters (p, q, Q, G, E). Here we use padding bits for encryption. If it is not valid, then it rejects the request by sending the message Inval_login. CH will use same master key as it knows RC of a particular UN.

Step 3 After getting the Val_login message UN collects all data after decryption and sends the response message Grant_login which contains H(RC ⊕ UID).

After following these steps, each user node of a cluster gets a valid login. Suppose node A and node B are two user nodes in a particular cluster wants to communicate with each other. First they will send a request to CH. Now following steps will be performed for mutual authentication and session key establishment as shown in Fig. 2.

(iii) *Key exchange phase* In this phase we follow ECDH protocol for key exchange and perform the following steps as shown in Table 3.

Step 1 CH will generate a Unique Session ID for these two nodes for building session and send to the nodes for generating public keys. Now node A generate public key $P_A = \eta_A \times G$ where η_A is A's private key. Node B selects a private key η_B and computes a public key P_B for node B. Now both of them exchange their public keys with Session ID.

Step 2 Node A generates the secret key $K = \eta_A \times P_B$. Node B generates the secret key $K = \eta_B \times P_A$ independently. The two calculations in this step will produce the same result because $\eta_A \times P_B = \eta_A \times (\eta_B \times G) = \eta_B \times (\eta_A \times G) = \eta_B \times P_A$.

Step 3 Node A send message set_id_A() which contains $UID_A||H(PIN_A)||T_A$.

Step 4 Node B calculate delay from its present timestamp and send a message set_id_B() which contains $UID_B||H(PIN_B)||T_B$ to node A.

(iv) *Mutual authentication and session key generation phase*

For mutual authentication and session key generation between two nodes, following steps will be performed as shown in Table 4.

Table 4 Flow of session key generation

Steps	Flow	Message	Description
1.	$A \rightarrow B$	Req_Sesn()	$E_K(UID_A \| \| T_1 \| T_s)$
2.	$B \rightarrow A$	Val_Sesn()	$E_K((H(PIN_A) \oplus UID_B) \| \| T_2)$
3.	$A \rightarrow B$	Grant_Sesn()	$E_K(RC \| \| UID_A)$

Step 1: Node A will send a request message Req_Sesn encrypted with K which carries nodes recent ID as UID_A, present timestamp T_1 and Session time interval T_s.

Step 2: After getting request message from node A, node B decrypt it and get the session time. If $T - T_1 \leq \Delta T$ where T is the present timestamp of B, then node B accepts the message otherwise rejects. After that Node B Check UID_A, if matches then B authenticate A. Now B send the encrypted message Val_Sesn contains $E_k(H(PIN_A) \oplus UID_B), T_2)$ to node A.

Step 3: Node A then decrypts it with K and found $H(PIN_A) \oplus UID_B$ and subsequent timestamp T_2. If $T - T_2 \leq \Delta T$ where T is the present timestamp of A, then node A accepts the message otherwise rejects. Node A recovers $H(PIN_A)$ by performing $\oplus$ operation with UID_B. If recovered $H(PIN_A)$ matches with its original $H(PIN_A)$ then A authenticates B.

Step 4: Now A sends Grant_Sesn() message which contains encrypted $(RC \| UID_A)$ which confirms that A build the session.

Step 5: Now node A and node B generate Common session key $K_s = H(UID_A||UID_B||K)$ for a particular session T_s. After each valid session a new session key will generate. This session key is used for message encryption and decryption.

In case of mutual authentication between two nodes in the different clusters, we assume that first two phases (registration and login phase) are completed. If node C of a cluster wants to communicate with node A of another cluster as shown in Fig. 1, then it first sends a request message to CH_3. CH_3 then forwards the request message to the concerned cluster head CH_2 of node A. Once CH_2 authenticates node C, then node C can communicate with node A after mutual authentication.

Hence for mutual authentication nodes also maintain a list for pair wise key. This list contains pair wise node Id with USID and secret key. For reliable mutual authentication each node will have a update phase for updating their list with the change of USID and RC. As the public parameters will change by the BS after time to time with RC, CH will send these parameters to its child nodes. For each session nodes will generate separate public key and private key and maintain a list.

(v) *Key Management and Update Phase*

In all the previous phases, different types of keys are generated for authentication purpose. So to manage these large no of keys this phase is very important. Prior to deployment, each node is preloaded with two keys: a master key to communicate with CH and a key that it shares with the BS only. Initially, the sensor node will store this two keys: one is encryption key $E_n = H(UID)$ that it shares with the BS only for communication. Another one is master key $K_m = H(RC)$ which will use to communicate with CH. Now these two keys will updated with each session. After each valid session the generator of BS will generate a new RC for each node. After each valid time interval, BS will send an updated list of records to CH including changed PIN, RC and CH will inform it to its member nodes in a encrypted form. CH will send changed RC and session ID using the previous key and then it discards the key. Each sensor node will maintain a key list and update the list with session ID.

Table 5 Key table for protection of anonymity of a sensor node

Session time	Session ID	Node ID	Node key with BS	Node key with CH	Function Output
T1	$USID_1$	UID	$E_1 = H(UID)$	$K1 = H(RC_1)$	$H_1 = H_{E1}[UID]$
T2	$USID_2$	H_1	$E_2 = H[H(UID)] = H[E_1]$	$K2 = H(RC_2)$	$H_2 = H_{E2}[UID]$
T3	$USID_3$	H_2	$E_3 = H[E_2]$	$K3 = H(RC_3)$	$H_3 = H_{E3}[UID]$

For sensor node privacy and security, the hashed UID is stored using a one-way keyed hash function F. This function is used for producing a sequence of hash values of ID of the node. The function will use the UID and H(UID) as input and produce output $H_1 = H_{En}[UID]$ using HMAC operation. This function is generating new ID for each session. Now for new session, the node will discard its old UID. Thus the node maintains a key table as shown in Table 5.

Similarly a node also maintains pair wise key table with public and private key.

As the sensor nodes are resource constrained devices, so they can store only three session details for t units of time. CH and BS maintain lists having node ID, Session ID and Key. They also update it with time to time.

(vi) *Signature Generation/Verification*

For a particular session each message block is signed by using following signature scheme. Here we modify ECDSA to create digital signature.

Signature Generation Algorithm:

Step 1: Select $k_1,\ k_2, 1 \leq k_1, k_2 < n$.
Step 2: Compute $k_1Q = (x_1, y_1), r_1 = x_1 (\text{mod } n)$
Step 3: Compute $k_2Q = (x_2, y_2), r_2 = x_2 (\text{mod } n)$
Step 4: Compute $s = k^{-1}\ (H(m)k_2 + x(r_1 \cdot r_2))(\text{mod } n)$

(r_1, s) is the Signature pair of node A.

This signature pair is sent by the sender node A with encrypted message block. On the receiver side node B will verify the signature and then accept the message and decrypt it with the common session key generated earlier.

Signature Verification Algorithm:

Step 1: Compute $w = s^{-1} (\text{mod } n)$
Step 2: Compute $u_1 = H(m)wk_2 (\text{mod } n)$
Step 3: Compute $u_2 = (r_1 \cdot r_2)\ w (\text{mod } n)$
Step 4: Compute $u_1G + u_2Q = (x_3, y_3)$,
Step 5: Compute $v = x_3 (\text{mod } n)$

If $v = r_1 \rightarrow$ accept the Signature
else reject.
This two algorithm will ensure the non-repudiation of message.

5 Security Analysis

The proposed protocol will be considered to be a secure authenticated protocol, if it satisfies the following properties:

Theorem 1 *This protocol can withstand man-in-middle attack even if an attacker E intercepts the message transmitted between two nodes.*

Proof In our protocol, no useful information about the secret key K is revealed during a successful run. Even if an attacker intercepts G, it cannot calculate K as public key P_A, P_B depend on the private key $n_A \times G$ and $n_B \times G$. To break this scheme, an attacker would require for compute n_A given G and $n_A G$, which is assumed hard.

Consider A and B are two communicating nodes. During key exchange phase, an attacker intercepts the message set_id_A() and get the UID_A, $H(PIN_A)$, T_A. Similarly an attacker intercepts the message set_id_B() and get the UID_B, $H(PIN_B)$, T_B. Before that it already receives PU_B from B and sends PU_C instead of PU_B to user A. Similarly the attacker sends PU_C instead of PU_A to user B. The attacker doesn't know the value of G. With a new value of G, he sets two secret keys K_1 (between A and C) and K_2 (between A and B) for encrypt/decrypt messages of both the party. But after that the nodes exchange Req_sesn(), Val_Sesn(), Grant_Sesn() for mutual authentication. He cannot able to decrypt the first two messages. The last message needs RC which is only available to the valid user (given to the valid user during registration phase). Hence the attacker is unsuccessful to build a session between the node A and B. Thus this protocol resists the man in-the-middle attack.

Theorem 2 *This protocol is secure against of dictionary attack even if any unauthorized malicious insider monitors the authentication process of the user and gather information of the login process.*

Proof In this protocol for valid login, the attacker has to guess the identity ID and password PIN corresponding to the user. Even after getting the valid ID of user, an attacker attempts to login the server by guessing different CID because $PIN = UID \oplus CID$. In such case, an attacker gets a very few chances to guess the identity and PIN because CH will suspect the node. Moreover it is not possible to guess identity and H(PIN) correctly at the same time. The attacker must use the same hash function to produce the same hashed value, otherwise with the correct PIN also he cannot get a valid login. Thus the proposed scheme resists on-line password guessing attack or dictionary attack. On the other hand, in an off-line password guessing attack, suppose the attacker knows all the user details like UID, H(PIN).

During login phase He sends the Req_login () and after verification CH sends Val_login(). Now in response of this message, the malicious node will send a Grant_login () message otherwise CH will not send the session parameters. As the malicious node doesn't know the RC of that UN, he cannot build a session. It is also impossible to get a valid login as after every session this H(PIN) is changed by BS. Hence this protocol is secure against of dictionary attack even if any unauthorized malicious insider monitors the authentication process of the user and gather information of the login process.

Theorem 3 *If any unauthorized malicious node modify or insert message on the communication channel with the hope of discovering important message, then also this protocol will resist this insertion attack.*

Proof Suppose an attacker wants to modify some message and insert the modified message to the communication channel so that a wrong message is passed to the receiver. In this case it has to know the common session key $K_s(H(UID_A||UID_B \| K))$ for a particular session T_s all the messages are encrypted by a common session key. Now to generate session key, the malicious node requires secret key K which is not transmitted in the communication channel.

Suppose he intercepts the messages containing public keys P_A, P_B. It is difficult to find the value of K, as public key P_A, P_B depend on the private key $n_A \times G$ and $n_B \times G$. To break

this scheme, an attacker would require for compute n_A given G and $n_A G$, which is assumed hard. Hence it is impossible to generate K from the public keys even if G is known. Also after a given time period the session key will be changed.

Another advantage of this protocol is, each time the sender sends a signed message to the receiver who accepts the message after verifying the signature. Thus he cannot modify the message as the session key is unknown to him. He can replace the message, but creating a same signed message is impossible. Hence this type of attack is not possible in our protocol.

Theorem 4 *This protocol is secure against the stolen-verifier attack even if the attacker may be able to steal the verification list from cluster heads.*

Proof In the registration phase, BS will assign a *CID* which is a unique no. for each node under a particular cluster. Then BS sends a message Reg_no () containing *H(PIN)* and *RC* to a sensor node where $PIN = UID \oplus CID$. After the deployment of the sensor nodes, BS will send Nod_list() message which is a list containing the *UID, RC, PIN* of all nodes of the clusters, to all CH in a confidential way. This verification list is stored in CH. Each time when login request comes from user nodes, the CH will verify from the list. Suppose an attacker has stolen the verification table from CHs and get the UID, PIN of a valid user. Now a malicious node use this ID and H(PIN) for login and CH will verify this UID, H(PIN) with the stored value. Now it will send the system parameters in a encrypted form. It will use master key $K_m = H(RC)$ for encryption and decryption. But the malicious node does not know the RC of the user. Hence it will unable to communicate with CH and other nodes. Also as BS is changing updated list after every valid period hence stolen information will be invalid after a time period. Thus our protocol resists this type of attack.

Theorem 5 *This protocol is secure against the node-compromise attack even if the attacker may be able to capture a node and steal stored secret information about the networks.*

Proof Suppose a user node is compromised and the attacker gets all stored information such as UID, H(PIN). Actually at the time of registration when user node submits its UID, that time BS sends a message Reg_no () which contains H(PIN) and RC. RC is the unique request code generated with request message and H(RC) is used as a master key. This code is not stored in node memory. Thus even if a node is compromised and stolen and attacker gets the information such as $UID||H(PIN)$, he will not be able to get the master key which is required to decrypt the message send by CH. This is because the master key is generated from hash value of *RC* in sensor node which is not known to the attacker and also it is periodically changed by BS.

Theorem 6 *If the node ID is compromised, this protocol never allows the adversary to determine the session key for past sessions and decrypt the cipher text. Thus the property of perfect forward secrecy is maintained.*

Proof Consider a case where after a successful session (session time is T_s), the adversary captured the node and get ID of the user with the H(PIN). It also want to get access of the System parameters (*p, q, Q, G, E*) in a encrypted form. Both CH and UN use same master key $K_m = H(RC)$ for encryption and decryption of system parameters. So he is unable to get the system parameters. Now after getting the identities of the parties, the adversary cannot wants to generate the past common session key K_s where $K_s = (H(UID_A||UID_B||K)$. But the attacker still cannot compute the previous session keys because K is unknown. It is difficult to find the value of K, as public key P_A, P_B depend on the private key $n_A \times G$ and

$n_B \times G$. To break this scheme, an attacker would require for compute n_A given G and $n_A G$, which is assumed hard. Hence it is impossible to generate K from the public keys even if G is known. Hence the property of perfect forward secrecy is satisfied by our proposed protocol.

Theorem 7 *If any unauthorized malicious user can send duplicate data repeatedly to the receiver which is already sent, the protocol will resist this replay attack.*

Proof In this protocol for a particular session a new session key will generate by applying the three steps as described previously. In each step the receiver check the timestamp value. In step 1, node A will send a request message Req_Sesn encrypted with K which carries UID_A, present timestamp T_1 and Session time interval T_s. After getting request message from node A, node B decrypt it and get the session time. If $T - T_1 \leq \Delta T$ where T is the present timestamp of B, then node B accepts the message otherwise rejects. After that Node B Checks UID_A, if matches then B authenticate A. Now B send the encrypted message Val_Sesn contains $E_k(H(PIN_A) \oplus UID_B), T_2)$ to node A. Node A then decrypts it with K and found $H(PIN_A) \oplus UID_B$ and subsequent timestamp T_2. If $T - T_2 \leq \Delta T$ where T is the present timestamp of A, then node A accepts the message otherwise rejects. In this way retransmission is resisted. This method is also follow in encryption and decryption method to avoid replay attack. In this protocol, after each valid session time Ts which is unknown to malicious user, a new session key will generate for encryption, so that replay attack is not possible.

Theorem 8 *If attacker is to announce itself to be the neighbour of another node by sending "HELLO" messages, the protocol will resist this HELLO Flood attack.*

Proof In this protocol, BS sends Nod_list() message which is a list containing the *UID, RC, PIN* of all nodes of the clusters, to all CH in a confidential way. After each valid time interval, BS will send updated list of records to CH including changed *PIN, RC* and CH will inform it to its member nodes in encrypted form. So this protocol doesn't require "HELLO" messages to be constantly exchanged among the sensor nodes to establish neighborhood tables. Here an attacker broadcasts HELLO message with high power and capture nodes to setup links with it. This type of attack is not possible because BS first broadcasts a message contain the list of Cluster Heads. So if a HELLO message comes from an adversary that the nodes will first check that it is a valid CH or not. We also restrict signal intensity by putting a threshold value. If signal intensity exceeds the threshold value then the adversary node is detected.

Theorem 9 *If any unauthorized user capture a node, then also due to this protocol anonymity of a sensor node is protected even when the key is compromised.*

Proof Assuming the hash function is shared and thus known to all the sensor nodes, if an adversary compromised one sensor node, it is clear that he could also compute the next ID for every node using the hash function. Thus we identify a keyed hash function that can grow IDs such that an adversary cannot link the input and output values of a keyed hash function without knowing the key. Also the adversary cannot determine if two messages are sent by the same sensor node, if he does not know the secret keys. Thus the anonymity of a message's sender is protected as long as the key is not compromised. A sensor node can delete its previous ID and generate a new one after completing a session. Then through physically capturing a sensor node, the adversary only knows the current ID and a secret key. Because of the one way hashing, the adversary cannot reverse the hash function to get the previous IDs used. Thus, the anonymity of a sensor node in the past is protected even when the key is compromised.

Table 6 Experimental results of ECC (prime field)

Elliptic curves over prime field	Base point generation	Public key PU_A	Public key PU_B	Node-A secret key K	Node-B secret key K	Signature generation	Message encryption (899 Bytes)	Message decryption (899 Bytes)	Signature verification
Field order—F(2^163)	(0x2fe13c0537bbc11acaa07d793de4e6d5e5c94eee8, 0x289070fb05d38ff58321f2e800536d538ccdaa3d9)	(947133209628870 17981246 54025926 00505387 264934967, 73672669 20766783 5965460110 642201 65929086 67634053)	(116711 2403993 5811037 2652537 0500852 0558774 14415739, 4429730 4733821 7101722 3088395 0052732 7798141 733910)	918 819082 17933032 6594279 6209771 7675483 6424180 185	918 819082 179330 326594 279620 977176 754836 424180 185	Signature = [34wCFH cxJFQMzs gRw5XCg dgSqFA,J yczA-hQop JdCldQuR ZRa7/0vb 30z49Bw EwAt]	Encryption done: plain. txt.enc:	Decryption done: plain. txt.enc. txt	Signature verification successful!

Table 6 continued

Elliptic curves over prime field	Base point generation	Public key PU_A	Public key PU_B	Node-A secret key K	Node-B secret key K	Signature generation	Message encryption (899 Bytes)	Message decryption (899 Bytes)	Signature verification
		(83 ms)	(110 ms)	(81 ms)	(81 ms)	Time in ms:125	(2,785 ms)	(1,282 ms)	(210 ms)
Field Order-F(2^233)	(0x172 32ba853 a7e731a f129f 22ff4 149563a 419c26 bf50a4c 9d6ee fad6126, 0x1db53 7dece81 9b7f707 555a67c 427a8c d9bf18ae b9b56e0 c11056f ae6a3)	(400 38985 859382 3418120 8384627 8085654 5517125 43647, 775066 0623866 1915992 668944 74906173 6386181 2331568)	(10458734 9861939 1841811 1849601 27943415 772594 836268, 2650995 7331596 2795531 467657 7342232 1201590 0760054)	2124800 567299 624176 1125423 1699815 3626760 81035589	212480 056729 962417 611254 2316998 153626 760810 35589	Signature = [FBACFE 4DxOhMZY 5PBa8 AQXMEt, DOym 3JAhRbIif 8OQIq6bf/ YDszvZ 4iCsg3Fw]	Encryption done: plain. txt.enc	Decryption done: plain. txt.enc.txt	Signature verification successful!
		(117 ms)	(140 ms)	(110 ms)	(110 ms)	Time in ms: 250	(3,928 ms)	(1,965 ms)	(521 ms)

Table 7 Performance comparison of our scheme with existing protocols

Computational load	Our protocol	Das [16]	Kumar et al. [18]
Registration phase	$1T_h + 2T_e$	$2\ T_h$	$3\ T_h$
Login phase	$1T_h + 1T_E + 1T_{PA}\,1T_{PM} + 2T_e$	$3\ T_h$	$3\ T_h$
Authentication & key generation phase on each side	$2\ T_h + 2T_{PM} + 2T_{PA} + 1T_E + 3T_e$	$5\ T_h$	$7\ T_h$

Table 8 Security feature comparison of our scheme with existing protocols

Attack	Our scheme	Benenson et al. [11]	Yeh et al. [19]	Kumar et al. [18]	Das [16]
Man-in-the-middle attack	Yes	Yes	Yes	Yes	Yes
Dictionary attack	Yes	–	Yes	Yes	Yes
Impersonation attack	Yes	No	No	Yes	Yes
Stolen-verifier attack	Yes	Yes	–	–	–
Node-compromise attack	Yes	Yes	Yes	Yes	No
Mutual authentication	Yes	No	No	Yes	No
Replay attack	Yes	No	Yes	Yes	No
Perfect forward secrecy	Yes	–	No	No	–

6 Performance Analysis

Our experimental result shows the timings of basic operations of Elliptic Curve based scheme with an 8-bit micro-processor (ATMega128L). For ECC implementation on different binary fields we have used NIST recommended elliptic curve parameters [20]. Here we have considered the elliptic curve $y^2 \equiv x^3 + x + 1$ over the finite field $\mathbb{F}_p$. Implementation results of our proposed protocol is shown in Table 6.

The proposed protocol is suitable for WSN as it requires less bandwidth and has low storage requirement for user side. Total no. of bits exchanged in the protocol during message transmission for authentication is 1,530 bits and storage space required to store public, secret and session key is 1,240 bits for ECC of key size 160 bits.

To calculate how much energy it consumes over time, we find that the cost of receiving one byte is 28.6 μJ and the cost of transmitting a byte is 59.2 μJ. So if a packet size is 41 byte (Payload 32 byte + Header 9 byte),then the cost of receiving message for authentication is 133.40 μJ. Also the cost of transmitting message for authentication is 276.14 μJ. We find that the energy cost of digital signature computations in ATMega128L is 24.12 μJ for signing and 46.08 μJ for verifying signature.

In calculating computation costs, we define the notation T_h as the hash computation time, T_{PA} as the elliptic curve point addition computation time, T_{PM} as the elliptic curve point multiplication computation time, T_E as the elliptic curve polynomial computation time, T_e as time for symmetric encryption/decryption.

The computational performance of our proposed protocol including registration phase, login and authentication phase, mutual authentication phase is favorably comparable with existing protocols as shown in Table 7.

Table 9 Comparison of our scheme with real time metrics

Real time metrics	Our scheme	Benenson et al. [11]	Yeh et al. [19]	Kumar et al. [18]	Das [16]
Delay	Low	High	–	High	High
Transmission rate usage	Moderate	–	Moderate	Low	High
Traffic Congestion	Low	High	High	High	–
Network life time	Moderate	High	Moderate	High	High

The computational performance of our proposed protocol includes registration phase (1H + 1X + 2Enc/Dec), login phase (1H + 1X + 2Enc/Dec), mutual authentication phase (2H + 1X + 3Enc/Dec) where H and X denotes hash and XOR operation. For signature generation/verification 1H is needed. Security Analysis shows that our scheme is favorably comparable with existing protocols as given in Table 8.

Moreover, looking in the comparison table, one can find that our computational cost is higher than Das protocol [16] and Kumar et al. protocol [18] due to point multiplication, exponentiation operation which is computationally expensive. But we have improved delay and traffic congestion with high level of security.

We also compare our algorithm with other real time metrics given in Table 9.

7 Conclusion

We propose a timestamp based mutual authentication protocol to enhance security during communication in WSN. Performance analysis of our proposed authentication protocol shows that it has light communicational load and consumes less energy for authentication process. Also it has improved delay and traffic congestion with high level of security. Detailed security analysis shows that our scheme resists the major vulnerable attacks in wireless sensor networks and is favorably comparable with existing protocols. Also the scheme is based on ECC, so it inherits the security and implementation properties of the elliptic curve cryptosystems. ECC offers the highest cryptographic strength per bit among the existing public-key cryptosystems.

References

1. Eschenauer, L. & Gligor. V. (2002). A key management scheme for distributed sensor networks. In *CCS '02: Proceedings of the 9th ACM conference on computer and communications security, New York, USA*.
2. Chan, H. Perrig, A. & Song, D. (2003). Random key pre-distribution schemes for sensor networks. In *Proceedings of the IEEE security and privacy symposium*.
3. Watro, R., Kong, D., Cuti, S. F., Gardiner, C., Lynn, C. & Kruus, P. (2004). TinyPK: Securing sensor networks with public key technology. In *SASN '04, New York, USA* (pp. 59–64).
4. Uhsadel, L., Poschmann, A. & Paar, C. (2007). An efficient general purpose elliptic curve cryptography module for ubiquitous sensor networks. In *SPEED*, www.crypto.rub.de
5. Raazi, S. M. K., & Lee, S. (2010). A survey on key management strategies for different application of wireless sensor networks. *Journal of Computing Science and Engineering*, *4*(1), 23–51.
6. Tsai, S. C., Tzeng, W. G., & Zhou, K. Y. (2009). Key establishment schemes against storage-bounded adversaries in wireless sensor networks. *IEEE Transactions on Wireless Communications*, *8*(3), 1218–1222.
7. Yu, Z., & Guan, Y. (2008). A key management scheme using deployment knowledge for wireless sensor networks. *IEEE Transactions on Parallel and Distributed Systems*, *19*(10), 1411–1425.

8. Liu, D., Ning, P., & Du, W. (2008). Group-based key predistribution for wireless sensor networks. *ACM Transactions on Sensor Networks (TOSN)*, *4*(2), 11:1–11:30.
9. Martin, K. M., Paterson, M. B., & Stinson, D. R. (2010). Key predistribution for homogeneous wireless sensor networks with group deployment of nodes. *ACM Transactions on Sensor Networks (TOSN), 7*(2): Article 11.
10. Chen, C.-Y., & Chao, H.-C. (2011). A survey of key distribution in wireless sensor networks. *Security Communication Networks*. doi:10.1002/sec.354.
11. Benenson, Z., Gedicke, N. & Raivio O. (2005). Realizing robust user authentication in sensor networks. In *Workshop on real-world wireless sensor network REALWSN'05*.
12. Wong, K. H. M., Zheng, Y., Cao J. & Wang S. (2006). A dynamic user authentication scheme for wireless sensor networks. In *IEEE SUTC'06* (pp. 244–251).
13. Tseng, H. R., Jan, R. H. & Yang, W. (2007). An improved dynamic user authentication scheme for wireless sensor networks. In *IEEE GLOBECOM 2007* (pp. 986–990).
14. Ko, L.-C. (2008). A novel dynamic user authentication scheme for wireless sensor networks. In *IEEE ISWCS 2008* (pp. 608–612).
15. Lee, T. H. (2008). Simple dynamic user authentication protocols for wireless sensor networks. In *International conference on sensor technologies and application (SENSORCOMM 2008)* (pp. 657–660).
16. Das, M. L. (2009). Two-factor user authentication in wireless sensor networks. *IEEE Transaction on Wireless Communication*, *8*(3), 1086–1090.
17. Nyang, D. H. & Lee, M. K. (2009). Improvement of Das's two-factor authentication protocol in wireless sensor networks. http://eprint.iacr.org/2009/631.pdf
18. Kumar, P., Sain, M. & Lee, H. J. (2011). An efficient two-factor user authentication framework for wireless sensor networks. In *ICACT 2011* (pp. 574–578).
19. Yeh, H. L., Chen, T. H., Liu, P. C., Kim, T. H. & Wei, H. W. (2011). A secured authentication protocol for wireless sensor networks using elliptic curves cryptography. *Sensors*, *11*(5), 4767–4779. doi:10.3390/s110504767.
20. Hankerson, D., Menezes, A., & Vanstone, S. (2004). *Guide to elliptic curve cryptography*. Springer publication, ISBN 0-387-95273-X.
21. Oh, B.-K., Ha, K.-C., & Oh, J. (2006). An improved baby-step-giant-step method for certain elliptic curves. *Journal of Applied Mathematics and Computing*, *20*(1–2), 485–489.
22. Blake, I. F., Seroussi, G., Smart, N. P. (2004). *Advances in elliptic curve cryptography*. London mathematical society lecture note series. Cambridge University Press, ISBN: 052160415X.
23. Karakoyunlu, D., Gurkaynak, F. K., Sunar, B., & Leblebici, Y. (2009). Efficient and side-channel-aware implementations of elliptic curve cryptosystems over prime fields. *IET Security*, *4*(1), 30–43.
24. Cohen, H., & Frey, G. (2006). *Handbook of elliptic and hyperelliptic curve cryptography*. London: Chapman & Hall/CRC Press.
25. Longa, P., & Gebotys, C. (2010). Efficient techniques for high speed elliptic curve cryptography. In *CHES 2010. LNCS 6225* (pp. 80–94).
26. Longa, P., & Gebotys, C. (2009). Novel precomputation schemes for elliptic curve cryptosystems. In *ACNS2009 LNCS* (Vol. 5536, pp. 71–88).
27. Longa, P., & Miri, A. (2008). Fast and flexible elliptic curve point arithmetic over prime fields. *IEEE Transactions on Computers*, *57*(3), 289–302.
28. Abi-char, P. E., Mhamed, A., & El Hassan, B. (2007). A secure authenticated key agreement protocol based on elliptic curve cryptography. In *International symposium on information assurance and security, IEEE* (Vol. 57, pp. 89–94).
29. Bringer, J., Hervé, C., & Thomas I. (2010). Password based key exchange protocols on elliptic curves which conceal the public parameters. In *ACNS 2010, lecture notes in computer science*(Vol. 6123/2010, pp. 291–308).
30. Chatterjee, K., & Gupta, D. (2009). Secure access of smart cards using elliptic curve cryptosystems. In *WiCOM 2009, IEEE Catalog No. CFP09WNM-CDR*.
31. Chatterjee, K., De, A., & Gupta, D. (2011). Timestamp based authentication protocol for smart card using ECC. In *Proceedings of international conference on web information system and mining (WISM 2011), LNCS 2008* (Vol. 6987, pp. 368–375).
32. Lim, M.-H., Yeoh, C.-M., Lee, S., Lim, H. & Lee, H. (2008) A secure and efficient three-pass authenticated key agreement protocol based on elliptic curves. In *Networking, LNCS 2008* (Vol. 4982/2008, pp. 170–182).
33. Wadaa, A., Olariu, S., Wilson, L., Eltoweissy, M. & Jones, K. On providing anonymity in wireless sensor networks. In *Proceedings of the tenth international conference on parallel and distributed systems (ICPADS'04)* (pp. 411–418).

34. Wan, C.-Y., Eisenman, S. & Campbell, A. (2003). CODA: Congestion detection and avoidance in sensor networks. In *Proceedings of the ACM sensor systems conference, Los Angeles, CA* (pp. 266–279).



Kakali Chatterjee is an Assistant Professor in Computer Science and Engineering Department of National Institute of Technology Patna, India. She has completed her Ph.D. from Delhi Technological University (formerly Delhi College of Engineering). She has done M.Tech from Centre for Development of Advanced Computing, a R&D and Academic centre of Govt. of India. She has many published research papers in LNCS (*Springer*) and reputed International Journals including CSI Transactions on ICT (*Springer*), Information Security Journal: A Global Perspective (*Taylor & Francis*). She is working in the field of Information Security and Cryptography.



Asok De received Ph.D. from IIT Kharagpur (India) in the area of Microstrip antenna. He was Professor in Delhi Technological University (formerly Delhi College of Engineering). He also worked as Principal, Ambedkar Institute of Advanced Communications Technologies & Research, Delhi. Presently he is Director, National Institute of Technology, Patna. His field of interest is Antennas, Numerical techniques in Electromagnetic, Information Security etc. He has published many research papers in reputed International Journals.



Daya Gupta is Professor of Computer Engineering Department of Delhi Technological University (formerly Delhi College of Engineering), India. She has done M.Sc. (Maths), Post M.Sc. Diploma (Computers Science) from IIT, Delhi and Ph.D. in Computer Science from Delhi University. She is a senior member of IEEE and a life member of CSI. Her field of interest is Software Engineering, Information Security etc. She has chaired many sessions and delivered invited talks at many conferences and has published many research papers in reputed International Journals.

ISSN (Online) : 2278-1021
ISSN (Print) : 2319-5940

International Journal of Advanced Research in Computer and Communication Engineering
Vol. 3, Issue 9, September 2014

A Survey on LTE Downlink Packet Scheduling

Vallari Sharma[1], Prof. P.K Chopra[2]

M.Tech - Student, Department of ECE, Ajay Kumar Garg Engineering College, Ghaziabad, India[1]

HOD, Department of ECE, Ajay Kumar Garg Engineering College, Ghaziabad, India[2]

Abstract: Long term evolution (LTE) is a 3GPP (Third Generation Partnership Project) 4G technology which enhances the development in the field of telecommunication and by improving the performance of the network for the different types of traffic flows. As it is an all IP technology so, it is the most emerging technology now a days. The fact that 3G long term evolution is a packet based networks brings some improvements in the form of higher bit rate, lower latencies and a variety of services. This paper presents a survey of the different proposed scheduling algorithms under variable conditions and accordingly, the variation in their results in terms of the performance metrics like throughput, packet loss, delay time, spectral efficiency, fairness etc.

Keywords: Long term evolution (LTE), Channel Quality Indicator (CQI), Physical downlink common control channel (PDCCH), User Equipment (UE), Quality of Service (QoS).

I. INTRODUCTION

LTE is a global standard for fourth generation of mobile broadband (4G) supported by all major players in the industry introduced by 3rd Generation Partnership Project in 2008. It is expected that LTE provide an extension in capacity and a performance improvement compared to the current HSPA (High Speed Packet Access) networks [1]. The basic objective of LTE is to develop a environment which provides benefits such as high data rates for proper

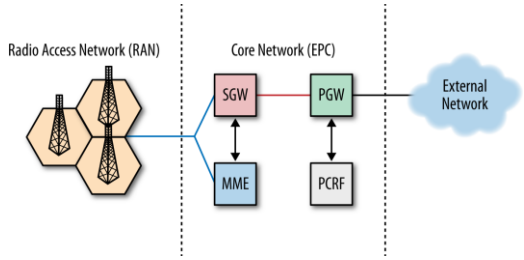


Fig 1 LTE Network

communication, minimum delay known as latency, high range of spectral efficiency over a wide range of bandwidth The main objective behind the evolution of LTE network is to increase the data-rate to fulfill the demands of the user.

The Radio resources are divided and shared efficiently among different active users while maintaining a satisfied level of QoS to all active users. To fulfill the requirements, the LTE system uses orthogonal frequency division multiple access (OFDMA) technology in the downlink. The OFDMA technology divides the available bandwidth into multiple narrow-band sub-carriers and allocates a group of sub-carriers to a user based on its requirements, current system load and system configuration [1] SC-FDMA (Single Carrier Frequency Division Multiple Access) in uplink and multi-antenna technology [3].

The transmission bandwidth can be selected between 1.4MHz and 20MHz [1].The 20MHz bandwidth can provide up to 150Mbps downlink user data rate with 2X2 MIMO and 300 Mbps with 4x4 MIMO. To support downlink data services with high transmission rates, a BS transmits data using shared channels where the data and information that comes from many users is multiplexed in time and frequency domains. So, the different scheduling strategies are proposed keeping in mind the different needs and requirements of the users along with the performance.

II. SCHEDULERS

1. Maximum Throughput Scheduler

The strategy known as Maximum Throughput (MT) aims at maximizing the overall throughput which assigns each Resource block to the user that can achieve the maximum throughput in the current TTI.

2. Proportional Fair Scheduler

A typical way to find a trade-off between requirements of fairness and spectral efficiency is the Proportional Fair (PF) scheme. The idea behind this is that the past average throughput can act as a weighting factor of the expected data rate, so that users in bad conditions will be served within a certain amount of time.

3. Modified Largest Weighted Delay First

The Modified LWDF (M-LWDF) is a channel-aware extension of LWDF and bounded packet delivering delay is provided. For, shaping the behavior of PF, MLWDF it uses information about the accumulated delay, assuring a good balance among spectral efficiency, fairness and QoS provisioning. It was developed to support multiple real time data users.

III. LITERATURE SURVEY

In 2013, Biswapratap singh Sahoo et.al [1] studied the downlink packet scheduling algorithms and mainly focuses on the three scheduling algorithms known as:

FLS (Frame level scheduler) in which basically two different algorithms are implemented in two different levels, EXP rule which explains the queue length and waiting time for servicing a queue and LOG rule which gives a balance between delay and robustness. Simulation is done in a vehicular environment by using LTE-Sim for the video traffic and the performance is analyze and the number of users taken for the simulation vary from 10 to 60 and the simulation is done in a region having radius of 1 km and is a bounded region. Simulation results showed that the FLS algorithm performed better than the rest two algorithms in terms of all the parameters.

In 2012, Ali Alfayly et.al [2] focused on analyzing the performance of the LTE algorithm in a single cell with a set of users at different speeds. As real-time flows like VoIP is considered to measure the impact on Quality of Experience (QoE). The LTE simulation was built based on LTE-Sim with three LTE scheduling algorithms (i.e., PF, EXP-PF, and MLWDF) for a single-cell scenario. Four different scenarios were developed using a single cell: static, pedestrian and vehicular scenarios using different speeds. EXP-PF is only considered for real time flows.PF has best end to end delay which is not suitable for VoIP applications and MLWDF and EXP-PF have less end to end delay.

In 2011, Wei Nie et.al [3] studied the scheduling problem and proposed a two- level scheduling scheme with support for quality of service and fairness guarantees for downlink traffic in a WiMAX network and analyzed the performance of the two- level scheduling scheme and compared it to round robin and weighted round robin algorithms.

In the two level scheduling, in first level strict priority packets are classified by scheduler according to the quality of service then they are arranged into different priority queues and in the second level fairness oriented scheduling schemes for different service flows are used. A simple WiMAX network is simulated by using OPNET simulation and concluded that as compared with round robin algorithm and weighted round robin algorithm, the QoS priority and fairness scheduling scheme for downlink traffic guarantees the delay requirement and maximize the throughput in the downlink.

In 2013, Oana IOSIF et.al [4] evaluated the performance of downlink LTE using System Level Simulator .Sector throughput, user throughput and Block error rate(BLER) are the performance indicators analyzed and in this basically three scheduling strategies are used i.e. Round Robin, Best CQI and Proportional Fair and the results showed for the different scenarios.

For the bandwidth of 20MHz, when the speed of user equipment is 5 Km/hr, the throughput and network BLER are higher as compared to the results for the user equipment speed of 20 Km/hr and for a bandwidth of 10 MHz, the results get halved. For 2x2 MIMO, the performance of Best CQI is better as compared to other two algorithms

In 2013, Arkadiusz Biernacki et.al [5] evaluated the performance of three scheduling algorithms proposed for LTE downlink transmission**.** The three scheduling algorithms i.e.PF, MLWDF and EXP/PF are used for the comparison. A proportional fair (PF) scheduler basically assigns the resources to the users considering the CQI and the past user throughput. The Modified Largest Weighted Delay First (M-LWDF) scheduler supports multiple data users with different QoS requirements. The EXP/PF algorithm supports the streaming services and the best-effort data services. Simulation results showed that the packet delay is maximum but the throughput is minimum in case of proportional fair scheduling algorithm and packet loss ratio performance is quite similar in case of MLWDF and EXP/PF scheduling.

In 2013, Bin Liu et.al [6] proposed a packet scheduling strategy known as Modified-Earliest Deadline First-Proportional Fair (M-EDF-PF) algorithm which is an extension of Earliest Deadline First (EDF) and Proportion Fair (PF) algorithm and having low complexity for real time traffics like video and VoIP in LTE systems. For, verifying the high efficiency of the proposed algorithm, several other well known algorithms are also taken such as EXP/PF, MLWDF etc. for the real time traffic and simulation is done. During the simulation, the proposed algorithm which is designed for the real time traffic services performed better than the other algorithms as it is having low complexity. The proposed algorithm is very efficient and is very suitable to use for the wireless systems.

In 2013, Huthaifa AL-Jaradat et.al [7] explored the performance of three well known packet scheduling algorithms i.e. Proportional Fair (PF) algorithm, Maximum Largest Weighted Delay First (MLWDF) and EXP/PF for the real time traffic. In this paper, LTE-Sim is used to perform the entire simulation.

A single cell of 1 km with inter cell interference is used and out of the total number of users half of them having VoIP flows and remaining half are having video flows. Performance of these scheduling algorithms is tested for five parameters i.e, fairness index, packet loss ratio, total spectral efficiency, packet throughput and packet delay. Simulation results showed that the MLWDF performed better than the PF and the EXP/PF algorithms in terms of all the parameters and for the both the traffics.

In 2013, A.S Sravani et.al [8] proposed two algorithms known as Max Round Robin and Max Throughput algorithms for high speed packet access giving higher capacity and fairness than other conventional algorithms

Max SNR, Round Robin and Proportional Fair are the three. As the users are not fixed and most probably they are randomly situated so for every instant, the active users are changed Simulation results showed that the two proposed algorithms achieved higher values of efficiency, average cell goodput etc.

Than the conventional algorithms but Max throughput scheduling is used in place of Max SNR because by using this, the performance is improved in terms of capacity of the system and fairness in all the users. So, the proposed scheduling algorithms performed better than the conventional algorithms.

In 2011, T. Ali- Yahiya et.al [9] investigated the performance of PF, M-LWDF and EXP/PF in LTE and in this a single cell with interference scenario is used. There are 40% of users using video flows, 40% of users using VoIP flows and 20% of users using best effort flows and considered that users are constantly moving at speed of 3kmph in random directions.

LTE simulator is used for the simulation because LTE – Sim provides a support for radio resource allocation in a time – frequency domain. This concluded that M-LWDF and EXP performed far better than PF when using real time flows.PF is not considered as a good solution for real time services.EXP/PF scheduling algorithm seems an optimal possible solution for guaranteeing a good QoS level.

In 2013, Deng Keke et.al [10] proposed an algorithm known as Energy-saving based Inter-group Proportional Fair (EIPF) for the LTE downlink multicast services. In this a proper transmission power is calculated first according to the available data rate then IPF principle is followed to allocate the resources among different multicast groups. One typical scheduling algorithm is Inter-group Proportional Fairness (IPF) for multicast services but its disadvantage is that in this data is transmitted at a fixed rate means for each Resource Block the scheduler picks one group to be scheduled on it according to the principle of IPF.

There is a amazing trade-off between throughput and fairness among different groups in IPF. In this paper, a scheduling algorithm is proposed known as Energy-saving based Inter-group Proportional Fair algorithm (EIPF).for utilizing rate of energy of the system. The simulated results showed that the average throughput and energy efficiency are best in EIPF as compared to IPF.

In 2013, Wei Kuang Lai et.al [11] proposed a scheduling algorithm known as Packet Prediction Mechanism (PPM) and compared it with the other schemes. Two typical methods Proportional fair and maximum throughput and other two real time applications MLWDF and EXP/PF were used for the comparison with the proposed algorithm. The results showed that the proposed mechanism performed better than the conventional mechanism in terms of average cell goodput, invalid packet rate, average delay time etc. for both fixed and moving user equipments.

IV. RESULT ANALYSIS

In 2011, T. Ali Yahiya et.al [9] analyzed the results for different parameter metrics. The value of fairness calculated in this is given by,

Scheduling Strategy	Fairness Index
ASA	0.774
RSA	0.830
Max. SNR	0.705
OFDM-TDMA	0.527

Table 1: Result Analysis of [9]

In 2013, Oana IOSIF et.al [4] analyzed the results i.e. the value of throughput for the different schedulers for variable bandwidth,

Schedulers	Throughput (Mbps)
ROUND ROBIN	45.06
PROPORTIONAL FAIR	63.89
BEST CQI	80.72

Table 2: Result Analysis of [4]

V. CONCLUSION

In this paper, different scheduling mechanism are studied for different downlink traffic flows in terms of parameter metrics i.e. throughput, packet loss, delay time, spectral efficiency and fairness index and analysed various results by comparing the parameters and scheduling mechanism proposed in the different papers.

ACKNOWLEDGMENT

We sincerely thank Ajay Kumar Garg Engineering College for providing the framework to accomplish our work

REFERENCES

[1] B. Sahoo, 2011"Performance Comparison of Packet Scheduling Algorithms for Video Traffic in LTE Cellular Network", IJMNCT, Vol.3 , No.3, pp 1307.
[2] A. Alfayly, I.H Mkwawa, L.Sun and Emmanuel, 2012"QoE-based Performance Evaluation of Scheduling Algorithms over LTE", IEEE , Vol8, No.4, pp 1362-1366.
[3] W. Nie, H.Wang, J.Hyuk Park, 2011 " Packet Scheduling with QoS and fairness for downlink traffic in WiMAX networks" , Journal of information processing system , Vol.7, No.2, pp 103-112.
[4] O.Iosif, I. Banica, 2013 "Performance Analysis of Downlink LTE using System level Simulator" , U.P.B.Sci.Bull.,Series C, Vol.75, Iss 1, pp 815-820.
[5] A.Biernacki, K.Tutschku, 2013 "Comparative Performance Study of LTE Downlink Schedulers", Springer, Vol.74, No.2, pp 585-599.
[6] B.Lui, H.Tang, L.Xu , 2013" An Efficient Downlink Packet Scheduling Algorithm for Real Time Traffics in LTE Systems", IEEE CCNC, Vol.44, No.3, pp 1-5.

[7] H. Al-Jaradat, K. Sandrasegaran, 2013 "On the Performance of PF, MLWDF and EXP/PF algorithms in LTE", IJCT , Vol8, No.1, pp 132-142.
[8] A. S. Sravani, K. Jagadeesh Babu , 2012 " Implementation of Scheduling Algorithm for LTE downlink ", ISSN, Vol.2, Issue-6, pp 52-59.
[9] T.AYahiya , 2011 "Performance Study of Opportunistic Scheduling in LTE Networks" , Springer Science , Vol.44, No.6, pp 167-180.
[10] D.Keke, W.bin, G.Hui, W.Wennai, 2013 "Energy saving scheduling for the LTE Multicast services", JOURNAL OF ELECTRONICS (CHINA), Vol.30, No.5, pp 423-429.
[11] W.Kuang Lai , C.LTang,2013 "QoS-aware downlink packet scheduling for LTE networks", Elsevier, Vol.57, No.7, pp 1689-1698.

BIOGRAPHIES



Vallari Sharma received her B.Tech degree from Uttar Pradesh Technical University, Lucknow, Now, She is pursuing M.Tech (ECE) from Ajay Kumar Garg Engineering College, Ghaziabad. Her area of interest is mobile and wireless communication



Prof. Pradeep Kumar Chopra entered the field of education in the year 2004 after 24 years of exemplary service in the technical branch of the Indian Air Force, He earned his Bachelor's degree in Engineering (Electronics) from Delhi college of Engineering in the year 1979 and Masters in Technology from IIT Delhi in the year 1985. He also has a Masters degree in Defense Studies from Madras University. While he was in the Indian Air Force he was part of and headed a number of important technical projects. For his exemplary services he was awarded "Vishist Seva Medal" by the President of India in the year 1993.He took premature retirement from the IAF in the year 2004 and entered the field of education. He is the Head of Dept. (Electronics and Communication) in Ajay Kumar Garg Engineering College in Ghaziabad.

Agile vs waterfall: A Comparative Analysis

Vaishnavi Kannan
Student
Delhi Technological University

Smita Jhajharia
Guest Faculty
Delhi Technological University

DR.Seema Verma
Associate Professor
Banasthali University

***Abstract*--Every software company requires to follow a well defined methodology for the proper development of its product. Software Development Life Cycle Models help companies to produce good quality software within the time limit and cost budget. Two widely used SDLC's are discussed in this paper. This paper also discusses their use along with their pro's and con's. Software development in Microsoft is also discussed .**

***Index Terms*--Software Development Life Cycle, Waterfall model, Agile models.**

I INTRODUCTION

SDLC is the process consisting of a series of well planned activities to develop or modify the software products [1]. They usually contain a series of steps that provide a model for the development and management. SDLC's aim at improving the quality of the software product and also of the development method. It helps produce a software that is cost-effective, competent and of high quality. Once an application is created, the SDLC maps the proper delivery and retirement of the .The SDLC's usually contain the following stages: requirements analysis, design, implementation (construction), testing, release and maintenance. There are two types of SDLC that are widely in use today: waterfall and agile. The waterfall model is more customary and requires a well thought out plan and defined set of requirements in contrast to the agile SDLC which has less stringent guidelines and makes adjustments as needed.

WATERFALL MODEL

It is considered as the most basic software development life cycle model and is a linear and sequential approach to developing software. In this model, each process requires the need to be completed before moving on to the next phase. Progress is compared to a waterfall which gives the model its name. Also just like natural waterfalls where once the water has flowed through the edge of the cliff and began flowing downwards never turns back to reach the top of the hill the progress in the waterfall model can never be reverted i.e. we cannot turn back from one phase to the previous one. We have only one option and that is to move forward. This model is also called the **classic life cycle model** as it suggests a systematic sequential and classical approach to software development[2]. In a waterfall process, normally a documents is the output of each phase which serves as the input to the next phase. Team members cannot change the outputs that the project has certified. However, requirements are subject to change. There is thus a need for a mechanism which ensures that the modifications are done in a controlled manner without affecting the product and its progress. Companies like Toyota use this model for development.

The phases of a waterfall model can be generalized as follows-

1. Requirement Analysis and Specification Phase It is probably the most error prone, time consuming and the costliest phase. This phase aims to understand, gather and document the requirements of the user. Requirements of the user are the main reason for the development of software and hence are needed to be noted with precision. Requirement elicitation is a joint effort of the customers and the developers as the goal is to document all the functions, performance and interfacing requirements of the software product. This phase leads to the development of a large document written in natural language and which contains the "what"of system without describing the "how". This resultant document is called the *software requirement specification* (SRS) document. The SRS may act as a contract between the developer and the customer. In case of failure to fulfill the

ISSN: 2278 – 7798 All Rights Reserved © 2014 IJSETR

requirements in the SRS, the product may be termed as a failure.

2. Design Phase – The SRS document produced in the previous stage serves as the input of this phase. The requirements are to be transformed into a structure suitable for design and implementation in some suitable programming language. The overall architecture is defined and the high level detailed and designed work is performed. The work / progress is documented and is known as the software design description document (SDD). The SDD may contain technical jargons and tells also about the "how "of the software. The information provided in the SDD should be sufficient to start the designing.

3. Implementation and Unit Testing - Based on the information provided by the SDD the designers have to start building/developing the software. If the SDD contains all the required information and is complete, consistent and accurate then this phase should go smoothly. Testing focuses on the examination, correction and modification of the code. In unit testing the software is tested one module at a time independent of the other. Usually, this process of integration and system testing requires reworking the modules and writing new code to correct problems in the operation or interactions of the pieces due to unforeseen problems as well as mistakes, miscommunications, or changes that have crept into the design of the parts during the project. If this integration work goes well, the team will ship the product when there are no serious bugs (errors or defects) remaining.

4. Integration and System Testing – Unit testing poses the following problems a) How do we test individual modules without a driver function? b) It doesn't tell us anything about how different modules interact with each other. System testing overcomes this issue by testing the software as a whole. Effective testing will ensure higher quality of our software, more satisfied users, lesser maintenance cost and more accurate and reliable results. This phase is a very expensive activity and consumes upto one-half the cost of the total software budget.

5. Operation and Maintenance Phase- It is the phase that comes after the software has been released, installed and is operational. The maintenance phase starts with the very release of the software and continues throughout the life cycle of the software. Software maintenance includes error correction, enhancement of functions and capabilities, introduction of new functions, removal of obsolete ones and optimization of the software [3].

DISADVANTAGES

1. It requires all the requirements to be specified at the very start which is not possible for real life projects mostly because customers are notorious for changing their stated requirements. Also unless the developers and the requirement specifiers are highly skilled, it is hard to know exactly what is needed a phase until some time is on that phase. Thus the software is required to be highly flexible and adaptable with taking into considerations that requirements are subject to change.

2. Since the model is linear it does not allow changes to be accommodated.

3. A working product is not available till late.

4. Real projects are rarely sequential and hence the waterfall model doesn't scale up well to large projects.

5. It doesn't accommodate risks and uncertainty. Unless there is iteration and feedback, there may be no way to improve initial imperfections in one of the later phases.

6. It is a poor model for large and ongoing projects.

7. It is difficult to measure the progress at every stage of the model .also the time and cost taken by each phase is not determinable.

8. Integration is done at the very end which doesn't help in the identification of challenges and business bottlenecks early in the life cycle.

9. A lot of time is wasted while waiting for one phase to be completed. For e.g., When the designers are busy designing the software the builder's time is wasted. Constant testing of the design, its implementation and verification of every phase is required to validate the phases preceding them. Some may argue that that if we follow a designed process and don't allow any room for mistakes then there should be no need to constantly validate the preceding phases.

10. Development of the SRS may take a lot of time for largeprojects.

11. Coordination of the work of a large group of people building different components of the software requires a high level of management that the simple

ISSN: 2278 – 7798 All Rights Reserved © 2014 IJSETR

sequence of activities in the waterfall model cannot guarantee. To implement this synchronization and simultaneously provide programmers with the required amount of freedom is perhaps an problem that managers face.

ADVANTAGES

1. The major advantage of the waterfall or lifecyclemodel is that it provides a structure for organizing and controlling a software development project.

2. Design details and errors are captured by the model before any software is written and hence saving time during the development.

3. A proper technical document is made that makes it easy or the customers to know what they should expect from the software.The documentation also help in the process of maintenance.

4. If the procedure are followed properly then the cost and time estimation can be accurately done.

5. Because of its sequential and linear nature faults in one phase can be detected before moving on to the other.

6. A lot of emphasis is done on paperwork. Any new worker joining the development team may find It easy to catch up with the help of these documents.

7. For smaller projects it is the best model to use. Also it requires less resources compared to the others.

8.It allows departmentalization and managerial control. This allows the product to be completed on time by setting a schedule for every phase.

9. A project plan can be utilized for indistinguishable or comparable projects in the future.

Best for projects that deal with services oriented and non physical deliverables like code, copywriting and design projects.

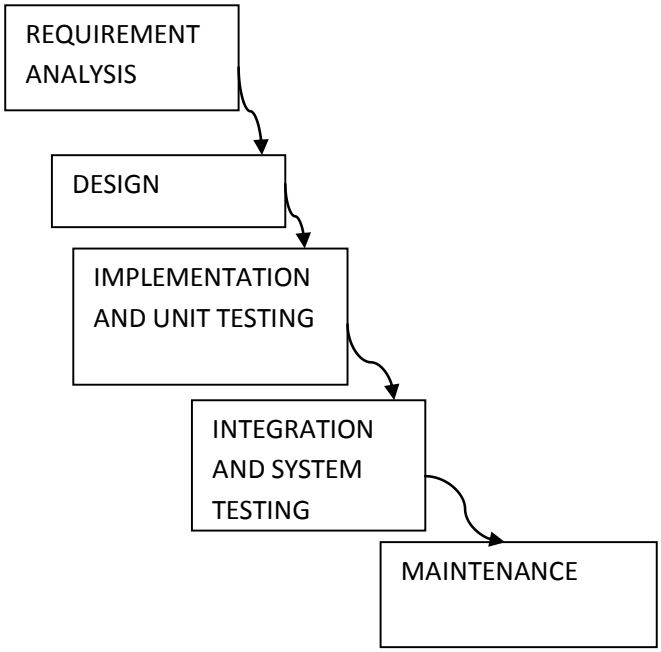
WHEN TO USE WATERFALL

1. When a clear picture of the final product is available.

2. When the requirements are well defined and understood and are not subject to change.

3. When the interest is on the final product to be developed rather that time being the concern.

The waterfall model works pretty well where the product development mainly consists of adding limited functionalities to an existing set of functionality. It also scales well for projects where changes in design can be introduced in a controlled way and the development can be continued without the requirement of customers or competitors. However waterfall model fails when there is so much new content or so many uncertainties to resolve that they become inevitable. For e.g. In the PC software market, for example, both hardware technologies and customer requirements change very rapidly. In such situations, capturing the specifications of a project at the very beginning is difficult. Consequently, the development cannot occur in a linear fashion. Any change in any part of the product for e.g., due to feedback from customers or evolution in particular hardware or software technologies, or even just to add a feature that a competitor has just introduced, may end up with pieces that no longer are compatible.



The testing fails. The project team now has to rework the pieces .Much of the developed product may now seem a waste .With these types of problems the software projects may exceed the time limit and end up being late, over budget, and with bugs. Alternatives to the waterfall have been proposed that use"iterative" approaches to development. These approaches see developers moving around in phases, vacillating between the designing, coding, and testing phase as the development of the software proceeds. This type of development in iteration is what many developers undergo in projects the though in an unplanned manner. Some companies refer to these iterations as "incremental builds". Many companies have started to move away from the classic waterfall model in practice although Companies still using elements of a waterfall process to plan and control software development can be found. For e.g., the U.S. Department of Defense, information system providers required the need to follow, as well as

ISSN: 2278 – 7798 All Rights Reserved © 2014 IJSETR

document their procedure and used the waterfall model.

AGILE MODEL

Agile development is in itself a huge umbrella term that includes other agile methodologies also. These initially include the Scrum, XP, Crystal, FDD, and DSDM [4]. However lean agile methodologies also have been included as they have emerged as valuable agile methodologies in the past. Agile models were specifically designed keeping the adaptability of changing requirements in mind. An agile method is a combination of iterative and incremental process models keeping in mind the flexibility and the timely delivery of the software. Agile models consider every development process to be different and believe that the existing methods need to be personalized in order to best suit the project requirements. Agile provides methods to assess the development and risks and also the direction throughout the development lifecycle.

The product is developed in a series of rounds known as iterations. Each iteration typically lasts for 2-3 weeks and involves various team's working simultaneously on various areas like requirement gathering, requirement elicitation, planning, design, coding and testing. Each iteration guarantees an enhancement in features of the product of the previous iteration and the final iteration product involves all the features demanded by the customer [5].Agile works on the following approaches-

1. Individuals and Interactions –In agile, self organization and encouragement are as important as are interactions like pair programming and co-location.

2. *Working Software*-Agile requires the need to develop a working prototype early in the life of a software and this prototype is often the best way to communicate with the stakeholders who can't appreciate the "how" of the software and technical jargons.

3. *Customer Involvement*-Since agile doesn't require all the requirements at the beginning of the software, it relies on customer interaction throughout the development.

***4. Quick Adaptability*-** Agile should be able to adapt to changing requirements quickly and as the need may be for the proper and timely development of the software. This "inspect and adapt" technique significantly decreases the development costs and time for shipment [6]. Teams can start developing their software in chorus with the requirement gathering process, which reduces the impact of the 'analysis paralysis 'on the progress. A team's work cycle is limited to 2 weeks because of which stakeholders have frequent opportunities to regulate releases for success. Agile helps develop the right software. It empowers companies to constantly enhance their products and plan their releases in order for better acceptance and greater success. Hence agile makes sure that the effort put in doesn't go waste and that the products market relevance doesn't drop and that the teams work doesn't wind up on a shelf, unreleased. An adaptive agile team will have difficulties describing how much progress will be observed in the next iteration or probably what risks might be encountered but it might be able to tell what are the functionalities that will be added to the product. The further away the deadline the vaguer is the idea. Each agile team contains a customer representative who is chosen by stakeholders to operate on their behalf and be available to answer questions that the developers have. At the end of each iteration, stakeholders and the customer representative evaluate the progress and reassess the priorities in order to optimize the return on investment (ROI) and for better alignment with customer needs and company goals. Companies like Pivotal Labs, Microsoft, RailsCarma etc use Agile mode of development.

ADVANTAGES

1. It takes the requirements and changing nature of software development in consideration and hence scales well for real life projects irrespective of their sizes.

2. It promotes team work. Everyone involved in the development process work together simultaneously on different areas of the software.

3. A working software product is available In the early phases of the software.

4. Agile doesn't dictate the need to document the work and minimal rules are employed. It also requires the minimum amount of resources compared to other models.

5. It makes planning just a voluntary phase and makes the process easy to manage and flexible.

ISSN: 2278 – 7798 All Rights Reserved © 2014 IJSETR

6. Developers and customers constantly communicate with each other and interaction with the customers is given more importance than the process and tools. This also helps in the understanding of what the users expect from the final product.

7. Best for projects that deal with services oriented and non physical deliverables like code, copywriting and design projects.

DISADVANTAGES

1. It is not suitable for handling complex dependencies and has more risk of extensibility, sustainability and maintainability. In case of some software deliverables it is difficult to assess the effort at the beginning of the process.

2. Though it doesn't require an initial planning phase it still requires an overall development plan. A good management system, an agile leader and a PM practice is required. Without them the project might not work.

3. Completion of work within a strict period of time with good quality and specified requirements makes it difficult to manage.

4. Customer involvement is a must. Without the cooperation of users the development process would be hampered and may lead to failure.

5. No importance on documentation is there and hence any new member joining the team may find it difficult to adjust. Also existing team members might need to reference the SRS sometimes and its absence can stir the development in a wrong direction.

6. Some decisions require the expertise of the senior software developers; hence novice developers are not really welcomed unless combined with experienced resources.

7. Due to development in iterations errors and risks are identified early.

8. Not suited for projects with strictly defined requirements and scope.

9. Requires vigilant backlog and documentation maintenance , and tech debt management.

WHEN TO USE AGILE

1. When the requirements of the software are not well specified or when the requirements are expected to change during later phases of the development process .In agile new changes can be implemented at a very low cost because of the frequency of new increments that are produced.

2. If freedom of options and time is required by both the developers and the stakeholders. Having options provides them with the facility to leave important decisions until more or better data are available and also the project can be continued without the fear of it being a failure.

II WHY NOT TRADITIONAL

Software is not hardware. Software cannot be developed like an automobile where each part is added in sequential phases , each phase depending on the previous one. *DR. Winston Royce* condemned the phase based approach in which there was a need to go sequentially in the order of requirement elicitation, design, implementation and then testing. He specifically dejected the idea of lack of communication between the customers and the developers.

It is easy to see why waterfall model is not feasible. Knowing all the requirements in the very start and not expecting them to change made no sense. A team might build the software on time with all the specifications taken care of but in the interim the realities might have changed dramatically that the product may seem irrelevant and may not be able to score well.

III AGILE VS TRADITIONAL

Agile Methods are considered to be at the opposite end of the "plan driven " or "disciplined" methods rainbow. Projects usually are considered as lying between the "adaptive" to "disciplined" range. Agile methods occupy the "adaptive" bandwidth. An adaptive agile team will have difficulties describing how much progress will be observed in the next iteration or probably what risks might be encountered but it might be able to tell what are the functionalities, that will be added to the product. The further away the deadline the more vague is the idea. Whereas the waterfall model is predictive which in contrast to the agile model focuses on planning for the future well ahead of time. A predictive can tell exactly how and by how much the software is going to develop and what changes might be observed. However the predictive teams are not ready for unidentified or unaccepted changes and have difficulty adjusting to them. The plan is set and accommodating new changes may mean that the

ISSN: 2278 – 7798 All Rights Reserved © 2014 IJSETR

process might have to be started all over again. Because of such an issue only the most important changes will be given a chance of being implemented[7].

IV WHAT IS YOUR METHODOLOGY?

Use Agile if...

1. If the requirements and functions are subject to change.

2. The product needs to be developed In a limited time.

3. A quick prototype with only certain functionalities is needed before the final product is available.

4. Agile requires the active participation of the stakeholders.

5. If the team is working on a highly collaborative, self organizing manner. Self organizing ensures that the team members are actively planning and estimating their own work.

6. If the team is willing to develop the software in installments.

Use Waterfall if...

1. The requirements are well defined and fixed.

2. There is no time limit or a reasonable amount of time is available to develop the software.

3. There is a need to document everything.

4. You need a safe software with a high reliability level.

5. You want to use the finished software.

6. You do not have resources for face-to-face everyday work.

V SIMILARITIES

1. Both provide methods, tools, techniques and well defined processes.

2. Both require a disciplined approach and have a pre decided finish time.

3. Both want customer satisfaction and want to adhere to the decided time and cost schedule.

VI MICROSOFT CASE STUDY

Many companies have begun to deviate from the waterfall style and make changes in order to be able to improve their capability to control changes in the software . One such company is Microsoft. After it had a number failed projects it could no longer have products involving small groups of programmers using *ad hoc* practices. As its customer support expanded there was a need to develop quality products and delivery problems became unacceptable. The dare Microsoft was facing was to introduce more structure and predictability into their loosely organized development practice and still have flexibility and creativity. Microsoft wanted a different process that would allow incremental approach to designing, respond to customer inputs, Build prototypes, and allows changes[8]. Microsoft includes the following phases in its product development.

1. Review and Planning- The number of releases required are planned with an explanation on why the particular release is required, and Their interdependencies with other products. The marketing team create sales forecasts on the basis of the product plans. The budget is then planned and the expected profit is calculated. Based on this analysis, a head-count is determined.

2. Development- Microsoft divides the development into three or four milestones, where each milestone has its own coding and testing phase. Groupings of features determine the milestones. The most difficult and important features are built first in contrast to the traditional SDLC's where the focus is on complete implementation of the specifications. As a result,
the pieces are put three or four times during the development with testing, debugging, and Integration activities all done in parallel in every milestone. Also it is assumed that specifications may change, so no specification documents are made at the start of a project. Microsoft creates a "build" of the product every day.

3.Testing Phase-Microsoft relies heavily on automated and manual testing by testers on a daily builds. Testing includes documentation, tutorials, set-up, hardware configurations, primary functions, and supporting utilities. Also, three types of beta tests are used to ensure better acceptance. Microsoft has introduced a parallel, incremental, and iterative but planned approach to product development that offers several benefits to the development organization:

1. It ***divides the large products into smaller controllable pieces*** (that can be created in a few months).

2. It ***enables projects to proceed methodically even when a complete and stable product cannot be determined*** at the project's beginning.

3. It ***allows large teams to work like small teams*** by dividing work into chunks, arranged in parallel but synchronized, and incremental.

VII CONCLUSION

Every project is different and requires to be handled differently. Hence, it is better not to grip on one particular methodology. the desires of the company

ISSN: 2278 – 7798 All Rights Reserved © 2014 IJSETR

and project are subject to change regularly, and one needs to be elastic in how to approach these projects for them to be successful. No single methodology is the panacea, so the trick is to determine which method works and tailor it to suit the individual needs.

VIII. ACKNOWLEDGMENT

I would like to take this opportunity to thank and express my deep respect and regard for ***MS.Smita Jhajharia(****Guest Faculty, DTU, Delhi****)*** *and* ***DR. Seema Verma (****Associate professor, Banasthali University)* for their exemplary guidance, constant encouragement and valuable feedback throughout the preperation of this paper.Their valuable suggestions were immensly helpful and working under them was a knowledgeable experience.

REFERENCES

[1] http://www.tutorialspoint.com/sdlc/

[2]http://www.codeproject.com/Articles/604417/Agile-software-development-methodologies-and-how-t

[3] Youssef Bassil " A Simulation Model for the Waterfall Software Development Life Cycle" International Journal of Engineering & Technology (IJET), ISSN: 2049-3444 May 2012

[4]http://en.wikibooks.org/wiki/Introduction_to_Software_Engineering/Process/Agile_Model

[5] Malik Hneif and Siew Hock Ow "Review Of Agile Methodologies In Software Development", International Journal of Research and Reviews in Applied Sciences ISSN: 2076-734X, October 2009

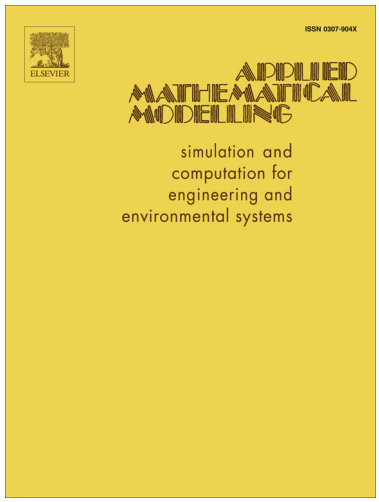
[6]http://www.ambysoft.com/essays/agileLifecycle.html

[7] http://www.base36.com/2012/12/agile-waterfall-methodologies-a-side-by-side-comparison/

[8] Michael A. Cusumano and Stanley Smith "Beyond the Waterfall:Software Development at Microsoft", August 16, 1995

ISSN: 2278 – 7798 All Rights Reserved © 2014 IJSETR

Accepted Manuscript



An Adaptive Mesh Strategy for Singularly Perturbed Convection Diffusion Problems

Vivek Kumar, Balaji Srinivasan

PII: S0307-904X(14)00492-2
DOI: http://dx.doi.org/10.1016/j.apm.2014.10.019
Reference: APM 10172

To appear in: *Appl. Math. Modelling*

Received Date: 25 October 2013
Revised Date: 9 August 2014
Accepted Date: 1 October 2014

Please cite this article as: V. Kumar, B. Srinivasan, An Adaptive Mesh Strategy for Singularly Perturbed Convection Diffusion Problems, *Appl. Math. Modelling* (2014), doi: http://dx.doi.org/10.1016/j.apm.2014.10.019

This is a PDF file of an unedited manuscript that has been accepted for publication. As a service to our customers we are providing this early version of the manuscript. The manuscript will undergo copyediting, typesetting, and review of the resulting proof before it is published in its final form. Please note that during the production process errors may be discovered which could affect the content, and all legal disclaimers that apply to the journal pertain.

ACCEPTED MANUSCRIPT

An Adaptive Mesh Strategy for Singularly Perturbed Convection Diffusion Problems

Vivek Kumar [1], **Balaji Srinivasan** [2]

Abstract

In this paper, a new adaptive mesh strategy has been developed for solving convection dominated, convection-diffusion singularly perturbed problems (SPP) using second order central difference schemes. Our strategy uses a novel, entropy-like variable as the adaptation parameter for convection diffusion SPP. Further, unlike the popular layer adapted meshes mainly by Bakhvalov (B-type) and Shishkin (S-type), no pre-knowledge of the location and width of the layers (boundary as well as interior) is needed. The method is completely free of arbitrary perturbation parameters ϵ (robust) and results in oscillation free solutions to a range of convection-diffusion SPP. Numerical results for various test problems: linear (boundary layers with and without turning points), nonlinear and systems of coupled equations are presented. This method is expected to aid in robust computations of convection dominated SPP.

Key Words

Central finite difference schemes, convection dominated singularly perturbed problems, layer-adaptive meshes.

1 Introduction

Singularly perturbed differential equations, which have non smooth solutions with singularities related boundary layers, and their numerical solutions have been quite an active field of research over the last few decades. Starting from late 60's by Bakhvalov [1], a large number of numerical techniques have been given by many researchers . Well developed techniques are now available for the numerical solutions of outside the layers regions but solving the problem inside the layers region is limited and still under investigation. To deal with such problems, robust layers resolving methods: methods which generates numerical approximation at each point in the domain for arbitrarily small values of the singular perturbation parameter ϵ are often needed in the real world applications. Layer adapted meshes have been first proposed by Bakhvalov for reaction diffusion equations and later on by Gartland [2] and others for convection diffusion equations. In early 90s , special piecewise uniform meshes have been introduced by Shishkin [3]. Because of simple structure of Shishkin meshes they have attracted much attention and are widely used for numerically approximation of SSP. The limitation with Shishkin meshes is the requirement of a-priori knowledge of the location of the layer regions. A detailed survey about

[1]Delhi Technological University, Deptt. of Applied Mathematics, Delhi - 110042, India, vivekkumar.ag@gmail.com

[2]Indian Institute of Technology, Deptt. of Applied Mechanics, Delhi - 110016, India, balaji.srinivasan@gmail.com

ACCEPTED MANUSCRIPT

layer adapted meshes for convection diffusion equations can be found in [5].

It is well known that whenever central finite difference schemes (second order or higher order central schemes, non-monotone methods) are applied to solve convection diffusion singularly perturbed problems numerically on uniform meshes, unphysical oscillations are observed in the numerical solution and their magnitude increases in the layers (boundary and interior) regions. The presence of these large unphysical oscillations in the approximated solution shows that central finite difference operators on the uniform meshes are unstable below a certain value of the singular perturbation parameter. To eliminate these oscillations while retaining the order of accuracy, one needs either a fine mesh at the layer. This maybe done either via uniformly fine meshing or via an adaptive mesh strategy. The former strategy increases significantly in computational cost as the perturbation parameter ϵ decreases. In this paper, we exploit such oscillations indirectly to locate the layers regions and then generate the layer adaptive meshes, via an entropy production operator which is positive automatically whenever the solution is unphysical, which effectively corresponds to insufficient resolution. We restrict ourselves to the class of SPPs which correspond to second order boundary value problems with a non-zero coefficient of the convection (first derivative) term.
Section 2 has been dedicated to adaptive mesh strategies and various numerical results have been discussed in section 3 followed by the conclusion.

2 Adaptive mesh strategy

2.1 Linear convection diffusion problems

We consider the following one dimensional steady-state convection diffusion problem as

$$\mathcal{L}u(x) = -\epsilon u''(x) - a(x)u'(x) + b(x)u(x) = f \in (0,1), u(0) = \alpha, u(1) = \beta \qquad (2.1)$$

with a small positive perturbation parameter ϵ. The above equation physically represents the steady state of transport of a passive scalar by a background velocity. For instance, $u(x)$ could represent the temperature and $a(x)$ could represent the (possibly spatially varying) background velocity and ϵ is the diffusion coefficient. As ϵ becomes smaller, convective processes start dominating over the diffusive processes [6]. Without loss of generality, we consider $b(x) \geq 0$ and $a(x)$ can change the sign (as in the case of turning point problem) in the given domain $[0,1]$. For $a(x) \geq \gamma > 0$, the above problem has unique solution and exhibit a boundary layer of $O(\epsilon)$ at $x = 0$. It was proved by Kellogg and Tsan [4] that u and its derivatives up to an arbitrary prescribed order q (depending on the smoothness of the data) can be bounded by

$$|u^{(k)}(x)| \leq C\{1 + \epsilon^{-k} e^{-\gamma x/\epsilon}\}, \quad \text{for } k = 0, 1, \ldots, q \text{ and } x \in [0,1],$$

where C denotes a generic positive constant independent of ϵ and the number of mesh points used.

We now define an auxiliary equation – the entropy production equation – by multiplying with an appropriate test function. From the case of scalar hyperbolic conservation

ACCEPTED MANUSCRIPT

laws [7] , it is well known that for scalar conservation laws, u^2 is always an appropraite entropy variable and, therefore, $2u(x)$ is a suitable multiplying test function. On mutiplying (component wise), we obtain

$$\mathcal{L}u * 2u = f * 2u; \tag{2.2}$$

after performing the calculation we can write the above equation (2.2) as

$$-\epsilon(S'' - 2(u')^2) - aS' + 2bS - 2uf = 0 \text{ where } S = u^2. \tag{2.3}$$

Rewriting the above equation , we get

$$-\epsilon S'' - aS' - 2uf = -2bS - 2\epsilon(u')^2. \tag{2.4}$$

We label the linear operator on the left hand side (LHS) in the above equation (2.4), as the entropy production operator with analogy to similar operators in hyperbolic conservation laws [7]. The continuous operator should obviously be negative for all $x \in [0, 1]$ (as right hand side (RHS) is always negative for all $x \in [0, 1]$).

Main Idea: As we know that if we solve the discrete analogue of equation (2.1) computationally using central difference method, we get non physical oscillations inside and near the boundary layer region. Similarly if we calculate the discrete analogue of the left hand side equation in (2.4) using the same central difference operator by taking $S_i = u_i^2$, where u_i is the central difference computed solution for equation (2.1), we observe that LHS is negative wherever the solution is smooth enough and positive where we have boundary layers (or oscillation in the computed solution of equation (2.1)). After investigation, we have found that if we write the RHS term $-2bu^2 - 2\epsilon(u')^2$ of equation (2.4) in difference operator at the ith mesh point, we get

$$-2b_i(u_i u_{i-1}) - 2\epsilon(\frac{u_i - u_{i-1}}{x_i - x_{i-1}})(\frac{u_{i+1} - u_i}{x_{i+1} - x_i}) \tag{2.5}$$

by applying a combination of forward and backward difference operator for u' and $(u_{i-1}u_i)$for u^2 which are of opposite sign wherever the oscillations occur and hence results in positive value of the difference operator as in equation (2.4) for the oscillatory numerical solution u_i. We exploit this property of the entropy production operator to precisely determine regions of insufficient resolution in what follows.

2.2 Adaptive mesh Generation Algorithm

To generate the adaptive mesh for the convection dominant SPP, we follow the following algorithm:
Step 1: Calculate the entropy with a minimum number of initial uniform mesh points (minimum 3 points in our case).
Step 2: Locate the mesh points where entropy S is positive and then choose the mesh point with the maximum entropy.
Step 3: Add one mesh point on the left and the right side of the location found in step 2.
Step 4: go to Step 1 till all the entropy becomes non positive over the complete mesh.
The resulting mesh is our adapted mesh which is represented by N_a.

ACCEPTED MANUSCRIPT

2.3 Entropy calculation at the boundaries

For a general Dirichlet boundary conditions (DBCs)

$$u(x_L) = u_L; u(x_R) = u_R$$

we introduce a ghost point say x_0 at the left of the node x_L and x_{n+1} on the right of the

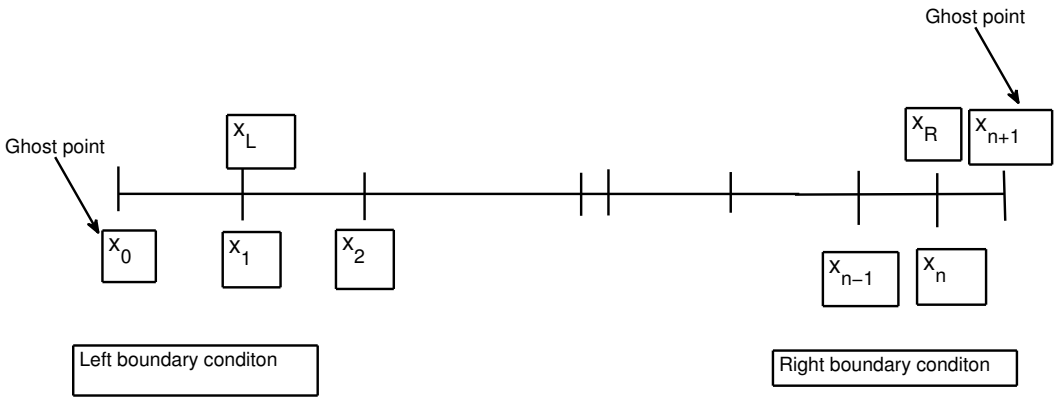


Figure 1: Ghost points at the left and the right boundaries.

node x_R as shown in the figure 1, then we calculate

$$-\epsilon\delta^2 u_1 - a_1 D^0 u_1 + b_1 u_1 = f_1 \quad (2.6)$$

$$-\epsilon\delta^2 u_n - a_n D^0 u_n + b_n u_n = f_n \quad (2.7)$$

As we already know the computed values of u_1, u_2 and then we calculate u_0 at the ghost point x_0 . Then we can find the entropy at the node x_L as usual (discussed above in equation (2.4)). Similarly we can calculate the entropy at the right boundary node x_R.

2.4 Finite Difference Operators for a Non-Uniform Mesh

Let u be any mesh function defined on a given non uniform (or adaptive mesh N_a) mesh $x_i,\ i = 0, 1, ...N;\ x_i \in (0, 1)$. The first order forward, backward and centered finite difference operators D^+, D^-, D^0 can be defined as:

$$\begin{aligned} D^+u(x_i) &= \tfrac{u(x_{i+1})-u(x_i)}{x_{i+1}-x_i}, \\ D^-u(x_i) &= \tfrac{u(x_i)-u(x_{i-1})}{x_i-x_{i-1}}, \\ D^0u(x_i) &= \tfrac{u(x_{i+1})-u(x_{i-1})}{x_{i+1}-x_{i-1}} \end{aligned} \quad (2.8)$$

ACCEPTED MANUSCRIPT

and the second order centered difference operator δ^2 is defined by

$$\delta^2 u(x_i) = \frac{2(D^+u(x_i) - D^-u(x_i))}{x_{i+1} - x_{i-1}}. \tag{2.9}$$

3 Numerical Results

In this section we solve different types of various examples to validate the proposed adaptive method. Without loss of generality, now onward we represent $u(x, \epsilon)$ as u.

3.1 One dimensional (1D) linear convection diffusion problems

Test case 1 [8]: We consider 1D linear convection-diffusion problem as

$$-\epsilon u'' - 2u' = 0; x \in (0, 1), 0 < \epsilon << 1, \tag{3.10}$$

with boundary conditions

$$u(0) = 1 \text{ and } \quad u(1) = 0; \tag{3.11}$$

The exact solution is

$$u = \frac{\exp(-2x/\epsilon) - \exp(-2/\epsilon)}{1 - \exp(-2/\epsilon)}. \tag{3.12}$$

This problem has regular boundary layers of width $O(\epsilon)$ at $x = 0$. When we apply central difference scheme on uniform mesh for this problem, we get

$$(\frac{-\epsilon}{h^2} + \frac{1}{h})u_{i-1} + \frac{2\epsilon}{h^2}u_i + (\frac{-\epsilon}{h^2} - \frac{1}{h})u_{i+1} = 0. \tag{3.13}$$

On solving the corresponding linear difference equation as given in the equation 3.13, we get

$$u_i = \frac{\tau^i - \tau^N}{1 - \tau^N}, \text{ where } \tau = \frac{1 - (1/\epsilon N)}{1 + (1/\epsilon N)}. \tag{3.14}$$

Where $h = 1/N$ with N number of mesh points. Now if we take $\epsilon < h$ then for ϵ sufficiently small, we have $\tau < 0$ and τ^i is positive or negative depending on whether i is even or odd. In that case the exact solution of the difference equation (3.13) will show some non physical oscillations, which increases unboundedly for N even and $\lim \epsilon \to 0$. This behaviour is completely different from the exact solution as given above (3.12), which is smooth and decreases from 1 to 0. The numerical approximated solution on a uniform mesh for $\epsilon = 10^{-5}$ and $N = 500$ is shown below in Figure 2(a). Figure 3(b) shows that the boundary layer is resolved very well with adaptive mesh containing only 30 points. Table 1 shows the maximum error computed for the corresponding adaptive meshes using central (CS) and upwind schemes (US) for various values of ϵ. Table 1 illustrates the uniformity in ϵ of the method.

The proposed method also satisfies $\epsilon \leq \frac{\gamma}{2}N_a^{-1}$ as is generally the case for discretizations of convection-dominated problems . As discussed in [5], the central difference discrete operator say L is (l_∞, l_1) stable for any mesh function u (computed solution in our case) given on any arbitarary mesh ω (adaptive mesh in our case) with

ACCEPTED MANUSCRIPT

$$||u||_{\infty,\omega} \leq \frac{81}{4\gamma} \sum_{i=1}^{N_a-1} \bar{h_i}|[Lu]_i| \text{ where } \bar{h_i} = \frac{h_i + h_{i+1}}{2}; \;\; h_i = x_i - x_{i-1}. \tag{3.15}$$

provided

$$|\prod_{i=1}^{N_a}(\frac{\epsilon}{h_i a_{i-1}} - \frac{1}{2})/(\frac{\epsilon}{h_i a_i} + \frac{1}{2})| \leq 1/4$$

and $h_i \leq ch_j$ for $i \leq j$ with some constant c. We have calculated the bound as given in equation (3.15) for various values of ϵ as shown in the table 2. Figure 3(a) shows the maximum error verses various values of ϵ and N_a using central and upwind schemes. We observe that results corresponding to central schemes are better than upwind scheme, which is of first order, using the proposed adaptive mesh. Therefore, we can claim that the proposed method is definitely better than first order but lesser than second order which is the case for uniform meshes for $\epsilon = 1$. Reduction in order of convergence is the price one has to pay for working with nonuniform adaptive meshes. Figure 3(b) illustrates the distribution of mesh points in the boundary layer region corresponding to different schemes.

Table 1: Maximum errors for central and upwind schemes using same adaptive mesh having points N_a for test case 1

ϵ	Central scheme	Upwind scheme	N_a
2^{-4}	0.1353352	0.2209561	07
2^{-6}	0.1353352	0.2218050	09
2^{-8}	0.1353352	0.2218075	11
2^{-10}	0.1353352	0.2218075	13
2^{-12}	0.1353352	0.2218075	15
2^{-14}	0.1353352	0.2218075	17
2^{-16}	0.1353352	0.2218075	19
2^{-18}	0.1353352	0.2218075	21

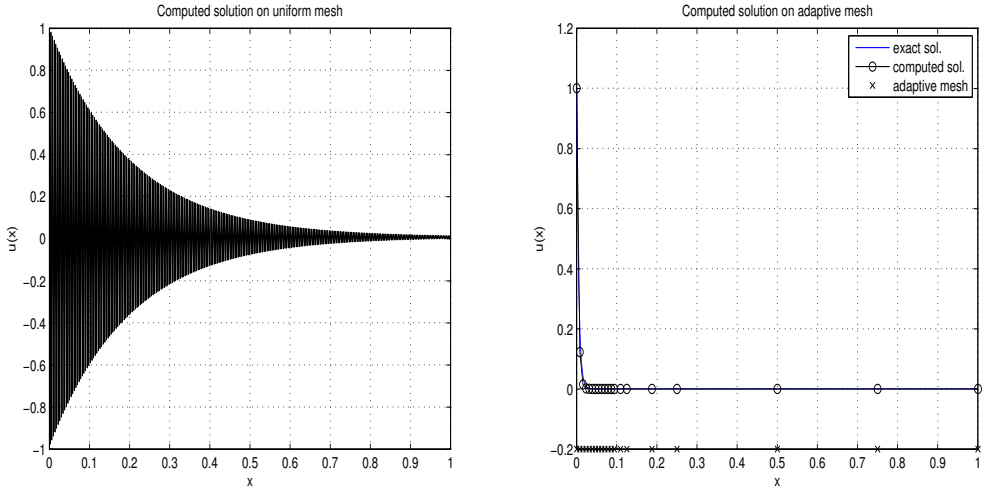
Table 2: Maximum errors, number of adaptive mesh points N_a and bounds (3.15) for u for the test case 1

ϵ	Max. error	N_a	bound (3.15) central	bounds (3.15) upwind
10^{-2}	0.0868	20	2.8350	9.0088
10^{-4}	0.0531	29	6.4638	12.0296
10^{-5}	0.0830	30	3.1460	9.2625
10^{-7}	0.0505	45	6.8619	12.3680
10^{-8}	0.0793	42	3.4645	9.5234

Test case 2 [9]: We consider another 1D linear convection-diffusion problem with non zero source term as

$$-\epsilon u'' + u' + u = \cos(\pi x); x \in (0,1), 0 < \epsilon << 1, \tag{3.16}$$

ACCEPTED MANUSCRIPT



(a) For uniform mesh with $N = 500$ mesh points (b) For adaptive mesh with $N_a = 30$ mesh points

Figure 2: Results for the test case 1 for $\epsilon = 10^{-5}$.

with boundary conditions

$$u(0) = 0 \text{ and } \quad u(1) = 0; \tag{3.17}$$

The exact solution is

$$u = a\cos(\pi x) + b\sin(\pi x) + A\exp(\lambda_0 x) + B\exp(-\lambda_1(1-x)). \tag{3.18}$$

where $\lambda_0 < 0$ and $\lambda_1 > 0$ are the real solutions of the characteristic equation $\epsilon\lambda^2+\lambda+1 = 0$, and

$$a = \frac{\epsilon\pi^2 + 1}{\pi^2 + (\epsilon\pi^2+1)^2}, b = \frac{\pi}{\pi^2 + (\epsilon\pi^2+1)^2}$$

$$A = -a\frac{1+\exp(-\lambda_1)}{1-\exp(\lambda_0-\lambda_1)}, B = a\frac{1+\exp(\lambda_0)}{1-\exp(\lambda_0-\lambda_1)}$$

Table 3 shows the maximum error computed for the corresponding adaptive meshes.

Test case 3 [9]: We consider another 1D linear convection-diffusion problem as

$$-\epsilon u'' + u' + (1+\epsilon)u = 0; x \in (0,1), 0 < \epsilon << 1, \tag{3.19}$$

with boundary conditions

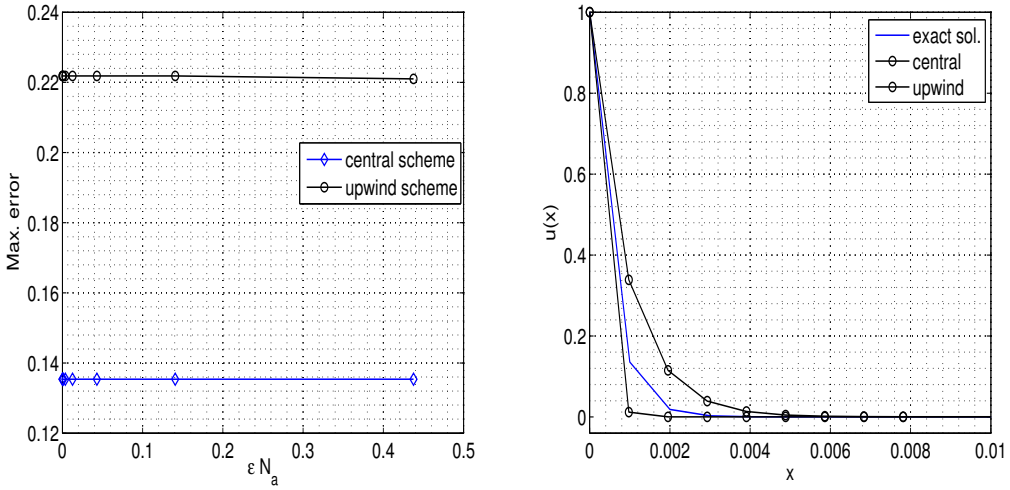
$$u(0) = 1 + \exp(-(1+\epsilon)/\epsilon) \text{ and } \quad u(1) = 1 + \exp(-1); \tag{3.20}$$

The exact solution is

$$u = \exp(\frac{(1+\epsilon)(x-1)}{\epsilon} + \exp(-x). \tag{3.21}$$

In this problem the coefficient of reaction term and left boundary condition are the function of perturbation parameter ϵ. Table 4 shows the maximum error computed for the corresponding adaptive meshes. We have calculated the bound as given in equation (3.15)

ACCEPTED MANUSCRIPT



(a) Max. error using central and upwind schemes for the same adaptive mesh

(b) Comparision of the boundary layer in the numerical solutions generated by central and upwind schemes

Figure 3: Results for the test cass 1

for various values of ϵ as shown in the table 4, that also varifies the uniform convergence of the proposed method. Figure 4(a) shows the maximum error verses various values of ϵ and N_a using central and upwind schemes. We again, observe that the results corresponding to central schemes are better than upwind scheme using the proposed adaptive mesh. Figure 4(b) illustrates the distribution of mesh points in the boundary layer region corresponding to different schemes.

Test case 4 : [10] We consider 1D linear convection-diffusion problem with turning point as

$$-\epsilon u'' + 2(2x-1)u' + 4u = 0; x \in (0,1), 0 < \epsilon << 1, \tag{3.22}$$

with boundary conditions

$$u(0) = 1 \text{ and } \quad u(1) = 1; \tag{3.23}$$

The exact solution is

$$u = \exp(\frac{-2x(1-x)}{\epsilon}). \tag{3.24}$$

This test case has a turning point at $x = 1/2$. In this case we have boundary layers at both the boundary points and the turning point does not coincide with the layer region. Such type of problems are hard to solve with the conventional methods. The proposed method gives quite impressive results as shown in the figures 5. Table 5 shows the maximum error computed for the corresponding adaptive meshes.

3.2 System of coupled convection diffusion problems

We also consider the coupled system of singularly perturbed convection diffusion problem given as

ACCEPTED MANUSCRIPT

Table 3: Maximum errors and Adaptive mesh points for test case 2, and starting number of uniform mesh points N=5

ϵ	Max. error	N_a
10^{-2}	0.0308	09
10^{-3}	0.0385	12
10^{-4}	0.0256	16
10^{-5}	0.0299	19
10^{-6}	0.0376	22
10^{-7}	0.0255	30
10^{-8}	0.0291	31
10^{-9}	0.0367	34
10^{-10}	0.0255	40

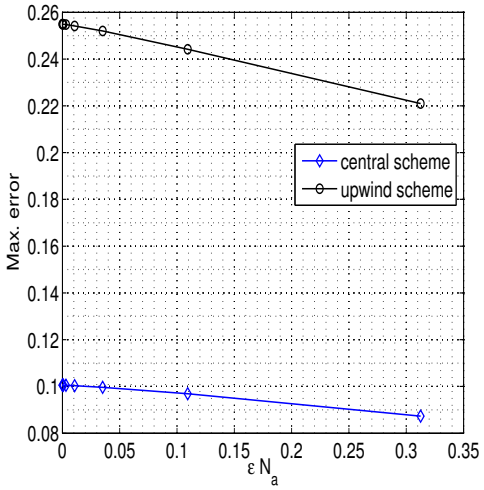
Table 4: Maximum errors, number of adaptive mesh points N_a and bounds (3.15) for u for the test case 3

ϵ	Max. error (CS)	Max. error (US)	N_a	bounds (3.15) (CS)	bounds (3.15) (US)
2^{-4}	0.0873306	0.2209864	5	12.656	20.196
2^{-6}	0.0968888	0.2442103	7	10.757	18.159
2^{-8}	0.0996411	0.2520102	9	10.283	17.606
2^{-10}	0.1003516	0.2541902	11	10.164	17.466
2^{-12}	0.1005307	0.2547530	13	10.134	17.431
2^{-14}	0.1005755	0.2548949	15	10.127	17.423
2^{-16}	0.1005868	0.2549305	17	10.125	17.420
2^{-18}	0.1005896	0.2549393	19	10.125	17.420

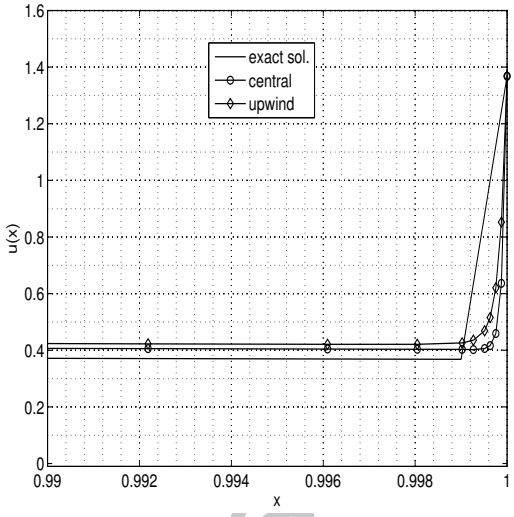
Table 5: Maximum errors and adaptive mesh points for test case 4, and starting no. of points N=3

ϵ	Max. error	N_a
10^{-2}	0.0825	35
10^{-3}	0.1293	29
10^{-4}	0.0530	53
10^{-5}	0.0830	55
10^{-6}	0.1248	49
10^{-7}	0.0505	85
10^{-8}	0.0793	79
10^{-9}	0.1197	69
10^{-10}	0.0480	109

ACCEPTED MANUSCRIPT



(a) Max. error using central and upwind schemes for the same adaptive mesh



(b) Comparision of the boundary layer in the numerical solutions generated by central and upwind schemes

Figure 4: Results for the test case 3

$$-\epsilon_1 u_1'' - a_1(x)u_1' + b_1(x)u_1 + c_1(x)u_2 = f_1(x), u_1(0) = \alpha_1, u_1(1) = \beta_1 \quad (3.25)$$
$$-\epsilon_2 u_2'' - a_2(x)u_2' + b_2(x)u_2 + c_2(x)u_1 = f_2(x), u_2(0) = \alpha_2, u_2(1) = \beta_2 \quad (3.26)$$

with two overlapping layers near x = 0 (assuming $a_1(x), a_2(x) \geq 0$). Such problems can have perturbation parameters ϵ_1, ϵ_2 of different magnitude. These types of problems have been solved widely using upwind methods on Shishkin type meshes and more literature can be found in paper [11]. The corresponding entropy production operator equations can be found by taking inner product of each of the equation of the coupled systems with respect to $2u_1(x)$ and $2u_2(x)$ respectively as given

$$-\epsilon_1(S_1'' - 2(u_1')^2) - a_1 S_1' + 2b_1 S_1 + 2c_1 u_1 u_2 = 2u_1 f_1 \quad (3.27)$$
$$-\epsilon_2(S_2'' - 2(u_2')^2) - a_2 S_2' + 2b_2 S_2 + 2c_2 u_1 u_2 = 2u_2 f_2. \quad (3.28)$$

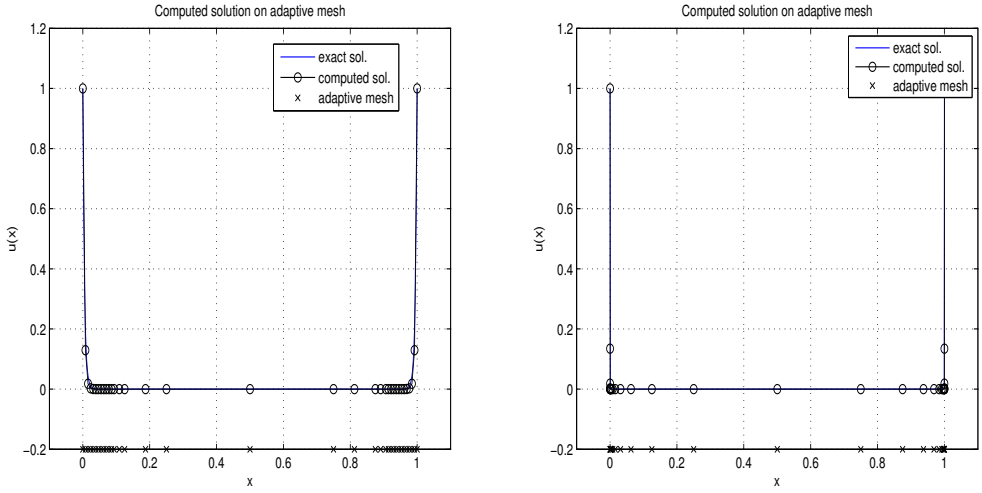
The entropies can be calculated at the boundaries points in the same way as done before in the linear case. Results by the proposed method are discussed for the following test case.

Test case 5 : We consider system of coupled convection-diffusion problem as [11]

$$-\epsilon_1 u_1'' - u_1' + 2u_1 - u_2 = \exp(x), u_1(0) = 0, u_1(1) = 0 \quad (3.29)$$
$$-\epsilon_2 u_2'' - 2u_2' + 4u_2 - u_1 = \cos(x), u_2(0) = 0, u_2(1) = 0 \quad (3.30)$$

which shows two overlapping layers near x = 0. The exact solution of this equation is not known. The results for various values of ϵ_1 and ϵ_2 for adaptive meshes have been shown in the figures 6 and 7. In the figure 6, we have generated the adaptive mesh by

ACCEPTED MANUSCRIPT



(a) For $\epsilon = 10^{-2}$ with $N_a = 35$ adaptive mesh points

(b) For $\epsilon = 10^{-5}$ with $N_a = 55$ adaptive mesh points

Figure 5: Results for test case 4.

taking maximum of the entropies S_1, S_2. The results show the required adaptive mesh but some unexpected adaptive mesh points can be seen near boundary point $x = 1$. So, we have generated the adaptive mesh by taking minimum of the entropies S_1, S_2 and the corresponding results are shown in the figure 7. The adaptive mesh seems better by taking choice of minimum as compared to maximum for the entropies S_1, S_2.

3.3 Nonlinear convection diffusion problems

We also consider the nonlinear singularly perturbed boundary value problem [12]

$$-\epsilon u''(x) - u(x)(u'(x) - 1) = 0 \in (0, 1), u(a) = \alpha, u(b) = \beta; a \leq x \leq b \tag{3.31}$$

The resulting finite difference equations give a system of non-linear equations. As suggested by [12], for efficient solution of these equations, we use Newton-Raphson iterations to determine the solution of the non-linear system. The initial guess for the solution is the approximate solution given by

$$u(x) = x - \bar{x} + w_0 \tanh(w_0(x - \bar{x})/(2\epsilon)) \tag{3.32}$$

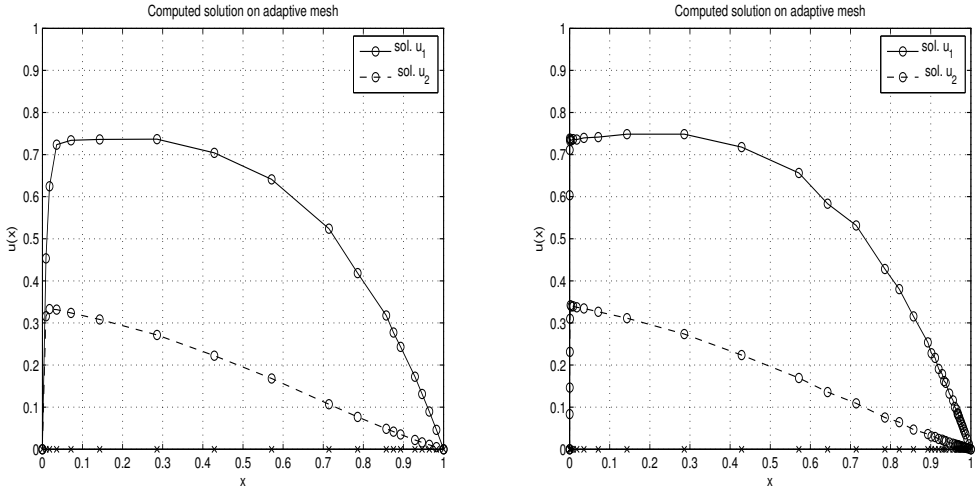
where

$$\bar{x} = 0.5(a + b - \alpha - \beta), w_0 = 0.5(a - b + \beta - \alpha).$$

This problem shows an interior layer at $x = 0.25$ for $a = 0, b = 1, \alpha = -1$ and $\beta = 1.5$. Its conservative form can be written as

$$-\epsilon u''(x) - (\frac{u^2(x)}{2})' + u(x) = 0 \in (0, 1), u(a) = \alpha, u(b) = \beta; a \leq x \leq b \tag{3.33}$$

ACCEPTED MANUSCRIPT



(a) Adaptive mesh points $N_a = 19$ for $\epsilon_1 = .01$ and $\epsilon_2 = .01$

(b) Adaptive mesh points $N_a = 45$ for $\epsilon_1 = .0001$ and $\epsilon_2 = .001$

Figure 6: Results for coupled case with starting uniform mesh for N=8, using maximum entropy condition.

There are several choices for the entropy production equation. Again, in analogy to the entropy equation in hyperbolic conservation laws, we use the conservative of the entropy equation which can be obtained as

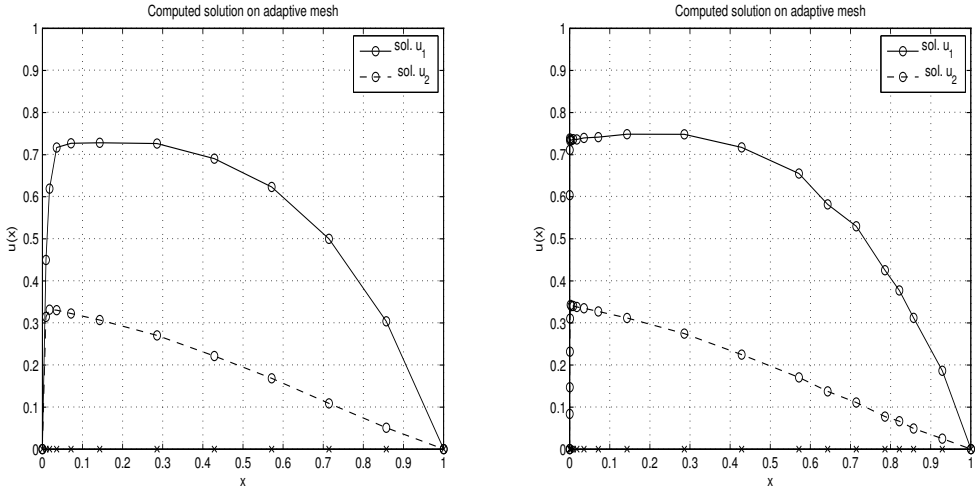
$$-\epsilon S''(x) - (\frac{2u^3(x)}{3})' + 2S(x) = -2\epsilon(u'(x))^2 \tag{3.34}$$

The above choice, with a conservative operator on the left, is the one that captures the correct location of the interior layer. Figures 8 and 9 show the result of the adapted mesh obtained for different values of the perturbation parameter. As can be seen, points are clustered correctly right around the location of the interior layer. This shows the robustness of the current approach as it works on both linear and non-linear problems with equal felicity.

4 Conclusions

In this paper we have presented a new type of robust layer resolving method to deal with oscillation produced by central finite difference method, which is a non-monotone ϵ uniform, when applied to convection dominated singularly perturbed problems with the help of entropy-like variable as the adaptation parameter. We have tested our proposed method for varieties of problems (linear problem with and without turning point, nonlinear and coupled systems of equations) and results seems worth when dealing with SPP. The proposed method can be considered as an initiative for an alternative to B-type or S-type meshes layers resolving meshes.
Our hope is to ultimately extend this method to the Navier-Stokes equations. The coupled and nonlinear cases presented above were done with this in mind. We believe this

ACCEPTED MANUSCRIPT



(a) Adaptive mesh points $N_a = 12$ for $\epsilon_1 = .01$ and $\epsilon_2 = .01$

(b) Adaptive mesh points $N_a = 22$ for $\epsilon_1 = .0001$ and $\epsilon_2 = .001$

Figure 7: Results for coupled case with starting unifrom mesh for N=8, using minimum entropy condition.

extension is possible since there is an essentially unique entropy variable for the three-dimensional Navier-Stokes equations. However, several essential gaps need to be filled before this may be attempted. Most importantly, we have found the method presented above to be particularly resistant to any usual methods of convergence analysis. We believe that the encouraging results obtained herein warrant a closer look at methods that could give estimates of convergence rates and convergence behavior. This would be an important step in determining the actual potential of the method.

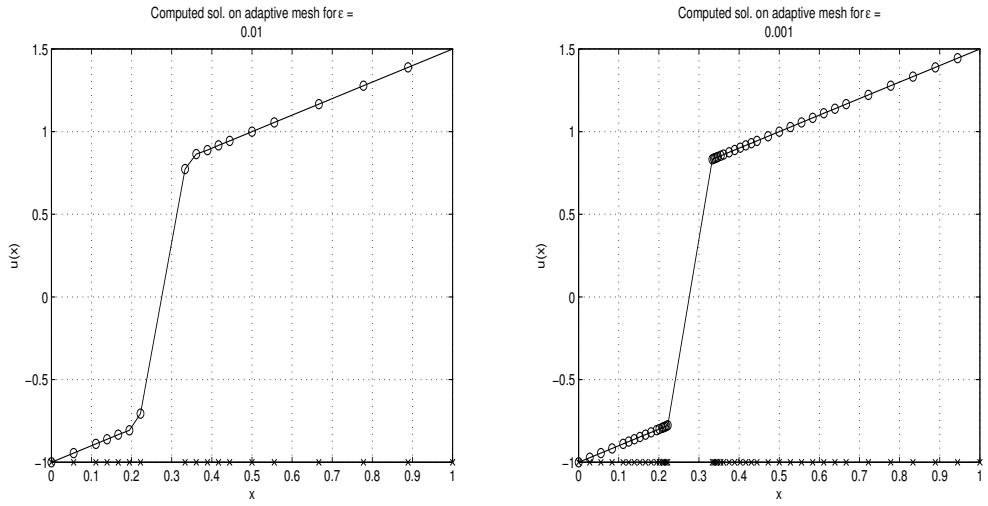
We know from the previous experience of using central difference schemes (non monotone method), one need to choose appropriate values of the turning parameters in order to suppress non-physical oscillations in the numerical solutions using piecewise uniform meshes of S-type and choice of the parameter is also ad hoc. In the proposed method this problems has already been taken care automatically. Also the proposed method seems to be ϵ uniform of order not less than the order of the first order upwind schemes. Only few theoretical analysis of the convergence of non monotone methods has been established so far by researchers for piecewise uniform meshes of S and B-type but is still in its infancy for a completely arbitrary (i.e. non pre-defined) meshes for SPP as discussed in this paper.

Finally, it must be mentioned that, in our experience, the above method is effective only for problems with non-zero convection coefficient. There exist BVPs such as the Bratu problem [13] which do not fall under this category and require other approaches.

Acknowledgement

We would like to thank the reviewers for their valuable and constructive comments and suggestions.

ACCEPTED MANUSCRIPT



(a) Adaptive mesh points $N_a = 18$ for $\epsilon = .01$ (b) Adaptive mesh points $N_a = 44$ for $\epsilon = .001$

Figure 8: Results for nonlinear case with starting uniform mesh with N=10.

References

[1] N.S. Bakhvalov " Towards optimization of methods for solving boundary value problems in the presence of boundary layers" *Zh. Vychisl. Mater. Fiz.* , 9, 1969, 841-859 (In Russian).

[2] E.C. Gartland " Graded-mesh difference schemes for singularly perturbed two-point boundary value problems" *Math. Comput.*, 51, 184, 1988, 631657.

[3] J.J.H. Miller, E. ORiordan, I.G. Shishkin " Fitted Numerical Methods for Singular Perturbation Problems" *World Scientific*, Singapore, 1996.

[4] R.B. Kellogg, A. Tsan "Analysis of some difference approximations for a singular perturbation problem without turning points", *Math. Comp.*, 32, 1978, 1025-1039.

[5] Torsten Linb " Layer-adapted meshes for convection - diffusion problems" *Comput. methods Appl. Mech. Engrg.* , 192, 2003, 1061-1105.

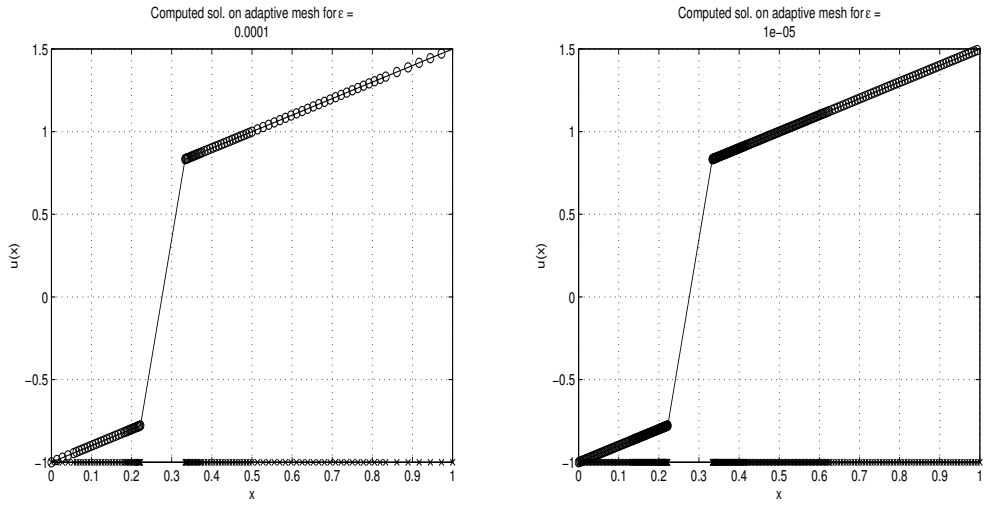
[6] S.V. Patankar " Numerical Heat Transfer and Fluid Flow" *Hemisphere*, Washington, DC, 1980.

[7] R. J. Leveque "Finite Volume Methods for Hyperbolic Problems" *Cambridge University Press* , 2002

[8] P.A. Farrell, A. Hegarty, J.J.H. Miller, E. O'Riordan, G.I. Shishkin "Robust Computational Techniques for Boundary Layers", *Chapman and Hall*, 2000.

[9] Mohan K. Kadalbajoo, Vikas Gupta " Numerical solution of singularly perturbed convectiondiffusion problem using parameter uniform B-spline collocation method" *J. Math. Anal. Appl.* , 355 (2009) 439452.

ACCEPTED MANUSCRIPT



(a) Adaptive mesh points $N_a = 100$ for $\epsilon = .0001$ (b) Adaptive mesh points $N_a = 272$ for $\epsilon = .00001$

Figure 9: Results for nonlinear case with starting uniform mesh with N=10.

[10] P.Lagerstrom " Matched Asymptotic Expansions" *Springer* , New York, 1988.

[11] Torsten Linb " Analysis of an upwind finite-difference scheme for a system of coupled singularly perturbed convection-diffusion equations" *Computing* , 79, 2007, 2332.

[12] R. J. Leveque " Finite difference methods for ordinary and partial differential equations" *SIAM* , 2007.

[13] A. Mohsen " A simple solution of the Bratu problem" *Computers and Mathematics with Applications*, 67, 2014, 2633.

Proceedings of the World Congress on Engineering 2014 Vol I,
WCE 2014, July 2 - 4, 2014, London, U.K.

Analysis of Software Project Reports for Defect Prediction Using KNN

Rajni Jindal, Ruchika Malhotra and Abha Jain

***Abstract*— Defect severity assessment is highly essential for the software practitioners so that they can focus their attention and resources on the defects having a higher priority than the other defects. This would directly impact resource allocation and planning of subsequent defect fixing activities. In this paper, we intend to predict a model which will be used to assign a severity level to each of the defect found during testing. The model is based on text mining and machine learning technique. We have used KNN machine learning method to predict the model employed on an open source NASA dataset available in the PITS database. Area Under the Curve (AUC) obtained from Receiver Operating Characteristics (ROC) analysis is used as the performance measure to validate and analyze the results. The obtained results show that the performance of KNN technique is exceptionally well in predicting the defects corresponding to top 100 words for all the severity levels. Its performance is less for top 5 words, better for top 25 words and still better for top 50 words. Hence, with these results, it is reasonable to claim that the performance of KNN is dependent on the number of words selected as independent features. As the number of words increases, the performance of KNN also gets better. Apart from this, it has been noted that KNN method works best for medium severity defects as compared to the other severity defects.**

***Index Terms*—Receiver Operating Characteristics, Text mining, Machine Learning, Defect, Severity, K-Nearest Neighbour**

I. Introduction

Now-a-days, various defect reporting/ tracking systems such as Bugzilla, CVS etc. are maintained for open source software repositories. These systems play an important role in tracking the defects which may be introduced in the source code [14]. These defects are then reported in a defect management system (DMS) for further analysis. Although, the issues of software are tracked using defect tracking systems which store the reported defects along with their details.

However, the data present in such systems is generally in unstructured form. Hence, text mining techniques in combination with machine learning techniques are required to analyze the data present in the defect tracking system.

Manuscript received March 14, 2014; March 31, 2014
Prof. Rajni Jindal is with Indira Gandhi Delhi Technical University for Women, Delhi, India (email: rajni.jindal@yahoo.co.in)
Dr. Ruchika Malhotra (Corresponding Author phone: 91-011-26431421) is with Delhi Technological University, Delhi, India (email: ruchikamalhotra2004@yahoo.com)
Abha Jain is with Delhi Technological University, Delhi, India (email: me_abha@yahoo.com)

In the present scenario, an automated tool is required to collect the data from software repositories so that it can be analyzed and interpreted in order to make generalized conclusions. The defects in the software may be associated with various severity levels. For instance, catastrophic defects are the most severe defects and a failure caused by such defects may lead to a whole system crash [1], [5].

In this paper, we mine the information from the NASA's database called PITS (Project and Issue Tracking System), by developing a tool that will first extract the relevant information from PITS using text mining techniques. After extraction, the tool will then predict the defect severities using machine learning techniques. The defects are classified into five categories of severity by NASA's engineers as very high, high, medium, low and very low. In this work, we have used K-nearest neighbor (KNN) technique to predict the defects at various levels of severity. The prediction of defect severity will help the researchers and software practitioners to allocate their testing resources on more severe areas of the software. The performance of the predicted model will be analyzed using Area Under the Curve (AUC) obtained from Receiver Operating Characteristics (ROC) analysis.

The rest of this paper is organized as follows: Section 2 reviews the key points of available literature in the domain. Section 3 describes the research method used for this study, which includes the data source and model evaluation criteria. Section 4 presents the result analysis. Section 5 concludes the paper and outlines directions for future work.

II. LITERATURE REVIEW

Nowadays, the analysis of defect project reports available in various open source software repositories has become the most essential step towards the successful completion of an error free software project. These defect reports are contained within the defect database and correspond to the defects which are encountered in the real-life systems. The defects occurring in such real-life systems are detected during testing by developer or anyone who is involved in the development of the product and are reported in a defect management system (DMS) or a bug tracking system. Later on, these defects are notified to the one responsible for the identification of its cause and its correction [18]. Each defect has its separate defect report which contains the detailed information about that defect. This information generally includes; ID of the defect, summary of the defect and associated severity of the defect. Till date, few authors have analyzed the defect project reports available in different open source software repositories

ISBN: 978-988-19252-7-5
ISSN: 2078-0958 (Print); ISSN: 2078-0966 (Online)

for software defect prediction i.e. for predicting whether a A very effective tool based on Natural Language Processing (NLP) was developed by Runeson et al. [18] and Wang et al. [22] that was used to detect duplicate reports. Cubranic and Murphy [4] analyzed an incoming bug report and proposed an automated method that would assist in bug triage to predict the developer that would work on the bug based on the bug description. Canfora and Cerulo [3] discussed how software repositories can help developers in managing a new change request, either a bug or an enhancement feature. Also, a lot of empirical work has been carried out in predicting the fault proneness of classes in object-oriented (OO) software systems using a number of OO design metrics [2], [5], [7], [8], [11], [12], [15], [16], [23], [25]. Although, these studies were based on finding the relationship between OO metrics and fault proneness of classes, but did not focus on the severity of faults. Till date, there are only a few studies which were based on finding the relationship between OO metrics and fault proneness of classes at different levels of severity of faults.

The most efficient work in the field of fault severity has been done by the authors Singh et al. [21]. They have analyzed the performance of models at high, medium and low severity faults and found that the model predicted at high severity faults has lower accuracy than the models predicted at medium and low severities. The validation of the proposed models was done using various OO metrics like CBO, WMC, RFC, SLOC, LCOM, NOC, DIT on the public domain NASA dataset KC1 using DT and ANN as the machine learning methods and LR as the statistical method. The conclusion drawn was that DT and ANN models outperformed the LR model and that CBO, WMC, RFC and SLOC metrics are significant across all severity of faults and DIT metric is not significant across any severity of faults. LCOM and NOC are not found to be significant with respect to LSF. Somewhat same results were also concluded in the paper by Zhou and Leung [24]. They have investigated the fault-proneness prediction performance of OO design metrics with regard to ungraded, high, and low severity faults by employing statistical (LR) and machine learning (Naïve Bayes, Random Forest, and NNge) methods. From both the above papers, it was summarized that the design metrics are able to predict low severity faults in fault-prone classes better than high severity faults in fault-prone classes. Bayesian approach was also used by the author Pai [17] in his work to find the relationship between software product metrics and fault proneness. Shatnawi and Li [20] focused on identifying error-prone classes in post-release software evolution process. They studied the effectiveness of software metrics and examined three releases of the Eclipse project. They observed that, the accuracy of the prediction decreased from release to release and that there are only a few metrics which can predict class proneness in three error-severity categories.

The work proposed in this paper is similar to the work done by Menzies and Marcus [13]. The authors have presented an automated method named SEVERIS (SEVERity Issue assessment) which is used to assign severity levels to the defect reports by using the data from NASA's Project and Issue Tracking System (PITS). Their method is based on the automated extraction and analysis of textual descriptions from issue reports in PITS by using various text mining techniques. particular part of the software is defective or not.

They have used a rule learning method as their classification method to assign the features with proper severity levels, based on the classification of the existing reports. Similar work has also been done by Sari and Siahaan [19]. They have also developed a model for the assignment of the bug severity level. They have used the same pre-processing tasks (tokenization, stop words removal and stemming) and feature selection method (InfoGain), but, have used SVM as their classification method. Lamkanfi et al. [10] have also analyzed the textual description using text mining algorithms in order to propose a technique that is used to predict the severity of a reported bug against three open – source projects viz. Mozilla, Eclipse and GNOME using Bugzilla as their bug tracking system and Naïve Bayes as their classifier.

III. RESEARCH METHODOLOGY

In this section, we present our research method. We first introduce the data source which elaborates on the dataset being used in our study followed by the text classification framework that we have used in order to extract the relevant words from the defect descriptions. Finally, we describe our model evaluation criteria.

A. Data Source

We have collected the defect data from an open source NASA's dataset called PITS (Project and Issue Tracking System). There are various projects that come under PITS database all of which were supplied by NASA's Software Verification and Validation (IV & V) Program. We have used PITS B project wherein the data has been collected for more than 10 years and includes all the issues that have been found in the robotic satellite missions and human rated system. The focus of our study is to investigate the predictiveness of the model with regard to the severity of defects. Therefore, we are interested in the number of defects at each severity level as shown in Table I.

NASA's engineers have classified severity 1 defects as Very High, severity 2 defects as High, severity 3 defects as Medium, severity 4 defects as Low and severity 5 defects as Very Low. We are interested only in the last four severity levels i.e. severity 2, severity 3, severity 4 and severity 5 as it can be seen from table 1 that there are no severity one issues in the defect data. This is so because these defects are of very high severity level and therefore possibility of such defects in the software become very rare.

We went through this dataset and extracted the summary of each defect from all the reports. We then analyzed these textual descriptions and applied the text mining techniques to extract the relevant words from each report. At a later stage, machine learning method was used to assign the severity level to each defect based on the classifications of existing reports. As we know that the standard machine learning methods work well only for the data with fewer number of attributes. Therefore, before we can apply machine learning to the results of text mining, we have to reduce the number of words, referred to as the dimensions (i.e. attributes) in the data.

ISBN: 978-988-19252-7-5
ISSN: 2078-0958 (Print); ISSN: 2078-0966 (Online)

Hence, we applied different methods of text mining for dimensionality reduction in the following order: tokenization, stop word removal, stemming, feature selection and weighting.

TABLE I. NUMBER OF DEFECT REPORTS OF PITS B DATASET AT EACH SEVERITY LEVEL

	Severity 1	Severity 2	Severity 3	Severity 4	Severity 5
Pits B	0	23	523	382	59

1)Pre-processing

Pre-processing is the first and foremost step of text mining which is done in order to remove the irrelevant words from the document. Irrelevant words are the words which are not important for the learning task and rather their usage can substantially degrade performance of machine learning methods. The three most popular methods which are used for pre-processing are tokenization, stop words removal and stemming. Tokenization is the process of converting a stream of characters into a sequence of tokens. We have done tokenization by replacing the punctuation with blank spaces, removing all the non-printable escape characters and converting all the words to lowercases. Thereafter, all the stop words like prepositions, conjunctions, articles, common verbs, nouns, pronouns, adverbs and adjectives were removed from the dataset by using a list of English stop words. Finally, stemming was performed which removes words with the same stem and keeps the stem as the feature. For example, the words "train", "training", "trainer" and "trains" can be replaced with "train". All the words obtained after preprocessing were called as 'features'.

2)Feature selection

Even after performing a series of pre-processing tasks, the number of words in the document can still be very large. Therefore, feature selection method is used in order to further reduce the dimensionality of the feature set. There are a number of such methods available in the literature like document frequency, term frequency, mutual information, information gain, odds ratio, χ2statistic, term strength etc. These methods use an evaluation function that is applied to a single word. Thereafter, all these words are ranked by their independently determined scores, and then the top scoring words are selected.

In this paper, InfoGain measure is used to rank all the features obtained after pre-processing and then the top 'N' scoring features are selected based on the rank. According to the InfoGain measure, the best words are those that most simplifies the target concept, which is in our case, the distribution of severities [13]. Suppose a data set has 80% severity=5 issues and 20% severity=1 issues. Then that data set has a class distribution C_0 with classes c(1) = severity5 and c(2) = severity1 with frequencies $n(1) = 0.8$ and $n(2) = 0.2$. The number of bits required to encode an arbitrary class distribution C_0 is $B(C_0)$ defined as follows:

$$B(C) = -\sum_{c \in C} [{}^{n(c)}/_{N}] \; log_2 \; [{}^{n(c)}/_{N}] \tag{1}$$

Where,

$$N = \sum_{c \in C} n(c) \tag{2}$$

If A is a set of attributes, then the number of bits required to encode a class after observing an attribute is:

$$B(C|A) = -\sum_{c \in A} \left[{}^{n(a)}/_{N}\right] \sum_{c \in C} p(c|a) log_2 \left(p(c|a)\right) \tag{3}$$

Where,

$$p(c) = {}^{n(c)}/_{N} \tag{4}$$

The highest ranked attribute A_i is the one with the largest information gain; i.e., the one that most reduces the encoding required for the data after using that attribute; i.e.

$$Infogain(A_i) = B(C) - B(C|A_i) \tag{5}$$

3)Weighting and Normalizing

Now, these 'N' features can be represented as $t_1, t_2, \ldots, t_N$. The ith document is then represented as an ordered set of N values, called an N-dimensional vector which is written as $(X_{i1}, X_{i2}, \ldots, X_{iN})$ where X_{ij} is a weight measuring the importance of the jth term t_j in the ith document. The complete set of vectors for all documents under consideration is called a vector space model or VSM.

There are various methods which can be used for weighting the terms. We have used TFIDF approach for calculating the weights, which stands for Term Frequency Inverse Document Frequency. Term frequency is simply the frequency of the jth term, i.e. t_j, in document i. This value makes the terms that are frequent in the given document more important than the others. The second value i.e. inverse document frequency is given by $\log (n/n_j)$ where n_j is the number of documents containing term t_j and n is the total number of documents. This value makes the terms that are rare across the collection of documents more important than the others.

Now, before we use the set of N-dimensional vectors, we will first need to normalize the values of the weights. It has been observed that 'normalizing' the feature vectors before submitting them to the learning algorithm is the most necessary and important condition.

B. *Model Evaluation*

As we all know, defect-prone documents are treated as the positive instances in the context of defect prediction [9]. On this basis, we can categorize the defect prediction results into four different types as defined below:

- TP (True Positive): defect-prone documents that are classified correctly;

ISBN: 978-988-19252-7-5
ISSN: 2078-0958 (Print); ISSN: 2078-0966 (Online)

- FN (False Negative): defect-prone documents that are wrongly classified to be defect- free;
- TN (True Negative): defect-free documents that are classified correctly;
- FP (False Positive): defect-free documents that are wrongly classified to be defect-prone.

To measure the performance of the predicted model, we have used the following performance evaluation measures:

1) Sensitivity

It measures the correctness of the predicted model and is defined as the percentage of the documents correctly predicted to be defect prone. It is also referred to as Recall. Mathematically we can define sensitivity as,

$$Sensitivity = \frac{TP}{TP + FN} * 100 \quad (6)$$

2) Receiver Operating Characteristics (ROC) analysis

ROC curve is defined as a plot of sensitivity on the y-coordinate versus its 1-specificity on the x- coordinates [6]. The main objective of constructing ROC curves is to obtain the required optimal cut-off point that maximizes both sensitivity and specificity. An overall indication of the accuracy of a ROC curve is the area under the curve (AUC). Values of AUC range from 0 to 1 and higher values indicate better prediction results.

3) Validation method used

The validation method used in our study is Hold-out validation (70-30 ratio) in which the entire dataset is divided into 70% training data and remaining 30% as test data. There are two methods by which we can assign the cases. Either we can randomly assign the cases based on relative number of cases or else we can use a partitioning variable. We have not randomly assigned the cases, but have rather used a partitioning variable to assign the cases. In other words, we have used a variable that splits the given dataset into training and testing samples in 70-30 ratio. This variable can have the value either 1 or 0. All the cases with the value of 1 for the variable are assigned to the training samples and all the other cases are assigned to the testing samples.

To get more generalized and accurate results, we have done validation using 10 separate partitioning variables. A single variable is used at a time on the basis of which the given dataset will be divided randomly in the ratio of 70-30. The corresponding training samples will be used by KNN in order to predict the model and the remaining testing samples will be used to validate the model. The same process is repeated for 10 runs corresponding to each partitioning variable.

IV. RESULT ANALYSIS

In this section, we have analyzed the results corresponding to the top-5, 25, 50 and 100 words in order to predict the best model that gives the highest accuracy using sensitivity, AUC and the cut-off point as the performance measures. Tables II-V present and summarize the results with respect to high, medium, low and very low severity levels.

TABLE II. RESULTS OF KNN FOR TOP-5 WORDS

	High Severity Defects			Medium Severity Defects			Low Severity Defects			Very Low Severity Defects		
Runs	AUC	Sens	Cut-Off	AUC	Sens	Cut-Off	AUC	Sens	Cut-Off	AUC	Sens	Cut-Off
1	0.495	00.0	0.214	0.544	66.0	0.357	0.550	59.0	0.214	0.493	10.5	0.214
2	0.496	00.0	1.000	0.548	66.7	0.357	0.556	43.3	0.357	0.495	16.7	0.214
3	0.568	14.3	0.214	0.555	37.5	0.500	0.581	58.9	0.214	0.528	17.6	0.214
4	0.559	12.5	0.214	0.520	48.0	0.500	0.554	53.7	0.214	0.473	04.8	0.214
5	0.495	00.0	0.214	0.538	40.1	0.500	0.564	58.1	0.214	0.492	10.5	0.214
6	0.498	00.0	0.214	0.564	50.7	0.500	0.550	49.6	0.214	0.437	05.0	0.357
7	0.568	14.3	0.214	0.475	32.4	0.500	0.512	56.0	0.214	0.464	05.9	0.214
8	0.582	16.7	0.214	0.596	47.3	0.500	0.584	62.0	0.214	0.489	09.1	0.357
9	0.561	12.5	0.214	0.515	43.1	0.500	0.531	55.8	0.214	0.477	04.2	0.214
10	0.628	33.3	0.214	0.545	58.9	0.357	0.539	52.4	0.214	0.542	20.0	0.214

TABLE III. RESULTS OF KNN FOR TOP-25 WORDS

	High Severity Defects			Medium Severity Defects			Low Severity Defects			Very Low Severity Defects		
Runs	AUC	Sens	Cut-Off	AUC	Sens	Cut-Off	AUC	Sens	Cut-Off	AUC	Sens	Cut-Off
1	0.596	25.0	0.214	0.708	70.1	0.357	0.646	39.3	0.357	0.533	21.1	0.214
2	0.691	40.0	0.214	0.739	73.7	0.357	0.697	48.6	0.357	0.595	33.3	0.214
3	0.620	28.6	0.214	0.682	69.4	0.357	0.650	46.8	0.357	0.548	23.5	0.214
4	0.795	62.5	0.214	0.726	71.1	0.357	0.669	51.2	0.357	0.587	28.6	0.214
5	0.659	33.3	0.214	0.729	70.4	0.357	0.681	51.3	0.357	0.566	26.3	0.214
6	0.684	40.0	0.214	0.696	70.9	0.357	0.653	51.3	0.357	0.632	40.0	0.214
7	0.701	42.9	0.214	0.690	69.9	0.357	0.666	45.7	0.357	0.575	29.4	0.214
8	0.590	20.0	0.214	0.708	63.2	0.357	0.639	49.6	0.357	0.530	25.0	0.214
9	0.699	44.4	0.214	0.754	71.4	0.357	0.692	51.6	0.357	0.567	25.0	0.214
10	0.822	66.7	0.214	0.738	67.4	0.357	0.677	50.9	0.357	0.573	25.0	0.214

TABLE IV. RESULTS OF KNN FOR TOP-50 WORDS

	High Severity Defects			Medium Severity Defects			Low Severity Defects			Very Low Severity Defects		
Runs	AUC	Sens	Cut-Off	AUC	Sens	Cut-Off	AUC	Sens	Cut-Off	AUC	Sens	Cut-Off

ISBN: 978-988-19252-7-5
ISSN: 2078-0958 (Print); ISSN: 2078-0966 (Online)

1	0.698	50.0	0.214	0.746	70.7	0.357	0.709	49.6	0.357	0.701	52.6	0.214
2	0.678	40.0	0.214	0.762	73.0	0.357	0.762	57.9	0.357	0.663	44.4	0.214
3	0.682	42.9	0.214	0.758	65.0	0.357	0.668	47.6	0.357	0.674	52.9	0.214
4	0.582	25.0	0.214	0.798	75.0	0.357	0.739	47.2	0.357	0.834	76.2	0.214
5	0.813	66.7	0.214	0.810	75.7	0.357	0.757	54.7	0.357	0.681	47.4	0.214
6	0.632	30.0	0.214	0.754	70.9	0.357	0.697	53.0	0.357	0.712	55.0	0.214
7	0.754	57.1	0.214	0.796	71.0	0.357	0.739	58.6	0.357	0.675	47.1	0.214
8	0.564	20.0	0.214	0.748	70.1	0.357	0.708	53.8	0.357	0.660	50.0	0.214
9	0.742	55.6	0.214	0.728	67.9	0.357	0.681	50.8	0.357	0.562	25.0	0.214
10	0.648	33.3	0.214	0.759	70.2	0.357	0.670	57.3	0.357	0.721	55.0	0.214

TABLE V. RESULTS OF KNN FOR TOP-100 WORDS

	High Severity Defects			Medium Severity Defects			Low Severity Defects			Very Low Severity Defects		
Runs	AUC	Sens	Cut-Off	AUC	Sens	Cut-Off	AUC	Sens	Cut-Off	AUC	Sens	Cut-Off
1	0.734	50.0	0.214	0.751	72.1	0.357	0.698	54.7	0.366	0.713	57.9	0.214
2	0.687	40.0	0.214	0.779	67.8	0.357	0.749	60.7	0.357	0.665	50.0	0.214
3	0.692	42.9	0.214	0.775	72.5	0.357	0.710	86.3	0.214	0.705	58.8	0.214
4	0.610	25.0	0.214	0.785	75.0	0.357	0.699	50.4	0.357	0.813	76.2	0.214
5	0.822	66.7	0.214	0.795	78.3	0.357	0.724	49.6	0.357	0.680	47.4	0.214
6	0.689	40.0	0.214	0.749	70.3	0.357	0.675	77.4	0.214	0.707	50.5	0.214
7	0.775	57.1	0.214	0.781	75.0	0.357	0.721	55.2	0.357	0.638	41.2	0.214
8	0.732	50.0	0.214	0.778	74.7	0.357	0.722	51.2	0.357	0.547	27.3	0.214
9	0.732	50.0	0.214	0.760	72.2	0.357	0.708	54.9	0.357	0.600	41.7	0.214
10	0.732	50.0	0.214	0.776	67.4	0.357	0.742	65.7	0.357	0.716	53.3	0.214

From table II, it becomes clear that the performance of the model is consistent for all the severity levels when AUC is considered for evaluation. This is so because the values of AUC lie in the range of 0.4 to 0.6 for all the 10 consecutive runs, irrespective of the severity levels. However, there is a huge difference in the model prediction if we look at the sensitivity column. The maximum value of sensitivity for medium and low severity level is 66.7%, whereas its maximum value corresponding to high and very low severity level is just 33.3%. This trend suggests that model can predict medium severity defects better than the defects having either high or very low severity level when the number of words is less. As we increase the number of words to 25, we can see from table III that the prediction capability of the model is again the best for the medium severity defects with AUC in the range of 0.68 to 0.74 and is worst for very low severity defects with the maximum value of AUC being 0.6. Also, the sensitivity values for very low severity defects are just in the range of 21.1% to 40.0%. This trend is suggesting that there should be maximum focus on the defects having medium severity level when the number of words considered is nominal.

A similar kind of trend can be seen from table IV, where the model has performed exceptionally well in predicting the medium severity defects as values for both AUC and sensitivity are highest as compared to other severity levels. But, it is evident from table V, that performance of the model is consistent with respect to all the four severity levels when considering AUC as the performance evaluation measure. However, the sensitivity values indicate that the model predicted with respect to medium and low severity defects should be preferred over the model predicted with respect to high and very low severity defects.

But if we compare the performance of the model in terms of the number of words considered for model prediction, then there is a very clear indication of the fact that the model performs exceptionally well when top 100 words were considered, and that its performance drastically reduces when the number of words considered for classification is less. Performance of the model is worst when top 5 words were taken into account, is still better for top 25 and 50 words, and best for top 100 words. Hence, with these results, it is reasonable to claim that the performance of KNN is dependent on the number of words selected as independent features. As the number of words increases, the performance of KNN also improves. Apart from this, we have also observed that KNN method works best for medium severity defects as compared to the other severity defects.

V. CONCLUSION

Due to the widespread use of open source software repositories, the use of defect tracking systems has become inevitable. The issues of the software are tracked using such systems which store the defects along with their details. Such defects introduced in the software may be of varying severity levels ranging from mild to catastrophic. Thus, defect tracking systems play an important role to capture the defect data. However, a common issue in such systems is that they are useful for storing day-to-day information. Moreover, the information contained within such systems is generally of unstructured form.

Hence in this paper, text mining and machine learning techniques were used to analyze the defect data present in such systems. We have used text mining techniques to mine the information from the database and thereafter KNN machine learning method was used to predict the defect severities. The results were validated using NASA dataset available in the PITS database and were analyzed using Area Under the Curve (AUC) obtained from Receiver Operating Characteristics (ROC) analysis. The obtained results showed that the performance of KNN is exceptionally well in predicting the defects corresponding to top 100 words for all the severity levels. Its performance is poor for top 5 words, better for top 25 words and still better for top 50 words. Hence, with these results, we concluded that the performance of KNN is dependent on the number of words selected as independent features. Apart from this, we have also observed

ISBN: 978-988-19252-7-5
ISSN: 2078-0958 (Print); ISSN: 2078-0966 (Online)

that KNN method works best for medium severity defects as compared to the other severity defects.

Although we analyzed only one project of PITS in our study so far, we believe that the research results can be generalized to the other projects available in the PITS database. So, our future work involves replication of this work in other projects of PITS.

REFERENCES

[1] K.K. Aggarwal, Y. Singh, A. Kaur and R. Malhotra, "Empirical analysis for investigating the effect of object-oriented metrics on fault proneness: A replicated case study," *Software Process: Improvement and Practice*, vol. 16, no.1, pp. 39-62, 2009.

[2] C. Catal and B. Diri, "A systematic review of software fault prediction studies," *Expert Systems with Applications*,vol.36, pp. 7346-7354, 2009.

[3] G. Canfora and L. Cerulo, "How Software Repositories can Help in Resolving a New Change Request," *Workshop on Empirical Studies in Reverse Engineering,* 2005.

[4] D. Cubranic and G.C. Murphy, "Automatic bug triage using text categorization," *Proceedings of the Sixteenth International Conference on Software Engineering and Knowledge Engineering*, 2004.

[5] K.E. Emam and W. Melo, "The Prediction of Faulty Classes Using Object-Oriented Design Metrics," *Technical report: NRC 43609*, 1999.

[6] K.E. Emam, S. Benlarbi, N. Goel and S. Rai, "A validation of object-oriented metrics," *NRC Technical report ERB-1063*, 1999.

[7] I. Gondra, "Applying machine learning to software fault-proneness prediction," *The Journal of Systems and Software*, vol.81, pp. 186-195, 2008.

[8] T. Gyimothy, R. Ferenc and I. Siket, "Empirical validation of object-oriented metrics on open source software for fault prediction," *IEEE Transactions on Software Engineering*, vol.31, no.10, pp. 897-910, 2005.

[9] Y. Jiang, B. Cukic and Y. Ma,"Techniques for evaluating fault prediction models," *Empirical. Software. Engineering*, vol.13, no. 15, pp. 561-595, 2008.

[10] A. Lamkanfi, D. Serge, E. Giger and B. Goethals, "Predicting the Severity of a Reported Bug," *7th IEEE working conference on Mining Software Repositories (MSR)*, pp. 1-10, 2010.

[11] R. Malhotra and Y. Singh, "On the Applicability of Machine Learning Techniques for Object- Oriented Software Fault Prediction," *Software Engineering: An International Journal*, vol.1, no.1, pp. 24-37, 2011.

[12] R. Malhotra and A. Jain, "Fault Prediction Using Statistical and Machine Learning Methods for Improving Software Quality," *Journal of Information Processing Systems*,vol. 8, no.2, pp. 241- 262, 2012.

[13] T. Menzies and A. Marcus, "Automated Severity Assessment of Software Defect Reports," *IEEE International Conference on Software Maintenance (ICSM)*, 2008.

[14] G. Myers, T. Badgett, T. Thomas and C. Sandler, "The Art of Software Testing," second ed., John Wiley & Sons, Inc., Hoboken, NJ, 2004.

[15] N. Ohlsson, M. Zhao, M and M. Helander , "Application of multivariate analysis for software fault prediction," *Software Quality Journal*, vol.7, pp.51-66, 1998.

[16] H. Olague, L. Etzkorn, S. Gholston and S. Quattlebaum, "Empirical validation of three software metrics suites to predict fault-proneness of object-oriented classes developed using highly iterative or agile software development processes," *IEEE Transactions on Software Engineering*, vol.33, no.8, pp. 402-419, 2007.

[17] G. Pai, "Empirical analysis of software fault content and fault proneness using Bayesian methods," *IEEE Transactions on Software Engineering*, vol. 33, no. 10, pp. 675-686, 2007.

[18] P. Runeson, M. Alexandersson and O. Nyholm, "Detection of Duplicate Defect Reports Using Natural Language Processing," *29th IEEE International Conference on Software Engineering (ICSE)*,pp. 499 – 508, 2007.

[19] G.I.P. Sari and D.O. Siahaan, "An attribute Selection For Severity level Determination According To The Support Vector Machine Classification Result," *Proceedings of The 1st International Conference on Information Systems For Business Competitiveness (ICISBC)*, 2011.

[20] R. Shatnawi and W. Li, "The effectiveness of software metrics in identifying error-prone classes in post-release software evolution process," *The Journal of Systems and Software*,vol. 81, pp. 1868-1882, 2008.

[21] Y. Singh, A. Kaur and R. Malhotra,"Empirical validation of object-oriented metrics for predicting fault proneness models," *Software Quality Journal*, vol.18, pp. 3-35, 2010.

[22] X. Wang, L. Zhang, T. Xie, J. Anvik and J. Sun, "An Approach to Detecting Duplicate Bug Reports using Natural Language and Execution Information," *Association for Computing Machinery*, 2008.

[23] P. Yu, T. Systa, and H. Muller, "Predicting fault-proneness using OO metrics: An industrial case study," *In Proceedings of Sixth European Conference on Software Maintenance and Reengineering*, Budapest, Hungary, pp.99-107, 2002.

[24] Y. Zhou, and H. Leung,"Empirical Analysis of Object-Oriented Design Metrics for Predicting High and Low Severity Faults," *IEEE Transactions on Software Engineering*, vol. 32, no. 10, pp. 771-789, 2006.

[25] Y. Zhou, B. Xu, and H. Leung,"On the ability of complexity metrics to predict fault-prone classes in object -oriented systems," *The journal of Systems and Software*, vol.83, pp.660-674, 2010.

ISBN: 978-988-19252-7-5
ISSN: 2078-0958 (Print); ISSN: 2078-0966 (Online)

Applied Water Science
© The Author(s) 2014
10.1007/s13201-014-0235-1

Original Article

Assessment of water quality and suitability analysis of River Ganga in Rishikesh, India

A. K. Haritash[1] , Shalini Gaur[1] and Sakshi Garg[1]

(1)
Department of Environmental Engineering, Delhi Technological University, Bawana Road, Shahbad, Delhi, 110042, India

A. K. Haritash
Email: akharitash@dce.ac.in

Received: 27 September 2013**Accepted:** 25 September 2014**Published online:** 12 October 2014

Abstract

The water samples were collected from River Ganga in Rishikesh during December 2008 to assess its suitability for drinking, irrigation, and industrial usages using various indices. Based on the values obtained and suggested designated best use, water in upper segment can be used for drinking but after disinfection (Class A); organized outdoor bathing in middle segment (Class B); and can be used as drinking water source (Class C) in lower segment in Rishikesh. All the parameters were within the specified limits for drinking water quality except *E. coli*. The indices of suitability for irrigation and industrial application were also evaluated. The irrigation quality ranged from good to excellent at almost all places with the exception of percent sodium. The abundance of major ions followed K^{+}> Ca^{2+}> Cl^{-} > HCO_3^{-} > Na^{+}> Mg^{2+}> CO_3^{2-} trend. The major cations suggested that the water is alkaline (Na + K) than alkaline earth (Ca + Mg) type. The heavy metals (Pb, Cu, Zn, Ni) were found either absent or within the limits specified. There was no specific industrial input of pollutants. Industrial applications of the river water should be limited since the water was found to be aggressive, based on Langelier saturation index (0.3) and Ryznar stability index (8.8), with the problem of heavy to intolerable corrosion. Water quality of Ganga in Rishikesh was good with exception of most probable number (MPN) which needs regular monitoring and measures to control.
Electronic supplementary material

The online version of this article (doi:10.1007/s13201-014-0235-1) contains supplementary material, which is available to authorized users.

Keywords

Ganga Designated best use (DBU) Rishikesh Residual sodium carbonate (RSC) Sodium adsorption ratio (SAR) Permeability index (PI) Langelier saturation index (LSI)

Introduction

Ganga River originates from Gangotri glacier situated between 30°43′22″ 30°50′49″ North latitude and 79°4′4″–79°16′34″ East longitude, about 4,100 m above mean sea level. It is a valley-type glacier with a length of 30.20 km, and width varying from 0.5 to 2.5 km (NRCD *2009*) situated in the Uttarkashi district of Garhwal Himalaya. Ganga river basin is the largest among river basins in India and the fourth largest in the world, with a catchment area of 8, 61, 404 sq km. and a total length of 2,525 km. It is one of the most densely populated river basins in the world, supporting 29 Class-I cities (population ≥ 100,000), 23 Class-II cities (population 50,000–99,999), 48 towns, and thousands of villages. Over 500 million people were estimated to be living in the entire Ganga river basin in 2000, and this number is expected to grow to over 1 billion by 2030 (Markandya and Murty *2004*). Nearly all the sewage from these cities enters the basin waterways partially treated or untreated, totalling 1.3 billion litres per day of human waste, and 260 million liters of industrial waste, primarily from agricultural fertilizers and pesticides (Markandya and Murty *2004*). In addition to these domestic and industrial pollutants, hundreds of human corpses and thousands of animal carcasses are released to the river each day for spiritual rebirth. Studies have reported that waste discharge exceeded available river water in the state of Uttar Pradesh, just prior to the yearly monsoon (Lacy *2006*; Vass et al. *2010*). Population pressures, lack of proper investment in water quality infrastructure, limited governmental initiatives, and a lack of empowerment of the people all continue to contribute to the deteriorating state of the Ganga (Mishra and Tripathi *2008*; Rai et al. *2010*). Till date, there have been various studies on river water quality with reference to geochemistry and pollution (NRCD *2008*, *2009*; Li et al. *2009*; Li and Zhang, *2010*; Trivedi *2010*; Seth et al. *2013*), and suitability assessment of groundwater for different uses (Kaushik et al. *2000*; Haritash et al. *2008*; Srinivas et al. *2013*; Sivasubramanian et al. *2013*). The water from River Ganga is used for irrigation primarily; and as a source for drinking water and industrial applications. It, therefore, becomes imperative to assess the suitability of water for different uses. The present study has been undertaken to assess the water quality of Ganga in Rishikesh town and its suitability for drinking, agricultural, and industrial use.

Rishikesh, surrounded by virgin forests at the toe of the Himalayas, is the first town on River Ganga taken up under the Ganga Action Plan (GAP) Phase-I for pollution abatement of the river. The GAP works in Rishikesh comprise sewerage works to tap the sewage outfalls through appropriate pumping station, and diversion of the sewage to a pond type STP at Lakkarghat between Haridwar and Rishikesh. Still hundreds of ashrams, temples, residences, hotels and other commercial establishments dot the banks and this immense human activity, in a narrow band along the length of the town on both the banks, generates millions of litres of sewage per day into river Ganga. Rishikesh, unlike other cities, is the first pilgrimage-cum-tourist destination after the river enters plains, and upstream-located industrial/anthropogenic sources of pollution which may affect the water quality are absent. Any addition upstream of Rishikesh may be treated as natural. Since natural flow of water in winters is lean; and tourist activity during December (Christmas and New Year) is more, it may affect water quality adversely particularly during this period. The present study was, therefore, carried out in

December to study the designated best use of water, and its suitability for different usages based on various indices of water quality.

Materials and methods

The study was carried out in Rishikesh town of Uttaranchal state. A total of 20 samples were collected along the banks of River Ganga from Mini Goa Beach (upstream of Rishikesh) to Bhardwaj Sthal (Downstream of Rishikesh) in December 2008. Sampling locations (Fig. 1) were identified on the basis of prominent activities of bathing, washing, addition of sewage/wastewater into the river. Bulk samples were collected from a distance at least five feet inside from the banks in pre-rinsed sterilized plastic bottles. The pH, electrical conductivity (EC), total dissolved solids (TDS), temperature, and salinity (as NaCl) were analysed on the site using HACH (USA) made HQ40-D-*Multi* model meter (Hossain et al. *2010*). Dissolved oxygen (DO) was also analysed on the site using DO probe fitted with HACH made HQ30-D-*Flexi* model meter. The samples were stored at 5 °C in an ice box, transported to the laboratory and analysed for other parameters within 6 h using standard methods of APHA (Eaton et al. *1995*). Fluoride (F^-) was measured using F^- ion electrode fitted with Thermo Orion model 720A20+ meter, and total organic carbon (TOC) was analysed on Analytik-jena Multi N/C-2100 TOC analyzer based on non-dispersive infra-red (NDIR) spectroscopy. Lead (Pb), Copper (Cu), Zinc (Zn), and Nickel (Ni) were analysed on Shimadzu made model AA-6300 atomic absorption spectrophotometer (AAS). In order to assess the suitability for irrigation residual sodium carbonate (RSC), soluble sodium percentage (SSP), sodium adsorption ratio (SAR), permeability index (PI), Kelley's ratio (KR), and magnesium hazard (Mg Haz.) was evaluated.

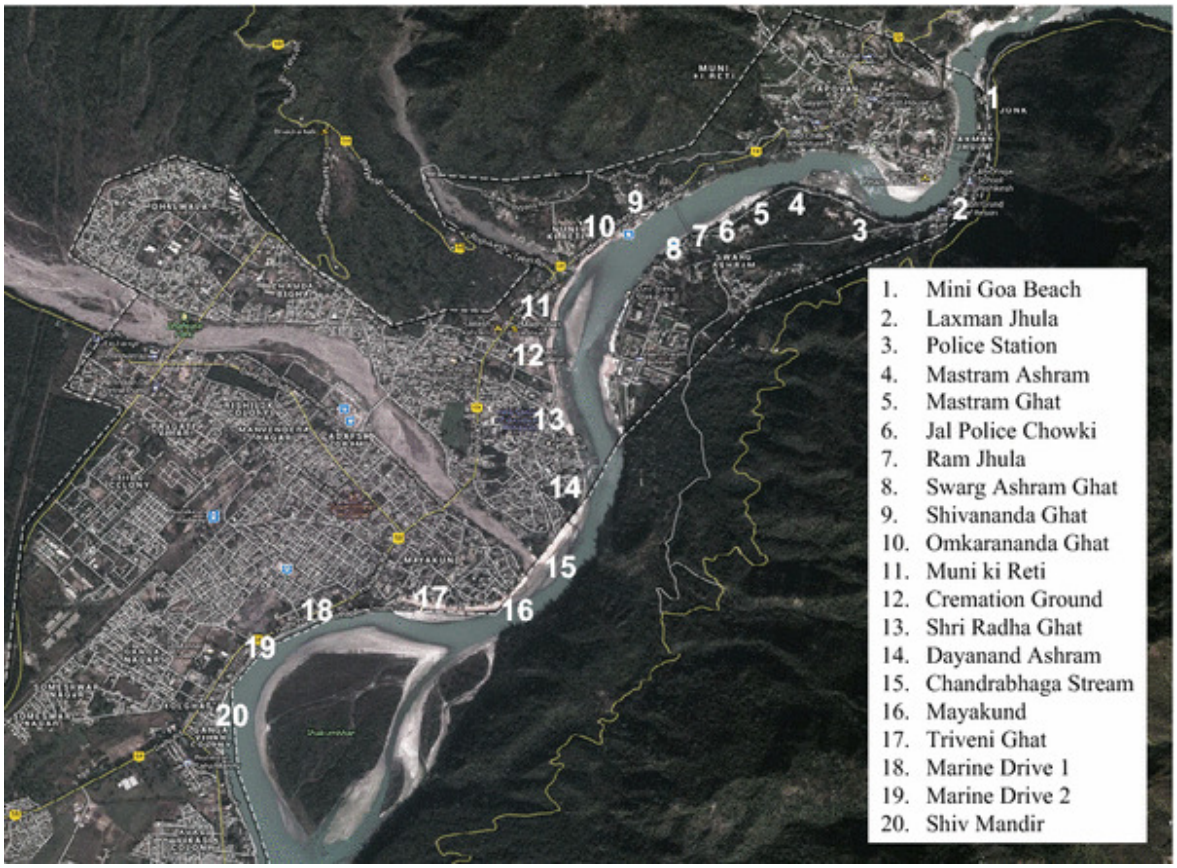


Fig. 1
Location of sampling sites in Rishikesh town

RSC = $(HCO_3^- + CO_3^{2-}) - (Ca^{2+} + Mg^{2+})$	(Eaton *1950*)
SSP = $[Na^+/(Ca^{2+} + Mg^{2+} + Na^+)] \times 100$	(Eaton *1950*)
SAR = $Na^+/(Ca^{2+} + Mg^{2+}/2)^{1/2}$	(Richards *1954*)
PI = $[Na^+ + (HCO_3^-)^{1/2}/(Ca^{2+} + Mg^{2+} + Na^+)] \times 100$	(Doneen *1962*)
KR = $Na^+/(Ca^{2+} + Mg^{2+})$	(Kelly *1963*)
Mg Haz. = $(Mg^{2+} \times 100)/(Ca^{2+} + Mg^{2+})$	(Paliwal *1972*)

All ionic concentrations are in milli equivalent per litre (meq/l).

Results and discussion

Suitability for drinking

The representative samples collected from the study area were analysed for their physical, chemical, and biological properties for determining their designated best use. The results

obtained are given in Table 1. The temperature of water was in the range of 10.2–21.0 with an average of 17.5. Comparatively higher temperatures at places could be attributed to the decreased flow rate or very shallow rocky river bed exposed to direct sunlight raising the temperature of water flowing through/over. So, temperature of the river water was observed to be a function of depth, turbulence, time of the day, and heat input from outer environment. The pH values of the samples were in the range of 9.0–10.5 with a mean value of 9.4 indicating that the water is slightly alkaline. Electrical conductivity (EC) represents the concentration of different ions present. EC varied from 38.0 to 170 µS/cm with the mean value of 85.2 µS/cm. Comparatively higher values were observed at location #10 and downstream owing to the external input of wastewater. Still higher values of EC from Dayanand Ashram to Triveni Ghat were a result of addition of sewage from Chandrabhaga stream and wastewater from the ashrams. The TDS ranged from 18.0 to 85.0 mg/l with an average value of 38.6. Higher values of TDS at location #11 and 12 may be attributed to addition of sewage and suspension of ashes from cremation ground near the locations. The desirable limit for TDS in drinking water is 500 mg/l. Salinity (expressed as per thousand) ranged from 0.01 to 0.08 with a mean value of 0.04. Alkalinity of the water exhibited more variation and ranged from 32.0 to 144.0 mg/l with an average value of 70.4 mg/l. About 90 % of the samples were having bicarbonate as the major species responsible for the alkalinity. As per the Bureau of Indian Standards (BIS) standards (*2012*) (Table 2), the limit of alkalinity in drinking water is 200 mg/l.

Table 1

Physico-bio-chemical characteristics of water of River Ganga in Rishikesh

Sample No.	Temp. (°C)	pH	EC (µS/cm)	TDS (mg/L)	Salinity ($^{o}/_{oo}$)	Alkalinity	DO	TH	CO_3^{2-}	HCO_3^-
1	16.0	9.6	77.0	31.0	0.04	80.0	9.6	64.0	9.6	4.9
2	16.0	9.3	59.0	23.0	0.03	80.0	9.4	64.0	0.0	24.4
3	16.0	9.5	67.0	31.0	0.03	48.0	9.2	68.0	0.0	14.6
4	17.0	9.0	63.0	31.0	0.02	48.0	9.5	80.0	0.0	14.6
5	20.0	9.2	63.0	30.0	0.01	48.0	9.5	76.0	0.0	14.6
6	21.0	10.5	68.0	18.0	0.03	80.0	11.1	76.0	0.0	24.4
7	19.0	10.0	40.0	32.0	0.03	48.0	10.6	76.0	0.0	14.6
8	16.2	9.4	38.0	25.0	0.01	32.0	9.5	72.0	0.0	9.8

Sample No.	Temp. (°C)	pH	EC (µS/cm)	TDS (mg/L)	Salinity ($^{o}/_{oo}$)	Alkalinity	DO	TH	CO_3^{2-}	HCO_3^-
9	17.0	9.1	52.0	25.0	0.02	64.0	9.3	64.0	0.0	19.5
10	17.5	9.6	72.0	34.0	0.02	144.0	9.5	72.0	0.0	19.5
11	20.0	9.5	125.0	60.0	0.06	64.0	7.8	212.0	4.8	34.2
12	17.8	9.5	102.0	48.0	0.05	64.0	9.0	116.0	4.8	9.8
13	17.0	9.3	75.0	22.0	0.03	64.0	9.2	80.0	0.0	19.5
14	19.2	9.0	118.0	30.0	0.05	96.0	10.6	120.0	4.8	19.5
15	20.3	9.0	170.0	85.0	0.08	80.0	9.3	168.0	4.8	19.5
16	19.5	9.2	152.0	76.0	0.07	64.0	10.2	124.0	0.0	24.4
17	18.0	9.3	117.0	54.0	0.05	64.0	10.8	120.0	0.0	19.5
18	17.3	9.3	97.0	46.0	0.04	48.0	10.5	92.0	0.0	19.5
19	15.7	9.2	76.0	35.0	0.03	144.0	10.2	80.0	0.0	14.6
20	10.2	9.2	73.0	35.0	0.03	48.0	16.1	200.0	4.8	34.2
Range	10.2–21.0	9.0–10.5	38.0–170.0	18.0–85.0	0.01–0.08	32.0–144.0	7.8–16.1	64.0–212.0	0.0–9.6	4.9–34.2
Mean ± SD	17.5 ± 2.38	9.4 ± 0.36	85.2 ± 35.54	38.6 ± 17.94	0.04 ± 0.02	70.4 ± 29.55	10.0 ± 1.62	101.2 ± 44.86	1.7 ± 2.82	18.8 ± 7.31

Sample No.	HCO_3^-	Cl^-	F^-	PO_4^{3-}	Na^+	Mg^{2+}	Ca^{2+}	TOC	BOD	MPN
1	4.9	15.0	0.25	3.6	10.1	0.0	25.6	14.5	5.4	125
2	24.4	10.0	0.27	3.8	9.8	5.0	17.6	13.3	5.6	na*
3	14.6	12.5	0.33	4.5	9.8	5.0	19.2	16.4	5.5	na
4	14.6	15.0	0.27	4.5	9.7	8.5	18.4	12.8	4.6	na
5	14.6	20.0	0.25	3.7	9.8	7.0	19.2	12.7	4.4	na
6	24.4	17.5	0.28	3.8	9.7	7.0	19.2	12.4	4.3	na
7	14.6	15.0	0.26	4.2	9.8	6.5	20.0	16.7	6.8	450
8	9.8	20.0	0.29	4.5	9.8	6.0	19.2	13.2	5.4	na
9	19.5	20.0	0.27	4.5	9.8	3.0	20.8	15.0	6.5	na
10	19.5	27.5	0.27	4.3	10.1	6.5	18.4	13.9	5.5	na
11	34.2	25.0	0.24	4.2	10.2	22.0	49.6	51.2	11.5	na
12	9.8	25.0	0.27	4.2	9.7	10.5	29.6	26.7	14.6	na
13	19.5	32.5	0.35	3.8	10.4	7.5	20.0	15.9	12.4	3000
14	19.5	30.0	0.25	4.0	10.5	8.5	34.4	28.6	15.2	na
15	19.5	25.0	0.15	4.5	10.5	14.5	44.0	42.3	18.3	2500
16	24.4	32.5	0.22	4.8	10.4	11.5	31.2	67.0	19.3	na
17	19.5	27.5	0.22	4.8	10.4	13.0	27.2	43.9	15.6	1200
18	19.5	25.0	0.22	4.0	9.8	8.5	23.2	108.3	19.5	na

Sample No.	HCO_3^-	Cl^-	F^-	PO_4^{3-}	Na^+	Mg^{2+}	Ca^{2+}	TOC	BOD	MPN
19	14.6	25.0	0.22	4.3	9.8	3.5	26.4	19.5	8.4	na
20	34.2	22.5	0.23	4.2	10.2	37.0	20.8	14.9	6.5	na
Range	4.9–34.2	10.0–32.5	0.15–0.35	3.6–4.8	9.7–10.5	0.0–37.0	17.6–49.6	12.4–108.3	4.3–19.5	125–3000
Mean ± SD	18.8 ± 7.31	22.1 ± 6.51	0.3 ± 0.04	4.2 ± 0.35	10.0 ± 0.33	6.6 ±8.0	25.2 ± 8.84	28.0 ± 24.41	9.8 ± 5.45	1455 ± 1257

All the values expressed in mg/l except Temperature (^oC), EC (µS/cm), salinity ($^o/_{oo}$), and MPN (No./100 ml); *na* Not Analysed

Table 2
Standards for drinking water (Bureau of Indian Standards (BIS) *2012*; IS: 10500)

S. No.	Parameter	Acceptable limit	Permissible limit in the absence of alternate source
1.	Colour (Hazen units)	5	15
2.	Odour	Agreeable	Agreeable
3.	pH value	6.5–8.5	No relaxation
4.	Taste	Agreeable	Agreeable
5.	Turbidity (NTU units)	1	5
6.	Total dissolved solids (mg/l)	500	2000
7.	Aluminium (mg/l)	0.03	0.2
8.	Ammonia (mg/l)	0.5	No relaxation
9.	Anionic detergents (as MBAS) (mg/l)	0.2	1.0

S. No.	Parameter	Acceptable limit	Permissible limit in the absence of alternate source
10.	Barium (as Ba) (mg/l)	0.7	No relaxation
11.	Boron (as B) (mg/l)	0.5	1.0
12.	Cadmium (mg/l)	0.003	No relaxation
13.	Calcium (as Ca) (mg/l)	75	200
14.	Chloramines (as Cl_2) (mg/l)	4.0	No relaxation
15.	Chloride (as Cl) (mg/l)	250	1,000
16.	Copper (mg/l)	0.05	1.5
17.	Fluoride (mg/l)	1.0	1.5
18.	Iron (mg/l)	0.3	No relaxation
19.	Lead (mg/l)	0.01	No relaxation
20.	Magnesium (mg/l)	30	100
21.	Mercury (mg/l)	0.001	No relaxation
22.	Nickel (mg/l)	0.02	No relaxation
23.	Nitrate (mg/l)	45	No relaxation
24.	Phenolic compounds (as C_6H_5OH) (mg/l)	0.001	0.002
25.	Selenium (as Se) (mg/l)	0.01	No relaxation
26.	Sulphate (as SO_4) (mg/l)	200	400
27.	Sulphide (as H_2S) (mg/l)	0.05	No relaxation
28.	Total alkalinity (as $CaCO_3$) (mg/l)	200	600
29.	Total arsenic (mg/l)	0.01	No relaxation
30.	Total chromium	0.05	No relaxation

S. No.	Parameter	Acceptable limit	Permissible limit in the absence of alternate source
31.	Total hardness (as $CaCO_3$) (mg/l)	200	600
32.	Zinc (mg/l)	5.0	15.0
33.	Aldrin/Dieldrin (µg/l)	0.03	No relaxation
34.	Chlorpyriphos (µg/l)	30	No relaxation
35.	2,4-D (µg/l)	30	No relaxation
36.	DDT (µg/l)	1.0	No relaxation
37.	Endosulfan (µg/l)	0.4	No relaxation
38.	Radioactive α emitters (Bq/l)	0.1	No relaxation
39.	Radioactive β emitters (Bq/l)	1.0	No relaxation
40.	Total *Coliform* bacteria	Shall not be detectable in any 100 ml sample	

The dissolved oxygen (DO) in water is an important parameter to monitor the biological quality of water, and ascertain its designated best use. It supports the aquatic life forms and regulates the biological degradation of organic impurities. DO level of River Ganga in Rishikesh during December was fairly good with an average of 10.0 mg/l. A slight decrease in DO at location #11 and at confluence with Chandrabhaga could be attributed to the addition of sewage upstream. It was observed that DO concentration in river water is a function of temperature, turbulence, depth, and organic matter present. The total hardness (TH) in river water is primarily regulated by the carbonates, bicarbonates, chlorides, sulphates, etc. of calcium and magnesium chiefly, whereas there are certain other chemical entities accounting for it. The hardness levels varied from 64.0 to 212.0 mg/l with a mean value of 101.2 mg/l. The observations revealed that the major source of hardness ions is the wastewater from domestic use. The desirable limit for total hardness in drinking water, as per BIS, India is 300 mg/l. These results revealed that wastewater from domestic use had a fair proportion of calcium bound ions adding to total hardness. The contribution of carbonate and bicarbonate ions towards hardness was analysed and it was observed that carbonate concentration was nil at most of the places except at the locations where a source of wastewater discharge was observed (4.8 mg/l). The bicarbonate concentration varied from 4.9 to 34.2 mg/l with a mean value of 18.8 mg/l. The chloride ions (Cl^-) account for the permanent hardness in water. Its concentration varied from 10.0 to 32.5 mg/l with a mean value of 22.1 mg/l, and lower concentration of chloride ions was observed at upstream locations. The concentration with respect to drinking quality was within the limit (250 mg/l) specified by BIS.

Phosphate in river water is the limiting factor for eutrophication. Phosphate levels varied from 3.6 to 4.8 mg/l with a mean value of 4.2 mg/l. Maximum concentration (4.8 mg/l) was noticed in the stretch from confluence with Chandrabhaga to Triveni Ghat and it was regulated by the wastewater added by the stream of Chandrabhaga. Fluoride is an important parameter for establishing quality of drinking water. It was found to be fairly lower than the standard limit of 1.0 mg/l (WHO *2006*). The concentration varied from 0.15 to 0.35 mg/l. The sodium (Na^+) concentration varied from 9.7 to 10.7 mg/l with a mean value of 10.0 mg/l. Lower concentrations were represented at the sampling locations in the first segment (location #1–10) and higher levels were reported at the locations where a source of discharge was observed (location #11–17). Similarly, calcium concentration ranged from 17.6 to 49.6 mg/l with a mean value of 25.2 mg/l. It was found to be well within the limits for drinking as the desirable limit for calcium, as per Indian Standard (BIS 10500: 2012) is 75 mg/l.

In order to measure the organic pollution in Ganga, biological oxygen demand (BOD_5) and total organic carbon (TOC) were determined. The BOD_5 ranged from 4.3 to 19.5 mg/l with a mean value of 9.8 mg/l. Maximum concentration (19.5 mg/l) was observed downstream of Triveni Ghat and the probable reason is offerings in the form of milk, flowers, sweets, and addition of wastewater by a thin channel immediately downstream of Triveni ghat. Lower levels were observed in the upper segment. Similarly, TOC values were lower in the upper segment and higher in the lower stretch owing to the sources located in the region. TOC concentration varied from 12.4 to 108.3 mg/l with a mean value of 28.0 mg/l. Maximum concentration of TOC was reported at location #18. The most probable number (MPN) was determined at five locations only (S. No. 01, 07, 13, 15, and 17). It was maximum (3,000/100 ml) at location #13 followed by confluence with Chandrabhaga stream (#15) (2,500/100 ml). The disposal of night soil in river bed in the vicinity of cremation ground; and discharge from Chandrabhaga stream add the *E. coli* bacteria to the river. It reveals that most of the pollution load in River Ganga in Rishikesh is from the domestic sector.

Heavy metal is another class of pollutants responsible for many of the diseases in exposed organisms. Nickel (Ni), copper (Cu), Zinc (Zn), and Lead (Pb) were analysed in the collected water samples (Table 3). Lead was below the detection limit in all the samples. Copper was present at all the locations and ranged from 0.0321 to 0.0581 mg/l with an average value of 0.0386 mg/l. Maximum concentration was reported in lower stretch. Zinc concentration varied from 0.0304 to 1.3497 mg/l. The probable reason for the high concentration could be addition from some anthropogenic source. Nickel ranged from 0.0105 to 0.0367 mg/l. The immediately higher values at location #18 might be a result of wastewater added by a channel downstream of Triveni Ghat. The desirable limit as per BIS is 0.05 and 5.0 mg/l for Copper/Nickel/Lead and Zinc, respectively.

Table 3

Concentration of heavy metals in water of River Ganga in Rishikesh

S. No.	Ni	Pb	Zn	Cu
1	0.0227	BDL	BDL	0.0445
2	0.0105	BDL	0.1489	0.0371
3	0.0245	BDL	BDL	0.0321
4	BDL	BDL	0.0760	0.0334
5	0.0175	BDL	0.3526	0.0346
6	0.0245	BDL	BDL	0.0358
7	BDL	BDL	0.0304	0.0346
8	0.0157	BDL	0.0365	0.0334
9	0.0140	BDL	0.0578	0.0358
10	BDL	BDL	BDL	0.0334
11	BDL	BDL	BDL	0.0334
12	BDL	BDL	BDL	0.0358
13	BDL	BDL	0.0426	0.0383
14	0.0367	BDL	BDL	0.0531
15	BDL	BDL	BDL	0.0408
16	BDL	BDL	0.0669	0.0433
17	BDL	BDL	0.1763	0.0346

S. No.	Ni	Pb	Zn	Cu
18	0.0314	BDL	1.3497	0.0420
19	BDL	BDL	BDL	0.0581
20	NA	NA	NA	NA

All the values expressed in mg/l

BDL Below the detection limit (0.01 mg/l), *NA* Not Analysed

As per the Designated Best Use (DBU) classification (CPCB *2008*), the water of River Ganga is suitable for drinking but after disinfection (Class A) in upper segment (location #1–7); is suitable for organized outdoor bathing (Class B) in middle segment (location # 8–10); and can be used as a drinking water source (Class C) in lower segment (location #11–20).

Suitability for irrigation

The criteria of suitability for drinking water, water for industrial purposes, and for agriculture are different. Therefore, water which is not fit for drinking and industrial uses may be suitable for irrigation. The suitability of waters for a specific purpose depends on the types and amounts of dissolved salts. Some of the dissolved salts or other constituents may be useful for crops. However, the suitability for irrigation is assessed in terms of the presence of undesirable constituents, and only in limited situations is irrigation water assessed as a source of plant nutrients (FAO *2008*).

The most important characteristics that determine the quality of irrigation water are: pH; total concentration of soluble salts assessed through EC; Relative proportion of Na to other cations such as Ca and Mg, referred to as the sodium adsorption ratio (SAR); concentration of Boron and other elements that may be toxic to plants; concentration of carbonates and bicarbonates as related to the concentration of Ca and Mg, referred to as residual sodium carbonate (RSC); content of anions such as chloride, sulphate and nitrate. The analytical data on the above parameters are used to describe the quality of irrigation water taking standards fixed for each aspect as an index (FAO *2008*). The parameters evaluated to determine the quality for irrigation are presented in Table 4. The statistical analysis of the results obtained was done on SPSS 7.5 statistical package. The suitability of the samples was analysed on the basis of results obtained and indices evaluated; comparing the obtained values with the classification as suggested by different authors (Table 5).

Table 4

Calculated values to assess the suitability for irrigation and industrial use

S. No.	RSC	SSP	SAR	Mg Hazard	KR	PI	LSI*	RSI*
1	−0.88	25.54	0.39	0.0	0.34	42	−0.05	9.7
2	−0.90	24.73	0.41	31.8	0.33	61	0.21	8.7
3	−1.14	23.64	0.39	29.9	0.31	51	0.21	9.1
4	−1.39	20.57	0.37	43.1	0.26	44	−0.28	9.6
5	−1.30	21.64	0.38	37.4	0.28	46	0.01	9.2
6	−1.14	21.46	0.38	37.4	0.27	54	1.50	7.4
7	−1.30	21.65	0.38	34.8	0.28	47	0.83	8.3
8	−1.30	22.59	0.39	33.9	0.29	44	−0.02	9.4
9	−0.97	24.83	0.39	19.1	0.33	58	0.01	9.1
10	−1.14	24.14	0.43	36.7	0.32	53	0.45	8.7
11	−3.59	9.32	0.24	42.1	0.10	25	1.00	7.4
12	−2.03	15.19	0.30	36.8	0.18	30	0.24	9.0
13	−1.31	21.77	0.39	38.1	0.28	49	0.17	9.0
14	−1.95	15.82	0.32	28.8	0.19	35	0.12	8.8
15	−2.93	11.81	0.27	35.1	0.13	26	0.21	8.6

S. No.	RSC	SSP	SAR	Mg Hazard	KR	PI	LSI*	RSI*
16	−2.12	15.22	0.32	37.7	0.18	37	0.36	8.2
17	−2.12	15.62	0.33	43.9	0.19	35	0.29	8.7
18	−1.55	18.57	0.35	37.5	0.23	43	0.22	8.9
19	−1.37	20.91	0.35	17.9	0.26	45	0.04	9.1
20	−3.40	9.71	0.28	74.5	0.11	26	0.18	8.8
Mean	−1.7	19.2	0.4	34.8	0.2	42.6	0.3	8.8
± SD	±0.8	±5.1	±0.05	±13.8	±0.08	±10.6	±0.4	±0.6

Table 5

Classification of water quality for irrigation

Quality	EC range		RSC		KR	SAR	Mg. Hazard
Very good	250[a]	<1,000[b]	<0[c]			0–10[e]	
Good	250–750	1,000–2,000	0–2.5	<1.25[d]	<1[g]	10–18	
Marginal	750–2,000	2,000–4,000	2.5–5.0	1.25–2.5	1–2		<50 %[f]
Poor	2,000–3,000	4,000–6,000	5.0–7.5			18–26	
Harmful	3,000	>6,000	>7.5	>2.5	>2	>26	>50 %

[a] Wilcox *1955*; [b] Bhumbla and Abrol *1972*; [c] Bishnoi et al. *1984*; [d] Eaton *1950*; [e] Richards *1954*; [f] Paliwal*1972*; [g] Kelly *1963*

Electrical conductivity

The concentration of total salt content in irrigation waters, estimated in terms of EC, is an important parameter for assessing the suitability of irrigation waters. Generally, all irrigation waters with an EC of less than 2250 µS/cm are considered suitable except in some situations, e.g. very sensitive crops and highly clayey soils of poor permeability. The ideal value is less than 750 µS/cm (Richards *1954*). In our study, Electrical conductivity (EC) (in µS/cm) varied in the range from 38 to 170 with a mean value of 85.2. All the water samples have EC below 750 µS/cm indicating good quality of irrigation water.

Sodium adsorption ratio (SAR)

The degree to which the irrigation water tends to enter into cation exchange reaction in soil can be indicated by the sodium adsorption ratio. Excess sodium gets adsorbed on soil particles, thus changes the soil properties and also reduces permeability (Ayers and Bronson *1975*). In this study, SAR was found in the range of 0.24–0.43. As per Richards (*1954*), water with SAR ≤ 10 is considered as of excellent quality. Figure 2 is a plot of SAR against EC for rating irrigation water in different classes which indicate the extent that the water can affect the soil in terms of salinity hazard. All the samples were found to lie in C1S1 class, i.e. low salinity and low sodium hazard class, thus excellent for irrigation purpose for almost all soils.

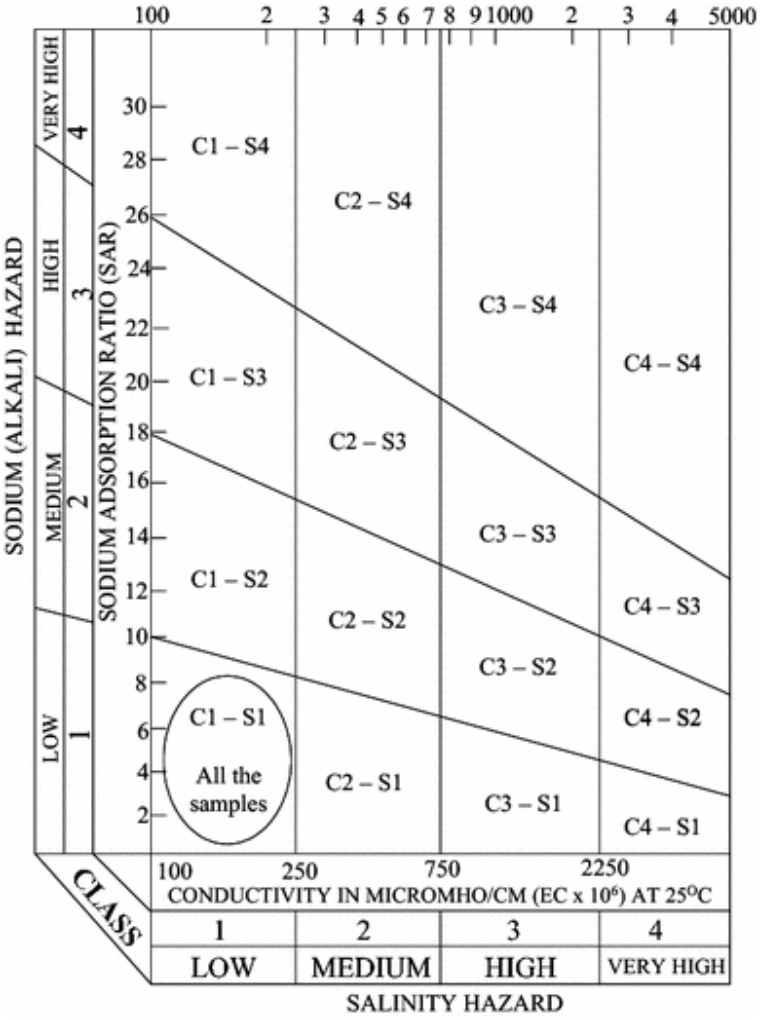


Fig. 2

Plot of calculated values of SAR and EC of water samples for classification of irrigation water (after US Salinity Laboratory Staff, *1954*)

Bicarbonate and residual sodium carbonate (RSC)

The concentration of bicarbonates was observed to be in the range of 4.9–34.2 with mean value of 18.8 mg/l. In water having a high concentration of bicarbonate, there is a tendency for calcium and magnesium to precipitate. When this happens, there is a reduction in the concentration of calcium and magnesium and a relative increase in sodium. The calcium and magnesium are precipitated as carbonates, and any residual carbonate or bicarbonate is left in solution as RSC or bicarbonate hazard. RSC remained negative for all the water samples in this study, showing that the water is of good quality for use in irrigation.

Soluble sodium percentage (SSP)

Water intended for agricultural use should have a lower concentration of sodium ions and higher concentrations of calcium and magnesium ions. This is just opposite for water in domestic use. Excessive amounts of Na^+ ions may cause a significant decrease in the permeability of agricultural soils receiving such irrigation water. SSP was found to be in the range of 9.71–25.54 with the mean value of 19.24. SSP values were observed to be in lower range with a non-significant effect on irrigation quality of water.

Magnesium hazard

It is widely reported that Ca and Mg do not behave identically in soil systems, and the Mg deteriorates soil structure particularly where waters are sodium dominated and highly saline. A high level of Mg usually promotes a higher development of exchangeable Na in irrigated soils (FAO *2008*). Water with magnesium hazard less than 50 is suitable for irrigation (Paliwal *1972*). In our study, it is observed that magnesium hazard was less than 50 in 95 % of samples. Thus, it can be safely used for irrigation except the water sample taken from the location 20, which had Mg hazard ratio as 74.8.

Kelly's ratio and permeability index (PI)

The Kelley's ratio of water samples collected at all the locations or sources ranged from 0.1 to 0.34 with mean value of 0.243, which is well below unity indicating that the water is free from sodicity hazard and can be used for irrigation purpose.

The soil permeability is affected by long-term irrigation influenced by Na^+, Ca^{2+}, Mg^{2+} and HCO_3^- contents of the soil. The permeability index values indicate the suitability of water for irrigation. The Doneen's diagram plots the permeability index, calculated from the relative proportions of sodium and bicarbonate ions on one hand, and the sum of the major cations on the other hand, against the total ion content of the water in milliequivalents per litre. The samples of the study area fall in Class II (25–75 %) and the water of the study area is of good quality for irrigation.

Chloride ion

Chloride ion up to a concentration of 70 mg/l is considered safe. It can cause several problems in crops at concentration >350 mg/l (Hopkins et al. *2007*). In our study, the values were found in the range of 10–32.5 with a mean value of 22.1. Thus, the water from these locations/sources is within the limits and found suitable for irrigation.

Each of the above parameters has a bearing on the quality of irrigation water. However, each water source will have its specific suitability or hazardous nature depending on the presence (and the degree) or absence of each of the constituents. Different chemical constituents interact with one another and cause a complex effect on soil properties and plant growth. Water with a low SAR and low EC is widely suitable. However, when a value of any one of these parameters (or both) increases in its content, the water becomes less suitable for irrigation purposes. The selection of crops for such situations becomes critical. Salt-tolerant crops can be grown in such areas. Soil type is also an important consideration under such situations (FAO*2008*).

Suitability for industrial application

Water for industrial use refers to applications such as cooling water, boiler feedwater, and in manufacturing processes. The water quality must be monitored to prevent pipe corrosion in utilities. For indicating the extent to which water flowing through pipes will precipitate or dissolve calcium carbonate, important factors such as Saturation Indices are used to test the quality of water. The Langelier saturation index is a calculated number used to predict the calcium carbonate stability of water. It indicates whether the water will precipitate, dissolve, or be in equilibrium with calcium carbonate. The LSI is expressed as the difference between the actual system pH and the saturation pH.

LSI = pH (measured)−pHs (Langlier *1936*)

If the actual pH of the water is below the calculated saturation pH, the LSI is negative and the water has a very limited scaling potential. If the actual pH exceeds pHs, the LSI is positive, and being supersaturated with $CaCO_3$, the water has a tendency to form scale. At increasing positive index values, the scaling potential increases. It is also worth noting that the LSI is temperature sensitive. The LSI becomes more positive as the water temperature increases. This increase in temperature can cause scaling, especially in cases such as hot water heaters. LSI was calculated for all the samples and it indicated that 85 % of the samples had LSI > 0. This indicates that the water at these sources is under saturated and will have a tendency to dissolve solid $CaCO_3$ protective coatings in pipelines and equipment.

The Ryznar stability index (RSI) uses a database of scale thickness measurements in municipal water systems to predict the effect of water chemistry.

Ryznar saturation index (RSI) is defined as:

RSI=2×pHs−pH (measured)

Ryznar gives only an indication about the aggressiveness of the water but carrier gives an indication about the scale and corrosion potential of the water (Table 6). RSI values indicated that 90 % water samples (RSI > 7.5) have heavy corrosion potential. 45 % water samples have intolerable water potential. As per Ryznar, all the water samples taken have aggressive water, thus unsuitable for transportation through pipes.

Table 6

Classification of water quality for industrial use

RSI	Inference (Ryznar *1944*)	RSI	Inference (Carrier *1965*)
<5.5	Heavy scale will form	4–5	Heavy scale
		5–6	Light scale
5.5–6.2	Scale will form	6–7	Little scale or corrosion
6.2–6.8	No difficulties	7–7.5	Corrosion significant
6.8–8.5	Water is aggressive	7.5–9	Heavy corrosion
>8.5	Water is very aggressive	>9	Corrosion intolerable

Conclusion

During the study, it was observed that the water quality of River Ganga was good at most of the locations in Rishikesh town. The upper segment of Ganga had good quality of water to be used for drinking with minimal treatment but after disinfection. Even the concentration of heavy metals was either non-detectable or within the safe limits. The middle and lower segments had higher levels of pollutants, especially the TDS, organic matter, and MPN. Such areas may be dedicated for organized outdoor bathing for tourists and pilgrims. Night soil disposal in river bed and wastewater discharge through open channels need immediate attention to control MPN and organic load. MPN was found to be a critical parameter which needs regular monitoring and measures to control. Addition of phosphate from wastewater channels is of concern since it may lead to eutrophication particularly in the time of year when the flow is lean. The channels may be intercepted and diverted to sewage treatment plants. The water was observed to be of good to excellent quality throughout with respect to its use in irrigation for a

long period of time. In industrial application, the water will not result in scale formation but may result in corrosion of pipes used for transporting the water. Such water may be used in different industrial processes with minimal pretreatment.

Acknowledgments

The authors acknowledge the help of Dr. Ankur Kansal, UEPPCB, Dehradun, Uttarakhand to determine BOD and MPN; and Er. Rajesh Nain, GJUS&T, Hisar, Haryana for his help in analysis of heavy metals.

Open Access This article is distributed under the terms of the Creative Commons Attribution License which permits any use, distribution, and reproduction in any medium, provided the original author(s) and the source are credited.

Electronic supplementary material

Below is the link to the electronic supplementary material.

Supplementary material 1 (XLS 20 kb)

References

Ayers RS, Bronson RL (1975) Guidelines for interpretation of water quality for agriculture. University of California, Extension Mimeographed, p 13

Bhumbla DR, Abrol IP (1972) Is your water suitable for irrigation. Indian Farming 22:15–17

Bishnoi SR, Brar SPS, Kumar D (1984) Underground water quality of Dhuri block, Distt. Sangrur, Punjab. Indian J Ecol 11(2):220–228

Bureau of Indian Standards (BIS) (2012) Indian standard drinking water specification (second revision) BIS 10500:2012, New Delhi

Carrier Air Conditioning Company (1965) Handbook of air conditioning system design. McGraw-Hill Books, New York

Central Pollution Control Board (CPCB) (2008) Guidelines for Water Quality Monitoring, MINARS/27/2007–08, New Delhi

Doneen LD (1962) The influence of crop and soil on percolating water. In: Proceedings of the 1961 Biennial conference on groundwater recharge, pp 156–163

Eaton EM (1950) Significance of carbonate in irrigation water. Soil Sci 69:123–133CrossRef

Eaton AD, Clesceri LS, Greenberg AE (1995) Standard methods for the examination of water and wastewater, 19th edn. APHA, New york

FAO (2008) Guide for laboratory establishment for plant nutrient analysis. FAO, Rome

Haritash AK, Kaushik CP, Kaushik A, Kansal A, Yadav AK (2008) Suitability assessment of groundwater in some villages of Rewari district in Haryana. Environ Monit Assess 145(1–3):397–406CrossRef

Hopkins BG, Horneck DA, Stevens RG, Ellsworth JW, Sullivan M (2007) Managing irrigation water quality for crops production in the Pacific Northwest. Pacific Northwest Extension Publication, Washington, p 597

Hossain F, Chang NB, Wanielista M, Xuan Z, Daranpob A (2010) Nitrification and denitrification in a passive on-site wastewater treatment system with a recirculation filtration tank. Water Qual Expo Health 2:31–46CrossRef

Kaushik A, Sharma HR, Mehta B, Pragya, Shilpa, Sapna, Ishita, Veenu (2000) Groundwater quality of Ambala and Nilokheri cities in Haryana in relation land use. Environ Ecol 18(3):616–623

Kelly WP (1963) Use of saline irrigation water. Soil Sci 95:355–391

Lacy S (2006) Modeling the efficacy of the ganga action plan's restoration of the Ganga River, India. Thesis, Natural Resources and Environment, University of Michigan

Langlier WF (1936) The analytical control of anti—corrosion water treatment. J Am Water Work Assoc 28:1500–1521

Li S, Zhang Q (2010) Risk assessment and seasonal variations of dissolved trace elements and heavy metals in upper Han River, China. J Haz Mat 181:1051–1058CrossRef

Li S, Xu Z, Wang H, Wang J, Zhang Q (2009) Geochemistry of upper Han River basin, China 3: anthropogenic inputs and chemical weathering to the dissolved load. Chem Geo 264:89–95CrossRef

Markandya A, Murty MN (2004) Cost benefit analysis of cleaning the Ganges: some emerging environment and development issues. In: Environment and development economics, vol 9, Issue 1, Cambridge University Press, Cambridge, p 61–81

Mishra A, Tripathi BD (2008) Heavy metal contamination of soil, and bioaccumulation in vegetables irrigated with treated waste water in the tropical city of Varanasi, India. Toxicol and Environ Chem 90(5):861–871CrossRef

National River Conservation Directorate (NRCD) (2008) Water quality monitoring for Ganga. Ministry of environment and forests, New Delhi

National River Conservation Directorate (NRCD) (2009) Status paper on River Ganga: State of Environment and Water Quality. Ministry of Environment and Forests, New Delhi

Paliwal KV (1972) Irrigation with saline water. IARI Monograph no 2 (New series), New Delhi, p 198

Rai PK, Mishra A, Tripathi BD (2010) Heavy metal and microbial pollution of River Ganga: a case study of water quality at Varanasi. Aquat Ecosyst Health Manag 13(4):352–361CrossRef

Richards LA (1954) Diagnosis and improvement of saline alkali soils. In: agriculture, handbook no 60. US Department of Agriculture, Washington, p 160

Ryznar JW (1944) A new index for determining amount of calcium carbonate scale formed by water. J AWWA 36(4):472

Seth R, Singh P, Mohan M, Singh R, Aswal RS (2013) Monitoring of phenolic compounds and surfactants in water of Ganga canal, Haridwar (India). Appl Water Sci. doi:10.1007/s13201-013-0116-z

Sivasubramanian P, Balasubramanian N, Soundranayagam JP, Chandrasekar N (2013) Hydrochemical characteristics of coastal aquifers of Kadaladi, Ramanathpuram District, Tamilnadu, India. Appl Water Sci 3:603–612CrossRef

Srinivas Y, Oliver DH, Raj AS, Chandrasekar N (2013) Evaluation of groundwater quality in and around Nagercoil town, Tamilnadu, India: an integrated geochemical and GIS approach. Appl Water Sci 3:631–651CrossRef

Trivedi RC (2010) Water quality of Ganga River—an overview. Aquat Ecosyst Health Manag 13(4):347–351CrossRef

U.S. Salinity Laboratory Staff (1954) Diagnosis and improvement of saline and alkali soils. USDA, Handbook No. 60, Wasington, p 160

Vass KK, Mondal SK, Samanta SS, Suresh VR, Katiha PK (2010) The environment and fishery status of River Ganges. Aquat Ecosyst Health Manag 13(4):385–394CrossRef

Wilcox LV (1955) Classification and use of irrigation water. USDA, Circular 969, Washington, DC, p 19

World Health Organization (WHO) (2006) Guidelines for drinking water quality. First addendum to third edn, vol 1, Geneva

Chaos based Joint Compression and Encryption Framework for End-to-End Communication Systems

Nidhi Goel[a], Balasubramanian Raman[b], Indra Gupta[c]

[a]*Department of Electronics & Communication Engineering, Delhi Technological University, New Delhi, India*
[b]*Department of Computer Science Engineering, Indian Institute of Technology, Roorkee, India*
[c]*Department of Electrical Engineering, Indian Institute of Technology, Roorkee, India*

Abstract

Augmentation in communication and coding technology has made encryption an integral part of secure multimedia communication systems. Security solution for end-to-end image transmission requires content adaptation at intermediate nodes, which consumes significant resources to decrypt, process and re-encrypt the secured data. To save the computational resources, this article proposes a network-friendly encryption technique, which can be implemented in transparency to content adaptation techniques. The proposed encryption technique maintains the compression efficiency of underlying entropy coder, and enables the processing of encrypted data. Thorough analysis of the technique, as regards various standard evaluation parameters and attack scenarios demonstrates its ability to withstand known-plaintext, ciphertext-only, and approximation attacks. This justifies its implementation for secure image transmission for end-to-end communication systems.

Keywords: Approximation attack, Content adaptation, End-to-end encryption, Huffman coding.

1. Introduction

The last decade has witnessed significant advancements in communication and networking technologies, paving the way for various distributed network multimedia applications and services. Wider availability of these multimedia services requires data dissemination over open-natured wired or wireless IP

networks, which makes the multimedia content vulnerable to eavesdropping. Consequently, preserving data confidentiality has become an important issue for secure transmission and distribution through wired/wireless networks.

Considering the resource constrained, bandwidth limited nature of these communication channels, encryption is performed during compression for better encryption efficiency with less computational resources [1, 2]. Such joint compression and encryption framework is achieved either by embedding key-controlled confusion and diffusion in these source-coding schemes or by incorporating compression in cryptographic algorithms [3, 4, 5, 6, 7].

Wen *et al.* [4] proposed the mapping of variable length codewords to fixed length indices, which are then encrypted using a conventional cipher. Spatial shuffling of macro block, coded 8 x 8 block or run level codeword has also been implemented in compressed domain [4]. Its security aspect has been improved upon by Kankanhalli *et al.* [5], by the last bit flipping of randomly chosen Huffman codeword. Wu *et al.* [8] proposed multiple Huffman table (MHT) based encryption, where each symbol is encoded with a different Huffman tree. These multiple trees have been generated by the mutation of four basic trees. However, this requires high computational resources for synchronizing the encoder-decoder pair. Also, the use of weak keys to select multiple Huffman trees makes the encrypted content vulnerable to basic cryptanalytic attacks [9, 10].

Though encryption is performed during compression, these techniques have an intrinsic security gap, especially, when the data is targeted for devices connected in a heterogeneous network. Such a network comprises of devices connected through different access networks having different bandwidth constraints and channel conditions. Further, these devices may have different computation capabilities, screen resolution, and data format requirements. For instance, same data may be required by a high speed workstation connected through a high quality link, and also by a PDA with limited computational capability and low screen resolution, connected through a wireless link. It is not feasible for a server to anticipate the user requirements and save multiple copies of the same data in different formats. An elegant solution to this problem is the implementation of adaptation procedures at the intermediate nodes. The adaptation procedures at the intermediate nodes would cater to varying requirements of different client devices without requiring any change in the existing client or server configuration.

However, most of the encryption processes disturb the data format, making it unsuitable for such processing operations. Consequently, this requires

the intermediate nodes to first decrypt, then process and re-encrypt the data using the same or new keys. This generates significant processing overhead, and also necessitates the intermediate modules to possess encryption/decryption capabilities. It also imposes an additional burden on the key management system for synchronizing the existing keys, or generating the new security keys. Further, a high level of trust is required between the end-points and the adaptation points, for sharing the security keys. Possession of security keys with all but one trusted node can break the security system, despite the strongest encryption technique implemented.

To alleviate this problem, encryption should be performed in a manner such that content adaptation can be accomplished with transparency to the content protection mechanism. Adaptation of encrypted content has been made possible in [4, 11, 12, 13], but these techniques adversely affect the compression efficiency of the entropy coder. Technique proposed in [8] maintains the compression efficiency, but the existence of invalid Huffman codewords in encrypted bitstream makes it infeasible to perform content adaptation without decryption. Validity of Huffman dictionary has been maintained in [5], but it consumes extra computational resources.

This necessitates a network-friendly encryption technique to achieve the twin objectives, *i.e.*, high compression efficiency and content adaptation of encrypted data, without increasing the computational resource consumption. Thus, a unique joint compression and encryption framework has been proposed to generate format-compliant encrypted bitstream, so that significant processing overhead can be saved at the intermediate nodes. The proposed technique employs chaos based logistic map to alter the Huffman dictionary at the entropy coding stage, without any change in the compressibility of the encoder. This would allow content adaptation of the encrypted data, and hence, would not compromise on security by sharing the security keys with intermediate nodes.

This article is organized as follows. Section 2 highlights the intricacies involved in Huffman coding from the viewpoint of the proposed image encryption technique. It also presents a snapshot of the one dimensional logistic map, which has been employed as a pseudorandom number generator. Section 3 describes the proposed technique that overcomes the limitations of existing dictionary-scrambling based encryption techniques. The performance, security, and comparative analysis have been discussed in Section 4. Finally, Section 5 concludes the paper.

2. Preliminaries

The use of Huffman encoding for compression and chaos based maps for cryptography has already been established [14, 15, 16]. This section gives a brief description of the Huffman encoding and the logistic map. Huffman encoding has been employed at the entropy coding stage to achieve compression, whereas the logistic map has been used as a pseudorandom number generator to scramble the generated dictionary.

2.1. Huffman Encoding Framework

Huffman encoding is a lossless entropy coding scheme, which requires *a priori* statistical input data generated from a discrete-time, discrete-amplitude information source, with a finite set of unique symbols, $S = \{s_0, s_1, ..., s_{n-1}\}$. At any given time, the probability that the source outputs symbol s_k, is $p_k = P(s_k)$, where $0 \leq k \leq n-1$, with $\sum_{k=0}^{n-1} p_k = 1$. In Huffman coding, for every distinct symbol $s_i \, \epsilon \, S$, a unique binary variable length codeword $c_i \, \epsilon \, C$ is generated, where $C = \{c_0, c_1, ..., c_{n-1}\}$ denotes the set of Huffman codewords. The length of these generated codewords is inversely proportional to the occurrence probability of their corresponding symbol in the input data set.

The symbols and their corresponding codewords are mapped to each other using a mapping function, M. This function maps the source symbol $s \, \epsilon \, S$ to the codeword $c \, \epsilon \, C$, *i.e.*, $M : s \rightarrow c$. Let M^{-1} be the inverse of M, then the encoding and decoding can be shown as $c = M(s)$ and $s = M^{-1}(c)$, respectively.

The symbols with their corresponding codewords are usually stored in a symbol-to-codeword mapping table, available to the encoder as well as the decoder. Huffman codes are uniquely decodable due to the imposed prefix condition on the distinct entries of symbol-to-codeword mapping table [17]. The optimality condition for this can be stated as:

1. No codeword in the dictionary can be a prefix of any other codeword.
2. If $P(s_k) > P(s_j)$ $(k \neq j)$, then $l_k < l_j$, where l_k and l_j are the lengths of the codewords assigned to symbols s_k and s_j, respectively.
3. If the symbols are listed in the order of their decreasing probabilities, the last two symbols in the ordered list are assigned codewords of the same length. These two codewords are alike, except for their final bit.

The formed symbol-to-codeword mapping table is also referred to as a dictionary in the current context. The validity of encrypted bitstream and Huffman dictionary has to be maintained to support adaptation on encrypted content. This can be attained *iff* the prefix condition of codewords is not violated in the modified dictionary.

2.2. Logistic Map

Single dimension logistic map can be mathematically represented as

$$x_{n+1} = rx_n(1 - x_n) \tag{1}$$

where, $0 \leq x_n \leq 1$

The parameter r and x_0 together form the initial conditions of the logistic map. This map exhibits high sensitivity to initial conditions for r varying between 3.57 and 4. Due to its high sensitivity, chaotic behaviour, and non-uniform probability density function, this map has been found suitable as a pseudorandom sequence generator [18].

Thus, the proposed work employs this map in the similar context. The initial conditions of the map are considered as a part of the security keys. However, while selecting the initial conditions, considerations have been made to comply with the key related requirements of chaos based cryptosystems [19]. Hence, the non-chaotic region existing between 3.82 and 3.845 has been carefully avoided to ensure a random sequence.

3. Proposed Technique

A block diagram indicating the placement of proposed encryption function in a communication food-chain is shown in Fig. 1. In the proposed encryption framework, an input image has been transformed into the frequency domain, where the quantized transform coefficients form the discrete-time, discrete-amplitude information source. After calculating the source statistics of this finite set of unique symbols, Huffman dictionary has been generated. This Huffman dictionary is then modified using the chaotic output obtained from logistic map. The modification is performed in terms of both symbol values as well as their corresponding codewords, keeping in mind the requirements of a valid Huffman dictionary. The modification of Huffman dictionary can be described as follows:

A Huffman dictionary consists of distinct symbols $s_i \; \epsilon \; S$ which corresponds to variable length codewords. The length of codeword varies from

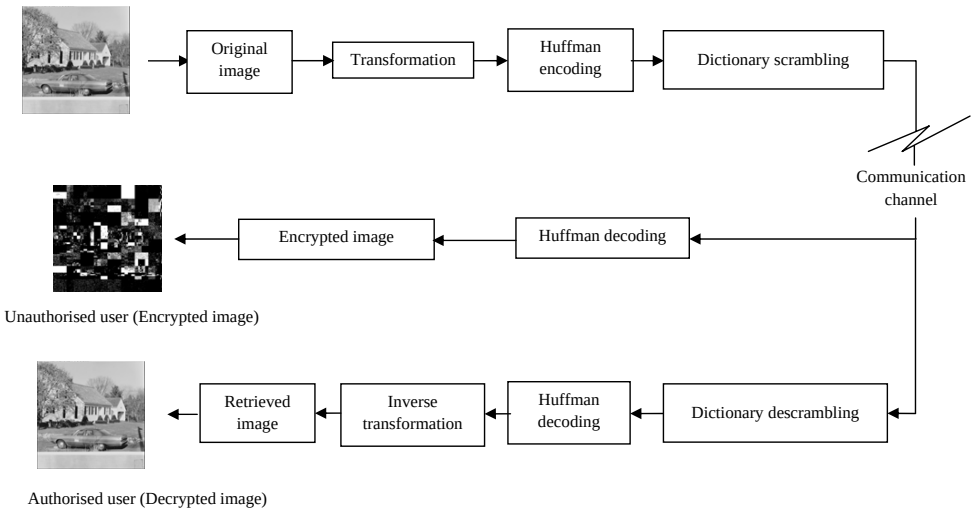


Figure 1: Block diagram for the proposed technique

l_{min} to l_{max}, where l_{min} and l_{max} denote the shortest and longest existing code-length, respectively. In the proposed technique, different disjoint sets are formed from the set S as per the length of codes, such that:

$$D_1 = \{x|\ x\ \epsilon\ S, \text{code-length}(x) = l_{min}\}$$
$$D_2 = \{x|\ x\ \epsilon\ S, \text{code-length}(x) = l_{min} + 1\}$$
$$.$$
$$.$$
$$.$$
$$D_{l_{max}-l_{min}+1} = \{x|\ x\ \epsilon\ S, \text{code-length}(x) = l_{max}\}$$
$$\text{and } S = \{D_1\ \cup\ D2\ \cup\ ...D_{l_{max}-l_{min}+1}\}$$

Logistic map is then iterated to generate a pseudorandom sequence of the size of a disjoint set D_i, where i varies from 1 to $l_{max} - l_{min} + 1$. The symbols within the formed disjoint subsets are then scrambled using the generated pseudorandom sequence. Different initial conditions of the map have been assumed for different subsets. This yields a different mapping function between symbols and the codewords for each subset.

Apart from changing the mapping function, the symbol values have also

Position No.	Original subset		Scrambling vector		Scrambled subset	
	Symbol	Code			Symbol	Code
1	210	000111010111	20		27	000111010111
2	168	010000111000	19		96	010000111000
3	156	010000111011	12		67	010000111011
4	147	000010101111	1		102	000010101111
5	75	000010101110	8		522	000010101110
6	82	000111010110	3		561	000111010110
7	140	010000111010	10	Reverse number for 1 and 2 digit symbols and shuffling vector '213' for 3 digit symbol.	271	010000111010
8	252	001101101011	9		261	001101101011
9	126	000110010111	5		57	000110010111
10	127	010111101001	17		88	010111101001
11	158	000110010001	14		37	000110010001
12	76	000110010110	16		58	000110010110
13	189	010111101000	2		681	010111101000
14	73	001101101010	6		28	001101101010
15	83	000011010001	11		581	000011010001
16	85	010111001010	4		471	010111001010
17	88	000110011101	7		401	000110011101
18	61	000001111100	15		38	000001111100
19	69	000110010000	13		891	000110010000
20	72	001101100010	18		16	001101100010

Figure 2: Dictionary scrambling process

been simultaneously modified on the basis of symbol length. It is observed that Huffman symbols are primarily t-digit decimal numbers, where t generally varies from 1 to 4. These symbols are altered according to the following rules.

1. All one digit and two digit symbols of the dictionary are modified by making LSB as MSB, and MSB as LSB. *E.g.* '5' is read as '05', thus giving a modified value of '50', '19' is converted to '91', and '27' is converted to '72'.
2. All three digit and four digit symbols have been scrambled according to distinct random shuffling vectors. E.g.: if LSB denotes position 1 and the shuffling vector for three digit symbols is '213', then the symbol '138' is converted to '381' and '672' is converted to '726'. Likewise, if shuffling vector is '2413' for four digit symbols, then the symbol '8725' is changed to '2857', and '3672' is modified to '7326'.

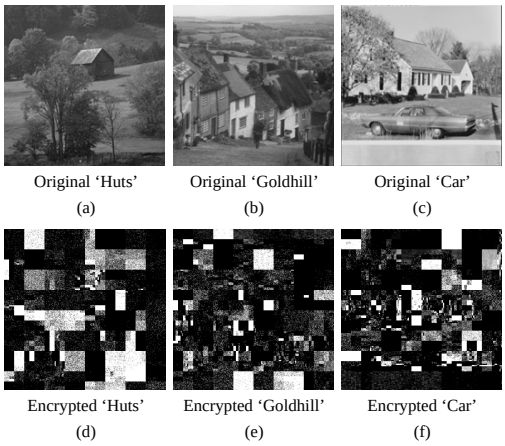


Figure 3: Encrypted results for huts, goldhill, and car image, top row: original images, bottom row: their encrypted counterparts

In this manner, the proposed encryption technique simultaneously changes the symbol values as well as their corresponding codewords. The original subsets are then replaced with their scrambled counterparts to generate an altered Huffman dictionary.

The technique uses distinct scrambling vectors for different subsets to change the mapping function, and same shuffling vector for same length symbols to modify their values. This former preserves the codestream length before and after encryption, while the later ensures distinct symbols even after modification. A snapshot of a subset from the original and the modified Huffman dictionary has been illustrated in Fig. 2.

4. Performance and Security Analysis

This section assesses the performance and security of the proposed technique, as regards different evaluation parameters and attack scenarios. Simulations for the proposed technique have been performed on various test images, however, results for only three images ('huts', 'goldhill' and 'car') are shown here.

4.1. Visual Degradation and Peak Signal to Noise Ratio

Decoding of images using scrambled dictionary provides the encrypted image. Subjective analysis of these encrypted images has been performed to

Table 1: PSNR obtained for various images

Image	PSNR (dB)
lena	0.2172
goldhill	0.9118
baboon	0.1864
car	0.2581
huts	2.3413
butterfly	1.3684
woman	0.1987

observe the amount of information leakage. The encrypted output for few test images is shown in Fig. 3. It is observed that the encrypted output is completely incomprehensible, and do not give any information about the original image.

To objectively verify the degradation introduced by the proposed technique, peak signal to noise ratio (PSNR) has also been evaluated, using

$$PSNR = 20 \times log_{10}(255/\sqrt{MSE}) \text{ dB} \tag{2}$$

where, MSE is Mean Square Error, and is given by

$$MSE = \frac{1}{MN} \sum_{i=1}^{M} \sum_{j=1}^{N} ||(I(i,j) - I'(i,j))||^2 \tag{3}$$

$I(i,j)$ and $I'(i,j)$ denote intensity of the original image and the encrypted image at pixel position (i,j).

PSNR obtained for different images using the proposed technique has been indicated in Table 1. It can be observed that a higher PSNR value is achieved by 'huts' image, in comparison to other images. This is due to the fact that 'huts' is a low contrast image, and generates a small dictionary with relatively small sized subsets. This offers a small scrambling space, as opposed to a large scrambling space for high contrast images. Thus, shuffling in small subsets causes high PSNR value, indicating that the performance of proposed technique strongly depends on contrast of the test image. Though

relatively higher PSNR has been obtained for low contrast images, it is still within the satisfactory limits.

4.2. Key Sensitivity

As per the Kerckhoff's principle, security keys are the most important part of any cryptosystem. Decryption using an incorrect key or an approximately correct key should not reveal any details of the original image [19]. To verify the key sensitivity of the proposed technique, three different cases, with slight modifications in decryption key, have been considered. First case considers wrong initial conditions of the logistic map for only one subset. This generates a wrong scrambling vector, which consequently leads to wrong mapping function for that particular set of symbols. Thus, all but one subset of the entire dictionary is correctly reshuffled. The obtained reshuffled dictionary (with one subset wrongly reshuffled) has been used to decode the output; the results for which are shown in Fig. 4 (1^{st} row). This illustrates that an incomprehensible mapping function for even one set of symbols does not give a clear view of the original image.

The second case considers an incorrect reshuffling vector during retrieval of values, for either 3 digit or 4 digit symbols. Third case considers both incorrect initial conditions and wrong reshuffling vector. Second case leads to wrong symbol values, whereas the third case leads to an incorrect descrambled dictionary, from the perspective of symbol values as well as their corresponding codewords. The decoded images for these two cases are illustrated in Fig. 4 (2^{nd} & 3^{rd} row), whereas Fig. 4 (last row) illustrates the decoded image when all the key parameters are correct. The results clearly indicate that an incorrectly descrambled dictionary leads to an incomprehensible image. It can be observed that no information has been leaked out even with decryption using a slightly different key. This depicts high key sensitivity of the proposed technique.

4.3. Compression Overhead

The proposed technique is also assessed for its impact on compression efficiency of the encoder. This can be quantified by the change in average code-length before and after encrypting the symbol source. Since symbol shuffling has been performed between symbols of same probability distribution, the length of codestream before and after encryption remains unaltered. Also, modification of the symbol values does not affect the length of their corresponding codewords. This has been verified for all the test images, however

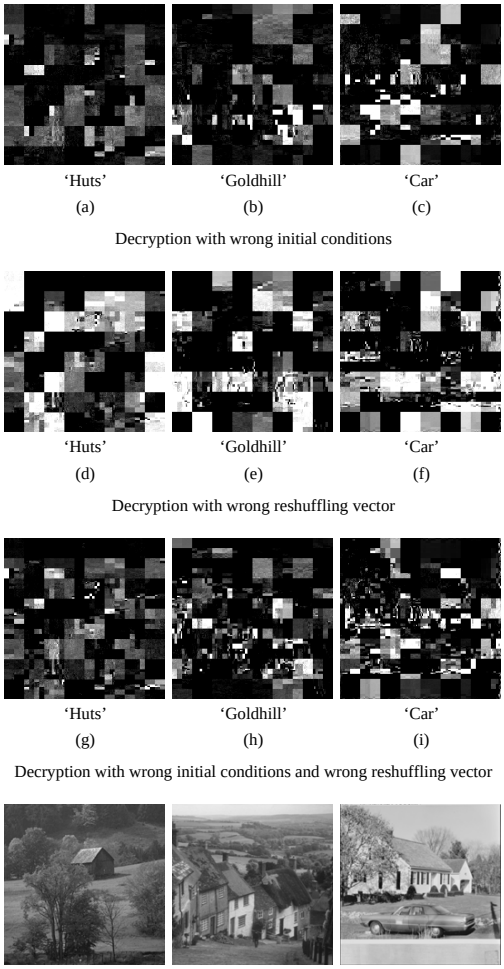


Figure 4: Key sensitivity results for huts, goldhill and car image

results for only 'Huts' image has been depicted graphically in Fig. 5. This clearly reflects that dictionary scrambling does not effect the compression efficiency of the encoder.

The impact on compression efficiency of the encoder is further evaluated by measuring the overhead generated in the entire process. The expression for overhead calculation in dictionary scrambling based encryption techniques

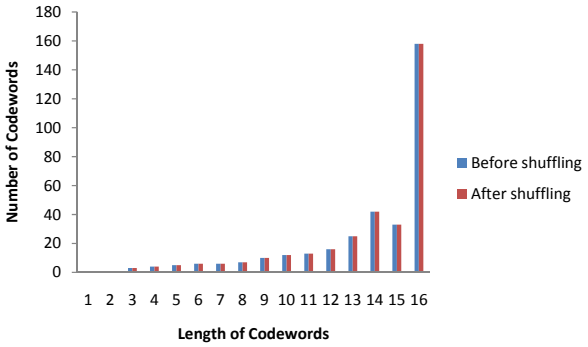


Figure 5: Effect of encryption on codeword length

can be given as [13]:

$$\delta L = (q_i - p_i)l_i, \tag{4}$$

where δL indicates the change in code length, p_i and q_i stand for probability mass function of the symbols, pre and post-encryption process. Codelength for distribution p_i is given by l_i. As the probability mass function of the symbols remain same before and after encryption, no change in the bitstream length has been observed. This also ascertains the avoidance of any adverse effect on the compression efficiency, due to the implementation of the proposed technique.

4.4. Brute-Force Attack Analysis

Since the number of subsets and the number of symbols within these subsets comes out to be different for different images; the trials required to retrieve the image without the knowledge of security keys has been discussed in a generalized manner. It has been proved that decoding a Huffman encoded bitstream without the knowledge of dictionary, is a NP-complete problem. Thus, the retrieval of plaintext, just by knowing the ciphertext is not possible [20, 21]. This ensures security against ciphertext-only attacks. Also, an intruder requires ${}^{2n-2}C_{n-1}/n$ (where n is the number of leaves) trials to retrieve information about the Huffman tree, if the probability distribution of source symbols is not known.

To break the proposed cryptosystem, an intruder would require the knowledge of correct symbol values as well as their corresponding codewords. The correct corresponding codewords can be obtained by either speculating the

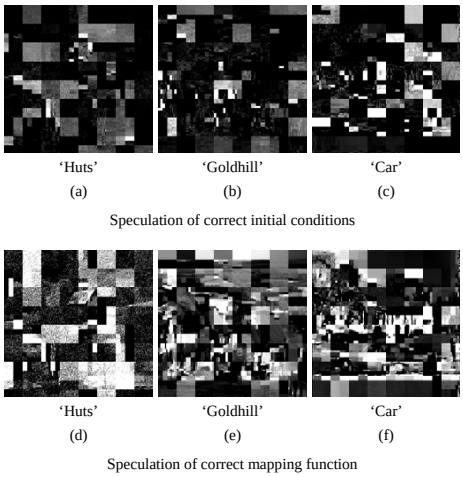


Figure 6: Brute force attack analysis

correct initial conditions, or try different mapping functions for different subsets. Both mathematical and simulation analysis has been performed to verify the resistance of proposed technique against brute force attack analysis.

Fig. 6 (first row) shows the obtained results when correct initial conditions has been speculated and Fig. 6 (second row) indicates the results when an assumption for correct mapping function has been made. The obtained visual results indicate that an assumption of the key will not lead to correct image and exact key would be required to break the cryptosystem. However, retrieving the correct key is not simple, the relevant mathematical analysis is explained hereafter.

The former way of obtaining the codewords, *i.e.*, finding the correct initial conditions would be difficult due to the high key sensitivity and large key space of the logistic map. Analysis shows that the two parameters denoting initial conditions of logistic map have a sensitivity of 10^{-13} and 10^{-14}, thus, giving a key space of $N \times 10^{27}$, where N is the total number of subsets. Thus, an intruder would require a large number of trials to obtain the correct key.

To retrieve the correct dictionary, second alternative is to attempt different mapping functions for different subsets. The number of trials required to find the correct mapping function for a subset depends upon its size, and can be described as hence. For a subset of cardinality n, there exist $n!$ different possible mapping functions. The dictionary can be correctly retrieved, *iff* all

the subsets are correctly reshuffled back to their original form. This would require $\prod_{j=1}^{N} n_j!$ trials, where n_j is the number of symbols in the subset j and N denotes the total number of disjoint subsets.

Along with the correct mapping function, an intruder would also require the correct symbol values to correctly decrypt and decode the encrypted data. The number of trials required for retrieving the correct symbol value can be given by $\prod_{k=1}^{4} t_k!$, where t_k denotes the symbol-length in the chosen subset. Due to the straightforward approach of modifying the single digit and two digits symbols, they have not been included in calculating the key space, or the trials required to break the cryptosystem. Thus, the total number of trials required for getting the correct dictionary comes out to be $\prod_{j=1}^{N} n_j! \times \prod_{k=3}^{4} t_k!$. Hence, an intruder needs to try keys from a large enough key space in an attempt to unscramble the dictionary and retrieve the plaintext.

4.5. Known-Plaintext Attack Analysis

Since, in the proposed technique, both symbol values and their corresponding codewords have been modified, the security against known-plaintext attacks has been achieved. For instance, in the example indicated in Fig. 2, an attempt by an intruder to find the codeword of original symbol value '72', in the modified dictionary would not lead to any codeword. This is due to the fact that the value '72' has changed to '27' in the modified dictionary. Let us suppose that the intruder correlates the symbol '72' and '27' (Fig. 2). In this case also, the codeword obtained by him will not be correct, as the mapping function is also modified in the scrambled dictionary. The symbol '72' correlated to '27' would return a codeword '000111010111' instead of actual codeword, '001101100010'.

Thus, even after getting the correct symbol values, the retrieval of correct corresponding codeword would not be easy. This is due to the modified symbol values as well as the mapping function. An attempt by an intruder to obtain a codeword corresponding to an original symbol would crash the decoder. This reflects the resistance of proposed technique against the known-plaintext attacks.

4.6. Approximation Attack Analysis

Security of the proposed technique has also been verified against approximation attacks [13]. In this attack, a part of unknown data is replaced with random data, in an attempt to obtain an approximate copy of the original content. In the proposed technique, replacement of an unknown symbol or codeword with an arbitrary symbol or codeword may lead to duplication of an existing dictionary entry. This would violate the prefix condition of Huffman symbol-to-codeword mapping table. Decoding of the data with an invalid partially assumed dictionary would not be successful. Hence, this will not result into even an incomprehensible or approximate image. This reflects the robustness of proposed technique against approximation attacks.

4.7. Comparative Analysis

This section performs the comparative analysis of the proposed technique with other Huffman encoding based encryption techniques. The comparative analysis has been summarised in Table 2 and discussed hereforth.

The first technique proposed by Wen *et al.* [4] initially maps the variable length codewords (VLC) to fixed length indices. These indices are then concatenated and encrypted using a conventional cipher. This result into an equivalent number of indices, but disturbs the compression efficiency of the encoder. This is due to the probability that an index of a short length codeword may get encrypted to an index of a long codeword. In contrast, the proposed technique contemplates the probability distribution of the symbols to change the mapping function. In the proposed technique modified mapping between same length codewords has been implemented, which does not alters the compression efficiency of the encoder.

Kankanhalli *et al.* [5] proposed to flip the last bit representing the codewords. This last bit flipping, however, violates the prefix condition of the dictionary, which can consequently crash the decoder. To avoid such a situation, a rule has been defined, which randomly flips the last bit, and modifies all other codewords to maintain the dictionary invalidity. Following this rule, validity of dictionary has been attained, but this would consume additional computational resources with every one bit flip in the dictionary. In contrast, the proposed technique neither disturbs the codeword, nor consumes any additional resources to maintain the dictionary validity. The symbol values are modified in a manner, such that a valid modified dictionary becomes a natural outcome of the scrambling process.

Table 2: Comparison of the proposed technique

Technique	Ideal	Wen *et al.* [4]	Kankanhalli *et al.* [5]	Wu *et al.* [8]	Proposed
Visual Degradation	High	High	High	-	High
PSNR	Low	-	-	-	Average
Key Sensitivity	High	Average	-	High	High
Compression Efficiency	High	Low	High	Average	High
Brute Force Trials	High	Average	High	High	High
Validity of Scrambled Dictionary	Yes	No	Yes	No	Yes
End-to-End Dictionary	Yes	Yes	No	No	Yes

In the technique proposed by Wu *et al.* [8], each symbol value has been encoded by a different Huffman tree, which are generated by mutation of four basic trees. To enhance the security level, randomly certain bits have been inserted in the codestream. Since, the multiple trees do not have the same length codewords, this technique adversely affects the compression efficiency, and consumes high computational resources in synchronizing the encoder-decoder pair. In addition to this, the random bit insertion disturbs the validity of the codestream, and hence, this does not support the content adaptation of the encrypted data. Thus, for processing operation at intermediate nodes, the communicating nodes need to either possess, or generate all the employed Huffman tables. This consumes additional resources. However, the present proposed technique neither disturbs the compression efficiency nor the validity of codestream of Huffman dictionary. As, the dictionary/codestream validity has been maintained in the proposed technique, content adaptation is possible even on the encrypted data. This saves the computational resources at the intermediate nodes and also do not require

the intermediate nodes to possess the security keys. Subsequently, this enhances the security level.

The comparative analysis reveals that the proposed technique neither affects the compression efficiency nor consumes additional resources to generate a valid scrambled dictionary. This is due to the consideration of probability distribution for source symbols and the fulfilment of prefix condition, while modifying the dictionary. This ensures data processing or decoding even on the encrypted data, and gives an advantage to the proposed technique over other dictionary-scrambling based techniques. This also justifies its implementation for real time secure end-to-end image transmission over insecure communication channel. Since the shuffling has been performed from the viewpoint of supporting adaption techniques on encrypted data, the proposed technique can be extended to video format or any other multimedia data that employs Huffman encoding at the entropy coding stage.

5. Conclusion

Joint compression and encryption framework provides high encryption and compression efficiency for real time secure multimedia applications. Existing such techniques consume significant overhead at intermediate nodes to decrypt, process and re-encrypt the secured content. This is also a potential security loophole despite the strongest encryption technique used.

Network-friendly encryption technique is thus proposed, so that the processing operations can directly be performed on the encrypted data. The proposed technique alters the Huffman dictionary using chaos based logistic map. With the contemplation of probability distribution for source symbols and the prefix condition of the Huffman dictionary, data decoding has been achieved even with the scrambled dictionary. Thorough analysis of the proposed technique has been done. This reflects the high perceptual degradation, low PSNR, high key sensitivity, and no adverse effect on the compressibility of the used encoder. Security analysis reveals the ability of the proposed technique to resist approximation and cryptanalytic attacks. The ability to support content adaptation, even on the encrypted content, would make the proposed technique a suitable candidate for real time secure end-to-end communication systems.

References

[1] W. Zeng, J. Lan, and X. Zhuang, "Security for multimedia adaptation: Architectures and solutions," *IEEE Multimedia*, vol. 13, no. 2, pp. 68-76, June 2006.

[2] J. Chen, J. Zhou, and K.W. Wong, "A modified chaos-based joint compression and encryption scheme," *IEEE Trans. Circuits Syst. II*, vol. 58, no. 2, pp. 110-114, Feb. 2011.

[3] A. Pande, P. Mohapatra, and J. Zambreno, "Securing multimedia content using joint compression and encryption," *IEEE MultiMedia*, vol. 20, no. 4, pp. 50-61, 2013.

[4] J. Wen, M. Severa, W. Zeng, M.H. Luttrell, and W. Jin, "A format-compliant configurable encryption framework for access control of video," *IEEE Trans. Circuits Syst. Video Technol.*, vol. 12, no. 6, pp. 545-557, June 2002.

[5] Mohan S. Kankanhalli and T.T. Guan, "Compressed domain scrambler/descrambler for digital video," *IEEE Trans. on Consumer Electron.*, vol. 48, no. 2, pp. 356-365, May 2002.

[6] Zhi-liang ZHU, Ying TANG, Qiong LIU, Wei ZHANG, Hai YU, "A chaos-based joint compression and encryption scheme using mutated adaptive Huffman Tree," *Int. Workshop on Chaos-fractals Theories and Applications*, pp. 212-216, 2012

[7] H. Shen, Li Zhuo, and Y. Zhao,"An efficient motion reference structure based selective encryption algorithm for H.264 videos," *IET Info. Secur.*, vol. 8, no. 3, pp. 199-206, 2014.

[8] C.P. Wu, and C.C. Jay Kuo, "Design of integrated multimedia compression and encryption systems," *IEEE Trans. Multimedia*, vol. 7, no. 5, pp. 828-839, Oct. 2005.

[9] Jiantao Zhou, Zhiqin Liang, Yan Chen, and O.C. Au, "Security analysis of multimedia encryption schemes based on multiple Huffman table," IEEE Sig. Process. Letters, vol. 14, no. 3, pp. 201-204, Mar. 2007.

[10] G. Jakimoski and K. P. Subbalakshmi, "Cryptanalysis of some multimedia encryption schemes," *IEEE Trans. Multimedia*, vol. 10, no. 3, pp. 330-338, Apr. 2008.

[11] M. Pazarci and V. Dipcin, "A MPEG2-transparent scrambling technique," *IEEE Trans. Consumer Electron.*, vol. 48, no. 2, pp. 345-355, May 2002.

[12] W. Zeng and S. Lei, "Efficient frequency domain video selective of digital video," *IEEE Trans. Multimedia*, vol. 5, no. 1, pp. 118-129, Mar. 2003.

[13] Yinian Mao and Min Wu, "A joint signal processing and cryptographic approach to multimedia encryption," *IEEE Trans. on Image Process.*, vol. 15, no. 7, pp. 2061-2075, July 2006.

[14] N. Taneja, B. Raman, and I. Gupta, "Selective image encryption in fractional wavelet transform," *Int. J. Electronics and Commun.*, vol. 65, issue 4, pp. 338-344, April 2011.

[15] N. Taneja, B. Raman, and I. Gupta, "Combinational domain encryption for still visual data," *Multimedia Tools Appl.*, vol. 59, pp. 775-793, 2012.

[16] N. Taneja, B. Raman, and I. Gupta, "Chaos based cryptosystem for still visual data," *Multimedia Tools Appl.*, vol. 61, pp. 281-298, 2012.

[17] D.S. Hirschberg and D.A. Lelewer, "Efficient decoding of prefix codes," *Comm. of the ACM*, vol. 33, no. 4, pp. 449-450, Apr. 1990.

[18] Dwight Kuo, "Chaos and its computing paradigm," *IEEE Potentials*, vol. 24, no. 2, pp. 13-15, 2005.

[19] Gonzalo Álvarez and Shujun Li, "Some basic cryptographic requirements for chaos-based cryptosystems," *Int. J. Bifurcation and Chaos*, vol. 16, no. 8, pp. 2129-2151, 2006.

[20] D. Gillman, M. Mohtashemi, and R. Rivest, "On breaking a Huffman code," *IEEE Trans. Inform. Theory*, vol. 42, no. 3, pp. 972-976, May 1996.

[21] Takeyuki Uehara, "Contribution to image encryption and authentication," Ph.D. Thesis, University of Wollongong, 2003.

Closure to "Fastest Rapid Loading Methods of Vertical and Radial Consolidations" by S. K. Tewatia, Pratima Rani Bose, and Asuri Sridharan

DOI: 10.1061/(ASCE)GM.1943-5622.0000213

S. K. Tewatia[1]; Pratima Rani Bose[2]; and Asuri Sridharan[3]

[1]Researcher, Central Soil and Materials Research Station, Ministry of Water Resources, Government of India, Hauz Khas, New Delhi 110016, India (corresponding author). E-mail: tewatiask_2000@yahoo.co.in

[2]Head, Engineering and Disaster Management, DDF Consultants, Pitampura, New Delhi 110034, India; formerly, Professor, Dept. of Civil Engineering, Delhi Technological Univ., Delhi 110052, India.

[3]Professor Emeritus, Dept. of Civil Engineering, Indian Institute of Science, Bangalore 560012, India.

The writers are thankful to the discussers for their valuable suggestions. They are correct that the term $(1 + e)$ is missing. Also, there is an error in Eq. (11) of the original paper; correcting that, Eq. (14) becomes

$$c_v = \frac{\pi}{2} m_1 \left[\frac{H}{(\delta_{100} - \delta_0)}\right]^2 = \frac{\pi}{2} m_1 \left[\frac{H}{\Delta H}\right]^2 = \frac{\pi}{2} m_1 \left[\frac{(1+e)}{C_c \log_{10}(\text{LIR}+1)}\right]^2 \quad (1)$$

when LIR = 1 (usually), Eq. (1) gives

$$C_c = 4.164(1+e)\sqrt{\frac{m_1}{c_v}} \quad (2)$$

The discussers assumed that void ratio $e = 1$, which cannot be expected at a very high pressure range of 800–1,600 kPa. If one inputs $e = 0.4$, Casagrande's (1939) $c_v = 2.62 \times 10^{-5}$ cm^2/s (Tewatia et al. 2007), and $m_1 = 156.5 \times 0.0002^2/60$ cm^2/s; then, from Eq. (2), $C_c = 0.368$.

Skempton and Jones (1944) showed the following relationship between C_c and liquid limit (LL):

$$C_c = 0.007(LL - 10\%) \quad (3)$$

For Sawan-Bhadon dam soil (in Fig. 5 of the original paper), $LL = 61\%$ and plastic limit $(PL) = 29\%$; therefore, from Eq. (3), $C_c = 0.357$, which compares well with the C_c found by using Eq. (2). If one uses true $c_v = 4.82 \times 10^{-5}$ cm^2/s (Tewatia et al. 2007), then Eq. (2) gives $C_c = 0.271$, which is less than that derived from Eq. (3). Eq. (2) can be written as

$$c_v = 17.33 m_1 \left(\frac{1+e}{C_c}\right)^2 \quad (4)$$

Inputting the value of C_c from Eq. (3)

$$c_v = 3.537 \times 10^5 m_1 \left(\frac{1+e}{LL-10}\right)^2 \quad (5)$$

Eq. (5) suggests that, for quick evaluation of c_v, one need not evaluate C_c. The LL and e are known at the beginning of load increment; just plot a few initial points to obtain m_1 and the test is over within a few minutes.

The $\delta - (dt/d\delta)$ and $\delta - \sqrt{t}$ plots are straight lines in the initial portion. By basic mathematics, it can be shown that, in the initial slope portion of the $\delta - dt/d\delta$ plot, m_1 is related to the slope of the $\delta - \sqrt{t}$ plot (say $m_{\sqrt{t}}$) by the following:

$$m_1 = \frac{1}{2} m_{\sqrt{t}}^2 \quad (6)$$

Substituting m_1 from Eq. (6) into Eqs. (1), (4), and (5)

$$c_v = \frac{\pi}{4}\left[\frac{(1+e)m_{\sqrt{t}}}{C_c \log_{10}(\text{LIR}+1)}\right]^2 \quad (7)$$

when (usually) LIR = 1 is adopted, Eq. (7) reduces to

$$c_v = 8.67\left[\frac{(1+e)m_{\sqrt{t}}}{C_c}\right]^2 \quad (8)$$

Inputting the value of C_c from Eq. (3)

$$c_v = 1.769 \times 10^5 \left[\frac{(1+e)m_{\sqrt{t}}}{(LL-10)}\right]^2 \quad (9)$$

Eqs. (7)–(9) suggest that the $\delta - \sqrt{t}$ plot also can be used in place of the $\delta - (dt/d\delta)$ plot for the fastest loading methods (this can be named *fastest* $\sqrt{t}$ *method*). The advantage of the $\sqrt{t}$ plot is that it does not require very precise observation as is the case in rate of settlement methods. The rate of settlement methods (Tewatia 1998; Tewatia et al. 1998, 2007; Tewatia 2010, 2013; Tewatia et al. 2012; Tewatia 2012; Tewatia et al. 2013) use settlement versus rate of settlement [$\delta - (d\delta/dt)$ or $\delta - (d\delta/d\sqrt{t})$] plots in various formats. That means settlement is plotted versus its slope. Quite often they use even the slope of settlement versus its slope. Therefore, the rate of settlement methods require very precise measurement of δ and t, because a small error in the measurement may cause a huge error in slope, particularly in curved portions where it may be difficult to normalize the scattered points (Tan and Chew 1998; Tewatia et al. 2013; Trivedi et al. 2014).

Quick Evaluation of True c_v, Taylor's c_v, and Casagrande's c_v by Fastest $\sqrt{t}$ Method

Eq. (9) can be generalized for various values of c_v as

$$c_v = \alpha \times 10^5 \left[\frac{(1+e)m_{\sqrt{t}}}{(LL-10)}\right]^2 \quad (10)$$

where α = dimensionless factor, the value of which depends on the choice of c_v. Fig. 5 of Tewatia (1998) showed the $\delta - \sqrt{t}$ plot of Sawan-Bhadon dam soil, from which $m_{\sqrt{t}} = 17.72 \times 0.0002/\sqrt{60}$ cm/$\sqrt{\text{s}}$, $LL = 61\%$, and $e = 0.4$. Tewatia et al. (2007) showed the following for the same soil: true $c_v = 4.82 \times 10^{-5}$ cm^2/s, Taylor's (1948) $c_v = 3.38 \times 10^{-5}$ cm^2/s, and Casagrande's $c_v = 2.62 \times 10^{-5}$ cm^2/s. Put these values into Eq. (10), then $\alpha_t = 3.06$, $\alpha_{\sqrt{t}} = 2.14$, and

Downloaded from ascelibrary.org by Delhi Technological University - Delhi College of Engg on 11/03/14. Copyright ASCE. For personal use only; all rights reserved.

$\alpha_c = 1.66$. Therefore, true c_v, Taylor's c_v, and Casagrande's c_v can be obtained quickly from Eq. (10) (as soon as a straight line starts on the $\delta - \sqrt{t}$ plot) by inputting the values of $\alpha_t = 3.06$, $\alpha_{\sqrt{t}} = 2.14$, and $\alpha_c = 1.66$, respectively.

However, such tests should be conducted on a wide variety of soils and Eq. (10) needs to be more generalized for better results. It calls for thorough investigation of the past data that leads to the various relationships of C_c with various index properties, such as *LL*, *PL*, shrinkage limit (*SL*), *e*, and so forth (Skempton and Jones 1944; Hough 1957; Sridharan and Nagaraj 2000). Hough (1957) suggested the following:

$$C_c = 0.3(e - 0.27) \tag{11}$$

Sridharan and Nagaraj (2000) showed experimentally that, instead of *LL* [Eq. (3)], shrinkage index [$SI(=LL - SL)$] gives a much better relation

$$C_c = 0.007(SI + 18) \tag{12}$$

Putting this value into Eq. (8)

$$c_v = 1.769 \times 10^5 \left[\frac{(1+e)m_{\sqrt{t}}}{(SI+18)}\right]^2 \tag{13}$$

Experimental Justification

Eq. (13) shows that c_v is inversely proportional to the square of *SI* (plus some constant) and this can be assumed roughly to be of the following type:

$$y = \frac{\alpha_1}{x^2} \tag{14}$$

where α_1 = constant. When *y* is plotted on log scale and *x* is plotted on linear scale, the curve (Fig. 1) is similar to the experimental curve of Sridharan and Nagaraj (2004), where c_v is plotted on the *y*-axis on log scale and *SI* is plotted on the *x*-axis on linear scale. If $x(=SI + 18)$ is plotted (instead of *SI*) in their (Sridharan and Nagaraj 2004) Figs. 4(c and d), the curve shape remains the same and it simply shifts toward the right-hand side by 18 units. Thus, Eq. (13) is the theoretical equation of the experimental $c_v - SI$ plot of Sridharan and Nagaraj (2004).

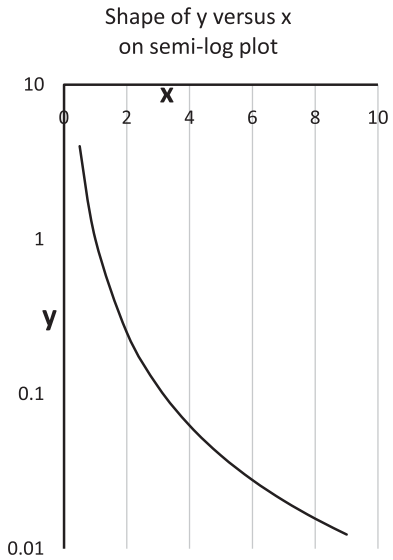


Fig. 1. Theoretical shape of $c_v - SI$ plot from Eqs. (13) and (14); this resembles the experimental $c_v - SI$ plot of Sridharan and Nagaraj (2004, Figs *4c* and *4d*)

This reinforces the concept that c_v and C_c are better correlated to *SI* instead of *LL* only (Sridharan and Nagaraj 2000, 2004). However, better correlation may be sought by using the following (but only after some experiments are conducted shall the degree of correlation be known):

$$c_v = \alpha \times 10^5 \left[\frac{(1 \pm a \times e)m_{\sqrt{t}}}{(LL - bSL \pm c)}\right]^2 \tag{15}$$

where *a*, *b*, and *c* = dimensionless constants like α. Eq. (15) has all the main four to five parameters described previously. This is just a hint of information and requires a separate paper. Unlike the determination of C_c, where four to five incremental loadings of long durations are required for 4–5 days, only one loading is required on four different soils that can be applied simultaneously in four different consolidometers in a few hours or 1 day. For every soil, true, Taylor's, and Casagrande's c_v are determined for Eq. (15) and three sets of α, *a*, *b*, and *c* are determined from Eq. (15) for true, Taylor's, and Casagrande's c_v, respectively.

Eqs. (12)–(15) show that *PL* has no role to play in consolidation; only *LL* and *SL* influence consolidation behavior of clays. It is similar to Mohr-Coulomb failure theory, where intermediate principal stress has no role to play and only major and minor principal stresses influence the strength of material. Therefore, in consolidation, instead of writing *LL* and *PL* with the names of clays, *LL* and *SL* should be used.

Fastest $\sqrt{t}$ Method in Three-Dimensional Consolidation

The following is the basic three-dimensional (3D) consolidation equation in Cartesian coordinates (Biot 1941):

$$\frac{\partial u}{\partial t} = c_x \frac{\partial^2 u}{\partial x^2} + c_y \frac{\partial^2 u}{\partial y^2} + c_z \frac{\partial^2 u}{\partial z^2} \tag{16}$$

where u = pore pressure; t = time; and c_x, c_y, and $c_z(=c_v)$ are coefficients of consolidation in the *x*-, *y*-, and *z*-directions, respectively. Eq. (1) in the original paper is

$$\frac{\partial u}{\partial t} = c_z \frac{\partial^2 u}{\partial z^2}$$

The above equation is just one part of Eq. (16) in the *z*-direction only. Eq. (2) in the original paper is the solution of the aforementioned equation, and is given here as

$$U = 1 - \frac{8}{\pi^2} \sum_{N=0}^{N=\infty} \frac{1}{(2N+1)^2} \exp\left\{-\frac{(2N+1)^2 \pi^2}{4} T\right\}$$

Suppose *L*, *B*, and *H* are the length, breadth, and height of a sample draining outward from all the six phases and settling in *z* or the vertical direction only. A Carillo (1942) solution of Eq. (16) is given by Tewatia (2013) as

$$(1 - U_{xyz}) = (1 - U_x)(1 - U_y)(1 - U_z) \tag{17}$$

Downloaded from ascelibrary.org by Delhi Technological University - Delhi College of Engg on 11/03/14. Copyright ASCE. For personal use only; all rights reserved.

and a Terzaghi (1923) solution of Eq. (16) is given by Tewatia (2010, 2012) as

$$U = 1 - \frac{8}{\pi^2} \sum_{N=0}^{N=\infty} \frac{1}{(2N+1)^2} \exp\left\{ -\frac{(2N+1)^2 \pi^2}{4} \lambda T \right\} \quad (18)$$

where λ is given as

$$\lambda = 1 + \frac{k_y H^2}{k_z B^2} + \frac{k_x H^2}{k_z L^2} \quad (19)$$

where k_x, k_y, and $k_z (= k_v)$ are the permeability of soil in the x-, y-, and z-directions, respectively. Comparing Eq. (2) in the original paper and Eq. (18) here shows that, in 3D consolidation, T for a particular t is increased by λ times or c_v is increased by λ times (Tewatia 2010, 2012).

Hence, U for a particular t increases. The shapes of $\delta - \sqrt{t}$ plots in vertical and 3D consolidations are the same, and only the slopes (of straight-line portions) differ. If $m_{\sqrt{t}3\mathrm{D}}$ is the slope of the straight-line portion in 3D consolidation, then, similar to Eqs. (7)–(9)

$$c_v = \frac{\pi}{4\lambda} \left[\frac{(1+e) m_{\sqrt{t}3\mathrm{D}}}{C_c \log_{10}(\mathrm{LIR}+1)} \right]^2 \quad (20)$$

when (usually) LIR = 1 is adopted, Eq. (20) reduces to

$$c_v = \frac{8.67}{\lambda} \left[\frac{(1+e) m_{\sqrt{t}3\mathrm{D}}}{C_c} \right]^2 \quad (21)$$

inputting C_c from Eq. (12)

$$c_v = \frac{1.769 \times 10^5}{\lambda} \left[\frac{(1+e) m_{\sqrt{t}3D}}{(SI+18)} \right]^2 \quad (22)$$

and

$$c_y = \frac{k_y}{k_v} c_v \quad (23)$$

$$c_x = \frac{k_x}{k_v} c_v \quad (24)$$

The fastest method to determine the coefficient of secondary consolidation, C_α, can be adopted as suggested by Tewatia et al. (2007) and Tewatia (2012), which is nothing but the slope of the $\delta - \log(d\delta/dt)$ plot that equals (in magnitude) the slope of the $\delta - \log(t)$ plot and always comes as a straight line in secondary consolidation or creep.

References

Biot, M. A. (1941). "General theory of three-dimensional consolidation." *J. Appl. Phys.*, 12(2), 155–164.

Carillo, N. (1942). "Simple two and three dimension cases in the theory of consolidation of soils." *J. Math. Phys.*, 21(1), 11–18.

Casagrande, A. (1939). "Notes on soil testing for engineering purposes." *Soil Mechanics Series No. 8, Graduate School of Engineering Publication No. 268*, Harvard Univ., Cambridge, MA.

Hough, B. K. (1957). *Basic soil engineering*, 1st Ed., Ronald Press, New York.

Skempton, A. W., and Jones, O. T. (1944). "Notes on the compressibility of clays." *Q. J. Geol. Soc. Lond.*, 100(Jan), 119–135.

Sridharan, A., and Nagaraj, H. B. (2000). "Compressibility behaviour of remoulded, fine-grained soils and correlation with index properties." *Can. Geotech. J.*, 37(3), 712–722.

Sridharan, A., and Nagaraj, H. B. (2004). "Coefficient of consolidation and its correlation with index properties of remolded soils." *Geotech. Test. J.*, 27(5), 1–6.

Tan, S. A., and Chew, S. H. (1998). "Closure for discussion on comparison of the hyperbolic and Asaoka observational methods of monitoring consolidation with vertical drains." *Soils Found.*, 38(2), 227.

Taylor, D. W. (1948). *Fundamentals of soil mechanics*, Wiley, New York, 238–242.

Terzaghi, K. (1923). "Die Berechnung der Durchlässigkeitsziffer des Tones aus dem Verlauf der hydrodynamischen Spannungserscheinungen." *Sitzungsber. Akad. Wiss. Wien, Math.-Naturwiss. Kl., Abt. 2a*, 132(3–4), 125–138 (in German).

Tewatia, S. K. (1998). "Evaluation of true C_v and instantaneous C_v, and isolation of secondary consolidation." *Geotech. Test. J.*, 21(2), 102–108.

Tewatia, S. K. (2010). "Time dependent behavior of clayey soils." Ph.D. thesis, Dept. of Civil Engineering, Delhi College of Engineering, Delhi Univ., New Delhi, India.

Tewatia, S. K. (2012). "Trend of settlement in primary and secondary consolidations." *Geomech. Geoeng.*, 8(2), 125–134.

Tewatia, S. K. (2013). "Equation of 3D consolidation in Cartesian coordinates." *Int. J. Geotech. Eng.*, 7(1), 105–108.

Tewatia, S. K., Bose, P. R., Sridharan, A., and Rath, S. (2007). "Stress induced time dependent behavior of clayey soils." *Geotech. Geol. Eng.*, 25(2), 239–255.

Tewatia, S. K., Huat, B. K., Rath, S., and Tewatia, K. (2013). "*U*-chart method for radial and 3D consolidation." *Proc. Inst. Civ. Eng. Ground Improv.*, 166(4), 188–195.

Tewatia, S. K., Sridharan, A., Singh, M., and Rath, S. (2012). "Theoretical equations of vertical and radial consolidation by equating degrees of consolidation by settlement analysis and dissipation of pore pressure." *Geotech. Geol. Eng.*, 30(4), 1037–1043.

Tewatia, S. K., Venkatachalam, K., and Sridharan, A. (1998). "T-Chart to evaluate consolidation test results." *Geotech. Test. J.*, 21(3), 270–274.

Trivedi, A., Banik, T., Sukumar, T., Kumar, N., Jain, A., and Kumar, A. (2014). "Consolidation of clayey gouge amid permeating rock masses." *Environ. Geotech.*, in press.

Downloaded from ascelibrary.org by Delhi Technological University - Delhi College of Engg on 11/03/14. Copyright ASCE. For personal use only; all rights reserved.

International Journal of Electronic and Electrical Engineering.
ISSN 0974-2174, Volume 7, Number 3 (2014), pp. 201-206
© International Research Publication House
http://www.irphouse.com

Comparison study of Vector Control of Induction Motor Using Rotor Flux Estimation by Two Different Methods

Ashish Chourasia[1], Vishal Srivastava[2], Abhishek Choudhary[3] and Sakshi Praliya[4]

[1,2,3,4]*Electrical Engineering Department, Delhi Technological University, Delhi.*

Abstract

The Speed Control of Induction motor is one of the important areas of research for the Electrical Engineers. Since the requirement and industrial applications of induction motors cannot be neglected, their fine speed control is one of the major objectives for the control drive engineers. The vector control of induction motors provide one of the most suitable and popular speed control technique presently used. The scalar control techniques available on the contrary were simple to implement but have the coupling effect ultimately responsible for the sluggish response which further made system prone to instability due to higher order system effect. This paper will show the comparison of vector control using PI Controller with the rotor flux estimation by two different methods and the analysis. The simulation study of results will form the basis of the conclusion.

Keywords: Vector Control, Speed Control, Scalar Control, Sluggish, Higher Order System Effect, PI Controller, Rotor Flux.

1. Introduction

An induction motor is an asynchronous AC (Alternating current) motor. The least expensive and most widely used induction motor is the squirrel cage induction motor. The interest in sensorless drives of induction motor has grown significantly over the past few years due to some of their advantages, such as mechanical robustness, simple construction and less maintenance. These applications include pumps and fans paper and textile mills, subway and locomotive propulsions, electric and hybrid vehicles, machine tools and robotics, home appliances, heat pumps and air conditioners, rolling mills, wind generation systems etc. So the induction motors have been used more in

the industrial variable speed drive system with development of vector control. This method requires a speed sensor such as shaft encoder for speed control.

The control and estimation of ac drives in general are considerably more complex than those of ac drives, and this complexity increases substantially if high performances are demanded.

2. Control schemes for speed control of three phase induction Motor

The different control schemes of induction motor drives are including scalar control, vector or field oriented control, direct torque control, and adaptive control etc. But induction motor control drives are broadly classified in two category i.e. scalar control and vector control.

2.1 Scalar Control

In this method the magnitude of the control variable is taken under variation irrespective of the coupling effect in machine. Scalar control is easy to implement, hence widely used in industries. But the performance of scalar controlled drives become inferior. To improve the performance of the scalar control method an encoder or speed tachometer is required to feed back the rotor angle or rotor speed signal and compensate the slip frequency. However, it is expensive and destroys the mechanical robustness of the induction motor. So these are the limitations of the scalar control which is overcome by Field Oriented Control or Vector Control of Induction motor drives.

2.2 Vector Control or Field Oriented Control (FOC)

Blaschke introduced the principle of vector control to realize the dc motor characteristics in an induction motor drive. For the same, he has used decoupled control of torque and flux in the motor and gives the name transvector control. In DC machine particularly separately excited dc motor, the field flux is perpendicular to the armature flux. Being orthogonal, these two fluxes produce no net interaction to each other. Adjusting the field current can therefore control DC machine flux, and the torque can be controlled independently of flux by adjusting the armature current. An ac machine is not so simple because of the interactions between the stator and rotor fields, whose orientations are not held at 90° but vary with operating conditions. We can obtain the DC machine like performance in holding a fixed and orthogonal orientation between the fields and armature fields in an AC machine by orienting the stator current with respect to rotor flux so as to attain independently controlled flux and torque. Such a scheme is called Vector Control or Field Oriented Control.

2.3 Indirect Vector control

There are essentially two general methods of vector control. One, called the direct or feed- back method, was invented by Blaschke [1], and the other, known as the indirect or feed forward method was invented by Hasse [2, 4].The two methods differ in the way the rotor angle is determined. In direct FOC the angle is obtained by the terminal

voltages and currents, while as in indirect FOC, the angle is obtained by using rotor position measurement and machine parameter's estimation. Field orientation has emerged as a powerful tool for controlling ac machines such as inverter-supplied induction motors/synchronous motors. The dynamic performance of such drives is comparable to that of a converter fed four quadrant dc drives. The complex functions required by field oriented control are executed by intelligent controllers using microcontrollers or digital signal processors (DSP), thus greatly reducing the necessary control hardware [3, 6].

An important requirement to obtain good control performance is to make the motor parameters in the field-oriented controller coincide with the actual parameters of the motor. The ability to inject currents into the motor with a current source opened up new possibilities for parameter determination. It was Takayoshi [4] who described a new identification technique utilizing injected negative sequence components. It is shown that the stator as well as rotor resistance and leakage inductance can be determined on line while the motor is driving the load. The theory is verified with a full-scale hybrid computer simulation of a field-oriented controlled PWM inverter based induction motor drive.

2.4 Direct Vector Control

In direct FOC [5] the rotor angle or control vector is obtained by the terminal voltages & currents directly by using flux estimators. The direct vector control is also known as feedback vector control scheme. Similar to Indirect Vector Control, various controllers have been implemented on direct vector controlled induction motor drives also to improve the performance of the drive.

While the direct method is inherently the most desirable control scheme, it suffers from high cost and the unreliability of the flux measurement. Although the indirect method can approach the performance of the direct measurement scheme, the major weakness of this approach is centered upon the accuracy of the control gains which, in turn, depend heavily on the motor parameters assumed in the feed forward control algorithm.

3. Mathematical equations governing IMFOC

Axis transformation is governed by following set of equations [7]

$$I_{dq0} = TI_{abc} = \frac{2}{3}\begin{bmatrix} Cos\theta & Cos\left(\theta - \frac{2\pi}{3}\right) & Cos\left(\theta + \frac{2\pi}{3}\right) \\ -Sin\theta & -Sin\left(\theta - \frac{2\pi}{3}\right) & -Sin\left(\theta + \frac{2\pi}{3}\right) \\ \frac{1}{2} & \frac{1}{2} & \frac{1}{2} \end{bmatrix}\begin{bmatrix} I_a \\ I_b \\ I_c \end{bmatrix} \quad \text{Eq. 1}$$

$$I_{abc} = Te^{-1}I_{dq0} = \frac{2}{3}\begin{bmatrix} Cos\theta & -Sin\theta & 1 \\ Cos\,(\theta - \frac{2\pi}{3}) & -Sin\,(\theta - \frac{2\pi}{3}) & 1 \\ Cos\,(\theta + \frac{2\pi}{3}) & -Sin\,(\theta + \frac{2\pi}{3}) & 1 \end{bmatrix}\begin{bmatrix} I_d \\ I_q \\ I_o \end{bmatrix} \quad \text{Eq. 2}$$

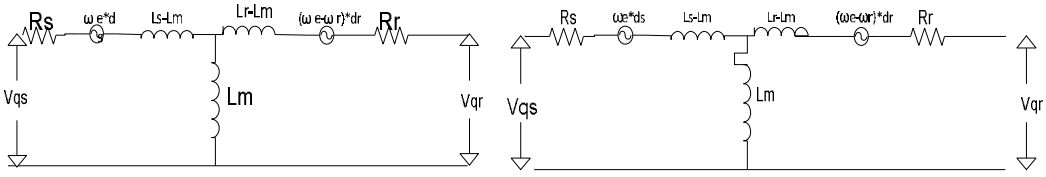


Fig. 1: Dynamic $d^e - q^e$ equivalent circuits of machine.

Voltage Equations are $V_{qs} = R_s * i_{qs} + \frac{d\psi_{qs}}{dt} + \omega_e\psi_{ds}$ Eq. 3

$$V_{ds} = R_s * i_{ds} + \frac{d\psi_{ds}}{dt} + \omega_e\psi_{qs} \quad \text{Eq.4}$$

$$V_{qr} = R_r * i_{qr} + \frac{d\psi_{qr}}{dt} + (\omega_e - \omega_r)\psi_{dr} \quad \text{Eq.5}$$

$$V_{dr} = R_r * i_{dr} + \frac{d\psi_{dr}}{dt} - (\omega_e - \omega_r)\psi_{qr} \quad \text{Eq.6}$$

Flux Equations are

$$\psi_{qs} = L_{ls} * i_{qs} + (i_{qs} + i_{qr})L_m \quad \text{Eq.7}$$

$$\psi_{qr} = L_{lr} * i_{qr} + (i_{qs} + i_{qr})L_m \quad \text{Eq.8}$$

$$\psi_{ds} = L_{ls} * i_{ds} + (i_{ds} + i_{dr})L_m \quad \text{Eq.9}$$

$$\psi_{dr} = L_{lr} * i_{dr} + (i_{ds} + i_{dr})L_m \quad \text{Eq.10}$$

4. Rotor Flux Estimation

In direct vector control method, it is necessary to estimate the rotor flux components ψ_{dr}^s *and* ψ_{qr}^s so that the unit vector and rotor flux can be calculated using equations

$$Cos\,\theta_e = \frac{\psi_{dr}^s}{\hat{\psi}_r} \quad \text{Eq. 11}$$

$$Sine\,\theta_e = \frac{\psi_{qr}^s}{\hat{\psi}_r} \quad \text{Eq. 12}$$

$$\hat{\psi}_r = \sqrt{\psi_{dr}^{s^2} + \psi_{qr}^{s^2}} \quad \text{Eq. 13}$$

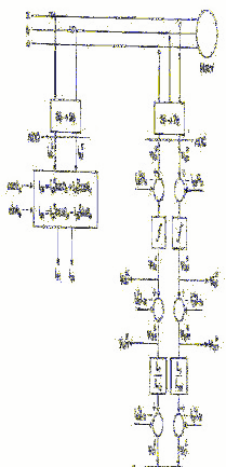


Fig. 3: Model from B.K. Bose

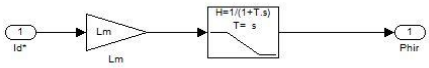


Fig. 4: Model using Constant

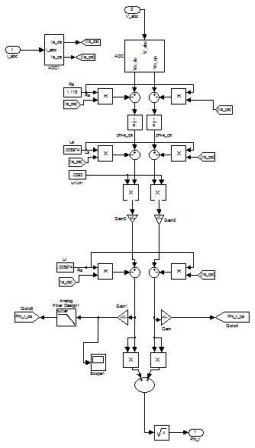


Fig. 5: Implemented Model from B.K. Bose

5. Simulation Results

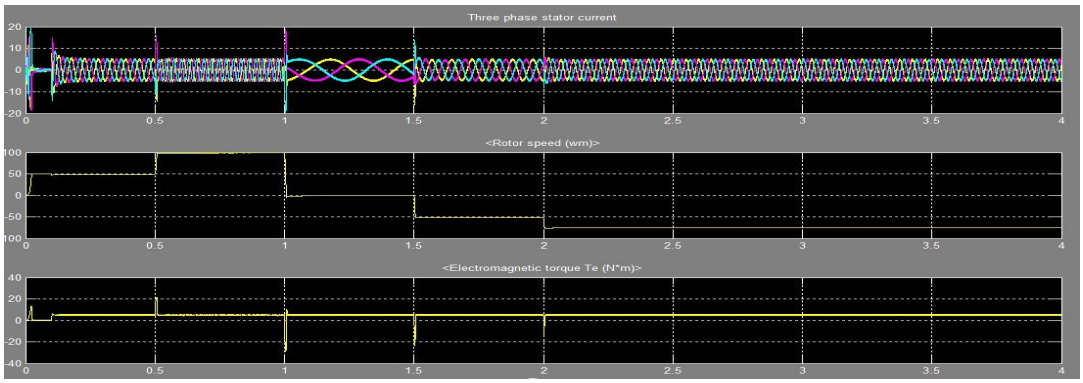


Fig. 4: Results 1 obtained using Rotor Flux Model.

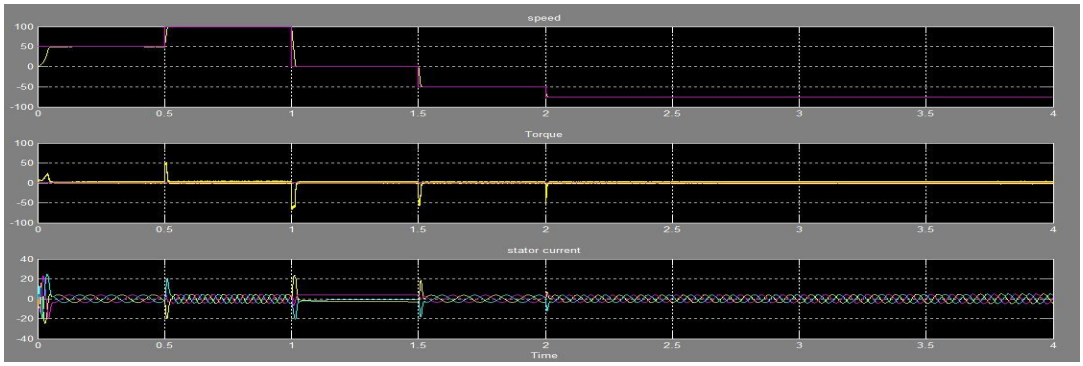


Fig. 5: Results 2 obtained using Rotor Flux Model.

6. Conclusion

From the above simulation results it was observed that the current waveforms are smoother as well as very less distortion in result 2 as compared to result 1. Moreover the torque waveforms are also better and the controller performance to track the reference speed is much more precise in results 2. Therefore it can be concluded that the vector control using model given in fig 5. It is obvious that the machine parameters and the PI controller parameters are same while performing the simulation in order to achieve the comparison.

References

[1] F. Blaschke, “Das VerfahrenDer Feldorientierung Zur RegelungDer Asynchronous machine",Siemens Forschungs-und Entwicklungsberichte1,1972.

[2] K. Hasse, "Zurdynamikdrehzahlgeregelter antriebemitstromrichtergespeisten asynchrony-kurzschlublaufenn- aschinen", Darmstadt, Techn. Hochsch, Diss., 1969.

[3] Rupprecht Gabriel. Werner Leonhard, and Craig J. Nord by, “Field-Oriented Control of a Standard AC Motor Using Microprocessors”, IEEE Transactions On Industrial ApplicationsVol.IA-16,No.2,March/April1980

[4] Takayoshi Matsuo and Thomas A. Lipo, “A Rotor Parameter Identification Scheme for Vector-Controlled Induction Motor Drives”, IEEE Transactions On Industry Applications,Vol.IA-21,No.4,May/June1985

[5] David M. Brod, and Donald W. Novotny, “Current Control of VSI-PWM Inverters”, IEEE Transactions On Industry Applications,Vol.IA-21. No. 4, May/June1985

[6] Masato Koyama, Masao Yano, Isao Kamiyama, And Sadanari Yano, “Microprocessor-Based Vector Control System For Induction Motor Drives With Rotor Time Constant Identification Function”, IEEE Transactions on Industry Applications,Vol.Ia-22,No.3,May/June1986.

[7] Bimal. K.Bose – “Modern Power Electronics & AC Drives”, Prentice Hall.

Med Chem Res
DOI 10.1007/s00044-014-1274-8

MEDICINAL CHEMISTRY RESEARCH

ORIGINAL RESEARCH

Curcumin-based IKKβ inhibiting anticancer lead design using novel fragment-based group QSAR modelling

Kunal Patel · Chetna Tyagi · Sukriti Goyal · Jaspreet Kaur Dhanjal · Navneeta Bharadvaja · Abhinav Grover

Received: 16 April 2014 / Accepted: 27 September 2014
© Springer Science+Business Media New York 2014

Abstract NF-κB transcription factor plays a vital role in the protection of transformed cells from apoptosis, thus resulting in the onset/progression of cancer. Activation of NF-κB is strictly controlled by IκB kinase, and therefore IκB kinase inhibition forms the basis for anticancer drug research. We present here a novel fragment-based QSAR model using 4-arylidene curcumin analogues having IκB kinase inhibitory properties. The insights into the contribution of each chemical fragment of the analogues in IκB kinase inhibitory activity were used to generate a combinatorial library containing 167,828 molecules and their inhibitory activities were predicted by the reported G-QSAR model. We report top two scoring compounds BEP and BHP possessing high docking scores of −9.21 and −8.98 kcal/mol, respectively. Molecular dynamics simulations studies showed that the trajectories of the IκB kinase complexed with BEP and BHP were stable over a considerably long time period (16 ns). The two compounds reported here showed high binding affinity and stability with IκB kinase and thus can be taken forward as promising anticancer leads. The G-QSAR model reported here will pave way for the development of novel leads by high-throughput activity prediction of similar compounds.

K. Patel · N. Bharadvaja
Department of Biotechnology, Delhi Technological University, Delhi 110042, India

C. Tyagi · J. K. Dhanjal · A. Grover (✉)
School of Biotechnology, Jawaharlal Nehru University, New Delhi 110067, India
e-mail: abhinavgr@gmail.com; agrover@jnu.ac.in

S. Goyal
Apaji Institute of Mathematics & Applied Computer Technology, Banasthali University, Tonk 304022, Rajasthan, India

Keywords Transcription factor · NF-κB · IκB kinase · Anticancer · Curcumin · QSAR · Simulations

Introduction

Cancer is a class of disease characterized by hyperproliferative cell growth resulting due to the imbalance between cell growth, cell division and apoptosis. Hyperproliferative cell growth results in tumour initiation and promotion, which ultimately leads to metastasis. Quest for a method to cure or control the disease has been going on for many years. In the last 25 years, few proteins have managed to have as profound influence in immunology and cancer biology as the transcription factor NF-κB. NF-κB was first discovered in the light chain of immunoglobulins by Sen and Baltimore while working on B cells in the year 1986 (Sen and Baltimore, 1986). Further studies have shown that it is a frequently expressed inducible transcription factor and plays a role in inflammatory responses, regulation of various genes which are involved in the regulation of cell cycle, cellular transformation, proliferation, invasion and angiogenesis (Baldwin, 2001; Collins *et al.*, 1995; Shishodia and Aggarwal, 2002; Yan *et al.*, 2000). NF-κB exists as a dimer in its functional state and is present in a number of combinations belonging to the Rel family of polypeptides. Various kinds of stimuli like growth factors and inflammatory cytokines activate NF-κB. In response to stimuli, IκB proteins which are bound to NF-κB undergo phosphorylation, ubiquitination and are degraded ultimately. Dissociation of NF-κB from IκBα is catalysed by an enzyme IκBα kinase (IKK) complex; it phosphorylates IκBα which is critical for initiation of pathway leading to the activation of NF-κB. IκBα kinase (IKK) complex has molecular mass of 700 kDa and it is composed of IKK-α,

Published online: 10 October 2014

IKK-β, IKK-γ (also known as NEMO) and a few unidentified proteins (Kabrun and Enrietto, 1994).

Previous researches have concluded that the NF-κB having implication in carcinogenesis that can't be neglected. Evidence indicates that NF-κB can lead to tumorigenesis thus establishing that agents which can suppress NF-κB activation can rescind carcinogenesis. NF-κB is needed in its active form for tumour cell invasion and its expression has been observed in most of the cancer cell types like breast, colon, leukaemia, lymphoma, melanoma, myeloma, prostate, pancreatic, neck and head squamous cell carcinoma (Baldwin, 2001; Bargou *et al*., 1997; Mori *et al*., 1999; Sarkar and Li, 2003). Thus, inhibition of NF-κB can be achieved by inhibiting IKKβ enzyme which is required for its activation. The IKK complex comprises two catalytic subunits, IKKα and IKKβ, and a regulatory subunit, IKKγ. Although both IKKα and IKKβ catalyse the phosphorylation of NF-κB, the latter subunit plays a central role (Delhase *et al*., 1999). Thus, the canonical pathway activating NF-κB can be disrupted by inhibiting IKKβ subunit.

Many natural food agents have been reported to inhibit NF-κB which includes soya isoflavone (Holmes-McNary and Baldwin, 2000) resveratrol (Plummer *et al*., 1999) and curcumin (Nautiyal *et al*., 2011). Turmeric, derived from *Curcuma longa* rhizome, has been used by mankind for centuries for various purposes. Curcuminoids, the main biologically active compounds present in *Curcuma longa*, are known to have therapeutic effect against leukaemia and cancer of brain, cervix, lung, prostate, breast, ovaries and bladder, and liver, pancreas and colorectal epithelial cancers (Hatcher *et al*., 2008; Huang *et al*., 1994; Wolanin *et al*., 2006).

It has been found that curcumin targets NF-κB cell signalling pathway by directly inhibiting IKK enzyme and the 26S proteasome (Leu and Maa, 2002; Milacic *et al*., 2008). However, due to poor bioavailability and comparatively low potency, it is not a widely used compound in medicine (Anand *et al*., 2007). To increase the potency against cancer, a series of 4-arylidene analogues were derived from curcumin by Qui *et al*. (2010). Four-arylidene analogue, a Knoevenagel condensate of 1,3-diketones, is found to have noticeably high IKK enzyme inhibition activity and is more cytotoxic for cancer cells than the parent compound curcumin but has low stability in the human body (Qiu *et al*., 2010).

To overcome the problem of low in vivo stability, identification of novel natural compounds which are more potent and more stable has become an urgent need. For this purpose, we require fast and reliable computational techniques for speedy, cost-effective evaluation of large databases of chemical compounds so that a limited set of candidates which have the potential to become lead drug compounds can be identified (Dhanjal *et al*., 2013; Tyagi *et al*., 2013; Goyal 2013; Goyal *et al*., 2014c; Dhanjal *et al*., 2014). Quantitative structure activity relationship (QSAR) is an effective and robust tool which has been used to establish statistically validated correlation model between the physiochemical characteristics of the chemical compounds and their biological activities (Tyagi *et al*., 2014; Vats *et al*., 2014; Goyal *et al*., 2014b; Goyal *et al*., 2014a). This QSAR model is then used for high-throughput activity prediction of new congeneric compound (Golbraikh and Tropsha, 2002). In this study, a novel and more efficient fragment-based QSAR model was developed based on 4-arylidene curcumin analogues (Afantitis *et al*., 2009). The 29 compounds were divided into training and test sets. This model determines the molecular features essential for the effective interaction between the inhibitors and the target enzyme IKKβ kinase. The information obtained from the G-QSAR model was then used to create a combinatorial library and biological activities of library compounds were predicted using the model which suggested some lead drug molecules for further experimental validation. This study will enhance our understanding of curcumin derivatives as a potent anticancer drug and key structural requirements needed for anticancer drug development by targeting IKK enzyme. This will aid in developing novel therapeutics for fighting cancer more effectively.

Materials and methods

Selection and preparation of data set

Marvin Sketch 5.12.01 was used to draw the structures of the 29 '4-arylidene curcumin analogues' in 2D (mol2) format. The inhibitory activity (IC50) values of these analogues were taken from the literature reported by Qiu *et al*. (2010) and converted into their logarithmic pIC50 values. The model generation and its analysis was performed using VlifeMDS (VLife, 2010), version4.3 on Intel® Xeon(R) CPU E31230 at 3.20 GHz with 8.00 GB RAM.

Optimization of the data set

The 2D structures were optimized using force field batch minimization module of Vlife Engine platform. For optimization, Merck Molecular Force Field (MMFF) and Gasteiger charges (Halgren, 1996) were used for 10,000 cycles, dielectric constant was taken (for vacuum) as 1.0 and root mean square gradient was kept at 0.01. This energy minimization confers a stable conformation to the structures. A common scaffold (template) representing all the reported 4-arylidene curcumin analogues with four substitution sites at 7th, 8th, 9th and 18th positions was drawn.

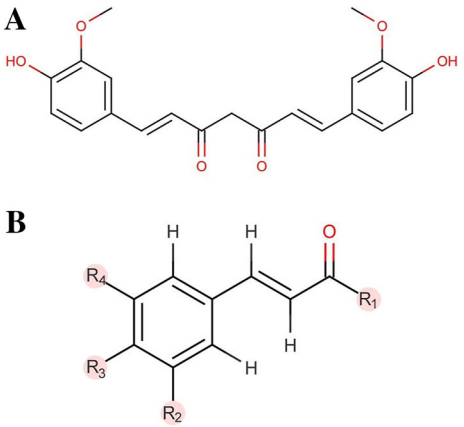


Fig. 1 **a** Structure of curcumin, **b** Diagrammatic representation of the substitution sites on the curcumin template

Calculation of 2D descriptors for G-QSAR model

Using the "Modify molecule" function, dummy atom (X) was assigned to specify the four substitution sites of the template molecule. The energy minimised set of molecules and template with dummy atom at substitution site are then used to build the G-QSAR model. The curcumin template and the substitution sites are depicted in Fig. 1. To build a robust G-QSAR model, calculation of 2D descriptors is one of the most important and inevitable step. The pIC50 values were provided manually for each optimized compound and the 2D descriptors describing various physicochemical properties of curcumin analogues were determined for all the functional groups present at different substitution points of the molecules.

Data selection and development of the G-QSAR model

To build the model, data are divided into two sets, training set is used to build the G-QSAR model and then the model obtained is evaluated for its performance using the test set. Both the data sets were chosen in a way with maximum diversity in terms of their activity value. Eight molecules, namely 7, 14, 20, 22, 25, 28, 31 and 33 were selected in test set data and the remaining 21 molecules were taken for the training set. To test the uniformity of molecules in both the data sets, the Unicolumn statistics were calculated and evaluated. Stepwise backward variable selection method coupled with Partial Least Square (PLS) regression method (Haaland and Thomas, 1988) was chosen for building the G-QSAR model. This algorithm begins by developing a model and adding independent variables one at a time and then examining the fitness of the model using the PLS cross-validation procedure which continuously improves the previous model by removing or adding a predictor variable till the best model is achieved.

The equation formed is:

$$Y = a1 * X1 + a2 * X2 + a3 * X3 + b$$

where X and Y are the independent and dependent variables, respectively, and '$a1$', '$a2$' and '$a3$' are regression coefficients for their corresponding X values and 'b' is a regression constant.

Validation of the developed G-QSAR model

Different statistical parameters were taken into account to examine goodness of fit of the developed G-QSAR model (Afantitis *et al*., 2009), such as r^2, q^2, pred_r^2, F test and standard error. A model is considered robust if the statistical parameters $r^2 > 0.6$, $q^2 > 0.6$ and pred_$r^2 > 0.5$ (Friesner *et al*., 2004; Halgren *et al*., 2004). The F test is also a very important parameter as it represents the ratio of actual variance observed and the variance caused due to error in the regression. Higher F test values show that the model is more statistically significant. Standard error terms of Pred_r^2se, q^2_se and r^2_se should be close to zero to have high fitness quality of the model.

Cross-validation of the model

To cross-validate the model, both external validation and internal validation were carried out. Leave-one-out (q^2, LOO) method was employed for internal validation. In this model, q^2 is calculated by consecutively removing each molecule from training set and then the same descriptor was used to refit the model. The refit model is used to predict the biological activity of the compounds which were removed earlier. The formula used for calculation of q^2 was

$$q^2 = 1 - \left(\frac{\sum(y_i - y)}{\sum(y_i - y_{\text{mean}})}\right)$$

where y_i represents the real activity and y represents the predicted activity, i is the number of molecules in the training set and y_{mean} represents the average activity of all molecules present in the training set. Once the model is generated from training set, it was used for external validation by predicting the test set data using the obtained model. The formula used is given below

$$\text{pred_}r^2 = 1 - \left(\frac{\sum(y_i - y)}{\sum(y_i - y_{\text{mean}})}\right)$$

where y_i represents the real activity and y represents the predicted activity, i is the number of molecules in the test set and y mean represents the average activity of all molecules present in the test set.

To test the robustness of the generated model, another test called Y randomisation was also carried out, in which

molecules were reshuffled to generate random sets and their activities in the training set were predicted. *Z*-score was calculated that determines the statistical significance of the model (Alexander and Alexander, 2002). The generated model is compared with the model derived from the random data sets. *Z*-score was determined by the formula:

$$Z\text{-score} = \frac{(h - \mu)}{\sigma}$$

where h represents q^2 value of the real data set, μ is mean of the all q^2 values and σ denotes standard deviation obtained for all the reiterations employing models built by various data sets chosen at random.

Generation of combinatorial library

The Leadgrow module of VLifeMDS was used for generating the combinatorial library using various moieties on all the four substitution sites—R1, R2, R3 and R4. Many libraries were created using various combinations of substitution groups like various atoms, alkyl group, alkenes, ketones, acids, aromatic rings, cyclic groups, $–OCH_3$, $–OCH_2CH_3$, NH_2 at all substitution sites. A library of 167,828 compounds was generated and the validated G-QSAR model was then used to predict the activity of these compounds. Activity prediction resulted in 233 compounds having high activity values than the curcumin analogues used for model building. They were selected for further evaluation to test their potency as anticancer candidates.

Preparation of protein and ligand for docking

The crystal structure of IkB kinase beta was retrieved from Protein Data Bank [PDB ID: 4KIK] (Liu *et al*., 2013). For the sake of reducing the computational time, only B chain was taken for docking and MD studies. After removal of water molecules and non-bonded heteroatoms, it was further prepared using Schrodinger's protein preparation wizard (Sastry *et al*., 2013), where hydrogen atoms were added and the structure was optimized. Also bad contacts were removed, bond lengths were optimized, missing disulphide bonds were created, terminal residues were capped and selenomethionines were converted to methionines. The 233 lead compounds obtained from the combinatorial library were also prepared before docking using Schrodinger's LigPrep ligand preparation protocol (Sastry *et al*., 2013). Different tautomeric, chiral, stereochemical and ionization variants of the lead compound were generated along with energy minimization and flexible filtering.

Using the Schrodinger's glide module (Friesner *et al*., 2006; Halgren *et al*., 2004), a cubic grid with sides of 20 Å was created around the active site of the protein target involving residues, Phe26, Val29, Ala42, Lys44, Met65, Val74, Ala76, Glu97, Tyr98, Cys99, Lys106, Val152 and Gly168 (Nagarajan *et al*., 2010). The grid was generated while keeping the centroid of the selected residues as the centre. The scaling factor was kept at a default value of 1.0, with a partial charge cut-off value of 0.25. No constraints were defined during the generation of the receptor grid. Glide's XP docking (Friesner *et al*., 2006) protocol was used to evaluate the binding affinities of top 233 compounds taken from the combinatorial library. The Glide score is an empirical scoring function that represents the ligand binding free energy. The terms included in the calculation either reward or penalize the interactions that influence ligand binding. The Glide XP Score specifically penalizes the poses that violate physical chemistry principles. The XP GlideScore function is given in Eq 1. The top two compounds having the least Glide score i.e., highest binding affinity were obtained and their molecular interactions were studied. The hydrogen bonds and hydrophobic interactions were plotted using Ligplot (Wallace *et al*., 1995).

$$\text{XP GlideScore} = E_{\text{coul}} + E_{\text{vdW}} + E_{\text{bind}} + E_{\text{penalty}}$$

where,

$$E_{\text{bind}} = E_{\text{hyd_enclosure}} + E_{\text{hb_nn_motif}} + E_{\text{hb_cc_motif}} + E_{\text{PI}} + E_{\text{hb_pair}} + E_{\text{phobic_pair}}$$

and,

$$E_{\text{penalty}} = E_{\text{desolv}} + E_{\text{ligand_strain}}$$

Molecular dynamics simulations studies

To get more insight into the protein–ligand complex and its stability, molecular dynamic study was performed using Desmond Molecular Dynamics module of Schrodinger maestro (Jorgensen *et al*., 1996) by applying optimized Potentials for Liquid Simulations (OPLS) all-atom force field 2005 (Kaminski *et al*., 2001). Prepared protein–ligand complexes were solvated with TI4P water model in a triclinic periodic boundary box for MD simulations. To prevent the direct interaction of protein complex with its own periodic image, a boundary box is created and the distance between protein complex and box wall is kept at 10 Å. Steepest descent method was used to minimise the energy of the prepared structures for a maximum of 5,000 steps till a threshold of 25 kcal/mol/Å is achieved, which was then followed by Low-memory Broyden–Fletcher–Goldfarb–Shanno quasi-Newtonian minimizer until a convergence threshold of 1 kcal/mol/Å was met. Other parameters were kept as default for system equilibration. MD simulations were carried out for 15 ns at a constant temperature of 300 K, pressure 1 atm and at time step of 2 femtoseconds (fs). Long-range electrostatic interactions were calculated

using smooth particle mesh Ewald method (Essmann *et al*., 1995), which were occurring during the MD simulations, and coulombic short-range interaction was calculated using a cut-off scheme, with a cut-off radius of 9 Å for calculation. The protein–ligand complex was prepared for MD simulations using the above-mentioned parameters. MD Simulation was then carried for a time period of 15 ns.

The root mean square deviation values (RMSD) for two top scoring ligands were calculated for the entire simulations trajectory with reference to their respective first frames. Radius of gyration (ROG) analyses were carried out for all the frames of 15 ns MD simulation of IkB kinase beta and ligand complex. Ligplot program was used for the hydrophobic interactions and H-bonds calculation.

Results and discussion

G-QSAR molecular modelling

Here we report a fragment-based group QSAR model that describes the structure–activity relationship for the 29 4-arylidene curcumin analogues. These curcumin analogues target IκB kinase beta by binding to its ATP-binding site, leading to inhibition of IKK complex enzyme which is required for the activation of NF-κB thereby inducing tumour cells to undergo apoptosis.

Unicolumn statistics for the chosen training and test set

The 4-arylidene analogues of curcumin prepared and reported by Qiu *et al*. along with their IC50 values, were divided into two datasets: 8 in test data set and remaining 21 in training data set. Unicolumn statistical analysis was performed to validate the selection of test and training set. Upon analysis, it was seen that the maximum of test set is equal to the maximum of training set and the minimum value of the test set is greater than the minimum value of training set (Table 1), which means that the test set lies within the preferable range of the training set and a better understanding of the relative variance of mean and point density distribution of the two sets can be analysed by mean and standard deviation data.

Table 1 Unicolumn statistics for the training and test set compounds

Data	Average	Maximum	Minimum	Standard deviation (SD)	Sum
Training set	5.5619	6.0000	4.4100	0.4491	116.8000
Test	5.6662	6.0000	5.1000	0.3323	45.3300

Analysis of the fragment-based QSAR model of 4-arylidene curcumin analogues

Many models were generated in the quest of a robust G-QSAR model which can explain the correlation between the physiochemical parameters and also the contribution of each fragment of curcumin derivatives. All the models were evaluated on the basis of various statistical parameters. Out of the many, the model with correlation coefficient r^2 value of 0.9556, cross-validated correlation coefficient q^2 value of 0.7113, pred_r^2 value of 0.8017, low standard error, r^2_se value of 0.1017, q^2_se value of 0.2594 and pred_r^2_se value of 0.1432 can be stated to be a robust one. The F test value of 193.8604 also supported the chosen model for its robustness by implying that the model is 99.999 % statistically accurate and chances of its failure are as low as 1 out of 10,000.

To further corroborate this claim of robustness, randomization test score can also be considered which indicates that the developed model predicts with confidence greater than 99.999 % (Alpha rand R2 = 0.00100) suggesting that it is not generated by chance and hence it is chosen as the G-QSAR model. Many other parameters like *Z*-score and random score are also taken into account and are presented in Table 2. The *Z*-score gives an idea about the deviation of observed value from the mean value. A Zscore_r^2 of 3.4004 gives 99.97 % area under the normal curve, Zscore_q^2 of 3.2858 gives 99.95 % area under the curve and Zscore_pred_r^2 of 1.4256 gives 92.30 % area under the curve which statistically validates the significance of the obtained G-QSAR model.

The linear graphical representation between actual and predicted activities of the 29 compounds along with the contribution plot for each descriptor in Fig. 2 gives a better understanding of the robustness of the model. It shows the extent of variation between the actual and predicted activities of the congeneric set; larger the deviation of training and test set points from the regression line, more is the difference between the actual and the predicted activity

Table 2 The statistical parameters calculated for developed G-QSAR model

Dep. variable	ZScore_r^2	Z-Score_q^2	Best rand r^2	Best rand q^2	Alpha rand r^2	Alpha rand q^2	Z-score_pred_r^2	Best rand pred r^2	Alpha rand pred_r^2
pIC50	3.4003	3.2858	0.64585	0.39488	0.00100	0.00100	1.42561	0.7635	0.10000

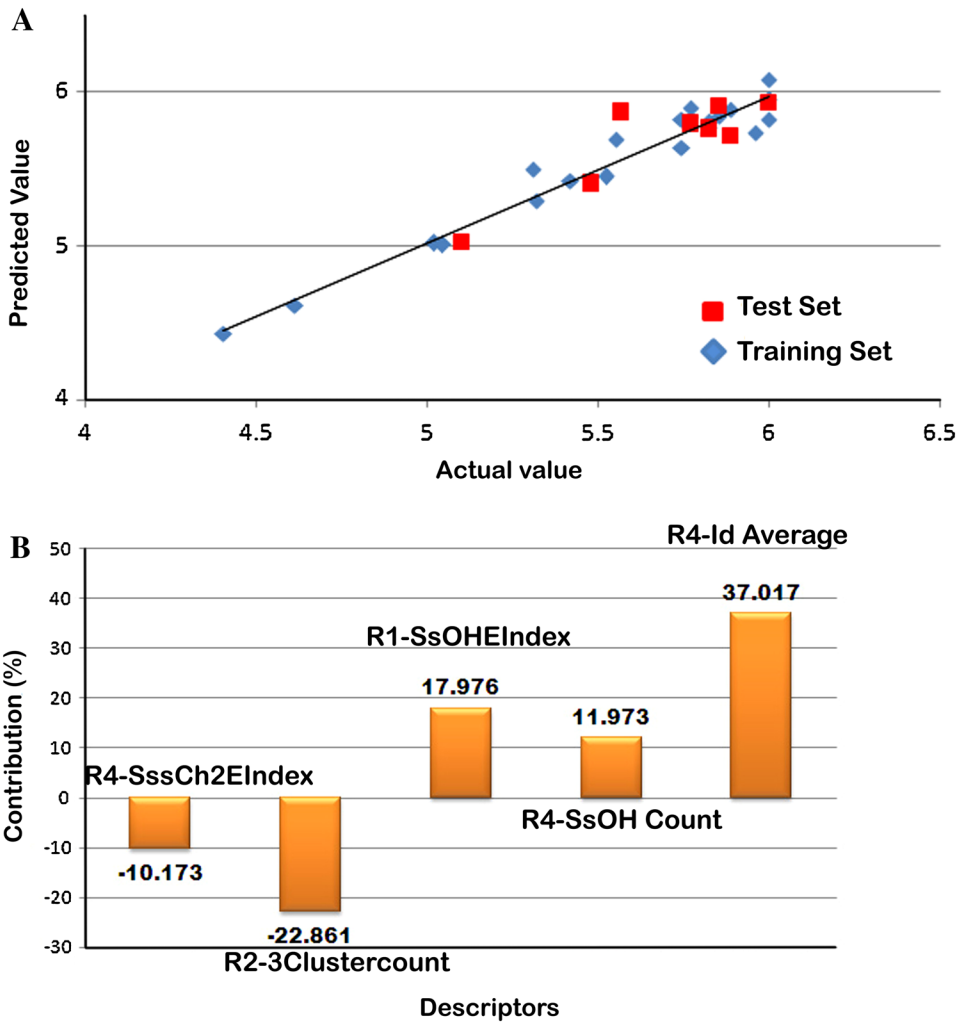


Fig. 2 **a** Fitness plot of the G-QSAR model obtained for actual and predicted activities. The other test set points overlap with the previous ones and hence cannot be differentiated. **b** Contribution plot of the selected descriptors R4-SssCH2E-index, R2-3ClusterCount, R1-SsOHE-index, R4-SsOHcount and R4-IdAverage

values. Contribution plot depicts the contribution of each descriptor and quantifies the effect of presence or absence of a property in lead molecule for enhancing its inhibitory activity. Presence of descriptors with positive contribution increases its inhibitory activity while descriptors with negative contribution decrease the same. Radar plots for training and test sets are shown in Fig. 3. These graphs depict the difference in the actual and predicted activities for the training and the test sets separately by the extent of overlap between blue (actual activity) and red (predicted activity) lines. The plot for training set represents a good r^2 value if the two lines show a good overlap, while for the test set, a good overlap represents high pred_r^2 value. Thus, it can be deduced from the analysis that the proposed model is reliable and predictive.

The correlation between the molecular descriptors representing the physiochemical parameters of the ligands and their biological activities is given by the following equation:

$$\begin{aligned}\textbf{pIC50} &= (0.0543626 \times \textbf{R1}-\textbf{SsOHE}-\textbf{index}) \\ &+ (-0.892346 \times \textbf{R2}-\textbf{3ClusterCount}) \\ &+ (-0.286261 \times \textbf{R4}-\textbf{SssCH2E}-\textbf{index}) \\ &+ (0.169529 \times \textbf{R4}-\textbf{SsOHcount}) \\ &+ (0.63639 \times \textbf{R4}-\textbf{IdAverage}) + 3.02689\end{aligned}$$

The equation obtained had five physiochemical descriptors which are explained below:

R1-SsOHE-index: This descriptor belongs to a class of Estate contributions. This descriptor signifies the number of –OH groups connected with one single bond at R1 substitution site. The contribution plot (Fig. 2b) shows that it has a positive contribution of 17.98 % which indicates that OH group at R1 has positive effect on its activity.

R2-3ClusterCount: This descriptor implies the presence of total number of cluster of third order fragments in the molecule. The contribution plot (Fig. 2b) shows that it has a negative contribution of 22.86 % which indicates that

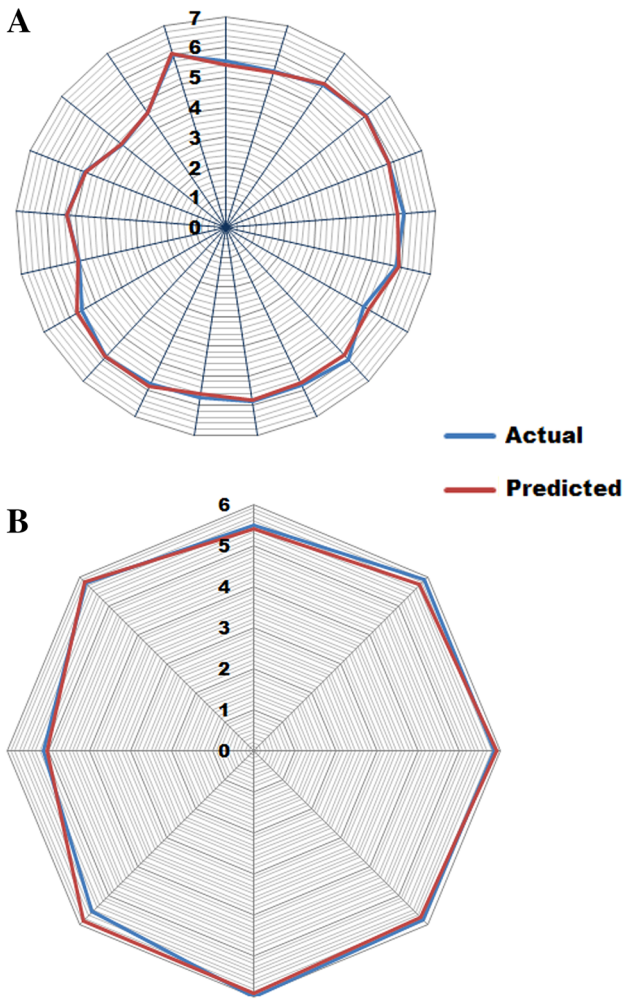


Fig. 3 Radar graphs plotting the predicted and actual activities for **a** training set and **b** test set

the presence of cluster fragment of third order at substitution site R2 reduces the biological activity.

R4-SssCH2E-index: This descriptor belongs to a class of estate number descriptors and describes the effect of total number of $–CH_2$ groups connected with two single bonds. The contribution plot (Fig. 2b) shows that it has a negative contribution of 10.17 % which indicates that $–CH_2$ group present at the R4 site has slight negative impact in enhancing the biological activity.

R4-SsOHcount: This descriptor belongs to a class of estate number descriptors. This descriptor describes the effect of total number of –OH groups attached with a single bond. The contribution plot (Fig. 2b) shows that it has a positive contribution of 11.97 % which indicates that OH group present at the R4 site has slight positive impact in enhancing the biological activity.

R4-IdAverage: This descriptor is a type of information theory-based descriptor and has a positive impact on the biological activity of curcumin analogues. The contribution plot shows that it has a positive contribution of 37.02 %.

Activity prediction of the combinatorial library using 4-arylidene curcumin moiety as template

Combinatorial libraries were generated using a common template and their biological activities were predicted using the obtained G-QSAR model. The different libraries were generated on the same template with different combinations of substitution group in a sequential order for e.g., atoms such as H, C, F, N, Cl, K, Br and aromatic rings like phenoxy, phenyl, furan, pyrrole, pyridine, imidazole, 2-thiophene, alkenes, acids, aliphatic rings and other groups such as $–O–CH_3$, $–O–C_2H_5$, amide, cyanide, cyanate, isocyanate, –C=N, –N=C, azo, hydrazo, benz etc. Each library consisted of thousands of molecules and a total of 167,828 molecules were generated and their biological activities were predicted. Only those molecules were considered for further docking studies whose predicted value was higher than the reported curcumin analogues ($pIC_{50} > 6.00$) and had extrapolation less than 2.4. This filtering gave us 233 compounds for proceeding further with modelling studies. Analysis of the substitution groups in top compounds revealed that the presence of groups such as $–OCH_3$, $–O–C_6H_5$, $–OCH_2CH_3$, Phenyl ring, Benzene ring, $–CH_2–CH_3$, $–CH_3$ and so on at R1 position and $–OCH_2CH_3$ at R4 position significantly enhanced inhibitory activity, while the presence of bulky groups at R2 position decreased the same. These findings were in accordance with the QSAR model obtained.

Interaction analysis of the predicted natural compounds using docking and molecular dynamics

Molecular docking analysis was carried out to get a better understanding of the probable inhibitory activity and binding poses of the top scoring candidates. The top 233 compounds with predicted pIC50 values greater than 6.00 were taken from the combinatorial library and docking was done against the crystal structure of IκB kinase using the Glide protocol. The two top scoring compounds, (2*E*)-3-(4-*benzyl*-3-*ethoxy*-5-*ethylphenyl*) *prop*-2-*Enal* [BEP] and (2*E*)-3-(4-*benzyl*-3-*hydroxyphenyl*) *prop*-2-*enal* [BHP] with glide score of −9.2069 and −8.9836 kcal/mol, respectively, (shown in Fig. 4a, b) were further examined to find their mode of interaction with the target protein. The first compound, BEP showed a good binding affinity with the active site of IκB kinase (Nagarajan *et al.*, 2010) and formed two Hydrogen bonds with Oxygen of Glu61 (2.83 Å) and Nitrogen of Leu167 (3.00 Å) of the catalytic domain. It also showed hydrophobic interactions with residues involving Ile165, Asp166, Met96, Val29, Leu21,

Asp103, Glu149, Met65, Gly22, Leu94, Glu97, Val152, Ala42, Tyr98, Cys99, Asn150, Glu61 and Leu167 (Fig. 5a). Some of these residues are part of the active site and some are present in close proximity. The second top scoring compound, BHP also showed good interaction with the active site IκB kinase via H-bonds and hydrophobic interactions. The ligand formed two hydrogen bonds with Asp166 (2.95 Å), Cys99 (2.98 Å) along with the hydrophobic interactions involved with the active site of IKKβ with surrounding residues namely Lys44, Glu97, Gly102, Val29, Ala42, Ile165 Asp103, Leu21, Tyr98, Ile165, Asp103 and Met96 (Fig. 5b). It was observed that both compounds have almost similar orientation or docking conformation as the ligands were docked at the same position. Hence, it is strongly suggested that these two compounds have the potential to inhibit enzymatic activity of IκB kinase effectively and thus inhibiting the formation of NF-κB.

Molecular dynamics studies were also carried out to evaluate the stability of protein–ligand complex in in vivo conditions. The 15-ns long simulations were run for two complexes BEP and BHP. RMSD was found to be quite high in the beginning of simulation of BHP but after 4000 ps, both the complexes started showing more stability and low RMSD variation for the rest 11 ns. BEP which was forming two H-bonds in docking studies was seen to be stabilized only by hydrophobic interaction with residues Leu21, Val29, Met96, Glu97, Gly102, Asp103, Val152, Ile165 and Asp166 (Fig. 5c). Also, RMSD plot showed that this loss of H-bond had minimal effect on the stability of the molecule as it showed strong hydrophobic interaction with the binding pocket. The 2nd compound BHP showed no change in H-bond formation and a slight change in hydrophobic interaction pattern during the simulations study. The residues involved in hydrophobic interactions (Table 3) were Val29, Ala42, Lys44, Met96, Glu97, Tyr98, Ile165 and Val152 (Fig. 5d). The first compound BEP (Glide score: −9.21 kcal/mol) was found stable for 11 ns at RMSD of 1.5 Å (Fig. 6a), while the second compound BHP (Glide score: −8.98 kcal/mol) (Table 4) was stable for 11 ns at RMSD of 2.5 Å (Fig. 6b). This indicates that the complex in presence of water molecules undergoes structural changes during the initial run of the simulations

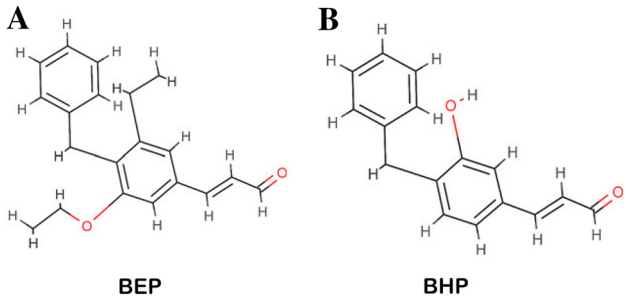


Fig. 4 The structures of top two scoring compounds **a** BEP, **b** BHP

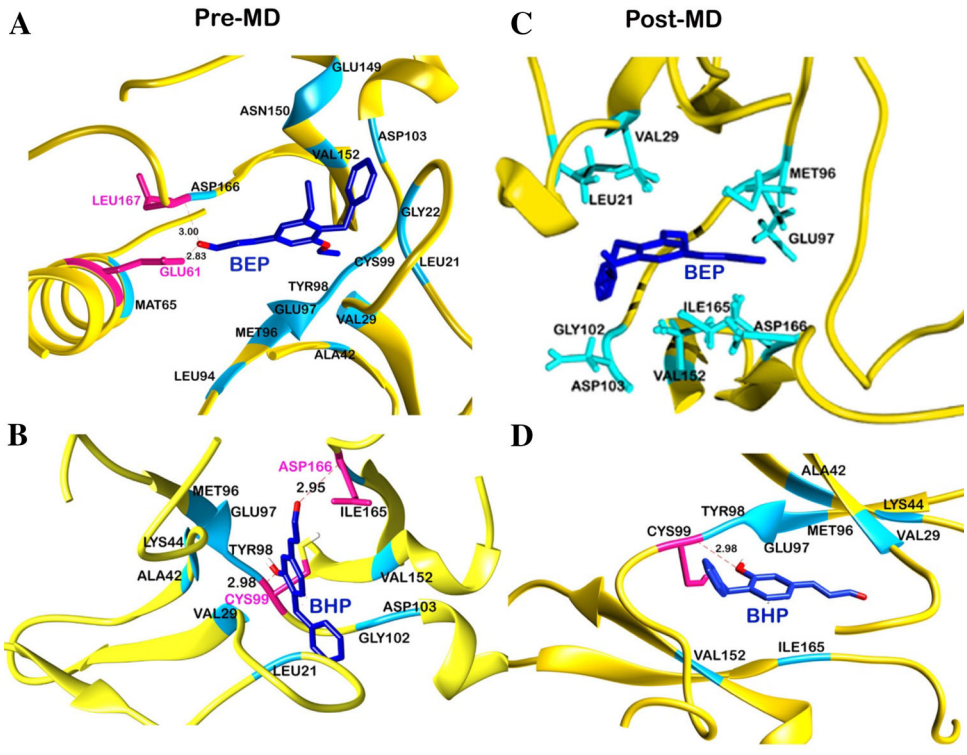


Fig. 5 Interactions present in the docked structures. **a** Residues involved in H-bond formation (*red*) and hydrophobic interactions (*blue*) with BEP and **b** residues involved in H-bond formation (*red*) and hydrophobic interactions with BHP. After molecular dynamics study, **c** residues involved in H-bond formation (*red*) and hydrophobic interactions with BEP (*blue*) and **d** residues involved in hydrophobic interactions with BHP (Color figure online)

and later slowly stabilizes for the rest part of the simulation studies. No instability was seen during MD study and RMSD plot showed that the ligand is forming a stable complex with the IKKβ. Molecular dynamics study showed that both the compounds are showing stable complex formation with IKKβ (Fig. 7).

Conclusion

In the above study, a novel G-QSAR model was developed for 29 curcumin-derived analogues exhibiting IKKβ inhibitory activity. A statistically sound G-QSAR model was generated with parameters indicating for its robustness and high predictive capability. The model equation consists of five physiochemical descriptors R4-SssCH2E-index, R2-3ClusterCount, R1-SsOHE-index, R4-SsOHcount and R4-IdAverage. Three of these descriptors R1-SsOHE-index, R4-SsOHcount and R4-IdAverage showed a positive contribution of 17.98, 11.97 and 37.02 %, respectively and the other two R4-SssCH2E-index and R2-3ClusterCount had negative contribution of −10.17 and −22.86 %, respectively. A combinatorial library was generated and their inhibitory activities were predicted using the developed G-QSAR model. Many compounds showing good inhibitory activity were picked for docking analysis. Docking analysis revealed important information about the binding pose and the kind of interactions involved with the catalytic domain of IκB kinase. On the basis of Glide's docking score, two compounds BEP and BHP with glide score of −9.2069 and −8.9836 kcal/mol among others were identified as the lead molecules. Further their stability as a complex with IKKβ was tested by doing molecular dynamics study in presence of water. The study showed that the two complexes which are very stable during MD simulations that mimic biological environment and processing have good inhibitory activity and thus may serve as lead molecules for anticancer drug development. This study utilizes the advancement made in the drug designing methodology and elucidates the crucial structural

Table 3 IκB kinase residues that are involved in hydrophobic interactions with BEP and BHP, respectively

	BEP	BHP
Residues involved in hydrophobic interactions	Leu 21, Val 29, Met 96, Glu 97, Gly 102, Asp 103, Val 152, Ile 165, Asp 166	Val 29, Ala 42, Lys 44, Met 96, Glu 97, Tyr 98, Ile 165, Val 152

Table 4 Top two scoring compounds, BEP and BHP with respective XP score values

Entry ID	Title	Potential energy	RMS derivative	Glide lignum score	GLIDE/XP GScore
1.	BEP	63.628124	0.015142	175	−9.2069
2.	BHP	72.243332	0.011819	78	−8.98364

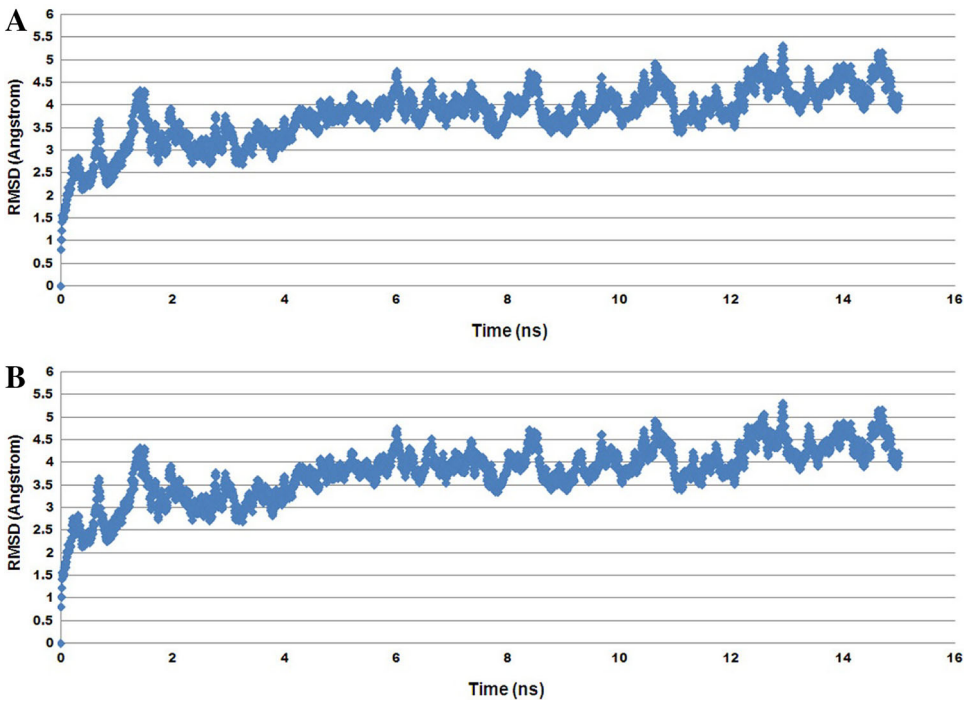


Fig. 6 RMSD plot of molecular dynamics simulations for compounds **a** BEP and **b** BHP

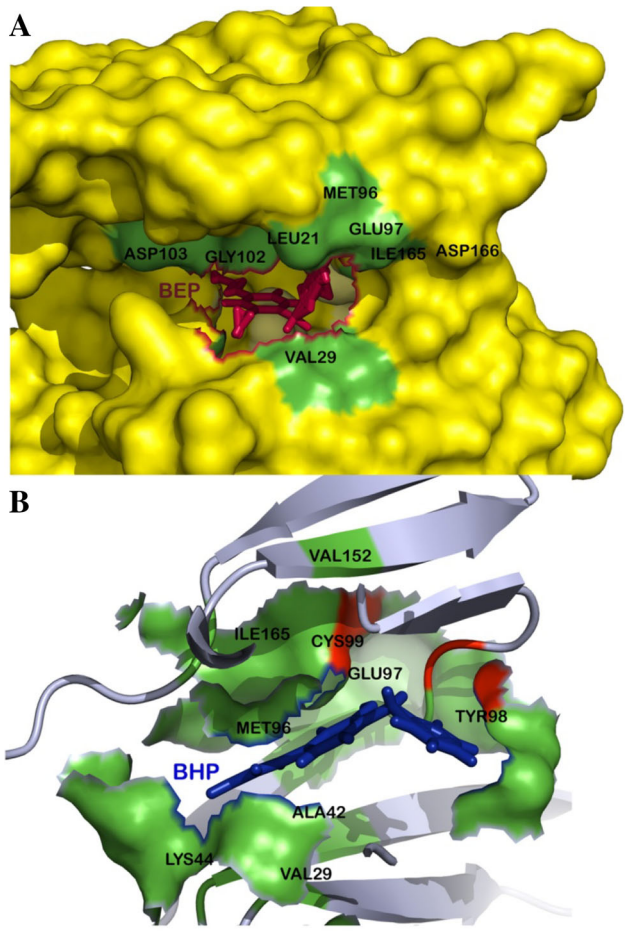


Fig. 7 Interactions present in the MD-simulated structures. **a** Diagrammatic representation of the ligand BEP interacting with active site residue by hydrophobic interaction (shown in *green*) and via H-bond (in *red*). **b** Diagrammatic representation of ligand BHP interaction in the cavity of IκB kinase with hydrophobic interaction (shown in *green*) and H-bond (in *red*) (Color figure online)

requirements of a potent anticancer compound. Study of inhibitory properties of a natural anticancer compound curcumin and its analogues resulted into a novel G-QSAR model. The fragment-based QSAR model developed in this study can be utilised in the identification and development of lead molecules by taking into account the importance of each substituents. This model confers an advantage over the traditional QSAR approaches whose predictive capability is limited as it makes use of properties of the molecules as a whole. The comprehensive analysis carried out in this study would provide a platform for the design and development of novel curcumin-based lead molecules as potent anticancer drugs.

Acknowledgments AG is thankful to Jawaharlal Nehru University for usage of all computational facilities. AG is grateful to University Grants Commission, India for the Faculty Recharge Position.

Conflict of interests The authors declare that there is no conflict of interests.

Ethical standards The manuscript does not contain clinical studies or medical data.

References

Afantitis A, Melagraki G, Sarimveis H, Igglessi-Markopoulou O, Kollias G (2009) A novel QSAR model for predicting the inhibition of CXCR3 receptor by 4-*N*-aryl-[1,4] diazepane ureas. Eur J Med Chem 44:877–884

Alexander G, Alexander T (2002) Beware of Q2! J Mol Gr Model 20:269–276

Anand P, Kunnumakkara AB, Newman RA, Aggarwal BB (2007) Bioavailability of curcumin: problems and promises. Mol Pharm 4:807–818

Baldwin AS (2001) Control of oncogenesis and cancer therapy resistance by the transcription factor NF-kappaB. J Clin Invest 107:241–246

Bargou RC, Emmerich F, Krappmann D, Bommert K, Mapara MY, Arnold W, Royer HD, Grinstein E, Greiner A, Scheidereit C, Dörken B (1997) Constitutive nuclear factor-kappaB-RelA activation is required for proliferation and survival of Hodgkin's disease tumor cells. J Clin Invest 100:2961

Collins T, Read M, Neish A, Whitley M, Thanos D, Maniatis T (1995) Transcriptional regulation of endothelial cell adhesion molecules: NF-kappa B and cytokine-inducible enhancers. FASEB J 9:899–909

Dhanjal JK, Goyal S, Sharma S, Hamid R, Grover A (2013) Mechanistic insights into mode of action of potent natural antagonists of BACE-1 for checking Alzheimer's plaque pathology. Biochem Bioph Res Co 443:1054–1059

Dhanjal JK, Grover S, Paruthi P, Sharma S, Grover A (2014) Mechanistic insights into mode of action of a potent natural antagonist of orexin receptor-1 by means of high throughput screening and molecular dynamics simulations. Com Chem High TScr 17:124–131

Delhase M, Hayakawa M, Chen Y, Karin M (1999) Positive and negative regulation of IκB kinase activity through IKKβ subunit phosphorylation. Science 284:309–313

Essmann U, Perera L, Berkowitz ML, Darden T, Lee H, Pedersen LG (1995) A smooth particle mesh Ewald method. J Chem Phys 103:8577–8593

Friesner RA, Banks JL, Murphy RB, Halgren TA, Klicic JJ, Mainz DT, Repasky MP, Knoll EH, Shelley M, Perry JK, Shaw DE, Francis P, Shenkin PS (2004) Glide: a new approach for rapid, accurate docking and scoring. 1. Method and assessment of docking accuracy. J Med Chem 47:1739–1749

Friesner RA, Murphy RB, Repasky MP, Frye LL, Greenwood JR, Halgren TA, Sanschagrin PC, Mainz DT (2006) Extra precision glide: docking and scoring incorporating a model of hydrophobic enclosure for protein-ligand complexes. J Med Chem 49:6177–6196

Golbraikh A, Tropsha A (2002) Predictive QSAR modeling based on diversity sampling of experimental datasets for the training and test set selection. Mol Divers 5:231–243

Goyal M, Grover S, Dhanjal JK, Goyal S, Tyagi C, Grover A (2013) Molecular modeling studies on flavonoid derivatives as dual site inhibitors of human acetyl cholinesterase using 3D-QSAR, pharmacophore and high throughput screening approaches. Med Chem Res 23:2122–2132

Goyal M, Dhanjal JK, Goyal S, Tyagi C, Hamid R, Grover A (2014a) Development of dual inhibitors against Alzheimer's disease

using fragment-based QSAR and molecular docking. Biomed Res Intl 2014:1–12

Goyal S, Dhanjal JK, Tyagi C, Goyal M, Grover A (2014b) Novel fragment based QSAR modelling and combinatorial design of pyrazole derived CRK3 inhibitors as potent anti-leishmanials. Chem Bio Drug Des 84:54–62

Goyal S, Grover S, Dhanjal JK, Goyal M, Tyagi C, Chacko S, Grover A (2014c) Mechanistic insights into mode of actions of novel oligopeptidase B inhibitors for combating leishmaniasis. J Mol Model 20:2099

Haaland DM, Thomas EV (1988) Partial least-squares methods for spectral analyses. 1. Relation to other quantitative calibration methods and the extraction of qualitative information. Anal Chem 60:1193–1202

Halgren TA (1996) Merck molecular force field. II. MMFF94 van der Waals and electrostatic parameters for intermolecular interactions. J Comput Chem 17:520–552

Halgren TA, Murphy RB, Friesner RA, Beard HS, Frye LL, Pollard WT, Banks JL (2004) Glide: a new approach for rapid, accurate docking and scoring. 2. Enrichment factors in database screening. J Med Chem 47:1750–1759

Hatcher H, Planalp R, Cho J, Torti FM, Torti SV (2008) Curcumin: from ancient medicine to current clinical trials. Cell Mol Life Sci 65:1631–1652

Holmes-McNary M, Baldwin AS (2000) Chemopreventive properties of trans-resveratrol are associated with inhibition of activation of the IκB kinase. Cancer Res 60:3477–3483

Huang MT, Lou YR, Ma W, Newmark HL, Reuhl KR, Conney AH (1994) Inhibitory effects of dietary curcumin on forestomach, duodenal, and colon carcinogenesis in mice. Cancer Res 54:5841–5847

Jorgensen WL, Maxwell DS, Tirado-Rives J (1996) Development and testing of the OPLS all-atom force field on conformational energetics and properties of organic liquids. J Am Chem Soc 118:11225–11236

Kabrun N, Enrietto PJ (1994) The Rel family of proteins in oncogenesis and differentiation. Semin Cancer Biol 5:103–112

Kaminski GA, Friesner RA, Tirado-Rives J, Jorgensen WL (2001) Evaluation and reparametrization of the OPLS-AA force field for proteins via comparison with accurate quantum chemical calculations on peptides. J Phys Chem B 105:6474–6487

Leu TH, Maa MC (2002) The molecular mechanisms for the antitumorigenic effect of curcumin. Curr Med Chem Anticancer Agents 2:357–370

Liu S, Misquitta YR, Olland A, Johnson MA, Kelleher KS, Kriz R, Lin LL, Stahl M, Mosyak L (2013) Crystal structure of a human IκB kinase β asymmetric dimer. J Biol Chem 288:22758–22767

Milacic V, Banerjee S, Landis-Piwowar KR, Sarkar FH, Majumdar AP, Dou QP (2008) Curcumin inhibits the proteasome activity in human colon cancer cells in vitro and in vivo. Cancer Res 68:7283–7292

Mori N, Fujii M, Ikeda S, Yamada Y, Tomonaga M, Ballard DW, Yamamoto N (1999) Constitutive activation of NF-kappaB in primary adult T-cell leukemia cells. Blood 93:2360–2368

Nagarajan S, Choo H, Cho Y, Shin KJ, Oh K-S, Lee B, Pae A (2010) IKKbeta inhibitor identification: a multi-filter driven novel scaffold. BMC Bioinform 11:S15

Nautiyal J, Banerjee S, Kanwar SS, Yu Y, Patel BB, Sarkar FH, Majumdar AP (2011) Curcumin enhances dasatinib-induced inhibition of growth and transformation of colon cancer cells. Int J Cancer 128:951–961

Plummer SM, Holloway KA, Manson MM, Munks RJ, Kaptein A, Farrow S, Howells L (1999) Inhibition of cyclo-oxygenase 2 expression in colon cells by the chemopreventive agent curcumin involves inhibition of NF-kappaB activation via the NIK/IKK signalling complex. Oncogene 18:6013–6020

Qiu X, Du Y, Lou B, Zuo Y, Shao W, Huo Y, Huang J, Yu Y, Zhou B, Du J, Fu H, Bu X (2010) Synthesis and identification of new 4-arylidene curcumin analogues as potential anticancer agents targeting nuclear factor-κB signaling pathway. J Med Chem 53:8260–8273

Sarkar FH, Li Y (2003) Soy isoflavones and cancer prevention: clinical science review. Cancer Invest 21:744–757

Sastry GM, Adzhigirey M, Day T, Annabhimoju R, Sherman W (2013) Protein and ligand preparation: parameters, protocols, and influence on virtual screening enrichments. J Comput Aided Mol Des 27:221–234

Sen R, Baltimore D (1986) Inducibility of κ immunoglobulin enhancer-binding protein NF-κB by a posttranslational mechanism. Cell 47:921–928

Shishodia S, Aggarwal BB (2002) Nuclear factor-kappaB activation: a question of life or death. J Biochem Mol Biol 35:28–40

Tyagi C, Grover S, Dhanjal JK, Goyal S, Goyal M, Grover A (2013) Mechanistic insights into mode of action of novel natural cathepsin L inhibitors. BMC Genomics 14:S10

Tyagi C, Gupta A, Goyal G, Dhanjal JK, Grover A (2014) Fragment based group QSAR and molecular dynamics mechanistic studies on arylthioindole derivatives targeting the α-β interfacial site of human tubulin. BMC Genomics 15:S6

Vats C, Dhanjal JK, Goyal S, Bharadvaja N, Grover A (2014) Computational design of novel flavonoid analogues as potential AChE inhibitors: analysis using group-based QSAR, molecular docking and molecular dynamics simulations. Struct Chem. doi:10.1007/s11224-014-0494-3

VLifeMDS: molecular design suite (2010) VLife Sciences Technologies Pvt. Ltd Pune, India

Wallace AC, Laskowski RA, Thornton JM (1995) LIGPLOT: a program to generate schematic diagrams of protein-ligand interactions. Protein Eng 8:127–134

Wolanin K, Magalska A, Mosieniak G, Klinger R, McKenna S, Vejda S, Sikora E, Piwocka K (2006) Curcumin affects components of the chromosomal passenger complex and induces mitotic catastrophe in apoptosis-resistant Bcr-Abl-expressing cells. Mol Cancer Res 4:457–469

Yan Z, Subbaramaiah K, Camilli T, Zhang F, Tanabe T, McCaffrey TA, Dannenberg AJ, Weksler BB (2000) Benzo[a]pyrene induces the transcription of cyclooxygenase-2 in vascular smooth muscle cells. Evidence for the involvement of extracellular signal-regulated kinase and NF-kappaB. J Biol Chem 275:4949–4955

International Journal of Electronic and Electrical Engineering.
ISSN 0974-2174, Volume 7, Number 1 (2014), pp. 19-24
© International Research Publication House
http://www.irphouse.com

Design and Implementation of PID Controller for Second Order Plant and Comparison of its Performance with Fuzzy Logic based Controller

Ashok Kumar Kumawat[1], Sandeep Rana[2] and Ashish Sharma[3]

[1,2]EE Department, Delhi Technological University, New Delhi-110042
[3] E&C Department, Jaipur Engineering College, Jaipur-303101

Abstract

Controller designing for various day to day practical processes has been a challenging task for designers. Several issues such as stability, steady state error, effect of parameter variations and speed etc. must be considered for designing a controller. In this communication, an arbitrarily underdamped second order plant is implemented which has highly oscillatory response. Then a PID controller is designed for improving the system stability. Further a fuzzy logic Controller is also designed for the same second order system and its result with PID controller is compared. Simulation of Fuzzy logic controller is done on MATLAB and for PID controller ORCAD PSPICE is used. Also hardware implementation of the system with PID controller is done using Op-Amp 741 IC.

Keywords: PID controller, Fuzzy logic controller, Op-amp 741.

1. Introduction

Though there is a huge advancement in advance control techniques, PID (Proportional-Integral-Derivative) controller is still widely used in process industries. The reason for preferring PID control strategy over others is its simple and well understood architecture [1]. If the plant model is known then the performance of PID controller is better than the other intelligent controllers. The major advantages of PID controller include its robustness and capability to withstand in wide operating conditions [5].

On the other hand, intelligent control technique like fuzzy logic based controller is used most frequently in the processes where plant model is not known. In Fuzzy logic controllers, the expert knowledge is translated into an automatic control scheme

[2],[3]. This control strategy is capable of finding precise solution from approximate information which makes it suitable for controlling non-linear and complex system.

In this paper PID controller is designed in hardware and software for an unstable system. Then further a fuzzy logic controller is designed for the same system and the performance of both types of controllers is compared. The paper is organised as follows; the section (II) describes the plant to be studied. Section (III) and (IV) is devoted to basic introduction of PID and Fuzzy Logic based controller respectively. The experimental work is discussed in section (V). Results are presented in section (VI) and at last paper is concluded in section (VI).

2. The Modelling of Plant

A second order underdamped plant [1] to be studied can be described in terms of its input output behaviour as follows:

$$\frac{v_{out}}{v_{in}} = \frac{K_1}{s^2+2\xi\omega_n s+\omega_n^2} \tag{1}$$

Above standard second order transfer function can be implemented with the help of Operational amplifier (Op-amp), resistors and capacitors [4]. The circuit diagram for this system is shown in Fig.1 and labelled as "system". The normal mathematical analysis leads the transfer function of "system" as in Eq. (1) where

$$K_1 = \frac{A_f}{(R_{16}R_{17}C_4C_5)}; \quad A_f = 1 + \frac{R_{19}}{R_{18}}; \quad \xi = \frac{3-A_f}{2}; \quad \omega_n = \frac{1}{\sqrt{(R_{16}R_{17}C_4C_5)}}$$

3. Proportional-Integral-Derivative Control

Proportional-Integral-Derivative (PID) Control is comprised of three type of control action;

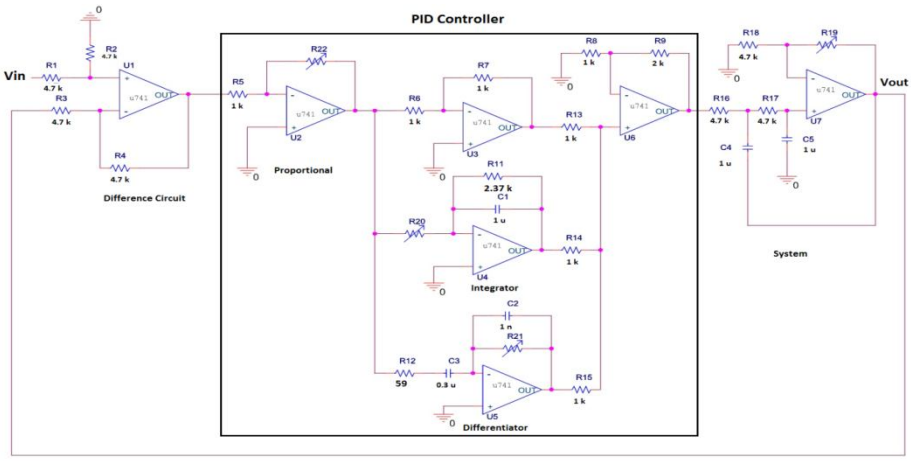


Fig. 1: Second order unstable System with PID controller.

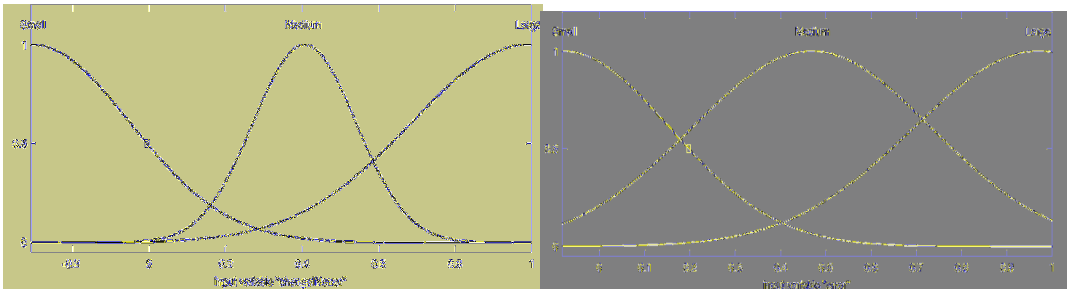
Proportional, integral and derivative. Proportional control provides the control action that is directly proportional to the error signal (the difference between the desired and measured variable). The integral control is used to eliminate steady state error but it degrades the quality of transient response. Finally the derivative control is used for improving the transient response. The actuating signal (control signal) in ideal PID is given as [1]:

$$e_a(t) = Ke(t) + K_i \int_0^t e(\tau)d\tau + K_d \frac{de(t)}{dt} \Rightarrow E_a(s) = \left[K + \frac{K_i}{s} + sK_d\right] E(s) \quad (1)$$

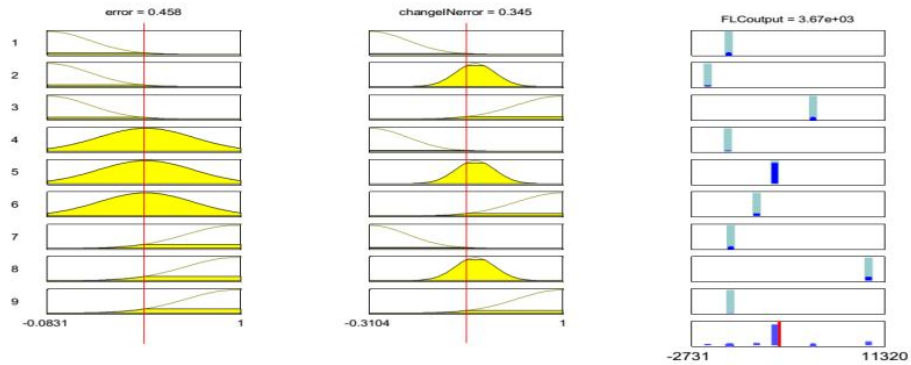
where K, K_i and K_d are proportional, integral and derivative constants respectively. PID controller with unstable system is shown in Fig. (1).

4. Fuzzy Logic Controller (FLC)

The FLC for the unstable system has two inputs, one output and nine fuzzy rules. Input membership functions are shown with suitable range by Fig.2 (a,b). The input variables 'Error' and 'change in error' are passed on these membership functions to generates input fuzzy variables which are then used (fuzzified) to evaluate the fuzzy rules (Fig.2(c)) and generate output fuzzy variables which are then defuzzified (Weight average method) to generate output as a input for the system[3].



(a) **(b)**



(c)

Fig. 2: (a) Input membership function of change in error (b) Input membership function of error (c) Rule Viewer for FLC

5. The Experimental work:

5.1 Open loop system

Simulation of step response for an open loop system of Fig.(1) is done on PSPICE using inbuilt model of uA741 with power supply ±15V. The required values of different components to make the plant highly unstable are taken as: $R_{16} = R_{17} = R_{18} = 4.7k\Omega, C_4 = C_5 = 1uF, R_{19} = 9.3k\Omega$. The simulation result of step response for open loop system is shown in Fig.(3) which shows highly oscillatory behaviour of open loop system.

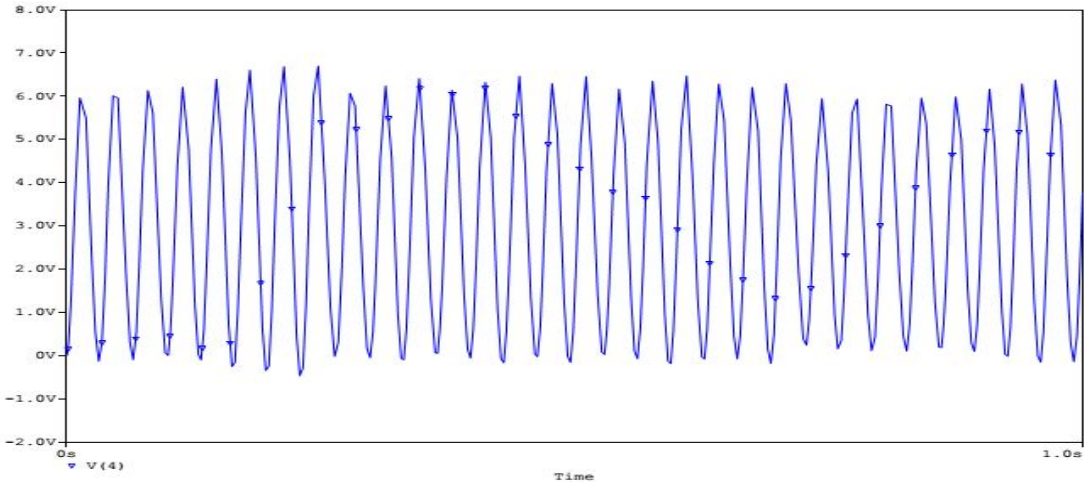
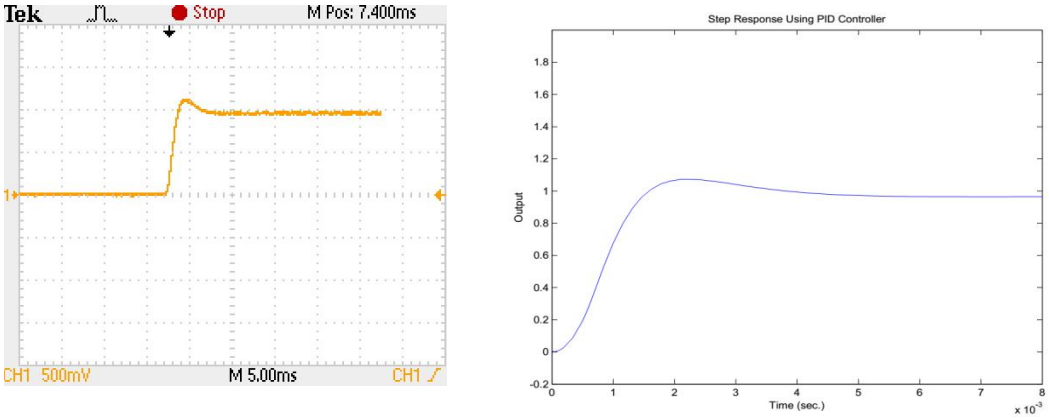


Fig. 3: PSPICE Simulation for the step response of open loop system.

5.2 Plant with PID controller

The circuit diagram for plant with PID controller is shown in Fig.(1) which is simulated in PSPICE as well as implemented in hardware by using components values as shown in Fig.(1). All variable resistances are used for tuning purpose.



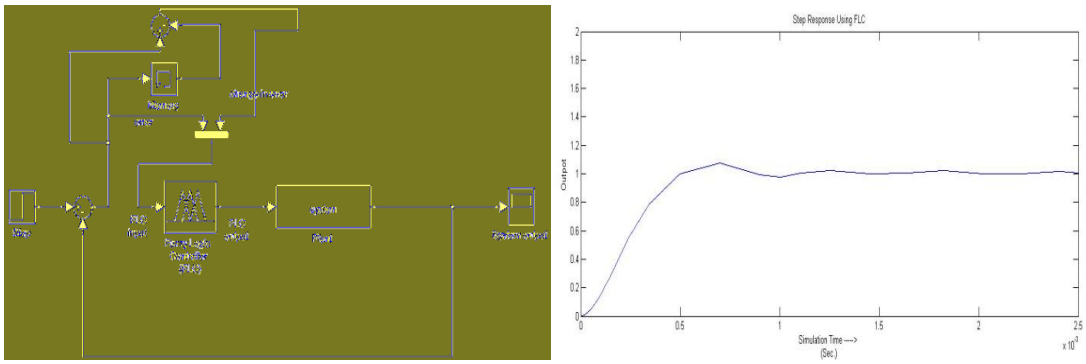
(a) **(b)**

Fig. 4: Step Response using PID controller (a) Hardware Result (b)PSPICE Simulation Result

The desired output response is obtained for the values of different variable resistances as 9.3kΩ, 23.7kΩ, 5.93kΩ and 8.1kΩ for R_{19}, R_{20}, R_{21} and R_{22} respectively. The simulation and practical results of step response for plant with PID controller is shown in Fig.(4).

5.3 Plant with Fuzzy Logic based Controller

FLC is designed by ANFIS toolbox of MATLAB. The Simulink block diagram and its step response is shown in Fig.(5)



(a) **(b)**

Fig. 5: (a) Simulink Block Diagram of FLC (b) Step Response of system using FLC.

6. Results

The system behaviour in terms of transient and steady state response for PID and fuzzy logic based controller is compared in Table (1).

Table 1: Comparative analysis of PID controller and FLC.

	Rise Time [ms]	**Maximum overshoot [%]**	**Settling Time(2%) [ms]**	**Steady state error [mV]**
PID (simulation)	0.9175	11.16167	1.4313	34.704
PID (practical)	1.4	12.24	3.6	30
FLC	0.49	5.39	1.37	20

7. Conclusion

The result of transient and steady state response for PID controller based system obtained from hardware and simulation, shows quite similarity as listed in Table (1). The FLC shows better transient and steady state response than PID controller which is quite obvious from Table (1).

References

[1] I.J. Nagrath, M.Gopal, "Control System Engineering" *Book*, New Age International Publishers, 2006

[2] T.J.Ross, "Fuzzy Logic with Engineering applications",Book,Wiley India,2009.

[3] T. Takagi and M. Sugeno, "Fuzzy identification of systems and its application to modelling and control", IEEE Transaction on systems, Man, Cybermetics, Vol.15,PP.116-132,1985.

[4] R.A. Gayakwad, "Op-Amps and Linear Integrated Circuits." *Book*, Pearson Prentice Hall, 2007.

[5] K.Astrom, K. and T. Hagglund, "PID Controllers: Theory, Design, and Tuning", Instrument Society of America, ISBN 1-55617-516-7, 1995.

Volume 2, Issue 3 (2014) 578-581 ISSN 2347 - 3258
International Journal of Advance Research and Innovation

Energy Exergy Analysis of a high pressure Claude Haylentsystem for liquefaction of Gases

Devender Kumar *, R. S. Mishra
Department of Mechanical Engineering, Delhi Technological University, Delhi, India

Article Info

Article history:
Received 20 July 2014
Received in revised form
10 August 2014
Accepted 20 August 2014
Available online 15 September 2014

Keywords

Thermodynamics Analysis Claude Haylentsystem,
Energy-Exergy Analysis,
First and second Law Analysis

Abstract

From various Cryogenics systems, lot of a detailed thermodynamic analysis ofcryosystems have been reported in literature however the modification of Claude systems for high pressure for high yield of liquefied mass of gases is very limited available in literature so far . A comprehensive energy and exergy analysis of Claude Heylandtcryogenic system for various gases is carried out in this paper by using various properties variables (i.e temperature, pressure etc) in system to find out the more efficient statics of system included exergy destructions in system .Numerical computations have been carried out for various gases in Claude Haylent system and it was observed that the Methane gas is more suitable than any other observed gas and 350 and 500 bar is best compressor pressure per kg of inlet gas.

Nomenculture

M	=	Total mass of gas
m_f	=	liqified mass of gas
m_4	=	mass of air in second heat exchanger
m_8	=	mass of air liquefied in the separator
h	=	Enthalpy
S	=	Entropy
X	=	Dryness fraction
T	=	temperature
P	=	Pressure
η_{comp}	=	Efficiency of compressor (approx. 80%)
$\eta_{expander}$	=	Efficiency of expander (approx. 80%)
$\eta_{2nd\ law}$	=	Second law efficiency
Ɛ	=	Effectiveness of heat exchanger (approx. 80%)
C	=	Specific heat capacity fluid or gas
W_t	=	Work of reversible isothermal compression
W_c	=	Shaft work supplied to compressor per unit mass
R	=	Universal gas constant
W_{net}	=	Net work done in system

1. Introduction

Cryogenic engineering is the application of low temperatures in which operating temperature below -150 ^oC .various gases like air, nitrogen, argon are liquefied. First vapour compression systems are used to achieve cryogenic temperature but used of these system worked is limited due to solidification temperature of the refrigerants .After this cryogenic industry find number of modes to achieve low temperature. Several liquefaction cycles exist [1]. Various processes are design and invent to achieve cryo temperature at different level of lower temperature Cryogenics is used in various important process at different level with different naming like cryobiology, cryonics, cryo-electronics, cryotrons, cryosurgery etc. Claude system is one of cryogenic system which is design to liquefy various particular gases like air, oxygen, nitrogen, feronetc,To improve perforamce of Claude system its modification is done in form of Haylentsystem. Haylent system is high pressure side Claude system but still Liquefaction plants are rather complicated with numerous components interacting with each other and consume a large amount of process energy, it is vital to develop efficient liquefaction processes for improving the overall system performance and economic competitiveness [2]. Various research and different method are employed to increase efficiency of cryo system. Exergy analysis is a strong method to identified inefficiencies of system and tells which part of system is critical and need to to be undertake study.From literature various data collected which help in optimization of cryosystem. The Bejan [3] work is bse of all exergetic analysis of heat exchangers. Various problems are studied related to exergy analysis which are mentioning or summarized in [4], from the vast study it noticed that most new methods differ only in the way that entropy generation is non-dimensional [5]. A good exergetic design of a heat exchanger would allow for an increase in the global efficiency of the process, by defining a thermodynamic cycle in which the exergetic losses would be limited [6]. The major cause of exergy loss is the use of compressors and to a lesser extent the use of turbines [7]. For optimization of Haylent system first and second law analysis is done but except to increase the whole Haylent system efficiency stress are done on particular parts of system and research are done on that systems. Air separation unit and compressor, condenser and evaporator of cryo system are the center of research because most of exergy destruction takes place in these parts. This paper mainly dealed with thermodynamic (exergy and anergy) analysis of Haylent system for determining the effect of every component of system with varying conditions for maximum second law efficiency

Corresponding Author,
E-mail address: devenderdahiya@in.com
All rights reserved: http://www.ijari.org

2. Thermo Analysis of Claude Haylent System for Liquefaction of Gases

Compressor work:

$$\eta_c = \frac{W_t}{W_{comp}} \quad (1)$$

$$W_t = mRT ln \frac{P_2}{P_1} \quad (2)$$

$$-W_c = m * (T_1 * (s_1 - s_2) - (h_1 - h_2) \quad (3)$$

$$W_{reversible} = W_{actual} - T_0 s_{gen} \quad (4)$$

$$W_{net} = W_c + W_e \quad (5)$$

Expander:

$$\frac{T_g}{T_s} = \left(\frac{P_g}{P_s}\right)^{\left(\frac{Y-1}{Y}\right)\eta_{expander}} \quad (6)$$

$$W_e = m_e * h_2 - m_e * h_e$$

"Control volume except compressor"

$$y = ((h_1 - h_2)/(h_1 - h_f)) + r * ((h_2 - h_e)/(h_1 - h_f)) \quad (8)$$

$$y = m_f/m$$

"Work done per mass of gas"

$$z = -W_{net}/m$$

"Work done per mass of liq gas"

$$t = -W_{net}/m_f$$

Coefficient of performance of system

$$COP = ((h_1 - h_f)/W_{net})$$

Second law analysis:

$$\eta_{2nd\ law} = ((((h_f - h_1) - T_0 * (s_f - s_1))/(W_{net}) * m_f) * 100)$$

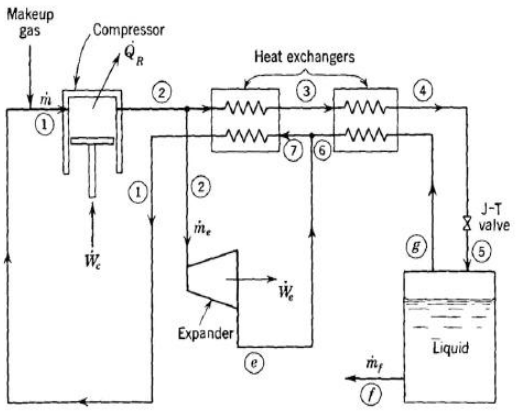


Fig: 1. Block Diagram of Haylent System

A complete analysis of Haylent Claude cycle is performing with the help of numerical computation technique for various gases. Haylent Claude cycle as shown in Fig 1 is taken for analysis. Haylent Claude system is almost same as simple Claude system except arrangement of first expander. In Haylentsystem expander intake is at high pressure side before first intial heat exchanger other than this it also consist a compressor, expander, two heat exchangers with throttle valve and separator. The fluids which have to liquefy first fed to compressor in its gaseous form at atmospheric pressure and temperature which circulate from all system and in last fractional mass of total mass get liquefied and remaining again fed in system with additional mass to recirculate in system again. Various results are drawn for particular inlet temperature, pressure and intermediate pressure for high pressure side of expander for different six type gases such oxygen, argon, methane, air ,fluorine and nitrogen are considered for study.

3. Results and Discussion

Various results are drawn on the basis of numerical equations of system. In fig 2 variation of liquefaction temperature is directly proportional to inlet pressure as we increseses the pressure Liquefaction temperature raises. Fig 3 show fall of liquefaction mass with increase of inlet temperature where as fig 4 shows first inctresse of liquification mass with increase of inlet pressure but after 3.5 bar it start decreasing, but this decriment with increase of inlet pressure is very slow. Fig 5-7 show variation in second law efficiency with intlet temperature, intermediate mass and inlet pressure respectively. Graph analysis of these 5-7 fig shows that second law efficiency is decreses with increase of inlet temperature and intermediate mass whereas it is increses with increase of inlet pressure. Fig 8 -9 show variation in COP of system with inlet pressure and temperature. They show that increase in pressure is desirable for system and COP of system is increses with increase in inlet pressure while it is decreseing with increase in inlet temperature. From above graph study it determinded that increses in inlet pressure is between 3 and 4 bar is desriable for system and increase in temperature in very concern reange is good for optimization of Haylentclaude system.

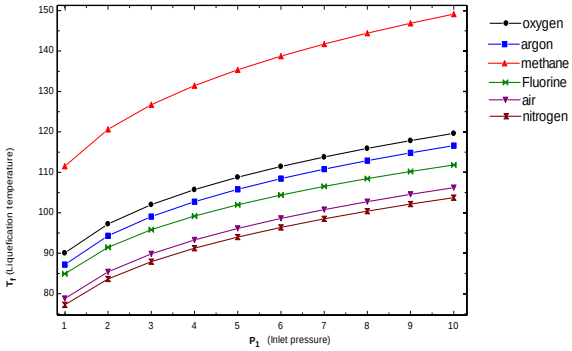


Fig: 2. Variation of liquefaction temperature with inlet Pressure

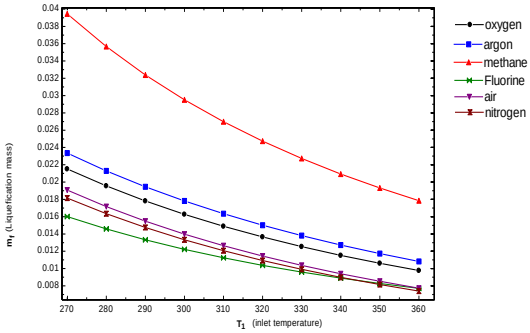


Fig: 3. Variation of Liquefied Mass with Inlet Temperature

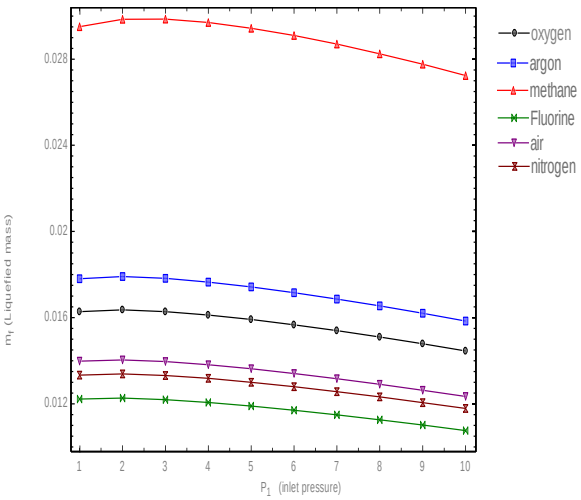


Fig: 4. Variation of Liquefied Mass with Inlet Pressure

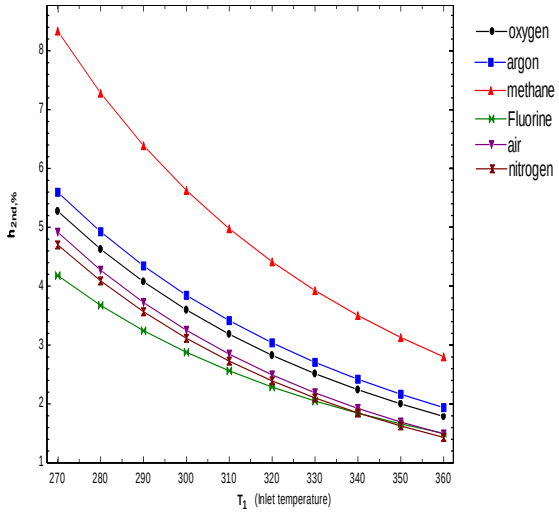


Fig: 5. Variation of 2nd law Efficiency with Inlet Temperature

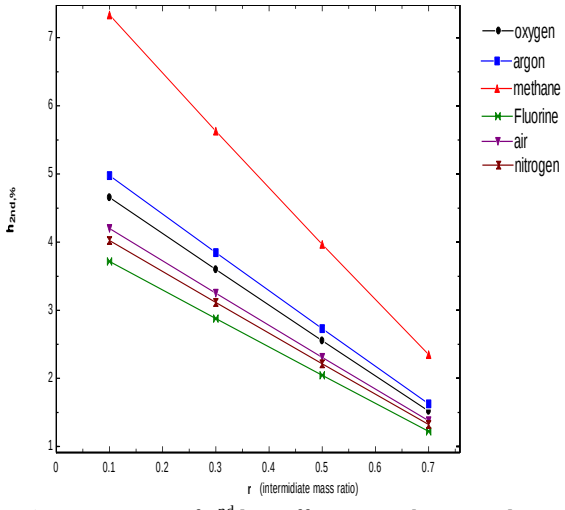


Fig: 6. Variation of 2nd law Efficiency with Intermediate Mass Ratio

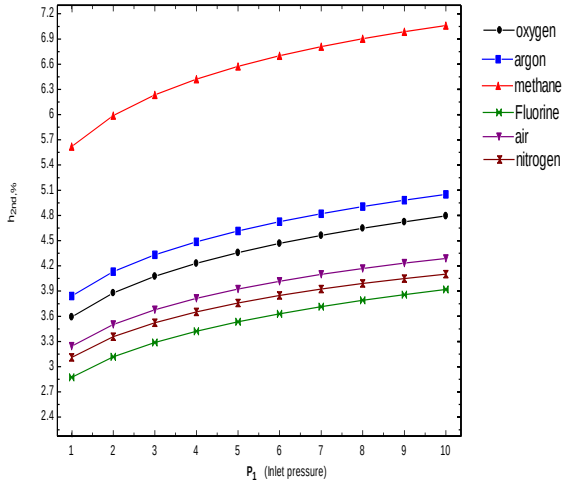


Fig: 7. Variation of 2nd law Efficiency with Inlet Pressure

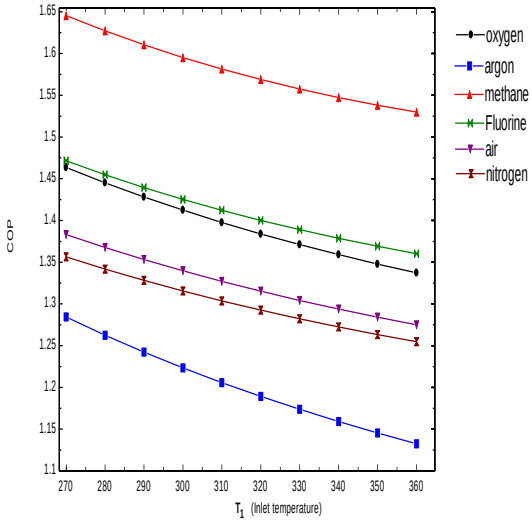


Fig: 8. Variation of COP with Inlet Temperature

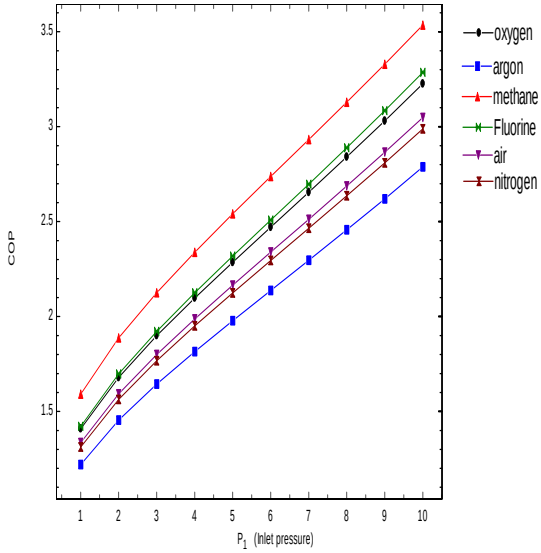


Fig: 9. Variation of COP with Inlet Pressure

4. Conclusion

From above study following results are concluded

1. The optimize range of inlet pressure is 3 .5 bar for considered variables such liquefaction mass, liquidation temperature and second law efficiency.
2. Intermediate pressure of high pressure side expander should be in minimum range for high second law efficiency.
3. Increase in inlet temperature deteriorate the performance of system and various Like COP, second law efficiency ,liquefaction mass are decrease with increase in inlet temperature

References

[1] G. Venkatarathnam, Cryogenic Mixed Refrigerant Processes, New York, 2008
[2] M. Kanoglu, Cryogenic turbine efficiencies. Exergy, Int J 2001; 1: 202–8
[3] A. Bejan, General criterion for rating heat-exchanger performance. Int. J. Heat Mass Transf. 1978, 21, 655–658
[4] M. Yilmaz, O. N. Sara, S. Karsli, Performance evaluation criteria for heat exchangers based onsecond law analysis. Exergy Int. J. 2001, 4, 278–294
[5] S. T. Wu, X. F. Yuan, Y. R. Li, L. Xiao, Exergy transfer effectiveness on heat exchanger for finitepressure drop. Energy 2006, 32, 2110–2120.
[6] T. J. Kotas, The Exergy Method of Thermal Plant Analysis; 1995 Ed.; Krieger Publishing Company:London, UK, 1985
[7] R. L. Cornelissen, G. G. Hirs, Exergy analysis of cryogenic air separation, Energy Conversion and Management, 39, 16–18, 1998, 1821-1826

ENHANCED BACK-CONTACT BACK-JUNCTION CRYSTALLINE SILICON SOLAR CELL PERFORMANCE WITH A SILICON-CARBIDE (SIC) BASED FRONT SURFACE PASSIVATION

Rahul Pandey[1], Rishu Chaujar[2]

[1]*Department of Engineering Physics, DTU, Delhi (India)*
[2] *Assistant Professor, Department of Engineering Physics, DTU, Delhi (India)*

ABSTRACT

In this work, a novel surface passivation scheme has been discussed with Back-Contact Back- Junction (BC-BJ) 10µm thin crystalline silicon Solar Cell which is 10-15 times thinner than the conventional c-Si solar cell. Presence of SiC as a surface passivation layer shows high quality passivation as compared to conventional antireflective front surface passivation layers. The hole concentration of 13-14 cm^{-3} has been achieved at the interface resulting in a significant 13.5% power conversion efficiency (PCE). Simulation results reveals that the presence of SiC makes BC-BJ silicon solar cell less prone to surface recombination of carriers. All the simulations have been done using DEVEDIT and ATLAS device simulator.

Keywords: ATLAS, Back-Contact Back-Junction (BC-BJ), Passivation, Simulation, Solar Cell.

I. INTRODUCTION

One of the growing research topic in the field of photovoltaics is the development of low cost and high efficiency silicon solar cell. In order to maximize solar cell efficiency, it is necessary to optimize both the electrical device characteristics and the optical absorption of the device [1-3]. There are several different cell concepts, such as PERL [4]. Sunpower corp. shows that it is posible to achive average cell efficiency upto 22% [5-6] in mass production with BC-BJ silicon solar cell structure. In BC-BJ solar cell, both the emitter and back surface field (BSF) are situated at the back side, opposite to the illuminated face of the device. The BC-BJ solar cell has many advantages, such as avoidance of optical shading losses at front side, higher absorption and current density. Here, we discussed new surface passivation scheme for BC-BJ silicon solar cell, which shows remarkably good characteristics over the conventional passivating antireflective coating of thermal SiO_2 or SiNx:H layers, higher field as well as low surface recombination is observed in simulation results. The new surface passivation scheme makes the device less prone to surface recombination by decreasing the concentration of holes at the interface. We have not incorporated the defected state which exists in silicon- silicon carbide heterojunction, since here, SiC layer is used for surface passivation.

IJATES

II. DEVICE STRUCTURE AND MODELS

The simulation device structure i.e. BC-BJ Si solar cell is shown in Fig.1. To simulate the solar cell properties, we specified the following: substrate was n type silicon with dimensions (100µm x 10µm) with doping density ($3x10^{15}$ cm^{-3}). The n+ and p+ region have a depth of 3µm and 2.5µm respectively, with doping density of $4x10^{20}$ cm^{-3}. Front surface of the device consists of passivation layer. We have defined our contacts as ohmic. This is done to avoid schottky barriers, and thus unnecessarily higher computation time. Table 1 shows the parameter used in simulations. Shockley-Read-Hall, Concentration dependent mobility and Auger recombination mechanisms were taken into account. Auger recombination is modeled according to [7] using the expression:

$$R_{Auger} = AUGN\,(pn^2 - nn_{ie}^2) + AUGN\,(np^2 - pn_{ie}^2) \quad (1)$$

Where, AUGN and AUGP are the Auger recombination coefficient for electrons and holes, respectively and nie is the intrinsic carrier concentration. The Shockley-Read-Hall recombination is modeled according to [7] using the expression:

$$R_{SRH} = \frac{pn - n_{ie}^2}{TAUP0\left[n + n_{ie}\exp\left(\frac{ETRAP}{kT_L}\right)\right] + TAUN0\left[p + n_{ie}\exp\left(\frac{-ETRAP}{kT_L}\right)\right]} \quad (2)$$

Where, ETRAP is the difference between the trap energy level and the intrinsic Fermi level, T_L is the lattice temperature in degrees Kelvin and TAUN0 and TAUP0 are the electron and hole lifetimes. The AM1.5G spectrum was used to simulate the current-voltage, (I-V) curve under one-sun illumination condition with intensity of $100mW/cm^2$.

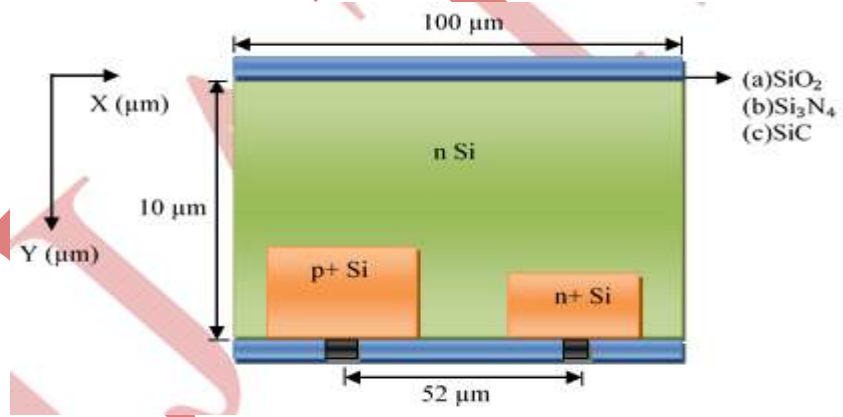


Fig. 1: Simulated device:-BC-BJ Si solar cell with surface passivation layer: (a) SiO_2 (b) Si_3N_4 (c) SiC

Table 1 Parameters Used In Simulation

Energy band gap (Eg)	1.08eV
Band density (Nc)	$2.8x10^{19}(cm^{-3})$
Band density (Nv)	$1.04x10^{19}(cm^{-3})$
Intrinsic carrier conc.	$1.45\ x10^{10}(cm^{-3})$
Minority carrier lifetime.	$1x10^{-5}s$
Minority carrier lifetime.	$1x10^{-5}s$
Electron mobility (μ_n)	1000 cm^2/Vs
Hole mobility (μ_p)	500 cm^2/Vs
Auger recombination coefficient for electrons	$2.8x10^{-31}\ cm^6\ s^{-1}$
Auger recombination coefficient for holes	$9.9x10^{-31}\ cm^6\ s^{-1}$

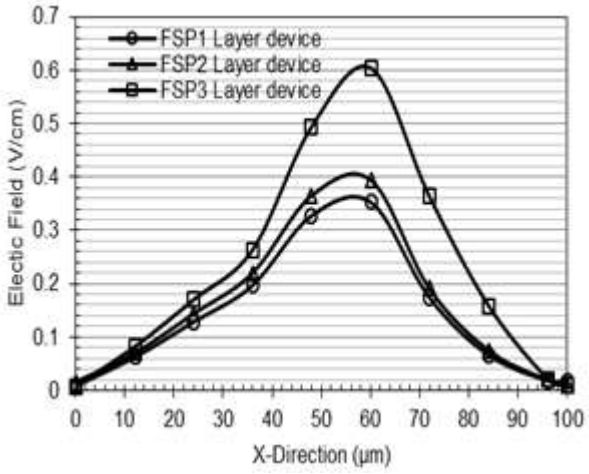


Fig. 3: Comparisons of electric field at interface for three different surface passivation layers

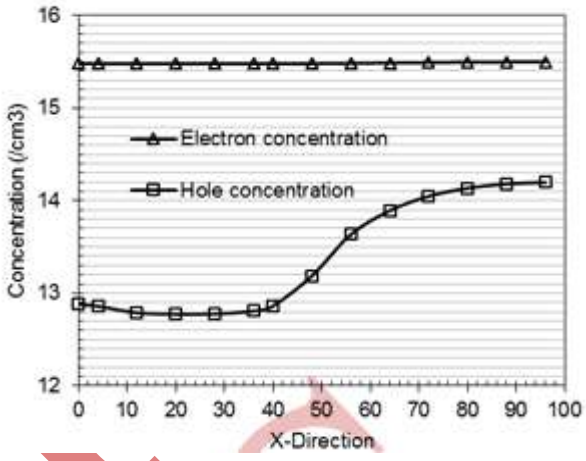


Fig. 4: Electrons and holes concentration at the interface in FSP3 layered device

III. RESULTS AND DISCUSSION

The front surface of most of the solar cell normally consists of well – passivated antireflective coating of thermal SiO2 or Si3N4 layers [8-9]. Here we study the effect of front surface passivation (FSP) on photovoltaic properties of BC-BJ silicon solar cell. We compare the impact of three different (FSP) schemes: single SiO2 named FSP1, Si3N4 named FSP2, and SiC named FSP3. Photogeneration rate contour within the device is shown in Fig.2. A higher generation rate as well as higher generation depth is observed in FSP3 layer device

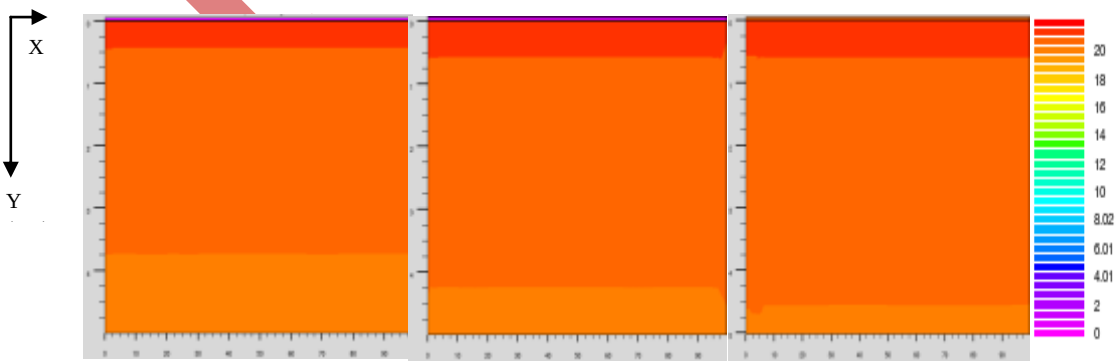
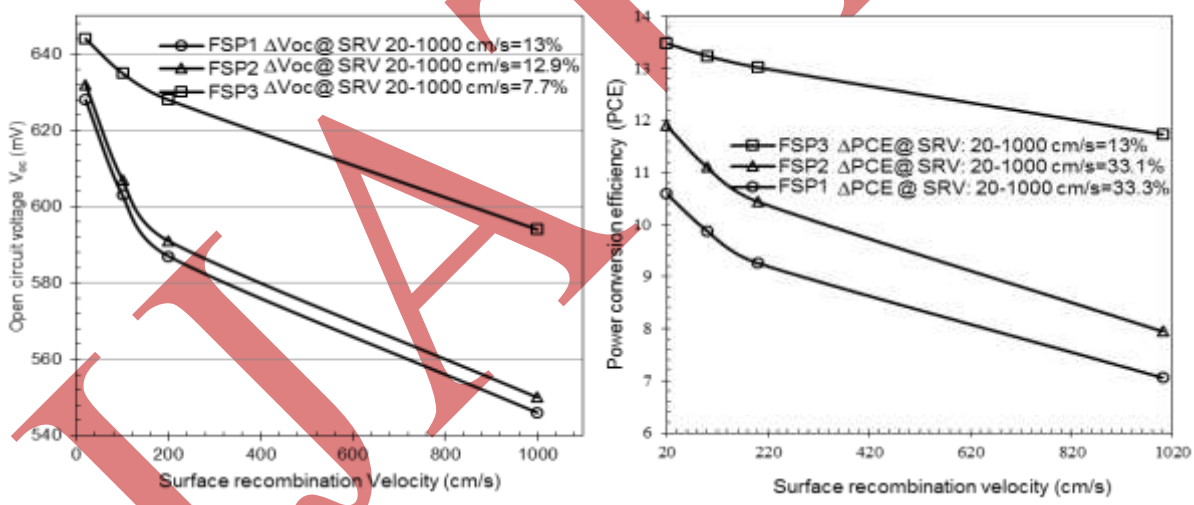


Fig.2: Photogeneration rate (/cm3s): (a) FSP1 layer device (b) FSP2 layer device (c) FSP3 layer device

because of the less reflectance at SiC layer. In surface recombination process, an electron from conduction band recombines with the hole in the valance band via a defect level within the bandgap [10]. This kind of recombination requires one electron and one hole for recombination and it would be maximum if no. of electrons is equal to the no. of holes at the interface. In addition, increased electric field at the interface is observed in FSP3 layer device (Fig.3), which assist the holes to moves towards the junction, resulting in low concentration of holes at the interface (Fig.4) and hence a lower surface recombination rate.

Furthermore, if the concentration of one comrade electrons or holes is drastically reduced, then recombination rate reduces strong. Fig.4, shows that the concentration of electrons at the interface is higher than the concentration of holes, resulting in low surface recombination rate in case of FSP3 layer device. Further, we obtained the influence of surface recombination velocity (SRV) on photovoltaic cell parameters as plotted in Fig. 5 (a) and (b). The open circuit voltage, in case of FSP3 layered device is less affected by SRV Fig.5(a), Also with surface recombination velocity of 20cm/s, FSP3 layer device shows 13.5 % power conversion efficiency (PCE), whereas for FSP1 and FSP2 layered devices, PCE is 10.59% and 11.9% respectively. Moreover, as the SRV is increased from 20 to 1000 cm/s, the efficiency of FSP3 changes from 13.5 to 11.73 with a percentage change of 13, whereas for FSP1 and FSP2 layered devices, it went down to 7.06% and 7.95% respectively, showing a percentage change of 33.1% and 33.3% respectively.



(a) (b)

Fig.5: Influence of SRV on: (a) Open circuit voltage (b) Power conversion efficiency

V. CONCLUSION

In this work, a novel surface passivation scheme for thin BC-BJ silicon photovoltaic has been proposed, and influence of front surface passivation scheme has been discussed based on TCAD analysis. For improving Front surface passivation of thin BC-BJ solar cells, it required to decrease the concentration of one partner electrons or holes at the interface. We achieved the concentration of electrons and holes, 15.5 cm^{-3} and 13-14 cm^{-3} respectively, at the interface, which makes the device insensitive to surface recombination phenomena, The presence of SiC layer improves all photovoltaic parameters: EQE> 85% spectrum range of 400-650 nm

IJATES

wavelength, fill factor 80% and a power conversion efficiency of 13.5%.

VI. ACKNOWLEDGEMENTS

The authors would like to thank Microelectronics Research Lab, Department of Engineering Physics, Delhi Technological University to carry out this work. Rahul Pandey (JRF) acknowledge UGC, Govt. of India for providing fellowship.

REFERENCES

[1] Deceglie, M.G., Ferry, V. E., Alivisatos, A., and Atwater, H. A., "Design of Nanostructured Solar Cells using Coupled Optical And Electrical Modeling", Nano Lett., 12 (6), 2012, 2894–2900.

[2] Tian, B., Zheng, X., Kempa, T.J., Fang, Y.,Yu , N., Yu , G., Jinlin & Charles Lieber, M., " Coaxial silicon nanowires as solar cells and nanoelectronic power sources", Nature, 449, 2007, 885-889.

[3] Deinega, A., Eyderman, S., and John, S., "Coupled optical and electrical modeling of solar cell based on conical pore silicon photonic crystals", J. Appl. Phys., 113(22), 2013, 224501(0-9).

[4] Green, M.A., "The path to 25% silicon solar cell efficiency: History of silicon cell evolution", Progress in Photovoltaics: Research and Applications, 17 (3), 2009, 183–189.

[5] Kluska, S., Granek, F., Rudiger, M., Hermle, M., Glunz, S.W., "Modeling and optimization study of industrial n-type high-efficiency back-contact back-junction silicon solar cells", Solar Energy Materials & Solar Cells, 94(3), 2010, 568–577.

[6] Ceuster, D. D., Cousins, P., Rose, D., Vicente, D., Tipones, P., Mulligan, W., "Low Cost, high volume production of >22% efficiency silicon solar cells", In 22nd European Photovoltaic Solar Energy Conference, 2007, 816-819.

[7] ATLAS User's Manual DEVICE SIMULATION SOFTWARE, 2013, 206-218.

[8] Swanson, R. M., Beckwith, S. K., Crane, R. A., Eades, W. D., Young, H.K., Sinton, R. A., and Swirhun, S. E., "Point-contact silicon solar cells", Electron Devices, IEEE Transactions, 31(5), 1984, 661-664.

[9] Diouf, D., Kleider, J.P., Desrues, T., Ribeyron, P.J., "Effect of front surface field in n-type interdigitated back contact silicon heterojunction solar cell", Energy Procedia, 2(1), 2010, 59–64.

[10] Aberle, A.G., "Surface Passivation of Crystalline Silicon Solar cell a review" Progress in photovoltaics research and applications, 8(5), 2000, 487-473.

Biographical Notes

Ms. Rahul Pandey is presently working as a Ph. D Research Scholar in Engineering Physics Department from Delhi Technological University (DTU), Delhi, India.

Dr. Rishu Chaujar is working as an Assistant Professor in Engineering Physics Department from Delhi Technological University (DTU), Delhi, India.

Examining the Effectiveness of Machine Learning Algorithms for Prediction of Change Prone Classes

Ruchika Malhotra
Department of Software Engineering
Delhi Technological University
Delhi- 110042, India
ruchikamalhotra2004@yahoo.com

Megha Khanna
Acharaya Narendra Dev College
University of Delhi
Delhi- 110019, India
meghakhanna86@gmail.com

***Abstract*—Managing change in the early stages of a software development life cycle is an effective strategy for developing a good quality software at low costs. In order to manage change, we use software quality models which can efficiently predict change prone classes and hence guide developers in appropriate distribution of limited resources. This study examines the effectiveness of ten machine learning algorithms for developing such software quality models on three object-oriented software data sets. We also compare the performance of machine learning algorithms with the widely used logistic regression technique and statistically rank various algorithms with the help of Friedman test.**

Keywords- Change proneness, Object- Oriented metrics, Open source, Software Quality

I. INTRODUCTION

With the growth in technology and ever increasing customer demands, the complexity of the software products is increasing day by day. Managing and controlling changes in such complex software products is one of the prime concerns of the software industry. A change could be because of existence of faults, progressive requirements or technology enhancements [1]. Thus, change prone classes in an Object-Oriented (OO) software represent weak areas of a software product. Identification of these change prone classes is important for effective resource management as we can focus more resources on these weak areas to yield a good quality and highly maintainable software products at low costs. These classes should be rigorously monitored and tracked during the maintenance and testing phases. Moreover, stringent verification activities like reviews and inspections should be performed on these change prone classes in order to identify the defects and changes in the early phases of software development life cycle [2].

A class in an OO software is termed as change prone if it is likely to change after the release of the software product [1]. In order to determine a class as change prone, researchers and software practitioners can develop software quality models which predict the change proneness attribute of a class with the help of various OO metrics [3-5] which measure inheritance, coupling, cohesion, size and other OO attributes. A few studies in the literature have tried to evaluate the change prone nature of a class in an OO software with the help of traditional statistical techniques [6-8]. However, this study aims to examine the effectiveness of the Machine Learning (ML) algorithms for determining change prone classes in an OO software.

The basic structure and functioning of the ML algorithms is quite different from the traditional statistical techniques. These algorithms have been successfully applied in various other domains of software engineering like defect prediction [9-12], effort prediction [13-14] and maintainability prediction [15]. Also various ML algorithms work differently on different data sets. Thus, there is a need to examine the applicability of these algorithms to the domain of change proneness prediction on different data sets. A brief description of the research questions explored in this study are as follows: (a) Which OO metrics are related to the change proneness attribute of a class? (b) Are the ML algorithms effective in ascertaining change prone classes in an OO software? (c) How do the ML algorithms compare to the statistical techniques for change proneness prediction?

In this study, we perform an empirical validation using three open source data sets developed in Java language to ascertain the capability of ten ML algorithms (Support vector machine (SVM), Gene Expression Programming (GEP), Multilayer Perceptron with conjugate learning (MLP-CG), Group Method Data Handling network (GMDH), K-means clustering, TreeBoost (TB), Bagging (BG), Naïve Bayes (NB), J48 decision tree and Random Forests (RF)) for developing change prediction models. We further analyze and compare the results of these algorithms with a statistical technique, logistic regression (LR). The comparison of various change prediction models developed using these algorithms was done by using the Receiver Operating characteristic (ROC) analysis, accuracy, precision and f-measure as performance indicators. We then statistically rank all the algorithms of the study with the help of Friedman's statistical test. Though there are few studies [1, 16-17] in the literature which evaluate the capability of ML algorithms for change proneness prediction, there has been no study till date which statistically compares the performance of a wide range of machine learning algorithms with the LR technique. The objective of large number of empirical studies is to evaluate the best software prediction model. Moreover, by using open source data sets and widely used performance measures the software industry and research community can ascertain the best change prediction model. The results show that ML algorithms are effective while predicting

978-1-4799-5313-4/14/$31.00 ©2014 IEEE

software change and even outperform the statistical LR technique.

This paper is organized as follows. Section II gives a brief description of the related work while Section III provides an introduction to variables of the study and the procedure for data collection. Section IV gives a brief overview of all the algorithms analyzed in the study. Section V states the analysis and results of the study while Section VI lists the threats to validity. Finally, Section VII summarizes the conclusions of the study.

II. Related Work

Evaluating the change prone nature of a class in an OO software is important for planning optimum use of constrained resources and improving the quality of the software product.

Elish et al. [7] proposed a set of evolution based metrics as efficient indicators of change. They concluded that these evolution based metrics along with the widely used Chidamber and Kemerer metric suite gave the most accurate results when predicting change prone nature of a class. Lu et al. [6] used statistical meta-analysis techniques to validate 62 OO metrics for prediction of change proneness attribute of a class in 102 systems developed using Java language. They found that the size metrics were highly correlated with change while the inheritance based metrics had the least capability of change prediction. Zhou et al. [8] investigated the relationship between OO metrics and change proneness using Eclipse data set and concluded that there exists a confounding effect of class size on this relationship.

Koru et al. [2] validated Pareto's principal on two open source projects and proposed a tree based model for prioritizing resources of a project. The resource prioritization was done by determining change prone classes. Arisholm et al. [18] analyzed the relationship between dynamic coupling and change proneness of a class. Amoui et al. [16] suggested a neural network based change prediction network which could predict "where" and "when" the changes would occur. The model was validated on two open source projects. Tsantalis et al. [19] proposed a probabilistic approach to ascertain change probability of a class and validated their approach on two open source projects. Bieman et al. [20] analyzed interactions amongst classes to determine a cluster of change prone classes, so that these classes can be effectively handled during maintenance. Han et al. [21] proposed Behavioral Dependency Measure (BDM), for predicting change proneness in UML 2.0 models.

Malhotra et al. [1] validated 22 OO metrics using three ML algorithms and concluded the existence of relationship between OO metrics and change proneness. They also found the ML algorithms to be better predictors than the LR technique. In another study, they evaluated the capability of inter-project validation of change proneness prediction using the ML algorithms on open source data sets [17]. However in this study, we evaluate a wide range of ML algorithms for software change prediction using three open source data sets. We also assign statistical ranks to all the algorithms using Friedman statistical test in order to ascertain whether ML algorithms are significantly better than the LR technique. Our aim is to establish empirical evidence to assess the best change prediction model. The results would help software practitioners to effectively choose an appropriate algorithm for developing change prediction models. These models would also help in efficient resource allocation and development of better quality software.

III. Research Background

This section gives a brief introduction of the dependent and the independent variables of the study and also explains the data collection procedure.

A. Independent Variables

The independent variables of this study is an OO metrics suite proposed by Chidamber and Kemerer [4]. This metrics suite consists of six OO metrics which measure different attributes of an OO software like coupling, inheritance, cohesion etc. The various metrics included in this suite are as follows: (1) Coupling Between Objects (CBO), (2) Number of Children (NOC), (3) Depth of Inheritance Tree (DIT), (4) Lack of Cohesion amongst Methods (LCOM), (5) Weighted Methods of a Class (WMC) and (6) Response for a class (RFC). Chidamber et al. [4] provide a detailed description of these metrics. Apart from these metrics, we also included Source Lines of Code (SLOC) as an independent variable. This metric is a measure of the length of code and excludes all comments. It is a count of all the lines containing the source code. This study calculates the above mentioned metrics with the help of Understand for Java (http://www.scitools.com/) tool.

B. Dependent Variable

The dependent variable of this study is change proneness. The change proneness attribute of a class in an OO software accounts for the likelihood of change in that particular class after the software has been released [1,17]. A change in a particular class can be accounted for by analyzing the number of SLOC added, modified or deleted in the class after the software is operational. Previous studies [1, 6, 8] have ascertained the existence of a relationship between OO metrics and change proneness.

TABLE I. Data Set Details

Name	Version	Release Date	Size
DrJava	r4668	04-09-2008	1,43,470
	r5686	18-08-2012	1,62,405
DSpace	1.6.0	02-03-2010	2,43,086
	1.8.1	15-12-2010	2,94,236
Robocode	1.7.2.2	04-11-2010	84,702
	1.7.4.4	21-11-2012	86,933

C. Empirical Data Collection

In order to empirically validate various ML algorithms, we collected data from three open source projects namely DrJava,

DSpace and Robocode. DrJava is a programming environment for Java which includes a program editor, debugger, unit testing tool and an interactions pane for program evaluation. DSpace is a system for managing digital assets by enabling services for accessing, provisioning, stewardship and reusing of digital assets. Robocode is a programming game where one can develop a robot battle tank to battle against other tanks. The source code of each of the three data sets was downloaded from http://sourceforge.net/. The versions chosen for each data set were stable versions of the corresponding data set. Table I provides the details of each data set which includes the version, release date and size of the data set.

In order to collect data, we first compute the various OO metrics for all the classes of the previous version (DrJava r4668, DSpace 1.6.0 & Robocode 1.7.2.2) in each data set. The metrics were collected with the help of Understand software available at http://www.scitools.com/. The next step was to extract all the common classes in both the versions of each software data set. We exclude all those classes which were present in only one version of the data set. Library classes and interface definition files were also excluded. Thereafter, all the common classes of each data set were analyzed line by line in both the versions of the data sets to obtain a count of SLOC added, deleted or modified. The comparison amongst the classes was aided by the Understand tool as it highlights the changes in two files. After the computation of the change statistics (SLOC added, deleted and modified), we also compute a binary variable named ALTER. The ALTER variable is assigned as "yes" if the total change (number of SLOC added, deleted or modified) > 0, otherwise it is set to "no". The data collection procedure is similar to that of Malhotra et al. [1].

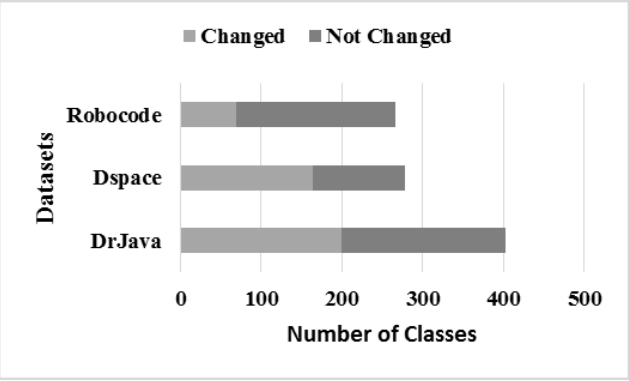


Figure 1. Statistics of Data Collection

A data point in a particular data set incorporates the various OO metrics for a particular class (which is common in both the versions of the data set) and its ALTER variable. Figure 1 shows the statistics of data collection where each bar represents an individual data set. A total of 402 classes were found common in DrJava data set. Out of these 402 classes, approximately 49% of the classes were found changed i.e. ALTER variable was set as "yes" for these classes. Similarly, 278 data points were computed for the DSpace data set, where 60% of the classes were found changed. The Robocode data set had 266 common classes with approximately 26% of changed classes.

We also evaluated a subset of all the OO metrics used in the study for developing efficient change prediction models. For this, we applied Correlation based Feature Selection (CFS) [22] technique. This technique reduces the dimensionality of the data set and eliminates all the redundant OO metrics. Thus, we extract those OO metrics which are highly effective in predicting change.

IV. RESEARCH METHODOLOGY

This section specifies in brief the various ML algorithms used in the study. Table II lists down the various parameter settings of each algorithm. These settings were the default settings of the WEKA [23] and the DTReg tool [24].

Support Vector Machine (SVM) is an algorithm which trains itself with the help of support vectors i.e. training examples. The SVM method formulates a hyperplane which segregates the input into different categories [25].

Gene Expression Programming (GEP) is evolutionary in nature. The chromosomes of a GEP algorithm are subject to various operators like mutation, selection and reproduction and form accurate expression trees until the desired fitness of the chromosome population is achieved [26].

Multilayer Perceptron (MLP) are prediction models which simulates biological neurons. They model complex relationships between the input and the output with a set of hidden layers [27]. In order to train the MLP model, we use the Conjugate Gradient method to find optimum weights of the network so that the difference between the output and the actual target values is minimum (MLP-CG) [24].

Group Method of Data Handling (GMDH) polynomial network is a self-organizing network. The connections between the neurons and the number of layers in the GMDH network is not fixed and is optimized to achieve the best accuracy without overfitting [24].

K-means clustering identifies clusters of data points with the same target category. The new instances are predicted based on the assumption that they are similar to the nearest cluster center [24].

Bagging (BG) creates a number of training sets and improves the classification model by training a different function for each of the set [28]. The different training sets are created with small changes. While predicting a binary variable, the vote given by the majority functions is selected as the output.

Naïve Bayes (NB) algorithm creates a probabilistic model based on the Bayes theorem [9]. In this algorithm, each of the features are considered independently. It requires only a small training set for classification.

J48 is the implementation of the decision tree C4.5 algorithm. The decision tree uses information gain as a splitting criteria in order to split the node on an attribute value test. The splitting should be such that it cultivates a particular target variable [29].

Random Forest (RF) is a collection of a number of decision tress at the training stage. It predicts the label of a particular instance by taking the mode of all the individual decision trees which are created randomly [30].

TreeBoost (TB) is quite similar to the RF algorithm. It creates a series of trees. However, while the RF algorithm uses voting for deciding the output, the TB algorithm improves the prediction accuracy with each tree in the series [24].

TABLE II. PARAMETER SETTINGS FOR ML ALGORITHMS

Algorithm	Parameters
SVM	Model Type: C; Kernel Function: RBF; Range of C: 0.1- 5,000; Range of Gamma: 0.001– 50; No. of intervals: 10.
GEP	Population Size: 50; Gene per chromosome: 4; Gene Head length: 8; Simplification generations: 500; Linking Funtion: Addition; Fitness Function: Accuarcy with penalty; Maximum Generations: 2,000; Stop if fitness reaches: 1; Mutation Rate: 0.044; Transposition rate: 0.1; Re-combination Rate: 0.3.
MLP-CG	No. of layers: 3; No. of hidden layer: 1; Training Method: Scaled Conjugate Gradient; No. of convergence tries: 4; Minimum iterations: 10,000; Hidden and Output layer ctivation function: logistic.
GMDH	Maximum network layers: 20; Maximum polynomial order: 16; Convergence to learn: 1.000e -004; Network layer connections: Previous layer and original input variables.
K-means	Minimum No. of Clusters: 2; Maximum no. of clusters: 200; Maximum steps without change: 50.
TB	Maximum No. of trees in series: 400; Depth of individual tree: 5; Minimum size of node to split: 10; Minimum No. of trees in series: 10.
BG	Bag sie percent: 100; Seed: 1; No. of iterations:10.
RF	No. of trees: 10; seed: 1.
J48	Confidence Factor: 0.25; Seed: 1; Minimum No. of objects: 2.

V. ANALYSIS AND RESULTS

This section gives a description of the analysis performed and lists down a number of performance measures evaluated for analyzing the developed model. In order to create the models, we have performed ten-fold cross validation. This involves dividing the complete data set into ten random subsets. A number of repetitions are performed. For each repetition cycle, we use nine subsets of the data for training and one remaining subset for validation. The procedure when repeated ten times gives the change proneness prediction of all the subsets [31]. The various performance measures used in this study are as follows:

- *Sensitivity and Specificity:* Sensitivity is defined as the percentage of correctly predicted classes which were change prone in nature. Specificity is defined as the percentage of correctly predicted classes which were not change prone in nature.
- *Accuracy:* It is the percentage of classes which are correctly predicted. They involve both correct change prone predictions as well as correct not change prone predictions.
- *Precision:* It is the proportion of correctly predicted classes of change prone nature to the total number classes predicted to be change prone by the model.
- *f- measure:* It denotes the harmonic mean of precision and sensitivity.
- *Receiver Operating Characteristic (ROC) Analysis:* This analysis involves the plotting of an ROC curve between sensitivity and 1-specificity measures. The model is evaluated by computing the Area Under the ROC curve (AUC). The larger the AUC value, the more effective is the model [32].

TABLE III. DRJAVA DESCRIPTIVE STATISTICS

Metric	Min.	Mean	SD	Max.	Median
CBO	0	5.55	9.98	157	3.5
NOC	0	0.36	3.61	71	0
DIT	1	2.46	1.11	7	2
LCOM	0	41.99	36.79	100	44.5
WMC	0	20.65	48.08	748	9
RFC	0	20.72	27.26	276	13
SLOC	1	154.23	409.91	7,011	58.5

TABLE IV. DSPACE DESCRIPTIVE STATISTICS

Metric	Min.	Mean	SD	Max.	Median
CBO	0	2.49	3.46	27	1
NOC	1	1.24	0.47	4	1
DIT	1	2.55	1.46	6	2
LCOM	0	50.70	32.64	100	51.5
WMC	1	21.03	25.27	178	12
RFC	1	20.43	16.96	64	14
SLOC	5	143.21	153.05	1,166	93.5

TABLE V. ROBOCODE DESCRIPTIVE STATISTICS

Metric	Min.	Mean	SD	Max.	Median
CBO	0	4.83	6.62	42	3
NOC	0	0.06	0.47	7	0
DIT	1	2.40	1.68	7	2
LCOM	0	45.83	37.83	100	57
WMC	0	22.71	37.47	414	11
RFC	0	38.29	56.47	202	16.5
SLOC	3	118.71	177.23	1,787	53.5

A. Descriptive Statistics

The values of the various OO metrics used in the study were analyzed for each of the open source data sets. Table III, IV and V lists the Minimum (Min.), Mean, Standard Deviation (SD), Maximum (Max.) and Median values for each metric of DrJava, DSpace and Robocode data sets

respectively. After analyzing the tables, the following observations were made:

- The class size of the DrJava data set ranges from 1–7,011 SLOC, that of the DSpace data set ranges from 5- 1,166 SLOC and for the Robocode data set ranges from 3- 1,787 SLOC.
- The mean values of the DIT metric (DrJava – 2.46, DSpace – 2.55 and Robocode – 2.40) and the NOC metric (DrJava – 0.36, DSpace – 1.24 and Robocode – 0.06) are poor in all the data sets. This means that there are only few subclasses and inheritance is not much used in the data sets. Similar results were observed by [1, 33].
- The value of LCOM measure is high (up to 100) in all the three data sets. This signifies the number of classes with no common attribute usage.

B. Ten-fold Cross Validation Results

This section describes the ten-fold cross validation results of all the algorithms on the three open source data sets used in the study.

As described in section III we first applied the CFS technique to get a set of OO metrics which are highly correlated with change. The results of the CFS technique is given in table VI. According to table VI, the CBO metric, the SLOC metric and the WMC metric were selected by the CFS technique in all the three data sets. Thus, these metrics are good predictors of change. The LCOM metric was selected for model inclusion by two data sets and is also highly correlated with change.

TABLE VI. CFS RESULTS

Dataset	OO Metrics Selected
DrJava	CBO, NOC, RFC, SLOC, LCOM, WMC
DSpace	CBO, SLOC, WMC
Robocode	CBO, SLOC, LCOM, WMC

The values of the performance measures for models developed using various algorithms is presented in table VII, VIII and IX. These tables list the Accuracy (Acc.), Sensitivity (Sens.), Specificity (Spec.), Precision (Prec.) and f- measure (f-mes.) values for the models developed using the various ML algorithms and the LR technique of DrJava, DSpace and Robocode data sets respectively.

According to table VII, the best performing model on the DrJava data set was developed using the MLP-CG algorithm. This model gave an accuracy measure of 74.13%, a precision value of 74.11%, a sensitivity value of 73.37%, a specificity value of 74.88% and an f-measure of 73.74%. Apart from the MLP-CG model, the SVM model and the GMDH model also performed well. These models gave better results than the LR model. The model giving the worst performance measures on the DrJava data set was the K-means model with a low accuracy measure of 57.21%.

TABLE VII. DRJAVA VALIDATION RESULTS

Algo.	Acc.	Sens.	Spec.	Prec.	f-mes.
SVM	72.39	71.36	73.40	72.45	71.90
GEP	70.40	71.86	68.97	69.42	70.62
MLP-CG	74.13	73.37	74.88	74.11	73.74
GMDH	72.39	68.84	76.85	74.46	71.54
K-Means	57.21	32.66	81.28	63.11	43.05
TB	70.65	69.85	71.43	70.56	70.20
BG	71.64	71.60	71.09	71.70	71.60
NB	66.40	66.40	60.69	74.30	63.30
RF	69.15	69.21	67.71	69.30	69.10
J48	70.39	70.40	70.00	74.40	70.40
LR	71.89	62.81	80.79	76.22	68.87

Table VIII lists the performance measure of various models developed on the DSpace data set. The best performing model on the DSpace data set was the SVM model with an accuracy of 78.78%, a precision value of 81.07%, a sensitivity value of 83.54%, a specificity value of 71.93% and an f-measure of 82.28%. Other models which performed well were the GEP model, the GMDH model, the MLP-CG model, the J48 model and the LR model. The model giving the worst performance measures on the DSpace data set was the NB model with an accuracy value of 64.02%.

TABLE VIII. DSPACE VALIDATION RESULTS

Algo.	Acc.	Sens.	Spec.	Prec.	f-mes.
SVM	78.78	83.54	71.93	81.07	82.28
GEP	78.78	89.63	63.16	77.78	83.29
MLP-CG	77.34	81.71	71.05	80.24	80.97
GMDH	77.70	87.20	64.04	77.72	82.18
K-Means	65.47	60.98	71.93	75.76	67.57
TB	77.34	85.37	65.79	78.21	81.63
BG	76.97	77.00	74.03	76.80	76.80
NB	64.02	64.00	53.76	72.10	63.30
RF	72.30	72.30	66.97	72.10	72.20
J48	78.41	78.40	77.55	78.30	78.10
LR	77.34	78.66	75.44	82.17	80.37

Table IX lists the results of ten-fold cross validation models on the Robocode data set. The BG model gave the best performance on the Robocode data set with an accuracy value of 80.45%, specificity and sensitivity values of 80.50% and 81.65% respectively. The precision and f-measure value of the BG model was 79.40% and 78.20% respectively. Other well performing models include the J48 model and the LR model. The worst performing model was the K-means model with an accuracy measure of 69.55%.

TABLE IX. ROBOCODE VALIDATION RESULTS

Algo.	Acc.	Sens.	Spec.	Prec.	f-mes.
SVM	77.44	27.54	94.92	65.52	38.78
GEP	75.19	31.88	90.36	53.66	40.00
MLP-CG	77.44	24.64	95.94	68.00	36.17
GMDH	77.07	30.43	93.40	61.76	40.78
K-Means	69.55	26.09	84.77	37.50	30.77
TB	75.56	40.58	87.82	53.85	46.28
BG	80.45	80.50	81.65	79.40	78.20
NB	75.18	75.20	78.54	72.40	72.60
RF	76.69	76.70	80.00	74.40	74.50
J48	77.81	77.80	81.94	76.30	76.60
LR	76.32	24.64	94.42	60.71	35.05

The models were also evaluated using the ROC analysis. Figure 2 shows a chart which depicts the AUC values on all the three data sets for all the algorithms employed in the study. For example, the AUC measure for the SVM model on the DrJava data set was 0.792, while the AUC measure on the DSpace data set for the SVM model was 0.824. The SVM model gave an AUC measure of 0.668 on the Robocode data set. Similarly, all other values for different models on each of the three data sets can be easily interpreted from Figure 2. The figure shows good AUC values for all the ML algorithms. These AUC values are comparable to the AUC values of the models developed using the LR technique. However, the values of the models using the K-means algorithm is relatively low when compared with other algorithms.

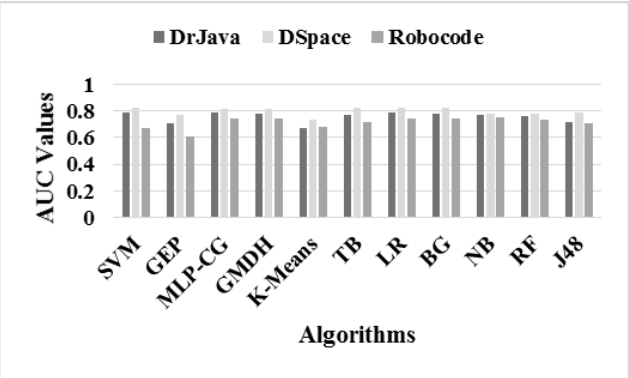


Figure 2. ROC Analysis of all Models

C. Friedman Test Results

This study analyzes a number of change prediction models using ten ML algorithms and the LR technique on three open source data sets. Though, there is difference in the performance of the models developed using various algorithms, we need to assess whether the difference is statistically significant. In order to do so, we perform Friedman statistical test [34]. Table X states the mean ranks obtained by each algorithm after application of Friedman test. The test was based on the classification accuracies of each model. According to the results, the best performing algorithm on all the three data sets was the SVM algorithm (ML), which obtained a mean rank of 2.50. The second rank was given to the MLP-CG algorithm which was closely followed by the GMDH algorithm. Two other ML algorithms, the J48 algorithm and the BG algorithm performed better than the statistical technique LR. The K-means algorithm was designated as the worst algorithm with a mean rank of 10.67.

The Friedman statistic value with ten degrees of freedom was calculated as 20.09 which is true for $\alpha = 0.05$. Furthermore, a p-value of 0.03 indicates that the results are true with a confidence interval of 95%. Thus, we reject the null hypothesis of the Friedman test which states that all algorithms are behaviorally same. The algorithms are significantly different in their behavior. The results also show that certain ML algorithms like SVM, MLP-CG, GMDH, J48 etc. perform better than the statistical technique LR.

TABLE X. FRIEDMAN TESE RESULTS

Algorithm	Mean Rank
SVM	2.50
MLP-CG	3.50
GMDH	3.83
J48	4.33
BG	4.67
LR	5.67
GEP	5.83
TB	6.67
RF	8.00
NB	10.33
K-means	10.67

D. Discussion of Results

This section presents an analysis of the various results presented in the study.

a) Which OO metrics are related to the change proneness attribute of a class?

OO metrics which are representative of various OO attributes like coupling, cohesion, size etc. can be effectively used for predicting change prone classes [1]. This study has evaluated a number of change prediction models which can efficiently predict change prone classes of a software product with OO metrics as the dependent variables. Moreover, we applied CFS technique to select OO metrics which are efficient predictors of change. Our results indicate that the CBO metric, the SLOC metric and the WMC metric are good indicators of change as these metrics were selected for developing the prediction model in all the three data sets used in the study. The WMC metric is also correlated with change in a class as it was selected in two data sets for model development. We also found that the inheritance metrics, DIT and NOC were not efficient change predictors. Similar results have been showed

by Lu et al. [6] where they found that the inheritance metrics were least effective while predicting change.

b) Are ML algorithms effective in ascertaining change prone classes in an OO software?

This study evaluates a number of change prediction models which were developed using the ML algorithms and the statistical technique, LR. The performance capability of the models were evaluated with a number of performance metrics i.e. accuracy, precision, specificity, sensitivity and AUC. All the models developed in the study yield good results i.e. accuracy values ranging from 64% to 80% and AUC values ranging from 0.61 to 0.83. These results show that the ML algorithms can be effectively used for developing good change prediction models. These models can be used by the software industry and researchers to identify change prone classes in the early phases of software development life cycle. Determining change prone classes would help in planning effective resource usage during the maintenance and testing phases of a software. It would further help in developing a better quality software by rigorous verification activities of these change prone classes.

c) How well the ML algorithms compare to statistical techniques for change proneness prediction?

In order to compare the performance of the ML algorithms with the LR, a statistical technique, we employed Friedman statistical test. The test ranks all the algorithms (ten ML and one statistical) using classification accuracies of the developed prediction models on the three open source data sets used in the study. The results of the test indicate that certain ML algorithms significantly outperform the LR technique. The SVM algorithm gave the best performing results and was assigned the first rank. The MLP-CG algorithm, the GMDH algorithm, the J48 algorithm and the BG algorithm were also given better ranks than the LR technique. The results of the Friedman statistical test were true for a confidence interval of 95%. Thus, we conclude that certain ML algorithms statistically outperform the LR technique and are effective for change proneness prediction.

VI. THREATS TO VALIDITY

This section briefly describes the various threats to validity of this study. This study does not consider the "casual" effect of various OO metrics on change proneness of a class. Thus, the threat to internal validity exists in the study [8]. Moreover, we have taken three open source medium sized software data sets for performing the empirical analysis. Thus, our results cannot be generalized to a large extent as we have not incorporated large sized software data sets. Future replicated studies should be conducted with different sized software data sets and development environments to reduce this threat to external validity. As the various OO metrics used in this study have been validated for their accuracy in previous studies [35-36], the threat to construct validity is minimized.

VII. CONCLUSIONS AND FUTURE WORK

The aim of this study was to evaluate a number of ML algorithms for their effectiveness in predicting software change. The empirical validation was done using three open source data sets. We further analyze and compare the performance of the ML algorithms with the statistical technique LR using the Friedman statistical test. Thus, the significance of this study include evaluation of an extensive set of ML algorithms for change proneness prediction problem and the statistical comparison amongst all the ML algorithms and statistical technique, LR. The main results of the study are concluded as follows:

- The CBO metric, the SLOC metric and the WMC metric are efficient predictors of change as they were included in the change prediction model using all the three open source data sets after application of the CFS technique.
- The results show that the SVM algorithm is the best ML algorithm which can be used for developing change prediction models. Certain other algorithms like the MLP-CG, GMDH, J48 and BG outperform the statistical technique, LR while developing change prediction models. Thus, ML algorithms are competitive while predicting software change and can be used by the software industry to effectively plan resource allocation and develop good quality software.

Future studies may replicate the use of ML algorithms on large-sized software data sets in order to yield generalized results. We may also employ a number of evolutionary algorithms to ascertain their applicability in developing software change prediction models.

REFERENCES

[1] R. Malhotra and M. Khanna, "Investigation of Relationship between Object-oriented Metrics and Change Proneness," *Int. J. Mach. Learn. & Cyber.*, Springer-Verlag, 4, pp. 273-286, 2013.

[2] A.G. Koru and H. Liu, "Identifying and characterizing change-prone classes in two large-scale open-source products," *Journal of Systems and Software,* vol. 80, pp. 63-73, 2007.

[3] K.K. Aggarwal, Y. Singh, A. Kaur and R. Malhotra, "Empirical Study of Object-oriented Metrics," *Journal of Object-Technology*, vol. 5, no. 8, pp. 149-173, 2006.

[4] S. Chidamber and C. Kemerer, "A Metric Suite for Object- Oriented design," *IEEE Transactions on Software Engineering*, vol. 20, no. 6, pp. 476-493, 1994.

[5] M. Lorenz and J. Kidd, *Object-Oriented Software Metrics*. Prentice Hall, 1995.

[6] H. Lu, Y. Zhou, B. Xu, H. Leung and L. Chen, "The ability of Object-Oriented metrics to predict Change-proneness: a meta-analysis," *Empirical Software Eng. Journal*, vol. 17, no. 3, pp. 200-242, 2012.

[7] M. O. Elish and M. A. Al-Khiaty, "A suite for quatifying historical changes to predict future change-prone classes in object-oriented software," *Journal of Software: Evolution and Process*, vol. 25, no. 5, pp. 407-437, 2013.

[8] Y. Zhou, H. Leung and B. Xu, "Examining the Potentially Confounding Effect of Class Size on the Associations between Object Metrics and Change proneness," *IEEE Transactions on Software Engineering*, vol. 35, no. 5, pp. 607-623, 2009.

[9] K. Dejaegaer, T. Verbraken and B. Basens, "Toward comprehensible software fault prediction models using bayesian network classifiers," *IEEE Transactions on Software Engineering*, vol. 39, no. 2, pp. 237-257, 2013.

[10] Y. Singh, A. Kaur and R. Malhotra, "Empirical Validation of Object-Oriented Metrics for Predicting fault-proneness Models," *Software Quality Journal*, Springer, vol. 18, no. 1, pp. 3-35, 2010.

[11] K. Elish and M. Elish, "Predicting Defect-prone Software modules using Support-Vector Machines," *Journal of System and Software*, vol. 81, no. 5, pp. 649-660, 2008.

[12] R. Malhotra, "Comparitive analysis of statistical and machine learning methods for predicting faulty modules," *Applied Soft Computing,* in press.

[13] A. Corazza, S.D. Martino, F. Ferucci, C, Gravino, F. Sarro and F. Mendes, "Using tabu search to configure support vector regression for effort estimation," *Empirical Software Engineering*, vol. 18, no. 3, pp. 506-546, 2013.

[14] V.K. Bardsiri, D.N.A. Jawawi, S.Z.M. Hashim, E. Khatibi, "A PSO-based model to increase the accuracy of software effort estimation," *Software Quality Journal,* vol. 21, no. 3, pp. 501-526, 2013.

[15] K.K. Aggarwal, Y. Singh, A. Kaur, R. Malhotra, "Application of Artificial Neural Network for Predicting Maintainability using Object-Oriented Metrics," *Transactions on Engineering, Computing and Technology*, vol. 15, Oct. 2006.

[16] M. Amoui, M. Salehie and L. Tahvildari, "Temporal software change prediction using neural network," *International Journal of Software Engineering and Knowledge Engineering*, vol. 19, no. 7, pp. 995-1014, 2009.

[17] R. Malhotra and M. Khanna, "Inter project Validation for Change Proneness Prediction using Object-Oriented Metrics", *Software engineering: An International Journal,* vol. 3, no. 1, pp. 21-31, 2013.

[18] E. Arisholm, L.C. Briand and A. Foyen, "Dynamic Coupling Measurement for Object-Oriented Software," *IEEE Transactions on Software Engineering*, vol. 30, no. 8, pp. 491-506, 2004.

[19] N. Tsantalis, A.Chatzigeorgiou and G. Stephanides, "Predicting the probability of change in object oriented systems," *IEEE transactions on Software Engineering,* vol. 31, no. 7, pp. 601-614, 2005.

[20] J.M. Bieman, A. A. Andrews and H. J. Yang, "Understanding Change-proneness in OO Software through Visualization," *IEEE International Workshop on Program Comprehension,* pp. 44-53, 2003.

[21] A.R. Han, S. Jeon, D. Bae and J. Hong, "Behavioral Dependency Measurement for Change-proneness Prediction in UML 2.0 Design Models," *Annual IEEE International Computer Software and Application Conference,* 2008.

[22] M.A. Hall, "Correlation-based Feature Selection for Discrete and Numeric Class Machine Learning," *Proceeding of the Seventeenth International Conference on Machine Learning*, pp. 359-366, 2000.

[23] Weka 3: Software Mining in Java. Available online at http://www.cs.waikato.ac.nz/ml/weka/

[24] Sherrod, P. 2003. DTreg Predictive Modeling Software. Available online at http://www.dtreg.com/gep.htm.

[25] C. Cortes and V. Vapnik, Support-Vector Networks, *Machine Learning,* Kluwer Academic Publishers, Boston, 20, 273-297, 1995.

[26] C. Ferreira, Gene Expression Programming: A New Adaptive Algorithm for Solving Problems, *Complex Systems*, vol. 13, pp. 87-129, 2001.D. Hosmer and S. Lemeshow, *Applied Logistic Regression*, New York, John Wiley & Sons, 1989.

[27] S. Haykin, *Neural Networks: A comprehensive Foundation*, Prentice Hall India, 2003.

[28] L. Brieman, Bagging Predictors, *Machine Learning,* vol. 24, pp. 123-140, 1996.

[29] J. Quinlan, *C4.5 Programs for Machine Learning*, Morgan Kaufmann Publishers, San Francisco, CA, 1993.

[30] L. Brieman, "Random Forests", *Machine Learning,* vol. 45, no. 1, pp. 5-32, 2001.

[31] M. Stone, "Cross-validatory choice and assessment of statistical predictions," J. Royal Stat. Soc., vol. 36, pp. 111-147, 1974.

[32] Fawcett, T., An introduction to ROC Analysis, *Journal of Pattern Recognition Letters,* 27, 8, (Dec 2005), 861-874.

[33] CartWright, M. and Shepperd, M., 2000. An Empirical Investigation of an Object-Oriented Software System, *In IEEE Transactions of Software Engineering,* 26, 8, 786-796.

[34] M. Friedman, "The use of ranks to avoid the assumption of normality implicit in the analysis of variance. *Journal of the American Statistical Association*, vol. 32, no. 2, pp. 675-701, 1937.

[35] L. Briand, J. Daly, and J. Wust, "A unified framework for coupling measurement in object-oriented systems", *In IEEE Transactions of Software Engineering,* vol. 25, no. 1, pp. 91-121, 1999.

[36] L. Briand, J. Wust, J. W. Daly and D. V. Porter, "Exploring the Relationships between Design Measures and Software Quality in Object-Oriented Systems," Journal of Systems and Software, vol. 51, no. 3, pp. 245-273, 2000.

Volume 2, Issue 3 (2014) 557-563 ISSN 2347 - 3258
International Journal of Advance Research and Innovation

Experimental Investigations on Friction Stir Processed Copper and Enhancement of Mechanical Properties of the Composite Material

V. Jeganathan Arulmoni *, R. S. Mishra
Department of Mechanical Engineering, Delhi Technological University, New Delhi, India

Article Info

Article history:
Received 25 July 2014
Received in revised form
10 August 2014
Accepted 30 August 2014
Available online 15 September 2014

Keywords

Surface Composites,
Process Parameters,
Mechanical Properties,
Friction Stir Processing of Copper

Abstract

This paper investigates the parameters affecting the friction stir processed copper and enhancement of the mechanical properties of the composite material. The results showed that the grain size of fabricated composite reduce, also it is indicated that in comparison to base metal (copper) micro hardness of friction stir processed composites in stir zone (SZ) increase significantly. The results obtained also indicated that the selected FSP parameters significantly influence the area of surface composite by the distribution of material particles. Higher tool rotational speed and lower processing speed produce an excellent distribution of material particles and higher area of surface composite due to higher frictional heat, increased stirring and material transportation.

1. Introduction

Friction stir processing (FSP) was developed for microstructural modification of metallic materials. In this review article, the current state of understanding and development of the FSW and FSP are discussed. At this stage, the technology diffusion has significantly outpaced the fundamental understanding of microstructural evolution and microstructure–property relationships. In FSP, a rotating tool is plunged into a material and high plastic deformation is produced. FSP is used to enhance ductility, induces super plasticity and improve corrosion resistance properties. Dynamic recrystallization of the deformed zone forms an ultrafine-grained structure. FSP has been successfully applied to various cast aluminium and magnesium and copper alloys to eliminate casting defects and thereby improve their mechanical properties.

Copper is a mostly used industrial and functional metal for various thermal, electrical and electronic applications, i.e. electronic packaging, electrical contacts and resistance welding electrodes. This is because of good thermal and electrical conductivity, high plasticity and excellent resistance to corrosion and oxidation. Nevertheless, low mechanical strength and poor wear resistance limit its applications.

Two modes of metal transfer during friction stir processing have been discussed [12]. The first mode of metal transfer is generated between the tool shoulder and the plate and takes place as layer-by-layer deposition of metal one over the other. The second mode of metal transfer is generated by the extrusion of metal around the tool pin, when it reaches a state of sufficient plasticity. Metal transfer, generated between the tool shoulder and the plate, plays an important role in influencing the mechanical properties during friction stir process. Modes of metal transfer are clearly visible in the microstructure characteristics, but they are not too distinct in macrostructure of most processed samples. Friction stir processing can be applied as a single-pass for processing a small area. For large engineering components in which the contact areas are relatively large, single pass FSP may not be adequate. Multi-pass FSP with a certain level of overlap between the successive passes is required for large contact areas. For both single and multi-pass processes, it is important to assess the microstructural evolution and its influence on the mechanical properties.

This paper mainly focused on friction stir processing (FSP) used to produce copper–graphite surface composites. Two tools with different pin profile were employed in order to achieve a comprehensive dispersion. Results showed that the tool with H13 steel triangular and threaded pins give rise to a better dispersion of graphite particles. Furthermore, copper–graphite composites containing different graphite content were prepared using the tool through repeating the process passes.

2. Literature Review

Bahram A. Et.al [1] has produced copper reinforced metal matrix composite (MMC) using micron sized chromium particles via friction stir processing (FSP) in order to study effects of adding Cr particles to copper based matrix by FSP. Microstructures, micro hardness and wear properties were studied in order to evaluate the microstructures and mechanical properties of fabricated composites. The microstructure properties were evaluated by optical microscopy (OM) and field emission scanning electron microscopy (FESEM). The mechanical behaviours of the samples were determined by micro hardness and wear tests. The results showed that the grain size of fabricated composite reduced. Also it was indicated that in comparison to base copper micro hardness of friction stir processed composites in stir zone (SZ) increased significantly. The results of wear test showed that in comparison with specimen with traverse speed of 80 mm/min, higher traverse speed of 160 mm/min increase wear rate of cylindrical pins. Akramifard H.R.et.al, [3**]** had investigated pure Cu sheets were reinforced with 25μm SiC particles to fabricate a composite surface layer by friction stir processing (FSP). In order to improve distribution of reinforcing SiC particles, a net of holes were designed by drill on the 4 surface of pure

Corresponding Author,
E-mail address: professor_rsmishra@yahoo.co.in
All rights reserved: http://www.ijari.org

Cu sheet. For evaluation of microstructure, Optical Microscope (OM) and Scanning Electron Microscope (SEM) were used. Microstructural observation confirmed fine and equiaxed grains in the stir zone (SZ) and showed that SiC particles act as heterogeneous nucleation sites in the dynamic recrystallization of Cu grains. Moreover, agglomeration of particles wasn't observed and fine particles had a good distribution in SZ. In the SEM micrographs, porosities were detected as microstructure defects. Microhardness measurements showed that surface hardness was two times as high as that of substrate. The rotational wear tests demonstrated that use of SiC particles enhanced wear resistance and increased average friction coefficient of pure Cu. No intermetallic compound was found in Cu/SiC composite as revealed by XRD analysis**..** Sarmadi H**,**et.al[4**]** mainly focused on friction stir processing (FSP) used to produce copper–graphite surface composites. Five tools with different pin profile were employed in order to achieve a comprehensive dispersion. Results showed that the tool with triangular pin give rise to a better dispersion of graphite particles. Furthermore, four copper–graphite composites containing different graphite content were prepared using triangular tool through repeating the process passes. Friction and wear performance of the composites were also studied using a pin-on-disctribometer. It was indicated that the friction coefficients of composites were lower than pure annealed copper and decreased with increase in graphite content. The reduction in friction coefficient is due to decrease in metal–metal contact points, originated from the presence of graphite particles as a solid lubricant. Wear loss of the composites was also decreased with increase in graphite content which was related to change in wear mechanism from adhesive to delamination wear and reduction of friction coefficient. Their work was concluded as mentioned below. Fabrication of copper–graphite composites by friction stir processing (FSP) is possible. Using this technique leads to more homogenous distribution of particles in surface of composite and prevents particle changing into clusters which was the most important problem in prior techniques such as powder metallurgy and centrifugal casting. It was also noted that in order to produce more heat and avoid wasting produced heat, rotating speed and transverse speed should be chosen high and low respectively and specimens should be isolated. Using tool with triangular pin leads to better distribution of particle rather than other tools which were because of flow pattern of materials against this tool. The area of composite produced with this tool was larger in comparison with compo- sites produced by other tools. Friction coefficient was decreased with increase in graphite content so that friction coefficient of Cu-4G composite containing about 22vol% graphite is79% lower than pure annealed copper. This was due to presence of graphite as a solid lubricant and decrease in number of metal to metal contact point. It was also observed that friction coefficient decreases to some extent as graphite con- tent increases and after a threshold value of graphite content, it remains constant. The threshold graphite content in their study was about 25vol%. Wear loss of specimens was decreased with increase in graphite content. Adding about 22vol% graphite to copper increases wear resistance of the composite by 65%. This was due to presence of graphite as a solid lubricant. Increase in graphite content results in increase in delamination wear and decrease in adhesive wear. Galvao I.et.al [5] in their work, 1 and 3 mm-thick copper-DHP plates were processed with the aim of simulating surface (SFSP) and bulk (VFSP) processing. The influence of the processing conditions on the microstructure and mechanical properties of the processed materials was analyzed. It was found that the tool geometry, which has a close relation with the plastic deformation and dynamic recrystallization kinetics inside the stirred volume, the processing parameters and the heat exchange conditions, which determine the extent of dynamic recrystallization and annealing phenomenon, are determinant in FSP. Kudzanayi Chiteka**[6]** conducted studied making a choice in selection of friction stir welding/processing (FSW/P) tool material which has become an important task in determining the quality of the weld produced. The tool material selection depends on the operational characteristics such as temperature, wear resistance and fracture toughness that determine the type of materials to be joined. Soft materials can be easily welded using tool steels while harder materials need harder tool materials such as carbide based materials and polycrystalline cubic boron nitride (PCBN). K. Surekha, A. Et.al. [7] Considered the objective of their study was to obtain a high strength, high conductivity copper by friction stir processing. Three milli meter thick pure copper plate was friction stir processed to a depth of 2.8 mm at low-heat input conditions by varying the travel speed from 50 to 250 mm/min at a constant rotation speed (300 rpm) to obtain fine grains. Grain size of the nugget decreased from 9 to 3 μm and the hardness increased from 102 to 114 HV by increasing the traverse speed from 50 to 250 mm/min. Yield strength, microhardness and ultimate tensile strength increased with decrease in grain size in the nugget region and the yield strength obeyed $\sigma s = 223.8 + 0.07d^{-1/2}$ Hall–Petch relationship, where d is the grain size in m.

3. Experimental Set Up

The machine used for Friction stir processing was a vertical milling machine in which necessary adjustments were made to make it suitable for use in friction stir processing. The collect chuck was used to hold the tool.Proper job holding fixture was used which could hold a 150 X 74 x 5 mm plate. Toe clamps were used to hold the job firmly. Collet used for holding the tool could hold a cylindrical (tapered/ untapered) tool of diameter 15- 16 mm. Two 150 x 37 x 5 mm 99% pure Copper Plates mounted on the fixture used for job holding one by one on Milling Machine for groove cutting. Two grooves of 1mm deep was made on 2 plates using a 1mm (width) saw cutter at equal linear distances. First plate (without grooves) was clamped firmly by using the toe clamps. Then H13 tool steel with shoulder dia 15mm and pin dia 5 mm and pin length 1.5mm was inserted in to the collet and tightened. The pin of the tool was brought just above the plate in such a way such that the centre of the pin lies just above the centre of the groove cut. First Pass, than a full pass is made along the length of the job. Second Pass, after cooling the plate for 5-10 minutes than a full pass is made along the length of the job. The job was allowed to cool for some time and then taken out from the fixtures. Graphite powder was filled into

the grooves of second and third plate using a Shoulder tool of diameter 15mm.



Fig: 1. Graphite Powder Filled in the Grooves of Copper Plate



Fig: 2. Tensile Specimens

The Graphite powder was filled into the grooves of second and third plate and process is repeated as per the following table. Process Parameters for first, second, third plate are mentioned in the table

Work Piece	Tool shape and size	Feed	rpm of spindle
99% pure Copper	H13 steel tool cylindrical Pin Shoulder Diameter-15mm Pin diameter-5mm Pin length-1.5 mm Pin shape- straight cylindrical threaded	10mm/min	1600 rev/ min

Specimen 1-- No. of Passes = 1
Specimen 2--Ist Groove, No. of Passes = 2
Specimen 3--IInd Groove, No. of Passes = 3
Specimen 4 --Ist Groove No. of Passes = 2
Specimen 5--IInd Groove,No. of Passes = 4

The processed pieces are now taken for the following tests:
Tensile Strength Test
Brinell hardness test
Microstructure test

3.1 Tensile Strength Test

After the FSP the specimen for tensile testing were cut from the job. The specimens are as shown in figure. The specification of specimen is as following:

1. Length of specimen- 101.6 mm
2. Gauge Length – 25.4 mm
3. Gauge width- 6mm
4. Gauge thickness- 5mm

Five specimens were chosen marked with marker on their ends. Care was taken to ensure that the specimens did not have any notching or cracks from manufacturing or any surface defects that would adversely affect the tensile tests. Before loading the specimens in the Instron machine, the computer system connected to the machine was given inputs such as gauge length and width of the specimen. The computer system was then prepared to record data and output necessary load-deflection graphs. The specimens were loaded into the Instron machine, and a tensile test was performed. The data was recorded electronically in text files and the load-deflection curve was shown on the computer screen as a visual representation. The average of different values of 3 specimens each from 2 jobs and parallel material was taken as the final values. The stress strain graphs and load elongations graph are shown for the ultimate strength of the specimen. The ultimate tensile strength of the processed material comes out to be lesser than the parallel material

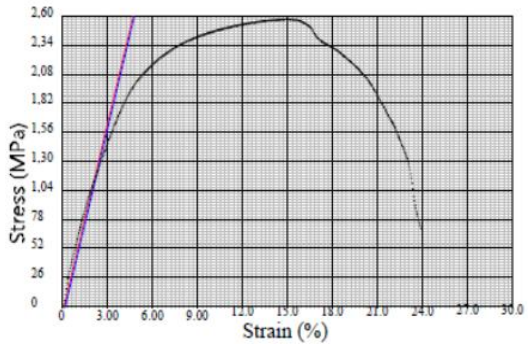


Fig: 3(a). Stress-Strain Curve for Specimen 1

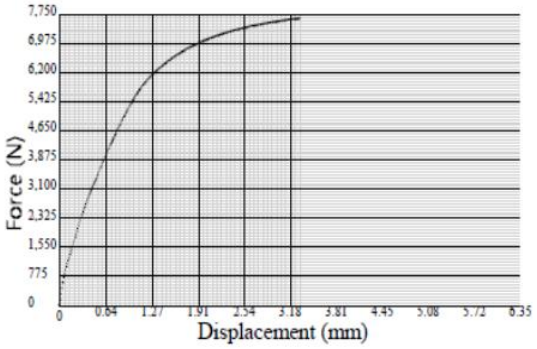


Fig: 3(b). Force-Displacement Curve Specimen 1

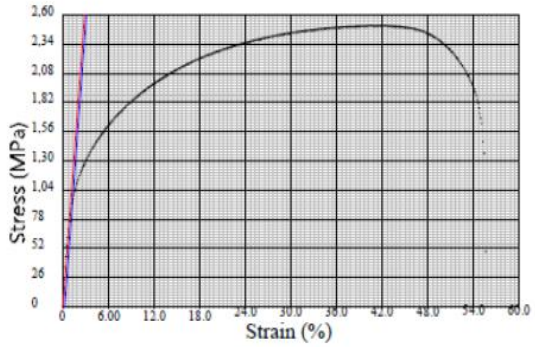


Fig: 3(c). Stress-Strain Curve for Specimen 3

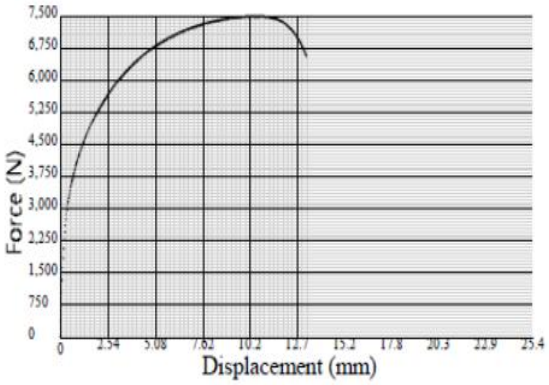


Fig: 3(d). Force-Displacement Curve Specimen 3

3.2 Brinell Hardness Test

The Brinell scale characterizes the indentation hardness of materials through the scale of penetration of an indenter, loaded on a material test-piece. It is one of several definitions of hardness in materials science. The brinell hardness was conducted on all 5 specimens each from 3 plates. The table below shows the BHN for different specimen:-

Specimen	Diameter of carbide sphere (D) (mm)	Diameter of impression (d)(mm)	BHN
1	10	6.5	79.5
2	10	6	95
3	10	5.5	115
4	10	6	95
5	10	5	142

As we can see the brinell hardness of the processed specimen increases as the number of passes are increased due to the more compact microstructure. The brinell hardness number comes out to be highest for specimen no. 5

4. Microstructure Ananlyis

The optical microscope is the principal tool used to characterize the internal grain structure of steel. Traditionally, the structure revealed by the microscope is called the **microstructure**. The mechanical properties of given steel are strongly influenced by its microstructure. An optical microscope uses reflected light to generate an image. A beam of light is directed down onto the surface and the image is generated either on film or the eye by light reflected along the same direction. This is performed on specimens either cut to size or mounted in a resin mold. The samples are polished to a fine finish, normally one micron diamond paste, and usually etched in an appropriate chemical solution prior to examination on a metallurgical microscope. For microstructure test we had 4 specimens. There are two examination methods in metallography:

1) Macroscopy
2) Microscopy

In macroscopy the examination of the structural characteristics or chemical characteristics of a metal or an alloy is done by the unaided eye or with the aid of a low-power microscope or binocular, usually under l0x. In microscopy similar examination is done with the prepared metal specimens, employing magnifications with the optical microscope of from 100x to as high as 2000x.

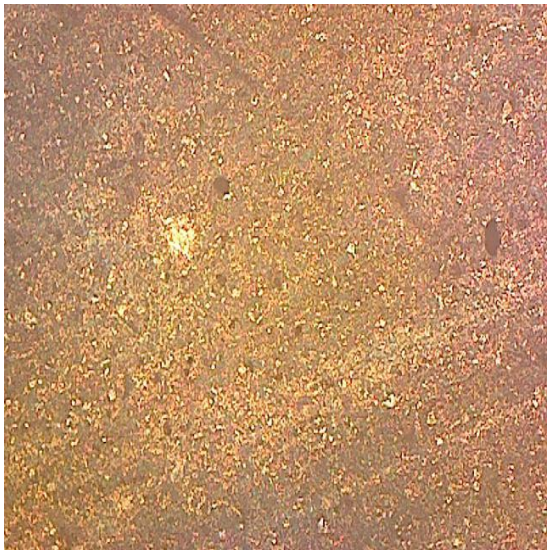


Fig: 4. Specimen 1--10x

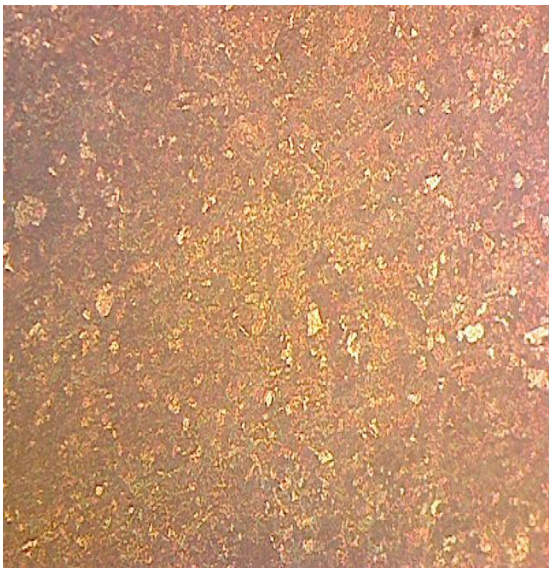


Fig: 5. Specimen 1--20x

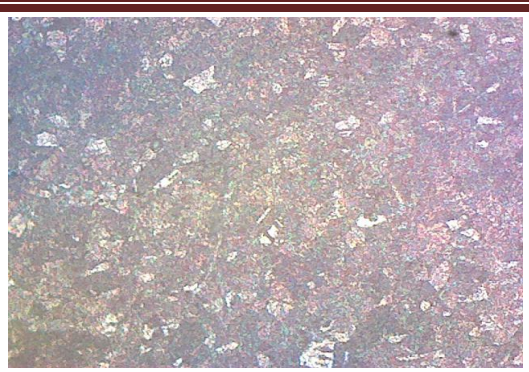


Fig: 6. Specimen 1--50x

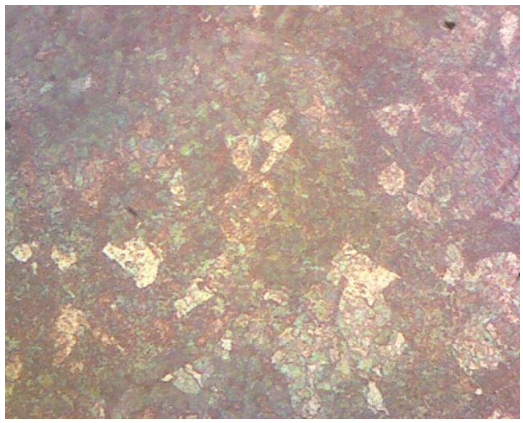


Fig: 7. Specimen 1--100x

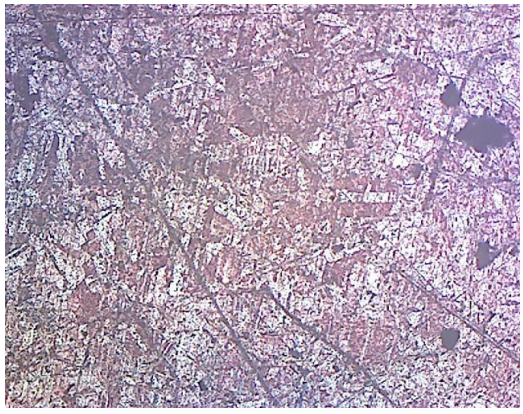


Fig: 8. Specimen 2--10x

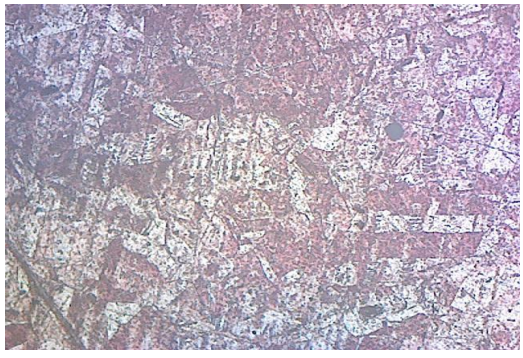


Fig: 9. Specimen 2--20x

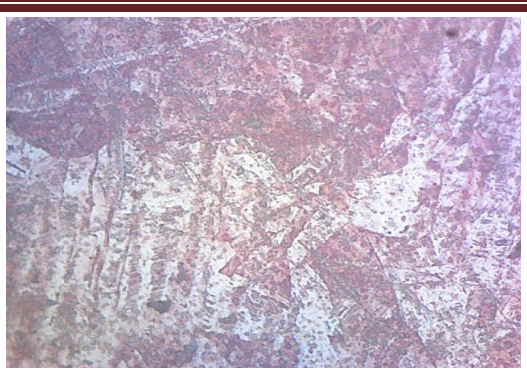


Fig: 10. Specimen 2--50x

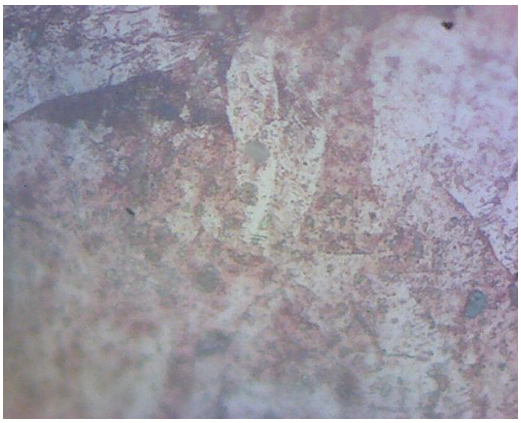


Fig: 11. Specimen 2--100x

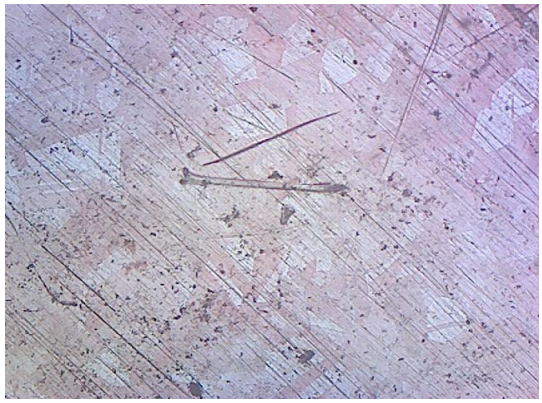


Fig: 12. Specimen 3--10x

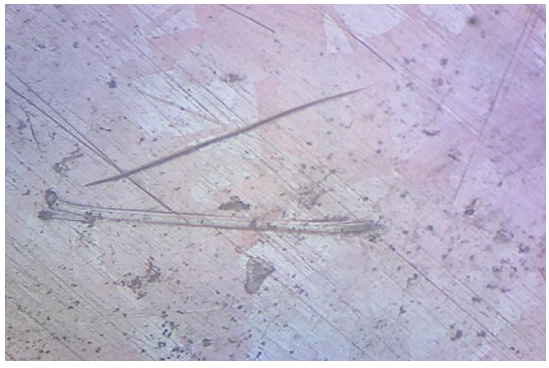


Fig: 13. Specimen 3--20x

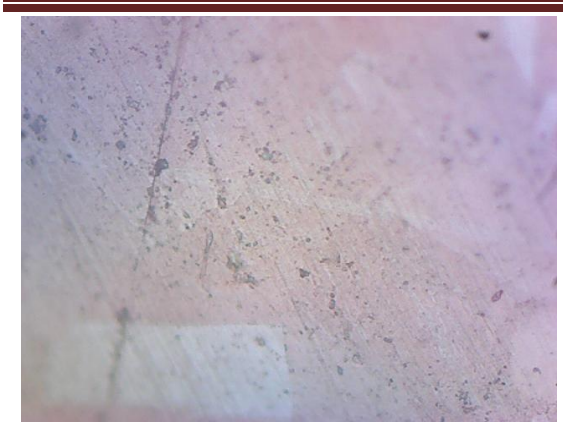


Fig: 14. Specimen 3--50x

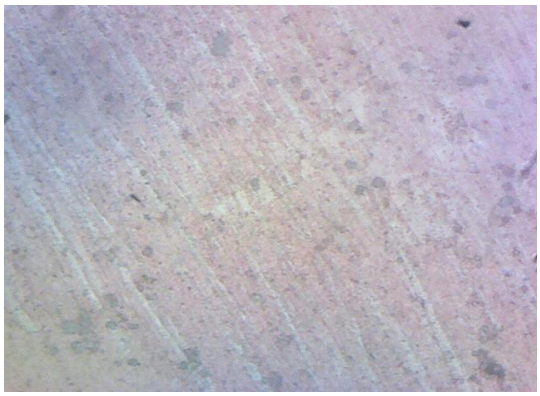


Fig: 15. Specimen 3--100x

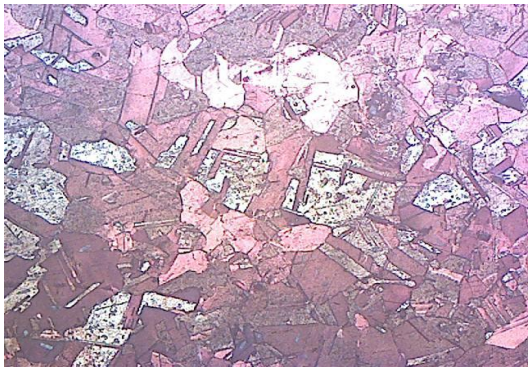


Fig: 16. Specimen 4--10x

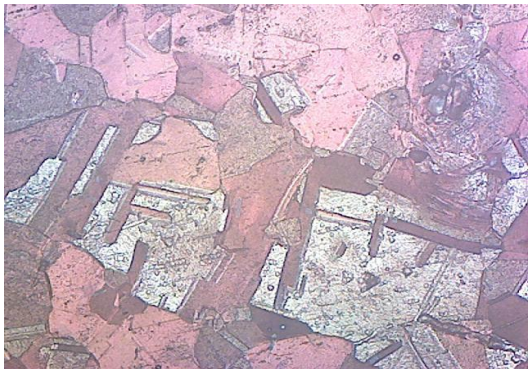


Fig: 17. Specimen 4--20x

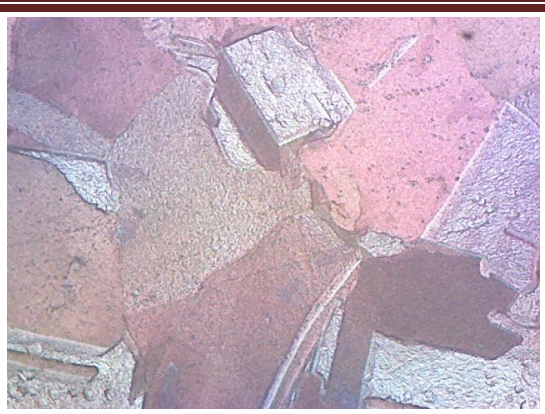


Fig: 18. Specimen 4--50x

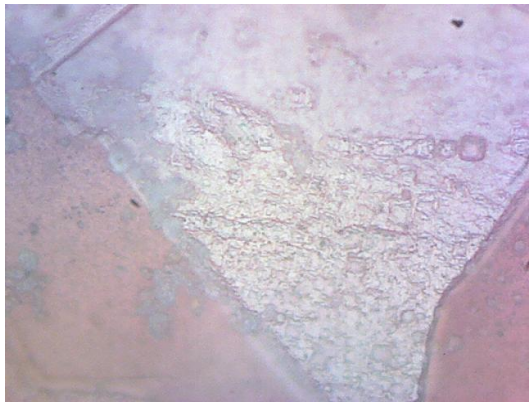


Fig: 19. Specimen 4--100x

Base metal microstructure (b) Boundary between NZ and HAZ in sample processed in adequate heat input (c) Cavities and cracks in samples processed at tool speed of 300 rpm, (d-f) Microstructure of NZ in sample processed at tool speed of 600 rpm and traverse speed of (d) 40 mm/min (f) 100 mm/min [16]

5. Conclusions

The effect of FSP parameters on copper material with graphite powder as composite material studied. Tensile strength, microstructure and micro hardness tests were conducted on the specimens prepared. The following conclusions have been made. Fabrication of copper–graphite composites by friction stir processing (FSP) is possible. Using this technique leads to more homogenous distribution of particles in surface of composite and prevents particle changing into clusters which was the most important problem in prior techniques such as powder metallurgy and centrifugal casting. It was also noted that in order to produce more heat and avoid wasting produced heat, rotating speed and transverse speed should be chosen high and low respectively and specimens should be isolated.

Using tool with threaded pin leads to better distribution of particle rather than other tools which were because of flow pattern of materials against this tool. The area of composite produced with this tool was larger in comparison with compo- sites produced by other tools. The microstructure for different specimens showed that as the no. of passes are increased microstructure gets more compact and no defects after processing. The ultimate

tensile strength of the processed pieces were more than the ultimate tensile strength of the unprocessed material. Also the processed surface formed by friction stir processing of 99% pure Copper by H13 steel tool has higher tensile strength than the base material. The processed plate specimen had higher brinell hardness number as compared to base material. Also as the number of passes are increased BHN number increases. This means friction stir processing of 99% pure copper by H 13 cylindrical threaded Pin provides a joint of hardness greater than the base material.

References

[1] Bahram A. Khiyavi, Abdolhossein Jalali Aghchai, Mohammadreza Arbabtafti, Mohammad Kazem Besharati Givi, Jalal Jafari, Effect of friction stir processing on mechanical properties of surface composite of Cu reinforced with Cr particles, Advanced Materials Research, 829, 2014, 851-856

[2] B. C. Liechty, B. W. Webb, Flow field characterization of friction stir processing using a particle-grid method, journal of materials processing technology 208, 2008 431–443

[3] H. R. Akramifard, M. Shamanian, M. Sabbaghian, M. Esmailzadeh, H.R. Akramifard, M. Shamanian, M. Sabbaghian, M. Esmailzadeh, Microstructure and mechanical properties of Cu/SiC metal matrix composite fabricated via friction stir processing Materials and Design, 2013

[4] H. Sarmadi , A. H. Kokabi, S. M. Seyed Reihani, Friction and wear performance of copper–graphite surface composites fabricated by friction stir processing (FSP) , Wear 304, 2013, 1–12

[5] I. Galvao, A. Loureiro, D. M. Rodrigues, Influence of process parameters on the mechanical enhancement of copper-DHP by FSP, Advanced Materials Research 445, 2012, 631-636

[6] Kudzanayi Chiteka, Friction Stir Welding/ Processing Tool Materials and Selection, International Journal of Engineering Research & Technology, 2(11), 2013, 8-18

[7] K. Surekha, A. Els-Botes, Development of high strength, high conductivity copper by friction stir processing, Materials and Design, 32, 2011, 911–916

[8] Mohsen Barmouz, Mohammad Kazem Besharati Givi, Fabrication of in situ Cu/SiC composites using multi-pass friction stir processing: Evaluation of microstructural, porosity, mechanical and electrical behaviour, Composites: Part A 42, 2011, 1445–1453

[9] Mohsen Barmouz, Mohammad Kazem Besharati Givi, Javad Seyfi, On the role of processing parameters in producing Cu/SiC metal matrix composites via friction stir processing: Investigating microstructure, icrohardness, wear and tensile behaviour, Materials Characterization 62, 2011, 108 – 117

[10] P. Xue, B. L. Xiao, Z. Y. Ma, Achieving Large-area Bulk Ultrafine Grained Cu via Submerged Multiple-pass Friction Stir Processing, J. Mater. Sci. Technol., 2013, 29(12), 1111-1115

[11] Q. Zhang, B. L. Xiao, P. Xue, Z. Y. Ma, Microstructural evolution and mechanical properties of ultrafine grained Al3Ti/Al–5.5Cu composites produced via hot pressing and subsequent friction stir processing, Materials Chemistry and Physics 134, 2012, 294– 301

[12] Rajiv S. Mishra, Murray W. Mahoney, Friction Stir Welding and Processing, ASM International, 2007

[13] R Sathiskumar, N Murugan, I Dinaharan and S J Vijay, Role of friction stir processing parameters on microstructure and microhardness of boron carbide particulate reinforced copper surface composites, Indian Academy of Sciences, Sadhana, 38(6), 2013, 1433–1450

[14] R. Sathiskumar, N. Murugan, I. Dinaharan, S. J. Vijay, Characterization of boron carbide particulate reinforced in situ copper surface composites synthesized using friction stir processing, Materials Characterization 84, 2013, 16 – 27

[15] R. Sathiskumar, N. Murugan, I. Dinaharan, S. J. Vijay, Prediction of mechanical and wear properties of copper surface composites fabricated using friction stir processing, Materials and Design 55, 2014, 224–234

[16] Salar Salahi, Vahid Rezazadeh, Fracture Mechanism in Friction Stir Processed Annealed Pure Copper Samples, World Applied Sciences Journal 23 (12): 54-58, 2013

[17] Scott F. Miller, New friction stir techniques for dissimilar materials processing, Manufacturing Letters 1, 2013, 21–24

[18] Yong X. Gan, Daniel Solomon 2 and Michael Reinbolt, Friction Stir Processing of Particle Reinforced Composite Materials, Materials 2010, 3, 329-350

[19] Z. Y. MA, Friction Stir Processing Technology: A Review, The Minerals, Metals & Materials Society and ASM International 2008

OPEN ACCESS

International
Journal
Of Modern Engineering Research (IJMER)

Failure of Piston in IC Engines: A Review

R. C. Singh[1], Roop. Lal[2], Ranganath M S[3], Rajiv Chaudhary[4]
[1]*Associate Professor,* [2]*Assistant Professor, Mechanical Engineering, Delhi Technological University, Delhi, India*

Abstract: *Piston in the internal combustion (IC) engine is robust, dynamically loaded tribo-pair that reciprocates continuously at varying temperature. Study has been made by various researchers on piston design, dynamics, fatigue and wear at the interface with other element in contact along with their effects on IC engines. It was found that the friction coefficient increases with increasing surface roughness of liner surface and thermal performance of the piston increases with increased coating thickness. The free material liberated due to deep scoring between the piston and liner snowballs, leads to seizure failure.*

Keywords: *Piston, Tribo-pair, IC Engines, Fatigue, Wear.*

I. INTRODUCTION

The current trend in the land transportation and power production is to develop IC engines of enhanced "power-capacity" and "reduced emissions" (to follow specified international intrinsic norms). Piston, piston rings and cylinder liner are important components of an IC engine. The prime function of piston is to transmit the motion produced by liberation of chemical energy of fuel to mechanical works. Piston rings dynamically seal the gap between the moving piston and the cylinder liner surface in order to prevent the escape of the combustion gases from the combustion chamber into the crankcase and the leakage of the oil from the crankcase into the combustion chamber.

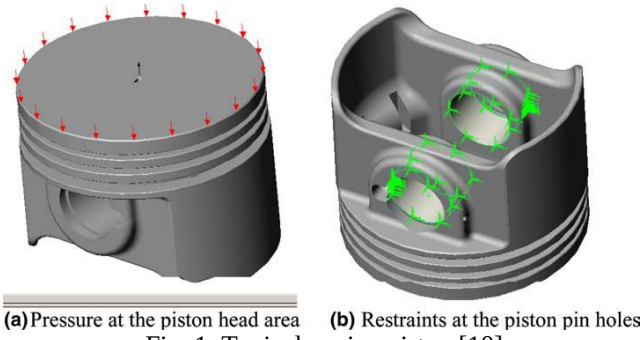


Fig. 1. Typical engine piston [10]

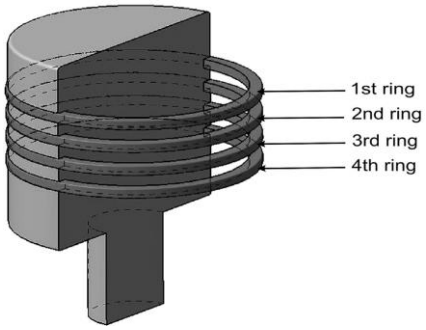


Fig. 2. Schematic illustration of a worn ring piece [25]

The manufacturing of cylinders includes boring, honing and plateau honing which has received much attention by manufacturers in recent times. The process of the surface changes which occurs during running of the engine is related to the wearing action caused by the piston ring on the bore. This action takes place of "transitional topography" where the surface generated exhibits the influence of the piston ring which modifies the machined surface. This has been made possible by improving the design of piston and reducing the failure i.e. scuffing, sculling, seizure of piston etc. The piston is one of the continuous moving parts of engine, is of pivotal importance. Piston has high dynamic loaded speed and heavy reciprocating weight develop high inertia forces, which are undesirable. The following factors may be considered for proper functioning of piston in IC Engine:

1. The piston should have enormous strength and heat resistance properties to withstand gas pressure and inertia forces. They should have minimum weight to minimize the inertia forces.
2. The material of the piston should have good and quick dissipation of heat from the crown to the rings and bearing area to the cylinder walls. It should form an effective gas and oil seal.
3. Material of the piston must possess good wearing qualities, so that the piston is able to maintain sufficient surface-hardness unto the operating temperatures.
4. Piston should have rigid construction to withstand thermal, mechanical distortion and sufficient area to prevent undue wear. It has even expansion under thermal loads so should be free as possible from discontinuities.

5. Piston should form tribo-pairs and have high reciprocation speed without noise, minimum work of friction and have little or no tendency towards corrosion and pitting-up.

II. LITERATURE REVIEW

Sunden and R. Schaub [12] presented a selection of some of the more practically orientated principles of the successful manufacture of grey cast iron piston rings greater than 175 mm in diameter, and shown that when considered with the sciences of strength of materials and diesel engineering, the subject of piston rings becomes an embodiment of the wider subject of tribology. A brief description of the most important topics of practical piston ring manufacture, and an indication of the vast size and complicated nature of an industry which concerns itself with one of the cheapest components of a diesel engine has been given. P. C. Nautiyal, et al, [23] investigated a large part of the top piston ring wear of an IC engine which takes place in boundary lubrication around top dead centre (TDC) position. A quantitative assessment of the frictional behavior using actual piston ring and cylinder liner under conditions close to TDC was made. The factors responsible for wear under these conditions have been identified as surface temperature, peak combustion pressure, total energy on the wearing surfaces and other physical properties of the material under sliding. T. H. C. Childs and F. Sabbagh [30] carried out tests to study the wear mechanisms responsible, particularly the relative importance of high cycle metal fatigue and chemical reaction film wear. Two types of cast iron used as piston rings (a grey and a carbidic iron) were used as pins and a cylinder bore material was used as the ring. Specific loads were varied from 20 to 400 M Pa and the sliding speed was 0.4 m s^{-1}. The wear mechanisms in the two types of test were possibly different, as the engine tests produced worn surfaces which when examined by an optical microscope were bright, whereas the pin-on-ring test surfaces were covered by patchy non-metallic films. Wear rates, friction coefficients, percentage metallic contact and plasticity index were measured in the pin-on-ring tests. Specific wear rates did not correlate with any parameters of contact stress severity.

D. J. Picken and H. A. Hassaan [6] paper described the theory and use of a method for estimating the service life of an internal combustion (i.c.) engine based on experimental evidence and the law of adhesive wear. A simple computer program described, which predicted the overhaul life of an IC engine from its design data and a typical sample of its particular running conditions. The use of the program for an engine generator set operating on biogas at a farm site used as an example. It was considered that the work reported showed that the limit of engine life occurred when the wear of the cylinder liner at the upper position of the piston ring became excessive. Based on this, and assuming marginal lubrication in this area was possible to do a calculation which predicted engine life for any given application. J. E. Willn [13] discussed various methods of characterizing and describing surface finish more accurately for specification purposes. Later, it was hoped that some part of the characterization may also form a correlation with the performance of the ring and bore surfaces with respect to scuffing failure. Complete surface finish characterization was a pre-requisite to ring and liner scuffing tests from which it could be possible to form some correlation between performance and some feature of the surface profile. Meanwhile, a practical and more precise method of specifying finish was required for insuring consistent results in production. Then established random analysis techniques offer a means of characterizing profiles which describe the variations more fully than the simple values of center line average or root mean square. In the majority of cases, the specimen profiles which were examined, varied randomly in amplitude but not in frequency. A. V. Sreenath and N. Raman [2] studied about the conformance between the liner and rings of an internal combustion engine and found that it depend upon mainly on the linear wear (dimensional loss) during running-in. Running-in wear studies, using the factorial design of experiments, on a compression ignition engine showed that at certain dead centre locations of piston rings the linear wear of the cylinder liner increases with increase in the initial surface roughness of the liner. The linear wear of the cast iron liner and rings decreased with increasing load but the mass wear increased with increasing load. Statistical analysis of the linear wear data showed that, during running-in, the initial surface roughness of the liner had a significant effect on running-in wear at and around such dead centre positions of rings where more than one compression ring slide over. It was observed that metal to metal contact occurs at the dead centre positions of rings during running-in. K. J. Stout and T. A. Spedding [17] considered the methods of producing engine bores and the surface profiles obtained by these methods were examined and attempted to characterize their surface topography made. The effects of wear studied and from a consideration of the surface topography of the initial machining process a characterization technique was proposed. The random part of the bored surface has a similar skewness and kurtosis to the honed surface which was due to the similarity of the effects of shearing and deformation on the surface during the two finishing operations.

William G. Agnew [33] reviewed the combustion research conducted by one automotive research laboratory of General Motors. Wieslaw Grabon et al, [32] carried out experiments on a reciprocating tester. The lubricant was supplied into the inlet side of the contact zone. The construction of tribological tester allowed to

measure the friction force between specimen and counter-specimen. Tribological behaviors of cylinder liners with and without oil pockets were compared. Specimens were cut from plateau honed cylinder liners made of grey cast iron. Counter-specimens were cut from grey cast iron piston rings. The results suggested that hydrodynamic oil pocket effect was of prime importance. The positive effect of additional cylinder liner surface texturing on frictional resistance under worse lubrication conditions was smaller. Height and slope of piston ring surface topographies decreased due to wear. S. Mezghani et al, [27] investigated the various aspects of the wear modeling that caused running- in problems in honed surfaces and its implications on ring-pack friction performance. Plateau honing experiments under different conditions were carried out on an instrumented vertical honing machine. The plateau honing experiments characterized the surface modifications during running-in wear of cast-iron engine bores using advanced characterization method. The predictions were in good agreement with the measurement data of plateau and valleys surface-height parameters. The simulation model of piston ring-pack contact developed to predict friction of cylinder surfaces after plateau honing showed that smooth surfaces lead to better friction performances despite the increases of the ratio between plateau and valleys height (non-plateaued surface). E.P. Becker and K.C Ludema [9] used a laboratory simulator to identify the important variables influencing cylinder bore wear. The same characteristics of wear were observed in the simulator as in running engines, even though the simulator did not attempt to duplicate all the conditions found within an engine. A new picture of wear in cylinders was presented, consistent with the data and previous work on boundary lubrication. The qualitative model accounted for the evolution of the cylinder running surface in terms of composition and texture changes. The model was used to determine the relative importance of the many variables that can influence wear behavior, including contributions from lubricant chemistry, material properties, and mechanical loading. J. Galligan et al, [14] developed a bench test in the first part of this work and the time to failure of ring bore contacts lubricated with a fully formulated motor oil. It was found that failure times correlated well with load, frequency, test temperature and quantity of oil, but that the effect of surface finish, though present, was more difficult to quantify. The main findings in this respect were that there is an optimum finish for long life, and that liner surfaces which were initially highly polished lived which are more dispersed than those with standard finishes. The time to failure in a bench test designed to simulate scuffing failure in the bores of IC engines was shown to be linearly related to load, frequency, temperature and quantity of oil. If the first three of these exceed a critical value, or if the quantity of oil falls below a critical value, scuffing was almost instantaneous. The time to scuff was related to liner surface finish as measured by the rms slope of the top half of its profile.

S.G. Chung et al,[29] employed three types of fixed piston samplers at Nakdong River Delta. The retrieved samples were equally divided into 100 mm long pieces. Quality was evaluated using suction, shear wave velocity, and consolidation tests. The constant rate of strain consolidation test, rather than the incremental loading test, produced a better correlation with the nondestructive test results. The results suggested that the difference in sample quality was principally caused by the mechanical disturbance attributed to the different penetration mechanisms (methods) of the sampling tubes. The tip angle of sampling tubes significantly affected sample quality, whereas the length-to-diameter ratio had a relatively insignificant effect. The three methods used are in the following order: oil-operated, mechanical, and hydraulic samplers. The difference in sample quality was primarily caused by the mechanical destructuration that occurs because of different penetration mechanisms. Sample quality tends to vary with the in-situ void ratio of the clay. M. Priest, C.M. Taylor [18] reviewed the nature of the surfaces encountered in the piston assembly, valve train and journal bearings of the internal combustion engine. The mathematical models of engine tribology endeavouring to cope with the extreme complexities for the incorporation of surface topography potentially were discussed. U.I. Sj¨odin, U.L.-O. Olofsson [31] investigated the wear interaction between piston ring and piston groove in a radial piston hydraulic motor in regard to mass loss and changes in form and surface roughness. A test rig was developed to simulate the tilting movements of pistons .The results showed that wear on the piston ring groove can be up to 10 times greater than the wear on the piston ring. Factorial design analysed that the form of the piston groove significantly influences the amount of wear, the dominant wear mechanism was mild wear.The most important design variable was the length of the support surface. The preferred design was a piston groove without any support plane. Zenon Krzyzak and Pawel Pawlus [36] analysed the surfaces of a large number of piston skirts surfaces under the "zero-wear" condition were analysed. The amplitude of worn piston skirt surfaces decreased, the ordinate distribution became asymmetric, summit density increased and lay direction changed from circumferential to axial during wear. The relationship between microgeometry parameters was studied using correlation and regression analysis. It was decided to determine the local wear of piston skirts based on the changes in amplitude parameters. An increase in the initial surface height caused and increase in piston skirt wear. The local linear wear of piston skirts was bigger on the thrust side than on the anti-thrust side of the cylinder . The worn piston skirt surfaces were observed to be smoothed. The ordinate distribution became asymmetric during "zerowear". The ratio of average slopes in axial and circumferential directions can monitor

piston skirt wear. Piston skirt wear was proportional to initial profile height. Change of height parameter during wear process was bigger on the thrust side than on the anti-thrust side of the cylinder. A. Skopp, et al, [1] compared the tribological behaviour of TinO2n−1 and TiO1.95−x coatings under lubricated conditions with uncoated specimen of grey cast iron. The interaction of the pairs with prototype engine oils based on esters and polyglycols were studied under mixed/boundary lubrication using the BAM test method. Lubricants were factory fill engine oils, ester-containing lubricants with low-SAP (sulphur–ash–phosphor) and/or bio-notox properties as well as polyglycole-based lubricants. The ester and polyglycole-based engine oils respond both to bio-no-tox criteria and were polymer-free. They followed different strategies to reduce zinc, phosphorus and sulphur to assure a low ash content. Based on the piston ring/cylinder liner simulation BAM test outside of engines under conditions of mixed/boundary lubrication, it is reasonable that thermally sprayed TiOx-based cylinder liner coatings can substitute commonly used uncoated grey cast iron liner materials. The coefficient of friction was more determined by the lubricants or by an individual interaction between lubricants and a specific material or tribopairing.

L. Ceschini, et al, [16] carried out both bench tests and laboratory dry sliding tests on components for hydraulic motors involved in a boundary lubricated sliding contact, with the aim of investigating the tribological behavior and improve the durability of the components. Bench tests were carried out on a rotating shaft, consisting of a quenched and tempered 36CrNiMo4 steel, coated by a Ni7Al layer deposited by Air Flame Spray, sliding against a carburized E470 steel contacting element. Failure analysis of real components after bench tests identified the main wear mechanism as two body abrasion. Laboratory dry sliding tests allowed the investigation of the influence of normal load and sliding distance on friction and wear behavior. Those tests also used in the subsequent steps of the work for ranking candidate alternative materials for the investigated tribo system. Rohollah Ghasemi and Lennart Elmquist [25] investigated the relationship between the deformation of the matrix and the closing tendency of flake graphite.

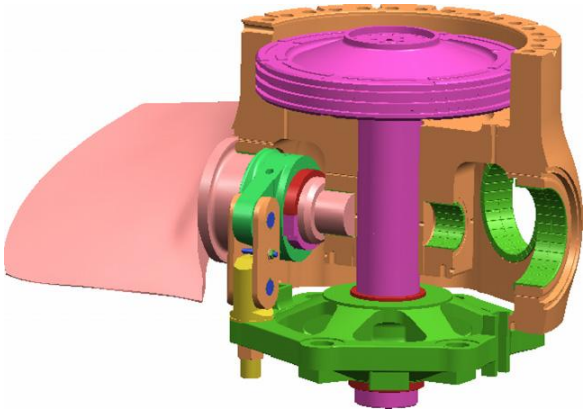


Fig. 3. Blade-control system for one blade.[35]

Two representative piston rings, which belonged to the same two-stroke marine engine but were operated for different periods of time, were studied. Initial micro structural observations indicated a uniform distribution of graphite flakes on unworn surfaces, where as worn surfaces demonstrated a tendency towards a preferred orientation. SEM and EDS analysis indicated substantial deformation of the matrix in the area around the flakes.

An insignificant corrosion attack was observed on both worn piston ring surfaces. As the orientation of the graphite flakes deviated more from the sliding direction, there was a higher chance of them maintaining their intrinsic self-lubricating nature and continuously supplying graphite to the sliding surface. C.W. Huanga and C.H. Hsuehb [5] selected Piston-on-three-ball tests by the International Organization for Standardization to establish ISO 6872 for the evaluation of the biaxial strength of dentistry–ceramic materials. The formula adopted in ISO 6872 for the fracture load-biaxial strength relationship was an approximate equation originally derived for piston-on-ring tests of mono layered discs. This formula was modified and extended to the case of multilayered discs subjected to piston-on-ring loadings recently. The purpose of their study was to evaluate the adequacy of applying the formula for piston-on-ring to piston-on-three-ball tests for both mono layered and multilayered discs. Finite element analyses were performed to simulate both piston-on-three-ball and piston-on-ring tests. Different degrees of friction between the specimen supporting surface and the loading fixture were considered in the simulations. The results depended on friction when the disc was supported by a ring, however the results became insensitive to friction when the disc was supported by three balls. The maximum tensile stress on the surface of the disc decreased when the friction increased. The results of finite element analyses demonstrated how the friction between the specimen supporting surface and the loading fixture affects the

biaxial strength evaluation in piston-on-ring and piston-on-three-ball tests. Results demonstrated that Hsueh et al.'s formulae predict well the biaxial tensile strength for mono layered systems.

Dacheng Li, et al, [7] proposed a capacity-regulation system based on a novel rotary control valve for reciprocating refrigeration compressor and designed for the first time. The regulation system was mainly composed of a rotary control valve and an adaptive regulation system. The parameters for the design and control of the rotary control valve are theoretically determined. To verify the feasibility and effectiveness of the proposed system, a three-cylinder reciprocating compressor was adopted as a test device. Experimental results showed that the technology was able to realize continuous stepless capacity regulation for the compressor within the range of (0)10e100%, and power consumption decreased correspondingly with the load reduction. S. Mezghania, et. al, [27] developed a prediction friction model in the hydrodynamic contact regime between the ring and cylinder liner taking into account the real topography of the cylinder liner. The properties of groove texture were related to the oil consumption. The friction performance in the piston ring/cylinder liner contact was associated with the plateau formation. Piston ring-pack friction reduction strategies through the cylinder liner groove texture optimization were analyzed. In their study, the groove texture (grooves balance, honing angle, etc.) have been demonstrated to greatly affect friction performance. This model aimed to solve the average Reynolds equation, which depends on the real surface topographies of the cylinder liner, and describes the influence of surface irregularities on the lubricant flow under hydrodynamic lubrication conditions, considering lubricant film rupture and cavitations. Muhammet Cerit [19] determined the temperature and the stress distributions in a partial ceramic coated spark ignition (SI) engine piston. Effects of coating thickness and width on temperature and stress distributions were investigated including comparisons with results from an uncoated piston. It was observed that the coating surface temperature increase with increasing the thickness in a decreasing rate. Surface temperature of the piston with 0.4 mm coating thickness was increased up to 82 °C. The normal stress on the coated surface decreases with coating thickness, up to approximately 1 mm for which the value of stress was the minimum. The optimum coating thickness was found to be near 1 mm under the given conditions. Results indicated that temperature distributions developed at the ceramic coated piston surface can be considerably higher than those of the uncoated piston surface. Thermal analysis results indicated that the coated section of the piston, which is close to the crevice and wall quenching regions, cause an increase in the temperature. As a result of increase in temperature, a slight amount of decrease in carbon monoxide emission may be expected since CO oxidation reactions strongly depend on temperature. The von Misses stress decreased with increased coating thickness. The shear stress which causes lateral cracks increased with the coating thickness increase and reached its maximum level at the inner edge of the coated region at the interface of the substrate. Finally, it was found that the optimum coating thickness for the ceramic coating was slightly below 1 mm.

C. Friedrich a, et al, [4] conducted experiments with coating development and model wear test results from PVD coatings on piston rings for combustion engines. Piston rings were examples for the application of thin films on commonly used mechanical components. The PVD CrxN coatings were deposited by RF magnetron sputtering and characterized by their fundamental mechanical properties like thickness, hardness, residual stress and adhesion, which are important for the tribological behavior of the coating substrate compound. The contact mechanics of the tribological system piston-ring–cylinder were determined by high mechanical loading and changing geometry caused by the sliding kinematics. Therefore, the range of thickness was about 7 mm. The selected rings were made of steel DIN 1.4112 (DIN X 90 Cr Mo V 18) with a bore diameter of 97.5 mm. The results of the coating substrate characterization — high hardness, moderate compressive residual stresses and sufficient adhesion on metallic substrates — provide good behaviour of coatings in this tribological application. This was confirmed by the results of the tribological test procedures which have been performed with ring-on-disc model-wear tests and a short-stroke test rig. The wear of piston rings was investigated with respect to PVD hard coatings as a surface finish with an adjustable profile of mechanical properties. Dhananjay Kumar Srivastava et al,[8] closely related the performance of a combustion engine with the friction force and wear between cylinder liner and piston rings. This friction force was significantly reduced by optimizing the surface topography of cylinder liners. The experiments were carried out for evaluating wear and friction in simulated engine conditions using Cameron–Plint wear testers, Pin-on-disk testers, SRV testers, etc. A non-firing engine simulator was developed in order to simulate engine conditions to a closer extent compared to these machines. This simulator operated at similar linear speed, stroke, and load as real engine and simulated almost all engine operating conditions, except firing pressures. Energy dispersive analysis (EDS) was carried out of liner and top ring for evaluating materials transfer. Coefficient of friction between three different liner segments and ring was evaluated using an SRV wear tester. Coefficient of friction in the piston ring–liner interface increases with increasing average surface roughness for liner. Surface profile and SEM tests were conducted on liner and rings at different stroke position, which reveal that highest amount

wear takes place at TDC location. Even at the BDC location, the wear was higher than the mid-stroke position because of failure of hydrodynamic lubrication regime. The major elements of liner material were iron, manganese, chromium and silicon. During the experiment, concentration of silica went up. In the ring, the hard chrome plating weared out with time and the base metals got exposed towards the end of the experiment. YujunLi et al, [34] developed a novel vibration-based fault diagnostic method to identify the vital components of a diesel engine that have abnormal clearance. The advantage of this method was that it does not require the comparison of current operating parameters to those collected as the baseline.The proposed method employs the timing of impacts caused by two contacting components as the prime diagnostic feature. To extract the features that distinguish the components with abnormal clearance from those with normal clearance, the characteristics of the vibrations generated by a diesel engine typically used in manufacturing were analyzed in this research.

F.S. Silva [10] analysed the fatigue-damaged pistons from petrol/diesel engines, as well as automobiles including trains. The study of damages initiation in the piston at the crown, ring grooves, pin holes and skirt was assessed. An assessment was made through the Case studies as well as the analysis of the thermal/mechanical fatigue damages the pistons. The stress distribution during the combustion was determined through the linear static stress analysis, using ''cosmos works''. Stresses at the piston crown, pin holes, grooves and skirt was also determined. For the confirmation of the crack initiation sites, a fractographic study was also done. The fatigue was a problem for the engine pistons, however, it was not responsible for being the largest part of the damaged pistons. The limitation of weight reduction promoted thinner walls, which cause higher stresses. The priority of fuel consumption reduction and more power was in contradiction as another constraint. Z.W. Wang et al, [35] predicted the failure conditions in the piston rods, in Kaplan turbines and the stresses were analyzed. The pressure oscillations over the turbine blades transfered the forces to the piston rods. The analysis of the dynamic stresses were done at thirteen operating conditions using CFD analyses of the flow, along with the analysis of the stresses to the dynamic loads.

The predicted position of the maximum stress concentration was in good agreement with the actual fracture position. The excessive dynamic stresses at the rated output resulted the crack to grow ending to fracture, in the AGC mode, The mean and dynamic stresses were smaller than that of the retainer ring structure due to the pre tightening force in the structure. G. Floweday et al, [11] Studed diesel engine piston failures, during a bench dynamometer engine durability test, which was aimed to evaluate the effects of various fuels on the life of the fuel system components in diesel engine cars. During the test, a number of pistons, cylinder heads and turbocharger failures were experienced. The study aimed at finding the reasons of the piston failures during the tests. Investigation of the fractured pistons revealed that due to excessive thermo-mechanical loading, thermo-mechanical fatigue initiation took place as a result of silicon phase cracking and subsequent micro-crack formation. Micro cracks with progressive formations lead to flaws upto sufficient magnitude for initiating the propagation by high cycle fatigue mechanisms.

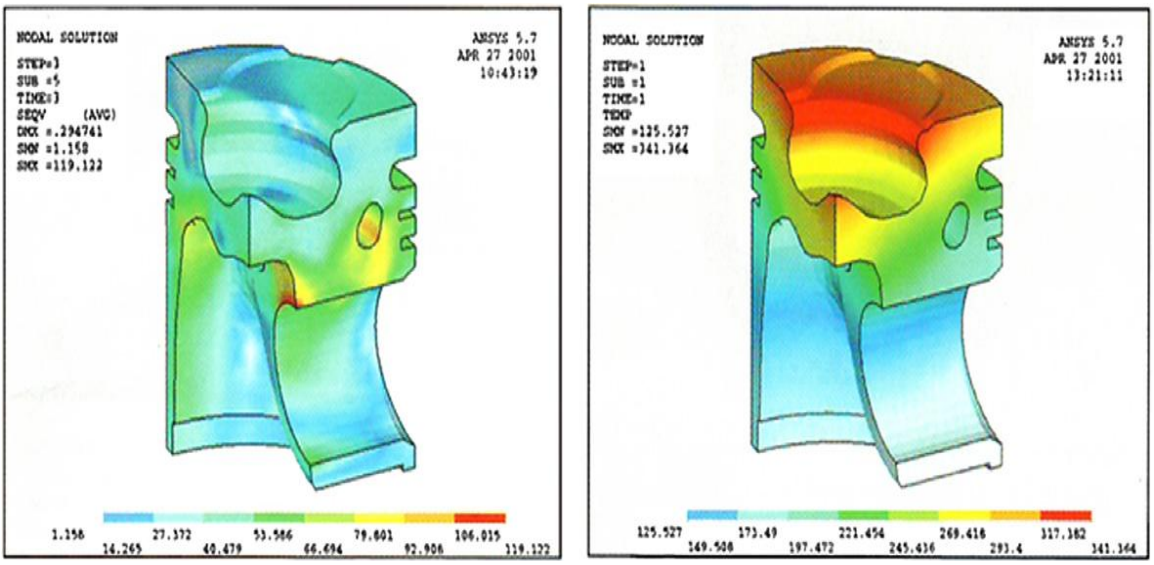


Fig. 4. Contour plot showing the distribution of stress (left) and temperature (right) in a diesel piston due to the combined thermal and pressure loads experienced in an engine. (Reprinted with permission from SAE R-345_2004 SAE International).[11]

Over-fuelling along with the combination of elevated and poorly controlled post intercooler air temperature caused the excessive thermo-mechanical piston loading. No evidence was found supporting the failures to be related with the test fuel formulations. The piston failure may be attributed to, minor over-fuelling and associated thermo-mechanical overload of the pistons, because of the use of neutral injector codes in the engine ECUs, as it deactivates the ECU's function of recalibration of the fuel injector. The damage of the Surface and hairline cracking of the reference fuelled engine piston, the indications of reduced radiation thermal loading as well as spray penetration with the test fuels gave strong indication that fuel formulations were not contributing to the piston failures. Roop Lal et al, [26] made studies on cylinder liner and piston rings interface. Published data on friction and wear was collected from various researchers and concluded. The oil film thichness played important roll and finally affected the performance of engine. Surface roughness of tribo pair material at the junction producing friction and it varied throughout the stroke length of piston. Loss of power in lubrication had the shear force due to boundary conditions. The tribological performance in IC engine could understood when friction and wear were considered. The necessaity to study the factors influencing reliability and performance along with wear was expressed . From the view point of tribo element it was very important to know the specific load, speeds and temperatures for the major components of engine like piston assembly, valve train, the journal bearing and lower viscocity engine oil for lubrication.

O.P. Singh et al, [22] investigated experimentally the seizure failure of piston with numerical simulation of thermal elasto-hydrodynamic lubrication (EHL).

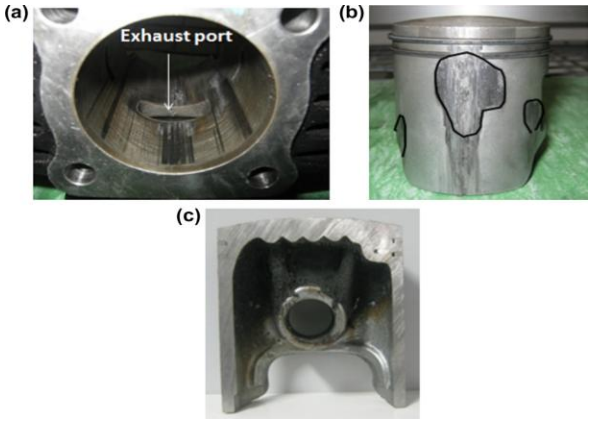


Fig. 5. (a) Seized cylinder liner, (b) seized piston and (c) cut section of the piston showing burnt oil under the crown and skirt. [22]

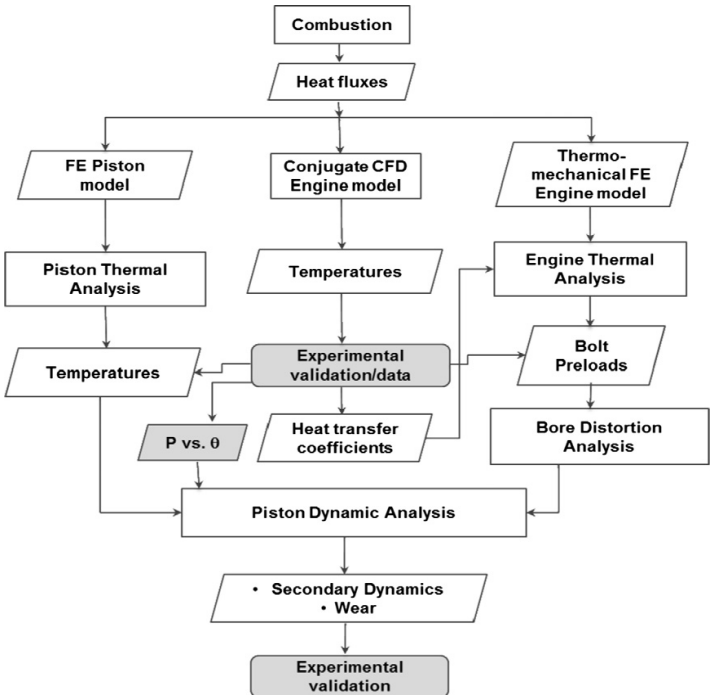


Fig. 6. Flow chart showing steps used in the numerical model of piston hydrodynamic simulation.[22]

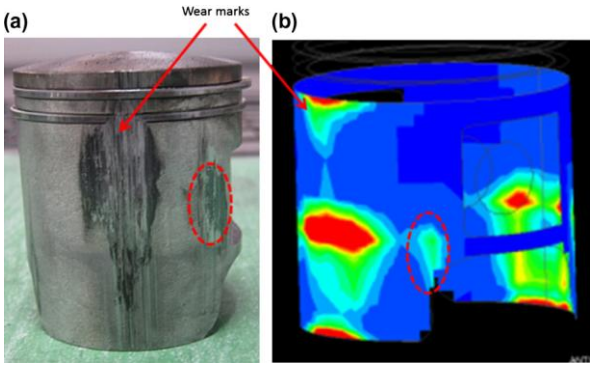


Fig. 7. Correlation of seized marks obtained from the test results and the cumulative wear plot from numerical simulation.[22]

A metallurgical investigation of the piston, rings and liner was done in terms of chemical composition, chemical analysis and hardness. The results indicated large decrease in clearances between the piston and liner at 28°C after TDC. The variation in frictional power over the cycle exhibited sudden increase in magnitude at that location after TDC. The predicted wear mark locations compared well with the test results. The overheating happened to be the root cause of the current piston seizure. Pistons coated with molybdenum material, although enhanced the piston life, but with the problem of skinning off the coating under severe conditions of temperatures and pressures. B. Zhang et al, [3] performed the design as well as experimental validation of a double acting free piston expander in which a slider-based control scheme was used for realizing a full expansion process for the expander. A model was developed for determining the geometric parameters of the expander along with the auxiliary compressor. The results showed that the expander worked stably in a wide range of pressure differences/ratios. R. Mikalsen and A.P. Roskilly [24] reviewed the history of free-piston I C engines, from the air compressors and gas generators used in the mid-20th century Salient features of the free-piston engine has been presented and the effects on engine operation has been discussed, along with comparative advantages and disadvantages with the conventional engines has been discussed.

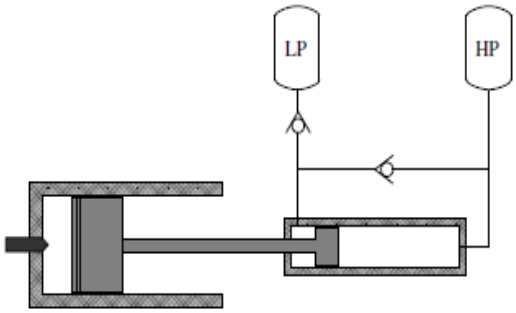


Fig. 8. Single piston hydraulic free-piston engine [24]

Muhammet Cerit and Mehmet Coban [20] improved the performance of a diesel engine, by finding out both temperature and thermal stress distributions on an aluminum piston crown with zirconia coating in a plasma sprayed magnesia-stabilized environment. Effects of the coating thickness varying between 0.2 to 1.6 mm has been investigated, and the results has been compared with that of an uncoated piston, using finite element method. Higher combustion chamber temperature was developed by means of TBC, resulting increase in thermal efficiency of the engine. The engine performance improved with reduction in the piston (substrate) surface temperature. The thermal performance of the piston also increased with increase in coating thickness. From the analysis it was found that the calculated stress values was lower than the allowable stress values of the materials.

III. SUMMARY

Experiments revealed that friction coefficient increases with increasing surface roughness of liner surface. The linear wear of the cast iron liner and rings decreased with increasing load but the mass wear increased with increasing load.

The thermal stress is related to coating thickness. It increases with the coating thickness on the SUBS. The greatest value of the normal stress which produces spalling of the ceramic is produced on the bond coat. It is nearly twice the value of the maximum normal stress on the substrate. The thermal performance of the piston

increases with increased coating thickness. Stress values obtained from FEA were compared with the mechanical properties of the aluminum alloy and zirconia material and it was concluded that calculated stress values were lower than the allowable stress values of the materials.

The ratio of average slopes in axial and circumferential directions can monitor piston skirt wear. The free material liberated due to deep scoring between the piston and liner snowballs, changes its phase from solid to molten state and finally makes its way into the rings. It locks the rings and thus leading the complete engine seizure failure.

Surface thermal damage and hairline cracking of the reference fuelled engine piston, as well as the indications of marginally reduced radiation thermal loading and spray penetration associated with the test fuels gave strong indication that the fuel formulations did not contribute to the piston failures. The fractographic and microstructural analyses reveal regarding selection of correct material for piston fabrication.

The piston failures were determined to have occurred due to Surface thermal damage of the piston bowl lip, Crack initiation by thermal micro-cracking and erosion of primary silicon particles, leading to threshold flaw size, Propagation by thermo-mechanical high and low cycle fatigue and Brittle fast fracture at the critical crack length. Subsequent fuel and flame impingement resulting in piston burn through and loss of engine compression.

The main causes contributing to the piston wear and failures was the use of neutral injector codes in the engine ECUs which deactivated the ECU's function of automatic recalibration of the fuel injector flow rates, resulting in minor over-fuelling and associated thermo-mechanical overload of the failed pistons. Further poorly controlled post intercooler air temperatures and an elevated set point, resulting in overheating of the piston and other combustion chamber components.

REFERENCES

[1] A. Skopp a,1, N. Kelling a,1, M. Woydta,1, L.-M. Berger b,, Thermally sprayed titanium sub oxide coatings for piston ring/cylinder liners under mixed lubrication and dry-running conditions, Wear 262 (2007) 1061–1070

[2] A. V. Sreenath And N. Raman, Running-In Wear Of A Compression Ignition Engine: Factors Influencing The Conformance Between Cylinder Liner And Piston Rings, Wear, 38 (1976) 271 – 289

[3] B. Zhang, X. Peng , Z. He, Z. Xing, P. Shu, Development of a double acting free piston expander for power recovery in trans critical CO2 cycle, Applied Thermal Engineering 27 (2007) 1629–1636

[4] C. Friedrich a,, G. Berg a, E. Broszeit a, F. Rick b, J. Holland b, PVD CrxN coatings for tribological application on piston rings, Surface and Coatings Technology 97 (1997) 661–668

[5] C.W. Huanga,, C.H. Hsuehb,c, Piston-on-three-ball versus piston-on-ring in evaluating the biaxial strength of dental ceramics, Dental materials 2 7 (2 0 1 1) e117–e123

[6] D. J. Picken; H. A. Hassaan, A Method for Estimating Overhaul Life of Internal Combustion Engines including Engines Operating, J. agric. Engng Res,28. (1983), 139-147

[7] Dacheng Li a,, Haiqi Wub, Jinji Gao b, Experimental study on stepless capacity regulation for reciprocating compressor based on novel rotary control valve, International journal of refrigeration 36 (2013) 1701 e1715

[8] Dhananjay Kumar Srivastava a, Avinash Kumar Agarwal a,, Jitendra Kumar b, Effect of liner surface properties on wear and friction in a non-firing engine simulator, Materials and Design 28 (2007) 1632–1640

[9] E.P. Becker a,, K.C Ludema b, A qualitative empirical model of cylinder bore wear, Wear, 225-229 (1999) 387-404

[10] F.S. Silva , Fatigue on engine pistons – A compendium of case studies, Engineering Failure Analysis 13 (2006) 480–492

[11] G. Floweday a, S. Petrov b, R.B. Tait b,, J. Press c, Thermo-mechanical fatigue damage and failure of modern high performance diesel pistons, Engineering Failure Analysis 18 (2011) 1664–1674

[12] H. Sunden and R. Schaub †, Piston rings for slow and speed diesel engines, Tribology International February 1979

[13] J. E. Willn, Characterisation Of Cylinder Bore Surface Finish A Review Of Profile Analysis, Wear - Elsevier Sequoia S.A., Lausanne - Printed in the Netherlands

[14] J. Galligan a, A.A. Torrance a,), G. Liraut b , A scuffing test for piston ring bore combinations: Pt. II. Formulated motor lubrication, Wear 236 (1999) 210–220

[15] Jarosław Milewski, Łukasz Szabłowski, Jerzy Kuta, Control strategy for an Internal Combustion engine fuelled by Natural Gas operating in Distributed Generation, Energy Procedia 14 (2011) 1478 – 1483

[16] L. Ceschini, A.Marconi, C.Martini n, A.Morri, Tribological behavior of components for radial piston hydraulic motors: Bench tests, failure analysis and laboratory dry sliding tests, Wear 305 (2013) 238 –247

[17] K. J. Stout And T. A. Spedding, The Characterization Of Internal Combustion Engine Bores, Wear, 83 (1982) 311 – 326

[18] M. Priest, C.M. Taylor, Automobile engine tribology — approaching the surface, Wear 241 (2000) 193–203

[19] Muhammet Cerit , Thermo mechanical analysis of a partially ceramic coated piston used in an SI engine, Surface & Coatings Technology 205 (2011) 3499–3505

[20] Muhammet Cerit and Mehmet Coban,Temperature and Thermal Stress analysis of a ceramic-coated aluminium alloy piston used in a diesel engine, International Journal of Thermal Sciences 77, (2014) 11-18

[21] Mustafa Canakci , Combustion characteristics of a turbocharged DI compression ignition engine fueled with petroleum diesel fuels and biodiesel, Bio resource Technology 98 (2007) 1167–1175

[22] O.P. Singh a,, Yogesh Umbarkar b, T. Sreenivasulu a, E. Vetrivendan a, M. Kannan a, Y.R. Babu a, Piston seizure investigation: Experiments, modeling and future challenges, Engineering Failure Analysis 28 (2013) 302–310

[23] P. C. Nautiyal, S. Singhal and J. P. Sharmat, Friction and wear processes in piston rings,Tribology International,1983
[24] R. Mikalsen, A.P. Roskilly , A review of free-piston engine history and applications, Applied Thermal Engineering 27 (2007) 2339–2352
[25] Rohollah Ghasemi, Lennart Elmquist. The relationship between flake graphite orientation, smearing effect, and closing tendency under abrasive wear conditions, Wear 317 (2014)153–162.
[26] Roop Lal, R C Singh, Ranganath M S and S Maji, Friction and Wear of Tribo-Elements in Power Producing Units for IC Engines- A Review, International Journal of Engineering Trends and Technology (IJETT) – Volume 14 Issue 5, 2014
[27] S. Mezghani a, n, I.Demirci a, M.Yousfi a,b, M.ElMansori a, Running-in wear modeling of honed surface for combustion engine cylinder liners, Wear 302 (2013) 1360–1369
[28] S. Mezghania, I. Demircia,, H. Zahouanib, M. El Mansoria, The effect of groove texture patterns on piston-ring pack friction, Precision Engineering 36 (2012) 210– 217
[29] S.G. Chung, J.M. Lee, W.Y. Jang, Comparing the Quality of Samples obtained by Three Types of Fixed Piston Samplers for Soft Sensitive Clay, Accepted manuscript, Engineering Geology, Accepted date: 21 June 2014
[30] T. H. C. Childs and F. Sabbagh, Boundary-Lubricated Wear Of Cast Irons To Simulate Automotive Piston Ring Wear Rates, Wear, 134 (1989) 81 – 97
[31] U.I. Sjodin, U.L.-O. Olofsson, Experimental study of wear interaction between piston ring and piston groove in a radial piston hydraulic motor, Wear 257 (2004) 1281–1287
[32] Wieslaw Grabon a, WaldemarKoszela a, PawelPawlus a,n, Slawomir Ochwat b a, Improving tribological behaviour of piston ring–cylinder liner frictional pair by liner surface texturing, Tribology International 61 (2013) 102–108
[33] William G. Agnew, Fifty Years Of Combustion Research At General Motors, Proc.Energy Combust. Scie. VoI 4, pp 115-155, 1978
[34] YujunLi a, PeterW.Tse a,, XinYang b, JianguoYang b, EMD-based fault diagnosis for abnormal clearance between contacting components in a diesel engine, Mechanical Systems and Signal Processing 24 (2010) 193–210
[35] Z.W. Wang a,, Y.Y. Luo a, L.J. Zhou b, R.F. Xiao a, G.J. Peng a, Computation of dynamic stresses in piston rods caused by unsteady hydraulic loads, Engineering Failure Analysis 15 (2008) 28–37
[36] Zenon Krzyzak, Pawel Pawlus, 'Zero-wear' of piston skirt surface topography, Wear,260 (2006) 554-561

Feasibility Study of a Solar Crematorium in India

Akhilesh Chandra Kashyap[1] ,Janardan Prasad Kesari[2]

[1]Research Scholar, *Department of Mechanical Engineering, Delhi Technological University, Delhi*
[2] Associate Professor, *Department of Mechanical Engineering, Delhi Technological University, Delhi*

***Abstract*- While cremation is an established Hindu ritual practice since ancient times and the Hindu religion permits the cremation of dead body in day-time only, there is much more scope of solar crematorium in this ritual; as solar power is also available in day-time only.Between 500 and 600 kg of wood are used to cremate a dead body. Many trees are felled to meet this requirement. As a result we are significantly contributing in global warming and polluting the atmospheric air much more. Therefore today, world is moving towards the sustainable energy sources which are renewable and biodegradable in nature. One of most sustainable energy source is sunlight that too is inexhaustible and available free of cost. The heat (energy) produced is very clean with no pollutants. So above environmental problems can be the addressed very well by using solar crematorium. Therefore anyone can be a firm believer of world powered by solar energy. In this paper, concept of solar crematorium and its feasibility in the India has been proposed.**

Keywords- Crematorium, Scheffler reflector, Concentration Ratio, Solar, Tracking, Religion, AntimSamakara, Cost etc.

I. INTRODUCTION

India is facing the twin problems of fast depletion of conventional fuels and environmental degradation. There is an urgent need to reduce dependence on petroleum and other conventional fuels for better economy and environment. Utilization of solar energy can address both these issues. The sun is the source of all the energies on earth. When one thinks of the word "solar", photovoltaic modules and panels automatically come to mind, which converts the sunlight into electricity but that is not the case here. Since the sunlight has very little part, only 20% of its energy as lighting effect and large portion, 80% as thermal effect. So energy of solar radiation can be utilized more in solar thermal power generation than in solar photo-voltaic (which utilizes only lighting effect of sunlight) for power generation. A crematorium too requires very large amount of heat energy which can be harnessed directly by solar concentrator. On the other hand, we can never suggest using of solar photo-voltaic panels to obtain such a large amount of heat indirectly for cremating a corpse. As firstly, PV panels convert only 20% (lighting effect) of solar energy into electricity, and then this electricity is converted into heat by passing through very high amount of resistance. This conversion of electricity into the heat is too associated with several losses. So employing solar PV panels will not be feasible for cremating a corpse. Although these PV panels can be used to get electricity for running the accessories like tubes, fans in office/cabins and necessary motors installed in tracking system.

II. LITERATURE REVIEW

Not much extensive and dedicated work is seen after studying a lot of different popular journals available. Few works has been reported and added in this paper for solar furnaces and cost estimation of solar equipments. The largest solar furnace is located in Font-Romeu at Odeillo in the Pyrenees Mountains in the Basque region of the French/Spanish border. It has been operational since 1970. This is the same area in which the world's first solar furnace was built; this solar furnace was put in place at Mont-Louis in 1949 by Professor Felix Trombe. Odeillo and Mont-Louis are within 15km of each other. The furnace makes use of an array of 10000 mirrors to reflect sunlight into a gigantic concave hemisphere which then focuses the energy onto an area roughly the size of a cooking pot. The flat mirrors track the sun in unison and redirect the solar thermal energy towards the crucible which is being used for melting steel. World's first solar crematorium is being developed in our country at Goraj village (30 km East of Baroda) in Gujarat state by Muni Seva Ashram with the help of Ronnie Sabawalla of Rashron Energy and Auto limited. In 1998 they started with a specially designed Scheffler reflector with 50m² mirror surfaces. But its initial concentration-factor of about C = 100 turned out to be by no means enough to allow proper cremation.

III. CREMATION PROCESS

A crematorium is a furnace that is able to generate temperatures of 760–1150°C to ensure disintegration of the corpse. Cremation is the process of burning a dead body at very high temperatures until there are only brittle, calcified bones left, which are then pulverized into "ashes." These ashes can be kept in an urn, buried, scattered or even incorporated into objects as part of the last rites of death. The heat raises the temperature of the cremator. During the cremation process, the greater portion of the body (especially the organs and other soft tissues) which is composed of 75 percent water is vaporized and oxidized by the intense heat; gases released are discharged through the exhaust system. As the soft tissues begin to tighten burn and vaporize from the heat, the skin becomes waxy, discolors, blisters and splits. The muscle begins to char, flexing and extending limbs as it tightens. The bones, which are the last to go, become calcified as they are exposed to the heat and begin to flake or crumble. The time required for cremation varies from body to body, and, in modern furnaces, the process may be as fast as one hour per 45 kg of body weight. An average human body takes from two to three hours to burn completely and will produce an average of 1.4 to 4.1 kg of ash.

IV. CONCEPT OF A SOLAR CREMATORIUM

The basic concept of solar crematorium is to ignite the dead body locally anywhere and anyhow with the help of a huge concentrating reflector having very high CR and to maintain the combustion of dead body by supplying the fresh atmospheric air with the help of blower. Once combustion of dead body starts within the cremation chamber, it also releases heat which automatically in combination with solar energy obtained from concentrating reflector maintains continuous burning of

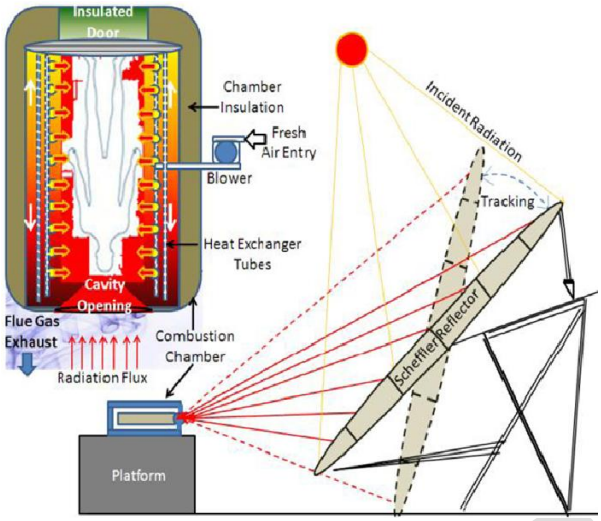


Fig. 1 : Block Diagram of Solar Crematorium

dead body until complete dead body gets converted into ash.Based on above mentioned concept, system of solar crematorium can be divided into following four components :Scheffler Reflector, Tracking System, Cremation Chamber, Backup system for non sunny hours.

V. SCHEFFLER REFLECTOR

Parabolic Scheffler Reflectors can provide (you with) high temperature heat for all types of cooking, steam generation and many other applications. Their speciality is a flexible surface curvature and a nonmoving focal area. Therefore their use is now becoming increasingly popular in many parts of the world, especially in India.

5.1 Designing a Scheffler Reflector

The **size** (Aperture Area) of Scheffler reflector is determined by reverse design procedure. Which is described step by step as following :

- First of all "**E**" (total energy) required to burn completely a single dead body is calculated. Since a traditional Hindu funeral pyre takes 2-3 hours and consumes 500–600kg of open wood pile to burn completely a corpse. But Mokshda, a Delhi-based non-governmental organization has created an alternative cremation system that reduces heat loss. With it, it takes up to two hours and 150–200 kilograms of wood to burn a corpse. According to Vinod Kumar Agarwal, the founder of Mokshda, with proper and complete combustion, 22 kg of wood is sufficient to burn down a body. Considering above facts, 100kg of wood is used for cremating a single corpse in 1 to 2Hrs if heat loss is optimized to minimum value by effective insulation of combustion chamber. Since calorific value of wood is 19700kJ/kg. Therefore

$$\boldsymbol{E = 100kg \times 19700kJ/kg = 1970000kJ = 1970MJ}$$

- Now "**P**" power (in MJ/hr) required to burn completely the body in combustion chamber is determined. If we design a reflector to cremate a dead body in 2hrs then this (total energy) "**E**" required to burn completely the dead body must be obtained/captured by the reflector within 2hrs. Therefore

$$\boldsymbol{P = \frac{1970MJ}{2Hrs} = 985MJ/Hrs}$$

- Finally "**A**", **size** (Aperture Area) of Scheffler reflector is determined. Since DNI (Direct Normal Irradiance) is 5MJ/m^{2}hr (≈ 4.9212 MJ/m^{2}hr = 1367W/m^2 X 3600sec). So Aperture Area "**A**" is obtained by dividing "**P**" (power) with DNI. i.e.

$$\boldsymbol{A = \frac{P}{DNI} = \frac{985MJ/Hr}{5MJ/m^2\,Hr} = 197m^2}$$

5.2 Material of Scheffler Reflector

The Scheffler reflectors are made up of several small double sided (two plane mirrors are joined on their each other silver coating sides) plane mirrors. Theoretically single sided mirror is sufficient for the Scheffler reflector, but double sided mirror is used to protect the silver material which is coated on the almost completely transparent glass. Because of intense heat and temperature of solar energy there is possibility of silver coatings to melt away from the rear surface of the glass. Therefore the rear side mirror protects the silver coating to melt away by reflecting back the sunlight if any from rear side, and simultaneously by avoiding the erosion and corrosion. This rear side mirror also provides the additional strength to the front mirror.

The efficiency/reflectivity of several plane mirrors in the Scheffler reflector ranges 90-95% when new. Though it is not important much more, because efficiency is greatly considered where we pay money for energy/fuels which (solar energy) is free here. Here efficiency/reflectivity of mirror is only considered to determine size (aperture area) of the Scheffler reflector.

5.3 Tracking System

Since combustion chamber of crematorium is stationary and not movable but solar concentrators require tracking the Sun, as a result a movable focus is obtained. This is major problem in designing a solar concentrator for the crematorium. This problem was shorted out by Wolfgang Scheffler who invented a new concentrator (scheffler reflector) tracking the Sun without changing it focus. In this paper, scheffler reflector is redesigned to determine required size (Aperture Area) of the concentrator to obtain sufficient heat energy for cremating a corpse. Since the speciality of Scheffler reflector is flexible surface

curvature and a nonmoving focal area. Their use is now becoming increasingly popular in many parts of the world, especially in India. Almost all concentrators have a rigid structure and the focus, the hot area where all light is concentrated, moves along with the direction of the sun. This makes its use a little bit impractical.

VI. BACKUP SYSTEM FOR NON-SUNNY HOURS

The actual harnessing of the solar energy can happen unless you're in a very hot sunny climate days but the need for energy is often greater in rainy, cloudy or, colder climates. So it can be unreliable. On the other hand we are intended to investigate the possibility of employing solar energy for Hindu ritual of cremation. This arise a concern regarding sentiments connected to the cremation process. As per Hindu ritual practice, there is an established sentimental fact of cremating the corpse completely at one goes. And there must not be left any un-burnt portion of the body. Otherwise the soul of that person will remain unsatisfied, and it will be converted into the devil or imp which will victimize or terrorize the concerned relatives for his/her satisfaction. Therefore there must be an arrangement of suitable and sufficient backup system to mitigate these situations. So the cremation chamber must be designed in such a way that other alternate fuels like Biogas/Biomass/LPG/CNG can be fired if required.

VII. DEVELOPMENT OF SOLAR CREMATORIUM

As the main challenge is to have a very small focal area, the whole frame has to be adjustable for exact positioning



Fig 2 : Concrete Reinforced Foundation Platform 6.3 X 9 m^2 under constructionWhere chamber will be placed

during the different seasons of the year. Electrical DC motors with gear boxes have to be installed and tested for an improved seasonal adjustment (+/-23.5 Degree). All the parts have to become very precise in order to have minimum mistakes in the focal area.

A place near a river is chosen as place for the new crematorium. The correct geographic North-South alignment is marked and so we are able to prepare the layout for the foundations on this piece of land belonging to village. The focus should be around 240mm diameter but in morning and evening positions the frame is twisted which results in a bigger focus. The stand, the rotating support and the wings of the frame and small parts got sandblasted and primer was sprayed twice as anti-corrosion measure. Finally painting is applied at the new place of erection (income generation in rural areas). The frame parts are mounted to the rotating support on the ground.As soon as the concrete is hardened, the stand and the back-crane of the stand (for lifting the stand up and down) got installed with the help of a mobile crane. The exact alignment of the stand (bearings parallel to polar axis) was adjusted. During the different phases of the project practical education is integrated in order to make the operator able to use the system properly. After the mirrors are all mounted on the crossbars of the frame (see Fig. : 3) we needed again a crane to lift the finished frame



Fig. 3 : Top View of the Cross-bar Stand

with the rotating support into the bearings of the stand. Before lifting up the stand with its back crane, all electrical installations have to be tested. The seasonal adjustments are now regulated so that the frame has the correct paraboloid for the day. On the right height and in the correct instance we prepare a provisorily stage for measuring the focal area because the platform for the chamber is not ready then. As mentioned in the Summary, the focal area has a diameter of 240 mm. In order to correct the twisting in the morning and the evening position, 8 instead of 4 wire ropes are connected to the 4



Fig. 4 : Chamber (front) arrives in; Focal-opening 240 mm diameter, Connection for air-blower at the side

edges of the frame with an elastic telescope column in the middle of the frame.

As soon as the platform is ready, the chamber can be tested. If the temperature inside the chamber is reaching at 800 degree Celsius, then small animals like e.g. dead dogs can be cremated in order to see, if the system can start to benefit human families soon.



Fig. 5 : Dead body being inserted in Crematorium

VIII. FEASIBILITY STUDY IN INDIA

Contrary to popular perception, electric crematoriums also lead to more pollution than the traditional Hindu style of cremation, involving burning the body on a pyre. The UNDP report informs that electric cremation is nearly seven times more intensive in terms of emission of green house gases as compared to the traditional Hindu style. Solar crematorium also appears to be a viable option, suggests V Ramesh of Karnataka Renewable Energy Development Limited. India is the front runner in this regard, with Baroda, a city in Gujarat equipped with the world's first solar crematorium. It was developed by Wolfgang Scheffler, a Swiss national and Ronnie Sabbawala of Rashron Energy and Auto limited. The body is burned exclusively using solar energy. The second solar crematorium is to be erected in Patna, Bihar, by 2015.

But this method also has certain disadvantages. Solar crematoriums are impossible in many parts of India during the winters and monsoons. Also, they can be used only during the day as long as the sun shines. Built with an investment of ₹3 Crores, the solar crematorium does not need electricity or gas. It makes it an energy and cost efficient.

Applications in Remote villages where wood is scarce and no electricity; Solar Crematoriums have high potential to be used in Gram-Panchayats& municipal corporations.

In north India, solar crematorium can be constructed at Yamuna Ghat near Nigam-Bodh Ghat in Delhi, at Bass-Ghat near Ganga in Patna and in Banaras as well as Haridwar and other places.

8.1Factors Influencing Crematorium

Key factors affecting demand for burial and cremation facilities are:

Population: Running cost of crematorium will be relatively where there is large population. Here in India, there is no problem of population as India is the second most populous country in the world. And population too is increasing at very high rate.

Age Structure: The general mortality rate conceals great variation according to age. Hence there is very high importance of examining the age structure of the given area (locality). Whilst the population is projected to grow, particularly in the pensionable age groups which have the highest death rates, the reducing death rates will result in a relatively small rise in the number of deaths. Mortality rates are highest amongst the elderly, who will represent and growing proportion of the population of India.

Mortality Rates: Mortality rates have fallen considerably over the last hundred years and will continue to fall because of improved medical facilities, resulting in falling numbers of deaths.

Religion and Ethnicity: Religious belief can play a significant role in people's choice between burial of cremation. Demand for burial and cremation facilities is thus influenced by the religious beliefs of the residents of an area. Ethnic origin, like religious belief, can influence people's choice of burial or cremation. For example, Cremation is permitted in Buddhism , Roman Catholic , Jews-Liberal, Roman Catholic, Church of Scotland, Church of England, Church in Wales, Church of Ireland, Presbyterians, Methodists where as it is necessary in Hindu and Sikh.

Availability of Cremation Facilities: People mind set are changing from burial to cremation. The same may be improved depending upon the available facility of cremation.

Location: A new crematorium has an opportunity to compete with existing crematoria on the basis not only of location, but also the quality of the facilities and the service it provides. Since as per religious ritual some burnt part of the dead body is allowed to flow in the water, therefore ideally, the new site should be located near the river, canal, pond, lake or sea. The main customers making the decision to use a particular crematorium are bereaved (whose relative is dead) people and the funeral directors. The influence of religious ministers is insignificant in my view, as the funeral location is usually chosen prior to their appointment to lead the service.

8.2 *Case Study of a Solar Crematorium in Gujarat*

A spiritual hermitage in Gujarat state, in the northwest of India, has become the home of the world's first solar-powered crematorium. The historic village of Gorajnear the town of Waghodia, in Vadodara district of Gujarat state is located in our country where an existing, but non-operational, the first solar crematorium is installed near Ashram at the "panchayat land" under the authority of ecologically conscious *Muni Seva Ashram*.

Introduction to the Problems : This installed crematorium is non-operational. There may be faulty design of solar crematorium because of which required sufficient temperature is probably not achieved to completely burn corpses or, aperture of collector may be small to collect

sufficient amount of solar heat energy for complete burning of dead body. Maybe people just don't come there because of any proper connectivity of road transport from nearby big cities like Vadodra and Ahemdabad or, maybe cremating cost per dead body is too high. Probably that place is geographically not suitable according to solar map or, there is no proper solar energy policy.

*Geographical Suitability of the Place***:** Today world is moving towards the sustainable energy sources which are renewable in nature and biodegradable because in this modern era, a lot of problems of pollution and global warming have been encountered in almost all developed countries. Gujarat is most developed state of our country so there is also problem of pollution and global warming. Since Gujarat state is situated in such a solar belt where average annual solar irradiance is 5.5 to 6.0 kwh/m^2/day. This quantity of solar irradiance is more than sufficient for solar powered equipments. The solar crematorium installed at *Muni Seva Ashram* is on the bank of Dev River which is basically a tributary of Dhadhar River. So this crematorium is suitable for performing religious ritual of *Antim-Sanskara*.

Government Policy: Since Gujarat is most developed state of our country so there is also problem of pollution and global warming. This problem of pollution and global warming has been noticed by the state government of Gujarat. Since Gujarat state is situated in such a solar belt where average annual solar irradiance is much more than sufficient for solar powered equipments therefore the GEDA have promoted installation of lot of solar powered projects in the state. Currently Gujarat is the state of most solar powered installations in the India.

***Design and Development* :**At the ecologically conscious Muni Seva Ashram, a 50m^2Scheffler dish will heat the oven which burns the dead bodies. The project was developed in cooperation with Wolfgang Scheffler (who designed the Scheffler mirrors from Germany) and Ronnie Sabawala (one of the owners of Vadodara-based Himalaya Engineering).

Opening Diameter of cremation chamber = d = 24cm

Receiver Area = $\boldsymbol{A_r = \frac{\pi}{4} d^2}$ = $\boldsymbol{\frac{\pi}{4}(24|100)^2}$ m^2 = 0.045238934 m^2

CR = $\boldsymbol{\frac{A_a}{A_r} = \frac{50}{A_r} = 1105.24266}$

As per the above calculations of **CR**, the target temperature is above 1000°C which can burn the human body very easily within approximately 40 to 60 min during a bright sunny day. The crematorium has been built as a chamber with special scheffler reflector developed specifically for this concept. The special reflectors are designed to heat a 2m long crematorium chamber to above 800°C. The facility was made operational on an experimental basis only.

As per our observation, size of scheffler collector is 50m^2 which doesn't suit as per our design of scheffler reflector described in preceding subsection. Since size (aperture area) of solar collector must be equal to 197m^2 otherwise, collector won't be able to collect sufficient amount of solar heat energy for complete burning of dead body within 2-3Hrs.

The Chamber is designed in such a way that the solar radiation gets reflected from its inner wall and concentrates on the plate where human body is kept. Thus, making full use of the solar energy and increasing the overall efficiency. Efficiency of cremation chamber insulation is about 80%.

Test with small pieces of meat was proved to be encouraging. However, Ashram will not be able to put the solar cremation chamber to use until a



Fig. 6 : Solar Crematorium which is visited at Goraj village near Waghodia town in Vadodara District of Gujarat State

biogas/biomass/CNG/PNG backup burner is installed. People across the region made clear that they will welcome the chamber if a backup burner takes over operation during cloudy hours. Otherwise, a body may only be half burnt which will hurt the sentiments of concerned relatives.

As per the conversation with Mr. Deepak Gadhia, Ashram is now searching for an eco-friendly solution with biogas, which is produced in a farm within 30 km of place of solar crematorium. As soon as the funds for the biogas backup are available, the bottled heat source can be delivered and the solar crematorium can finally start to operate.

IX. ECONOMIC ANALYSIS

Although solar radiant energy is free, the equipment required to convert it into useful form (thermal or electrical) is not free. Therefore a cost must be assigned to solar thermal/electrical energy that reflects the conversion equipment cost pro-rated by no. of kwh delivered by solar equipment. If solar cost is less than that of other energy sources that can perform the same task, there is an economic incentive to solar energy. The purpose of economic analysis is to maximize savings resulting from use of solar energy.

It is rarely cost effective to provide all energy requirements of thermal or mechanical system by means of solar energy. If this done, solar system would be capable to provide 100% of energy demand for the worst set of operating conditions ever expected: inclement weather, maximum demand and no sunshine. A solar system capable of providing peak demand for lengthy period would be oversized for all sever conditions; it would thus be greatly oversized. An oversized system delivers more energy than the requirement. A solar system

with such a low load factor is uneconomical and impractical. Therefore best use of solar equipment is in conjunction with conventional fuels which are used auxiliary source for special high demand situations.

Non solar systems usually have relatively small initial costs and high operating costs reflecting lower lifetime. Solar systems however are relatively expensive initially but have negligible running cost during lifetime. Therefore if selection of equipment is made on basis of initial cost only, solar system would rarely be selected.

9.1 Factors Affecting Cost of New Crematorium

Factors Affecting cost of new Crematorium	
Factors	**Influence**
Location	Cost of land Cost of access and internal roads Cost of installing new utilities
Design	Size Type of construction and materials Number of cremators and abatement equipment

Ideally, the new site should be 7 to 8 acres (2.83 to 3.24 hectare) and located near river, canal, pond, lake or sea as per religious ritual some burnt part of the dead body is allowed to flow in the water. The crematorium should have good connectivity to main roads. Land values vary tremendously, particularly where landowners hope to sell their land at some point in the future for housing development.

Installation of mains gas, electricity and water supplies can form a significant part of the budget, depending upon proximity to suitable supplies. For example, where suitable mains are available adjacent to the site, gas installation will costs in the region of ₹60000 and electricity ₹68000. However, costs can rise exponentially with distance: for example, an onsite electrical transformer can cost ₹216000. In broad terms, the construction costs of a crematorium would be grouped under the following headings with appropriate guide costs:

Installation Cost	
Items	Estimate in ₹
Professional fees	800000
Site survey, ground works, roads and car parking	3200000
Building structure	6000000
Building furniture and fittings	800000
Cremation equipment (single cremator)	4400000
Net total estimate	**15200000**

This estimate excludes the cost of land and any exceptional utility installation costs. Sufficient land would likely cost at least ₹600000. Thus a reasonable round figure for the cost of building a new crematorium in India would be ₹2 crores.

Thus based on above discussions, cost of crematorium can be divided into following sub-parts

:Operating Cost, Cost of cremation equipments, Premises cost.

9.2 Operating Costs

The key operational costs associated with operating a crematorium are:

- Personnel
- Operation and Maintenance of cremation equipment
- Maintenance of buildings and grounds

The number of staff varies between crematoria, with generally less employed at privately owned sites. Clearly, the unit cost per cremation of the staff and any other cost item is reduced by greater cremation numbers.

In order to provide a high quality service, there must be sufficient trained staff. The conditions of employment and job descriptions for crematorium staff at a new crematorium would be different from existing practices that have established over many years. Flexibility amongst employees is the key to success. The chart below shows the personnel that we may recommend for a new crematorium in big Indian cities like Delhi or, Patna :

Operating Cost of Employee			
Position	**Annual Salary in ₹**	**Number**	**Total Costs in ₹**
Manager	360000	1	360000
Administration	300000	1	300000
Operator	240000	2	480000
Total			**1140000**

These costs equate to ₹1140 per cremation based on 1000 cremations per year.

9.3 Cost of the Crematorium Equipment

Traditionally, crematoria have installed the maximum number of cremators possible to enable the cremation of all bodies on the same day as the funeral. This has still reduced significant overtime working.

It is now widely recognised that a crematorium should operate as few cremators as possible in order to minimise the environmental impact of cremation. National codes of practice have been changed to enable the retention of coffins overnight to enable the most efficient use of cremators.

If the private sector is building and operating a new crematorium undertaking 1000 to 1200 cremations per year, they would likely install only one cremator. This would minimize the capital and operational costs as well as the environmental impact. Cremators work most efficiently and cause least impact to the environment if they are used continuously, rather than being allowed to cool down. 5 day operation inevitably means that a cremator cools over the weekend, but storing coffins overnight as appropriate enables the number of daily cremations to be evened out to assist in reducing temperature variations and consequent thermal shock on the refractories.

The difficulty that a single cremator installation poses is that roughly every 5 years the cremator needs to be taken off line for a full re-line of the refractory brickwork. This work takes up to 18 days, during which the cremator cannot be used for cremations.

One way around this issue would be to initially install only a single cremator, but with a twin abatement plant. In the 4th year of operation, a second cremator could be added, enabling the crematorium to continue operating during the re-line of the first cremator in 5th year.

This option would reduce the initial capital requirement and maximize the efficiency of the first cremator during the first 4 years. Once 2 cremators were installed, the most efficient operation could be achieved by using each for 2 weeks alternately.

The design of the building should allow for easy delivery, installation and future maintenance of the equipment. Management should have flexible staff rota systems to ensure the most efficient operation of the equipment. The costs associated with cremation equipment include **:Purchase costs, Operating costs, Maintenance costs**.

Equipment Purchase Costs :Currently Facultatieve Technologies are the UK market leader in terms of the installation of cremators and abatement equipment. A single **FT111** cremator would cost in the range of ₹3832000. This includes: construction and installation of the equipment, automatic cleaning of the boiler, waste gas ducting, hot plate heat exchanger, electrical and mechanical installation, commissioning and testing, staff training. In addition to these cost, the crematorium would need : coffin charging system, cremated remains treatment equipment, coffin storage. These items would cost in the range of ₹336000. The installation costs associated with the cremation equipment would therefore total be ₹4166960. If the intention was to fit a second cremator in 4th year, the initial abatement plant cost would be higher, giving an initial installation total of ₹4446960. A second cremator would cost approximately ₹1080000 at current prices.

***Equipment Operating Costs* :**Unit costs can be dramatically reduced by increased throughput, as much of the energy used in heating a cremator is lost through intermittent operation. Cremators that receive five or more cremations per day retain heat energy and as numbers increase, fuel consumption per cremation decreases. Based upon annual figures of 1000 cremations, 50 operational weeks (allowing for Bank Holidays) and a 5 day working week, a crematorium would only receive an average of 4 cremations per day.

Cremation times using modern cremators can be on average between 70 and 90 minutes. Allowing for a 90 minutes cremation cycle, the cremator would be in use for 6 hours per working day. Certain days of the week attract more funerals than others and demand on the cremator could be evened out by the storage of coffins overnight, in accordance with national codes of practice.

Costs vary with the number of cremators and cremations and the way that the equipment is used. However, we may offer the following guide prices for the purposes of this feasibility study based on the efficient use of one FT111 cremator to cremate 1000 cremations per year. At today's rates, the operating costs of the cremator per cremation would be approximately:

Equipment Operating Cost	
Item	**Cost in ₹**
Gas	1200
Electricity	50
Reagent and disposal	100
Total	**1350**

Equipment Maintenance Costs :Excluding call-outs and all refractory repairs, the servicing of an FT111 cremator and abatement plant would be in the range of ₹112000 per year, i.e. ₹120 per cremation.

Refractory brickwork will require replacement from time to time due to wear from thermal shock and chemical erosion. A full re-line of the cremator currently costs in the region of ₹240000 and would likely be required every 5 years, with hearth replacements required twice as often. We can recommend an all-inclusive fixed-price maintenance contract for a 5 year period to facilitate budgeting and maintenance of the equipment.

9.4 Premises Costs

The maintenance costs of a new building should be low by virtue of good design, controlled construction and planned maintenance. In my opinion, high maintenance costs are the result of poor design. As in any building, it is essential that sufficient thought has gone into the roof and rainwater issues.

At Wrexham crematorium, Flat roofs needed continuous maintenance and the main sloping chapel roof required replacement after 30 years due to poor design of gutters and use of copperised felt to create a relatively low cost roof. At Harwood Park, a state-of-the-art computerised central heating system failed to adequately heat and ventilate the main chapel whilst over-heating other areas: this was in my view as a result of poorly-informed design.

The use of abatement equipment will necessitate the cooling of cremator exhaust gases prior to filtration. This will be an opportunity to utilise heat-recovery equipment to use this surplus energy to heat the building. The greatest demand for heating is during the winter months when cremation numbers are at their highest. Whilst this option would increase capital costs, it would provide significant long term savings and accord with the Indian Environmental Policy.

I recommend separate meters to accurately monitor utilities consumption for cremation and heating. Careful planning of the grounds will enable cost-effective maintenance. The areas used for memorials must be maintained to a high standard. This is appropriate evidence of customer care and also encourages memorial sales.

9.5 Expenditure Summary

In simple terms, the operational costs per cremation of the crematorium undertaking 1000 cremations per year would be between the following figures :

Expenditure Summary	
Item	**Cost in ₹**
Personnel	1140
Cremator Operation	1350
Cremator Maintenance	120
Total	**2610**

Additional costs would include capital charges, central support charges, business rates, buildings and grounds maintenance

9.5 Crematorium Income

Income is primarily received as charges for cremations and for memorials. There is variation in the type of provision and the charges made for these services. A new crematorium in India completing 1000 cremations per year could expect an annual income of ₹2610000 from a charge of ₹2610 per cremation. This fee would place India in a comparable yet competitive situation with other crematoria in the world. Some crematoria make a surcharge for cremations originating outside of their area, in the same way as many burial authorities impose higher burial fees. This system is not employed by the private sector and in my experience discourages funerals from outside the local area. This is self-defeating as there are fixed costs in operating a crematorium and the greater the number of cremations the greater the ability to pay off capital and make a profit. Cremation income is obviously proportional to the number of cremations. Each additional cremation represents the potential for additional income from memorials like book of remembrance, wall tablet, ashes retained, private gardens, tree, and columbaria.

Memorial income cannot be guaranteed. The legislation relating to the sale of memorials by local authorities in England was recently clarified by the Local Government Act 2003. It basically means that local authorities cannot lawfully make a profit out of memorial sales, whether at a cemetery or crematorium. However, the costs of providing memorials at a new Indian crematorium would include a contribution to the capital and operational costs of the facility. In my view, the Council would be able to sell memorials at a higher price than the simple direct cost of the memorial. It is possible for a local authority to engage with the private sector to provide memorials for profit on its behalf. I am not aware of this procedure actually being adopted at a UK crematorium. In general terms, memorial income is only likely from funerals where the cremated remains are disposed of within the crematorium Garden of Remembrance. People who choose to remove the cremated remains for disposal elsewhere are unlikely to see the benefit of having a memorial at the crematorium.

X. CONCLUSION

- While cremation is an established Hindu ritual practiced since ancient times and the Hindu religion permits the cremation of dead body in day-time only, there is much scope of solar crematorium in this ritual; as solar power is also available in day-time only.
- Between 500 and 600 kg of wood are used to cremate a dead body. So we are significantly contributing in global warming and atmospheric air pollution much more and forest are depleting day by day. The most sustainable energy source is sunlight that too is totally inexhaustible and available free of cost. It mitigates all the above problems.
- India is situated in high solar insolation belt with about 300 clear sunny days in a year and the daily average solar energy incident over India varies from 4 to 7 kWh/m^2. All these are an ideal combination for using solar power in India, So solar crematorium will be a viable option.
- We should never suggest of using solar photo-voltaic panels to obtain such a large amount of heat for cremation, as the sunlight has very little part, only 20% of its energy as lighting effect and large portion of 80% as thermal effect. So energy of solar radiation can be utilized more in solar thermal power generation than in solar photo-voltaic (which utilizes only lighting effect of sunlight) power.
- There must be an arrangement of suitable and sufficient backup system for non-sunny hours to meet the Hindu ritual sentiment of burning the corpse at one goes.
- Ideally the solar crematorium should be built near river, pond or lake and there must be facility to collect ashes for emerging in open flow of water.
- Building solar crematorium is very expensive, since solar reflector costs a great amount of money. But in solar cremation, since we don't have to pay for fuels, as in conventional cremation large amount of wooden pile or electricity are required. So money can saved in the long run.
- Central and state governments have several policies which promote using solar power by providing various subsidies, incentives and interest free loans.
- Cost of cremating a corpse solar crematorium is very genuine of ₹2610 on the basis of 1000 cremations per year, though it doesn't include land cost, capital charges, and central support charges.
- 800°C is at the low end of incineration temperatures, so this method would be more time consuming and adoption of this method may be difficult for families and operators. So to achieve high temperature, there is need of further research in the field of advance technologies for designing reflector and combustion chamber. Universities can be contacted in order to benefit students who want to work with solar energy developments.
- In conclusion, we will definitely be able to cremate a corpse through solar crematorium built with a well designedscheffler reflector and an efficient combustion chamber. The project may go through many stops and goes, but in the last we will be able to make working prototype Solar Crematorium.

REFERENCES

[1]. Agravat S., (2011). Jani O, "Feasibility Study of Solar Crematorium : Technical Report", Report No. GERMI/2011/Solar/107) March 14, 2011.

[2]. Gadhia D., (2009). "Parabolic solar concentrators for cooking and food processing", Valsad, Gujarat, International solar food conference.

[3]. Gagneux A., (2008). "Installation of the first 50 m^2Scheffler Solar Crematorium" April 2008.

[4]. Garg H. P., (1985). "Solar Thermal Energy Storage", D. Reidel Publishing Company, Dordrecht/Boston/Lancaster, ISBN 90-277-1930-6.

[5]. Hauer A., Kempener R., Simbolotti G., Tosato G., (2013) "Thermal Energy Storage Technology Brief", January 2013.

[6]. Hauer A., (2011). "Storage Technology Issues and Opportunities", Committee on Energy Research and Technology (International

Energy Agency), International Low-Carbon Energy Technology Platform, Strategic and Cross-Cutting Workshop Energy Storage– Issues and Opportunities", 15 February 2011, Paris, France.
[7]. Kesari J. P., Krishen, Sharma P. B., (2012). "Solar Power is a Panacea for Changing Rural India-The role of CSP under Indo-Japan Collaboration", Proceedings of 2nd International Symposium –collaborative research project of CSP for India and Japan, 25 April 2012, Tokyo Institute of Technology, Tokyo, Japan.
[8]. Kesari J. P., Sharma P. B., (2012). "Empowering India with Solar Energy Technology: A Roadmap at International Conference on Climate Change and Sustainable management of rural Resources", 5th to 7th Feb 2012, ITM University Gwalior.
[9]. Patil R., Awari G. K., Singh M., (2011). "Experimental Analysis of Scheffler Reflector Water Heater", Thermal Science, 2011, Vol. 15, No. 3, pp. 599-604.
[10]. Patra D. C., (2013) "India's Energy Scenario in 2013–Challenges & Prospects", Hydrocarbon Asia, Jan-Mar 2013.
[11]. Rapp J., Schwartz P., (2010) "Construction and Improvement of a Scheffler Reflector and Thermal Storage Device", Cal Poly Physics – November 2010.
[12]. Reuss M., (2011). "Solar District Heating in Germany – Findings and Prospects", Proceedings of the ISES Solar World Congress 2011, 28 August – 2 September 2011, Kassel, Germany.
[13]. Ristic S., Henninger V., Kaucic, (2013). "Water absorption of composite CaCl2-FeKIL-2 for solar thermal energy storage", 5th Croatian-Slovenian-Serbian Symposium on Zeolites, 30.5.-2.6. Zlatibor, Serbia.
[14]. Scheffler W., (2006). "Development of a solar crematorium", International conference on Solar Cooker, Spain, 15-16th July 2006.
[15]. Scheffler W., (2006) "Introduction to the Revolutionary Design of Scheffler Reflectors", International conference on Solar Coockers, Spain, 15-16, July 2006.
[16]. Subramuniyaswami S. S., "Living With Siva: Hinduism's Contemporary Culture", Himalayan Academy ISBN 0-945497-98-9; 750.
[17]. Tyagi A. .P, Dir. Gen., (2009). "Report on Solar Radiant energy Over India-2009", Chapter-5, 2009, Ministry of Earth Sciences, New Delhi.

Acknowledgement : We acknowledge kind support of Mr. **Deepak Gadhia** at **Muni Seva Ashram**.

INFLUENCE OF HETEROGENEOUS GATE DIELECTRIC ON HETERO-DIELECTRIC-DMG-GAA-TFET FOR IMPROVED TUNNELING CURRENT

Jaya Madan[1], R.S. Gupta[2], Rishu Chaujar[3]
[1]*Department of Engineering physics, DTU, Delhi (India)*
[2]*Professor & Head in Department of ECE, MAIT, Delhi (India)*
[3]*Assistant Professor, Department of Engineering physics, DTU, Delhi (India)*

ABSTRACT

In this paper, we propose and validate a Heterogate Dielectric- Dual Material Gate-Gate All Around, Tunnel Field Effect Transistor (HD-DMG-GAA-TFET). A comparative study for different values of high-k has been done, and it has been clearly shown that the problem of lower I_{ON} (which hinders the circuit performance of TFET) can be overcome by using the dielectric engineered hetero-gate architecture. The HD-DMG-GAA-TFET shows an enhanced I_{ON} of the order of 10^{-4}A and an I_{ON}/I_{OFF} of the order of 10^{12} (approximately). The perfect saturation of drain current is obtained and hence the device is a worthy candidate for sub nanometre range, for low power analog application. Further, the comparison of the proposed device with conventional Gate All Around Tunnel Field Effect Transistor (GAA-TFET), has been done and it has been found that the proposed device has greater tunneling current driving capacity.

Keywords- Ambipolarity, ATLAS-3D, band to band tunneling (BTBT), barrier width, heterogate dielectric, high-k, subthreshold swing (SS), TFET (tunneling field effect transistor).

I. INTRODUCTION

The miniaturizing of semiconductor devices for increasing the speed of the device, decreasing the area occupied and power consumed by the circuit results into increase in leakage currents, short channel effects and static power consumption for the integrated circuits. Numerous kinds of novel electron devices have been introduced to overcome the scaling limit of MOSFETs [1-3]. But all the MOSFETs use the diffusion over the thermal barrier and hence have a fundamental limit of (KT/q).ln10~60mV/dec; which leads to increase in static power consumption. Hence, the devices which use a new carrier transport mechanism other than diffusion over a thermal barrier came into existence. Among these devices, Tunnel Field Effect Transistor (TFET), which uses a band to band tunneling (BTBT) mechanism; to overcome this fundamental limit of subthreshold swing, acts as a promising candidate for further extending the Moore's law. Due to its immunity to short channel effects, lower subthreshold swing (SS) and lower off current (I_{OFF}), TFET is found to be the potential candidate to replace the MOSFET [4-6]. Due to lower I_{OFF} of the TFET, switching characteristics of TFET are far better than MOSFET. The major challenge in adopting TFET for wide scale application is its lower I_{ON}; in order to tackle this problem many novel device designs and materials such as double-gate, delta layer, SiGe, and

IJATES

PNPN structures have been proposed [7-11]. To enhance I_{ON}, a high-k material has been locally inserted (near the source side) in the gate dielectric to form heterogate-dielectric (HD) TFETs [12]. In HD-TFETs the gate dielectric is split into two regions; high-k dielectric near the source side and low-k dielectric near the drain side The presence of high-k results into a higher band bending due to increase in surface potential (at a constant gate bias) [13]. Another practical problem that needs to be tackled with TFET is high threshold voltage. To resolve this issue many structures were proposed such as, tunnel bandgap modulation, gate work function engineering, vertical tunnel field effect transistor (TFET) with SiGe delta doped layer, and high-k gate dielectric with double gate, higher source doping and abrupt doping profile [14-19]. Another major problem with TFET is ambipolarity. The ambipolarity in the device is the conduction for both high positive and high negative V_{GS}, while keeping the V_{DS} only in one direction (negative for p-type devices and positive for n-type devices) [20]. A higher ambipolar behaviour deteriorates the SS and standby power consumption of devices. When a high-k material is applied to the entire gate dielectric ambipolar behaviour increases, and hence causes a higher OFF current. This ambipolarity effect can be reduced by using a hetero gate dielectric structure. The higher value of dielectric improves the electrical coupling between the gate and the tunneling junction (the source-channel junction) and hence, increases the tunneling rate. The dual material gate further helps in the improvement of ON/OFF characteristics. Lower work function metal near the source side, increases the band overlap and hence reduces the tunneling barrier width. This reduced tunneling barrier increases the tunneling probability and the generation rate which results in higher I_{ON} and the higher value of work function near the drain side increases the tunneling barrier width and hence helps in reducing the I_{OFF}. So an optimum value of metal work function value at source and drain side should be chosen to trade-off between ON and OFF characteristics. In this work, a heterogate dielectric, dual material gate, gate-all around (GAA) structure has been applied to TFETs with the aim of higher I_{ON} and to improve the device characteristics.

II. DEVICE STRUCTURE: PARAMETERS AND SIMULATION MODELS

The Gate All Around (GAA) geometry is considered with radius (R) of 10nm, channel length (L_g) of 50nm which is basically equal to the sum of length of region 1 and region 2 respectively (L_1 (20nm) and L_2 (30nm)), in case of HD-DMG-GAA-TFET and gate oxide thickness (t_{ox}) of 2nm. The source is p+ type doped ($1\times10^{20}cm^{-3}$) and drain is n+ doped (5×10^{18} cm^{-3}) and body is lightly p type doped ($1\times10^{16}cm^{-3}$). To reduce ambipolarity effect source and drain are doped asymmetrically. In case of HD-DMG-GAA-TFET region 1 consists of dielectric constant ε_1=21 (high-k) and metal work function Φ_{M1}=4.1eV (near the source) and region 2 consists of ε_2=3.9 (low-k) and Φ_{M2}=4.4eV (near the drain). While studying the effect of high-k ε_1=7.5, 21 and 29 corresponding to Si_3N_4, HfO_2 and ZrO_2 respectively and ε_2=3.9 (SiO_2) were used. In case of GAA-TFET the dielectric constant 3.9 and gate metal work function 4.1eV is used. The source and drain junctions are abruptly doped for an effective band to band tunneling. Fig.1 shows the simulation device structure i.e. HD-DMG-GAA-TFET consisting of heterogate dielectric and dual material gate. All simulations have been performed using the ATLAS device simulator. The models activated during simulation are as follows: concentration and field dependent mobility model, non-local band to band tunneling, Shockley-Read-Hall for carrier recombination, band gap narrowing and Fermi Dirac statistics [21].

IJATES

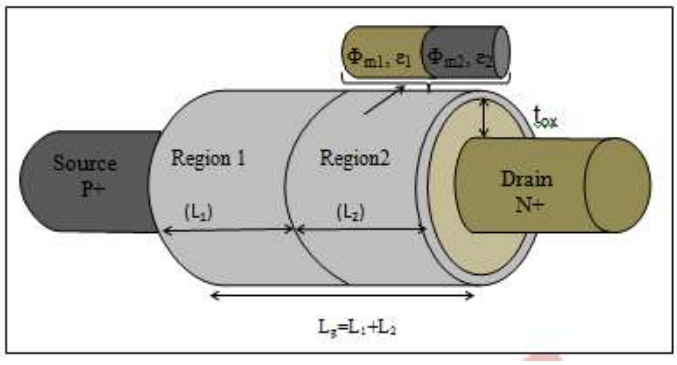


Fig.1: Structure of Heterogate Dielectric-Dual Material Gate-Gate All Around-Tunnel MOSFET (HD-DMG-GAA-TFET).

III. RESULT AND DISCUSSION

IMPACT OF HETERO-GATE DIELECTRIC

The drain current characteristics, transconductance, output characteristics have been studied and simultaneously the impact of high-k is considered. The presence of high-k near the source results into a higher band bending due to increase in surface potential (at a constant gate bias). The higher band bending results into reduction of tunneling barrier width, which further enhances the generation rate and hence the I_{ON}. It is evident from Fig.2 that among the three dielectric constants, the higher value of dielectric constant corresponds to higher current driving capability; this is because of the increase in band bending with higher dielectric constant, which reduces the tunneling barrier width and hence, enhances the generation rate. But the counter effect is the degradation of OFF characteristics; due to comparative higher band bending at higher gate dielectric resulting in tunneling of electrons at lower gate voltage. This results in higher leakage current which eventually results in higher static power dissipation. Hence we have to trade-off between I_{ON} and I_{OFF} to optimise the I_{ON}/I_{OFF} ratio and the subthreshold swing. The highest I_{ON}/I_{OFF} ratio is for Si_3N_4 (ε_1=7.5). Further it is evident that the GAA-TFET has 100 times lower I_{ON} as compared to HD-DMG-GAA-TFET. Transconductance g_m, or device gain which is basically the first order derivative of the drain current with respect to the gate voltage at constant drain bias, is shown in Fig.3. The peak of transconductance curve gives the optimum bias point if device is to be used as an amplifier. It clearly shows that among the three dielectric constants and GAA-TFET the gain of the device is higher for higher dielectric constant, due to the enhanced electrical coupling between the gate and the tunneling junction (the source-channel junction) with higher dielectric constant, which further enhances the tunneling rate.

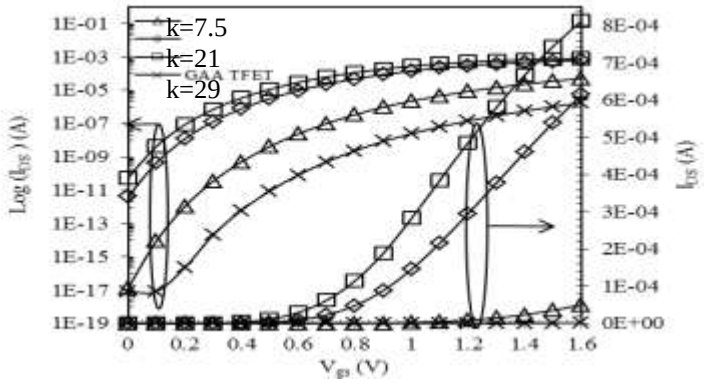


Fig.2: Drain current as a function of gate voltage (V_{GS}) for different values of high-k and for GAA-TFET at V_{DS}=0.8V.

Hence, the more number of electrons tunnel through the barrier which eventually leads to enhancement in drain current and transconductance. Fig.3 (inset) indicates the transconductance for GAA-TFET; clearly the gain is around 100 times lower as compared to HD-DMG-GAA-TFET.

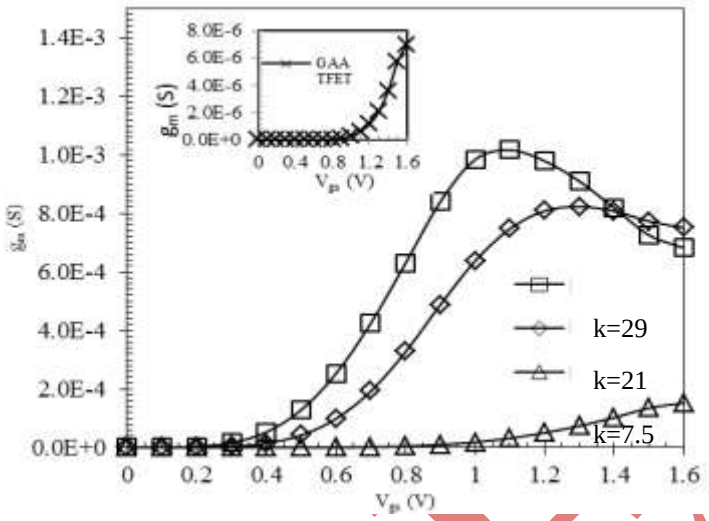


Fig.3: Transconductance as a function of gate voltage (V_{GS}) for different values of high-k and for GAA-TFET at V_{DS}=0.8V.

The output characteristic (I_{DS}-V_{DS}) at a constant V_{GS} = 1.0 V is illustrated in Fig.4. It is clear that the device predicts a qualitatively agreement in linear regime and also shows a well saturation in drain current for higher drain voltages. It has been obtained that the ZrO_2 has the better output characteristics as compared to Si_3N_4, HfO_2 and GAA-TFET. The output characteristics of GAA-TFET shown in Fig.4 (inset) for V_{GS}=1.0 V; Again the output current is much lower in case of GAA-TFET.

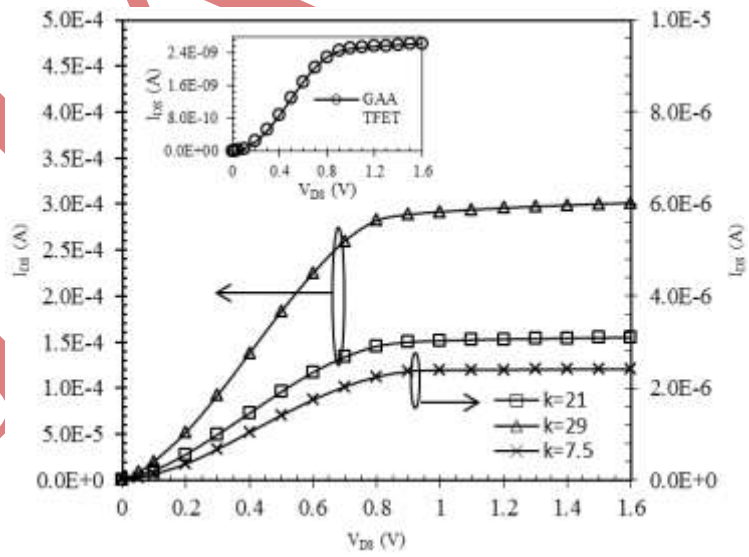


Fig.4: Drain current as a function of drain voltage (V_{DS}) for different values of high-k at V_{GS}=1.0 V and for GAA-TFET.

Output-conductance g_d, which is first order derivative of the drain current with respect to the drain voltage at a constant gate voltage, is shown in Fig.5. Again the output conductance has a higher peak for ZrO_2, increased by

an order of 100 (approximately) with respect to Si_3N_4. The output conductance for GAA-TFET is shown in Fig.5 (inset); g_d of GAA-TFET is manifold lower than that of HD-DMG-GAA-TFET.

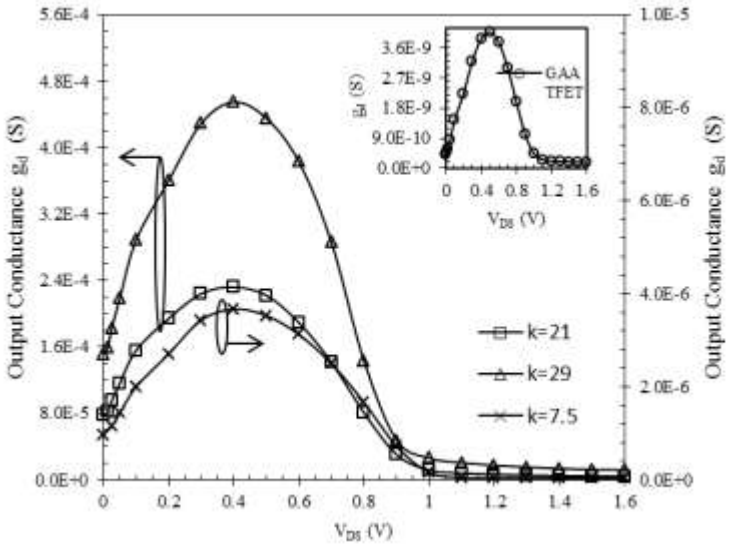


Fig.5: Output conductance as a function of drain voltage (V_{DS}) for different values of high-k and for GAA-TFET at V_{GS}=1.0 V.

IV. CONCLUSION

In conclusion the impact of high-k gate dielectric and comparison with GAA-TFET has been studied on the device performance. By using a high-k dielectric near the source side I_{ON} and transconductance has been enhanced. The output characteristic shows a very good saturation for higher drain bias. As in most of the conventional amplifiers, MOSFET is operated in saturation region or in linear region; therefore the device is well suited for analog applications and sub nanometre devices. But the counter effect of high-k is the degradation of OFF characteristics. Optimization of I_{ON}/I_{OFF} ratio depending on the application has to be done for sub nanometre devices. Both the static power dissipation and the higher I_{ON}/I_{OFF} ratio make the device an effective candidate for the analog application. While comparing the two devices; it is found that GAA-TFET has lower I_{ON} and device gain with respect to HD-DMG-GAA-TFET and hence HD-DMG-GAA-TFET is comparatively better candidate for analog performance.

V. ACKNOWLEDGMENT

The authors would like to thank to Microelectronics Research Lab, Department of Engineering Physics Delhi Technological University to carry out this work. Author would also like to thank University Grants Commission, Government of India, for the financial assistance during the course of this research work.

REFERENCES

[1] William M. R. and Gehan A. J. A., “Silicon surface tunnel transistor”, Appl. Phys. Lett., 67(4), Jul. 1995, 494–496.

[2] Qin Z., Wei Z., and Sea Baugh A, “Low-subthreshold-swing tunnel transistors”, IEEE Electron Device Lett., 27(4), Apr. 2006, 297–300.

[3] Boucart K. and A. M Ionescu, "Double-gate tunnel FET with high-K gate dielectric", IEEE Trans. Electron Devices, 54(7), Jul. 2007, 1725–1733.

[4] Nirschl Th., Wang P.-F., Weber C., Sedlmeir J., Heinrich R., Kakoschke R., Schrufer K., Holz J., Pacha C., Schulz T., Ostermayr M., Olbrich A., Georgakos G., Ruderer E., Hansch W., and Schmitt-Landsiedel D., "The tunneling field effect transistor (TFET) as an add-on for ultra-low voltage analog and digital processes", IEDM Tech. Dig., 2004, 195 – 198.

[5] Choi W. Y., Park B.G., Lee J. D. and Liu T.J.K., "Tunneling field effect transistors (TFETs) with subthreshold swing (SS) less than 60 mV/dec", IEEE Electron Device Lett., 28(8), Aug. 2007, 743–745,.

[6] Bhuwalka K. K., Schulze J. and Eisele I., "Performance enhancement of vertical tunnel field-effect transistor with SiGe in the δp+layer", Jpn. J.Appl. Phys., 43(7A), Jul. 2004, 4073–4078.

[7] Toh E.H., Wang G. H., Chan L., Sylvester D., Heng C.H., Samudra G. S., and Lee Y.C., "Device design and scalability of a double gate tunneling field-effect transistor with silicon– germanium source", Jpn. J. Appl. Phys., 47(4), Apr. 2008, 2593–2597.

[8] Karthigai Pandian M. and Balamurugan N.B., "Analytical Threshold Voltage Modeling of Surrounding Gate Silicon Nanowire Transistors with Different Geometries", J Electr Eng Technol, 9, March. 2014, 742-751.

[9] Schlosser M, Bhuwalka KK, Sauter M, Zilbauer T, Sulima T, Eisele I., "Fringing induced drain current improvement in the tunnel field-effect transistor with high-k gate dielectrics", IEEE Trans Electron Device 56(1), January 2009, 100–8.

[10] Gandhi R, Chen Z, Singh N, Banerjee K, Lee S., "Vertical Si-nanowire n-type tunneling FETs with low subthreshold swing (650 mV/decade) at room temperature". IEEE Electron Dev Lett, 32(4), 2011, 437–9.

[11] Nayfeh O. M., Chleirigh C. N., Hennessy J., Gomez L., Hoyt J. L., and Antoniadis D. A., "Design of tunneling field-effect transistors using strained-silicon/strained-germanium type-II staggered heterojunctions," IEEE Electron Device Lett., 29(9), Sep. 2008, 1074–1077.

[12] Anghel C, Chilagani P, Amara A, Vladimirescu A., "Tunnel field effect transistor with increased ON current, low-k spacer and high-k dielectric". Appl Phys Lett , 96(12), 2010, 122104

[13] Pal A., Sachid A. B., Gossner H., and Rao V. R., "Insights into device design Insights Into the Design and Optimization of Tunnel -FET Devices and Circuits", IEEE Transactions on Electron Devices, 58, April 2011, 1045 – 1053.

[14] Jiao G.F., Chen Z.X., Yu H.Y., Huang X.Y., Huang D. M., Singh N., G. Q. Lo G. Q., Kwong D.L., Ming-Fu. Li, "New Degradation Mechanisms and Reliability Performance in Tunneling Field Effect Transistors", Electron Devices Meeting, December 2009, 741-744.

[15] Moselund K. E., Ghoneim H., Bjork M. T., Schmid H., Karg S., Lortscher E., Riess W., and Riel H., "Comparison of VLSI grown Si-NW tunnel FETs with different gate stacks", in Proc. ESSDERC, Sep. 2009, 448–451.

[16] Anghel C., Hraziia G., Gupta A., Amara A., and Vladimirescu A., "30-nm tunnel FET with improved performance and reduced ambipolar current", IEEE Trans. Electron Devices, 58(6), Jun. 2011, 1649–1654.

[17] Hraziia A., Vladimirescu A., Amara, Anghel C., "An analysis on the ambipolar current in Si double-gate tunnel FETs", J. Solid-State Electron. 70 (2012) 67–72.

[18] Mallik A., Chattopadhyay A., "Drain-dependence of tunnel field-effect transistor characteristics: the role of the channel", IEEE Trans. Electron Devices, 58 (12) (2011) 4250–4257.

IJATES

[19] Nagavarapu V., Jhaveri R., Woo J.C.S., "The tunnel source (PNPN) n-MOSFET: a novel high performance transistor", IEEE Trans. Electron Devices, 55 (4) (2008) 1013–1019.

[20] Saurabh S. and kumar M.J, "Novel attributes of a Dual Material gate nanoscale tunnel field effect transistor", IEEE Trans. Electron Devices, vol no. 58 (2) (2011), 404-410

[21] ATLAS User's guide, SILVACO International, Version 5.14.0.R, 2010.

Biographical Notes

Miss. Jaya Madan is presently pursuing Ph.D. in Engineering physics Department from DTU Delhi, India.

Dr. Rishu Chaujar is working as an Assistant Professor in Engineering physics Department, DTU Delhi, India.

Prof. R. S. Gupta is working as a Professor & Head in Department of ECE, MAIT, Delhi, India.

IJATES

INVESTIGATION OF FREQUENCY DEPENDENT PARAMETER OF GEWE-SiNW MOSFET FOR MICROWAVE AND RF APPLICATIONS

Neha Gupta[1], Ajay Kumar[2] and Rishu Chaujar[3]
[1]*Department of Engineering Physics, DTU, Delhi (India)*
[2]*Department of Engineering Physics, DTU, Delhi (India)*
[3] *Assistant Professor, Department of Engineering Physics, DTU, Delhi (India)*

ABSTRACT

This paper presents the RF and high frequency performance of Gate Electrode Workfunction Engineered-Silicon Nanowire (GEWE-SiNW) MOSFET and the results so obtained are compared with Silicon Nanowire (SiNW) and Conventional MOSFET by using DEVEDIT-3D and ATLAS device simulator. The simulation results unfold the reduction in parasitic capacitances and lowering of intrinsic delay in GEWE-SiNW MOSFET. Furthermore, significant improvement in stern stability factor (K) has also been observed for GEWE-SiNW MOSFET as compared to conventional and SiNW MOSFETs, thus, reinforcing its use for high frequency wireless applications.

Keywords: Cut-Off Frequency (F_t), GEWE, Maximum Frequency (F_{max}), RF, Stability.

I. INTRODUCTION

The rapid growth of the mobile telecommunication markets emphasizes the need for reliable analog IC design at high frequencies. The RF performance of the Silicon MOSFET has been improved considerably during the late 1990s and early 2000s due to scaling of MOSFET. The reduction of the channel length in CMOS technologies has significantly improved the high frequency properties of the MOSFETs, making CMOS technology suitable for wireless communications and other RF applications [1-2]. Although, scaled technologies leads to undesirable effects such as short channel effects, leakage current, hot carrier effects (HCE), parasitic capacitances which results in degradation of device characteristics such as transconductance, voltage gains, subthreshold slope etc., which is unsuitable for RF/wireless applications [3]. GAA SiNW MOSET [4] is getting more attention for its advantages of small DIBL, small subthreshold swing etc. Also, it has found that their cut-off frequency can be much larger than that of planar Si-MOSFET [5]. Further, to enhance the carrier efficiency of a device, Zhou and Long [6] in 1999 proposed the concept of GEWE. With this scheme there is appreciable reduction in short channel effects and improvement in on-current due to step potential profile at the interface of metal gates owing to difference in metal workfunctions which results in enhanced lateral electric field allowing the carriers to travel faster hence improving the gate transport efficiency. Moreover, integration of GEWE scheme onto SiNW MOSFET ameliorates device efficiency, enhanced driving capability, minimizes short channel effects etc. [7-8]. Also, due to the increased demand for high-speed electronics products, the accurate analysis of the MOSFET at high frequencies (HF) is requisite to represent the behavior of device in microwave circuits and systems [9]. In

IJATES

this work, TCAD simulation tool is used to evaluate RF figure of merits of GEWE-SiNW MOSFET in terms of enhanced digital and RF performance of scaled devices in comparison to its conventional counterparts.

II. DEVICE STRUCTURE AND SIMULATION

Fig.1 shows a schematic cross-sectional view of GEWE-SiNW MOSFET where L1 and L2 are lengths of two different gate materials with workfunction Φ_{M1}=4.8eV and Φ_{M2}=4.4eV respectively. For n-channel MOSFET, we select two gate materials in such a way that the gate material having highest work function is placed near the source end and the gate material having lowest workfunction is placed near the drain end.

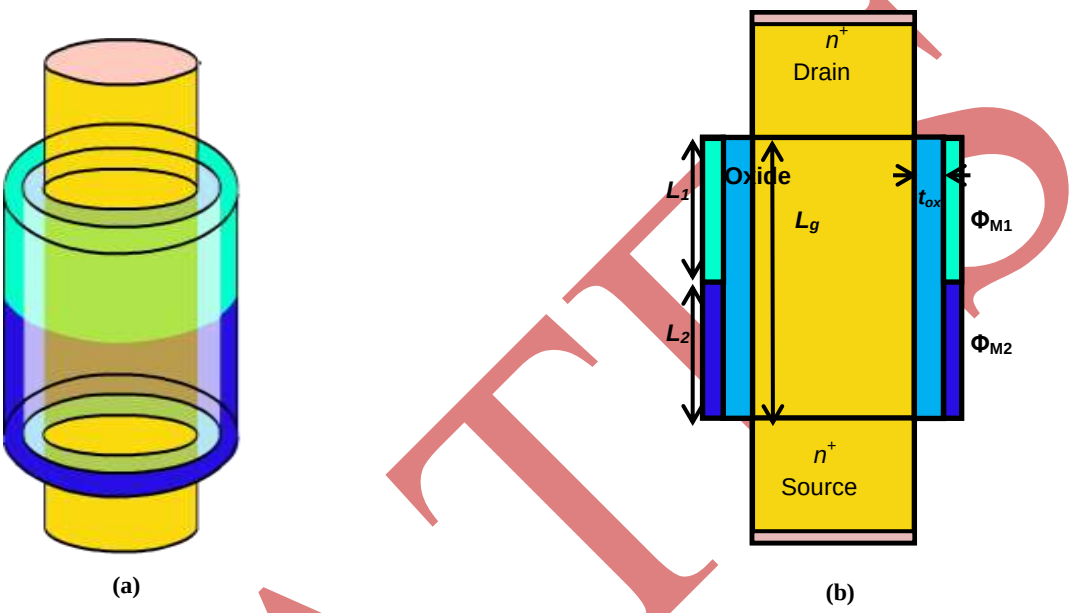
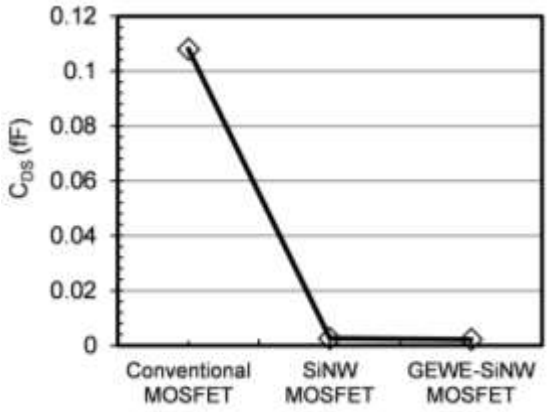


Fig. 1(a-b): Simulated structure and cross section of GEWE-SiNW MOSFET respectively

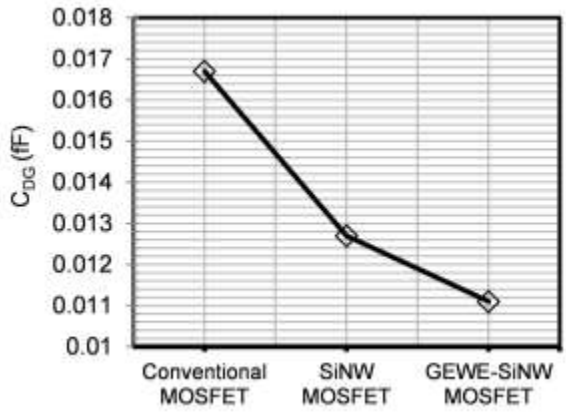
All the simulations have been performed using physical models accounting for the electric field-dependent and concentration-dependent carrier mobilities, Shockley–Read–Hall recombination/generation with doping dependent carrier lifetime, inversion layer Lombardi CVT mobility model, wherein concentration-dependent mobility, high field saturation model are all included [10]. In our simulation, we have adopted the hydrodynamic energy transport model which includes all nonlocal effects and is more accurate than the drift-diffusion method.

III. RESULTS AND DISCUSSION

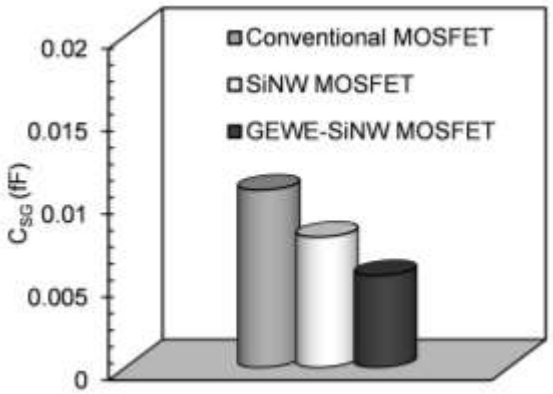
In this paper, we compare GEWE-SiNW MOSFET with its conventional counterparts. The present analysis is carried out for a channel length, L_g=30 nm, radius of NW, R=5nm and thickness of oxide, t_{ox}= 1.5 nm, substrate doping concentration is $1\times10^{16}cm^{-3}$. It is evident from Fig. 2(a-c) that GEWE-SiNW exhibits smaller C_{SG}, C_{DG} and C_{DS} in comparison to its conventional MOSFET at 240 GHz due to metal gate workfunction difference which results in improved screening of conducting channel from drain variations. In addition, due to Silicon nanowire carrier mobility across the channel is enhanced [11-12], thereby reducing the parasitic capacitances. The higher value of these capacitances acts as an obstruction in device switching performance due to increase in the turn-on delay time.



2(a)



2(b)



2(c)

Fig. 2 (a-c): Parasitic capacitance (femto farad) of Drain to source, Drain to Gate and Source to gate for Conventional, SiNW and GEWE-SiNW MOSFET respectively at 240 GHz.

The stern stability factor (K) determines the stability of a device. This factor estimates whether the device is conditionally/unconditionally stable. It must satisfy the condition K>1 for a device to be unconditionally stable [13-15].

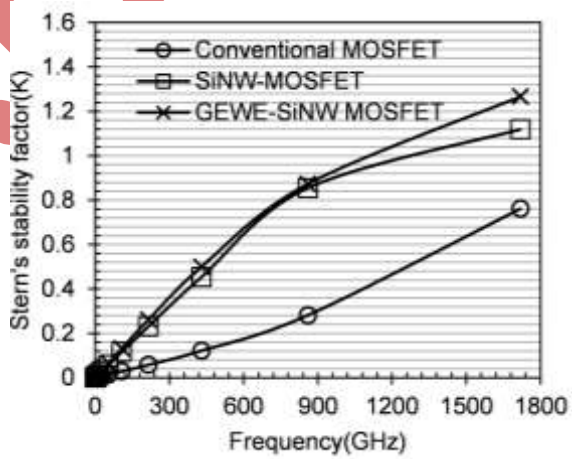
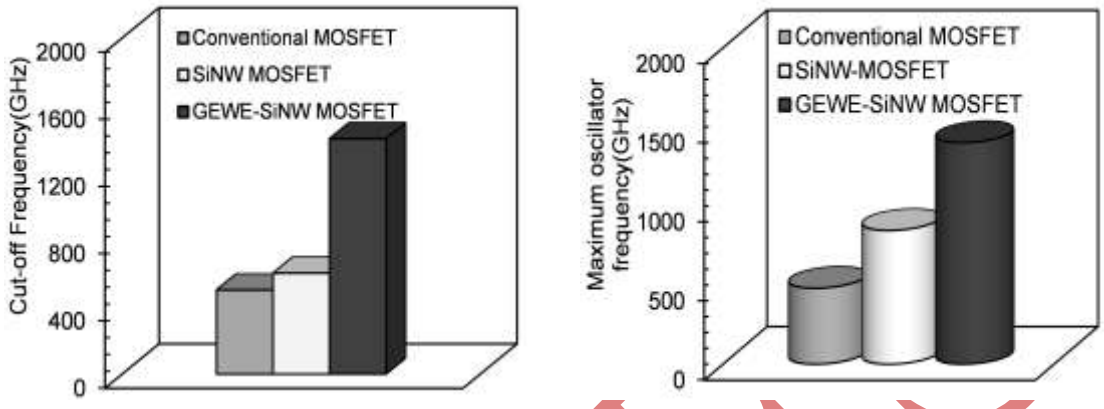


Fig. 3: Variation of Stern's stability (K) factor for Conventional, SiNW and GEWE-SiNW MOSFET

Fig. 3 shows the variation of stern's stability factor at higher frequencies. As is clear from the figure, K is significantly larger (greater than 1) as frequency increases, for GEWE-SiNW MOSFET in comparison to its counterpart where K is approaching 1.1 in SiNW MOSFET and 0.76 in conventional MOSFET. This is due to increased control of gate, which causes maximum power transfer from source to load. Hence, GEWE-SiNW is suitable for Low noise amplifier and RF applications.



4(a) **4(b)**

Fig. 4: (a-b) Maximum oscillator frequency and Cut-off frequency for Conventional, SiNW and GEWE-SiNW MOSFET respectively

Further, the cut-off frequency f_T is the frequency when the current gain is unity, whereas f_{MAX} is the frequency when the power gain is unity [16-17]. f_T is a specification for high-speed digital applications (speed and high swing) while f_{MAX} analogous to the transit frequency of the maximum available power gain that is a realistic parameter of the optimization of microwave amplifiers. The f_{MAX}, as is seen from Fig.4 (a), for GEWE-SiNW MOSFET, is higher than for SiNW and Conventional MOSFET, which shows large parasitic capacitance in the conventional and SiNW MOSFET, thereby giving the GEWE-SiNW design a new strength for switching applications and wireless communication. Also, the use of metal gates results in reduced gate resistance, and hence increases in f_{MAX}. Fig. 4(b) shows the cut-off frequency of GEWE-SiNW MOSFET is greater than the cut-off frequency for bulk MOSFET. Due to the enhanced gate control over channel and screening of potential from drain side, it reduces the short channel effects and enhances the transconductance, leading to increase the cut-off frequency and packing density, thereby making the device suitable for CMOS wireless applications.

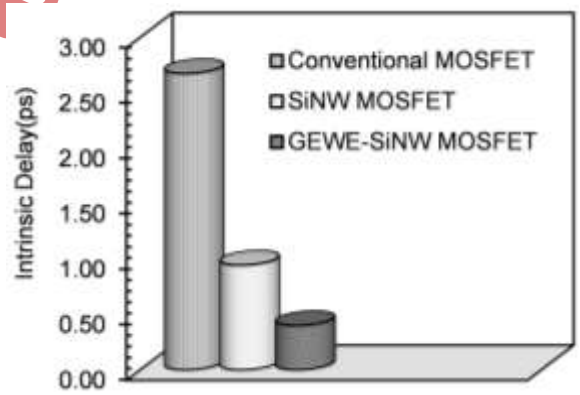


Fig. 5: Intrinsic Delay for Conventional, SiNW and GEWE-SiNW MOSFET

The increasing capacitance between the gate and the overlapped S/D region degrades the intrinsic gate delay. Fig. 5 shows the comparison of GEWE-SiNW with SiNW and conventional MOSFET in terms of intrinsic delay parameter. As is evident from the figure, there is notable reduction in intrinsic delay of GEWE-SiNW MOSFET than its conventional counterparts due to cylindrical gate which increases on-current, reduces parasitic capacitances and incorporation of two dissimilar metal gates, which leads to considerable reduction of intrinsic delay by 55.5%.

IV. CONCLUSION

In this work, we have investigated the improved RF performance of GEWE-SiNW MOSFET and compared it with conventional and SiNW MOSFET, it has been scrutinized that GEWE SiNW MOSFET exhibit lower parasitic capacitances, enhanced cut-off and maximum frequency with an appreciably low intrinsic delay, hence suitable for RF/wireless applications. Furthermore, GEWE-SiNW is found to be more stable than its conventional counterparts, thereby providing its efficacy for high-performance RF applications.

V. ACKNOWLEDGMENT

The authors would like to thank the Microelectronics Research Lab, Department of Engineering Physics, Delhi Technological University (formerly DCE) and one of the authors (Neha Gupta) is grateful to the University Grant Commission (UGC) for providing the necessary financial assistance to carry out this research work.

REFERENCES

[1] Larson, L. E., "Silicon technology tradeoffs for radio-frequency/mixed-signal system-on-a-chip", IEEE Trans Electron Devices 50(3), 2003, 683–99.

[2] Saijets. J., Andersson. M. and Berg. M. A., "A Comparative Study of Various MOSFET Models at Radio Frequencies", Analog Integrated Circuits and Signal Processing 33(1), 2002, 5–17

[3] Chen. Q., "Compact Modeling of Multi-Gate MOSFETs for RF Designs", IEEE International Wireless Symposium, Bejing , 2013, 1-4

[4] Kim. D. W., Yeo. K. H., Suk. S. D., Li. M., Yeoh. Y. Y., Kyun. S. D. and Chung. C., "Fabrication and electrical characteristics of self-aligned (SA) gate-all-around (GAA) Si nanowire MOSFETs (SNWFET)", IC Design and Technology (ICICDT), IEEE International Conference, 2010, Grenoble, 63-66.

[5] Wang. C., Zhuge. C., Huang. R., Tian. Y., Xiao. H., Zhang. L., Li. C., Zhang. X. and Wang. Y., "Analog/RF performance of Si nanowire MOSFETs and the impact of process variation", IEEE Trans. Electron Devices 54(6), 2007, 1288–1294.

[6] Long. W. and Chin. K. K.**, "**Dual Material Gate Field Effect Transistor (DMGFET)", Electron Devices Meeting Tech Dig., 1999, Washington, DC, USA, 549-552.

[7] Gupta. N and Chaujar. R, "Implications of Transport models on the analog performance of gate electrode workfunction engineered (GEWE) SiNW MOSFET", IEEE Second International conference on Devices, Circuits and Systems (ICDCS'2014), 2014, Coimbatore, India, 278-282.

IJATES

[8] Gupta. N, Chaujar. R and Kumar. A, "Simulation analysis of Gate Electrode Workfunction Engineered (GEWE) Silicon Nanowire MOSFET for hot carrier reliability", IEEE 1st International conference on Microelectronics, Circuits and Systems, 2014, Kolkata, India, 150-153

[9] Doan. C.H., Emami. S., Niknejad. A.M. and Brodersen. R.W., "Millimeter-wave CMOS design", IEEE J. Solid-State Circuits 40(1), 2005, 144–155.

[10] ATLAS User's Manual, SILVACO Int., Santa Clara, 2011, CA.

[11] Frey. M., Esposito. A. and Schenk. A., "Computational comparison of conductivity and mobility models for silicon nanowire devices", J. Appl. Phys. 109(8), 2011, 083707 - 083707-6

[12] Ramayya. E. B., Vasileska. D., Goodnick. R.W. and Knezevic. I., "Electron Mobility in Silicon Nanowires", IEEE Transactions on Nanotechnology, 6(1), 2008, 113-116.

[13] Voldman. S. H., (ESD: RF technology and circuits, Wiley, 2006)

[14] Cho. S., Kim. K. R., Park. B. G. and Kang. I. M., "RF performance and small-signal parameter extraction of junctionless silicon nanowire MOSFETs", IEEE Trans. Electron Devices 58(5), 2011, 1388–1396.

[15] Oh. Y. and Rieh. J. S., "Effect of Device Layout on the Stability of RF MOSFETs", IEEE Transactions on Microwave Theory and Techniques 61(5), 2013, 1861-1869.

[16] Nae. B., Lazaro. A. and Iniguez. B., "High Frequency and Noise Model of Gate-All-Around MOSFETs, Spanish Conference on Electron Devices", 2009, Santiago de Compostela, 112-115.

[17] Sarkar. A., De. S., Dey. A. and Sarkar. C. K., "Analog and RF performance investigation of cylindrical surrounding-gate MOSFET with an analytical pseudo-2D model", Journal of Computational Electronics, 2012, 11(2), 182-185.

Biographical Notes

Mrs. Neha Gupta is presently working as a Ph. D Research Scholar in Engineering Physics Department from Delhi Technological University (DTU), Delhi, India.

Mr. Ajay Kumar is presently working as Ph. D Research Scholar in Engineering Physics Department from Delhi Technological University (DTU), Delhi, India.

Dr. Rishu Chaujar is working as an Assistant Professor in Engineering Physics Department from Delhi Technological University (DTU), Delhi, India.

IJATES

IOSR Journal of Environmental Science, Toxicology and Food Technology (IOSR-JESTFT)
e-ISSN: 2319-2402,p- ISSN: 2319-2399.Volume 8, Issue 10 Ver. III (Oct. 2014), PP 01-07
www.iosrjournals.org

Leachate characterization and evaluating its impact on groundwa ter quality in vicinity of landfill site area

Lovleen Gupta[1], Swati Rani[2]
[1](Assistant Professor, Environmental Engineering Department, Delhi Technological University, India)
[2](Student, Environmental Engineering Department, Delhi Technological University, India)

Abstract: *An experimental study is performed for understanding the characteristics of leachate from the landfill site and groundwater in the vicinity area of sanitary landfill. Leachate and groundwater samples are collected from Narela- Bawana (New Delhi, India) landfill site. High Concentrations of various physicochemical parameters are observed in collected samples are reported including heavy metals (Cr, Cu, Fe, Ni, Fe and Zn). The present study deals with the determination of likely concentrations of hazardous contaminants in the groundwater over a period of time due to the discharge of such contaminants from landfill leachates to the nearby soil and finally to groundwater. Results clearly indicated that the likely contamination of groundwater due to leachate released from landfill. Results are further compared with Bureau of Indian Standards for drinking water. Presence of contaminants in groundwater particularly near the landfill sites warns its quality and thus renders the associated aquifer unreliable for domestic water supply and other uses.*
Keywords: *Delhi, Groundwater characteristics, Landfill, Leachate characteristics.*

I. Introduction

Rapid population growth and urbanization in developing countries have led to the generation of enormous quantities of Municipal Solid Wastes (MSW) and consequential environmental degradation. Safe and reliable disposal of MSW and residues is an important component of integrated waste management. One of the most common waste disposal methods is land filling due to its favorable economics, it may lead to the potential sources of groundwater contamination, which is practiced almost everywhere on large scale worldwide.

An MSW landfill is not a safe repository of discarded material; it is a biochemically active unit where toxic substances are leached or created from combinations of non-toxic or toxic precursors as a result of physical, chemical and biological processes in landfills combined with waste components and landfill water regime [1]. These are gradually released into the surrounding environment over a period of decade's and causes large amounts of hazardous and otherwise deleterious chemicals to reach nearby groundwater, surface water and soil also to the air, via leachate and landfill gas. The solid waste composition, particle size, degree of compaction, hydrology, and age of the landfill, moisture, temperature and available oxygen are the controlling factors that determine the rate of production and characteristics of the leachate [2, 3]. The effectiveness of landfill liner systems in preventing leachate migration is eventually compromised with time after installation and deteriorates over time allowing increasing amounts of leachate to pass through the liner into the groundwater system hydraulically connected to the bottom of the landfill.

In recent times, the impact of leachate on groundwater and other water resources such as surface water has attracted a lot of attention because of its overwhelming environmental significance and has given rise to a number of studies in recent years [2, 4, 5, 6, 7].

II. Materials and Methods

2.1 Site description

The Narela - Bawana landfill site is located in Delhi, the capital city of India. Delhi sprawls over 1483 km2 area and ranks second in population among other Indian metropolitan cities and is situated in North India at an altitude of 293 m above mean sea level [2]. Delhi is estimated to generate about 7000 metric tons of MSW daily [8]. Per capita generation of solid waste in Delhi ranging from 150 gm/d to 600 gm/d [5] depending upon the economic status of the community involved and mainly includes waste from household, industries and medical establishments.

Narela-Bawana is a sanitary landfill which came in operation from July 2011. Specific co-ordinates of t he site are 28048□ 21□ □ Nand 77004□ 14□ □ E(Google map) located in Northern part of Delhi along Haryana border. MSW site is constructed of the in different phases. Currently second phase of construction is being under taken, once fully functional 4000 tonnes/day of waste would be dumped in concerned landfill site. The site is being claimed to be efficiently installed with instrument which leads to effective management of waste produced and waste reduction and generation of electricity from waste. It has area approximately of 40 ha, out of which material recovery facility, including Refuse Derived Fuel (RDF) recovery which covers an area of 0.27 ha [9]. Compost Plant and Recyclables storage area are said to be placed in 2.7 ha and 0.27 ha respectively. Power plant

has an area of 13.1 ha and landfill occupy majority of land which is around 16.1 ha. It is claimed that the landfill is lined with two layers of clay and a High Density Polythene layer in between. Once the RDF plant becomes operational, there is a place to collect the harmful gases and flare it before releasing in the atmosphere which will be produced when RDF would be burned.

2.2 Leachate sample collection

Leachate sample were collected on 20th March 2014 from the slump pond in the center of the MSW landfill site. The leachate treatment plant was not operational at the time of sample collection, thus leachate sample post treatment could not be collected. Leachate samples were collected in BOD bottles which were sterilized before use by heating at 180°C together with their stoppers for some time. After collection, all samples were properly labeled with details of the source, date of sampling, time of sampling.

2.3 Groundwater sample collection

Six ground water samples (GW-1, GW-2, GW-3, GW-4, GW-5 and GW-6) were collected from specific tube wells, bore wells and hand pumps.



Figure 1: location of various existing landfills in Delhi. [10]

GW-1 was collected from a Hand Pump located in a house located at 28º48□ 20.4□ □ N and 77º04□ 36.6□ □ E, GW-2 was collected from 28º48□ 27.5□ □ N and 77º03□ 19.6□ □ E, and similarly GW-3 was located at 28º49 □ 17.2 □ □ N and 77º03□ 28.4□ □ E. GW-4 was collected from 28º47□ 12.7□ □ N and 77º05□ 36.3□ □ E, coordinates of GW-5 and GW-6 28º49□ 49.6□ □ N and 77º05□ 49.6□ □ E and 28º46□ 45.1□ □ N and 77º05□ 45.8 □ □ E respectively. The sampling points were located at 0.725 km, 1.5 km, 2.32 km, 3.0 km, 3.4km and lastly at 3.8 km from the landfill dumping point.



Figure. 2: location of MSW landfill and GW sampling

Priority was kept to take sample nearest to landfill, as considered landfill is situated in industrial area; p recaution of not collecting sample nearby the industrial area was kept in mind. Landfill at one side was also confined by Yamuna canal thus it was kept in mind to not collect sample beyond Yamuna canal. For ground water sample collection, 500ml poly vinyl chloride sampling bottles for ground water were used, which were rinsed 2-3times with the sample water which was to be collected. To prevent the loss of certain cations such as Cd, Cu, Cr, Ni and Zn etc by adsorption, or ion exchange with the walls of glass containers, some sampling bottles were acidified with concentrated HCl to pH below 2.0. Fig. 2 indicates the location of groundwater samples and the

landfill on the google map.

2.4 Sample storage, shipment and preservation

The sample are tested is 16.1 km which takes about 45 minutes in transportation. As soon as the sample s reached the DTU laboratory, they were kept in a refrigerator at 4°C for preservation. The samples were tested in laboratory within 24 hours from the time of collection.

2.5 Laboratory analysis

The chemical analysis was done in accordance with the APHA methods [11]. The pH, EC and TDS was measured using conductivity meter; Sodium and potassium by Flame photometer; Calcium, Magnesium and Chlorine by Titration method; COD by Open reflux digestion method & titration; BOD by Winkler method; Sulphate, Phosphate and Iron by Spectrophotometer and Heavy metals (Cr, Cu, Zn, Ni) by Atomic Absorption Spectrometer.

III. Results

3.1 Leachate characteristics

Physicochemical characteristics of the leachate samples collected from the Narela-Bawana MSW landfill site are presented in TABLE 1.

Table 1 Physicochemical concentration in leachate sample

After collection, leachate	pH	EC	TDS	Cl	SO4	PO4	COD	BOD	Ca	Na	K	Mg
Units		µS/cm	mg/l	mg/l	mg/l	mg/l	mg/l	mg/l	mg/l	mg/l	mg/l	mg/l
Value	8.4	965	26320	4466.10	N.D	251.92	47600	13094	133.6	3532	3218	330.7

Physicochemical characteristics of the leachate depend primarily upon the waste composition and water content of total waste. High value of pH is obtained for leachate sample, this indicates as phase of decomposition of wastes characterized by the production of volatile fatty acids and carbon dioxide [12]. Value of EC which is observed as 965µS/cm in given leachate sample reflects presence of anions or inorganic materials. High values of TDS of the order of 26320 mg/l is observed which indicates the presence of inorganic material in the samples. Value of BOD5 in leachate is observed around 13094 mg/l which tends to indicate the maturity of the landfill and shows that microbial activity in the decomposing leachate is yet to attain stability. Value of COD and BOD observed are 47600 and 13094 respectively, thus Ratio of BOD5/COD comes out to be 0.275. COD is an important parameter for its usefulness in determining the relative degree of solid waste decomposition, leachate treatment technique, detection of contaminant migration, and organic contamination. [13] Value of Chloride observed was very high of 4466.10mg/l. The presence of Phosphate (251.92 mg/l) in such a high concentration in leachate is dangerous as its presence in water promotes the growth of algae and correspondingly increases eutrophication.

Table 2 Heavy metals concentration in leachate sample

Parameter	Fe	Cr	Cu	Ni	Zn
Units	mg/l	mg/l	mg/l	mg/l	mg/l
Value	23.26	0.21	3.52	N.D	1.096

TABLE 2 shows Heavy metals contents of the leachate samples obtained from laboratory analysis inclu de Zinc, Iron, Copper, and Chromium. Iron has the highest concentration of all the heavy metals present in the leachate followed by Cu, Zn, Cr whereas the concentration levels of Ni went undetected. The high level of total iron (23.26mg/l), in the leachate samples is evidence of dumping of iron and steel scraps wastes in the dumpsite, which is justified as there is a huge industrial area called as Bawana industrial area in the proximity of landfill, although it is a MSW site. Concentration of Copper observed was 3.52mg/l and potential source of Cu is thought to have originated from the dumping of waste related to cement like bags in the dumpsite. On the other hand, the concentration of Zn which was around 1.096mg/l was less than permissible limit. It depicts that dumping of batteries and fluorescent lamps in the landfill could be a possible source of it. The presence of Cr (0.21 mg/l) in the leachate samples may have originated from the emission of automobile exhaust of diesel tanker vehicles which use Parameter the vicinity of the dumpsite as a garage and other vehicle which ply the road that leads to oil refinery in the city. The different heavy metals detected are indication that the Narela-Bawana landfill site receives variety of wastes from both industrial and residential sources.

3.2 Physicochemical characteristics of Ground Water

The ground water of the study area is used for domestic and agricultural purposes. TABLE 2 shows the concentration various parameters present in the groundwater samples from which the quality of groundwater can

be understood, as it is compared with the acceptable limit of BIS [14] and WHO [15] standards under normal circumstance there should be no variation in the concentration of the constituents of water. On the contrary variation in the ionic concentration of groundwater is expected in the direction of groundwater flow specifically nearby landfill site. The pH value for groundwater samples is slightly acidic to neutral in which the range is from 5.15-8.93. These values are exceeding WHO limits and the B.I.S standards permissible limit for portable drinking water.

The pH value of water has no obvious effects on the consumers, but gives an indication that water is sli ghtly acidic for GW-4 and GW-5 and was found basic for GW-1. The EC of water is reflection of the quantity of ionic constituents dissolved in it. The obtained EC ranges between 3360-4620µS/cm for groundwater samples. The maximum value of 4620µS/cm was measured for GW5; this value is higher than the recommended standard by WHO and B.I.S for potable water. Highest value was observed for GW1, which is a strong indication of contaminant through landfill site. The concentration of TDS in water gives assistance in knowing the nature of quality or its salinity.

Table 2 Physicochemical charactertics of groundwater in Bawana area

	Unit	GW1	GW2	GW3	GW4	GW5	GW6	BIS max Limit	WHO max limit
pH		8.93	6.37	7.47	5.15	5.77	6.04	6.5-8.5	9.2
EC	µS/cm	4583	4280	4440	4387	4620	3360	-	-
TDS	mg/l	2220	2160.67	2112.3	1542.96	1564.6	1685.3	2000	1500
Cl	mg/l	1585	1693.98	1108.74	1202.86	428.10	807.21	1000	600
SO4	mg/l	73.91	96.89	186.4	112.4	84.7	73.42	400	400
PO4	mg/l	0.572	0.44	0.256	0.10	0.34	0.62		
COD	mg/l	-	-	-	-	-	-	-	-
BOD	mg/l	-	-	-	-	-	-	-	-
Ca	mg/l	86.61	113.58	92.01	78.27	68.28	87.24	200	200
Na	mg/l	85.62	64.29	56.23	33.53	54.58	48.25	-	200
K	mg/l	28.67	18.66	15.93	14.91	13.86	9.47	-	200
Mg	mg/l	58.64	54.02	40.64	28.16	19.5	17.68	30	150
Fe	mg/l	0.542	0.660	0.342	0.101	0.090	0.070	0.3	0.3
Cr	mg/l	0.116	0.112	0.088	0.076	0.064	0.085	0.05	
Cu	mg/l	0.291	0.265	.250	0.219	0.092	N.D	1.5	
Ni	mg/l	N.D	N.D	N.D	N.D	N.D	N.D		
Zn	mg/l	0.861	N.D	0.363	N.D	N.D	N.D	5.0	5.0
	Unit	GW1	GW2	GW3	GW4	GW5	GW6	BIS max Limit	WHO max limit
pH		8.93	6.37	7.47	5.15	5.77	6.04	6.5-8.5	9.2
EC	µS/cm	4583	4280	4440	4387	4620	3360	-	-
TDS	mg/l	2220	2160.67	2112.3	1542.96	1564.6	1685.3	2000	1500
Cl	mg/l	1585	1693.98	1108.74	1202.86	428.10	807.21	1000	600
SO4	mg/l	73.91	96.89	186.4	112.4	84.7	73.42	400	400
PO4	mg/l	0.572	0.44	0.256	0.10	0.34	0.62		
COD	mg/l	-	-	-	-	-	-	-	-
BOD	mg/l	-	-	-	-	-	-	-	-
Ca	mg/l	86.61	113.58	92.01	78.27	68.28	87.24	200	200
Na	mg/l	85.62	64.29	56.23	33.53	54.58	48.25	-	200
K	mg/l	28.67	18.66	15.93	14.91	13.86	9.47	-	200
Mg	mg/l	58.64	54.02	40.64	28.16	19.5	17.68	30	150
Fe	mg/l	0.542	0.660	0.342	0.101	0.090	0.070	0.3	0.3
Cr	mg/l	0.116	0.112	0.088	0.076	0.064	0.085	0.05	
Cu	mg/l	0.291	0.265	.250	0.219	0.092	N.D	1.5	
Ni	mg/l	N.D	N.D	N.D	N.D	N.D	N.D		
Zn	mg/l	0.861	N.D	0.363	N.D	N.D	N.D	5.0	5.0

The obtained concentrations of TDS in GW in the study area vary between 1542.96- 2220mg/l. A high value of2220 mg/l is measured for GW1, followed by GW2 with a value of 2160 mg/l and least value is observe d of 1542.96 mg/l for GW4. According to WHO high level of TDS may be responsible for reduction in the palatability of water, inflict gastro-intestinal inconveniences in human and may also cause laxative effect particularly upon transits. These TDS values tend to decrease with distance of groundwater wells from the refuse dumpsite, along groundwater flow paths in down gradient direction. In addition, the work of [16] has established measurable high level of TDS concentration as an indication of contamination of groundwater near refused dumpsite. High concentrations of dissolved solids increases the density of water, affects regulation of fresh water organism, and reduces solubility of gases like oxygen and utility of water for drinking, irrigational and industrial purposes. The concentration of Ca^{2+} and Mg^{2+} ions in natural water influences its hardness, which is the ability of the water to form lather with soap. Total hardness actually reflects the total concentration of Ca^{2+} and Mg^{2+} in mg/l, equivalent $CaCO_3$. Source of calcium and magnesium can also be through weathering of underground rocks present. The value of Ca^{2+} ranged from 68.28 to 113.58 mg/l, the highest recorded value, is for GW2 and the least

value for GW4. The concentration of Ca2+ is below permissible range of WHO and BIS standards for potable groundwater, it has been known that consumption of water with very high concentration of Ca2+ may leads to concretion in kidney or bladder stone and also causes irritation in urinary passage [5]. Magnesium concentration is between 17.68 - 58.64 mg/l, highest at 1st, also at 2nd, 3rd location are more than BIS standard but are under WHO standards. The concentrations of Chloride is in the range of 1693.98 to 428.10 mg/l and significant proportion was found in GW2 and GW1 sampling location. High quantity of Chloride concentrations in water is indicator for pollution and as tracer for groundwater contamination [17]. Domestic effluents, fertilizers, septic tank and natural sources such as rainfall and dissolution of fluid inclusion are some of the sources that may contribute to high Chloride concentration in groundwater and thus causing pollution, other than leaching from landfill and high concentration of Cl- is detrimental to people with heart diseases and Kidney problem. The value of Na+ ions in the water samples varied from 85.62 to 33.53 mg/l. The highest value is associated with GW1 and lowest with GW4. Comparatively higher values are observed at GW5 that may have been due to geology of area or due to anthropogenic source. The consumption of water with high concentration of Na+ ions is inimical to people with cardiac, renal and circulatory diseases [5] Testing of sample has demonstrated the presence of potassium in groundwater sample. The value of K+ in the groundwater samples varied from 28.67 to 9.4 mg/l, highest at GW1 and lowest being at GW6. Phosphate is found to be present in minimal quantity of 0.62 to 0.1 mg/l, with GW6 having the maximum value of 0.62mg/l, source of it might the agricultural activities which being carried out in the area on small scale GW4 with a minimum value of 0.1. A minute value of phosphate as low as 0.01mg/l in groundwater may result in the water being slimy and also promotes the growth of algal [18]. The range of the concentration of sulphate in ground water samples varied from 186.40mg/l to 73.42 mg/l and was significantly higher in GW3 than the other. High quantity of sulphate in water is dangerous as it causes dehydration and diarrhea in children than adults [19]. COD concentration was not detected in any location.

Among the heavy metals analyzed, Fe2+ has the maximum concentration of 0.66 mg/l. The obtained va lue for GW1, GW2 are evidently higher than the 0.3mg/l standard requirement for portable drinking water but GW4, GW5 and GW6 fall within the standard stipulated by the B.I.S and WHO standards. The colour of ground water samples at all locations was colorless this however conforms to [20] findings, that a change in colour is often expected in groundwater which contains Fe2+. Total chromium present, varied from 0.116 to 0.085mg/l and concentration in groundwater is above permissible limit at all locations, highest is observed at GW1. Heavy doses of chromium salts even though are rapidly eliminated from human body, could corrode the intestinal tract [14]. There is minute concentrations of the following heavy metals are detected in the groundwater samples and are below the required standard for portable drinking water of B.I.S and WHO. This includes Cu with a concentration of 0.259mg/l and went undetected for GW6, at all location is well under limits. Consumption of high levels of copper can cause nausea, vomiting, diarrhea, gastric complaints and headaches. Long term exposure over many months and years can cause liver damage and death's was detected at only 1st and 3rd location of sample locations and are 0.861 and 0.363 mg/l respectively. These are in the minute concentrations and assumption has been made that they have come from the underground soil stratum. Nickel was not detected at any locations nearby landfill, which is acceptable as there was no concentration achieved in leachate also. The groundwater samples analyzed indicated trend of reducing contaminant concentration at increasing radial distances away from the landfill site for all contaminants studied but variation of concentration is totally justified as the concerned area is confined by various industries of plastic, metals etc.

3.3 Correlation Coefficient analysis

Pearson correlation is a descriptive method used to evaluate the degree of interrelation and association between two different variables. A correlation of positive sign indicates a perfect positive relationship between two variables. A correlation of negative sign indicates that one variable changes inversely with relation to the other.

Table 2. Correlation matrix for different ground water quality parameters

Parameter	pH	EC	TDS	Cl	Ca	Mg	Po4	Na	K	COD	BOD	Fe	Cu	Cr	Zn
pH	1														
EC	-0.96	1													
TDS	0.19	0.102	1												
Cl	0.083	0.21	0.994	1											
Ca	0.668	-0.42	0.857	0.796	1										
Mg	0.797	-0.59	0.745	0.668	0.982	1									
Po4	-0.84	0.961	0.371	0.47	-0.159	-0.342	1								
Na	0.87	-0.98	-0.317	-0.418	0.215	0.396	-0.998	1							
K	0.858	-0.97	-0.339	-0.439	0.192	0.374	-0.999	0.999	1						
COD	-0.68	0.434	-0.851	-0.789	-0.999	-0.984	0.17	-0.226	-0.2	1					
BOD	-0.48	0.203	-0.952	-0.914	-0.973	-0.912	-0.072	0.015	0.039	0.97	1				
Fe	0.28	0.011	0.995	0.979	0.901	0.803	0.284	-0.229	-0.25	-0.896	-0.98	1			
Cu	-0.54	0.76	-0.425	0.794	-0.83	-0.92	0.682	-0.723	-0.71	-0.254	0.679	-0.5	1		
Cr	0.687	-0.87	0.581	0.666	0.08	-0.109	0.971	-0.956	-0.96	-0.068	-0.31	0.5	0.49	1	
Zn	-0.72	0.88	0.55	0.637	0.042	-0.147	0.979	-0.966	-0.97	-0.03	-0.27	0.5	0.52	1	1

A correlation of zero indicates that there is no relationship between the two variables. TABLE 2 represents the correlation matrix table among fifteen ground water quality parameters of groundwater of the study area. TDS showed a higher significant positive correlation with most of water quality parameters like Cl (r=0.994), Ca (r=0.857), Mg (r=0.745), Fe (0.995), which indicates that presence of TDS in leachate effects presence of above parameters also. Similarly positive correlation of chlorine with magnesium, iron, copper, chromium, zinc was obtained. This suggested that presence of TDS, pH strongly influences the presence of chloride, calcium, iron, copper and various other compounds whose value is obtained more than 0.55. Most of the parameters were found to bear statistically significant correlation with each other indicating close association of these parameter with each other.

IV. Conclusion

The study primarily indicated that Narela-Bawana landfill cumulatively generates significant amount of leachate which contains higher concentration of heavy metals and other cations. The groundwater samples around all these landfills is also contaminated having heavy metals and other cations and anions more than recommended by BIS and WHO standard for drinking water. The spatial, distributions of all these heavy metals indicate possible leaching of contaminant from landfill. The analyzed groundwater samples obtained from the vicinity of the landfill dump site did not evidently reflect water quality that is affected by the leachates collected from the refuse landfill site.

Nevertheless the elevated values of EC, TDS, chloride, iron, copper and chromium obtained, strongly depict the influence of leachates on the groundwater quality and may pose serious threat to groundwater quality in the distant future. The groundwater sample analysis result clearly indicated that the trend of reducing contaminant concentration at increasing radial distances away from the landfill site for all contaminates studied.

REFERENCES

[1]. Naveen, A.K. Sharma, P.V. Sivapullaiah, Sitharam, Characteristics of the leachate from MSW landfill, Bangalore, journal of Geosynthetics India, 2013, 23-29.

[2]. Ohwoghere–Asuma, Leachate Characterization and Assessment of Groundwater and Surface Water Qualities Near Municipal Solid Waste Dump Site in Effurun, Delta State, Nigeria, Journal of Environment and Earth Science 2013 3(9)

[3]. Bharat J. and Singh S. Groundwater contamination due to Bhalaswa landfill site in New Delhi, International Conference on energy and environment. India, 2009, 2070-3740.

[4]. S. Kanmani, R. Gandhimathi, Investigation of physicochemical characteristics and heavy metal distribution in ground water system around open dump site, Appl Water Sci 2013, 10, 1-13

[5]. Suman Mor, Khaiwal Ravindra, R. P. Dahiya and A. Chandra, Leachate Characterization and assessment of groundwater pollution near municipal solid waste landfill site, Waste Manage 2006, 26(4):381–388.

[6]. Vijaya Singh and A.K.Mittal, Toxicity analysis and public health aspects of municipal landfill leachate: a case study of Okhla landfill, Delhi, 2009, 8 World Wide Workshop for Young Environmental Scientists

[7]. Rajkumar Nagarajan, Subramani Thirumalaisamy and Elango Lakshumanan, Impact of leachate on groundwater pollution due to non-engineered municipal solid waste landfill sites of erode city, Tamil Nadu, India, Iranian journal of Environmental Health Science &Engineering 2012, 9, 35.

[8]. Vikash Talyan , R.P. Dahiya , T.R. Sreekrishnan, State of municipal solid waste management in Delhi, the capital of India, Waste Management , 2008, 28, 1276–1287

[9]. [Ramky Enviro Engineers limited Establishment of integrated municipal solid waste management facility" at Narela- Bawana notified site, Delhi, 2010

[10]. Delhi urban environment and infrastructure improvement project. Government of National Capital Territory of Delhi, 2001.

[11]. APHA Standard methods for the examination of water and wastewater Washington, American Public Health Assoc 1994, 20th ed

[12]. Kjeldsen, P., Barlaz, M.A., Rooker, A.P., Baun, A., Ledin, A. and Christensen, T.H. Present and long-term composition of MSW landfill leachate. Env. Sci. Technol., 2002, 32, 4, 297-336.

[13]. Stephen C. James, BS, MSCE; Metals in Municipal Landfill Leachate and Their Health Effects, AJPH 1977, 67, 5

[14]. Bureau of Indian Standards (BIS), Indian standard specification for drinking water, IS 1991, 10500, 2-4.

[15]. WHO (World Health Organization), Guideline for drinking water quality, 1997, 2(2), Geneva, pp 940-949

[16]. Olaniya, M.S. and K.L. Saxena.: Groundwater pollution by open refuse dumps at Jaipur. Environ. Hlth.1977, 19, 176-188.
[17]. Loizidou, M., and E. Kapetanios, Effect of leachate from landfills on underground water quality, Sci. Total Environ, 1993 128, 69–81.
[18]. Adekunle, I.M., M.T. Adetunji, A.M. Gbadebo, and O.B. Banjoko, Assessment of Groundwater Quality in a Typical Rural Settlement in Southwest, Nigeria. Int. Journal of Environment and Public Health, 2007, 4(4), 307-318.
[19]. Longe, E.O. and M.R. Balogun., Groundwater Quality Assessment near a Municipal Landfill, Lagos, Nigeri., Research J. of Applied Sci, Eng and Technology, 2010, 2(1): 39-44.
[20]. Rowe, R. K., R. Q. Quigley and J. R. Booker, 1995. Clay Barrier Systems for Waste Disposal Facilities, E & FN Spon, London, UK

ISSN: 2319-5967
ISO 9001:2008 Certified
International Journal of Engineering Science and Innovative Technology (IJESIT)
Volume 3, Issue 5, September 2014

Modelling of Contaminant Transport from Landfills

Archana Chawla[1], Dr. S.K. Singh[2]
[1]Research Scholar, [2]Professor and HOD
Department of Environmental Engineering, Delhi Technological University, New Delhi

Abstract: ***Amongst all hydrological and environmental problems the most typical one is ground water contamination. Waste material is to be placed in engineered landfill as ground water contamination can take place due to landfill leachate. In order to design engineered landfill mathematical models proposed for the landfill. The general model of the ground water layer include various hydro geological process as contaminant transport, mechanical dispersion, molecular diffusion, sorption, chemical reactions, etc. the time behaviour of a contaminated ground water layer is to be predicted for practical situation. Realistic data for mathematical model is to be analysed using realistic results. Various soil parameters porosity, dispersivities, sorption, coefficients etc. are to be used in the model. The objective of this study is to develop and validate mathematical model that would address the problem of migration of contaminants from the bottom of landfill. This concentration was found to be in a consonance with the simulated concentration with chloride and sodium in ground water considering one dimensional transport model. Governing equation of contaminant transport involving advection-diffusion using explicit finite difference method with upwind correction.***

Keywords- **Groundwater, Sodium, Chloride, Solid Waste.**

I. INTRODUCTION

Human activities create waste, and the disposal of these wastes has been an important issue for human society. The methods of handling, storing, collecting and disposing of these wastes can pose risk to the environment and to public health [1]. A landfill site is defined as a tip, dump, rubbish or dumping ground and it is a site for the disposal of waste material by burial. It is one of the oldest methods to treat waste. Landfills are an essential part of everyday living but they may contaminate groundwater as well as surface water. In the United States, plastic liners were used to protect groundwater quality. The design and operation of landfill facilities are essential with respect to aesthetic, safety, and health problems [2]. To minimize the environmental impacts the design, construction and operation of the Modern landfill sites or engineered landfill sites are necessary. Production of leachate from landfill sites cause groundwater and surface water pollution. Also the generation of the landfill gas cause adverse health effects, explosive conditions, and global warming [3][4].

II. MECHANISMS OF CONTAMINANT TRANSPORT

When the leachate drifts over the top of liner, the leachate from landfill tends to migrate to the bottom of the aquifer carrying away with contaminant leached [5]. There is various mechanisms which account for the migration of leachate contaminant from landfill into barrier. The first mechanism consider in the groundwater system is due to advection transport which associated with mean flow or currents, such as rivers, streams, or tidal motion [6]. The second mechanism is diffusive transport of contaminant due to concentration gradient. Third mechanism is dispersion which involves the mixing of contaminant at relatively high flow[7]. Fourth mechanism is sorption which indicates a physical and chemical process by which one substance becomes attached to another [8].

Now considering the conservation of mass it is deduced that the increase in contaminant concentration within smaller region can be calculated from addition of increase in mass due to advective diffusion and decrease in mass due to sorption, which is given by equation (1)[9]. Where, f is the total mass flux represent by equation (2) which is the summation of flux due to advection, diffusion and dispersion, But in mathematical modelling diffusion and dispersion processes are lumped together to form a composite parameter, which is denoted by D_h called hydrodynamic dispersion coefficient. Which is given by summing these two coefficient i.e. $D_h = D_e + D_{md}$. (Hydrodynamic dispersion coefficient = effective molecular diffusion + mechanical dispersion)[10]. In clayey soil diffusion will usually control parameter than dispersion or diffusion can be important in vapour transport in unsaturated zone. In aquifer or saturated ground water flow dispersion is an important factor which dominant diffusion. So the governing equation of contaminant transport is expressed by equation (3). Where, R_f is

ISSN: 2319-5967
ISO 9001:2008 Certified
International Journal of Engineering Science and Innovative Technology (IJESIT)
Volume 3, Issue 5, September 2014

Retardation coefficient for freundlich isotherm, $R_f = 1 + \frac{\rho_d K_f c^{b-1} b}{n}$ where, b and K_f are the material constants for the soil- solute system and ρ_d is dry density[11][12][13].

$$n\frac{\partial c}{\partial t} = -\frac{\partial f}{\partial x} - \rho_d \frac{\partial S}{\partial t} \quad (1)$$

$$f = n v_a c - n D_h \frac{\partial c}{\partial x} \quad (2)$$

$$\frac{\partial c}{\partial t} = \frac{D_h}{R_f}\frac{\partial^2 c}{\partial x} - \frac{v_a}{R_f}\frac{\partial c}{\partial x} \quad (3)$$

This is the equation of advection diffusion which represents mathematical model of contaminant transport from landfill. Both boundary condition and initial conditions are needed to obtain solutions to any differential equation, and the advection Diffusion equation is one of them. Boundary conditions apply to specific locations in the modelled physical domain, and are usually specified in one of three ways[14].

Specify concentration (e.g. $C = C_0$ at $x = 0$), possibly time dependent. In combination with velocity, this gives advective flux.
Specify gradient (also possibly time-dependent), which in combination with the diffusivity, gives diffusive flux.
Specify total flux, as a (linear) combination of both diffusive and advective fluxes.

Boundary condition play a very important role in determining the behaviour of a particular solution, and care should be taken in specifying the correct condition for any given problem.

Initial condition $C (x \geq 0, t = 0) = 0$

Boundary condition $C (x = 0, t \geq 0) = C_0$

Boundary condition $C (x = \infty, t \geq 0) = 0$

III. NUMERICAL SOLUTION TO THE ADVECTION DIFFUSION EQUATION

The solution to the contaminant transport model represent by equation (3) subjected to boundary conditions and was implemented using the numerical method, explicit finite difference method with upwind correction describing the contaminant transport model for landfill include terms representing derivatives of continuous variable[15]. Finite difference method is based on the approximation of these derivatives by discrete linear changes over small discrete intervals of space and time.

General finite difference formulation for the solution to the one dimensional advection-diffusion equation assuming a conservative substance (no reactions) and constant v_a and D_h using a forward difference for the time derivative is given by equation (4). Where, ω is weighting factor that allows different weighting for implicit and explicit terms, with ω = 1 method is fully explicit Where α is the weighting factor for first spatial derivative α = 0, for backward difference, $\alpha = \frac{1}{2}$, for central difference put, $\alpha = \frac{1}{2}$ in equation (4) and resulting equation is given by equation (5) and References[16][17].

$$\frac{C_i^{m+1} + C_i^m}{\Delta t} = \frac{D_h}{R_f \Delta x^2}\{(1-\omega)\times(C_{i+1}^{m+1} - 2C_i^{m+1} + C_{i+1}^{m+1}) + \omega\times(C_{i+1}^m - 2C_i^m + C_{i-1}^m)\} - \frac{v_a}{R_f \Delta x}\{(1-\omega)$$

$$[\alpha\,(C_{i+1}^{m+1} - C_i^{m+1}) + (1-\alpha)(C_i^{m+1} - C_{i-1}^{m+1})] + \omega\,[\alpha(C_{i+1}^m - C_i^m)] + (1-\alpha)(C_i^m - C_{i-1}^m)\} \quad (4)$$

$$C_i^{m+1} = C_i^m - \frac{v_a \Delta t}{R_f \Delta x} \times \frac{1}{2}(C_i^m - C_{i-1}^m) + \frac{D_h \Delta t}{R_f \Delta x^2}(C_{i+1}^m - 2C_i^m + C_{i-1}^m) \quad (5)$$

ISSN: 2319-5967
ISO 9001:2008 Certified
International Journal of Engineering Science and Innovative Technology (IJESIT)
Volume 3, Issue 5, September 2014

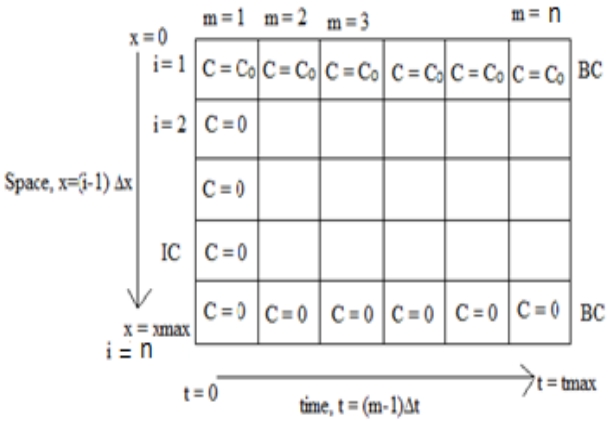


Fig 1: Schematic diagram of Finite Difference Method

The above equation can be arranged by keeping$K_1 = \frac{1}{2} \times \frac{v_a \Delta t}{R_f \Delta x}$, $K_2 = \frac{D_h \Delta t}{R_f \Delta x^2}$

$$C_i^{m+1} = C_i^m \times (1\text{-}2K_1\text{-}2K_2) + C_{i+1}^m \times K_2 + C_{i-1}^m \times (2K_1+K_2) \qquad (6)$$

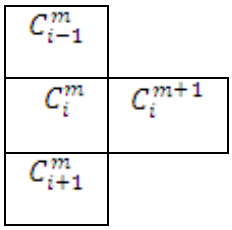


Fig 2: Finite Difference Method Node

Under condition of space Δx and time step Δt is the explicit 1-D finite method stable. The accuracy of explicit formulation is 0, (Δt, Δx^2) and for 1-D method it is numerically stable (stable means that the solution remain bonded) so long as the following stability criterion is met $\frac{D_h \Delta t}{R_f \Delta x^2} + \frac{1}{2} \times \frac{v_a \Delta t}{R_f \Delta x} \leq \frac{1}{2}$. Thus entire domain divided into m_n= T/Δt, and i_n = Z/Δx. Initial and boundary conditions are considered by keeping C_i^m at beginning of solution zero everywhere at the entire depth of the domain [18].

IV. VALIDATION OF MODEL

Model developed in this study was tested for two parameters of field data for an uncontrolled landfill at Huainan, China [19].Field data from this site was adopted to use to validate the numerical model. The field profile of chloride in the media was compared with the numerical model developed in the study. The results obtained by the mathematical model assuming pure diffusion. The effective diffusion coefficient of sodium for the soils was assumed to be 0.025 m^2/yr on the basis of the published data [20]. The retardation factor of the soils was assumed to be 1.5. This value is in the range of the published data (i.e., 1–5) provided by Rowe et al. (2004). The predicted migration depth of sodium assuming pure diffusion was about 2m. This value also underestimate the observed migration depth (i.e., about 4 m). The observed data fall into the range of the predicted curves using the advection–dispersion model. However, it is also difficult to obtain a well-fitted curve using the advection–dispersion model. The source concentrations of sodium, i.e., 5500 mg/L were used in the simulations. The data used for simulation of sodium and chloride are given below.

ISSN: 2319-5967
ISO 9001:2008 Certified
International Journal of Engineering Science and Innovative Technology (IJESIT)
Volume 3, Issue 5, September 2014

Table 1: Model parameters for Chloride (T.L.T. Zhan et al. 2014)

S.No.	Model Parameter	Unit	Value
1	Depth	m	7
2	Effective molecular diffusion coefficient	m^2/yr	0.023
3	Porosity		0.40
4	Retardation Factor		1.0
5	Advective Velocity	m/yr	0.04
6	Dispersivity	m	0.05

Table 2: Model parameters for Sodium (T.L.T. Zhan et al. 2014)

S.No.	Model Parameter	Unit	Value
1	Depth	m	4
2	Effective molecular diffusion coefficient	m^2/yr	0.025
3	Porosity		0.40
4	Retardation Factor		1.5
5	Advective Velocity	m/yr	0.275
6	Dispersivity	m	0.14

V. RESULTS AND DISCUSSION

The result of simulations was obtained for these cases are compared with the observed field data. The possible uncertainties in the chloride source function, comparison of the field data and numerical results were considered to be good if the model simulation fit the declining concentrations in the top 2-3 m of the profile. For greater depths, their model results did not agree with the observed data and the sharp localized concentration changes identified beyond 3 m were attributed to the variations in the source concentration within the landfill and due to unidentified changes in local geochemistry. In case of sodium simulated results match well with the observed values. The uncertainties in the sodium source function, is quite less as compared to chloride at the depths up to 9m. The simulated concentration of chloride and sodium with respect to depth is given in tables 3 and 4.

Table 3: Simulated and observed Chloride Concentration (17 years)

Depth (m)	Observed Chloride Concentration (mg/l)	Simulated Chloride Concentration (mg/l)
0.5	2528	2358
1.0	2253	1817
2.0	1209	1365
3.0	659	1146
4.0	604	1010
5.0	549	914
6.0	425	843
7.0	502	786

Table 4: Simulated and observed Sodium Concentration (17 years)

Depth (m)	Observed Sodium Concentration (mg/l)	Simulated Sodium Concentration (mg/l)
0.5	2803	2915
1.0	2441	2265
2.0	2441	1726
3.0	1265	1446
4.0	1305	1304
5.0	1185	1191
6.0	1157	1106
7.0	1129	1038

ISSN: 2319-5967
ISO 9001:2008 Certified
International Journal of Engineering Science and Innovative Technology (IJESIT)
Volume 3, Issue 5, September 2014

8.0	457	738		8.0	1156	981
9.0	412	697		9.0	1074	931

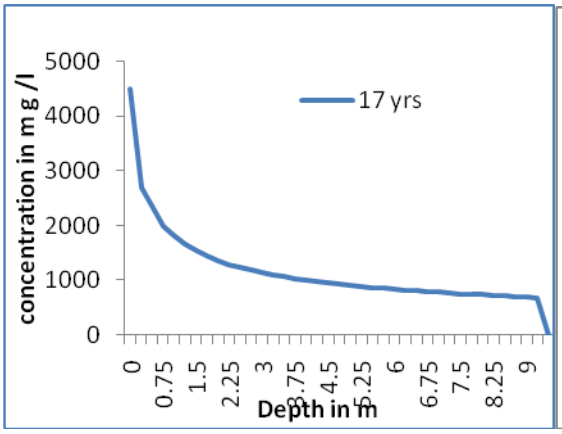


Fig 3: Results of chloride Concentration using Numerical Model of diffusion and advection

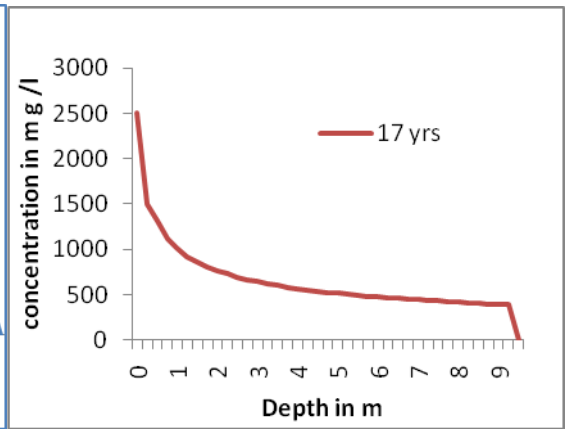


Fig 4: Results of sodiumConcentration using Numerical Model of diffusion and advection

VI. CONCLUSION

Mass transport of chloride and sodium from landfill leachate was modelled was taking into account the mechanism of contaminant transport advection and diffusion-dispersion and using the finite difference method with upwind correction. The model was solved and validated with the field data of solute transport (T.L.T. Zhan et al. 2014). Simulation of the validate model rum for two parameters. The possible uncertainties in the chloride source function, comparison of the field data and numerical results were considered to be good if the model simulation fit the declining concentrations in the top 2-3 m of the profile. For greater depths, their model results did not agree with the observed data and the sharp localized concentration changes identified beyond 3 m were attributed to the variations in the source concentration within the landfill and due to unidentified changes in local geochemistry.

The severity of the groundwater contamination is significant on account of associated complexity in pollution source identification, limited feasible options for treatment of groundwater all being cost prohibitive, complicated process in fixing geophysical boundaries, difficulty in prediction of movement, insufficient dilution, slow movement, lack of any natural cleansing capability. As a sizeable population in India is dependent on groundwater as the only source particularly densely populated, urgent attention to activities of solid waste disposal by land filling is highly needed.

REFERENCES

[1] Chris Zurbrugg (2003). "Solid Waste Management in Developing Countries", SWM introductory text on www. Sanicon.net.

[2] A.L. Ramanathan (2006). "Study of Groundwater Contamination through landfill site, NCT Delhi".

[3] Rowe RK and Quigely RM, Brachman RWI, Booker JR, (2004). "Barrier system for waste disposal facilities", London: Taylor and Francis.

[4] Young, A. (1989). "Mathematical modelling of landfill gas extraction, Journal of Environmental Engineering (ASCE), Vol. 115, pp 1973-1989.

[5] Kelley, W.E.(1976). "Groundwater pollution near a landfill", journal of environmental Engineering (ASCE), Vol. 10 pp 1129-1134.

[6] Rowe, R.k. and Badv, K. (1996a). "Advective-diffusive contaminant migration in unsaturated sand and gravel", Journal of Geotechnical Engineering (ASCE), Vol. 122, pp 965-975.

ISSN: 2319-5967
ISO 9001:2008 Certified
International Journal of Engineering Science and Innovative Technology (IJESIT)
Volume 3, Issue 5, September 2014

[7] Hillel Rubin, Joseph Atkinson, (July 2001). "Environmental Fluid mechanics", publisher Taylor and Francis, Edition 2 illustrated pp 423-488.

[8] Daichao sheng and David W. Smith (1999). "Analytic Solutions to the Advective Contaminant Transport Equation with Non-Linear Sorption", International journal for numerical and analytical methods in Geomechanics, Vol. 23, pp 853-879.

[9] Thornthwaite, C.W. and Mather, J.R. (1995). "The water balance", climatology, Vol. 8, pp 419-615.

[10] Bharat Jhamnani and SK Singh (2009). "Chloride Transport from Landfill". Journal of IPHE India. Vol 2009 2010, pp 2.

[11] Rowe, R.K. and Nadarajah, (1993). "Evaluation of the Hydraulic Conductivity of Aquitarde", Canadian Geotechnical Journal Vol. 30,No 5, pp 781-800.

[12] Conca, J.L. and Wright, (1990). "Diffusion coefficient in gravel under unsaturated conditions", Water resources research, Vol. 26, pp 1055-1066.

[13] Shakelford, CD., and Daniel, D.E. (1991). "Diffusion in Saturated Soil II: Results for Compacted Clay", Journal of Geotechnical Engineering (ASCE), Vol. 117, pp 485-506.

[14] Hillel Rubin, Joseph Atkinson, (July 2001). "Environmental Fluid mechanics", publisher Taylor and francis, Edition 2 illustrated, pp 423-488.

[15] B. Brunone, M. Ferrante, N. Romano and A. Santini, "Numerical Simulations of One-Dimensional Infiltration into Layered Soils with the Richards Equation Using Different Estimates of the Interlayer Conductivity."

[16] P.H. Benito (2004). "Finite Difference Approach to Solving ADE".

[17] Bharat Jhamnani and S.K. Singh, (2009). "Migration of Organic Contaminants from Landfill: Minimum Thickness of Barriers". The Open Environmental Pollution & Toxicology Journal, Vol. 1, pp 18-26.

[18] Bharat Jhamnani and SK Singh (2009). "Groundwater Contamination due to Bhalaswa Landfill Site in New Delhi", World Academy of Science, Engineering and Technology Vol. 3 pp 03-26

[19] T.L.T. Zhan, C. Guan, H.J. Xie, Y.M. Chen, (2014). "Vertical migration of leachate pollutants in clayey soils beneath an uncontrolled landfill at Huainan, China: A field and theoretical investigation", Science of the total Environment, Vol. 470-471, pp 290-298.

[20] Rowe RK and Quigely RM, Brachman RWI, Booker JR, (2004). "Barrier system for waste disposal facilities", London: Taylor and Francis.

Investigation on Multi-Response Parameter Optimization of Cold Spray Coating Process

Tarun Goyal[1]*, R.S. Walia[2] and T.S. Sidhu[3]
[1]*Professor, SUS College of Engineering and Technology, Tangori, Mohali, Chandigarh, India–140306*
[2]*Associate Professor, Delhi Technological University, Delhi, India–110042*
[3]*Director, SBSCET, Ferozepur, Punjab, India–152004*
*E-mail: *goyaltarun1@gmail.com, tarun_goyal2@rediffmail.com*

Abstract—*Cold spray (CS) process is a relatively new coating deposition thermal spray process and a lot of research is being carried out throughout the world towards the optimization of the process with an aim towards the performance improvement of the process. For optimization of process parameters, most of the existing approaches for multi response optimization of process parameters focus upon the subjective and practical knowledge available about the process. Keeping in view these limitations, an approach based on a Utility theory and Taguchi quality loss function (TQLF) has been applied to low-pressure cold spray (LPCS) process to deposit copper coatings, for simultaneous optimization of more than one response characteristics. In the present paper two potential response parameters i.e. coating thickness (CT) and micro hardness (MH) have been selected. Utility values based upon these response parameters have been analyzed for optimization by using Taguchi approach.*

Keywords: *Cold Spray (CS), Optimization, Taguchi Method, Utility Concept, Coating Thickness, Micro Hardness*

INTRODUCTION

The cold gas-dynamic spray method (CGSM), hereafter referred to simply as cold spray (CS), is a relatively new process by which coatings of ductile materials (or composite materials with significant ductile phase content) can be produced without significant heating of the sprayed powder. The kinetic energy of the particles is sufficient to produce large deformations and high interfacial pressures and temperatures, which appear to produce a solid-state bond [1]. Cold-spray processing was developed in the former Soviet Union more than a decade ago as an offshoot of supersonic wind tunnel testing [2, 3].

CS is a process of applying coatings by exposing a metallic or dielectric substrate to a high velocity (300–1200 m/s) jet of small (1–50 μm) particles accelerated by a supersonic jet of compressed gas. The two main clear cut distinctions of the Low pressure cold gas-dynamic spray (LPCGDS) system from the High pressure cold gas-dynamic spray (HPCGDS) system are: the utilization of low pressure gas (5–10 bars instead of 25–30 bars) and the radial injection of powder instead of axial injection. The accelerating gas (usually air or N_2) is injected at low pressure (5–10 bars) and preheated within the gas heater to temperatures up to about 400 °C to optimize its aerodynamic properties. Solid powder particles are radially introduced downstream of the throat section of the supersonic nozzle thus eliminating the need for a high pressure delivery system, which increases system portability, operational safety and significantly reduces spraying costs. Within the nozzle, static pressure is maintained below the atmospheric pressure ensuring that feedstock particles are effectively drawn in from the powder feeder by Venturi effect [4]. Fig. 1 shows a schematic of the LPCGDS system.

In the modern competitive non-conventional manufacturing scenario, it is most vital to optimize the parameters of a process to exploit its full utility. Practically,

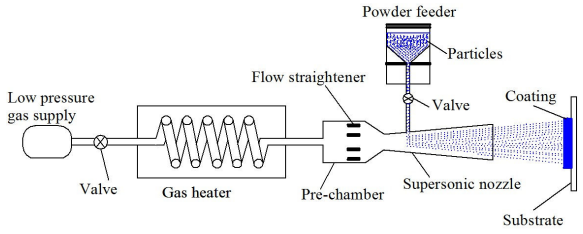


Fig. 1: A Typical LPCGDS Device [5]

it is seen that one particular setting of input parameters for a response characteristics may not be suitable for other characteristics of the process/product. In most of the manufacturing processes, more than one quality characteristics has to be considered for optimization of process parameters making it necessary that several response characteristics have to be simultaneously optimized. Based on the foregoing discussions, in this paper, Taguchi method is briefly reviewed for the multi-response optimization. The multi-response optimization of the response parameters of LPCS process is presented by using the experimental data. Optimization models have been developed by combination of the Taguchi Method and the Utility concept. The multi-response optimization of quality characteristics i.e. coating thickness and micro hardness of LPCS has been carried.

EXPERIMENTAL PROCEDURE

Table 1 show the process parameters that were identified as potential important in affecting the quality characteristics of the LPCS process under consideration [6]. The process parameters, their designated symbols and ranges are also given in Table 1.

The Taguchi's mixed level design was selected as it was decided to keep two levels of powder feeding arrangement. The rest four parameters were studied at three levels. The effect of selected process parameters was studied on the following response characteristics of LPCS process:

Table 1: Process Parameters and Their Range

Symbol	Process Parameters	Range	Level 1	Level 2	Level 3
A	Feed Type	Gravity, Argon	Gravity	Argon	--------
B	Substrate Material	Al alloy, Brass, Ni alloy	Al alloy	Brass	Ni alloy
C	Stagnation pressure	104–120 psi	104	112	120
D	Stagnation temperature	350–400^0 C	350	375	400
E	Stand-off distance	2.5–7.5 mm	2.5	5.0	7.5
Nozzle type: Converging-diverging, Carrier gas: Air, Powder size: < 45 μm					

Table 2: Experimental Results of Various Response Characteristics

Exp No.	Coating Thickness (mils) CT			S/N Ratio	Micro hardness ($H_{v0.3}$) MH			S/N Ratio
	R1	R2	R3	(dB)	R1	R2	R3	(dB)
1	28	26.2	30.4	28.95	122	126	124	41.86
2	52	51.5	52.2	34.30	134	129	132	42.38
3	74.5	74.2	74.7	37.43	131	132	122	42.15
4	58.4	58.2	58.7	35.33	126	128	124	42.00
5	44.7	44.1	45.4	33.01	124	125	128	41.98
6	25.8	24.3	25.5	28.01	126	127	128	42.07
7	14.7	11.2	14.6	22.39	129	131	132	42.32
8	55.1	55.6	55.5	34.86	137	133	134	42.58
9	53.9	54.5	54.3	34.68	134	135	139	42.66
10	68.9	64.1	69.7	36.57	123	118	111	41.36
11	38.6	38.2	38.7	31.70	119	115	117	41.36
12	58.2	57.5	57.9	35.24	126	131	129	42.18
13	43.2	43.3	43.6	32.74	125	121	122	41.77
14	28.3	27.2	25.5	28.60	110	119	113	41.12
15	64.8	65.4	64.6	36.24	122	120	124	41.72
16	56.9	57.1	59.5	35.23	129	125	127	42.07
17	57.9	56.2	56.7	35.10	125	127	128	42.05
18	17.3	19.1	16.7	24.91	123	128	132	42.11
Total	841.2	827.9	844.2	585.4	2265	2270	2266	755.80
	$\overline{T}_{CT}$ = overall mean of CT= 46.54				$\overline{T}_{MH}$ = overall mean of MH = 125.94			
R1, R2, and R3 represent repetitions								

a. Coating thickness (CT)

b. Micro hardness (MH)

Coating thickness and micro hardness are "higher the better" type of quality characteristics. A simplified multi-criterion methodology based on Taguchi's approach and utility concept (given below) is used to achieve the objective of this study. The observed values of response parameters are given in Table 2.

Utility Concept

Utility can be defined as the usefulness of a product or a process in reference to the expectations of the users. The overall usefulness of a process/product can be represented by a unified index termed as *Utility* which is the sum of the individual utilities of various quality characteristics of the process/ product. The methodological basis for Utility approach is to transform the estimated response of each quality characteristic into a common index.

If X_i is the measure of effectiveness of an attribute (or quality characteristic) i and there are n attributes evaluating the outcome space, then the joint Utility function can be expressed [7] as:

$$U(X_1, X_2, ...X_n) = f(U_1(X_1), U_2(X_2)....U_n(X_n)) \quad (1)$$

where $U_i(X_i)$ is the utility of the i^{th} attribute.

The overall Utility function is the sum of individual utilities if the attributes are independent, and is given as follows:

$$U(X_1, X_2, ...X_n) = \sum_{i=1}^{n} U_i(X_i) \quad (2)$$

The attributes may be assigned weights depending upon the relative importance or priorities of the characteristics. The overall utility function after assigning weights to the attributes can be expressed as:

$$U(X_1, X_2, ...X_n) = \sum_{i=1}^{n} W_i U_i(X_i) \quad (3)$$

where W_i is the weight assigned to the attribute i, the sum of the weights for all the attributes must be equal to 1.

Determination of Utility Value

A preference scale for each quality characteristic is constructed for determining its utility value. Two arbitrary

numerical values (preference number) 0 and 9 are assigned to the just acceptable and the best value of the quality characteristic respectively. The preference number (P_i) can be expressed on a logarithmic scale as follows [8, 9]:

$$P_i = A \times \log\left(\frac{X_i}{X_i'}\right) \quad (4)$$

where X_i = value of any quality characteristic or attribute *i*

X_i' = just acceptable value of quality characteristic or attribute *i*

A = constant

The value of *A* can be found by the condition that if $X_i = X^*$ (where X^* is the optimal or best value), then $P_i = 9$

Therefore, $$A = \frac{9}{\log \frac{X^*}{X_i'}}$$

The overall utility can be calculated as follows:

$$U = \sum_{i=1}^{n} W_i P_i \quad (5)$$

subject to the condition: $\sum_{i=1}^{n} W_i = 1$

Among various quality characteristics type viz. smaller the better, higher the better, and nominal the better, suggested by Taguchi, the Utility function would be higher the better type. Therefore, if the Utility function is maximized, the quality characteristics considered for its evaluation will automatically be optimized (maximized or minimized as the case may be).

ANALYSIS AND DISCUSSIONS

Based upon the methodology developed in the previous section, following case have been considered to obtain the optimal settings of the process parameters of LPCS for predicting the optimal values of combined responses. Two quality characteristics i.e. Coating Thickness (CT) and Micro hardness (MH) have been included in utility response.

Taguchi L_{18} orthogonal array (OA) [10] has been adopted for conducting the experiments. Powder feeding arrangement (A), Substrate material (B), air stagnation pressure (C), air stagnation temperature (D), and stand-off distance (E) were selected as input parameters. Response parameters (quality characteristics*)* were coating thickness and micro hardness, when they are optimized individually; the summary of results is produced in Table 3.

Table 3: Optimal Setting and Values of Process Parameters

Response Characteristics	Optimal Level of Process Parameters	Significant Process Parameters	Predicted Optimal Value of Quality Characteristics
CT	A2, B1, C3, D3, E2	A, B, C, D, E	72.36 mils
MH	A1, B3, C3, D2, E2	A, B, C, D, E	138.36 $H_{v0.3}$

Following is the stepwise procedure for transforming experimental data into utility data.

Construction of Preference Scales

(a) Preference scale for CT (P_{CT}):

X^* = Optimal value of CT = 72.36 (refer Table III)

X_i' = Just acceptable value of CT = 11 (All the observed values of CT are greater than 11)

Following equation is obtained from equation 4:

$$P_{CT} = 11.00 \times \log\left(\frac{X_{CT}}{11}\right) \quad (6)$$

(b) Preference scale for MH (P_{MH}):

X^* = Optimal value of MH = 138.36 (refer Table III)

X_i' = Just acceptable value of MH = 110 (All the observed values of MH are greater than 110)

Following equation is obtained from equation 4:

$$P_{MH} = 90.34 \times \log\left(\frac{X_{MH}}{110}\right) \quad (7)$$

Calculation of Utility Value

Equal weights (1/2 each) have been assigned to the selected quality characteristics assuming both the quality characteristics, are equally important. However, these weights can be varied depending upon the case or user requirements, if any.

The following relation was used to calculate the utility function based upon the experimental trials:

$$U(n,r) = P_{CT}(n,r) \times W_{CT} + P_{MH}(n,r) \times W_{MH} \quad (8)$$

where

$$W_{CT} = \frac{1}{2}; \qquad W_{MH} = \frac{1}{2}$$

n is the trial number (n = 1, 2, 3, …., 18) and *r* is the repetition number (r = 1, 2, 3). The calculated Utility values are shown in Table 4.

Analysis of Utility Data for Optimal Setting of Process Parameters

The average and main response in terms of Utility values and S/N ratio (Tables 5 and 6) are plotted in Figure 2. It can be observed from Figure 2 (i) to (v) that first level of powder feed arrangement (A1), Third level of substrate material (B3), Third level of air stagnation pressure (C3), first level of air stagnation temperature (D1) and Second level of stand-off distance (E2) are expected to yield a maximum values of the utility and S/N ratio within the experimental space.

The pooled version of ANOVA for utility data and S/N ratio are given in Tables 7 and 8 respectively. It can be noticed from Table 7 that all the input parameters have significant effect (at 95% confidence level) on the utility function. Similarly, it had been found from Table 8 that all the chosen parameters in study have significant effect on the S/N ratio of utility function.

Table 4: Calculated Utility Data Based on Responses CT and MH

Trial Number	Utility Values			S/N Ratio (dB)
	R1	R2	R3	
1	4.26	4.74	4.78	13.20
2	7.58	6.81	7.30	17.15
3	8.00	8.14	6.61	17.47
4	6.65	6.95	6.35	16.44
5	5.70	5.82	5.36	14.99
6	3.70	3.71	3.98	11.57
7	3.82	3.47	4.25	11.61
8	8.16	7.60	7.74	17.86
9	7.67	7.84	8.40	18.01
10	6.57	5.59	4.59	14.65
11	4.54	3.85	4.22	12.40
12	6.64	7.38	7.09	16.92
13	5.18	5.14	5.02	14.17
14	2.26	3.71	2.54	8.49
15	6.77	6.97	6.58	16.60
16	7.05	6.44	6.85	16.60
17	6.48	6.72	6.89	16.50
18	4.27	4.29	4.57	12.81

R1, R2, R3 = repetitions of experiments against each of the trial conditions

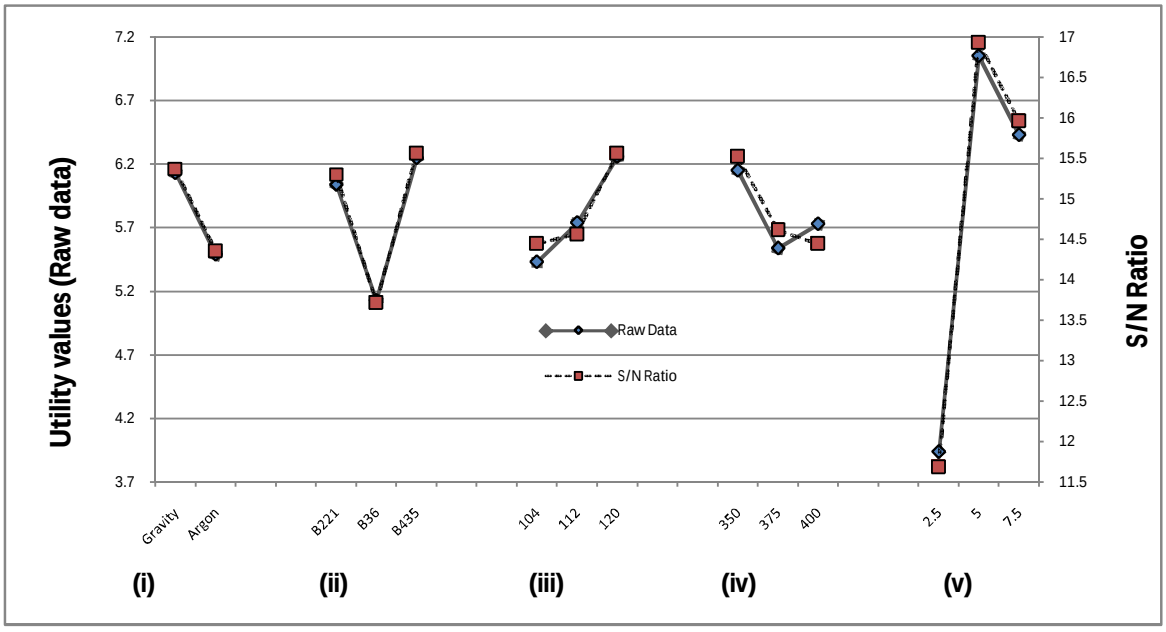


Fig. 2: Average and Main Response in Terms of Utility Values and S/N Ratio

Table 5: Average and Main Effects (Raw Data: CT and MH)

Process Parameter Designation	Average Utility Values			Main Effects		Difference
	L1	L2	L3	L2-L1	L3-L2	(L3-L2)-(L2-L1)
A	6.13	5.49	-	-0.64	-	-0.64
B	6.04	5.13	6.25	-0.91	1.12	2.03
C	5.43	5.74	6.26	0.31	0.52	0.21
D	6.15	5.54	5.73	-0.61	0.19	0.80
E	3.94	7.05	6.43	3.11	-0.62	-3.73

L1, L2 and L3 represents average values of raw data of corresponding parameters at levels 1, 2 and 3 respectively. L2-L1 is the average main effect when the corresponding parameter changes from level 1 to level 2. L3-L2 is average main effect when the corresponding parameter changes from level 2 to level 3.
A-Powder feed arrangement, B- Substrate material, C-air stagnation pressure, D-air stagnation temperature, E-stand-off distance.

Table 6: Average S/N Values and Main Effects (Raw Data: CT and MH)

Process Parameter Designation	S/N Average Values			Main Effects (dB)		Difference
	L1	L2	L3	L2-L1	L3-L2	(L3-L2)-(L2-L1)
A	15.37	14.35	-	-1.02	-	-1.02
B	15.30	13.71	15.56	-1.59	1.85	3.45
C	14.44	14.56	15.56	0.12	1.00	0.88
D	15.52	14.61	14.44	-0.91	-0.17	0.75
E	11.68	16.93	15.96	5.25	-0.97	-6.21

L1, L2 and L3 represents average values of S/N data of corresponding parameters at levels 1, 2 and 3 respectively. L2-L1 is the average main effect when the corresponding parameter changes from level 1 to level 2. L3-L2 is average main effect when the corresponding parameter changes from level 2 to level 3.
A-Powder feed arrangement, B- Substrate material, C-air stagnation pressure, D-air stagnation temperature, E-stand-off distance.

Table 7: Pooled ANOVA (Raw Data: CT and MH)

Source	SS	DOF	V	F-Ratio	SS'	P %
A	5.48	1	5.48	47.94*	5.37	4.01
B	12.68	2	6.34	55.48*	12.46	9.32
C	6.30	2	3.15	47.94*	6.08	4.54
D	3.46	2	1.73	15.13*	3.23	2.42
E	100.79	2	50.39	440.70*	100.56	75.18
E (Pooled)	5.03	44	0.11	-	6.06	4.53
Total (T)	133.76	53	-	-	133.76	100

*Significant at 95% confidence level. SS= Sum of Squares,
DOF= Degree of Freedom, V= Variance, SS'= Pure Sum of Squares

Table 8: S/N Pooled ANOVA (Raw Data: CT and MH)

Source	SS	DOF	V	F-Ratio	SS'	P %
A	4.65	1	4.65	12.53*	4.28	3.51
B	12.01	2	6.04	16.31*	11.36	9.31
C	4.52	2	2.26	6.10*	3.78	3.10
D	4.08	2	2.04	5.50*	3.34	2.74
E	93.63	2	46.82	126.22*	92.90	76.16
E (Pooled)	2.97	8	0.37	-	6.30	5.17
Total (T)	121.96	17	-	-	121.96	100

*Significant at 95% confidence level. SS= Sum of Squares,
DOF= Degree of Freedom, V= Variance, SS'= Pure Sum of Squares

Optimal Values of Quality Characteristics (Predicted Means)

The optimal values of utility and thus the optimal values of response characteristics in consideration are predicted at the above levels of significant parameters.

The average values of all the response characteristics at the optimum levels of significant parameters with respect to Utility function are recorded in Table 9.

The optimal values of the predicted means (μ) of different response characteristics can be obtained from the following equation:

$$\mu = A1 + B3 + C3 + D1 + E2 - 4T \quad (9)$$

where, A1-First level of powder feed arrangement, B3-Third level of substrate material, C3- Third level of air stagnation pressure, D1- first level of air stagnation temperature and E2-Second level of stand-off distance.

Table 9: Average Values of Various Responses at Optimal Levels of Utility Function

Levels	Coating Thickness, CT (mils)	Micro hardness MH (HVN)
A1	45.12	129.33
B3	42.60	130.44
C3	49.07	128.28
D1	50.21	125.28
E2	57.73	128.33

Note: The above average values are taken from experimental data

The 95% confidence interval of confirmation experiments (CI_{CE}) can be computed [10] by using the following equation:

$$CI_{CE} = \sqrt{F_{\alpha}(1, f_e) V_e \left[\frac{1}{n_{eff}} + \frac{1}{R}\right]} \quad (10)$$

where,

$F_{\alpha}(1, f_e)$ = The F-ratio at the confidence level of (1-α) against DOF 1 and error degree of freedom f_e , R = Sample size for conformation experiments, V_e = Error variance, $n_{eff} = \frac{N}{1+DOF}$ N= total number of trials, and DOF= Total degrees of freedom associated in the estimate of mean response.

(a) For Coating Thickness (CT)

$$\mu_{CT} = A1 + B3 + C3 + D1 + E2 - 4T_{CT} = 58.57$$

where A1 = 45.12, B3 = 42.60, C3 = 49.07, D1= 50.21, E2 = 57.73 (Table 9):

T_{CT} = 46.54 (Table 2)

The following values have been obtained by the ANOVA:

N = 54, f_e = 44, v_e = 2.00, n_{eff} = 5.4, R= 3, $F_{0.05}$ (1, 44) = 4.064

From equation 10, $CI_{CE} = \pm 2.05$

The predicted optimal range (for conformation runs of three experiments) for CT is given by

CI_{CE}: 56.52 < μ_{CT} < 60.62

(b) For Micro hardness (MH)

$$\mu_{MH} = A1 + B3 + C3 + D1 + E2 - 4T_{MH} = 137.9$$

where

A1 = 129.33, B3 = 130.44, C3 = 128.28, D1= 125.28, E2 = 128.33, (Table 9):

T_{MH} = 125.94 (Table 2)

The following values have been obtained by the ANOVA:

N = 54, f_e = 44; v_e = 19.77, n_{eff} = 5.4, R= 3, $F_{0.05}$ (1, 44) = 4.064

From equation 10, $CI_{CE} = \pm 6.45$

The predicted optimal range (for conformation runs of three experiments) for MH is given by

CI_{CE}: 131.45 < μ_{MH} < 144.35

Confirmation Experiment

For confirmation of experimental results, three experiments were performed at optimal settings as suggested by Taguchi analysis of Utility data. The observed values of various response characteristics have been given in Table 10. It can be noticed that overall average of the observed values of the response characteristics fall well within the 95% CI_{CE} of the optimal range of the respective response characteristics.

Table 10: Observed Values of Quality Characteristics (Confirmation Experiment)

Exp. No.	CT (mils)			MH ($H_{v0.3}$)		
	r_1	r_2	r_3	r_1	r_2	r_3
1	58.2	57.6	59.3	134	136	139
2	57.9	59.2	57.5	141	138	142
3	59.4	60.1	58.7	137	140	133
Overall Average	58.6			137.78		

CONCLUSION

The important conclusions of this research work are enlisted below:

1. Quality of coatings produced by LPCS process can be improved using Taguchi and Utility approach.
2. The selected input parameter significantly improves the Utility function (raw data and S/N ratio) comprising of quality characteristics (coating thickness and micro hardness).
3. The optimal setting of the process parameters for a multi-characteristic product can be predicted using the model.
4. The decreasing order of percentage contribution of the parameters to achieve a higher value of utility function is: stand-off distance (75.18%), substrate material (9.32%), air stagnation pressure (4.54%), powder feeding arrangement (4.01%) and air stagnation temperature (2.42%).

REFERENCES

[1] Papyrin, A.N. (2006), "Cold Spray: State of the Art and Applications", *Cold Spray Technology,* Albuquerque, NM, USA, pp. 1–2.

[2] Davis, J.R. (Ed.) *et al.* (2004), *Handbook of Thermal Spray Technology*, Materials Park, OH, USA, ASM International®, 1st Ed.

[3] Papyrin, A., Kosarev, V., Klinkov, S., Alkhimov, A. and Fomin, V. (2007), *Cold Spray Technology*, London, Elsevier.

[4] Maev, R. Gr. and Leshchynsky, V. (2008), *Introduction to Low Pressure Gas Dynamic Spray Physics and Technology*, Weinheim, Wiley2VCH.

[5] Grujicic, M., Zhao, C.L., Tong, C., DeRosset, W.S. and Helfritch, D. (2004), "Analysis of the Impact Velocity of Powder Particles in the Cold-gas Dynamic-spray Process", *Materials Science and Engineering A368, Elsevier*, pp. 222–230.

[6] Goyal, Tarun, Walia, R.S. and Sidhu, T.S. (2011), "Effect of Parameters on Coating Thickness for Cold Spray Process", *J. Materials and Manufacturing Processes*, Vol. 27, No. 2, pp. 185–192.

[7] Bunn, Derek W. (1982), *Analysis for Optimal Decisions*, New York, John Wiley and Sons, p. 275.

[8] Gupta, V. and Murthy, P.N. (1980), *An introduction to Engineering Design Methods*, New Delhi, Tata McGraw Hill, pp. 78–98.

[9] Kumar, P., Barua, P.B. and Gaindhar, J.L. (2000), "Quality Optimization (Multi-Characteristics) through Taguchi Technique and Utility Concept", *J. Quality and Reliability Engineering International*, Vol. 16, pp. 475–485.

[10] Roy, R.K. (1990), *A Primer on Taguchi Method*, New York, Van Nostrand Reinhold.

ISBN: 978-93-83083-98-5

3rd International Conference
On
"Innovative Approach in Applied Physical, Mathematical/Statistical, Chemical Sciences and Emerging Energy Technology for Sustainable Development"

(APMSCSET-2014)

CONFERENCE PROCEEDING

Editors:
Dr. B. B. Singh
Dr. G. C. Mishra
Dr. S. K. Yadav

Organized By
"Social Welfare Foundation"
In Association with "Krishi Sanskriti"
at
Jawaharlal Nehru University, New Delhi

Website link:
www.krishisanskriti.org/proceedings.html

First Impression: 2014

© Krishi Sanskriti
www.krishisanskriti.org

No part of this publication may be reproduced or transmitted in any form by any means, electronic or mechanical, including photocopy, recording, or any information storage and retrieval system, without permission in writing from the copyright owners.

DISCLAIMER

The authors are solely responsible for the contents of the papers compiled in this volume. The publishers or editors do not take any responsibility for the same in any manner. Errors, if any, are purely unintentional and readers are requested to communicate such errors to the editors or publishers to avoid discrepancies in future.

ISBN: 978-93-83083-98-5

Published by:
Krishi Sanskriti Publications
E-47, Rajpur Khurd Extn., Post Office – I.G.N.O.U. (Maidangarhi)
New Delhi-110068, INDIA
Contact No. +91-8527006560
Website: www.krishisanskriti.org

Typeset by
EXCELLENT PUBLISHING HOUSE
Kishangarh, Vasant Kunj, New Delhi – 110070
Tel.: 9910948516, 9958167102
E-mail: exlpubservices@gmail.com

3rd International Conference
On
"Innovative Approach in Applied Physical, Mathematical/Statistical, Chemical Sciences and Emerging Energy Technology for Sustainable Development"

(APMSCSET-2014)

ISBN: 978-93-83083-98-5

CONFERENCE PROCEEDING

3rd International Conference
On
"Innovative Approach in Applied Physical, Mathematical/Statistical, Chemical Sciences and Emerging Energy Technology for Sustainable Development"
(APMSCSET-2014)

Editors:
Dr. B. B. Singh
Dr. G. C. Mishra
Dr. S. K. Yadav

Published by:
Krishi Sanskriti Publications
E-47, Rajpur Khurd Extn., Post Office – I.G.N.O.U. (Maidangarhi)
New Delhi-110068, INDIA
Contact No. +91-8527006560
Website: www.krishisanskriti.org

Typeset by:
Excellent Publication Services
New Delhi-110070

Preface

September 28th, 2014

From the Desk of Editors……

On behalf of organizing committee, I extend my heartiest and warmth welcome to the distinguished delegates and participants of the ***3rd International Conference on Innovative Approach in Applied Physical, Mathematical/Statistical, Chemical Sciences and Emerging Energy Technology for Sustainable Development"*** *(APMSCSET-2014)* being held at Jawaharlal Nehru University, New Delhi, on 28th September, 2014, organized by Krishi Sanskriti. Surely, this Conference will help a lot to increase your knowledge bank. The conference is a source of powerful influence as it draws upon the expertise from various disciplines and also able to bring together leading authorities from academia, industry, R&D Institutions and sustainable management societies for focusing on innovative trends in *Applied Physical, Mathematical, Statistical, Chemical Sciences and Emerging Energy Technology* in order to achieve universal goal of sustainable development. The importance of this conference lies in the fact that during this duration, the feasibility of certain policies for innovations within the applied sciences and emerging energy technology as well as other applied engineering subjects with a special emphasis in physical, mathematical, statistical, chemical sciences in terms of harnessing eco-friendly technologies and its proper utilization in order to achieve sustainable development will be explored.

This conference will act as a major forum for the presentation of innovative ideas, approaches, developments and research projects in the area of theoretical as well as applied aspects for sustainable development. The (APMSCSET-2014) committee invited original Submissions from researchers, faculties, scientists and students that illustrate analytical research results, review works, projects, survey works and industrial experiences describing significant advances in the areas related to the relevant themes and tracks of the conferences. This effort guaranteed submissions from an unparalleled number of recognized top-level researchers. All the submissions underwent a strenuous peer-review process which comprised expert reviewers. Besides the members of the Technical Program Committee, external reviewers were invited on the basis of their specialization and expertise. The papers were reviewed based on their technical content, originality and clarity. The entire process which includes the submission, review and acceptance processes was done electronically. There were a total 110 submissions to the conference and the Technical Program Committee selected 60 papers for presentation at the conference and Subsequent publication in the International Journal as special issue. This small introduction would be incomplete without expressing our gratitude and thanks to the General and Program Chairs, members of the Technical Program Committees, and external reviewers for their excellent and diligent work. Thanks to the Jawaharlal Nehru University, New Delhi, for providing venue for this conference. Finally, we thank all the authors who contributed to the success of the conference. We also sincerely wish that all attendees will get benefited academically from the conference and wish them every success in their research Endeavour.



Dr. B. B. Singh
Editor



Dr. G. C. Mishra
Editor



Dr. S. K. Yadav
Editor

Contents

Preface **I**

RESEARCH PAPERS

1. **Upshot of Magnetic Field on Free and Force Convection FLOW in a Vertical Channel with Heat Transfer** **3**
   Abu Taher Mollah, Bidyapati Kumar
2. **On m-Open Sets in Topology** **7**
   Ankit Gupta, Ratna Dev Sarma
3. **Sustainable Development for All** **12**
   Ankur Singh
4. **Cost-Benefit Analysis of a Cold Standby System with Two-Stage Repair and Waiting Time Subject to Arrival Time of the Server** **14**
   Ashish Kumar, Monika Saini
5. **A Study of Exponential Mixture ROC Model** **18**
   Sudesh Pundir, Azharuddin
6. **Assessment of Soil Physico-Chemical Parameter for Sustainable Crop Planning in a Hilly Terrain of Assam** **27**
   Laxmi Narayan Sethi, Bornika Mandal, Racktackshree Chelleng
7. **Changing Role of Consumers in Imminent Smart Grids** **33**
   Damanjeet Kaur
8. **Application of Laplace-Differential Transform Method to Solve Non-linear PDEs with Boundary Conditions** **35**
   Kiranta Kumari, Praveen Kumar Gupta
9. **Inter-Annual and Spatial Rainfall Analysis for Environmental Restoration in Barak Valley of Assam** **41**
   Laxmi Narayan Sethi, Nitin Kumar, Doksiri Pegu
10. **Fritz John Type Optimality Criteria for Optimal Solution of Nonlinear Programming Problem** **47**
    Prashant Chauhan, Paras Bhatnagar
11. **On the k-Numbers of Some Generalized Kuratowski Operators in Topology** **50**
    Ratna Dev Sarma, Ankit Gupta
12. **Chi Square Divergence Measure and Their Bounds** **55**
    Ram Naresh Saraswat
13. **Mixture of Gompertz Regression Model with Different Frailty Distributions** **61**
    Richa Sharma, David D. Hanagal
14. **On Simultaneous Variation of Some Cosmological Parameters** **69**
    S K J Pacif, Abdussattar
15. **Application of Nanotechnology in Food Processing: A Promising Prospective with Considerable Risk** **75**
    Sanjib K. Paul, Sudipto Sarkar, Laxmi Narayan Sethi, Sujit K. Ghosh
16. **An Open Loop Method for Time Minimizing Transportation Problem with Mixed Constraints** **83**
    Swati Agarwal, Shambhu Sharma

17. **On Petri Net Generating all the Standard Basis for *n*-Dimensional Euclidean Space** **90**
Gajendra Pratap Singh

18. **Support Vector Regression (SVR) Model to Predict the Boiling/Non-boiling Length of the Heated Tube in a Vertical Tube Thermosiphon Reboiler** **93**
Sadaf Zaidi

19. **Temperature Dependent Effective Mass and Scattering Rate for the Heavy Electron System $CeAl3$** **103**
Prajwalit Shikha

20. **Experimental Evaporative Coolers for Vegetable Preservation** **106**
Ajay Kale, Kalyan Sundaram

21. **Application of Virtual Reality in Assessment and Enhancement of Cognitive Abilities of Military Personnel** **112**
Khushboo Bhargava, Kusum Gupta, Sushil Chandra, Ahsan Z Rizvi

22. **Data Science – A Statistical Modelling in Health Science** **115**
Sarojini G. Deshmukh, U. B. Aithal

ABSTRACTS

1. **Recent Developments and Future Role of Hydropower, Solar and Wind Energy Resources in India** **121**
Aditya Chauhan, Ganesh Panday, Sachin Chauhan, Jagdish Singh Mehta

2. **Construction of PBIB Designs through Chosen Lines and Triangles of Graphs** **122**
Davinder Kumar Garg, Syed Aadil Farooq

3. **Comparative Study of Various Evapo Transpiration Methods** **123**
Er. Daria Singh, Jodhpur

4. **Impedance and Dielectric Spectroscopy of Nano-Graphite Reinforced Silicon Elastomer Nanocomposites** **124**
Janita. Saji, A. Khare, S.P. Mahapatra

5. **Moments of Order Statistics from Lindley Distribution in the Presence of Multiple Outliers** **125**
Mahesh Kumar Panda

6. **Vapor Phase Alkylation of Aniline Over Ferrite Nanoparticles** **126**
Malvika Kadian, R.K Gupta

7. **Sequential Testing Procedures in a Family of Lifetime Distributions with Applications** **127**
Md. Wasi Alam

8. **Chaos in Science and Engineering** **128**
Mohammad Sajid

9. **Axisymmetric Deformation in Transversely Isotropic Thermoelastic Media** **129**
Nidhi Sharma, Parveen Lata

10. **Impact of two Temperature in Thermoelastic Media** **130**
Nidhi Sharma, Parveen Lata

11. **Schiff Bases of Heterocycles and their Metal Complexes: Synthesis, Spectral, Thermo- analytical and Biological Applications** **131**
Sangamesh A. Patil, Bhimashankar M. Halasangi, Prema S. Badami

12. **Application of Electro-chromic Tungsten Oxide Nano Wires to Determine Bioelectrogenesis in Microbial Fuel Cells** **132**
Sharma I., Ghangrekar M.M.

13. **Evaluation of Selected Medicinal Plants to judge their Confirmation as Anti-Diabetic Using Mathematical and Statistical Techniques** **133**
Sonia Sharma, Rachit Kumar, Hemlatha Vasishtha, Deepankar Sharma

14. **Probabilistic Analysis of a Standby System with Provision of Priority of Repair** **134**
Upasana Sharma, Jaswinder Kaur

15. **Synthesis and Characterization of Porous Coordination Complex/Polymer from Cashew Nut Shell Liquid (CNSL): A Sustainable Development** **135**
Fahmina Zafar, Hina Zafar, Eram Sharmin, Nahid Nishat

16. **Use of Adomian and Restarted Adomian Methods for Solving Algebraic Equations** **136**
Mohammad Danish

17. **Biologically Active and Thermally Stable Polymeric Schiff Base and Its Coordination Polymers with Some Divalent Transition Metals Ions** **137**
Raza Rasool, Nahid Nishat

18. **Homogeneous CO_2 Emission using Fuzzy Clustering** **138**
K. Ranganathan, Manish Kumar Goyal

19. **Application of Nanotechnology in Medical Sciences Specially for Treating Cancer and Tumor** **139**
Vineeta Jain

RESEARCH PAPERS

Upshot of Magnetic Field on Free and Force Convection FLOW in a Vertical Channel with Heat Transfer

Abu Taher Mollah[1], Bidyapati Kumar[2]

[1]*Dept. Mathematics, Pramathesh Barua College, Gauripur, Dist. Dhubri, Assam, Pin. 783331, India*
[2]*Professor, University Department of Mathematics, B.R. A. B. University, Muzaffarpur*

Abstract: **The problem of applied magnetic field on free convective flow in a vertical channel with heat transfer is taken for discussion to understand the magnetic upshots. A uniform magnetic field is applied normal to the plate. The equation governing the fluid flow and heat transfer have been solved subject to the relevant basic equations and boundary conditions. It is noticed that the magnetic field M has considerable effect on u, θ, τ_W, τ_1, Nu_1 . All the profiles increases with M. The behaviour of the fluid velocity U for α > 0 is reversed to the normal velocity V for α = 0, however both are diminishing sharply.**

1. INTRODUCTION

In recent years the problem of the free convective flow of a viscous fluid over a uniformly moving long vertical wavy wall and a parallel flat wall has got a threadbare response from research scholars with a view to understanding its application in transportation cooling of re-entry vehicles and rocket boosters, cross- hatching on ablative surfaces and film vaporization in combustion chambers. Lekoudias, Nayfeh and Saric are pioneering contributor in this field because they have discussed linear analysis of compressible boundary layer flows over a wavy wall. The Rayleigh problem for a wavy wall and amplitude wall waviness upon the stability of the laminar boundary layer have been discussed by lessen and Gangwani (1976). The free convection heat transfer in viscous incompressible fluid between a long vertical wavy wall and a parallel flat wall was presented by Vajravelu and Sastri (1978). Free convection heat transfer in a viscous incompressible fluid between a uniformly moving long vertical wavy wall and a parallel flat wall have been discussed by S. Ahmed et al. (2002). The aim of the present exploration is to find out the effects on the uniform magnetic field applied normal to the direction of main flow with a view to make an extension of the study done so far by S. Ahmed et al. (2002) in this field.

2. BASIC EQUATIONS

We consider the two dimensional steady laminar free convective MHD flow along the vertical channel as shown in Fig. 1.

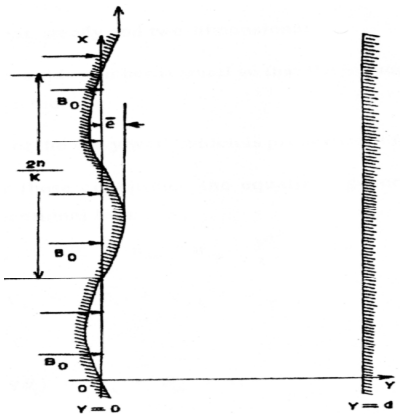


Fig. 1. Flow Configuration

In the channel, $\bar{X}$-axis is taken along the flat wall and the $\bar{Y}$-axis is taken perpendicular to it. Moreover, $\bar{T}_W$ and $\bar{T}_1$ are the constant temperatures at the respective wavy wall $\bar{Y}=\bar{\varepsilon}\cos\bar{k}\bar{x}$ and the flat wall $\bar{Y}$= d.

In view of this, we consider that:

1) Except density in the resilience force, fluid properties are constant.

2) In energy equation, the viscous and magnetic dissipative are meant to be ignored.

3) In context volumetric heat either source or sink does not change its energy equation.

4) The flow is laminar, balanced and two dimensional.

5) The magnetic Reynolds number is small so that the stimulated magnetic field can be abandoned.

6) The wave length of the wavy wall, which is proportional to K^{-1}, is large.

Under these conditions, the equations governing the fluid motion in non-dimensional form are:

$$uu_x + vu_y = -p_x + u_{xx} + u_{yy} - 1\frac{gd^3}{v^2} - Mu \qquad (4.2.1)$$

$$uv_x + vv_y = -P_y + V_{xx} + V_{yy}, \qquad (4.2.2)$$

$$u_x + v_y = 0, \qquad (4.2.3)$$

$$p(u\theta_x + v\theta_y) = \theta_{xx} + \theta_{yy} + \alpha \qquad (4.2.4)$$

Subject to the boundary conditions:

$$\left.\begin{array}{l} u = A,\ v = 0,\ \theta = 1, \text{ at } y = \varepsilon\cos\lambda x \\ u = v = 0,\ \theta = m \quad \text{at } y = 1 \end{array}\right\} \qquad (4.2.5)$$

The non-dimensional quantities introduced in the above equations are:

$x = \bar{x}/d$, $y = \bar{y}/d$, $u = d/\bar{u}$, $v = d/\bar{v}$,

$p = \bar{p}/\rho(\upsilon / d)^2$, $\theta = (\bar{T} - \bar{T}_s) / (\bar{T}_w - \bar{T}_s)$

$m = (\bar{T}_1 - \bar{T}_s) / (\bar{T}_w - \bar{T}_s)$, the wall temperature ratio,

$\alpha = Qd^2 / k (\bar{T}_w - \bar{T}_s)$, the heat source / sink parameter,

$P = \mu Cp / k$, the Prandtl number,

$\varepsilon = \bar{\varepsilon}/d$, the amplitude parameter

$\gamma = \bar{k}/d$, the frequency parameter,

$G = d^3 g\beta (\bar{T}_w - \bar{T}_s) / \upsilon^2$, the grashof number or free convection parameter,

$M = \sigma B_0^2 d^2/p\upsilon$, the Hartmann number

Where $\bar{u}$, $\bar{v}$ are velocity components, $\bar{p}$ fluid pressure, ρg the buoyancy force, Q the constant

Heat addition or absorption, B_0 the magnetic induction and the other symbols have their usual meanings.

Under the perturbations technique, let us assume that the flow field and temperature field are to be:

$$\left.\begin{array}{l} u(x, y) = u_0(y) + u_1(x, y), \\ v(x, y) = v_1(x, y) \\ p(x, y) = p_0(x) + p_1(x, y), \\ \theta(x, y) = \theta_0(y) + \theta_1(x, y), \end{array}\right\} \qquad (4,2,6)$$

Where the perturbations u_1, v_1, p_1 and θ_1 are small compared with the mean or the zeroth-order quantities.

On using (4.2.5), the equations (4.2.1) to (4.2.4), transformed to the non-dimensional form:

For zeroth order :

$$u_0'' - Mu_0 + G\theta_0 = C, \quad = \theta_0'' \qquad (4.2.7)$$

And for the first order:

$$u_o u_{1,x} + v_1 u_0' = -P_{1,x} + u_{1,xx} + u_{1,yy} + G\theta_1 - Mu_1 \qquad (4.2.8)$$

$$u_o v_{1,x} = -P_{1,y} + v_{1,xx} + v_{1,yy} \qquad (4.2.9)$$

$$u_{1,x} + v_{1,y} = 0 \qquad (4.2.10)$$

$$P(u_o\theta_{1,x} + v_1\theta_0') = \theta_{1,xx} + \theta_{1,yy} \qquad (4.2.11)$$

Where $c = (\frac{\partial p_0}{\partial x} - p_s)$ is the constant pressure gradient term and is taken equal to zero following Ostrach (1952) and subscript 's' stands for static fluid condition.

With the help of (4.2.6), the boundary conditions (4.2.5) can be split up into the following two parts:

$$\begin{array}{l} y = 0 : u_o = A,\ \theta_0 = 1 \\ y = 1 : u_o = 0\ \theta_0 = m \end{array} \qquad (4.2.12)$$

and

$u_1 = -\text{Re}\{\varepsilon u_0' e^{i\lambda x}\}$, $v_1 = 0$, $\theta_1 = -\text{Re}\{\varepsilon\theta_0' e^{i\lambda x}\}$ at $y = 0$

$$u_1 = 0,\ v_1 = 0,\ \theta_1 = 0 \text{ at } y = 1 \qquad (4.2.13)$$

Where the prime denotes differentiation w.r.t y.

3. METHOD OF SOLUTION FOR BOTH THE ORDERS

With the help of (4.2.12), the zeroth order solutions from the equations (4.2.7) have been obtained but are not presented here due to sake of brevity.

To find the first order solutions from the equations (4.2.8) to (4.2.11), let us introduce the stream function Ψ_1, defined by

$$u_1 = -\bar{\Psi}_{1,y}\ v_1 = \bar{\Psi}_{1,x} \qquad (4.3.1)$$

Where, $\bar{\Psi}_1(x,y) = \varepsilon e^{i\lambda x}\Psi(y)$, $\theta_1(x,y) = \varepsilon e^{i\lambda x}t(y)$

For small value of 1 (or K << 1), we consider:

$$\Psi(\lambda,y) = \sum_{i=0}^{2} \Psi_i,\ t(\lambda,y) = \lambda^i t_i \sum_{i=0}^{2} \qquad (4.3.2)$$

On using (3.1) and (3.2) into (2.8) – (2.11), to the order λ^2, the following sets of ordinary differential equations and corresponding boundary conditions :

$$\Psi^{IV}_0 - M\,\Psi_0'' = Gt_0',\ t_0'' = 0 \qquad (4.3.3)$$

$$\left.\begin{aligned} &\Psi^{IV}_1 - M\,\Psi_1'' = i(u_0\Psi_0'' - \Psi_0 u_0'') + Gt_1 \\ &t_1'' = iP\,(u_0 t_0 + \Psi_0 \theta_0') \end{aligned}\right\} \qquad 4.3.4)$$

$$\left.\begin{aligned} &\Psi^{IV}_2 - M\,\Psi_2'' = 2\Psi_0'' + i(u_0\Psi_1'' - \Psi_1 u_0'') + Gt_2'' \\ &t_2'' = iP\,(u_0 t_1 + \Psi_1 \theta_0') + t_0 \end{aligned}\right\} \qquad (4.3.5)$$

$$\left.\begin{aligned} &\text{and } \Psi_0' = u_0',\ \Psi = 0,\ t_o = -\theta'_0 \text{ at } y = 0 \\ &\Psi_{0/} = 0,\ \Psi_o = 0,\quad t_o = 0 \text{ at } y = 1 \end{aligned}\right\} \qquad (4.3.6)$$

$$\left.\begin{aligned} &\Psi_i' = \Psi_i = t_i = 0 \quad \text{at } y = 0 \\ &\Psi_i' = \Psi_i = t_i = 0 \text{ at } y = 1 \end{aligned}\right\} \text{ for } i \geq 1 \qquad (4.3.7)$$

With the help of (4.3.6) to (4.3.7), the solutions of the equations (4.3.3) to (4.3.4) have been obtained but not presented here due to sake of brevity. From these solutions, due to waviness of the wall, the expressions for u_1, v_1 and θ_1 are the first order solutions or the disturbed parts and they can be put into the form :

$$\left.\begin{aligned} &u_1 = \varepsilon[\Psi_i' \sin\lambda x - \Psi_r' \cos\lambda x], \\ &v_1 = -\varepsilon\lambda[\Psi_r \sin\lambda x - \Psi_i \cos\lambda x], \\ &\theta_1 = \varepsilon[t_r \cos\lambda x - t_i \sin\lambda x], \\ &\text{where}\quad \Psi = \Psi_1 + i\Psi_i \quad t = t_r + it_i \end{aligned}\right\} \qquad (4.3.8)$$

4. SKIN FRICTION AND HEAT TRANSFER COEFFICIENT AT THE WALLS

The non-dimensional skin friction at the wavy wall y = $\varepsilon\cos\lambda x$ and at the flat wall y = 1 are respectively:

$$\tau_u = \tau^0_0 + \varepsilon\cos\lambda x\,[u_0''(0) + \bar{u}'(0)], \qquad (4.4.1)$$

$$\tau_l = \tau^0_1 + \varepsilon\ \bar{u}_1(1)\cos\lambda x, \qquad (4.4.2)$$

Where $\tau^0_0 = u_0'(0)$ and $\tau^0_1 = u_0'(1)$ are the zeroth order skin frictions at the walls and

$u_1(x, y) = \varepsilon e^{i\lambda x}\bar{u}_1(y)$ and $v_1(x,y) = \varepsilon e^{i\lambda x}\bar{v}_1(y)$

The non-dimensional Nusselt Nu at the wavy wall y= $\varepsilon\cos\lambda x$ and at the flat wall y = 1 respectively:

$$Nu_w = Nu^0_0 + \varepsilon\cos\lambda x\,[\theta_0''(0) + t'(0)], \qquad (4.4.3)$$

$$Nu_1 = Nu^0_1 + \varepsilon\cos\lambda x\,[t'(1)], \qquad (4.4.4)$$

where $Nu^0_0 = \theta_0'(0)$ and $Nu^0_1 = \theta_0'(1)$ are the zeroth order skin frictions at the walls.

5. OUTCOME ANDDISCUSSION

All Mathematical computation are done in order to $\varepsilon = 0.05$, $\lambda = 0.5$. The action of the velocity profiles u, v and the temperature profile θ are illustrated in figs. 2 – 4 and they have been schemed against y as abscissa.

When $\alpha = 5$, the fluid velocity u increase as M (I, II, III) and A (I, IV, V), while it drop off with the augment of P (I, VI, VII). When $\alpha = 0$, the normal velocity v reduces with the boost of M and A, whereas v raises as K. When $\alpha = -5$, the q increases as M and P, but θ decreases with the increase of A.

Figures 5 to 8 show the behaviour of the skin frictions and the Nusselt numbers at the channel walls and they have been designed against α as abscissa. When G=0, the skin friction τ_w raises as raises as M and A, whereas τ_1 reduces with the increase of P. When G=0, the heat transfer coefficient Nu_w decreases with the increase of M, while Nu_w increases as A and P. Atlength, when G = 10, the Nu_1 heaves as M and P, but Nu_1 drops with the enhancement of A.

6. INFERENCE

The above mentioned outlines have made the following inferences -

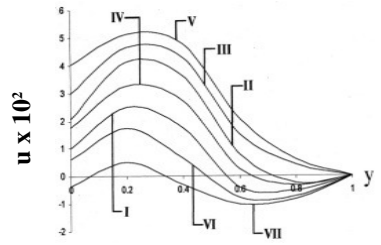
(i) The magnatic field M has considerably important effect on u, θ, τ_w, τ_1 and Nu_1. The outlines have augment inference.

(ii) The upshots of the parameters K, M, G on Nu_w for the air has been reversed to Nu_1 for the water.

(iii) The movement of the fluid velocity u for α>0 is not being directed to the normal velocity v for $\alpha = 0$, however both are diminishing keenly.

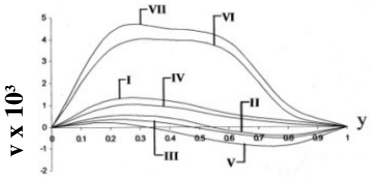
(iv) The result of v, θ, τ_w, Nu_w and Nu_1 is not being droped off with the P; but this result is reversed for u and τ_1.

(v) We see that u, τ_w, τ_l and Nu_w raised with or without plate velocity A. While this result is reversed to v, θ and Nu_l.



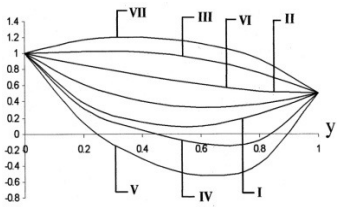
	M	A	P
I	1	0	0.71
II	7	0	0.71
III	15	0	0.71
IV	1	6	0.71
V	1	10	0.71
VI	1	0	7
VII	1	0	15

Fig. 2: Velocity profile u against y when m = 2, G =10, λx = 0



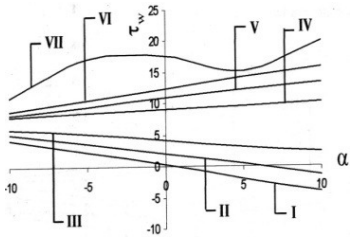
	M	A	P
I	1	0	0.71
II	7	0	0.71
III	15	0	0.71
IV	1	6	0.71
V	1	10	0.71
VI	1	0	7
VII	1	0	15

Fig. 3: Velocity profile V against y when m = 2, G =10, λx = $\frac{\pi}{2}$



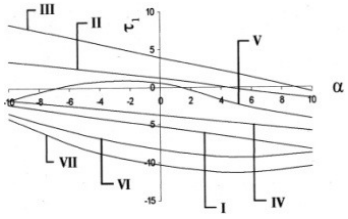
M	A	P	
I	1	0	0.71
II	7	0	0.71
III	15	0	0.71
IV	1	6	0.71
V	1	10	0.71
VI	1	0	7
VII	1	0	15

Fig. 4: Velocity profile V against y when m = 2, G =10, λx = $\frac{\pi}{2}$



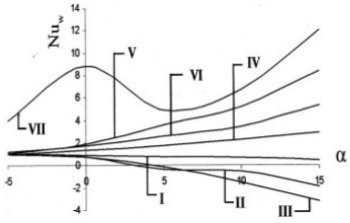
	M	A	P
I	1	0	0.71
II	7	0	0.71
III	15	0	0.71
IV	1	6	0.71
V	1	10	0.71
VI	1	0	7
VII	1	0	15

Fig. 5: Skin friction τ_w at y = 0 against α when m = 2, G = 0, λx = 0



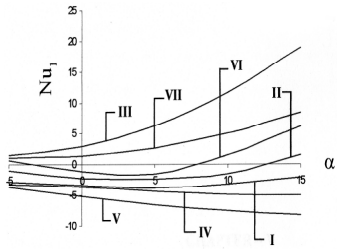
	M	A	P
I	1	0	0.71
II	7	0	0.71
III	15	0	0.71
IV	1	6	0.71
V	1	10	0.71
VI	1	0	7
VII	1	0	15

Fig. 6: Skin friction τ_l at y = 1 against α when m = 2, G = 10, λx = 0



	M	A	P
I	1	0	0.71
II	7	0	0.71
III	15	0	0.71
IV	1	6	0.71
V	1	10	0.71
VI	1	0	7
VII	1	0	15

Fig. 7: Heat transfer coefficient Nu_l at y = 0 against α when m = 2, G = 0, λx = 0



	M	A	P
I	1	0	0.71
II	7	0	0.71
III	15	0	0.71
IV	1	6	0.71
V	1	10	0.71
VI	1	0	7
VII	1	0	15

Fig. 8: Heat transfer coefficient Nu_1 at y = 1 against α when m = 2, G = 10, λx = 0

REFERENCE

[1] Lesen, M &Gangwani, S.T. (1976): Phys. Fluids 19, pp.510-513

[2] Vajravelu, K. (1978): Proc. Indian Acad.Sci., vol.87A, No.9 pp237

[3] Vajravelu, K Sastri, K.S. (1978): J.FluidMech, Vol.86, pt.2 pp. 365-83

[4] Vajravelu, K Sastri, K.S. (1980): Int, J. Heat and Mass transfer, Vol.23, pp-408

[5] Ahmed, Sahin (2002): J.CalMath.Soc. India, 100,(4) pp. 349-358

On m-Open Sets in Topology

Ankit Gupta[1], Ratna Dev Sarma[2]

[1]*Department of Mathematics, University of Delhi, Delhi 110007, India.*
[2]*Department of Mathematics, Rajdhani College, University of Delhi, Delhi 110015, India*

Abstract: **Minimal open sets or m-open sets for a topology are defined and investigated. They are found to form an Alexandroff space on X. Decompositions of open sets and continuity are provided using$m$-open sets.Also$m$-regularity and m-normalityare defined and studied. While Hausdorffness implies m-regularity, the product of normal spaces are found to be m-normal. 2010 Mathematics Subject Classification: Primary 54A05, 54A10, 54C08.**

Keywords and phrases: **Open set, Continuity, regularity. Corresponding author: Ratna Dev Sarma.**

1. INTRODUCTION

Now a days topological approaches are being investigated in a big way in various diverse field such as computer graphics, evolutionary theory, robotics etc.[6, 9, 16] to name a few. One such approach to computer graphics utilizes finite, connected order topological space[8]. In a finite topological space, the intersection of all open neighbourhoods of a point p is again an open neighbourhood of p, which is the smallest one. It is called the *minimal neighbourhood* of p. The topology of a finite space is completely determined by its minimal neighbourhoods. However, in a general framework of all topological spaces this is not true. Nevertheless, the sets which are realized as arbitrary intersection of open sets in topology are quite interesting. In this paper, we have made an investigation of all these type of sets. The m-open sets, as we call them, being a weaker form of open sets, are studied here in the light of other generalized form of open sets.

The m-open sets of a given topology on a set X again forms a topology on X. This is a departure from the fact that weaker forms of open sets usually form a "generalized topology"[4], not a topology. This development has led to few decompositions of open sets as well as decomposition of continuous mappings. A weaker form of regularity is defined using m-open sets. The product of m-regular spaces are found to be m-regular.

2. PRELIMINARIES

We recall some known definitions:

Definition 2.1 Let (X, τ) be a topological space. Then a subset A of (X, τ) is called,

i.)semi-open[10] if $A \subseteq cl\ int(A)$.

ii.)α-open [13] if $A \subseteq int\ cl\ int(A)$.

iii.)pre-open[11] if $A \subseteq int\ cl(A)$.

iv.)β-open[1] if $A \subseteq cl\ int\ cl(A)$.

v.)regular open (*regular closed* resp.,) [5] if $A = int\ cl(A)$ ($A = cl\ int(A)$ resp.,).

The complement of a semi-open (resp. α-open, pre-open, β-open) set is known as semi-closed (resp. α-closed, pre-closed, β-closed) set.

Definition 2.2 A subset$S$of a topological space$(X, \tau)$is said to be

*i.)*an A-set[14] if $S = U \cap C$, where U is open and C is regular closed.

*ii.)*a t-set[15] if $int(clS) = intS$.

iii.) a B-set[15] if there is an open set U and a t-set A in X such that $S = U \cap A$.

Let $f: X \to Y$ be a mapping, V be an arbitrary open set in Y. Then f is said to be*semi-continuous*[10] (resp. *pre-continuous*[11], α*-continuous*[12], β*-continuous*[14]) if $f^{-1}(V)$ is semi-open (resp. pre-open, α-open, β-open) in X. f is said to be A-continuous [14] (resp. B-continuous[15]) if $f^{-1}(V)$ is an A-set (resp. B-set) in X whenever V is open in Y. It is known that α-continuity implies pre-continuity and semi-continuity, A-continuity implies semi-continuity[14]. It can be shown that a subset S in X is open if and only if it is an A-set and an α-set[14] or equivalently, it is a pre-open set and B-set[15].

3. m-OPEN SETS

In this section, first we define m-open sets in a topology. It is shown that although, m-open sets are weaker form of open sets of the given topology, yet they also form a topology on their own.

Definition 3.1 Let(X, τ)be a topological space. A set$A \subseteq X$is called *minimal open or* m*-open* if Acan be expressed as intersection of a subfamily of open sets.

The collection of m-open sets of a topology (X, τ) is denoted by $\mathcal{M}$.

Clearly, every open set is m-open. In a finite space, open sets are the only m-open sets.

The following example gives an idea about the abundance of m-open sets.

Example 3.2 Let$X = \mathbb{N}$, the set of natural numbers, equipped with the cofinite topology. Then every subset of X is$m$*-open.*

Result 3.3 For a topological space(X, τ)
i.)$\emptyset, X \in \mathcal{M}$,
ii.) $\mathcal{M}$ is closed under arbitrary union,
iii.) $\mathcal{M}$ is closed under arbitrary intersection.

Proof.$i), iii)$ are obvious.

$ii)$ holds in view of the fact that $P(X)$, the power set of X forms a completely distributive lattice under union and intersection of sets.

Definition 3.4 Let (X, τ) be a topological space and$A \subseteq X$. Then minimal cover of A, denoted by$\mathcal{C}_m(A)$, is defined as$\mathcal{C}_m(A) = \bigcap\{U: U \in \tau, A \subseteq U\}$.

From the definition, it follows that $\mathcal{C}_m(A)$ is the smallest m-open set containing A.

Theorem 3.5 *Let* (X, τ) *be a topological space and* A, B *be subsets of* X*. Then the following hold:*
i.) $A \subseteq \mathcal{C}_m(A)$;
ii.) $\mathcal{C}_m(\mathcal{C}_m(A)) = \mathcal{C}_m(A)$;
iii.) If $A \subseteq B$ then $\mathcal{C}_m(A) \subseteq \mathcal{C}_m(B)$;
iv.)$\mathcal{C}_m(A \cup B) = \mathcal{C}_m(A) \cup \mathcal{C}_m(B)$;
v.) $\mathcal{C}_m(\emptyset) = \emptyset$.

Proof. Obvious from the definition of minimal cover of A.

This shows that $\mathcal{C}_m(A)$ is a closure operator. An operator similar to $\mathcal{C}_m$ was defined for generalized topological spaces in [3]. However the definition in [3] seems to erroneous or incomplete.

Theorem 3.6 *Let* (X, τ) *be a topological space. We define*
$$\mathfrak{T} = \{A \subseteq X: \mathcal{C}_m(A) = A\}.$$

Then $(X, \mathfrak{T})$ is a topological space and $\tau \subseteq \mathfrak{T}$.

Proof. Clearly $\emptyset, X \in \mathfrak{T}$. Let $A_i \in \mathfrak{T}$ where $i \in \wedge$, $A = \bigcup_{i\in\wedge} A_i$.

Since $A_i \subseteq \bigcup_{i\in\wedge} A_i$, thus $\mathcal{C}_m(A_i) \subseteq \mathcal{C}_m(\bigcup_{i\in\wedge} A_i)$ and hence $\bigcup_{i\in\wedge} \mathcal{C}_m(A_i) \subseteq \mathcal{C}_m(\bigcup_{i\in\wedge} A_i)$. Conversely, suppose that $x \notin \bigcup_{i\in\wedge} \mathcal{C}_m(A_i)$. Then $x \notin \mathcal{C}_m(A_i)$ for each $i \in \wedge$ and hence there exists an open set U_i containing A_i for each i, such that $x \notin U_i$.

Therefore $x \notin \bigcup_{i\in\wedge} U_i$, which contains $\bigcup_{i\in\wedge} A_i$. Hence $x \notin \mathcal{C}_m(\bigcup_{i\in\wedge} A_i)$.Therefore $\bigcup_{i\in\wedge} \mathcal{C}_m(A_i) = \mathcal{C}_m(\bigcup_{i\in\wedge} A_i)$.Hence
$\bigcup_{i\in\wedge} A_i = \bigcup_{i\in\wedge} \mathcal{C}_m(A_i) = \mathcal{C}_m(\bigcup_{i\in\wedge} A_i) \supseteq \bigcup_{i\in\wedge} A_i$. Lastly we show that if $A, B \in \mathfrak{T}$ then $A \cap B \in \mathfrak{T}$. We know that $\mathcal{C}_m(A \cap B) \subseteq \mathcal{C}_m(A) \cap \mathcal{C}_m(B) = A \cap B$. But $A \cap B \subseteq \mathcal{C}_m(A \cap B)$ and hence $\mathcal{C}_m(A \cap B) = A \cap B$. Thus $\mathfrak{T}$ forms a topology.
Furthermore let $U \in \tau$, then $\mathcal{C}_m(U) = U$. Thus $U \in \mathfrak{T}$. Hence $\tau \subseteq \mathfrak{T}$.

Theorem 3.7 *Let* (X, τ) *be a topological space. Then* $(X, \mathfrak{T})$ *forms an Alexandroff space[2], that is, it is closed under arbitrary intersection also.*

Proof. Let $A_i \in \mathfrak{T}$ for each $i \in \wedge$ then $\mathcal{C}_m(\bigcap_{i\in\wedge} A_i) \subseteq \mathcal{C}_m(A_i) = A_i$ for each i. Thus $\mathcal{C}_m(\bigcap_{i\in\wedge} A_i) \subseteq \bigcap_{i\in\wedge} A_i$.Again $\bigcap_{i\in\wedge} A_i \subseteq \mathcal{C}_m(\bigcap_{i\in\wedge} A_i)$.Hence $\mathcal{C}_m(\bigcap_{i\in\wedge} A_i) = \bigcap_{i\in\wedge} A_i$.Therefore if $A_i \in \mathfrak{T}$ then $\bigcap_{i\in\wedge} A_i \in \mathfrak{T}$.

From **Theorem** 3.5 and **Theorem** 3.7 , one can observe that $\mathfrak{T}^c = \{A^c | A \subseteq X: \mathcal{C}_m(A) = A\}$ is also a topology.

The members of $\mathfrak{T}$ are called the minimal open or m-open sets of τ. If X is finite, then $\tau = \mathfrak{T}$.

In the following, we study the interrelationship of m-open sets with other existing notions and finally obtain a decomposition of open set.

4. A DECOMPOSITION OF OPEN SETS

The operator $\mathcal{C}_m$ defined in the previous section can be used to define new weaker forms of open sets. We show that these weaker forms provide decomposition of open sets as well as that of continuity.

Definition 4.1 Let(X, τ)be a topological space. A subset$S \subseteq X$is said to be
i.)$\mathcal{C}_m$*-pre-open* if $S \subseteq int(\mathcal{C}_m(S))$,
ii.) $\mathcal{C}_m$*-t-set* if $int(S) = int(\mathcal{C}_m(S))$.
where int is the interior operator.

One can observe that every open set is $\mathcal{C}_m$-pre open set as well as $\mathcal{C}_m$-t-set. But converse is not true in general. In fact, we have the following example:

Example 4.2 Let$X = \mathbb{R}$, the set of real numbers with the usual topology. Take$A = (5,6) \cap \mathbb{Q}$. Then $A$is neither open nor semi-open and α-open set. But$A$is$\mathcal{C}_m$*-pre open-set as* $\mathcal{C}_m((5,6) \cap \mathbb{Q}) = (5,6)$.

Similarly if we take $B = (5,6]$, then B is $\mathcal{C}_m$-t-set but not open.

We can observe that if X is finite, then the class of $\mathcal{C}_m$-pre-open sets always forms a discrete topology. Because if X is finite then $\mathcal{C}_m(A)$ is an open set containing A.

Remark 4.3 A closed set need not be a $\mathcal{C}_m$-t-set.
We have the following example:

Example 4.4 Let$X = \{a, b, c, d\}$with topology$\tau = \{\emptyset, X, \{a\}, \{b\}, \{a, b\}, \{a, b, c\}\}$. If we take$A = \{d\}$. Then$A$is closed but not$\mathcal{C}_m$-$t$-*set.*

In **Example** 4.4, we see that $A = \{d\}$ is a t-set but not $\mathcal{C}_m$-t-set whereas $B = \{a, b, c\}$, being an open set is a $\mathcal{C}_m$-t-set, but not a t-set. Thus we can conclude that $\mathcal{C}_m$-t-set is independent of t-set.

Our next examples establish a fact that a $\mathcal{C}_m$-t-set is independent of open, semi-open, pre-open, α-open and β-open sets.

Example 4.5 Let$X = \mathbb{R}$, the set of real numbers with the usual topology. Take$A = (5,6) \cup \{\pi\}$. Then$A$is neither semi-open, pre-open, α-open and β-open set. But$A$ *is* $\mathcal{C}_m$-t-*set.*

Example 4.6 Let$X = \{a, b, c, d\}$with topology$\tau = \{\emptyset, X, \{a\}, \{b\}, \{a, b\}, \{a, b, c\}\}$. If we take$A = \{a, b, d\}$. Then $A$is α-open set and hence pre-open, semi-open and β-open set. But$A$is not$\mathcal{C}_m$-t-*set* because$\mathcal{C}_m(A) = X$.

Also a $\mathcal{C}_m$-t-set is independent from A-set and B-set. We have the following examples:

Example 4.7 Let$X = \{a, b, c, d\}$with topology $\tau = \{\emptyset, X, \{a\}, \{b\}, \{a, b\}, \{a, b, c\}\}$. If we take$A = \{b, c, d\}$, then $A$is aB-*set* because$A$is closed. But$A$is not a$\mathcal{C}_m$-t-*set.*

Example 4.8 Let$X = \{a, b, c, d\}$with topology $\tau = \{\emptyset, X, \{c\}, \{a, b\}, \{a, b, c\}\}$. If we take$A = \{c, d\}$, then$A$is an$A$-*set.* But$A$is not a$\mathcal{C}_m$-$t$-*set.*

5. SIMILARLY, WE HAVE

Example 4.9 Let$X = \mathbb{R}$, the set of real numbers with the usual topology. Take $B = [0,1) \cup (1,2) \cup \{\pi\}$. Then$Bis\mathcal{C}_m$-$t$-*set.* But not a$B$-*set.* If we take$A = (5,6) \cup \{\pi\}$is a$\mathcal{C}_m$-$t$-set but not an$A$-*set* because$A$is not a semi-open set.

Hence a $\mathcal{C}_m$-t-set is independent from A-set and B-set.

Proposition 4.10 If $A, B$are two$\mathcal{C}_m$-t-set, then$A \cap B$is also a$\mathcal{C}_m$-t-set.

Proof. Let A, B be two $\mathcal{C}_m$-t-sets. Then $int(A \cap B) \subseteq int(\mathcal{C}_m(A \cap B)) \subseteq int(\mathcal{C}_m(A) \cap \mathcal{C}_m(B)) = int(\mathcal{C}_m(A)) \cap int(\mathcal{C}_m(B)) = int(A) \cap int(B) = int(A \cap B)$.

Therefore $int(A \cap B) = int(\mathcal{C}_m(A \cap B))$. Hence $A \cap B$ is $\mathcal{C}_m$-t-set.

Thus the family of $\mathcal{C}_m$-t-set forms an infratopology[7], where an infratopology[7] on a set X is a collection τ of subsets of X having the following properties:

i.) $\emptyset$ and X are in τ.

ii.) The intersection of the elements of any finite sub collection of τ is in τ.

In our next theorem, we provide a decomposition of open set in terms of $\mathcal{C}_m$-pre-open and $\mathcal{C}_m$-t-set.

Theorem 4.11 *Let (X, τ) be a topological space. A subset $S \subseteq X$ is open if and only if S is $\mathcal{C}_m$-pre-open and $\mathcal{C}_m$-t-set.*

Proof. Let $S \subseteq X$ be an open set. Therefore S is $\mathcal{C}_m$-pre-open as well as $\mathcal{C}_m$-t-set.

Conversely, let S be a $\mathcal{C}_m$-pre-open and $\mathcal{C}_m$-t-set. We have $S \subseteq int(\mathcal{C}_m(S)) = int(S) \subseteq S$. Hence S is open.

Now we proceed to provide a decomposition for continuous mappings.

Definition 4.12 Let$f: X \to Y$be a mapping. Then f is said to be

i.) $\mathcal{C}_m$-*pre-continuous* if $f^{-1}(V)$ is $\mathcal{C}_m$-pre-open,

ii.)$\mathcal{C}_m$-t-*continuous* if $f^{-1}(V)$ is a $\mathcal{C}_m$-t-set,

where V is any arbitrary open set in Y.

From the discussion provide above, it follow that $\mathcal{C}_m$-t-continuity does not imply semi-continuity, hence does not imply continuity, α-continuity or A-continuity. We have the following examples in this regard.

Example 4.13 Let$X = \mathbb{R}$, the set of real numbers with the usual topology and$Y = \{a, b\}$with the topology$\mu = \{\emptyset, \{a\}, Y\}$. Let$f: X \to Y$be defined as*:*

$$f(x) = a \quad where\ A = (5,6) \cap \mathbb{Q}$$

$$= b\ if\ x \notin A$$

Then f is $\mathcal{C}_m$-t-continuous but neither semi-continuous nor continuous.

$\mathcal{C}_m$-t-continuity is independent from B-continuity and A-continuity also. Here are the examples:

Example 4.14 Let$X = \mathbb{R}$, the set of real numbers with the usual topology and$Y = \{a, b\}$with the topology$\mu = \{\emptyset, \{a\}, Y\}$. Let$f: X \to Y$be defined as:

$$f(x) = a \text{ where } A = [5,6) \cup (6,7) \cup \{\pi\}$$

$$= b \quad if x \notin A$$

Then f is $\mathcal{C}_m$-t-continuous but not B-continuous.

Example 4.15 Let $X = \{a, b, c, d\}$, with the topology $\tau = \{\emptyset, X, \{a\}, \{b\}, \{a, b\}, \{a, b, c\}\}$ and $Y = \{x, y\}$ with the topology $\mu = \{\emptyset, \{x\}, Y\}$. Let $f: X \to Y$ be defined as: $f(a) = y, f(b) = f(c) = f(d) = x$. Then f is B-continuous but not $\mathcal{C}_m$-t-continuous.

Similarly,

Example 4.16 Let $X = Y = \{a, b, c, d\}$, with the topology $\tau = \{\emptyset, X, \{a\}, \{b\}, \{a, b\}, \{a, b, c\}\}$ on X and topology $\mu = \{\emptyset, \{c\}, \{c, d\}, \{a, b, c\}, Y\}$. Let $f: X \to Y$ be defined as identity map. Then f is A-continuous but not $\mathcal{C}_m$-t-continuous because $\{c, d\}$ is not a $\mathcal{C}_m$-t-set in X.

From **Theorem** 4.11, we have a decomposition of continuity in the following manner:

Theorem 4.17 *A mapping $f: X \to Y$ is continuous if and only if it is both $\mathcal{C}_m$-pre continuous and $\mathcal{C}_m$-t-continuous.*

6. m-REGULARITY

In this section, we further use the concept of m-open sets to define a weaker form of regularity. Some interesting results are obtained here. While Hausdorffness implies m-regularity. Also the product of normal spaces are found to be m-normal.

Definition 5.1 A topological space X is said to be *m-regular* if for each pair consist of a point x and a closed set B not containing x, there exist a disjoint pair of m-open set and an open set, containing x and B respectively.

Since every open set is m-open therefore every regular space is m-regular as well. Converse is however not true. Here is an example.

Example 5.2 Let $X = \mathbb{N}$, the set of natural numbers, equipped with the cofinite topology. Then every subset of X is *m-open.* Then X is a *m-regular* space but not a regular space.

Theorem 5.3 *Let X be a topological space then X is m-regular if and only if given a point $x \in X$ and an open neighbourhood U of x, there exists an m-open neighbourhood V of x such that $x \in V \subseteq cl(V) \subseteq U$.*

Proof. Suppose that X is m-regular space and x and an open neighbourhood U of x are given. Then $B = X \backslash U$, is a closed set not containing x. By the hypothesis, there exists a pair of disjoint m-open set V and open set W, containing x and B respectively, that is, $x \in V$ and $B \subseteq W$. Then $cl(V)$ is disjoint from B and hence $x \in V \subseteq cl(V) \subseteq X \backslash W \subseteq X \backslash B \subseteq U$, that is $cl(V) \subseteq U$.

Conversely, suppose that a point x and a closed set B not containing x are given. Then $U = X \backslash B$, is an open set containing x. Therefore there is a m-open neighbourhood V of x such that $cl(V) \subseteq U$. Then the m-open sets V and the open set $X \backslash cl(V)$, are disjoint sets containing x and B respectively. Thus (X, τ) is m-regular.

Theorem 5.4 *Every Hausdorff space is m-regular.*

Proof. Let X be a Hausdorff space. Let x and B be a pair of a point and a closed set not containing the point x. Then for every $y \in B$, we have $x \neq y$. Therefore by the given hypothesis, there exist disjoint open sets U_y and V_y such that $x \in U_y$, $y \in V_y$ and $U_y \cap V_y = \phi$. Then $\{V_y | y \in B\}$ is an open cover of B and $U = \bigcap_{y \in B} U_y$, is an m-open set containing x such that $U \cap V = \phi$. Therefore X is m-regular.

Our next theorem is on the product of m-regular spaces.

Theorem 5.5 *Product of m-regular spaces is again m-regular.*

Proof. Let $\{X_\alpha\}$ be a family of m-regular spaces. Let $X = \prod_\alpha X_\alpha$. Let $x = \{x_\alpha\}$ be a point of X and U be an open neighbourhood of $x \in X$. We choose a basis element $\prod_\alpha U_\alpha$ about x contained in U. Then $x_\alpha \in U_\alpha$ for each α. As X_α is m-regular, there exists an m-open set V_α in X_α such that $x_\alpha \in V_\alpha \subseteq cl(V_\alpha) \subseteq U_\alpha$. Now, V_α being m-open, we have, $V_\alpha = \bigcap_j V_{\alpha_j}$, where V_{α_j} is open in X_α. If $U_\alpha = X_\alpha$, we simply choose $V_\alpha = X_\alpha$. Then by using the fact [5] that $\bigcap_\beta (\prod_\alpha A_{\alpha,\beta}) = \prod_\alpha (\bigcap_\beta A_{\alpha,\beta})$, we find that $V = \prod_\alpha V_\alpha$ is an m-open set in $\prod_\alpha X_\alpha$. Since $cl(V) = cl(\prod_\alpha V_\alpha) = \prod_\alpha cl(V_\alpha)$, it follows that $x \in V \subseteq cl(V) \subseteq \prod_\alpha U_\alpha \subseteq U$. Hence X is m-regular.

Definition 5.6 A topological space X is said to be *m-normal* if every pair of disjoint closed sets are contained in disjoint *m-open* sets.

One can observe that every normal space is m-normal. But converse is not true in general.

In **Example** 5.2, X is m-normal but not normal.

In our next theorem, we provide that m-regular spaces are m-normal.

Theorem 5.7 *Every m-regular space is m-normal.*

Proof. Let X be m-regular space. Let A and B be disjoint closed subsets of X. Then for each $x \in A$ has an open neighbourhood $X \backslash B$, because $A \subseteq X \backslash B$. By the given hypothesis, there exists an m-open set V_x such that $cl(V_x)$ doesn't intersect B, that is $x \in V_x \subseteq cl(V_x) \subseteq X \backslash B$.

Therefore $\{V_x | x \in A\}$ forms an m-open covering of A. In the same way, $\{U_x | x \in B\}$ is also an m-open covering of B. Thus $V = \bigcup_{a\in A} V_a$ and $U = \bigcup_{b\in B} U_b$ are m-open sets containing A and B respectively.

Now we define $U_i' = U_i \setminus \bigcup_{a\in A, a\neq i} cl(V_a)$ and $V_i' = V_i \setminus \bigcup_{b\in \Lambda', b\neq i} cl(U_b)$. Here U_i' and V_i' are m-open sets. Since arbitrary union of closed sets are m-closed, therefore $\bigcup_{a\in A, a\neq i} cl(V_a)$ is m-closed. (Because if A is m-open, then $A = \bigcap_n \{V_n,$ where V_n is open$\}$. Thus $X\setminus A = X\setminus \bigcap_n V_n = \bigcup_n (X\setminus V_n) = \bigcup_n U_n,$ where $U_n = X\setminus V_n,$ closed sets).Thus $U_i \setminus \bigcup_{a\in A, a\neq i} cl(V_a) = U_i \cap [\bigcup_{a\in A, a\neq i} cl(V_a)]^c$. Here $[\bigcup_{a\in A, a\neq i} cl(V_a)]^c$ is an m-open set in X, therefore $U_i' = U_i \setminus \bigcup_{a\in A, a\neq i} cl(V_a)$ is again an m-open set in X. Similarly, V_i' is m-open. Now, we have $U' = \bigcup U_i'$ and $V' = \bigcup V_i'$ are disjoint m-open covers containing A and B respectively. Therefore X is m-normal space.

Corollary 5.8 Thus from the **Theorem***5.7* and *5.5,* we can say that the product of normal T_1-space is coming out be *m-normal.*

ACKNOWLEDGEMENT

This work is a part of a research work financed by the University Grant Commission (India).

REFERENCES

[1] Abd EI-Monsef, M. E., Mahmoud, R. A., and El-Deeb, S. N., "β–open sets and β −continuous mappings", *Bull. Fac. Sci. Assiut Univ.*, 12 (1966),pp. 77 – 90.

[2] Alexandroff, P., Diskrete Räume, *Mat. Sb. (N.S.)* 2 (1937),pp. 501-518.

[3] Boonpok, C.,"ζ_μ-sets in generalized topological spaces", *Acta Math. Hungar.*, 134 (3), (2012), pp.269–285.

[4] Császár, Á.,"Generalized Topology, Generalized Continuity", *Acta Math. Hungar.*, 96 (2002), pp.351 – 357.

[5] Dugundji, J., Topology, Allyn and Bacon (Boston, 1972).

[6] Fabrizi, E. and Saffiotti, A.,"Behavioural Navigation on Topology-based Maps", *proc. of the 8th symp. on robotics with applications, Maui, Hawaii* , 2000.

[7] Husain, T. , Topology and Maps, Plenum Press(1977).

[8] Khalimsky, E. D. ,"Applications of Connected Ordered Topological Spaces in Topology", in: Conference of Math. Department of Povolsia (1970).

[9] Kovalesky, V., and Kopperman, R.,"Some Topology-Based Imaged Processing Algorithms", *Ann. Ny. Acad. Sci.*, 728 (1994), pp. 174 – 182.

[10] Levine,N.,"Semi-open Sets and Semi-Continuity in Topological Spaces", *The American Mathematical monthly*, 70 (1963), pp. 36 – 41.

[11] Mashhour, A. S., Abd EI-Monsef, M. E., and El-Deeb, S. N.,"On Pre continuous and Weak Precontinuous Mappings", *Proc. Math. and Phys. Soc. Egypt*, 51 (1981).

[12] Mashhour, A. S. , Hasanein, I. A., and E1-Deeb, S. N.,"α-continuous and α –open mappings", *Acta Math. Hungar.*, 41 (1983), pp. 213–218.

[13] Njăstad, O., "On Some Classes of nearly Open Sets", *Pacific J. Math.*, 15 (1965),pp. 961–970.

[14] Tong, J.,"A Decomposition of Continuity", *Acta Math. Hungar.*, 48 (1986), pp. 11–15.

[15] Tong, J.,"A Decomposition of Continuity in Topological Spaces", *Acta Math. Hungar.*, 54 (1989), pp. 51–55.

[16] Stadler,B̈. M. R., and Stadler, P. F., "Generalized Topological Spaces in Evolutionary Theory and Combinatorial Chemistry", 2001. *J. Chem. Inf. Comput. Sci.* 42 (2002) pp. 577-585.

Sustainable Development for All

Ankur Singh

ISTE, Rajasthan Section

Abstract: Sustainable Development : Sustainable development is a process that lasts i.e. the current generations should 'meet their needs without compromising the ability of future generations to meet their own needs'. But the world and our country as well are today developing destructively. The sustaining green cover is shrinking rapidly.

The country's forest cover is only 20 % while ideally it should be 33 % for the health of the country. Over-Population + GREED + lavish lifestyles of man has resulted in a highly destructive growth everywhere which is irreversible.

Impact of Destructive Development in India :

The destructive development has played havoc with the life of the people. It has painted an alarming picture on the national front. The Natural Hazards in India caused by man are easily seen in print and electronic media.

How to Bring Sustainable Development :

In order to achieve sustainable development, environmental protection shall constitute an integral part of the development process and cannot be considered in isolation from it . For sustainable development, we have to be eco-friendly ! We should maximize the economic growth with minimum environmental damage.

1. SUSTAINABLE DEVELOPMENT

Sustainable development is a process that lasts i.e. the current generations should 'meet their needs without compromising the ability of future generations to meet their own needs'. But the world and our country as well are today developing destructively. The sustaining green cover is shrinking rapidly.

If we are to avoid tipping the planet over a widely accepted danger threshold of 450 parts per million of atmospheric carbon dioxide, we can only afford to burn fossil fuels in a low quantity of carbon. Industry estimates suggest that remaining oil deposits alone exceeds the danger figure. If we are to avoid climate catastrophe, developing nations should not see developed nations as their role models.

As far as India is concerned, the country's forest cover is only 20 % while ideally it should be 33 % for the health of the country. **Over-Population + GREED + lavish lifestyles** of manhas resulted in a highly destructive growth everywhere which is irreversible.



Asia including India is facing the brunt of climate change and will see severe stress on water resources and food-grain production in the future, increasing the risk of armed conflict among India, Pakistan, Bangladesh and China, the latest report of a UN panel has warned.

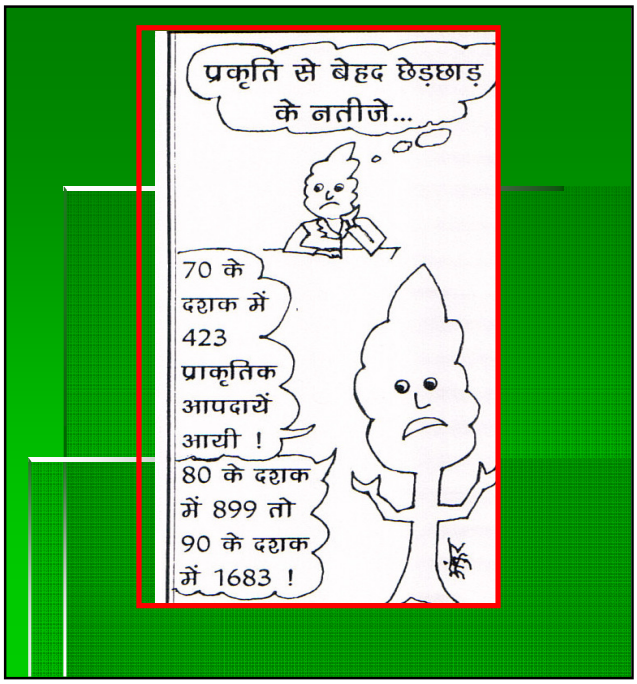
Maldives, China, India, Pakistan, Bangladesh and Sri Lanka will be among the most affected countries in Asia. Severe stress on fresh water resources in South Asia and China (Himalayan river basins) may become a reason for armed conflict in the region in near future.

2. IMPACT OF DESTRUCTIVE DEVELOPMENT IN INDIA:

The destructive development has played havoc with the life of the people. It has painted an alarming picture on the national and international front.

The Natural Hazards in India and the world over, caused by man are doubling in each decade in number and its intensity. Recent disasters in Kedar Nath and Kashmir or cyclone Phailin in Odisha underline this fact. Frequent floods and droughts are common these days in many parts of India.

India, like other developing economies, may lose up to 1.7% of its Gross Domestic Product (GDP) if the annual mean temperature rises by 1 degree Celsius compared to pre-industrialization level, hitting the poor the most.

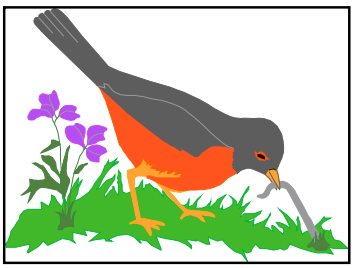


3. HOW TO BRING SUSTAINABLE DEVELOPMENT:

In order to achieve sustainable development, environmental protection shall constitute an integral part of the development process and cannot be considered in isolation from it . For sustainable development, we have to be eco-friendly ! We should maximize the economic growth with **minimum** environmental damage. We need to invest heavily in the development of solar power capacity of the country.

Our Prime Minister Sh. Narendra Modi in his maiden Independence Day speech spoke on the need to channelise the talent of the youth. We have to utilize our youth manpower for clean and green technology development and deployment of this technology from lab to land.

For improving the health of the country, we need to conserve our green cover, especially the forests. Tiger conservation is essential part of it. Side by side we have to promote sustainable life-styles, control our population and greed both, at the earliest.





For controlling the adverse effects of global warming and climate change, Govt. of India had launched 8 National Missions :

- National Solar Mission
- National Mission for Enhanced Energy Efficiency
- National Mission on Sustainable Habitat
- National Water Mission
- National Mission for Sustaining the Himalayan Ecosystem
- National Mission for a "Green India"
- National Mission for Sustainable Agriculture
- National Mission on Strategic Knowledge for Climate Change

We all have to help in implementation of these National Missions seriously. Only then, we will be able to avoid disasters like Kedar Nath and Kashmir or cyclone Phailin in Odisha.



Help Each other to save the Mother Earth !

Cost-Benefit Analysis of a Cold Standby System with Two-Stage Repair and Waiting Time Subject to Arrival Time of the Server

Ashish Kumar[1], Monika Saini [2]

[1,2]*Department of Mathematics, School of Basic Sciences and Humanities, Manipal University Jaipur, Jaipur-303007, Rajasthan, India*

Abstract: **The main objective of this investigation is to carry out the cost-benefit analysis of a two-unit cold standby system using the concepts of arrival time of the server, normal failure and two-stage repair of a failed unit. Here the concept of waiting time with two-stage repair for a two-unit cold standby system is discussed. There is a single server who takes some time to visit the system to do repair of the unit. The repair process is divided into two stages. In the first stage, the repairing process of the unit is started but it does not get completed; instead the process is completed in the second stage. The elapsed time between two stages is called the waiting time. The failure time of the unit follows negative exponential distribution while the distribution of repair times and waiting time of the unit are taken as arbitrary with different probability density functions. The unit works as new after repair and preventive maintenance. All random variables are statistically independent. Switch devices are perfect. The system has been analyzed stochastically in detail using semi-Markov process and regenerative point technique. The behavior of some important measures of system effectiveness has been observed numerically with respect to failure rate by giving particular values to other parameters.**

Keywords: **Cold Standby System, Arrival Time of the Server, Waiting Time, Two-Stage repair and Profit Analysis.**

1. INTRODUCTION

Two-unit cold standby redundant systems have been extensively studied by several authors such as Kumar and Malik (2012), Sridharan and Mohanavadivu (1998) and Goel and Sharma (1989) in the past by a common assumption of single server. Singh and Singh (1989) carried out the profit of a cold stand by system with provision of rest. A two-unit cold standby system is considered. The failure rate of a unit is a constant and the repair time distribution is a two-stage Erlang distribution is presented by Shandrasekhar et al. (2004). Mokaddis and El-Said (1990) developed a stochastic model for availability function and the mean time to the first failure for two models of a cold standby redundant system with two different types of repair. El-Said and El-Sherbeny (2005) considered the reliability of two units cold standby system with single repair and additional preventive maintenance of operative and the standby units. El-Said and El-Sherbeny (2010) developed a stochastic model for a cold standby system with two stage repair and waiting time.

In the present paper the idea of waiting time with two- stage repair for a two-unit cold stand by system is discuss subject to arrival time of the server. There is a single server who takes some time to visit the system to do repair of the unit. The repair process is divided into two stages. In the first stage, the repairing process of the unit is started but it does not get completed; instead the process is completed in the second stage. The elapsed time between two stages is called the waiting time. The failure time of the unit follows negative exponential distribution while the distribution of repair times and waiting time of the unit are taken as arbitrary with different probability density functions. The unit works as new after repair and preventive maintenance. All random variables are statistically independent. Switch devices are perfect. The system has been analyzed stochastically in detail using semi-Markov process and regenerative point technique. The behavior of some important measures of system effectiveness has been observed numerically with respect to failure rate by giving particular values to other parameters.

2. NOTATIONS

λ	Constant failure rate of the unit
h(t) / H(t)	pdf / cdf of the waiting time
g(t) / G(t)	pdf / cdf of repair time of the server
w(t) / W(t)	pdf / cdf of arrival time of the server
q_{ij} (t)/ Q_{ij}(t) :	pdf / cdf of passage time from regenerative state i to a regenerative state j or to a failed state j without visiting any other regenerative state in (0, t]
pdf / cdf	Probability density function/ Cumulative density function
$q_{ij.kr}$ (t)/$Q_{ij.kr}$(t)	pdf/cdf of direct transition time from regenerative state i to a regenerative state j or to

a failed state j visiting state k, r once in (0, t]

$\mu_i(t)$ Probability that the system up initially in state $S_i \varepsilon E$ is up at time t without visiting to any regenerative state

$W_i(t)$: Probability that the server is busy in the state S_i up to time 't' without making any transition to any other regenerative state or returning to the same state via one or more non-regenerative states.

m_{ij} Contribution to mean sojourn time $\mu_i(t)$ in state S_i when system transit directly to state S_j so that $\mu_i = \sum_j m_{ij}$ and $m_{ij} = \int t dQ_{ij}(t) = -q_{ij}^{*'}(0)$

® /© Symbol for Laplace-Stieltjes convolution/Laplace convolution

~ / * Symbol for Laplace –Steiltjes Transform (LST) / Laplace Transform (LT)

3. TRANSITION PROBABILITIES AND MEAN SOJOURN TIMES

Simple probabilistic considerations yield the following expressions for the non-zero elements

$$p_{ij} = Q_{ij}(\infty) = \int_0^\infty q_{ij}(t)dt \text{ as} \quad (1)$$

$p_{01}=1= p_{86} = p_{62}= p_{72} = p_{45}= p_{56}$, $p_{14}= \frac{\lambda}{\gamma+\lambda}$,

$p_{12} = \frac{\gamma}{\gamma+\lambda} = p_{12.456}$, $p_{28} = \frac{\lambda}{\beta+\lambda} = p_{22.8,6}$,

$p_{23} = \frac{\beta}{\beta+\lambda}$, $p_{32.7} = p_{37} = \frac{\lambda}{\theta+\lambda}$, $p_{30} = \frac{\theta}{\theta+\lambda}$ (2)

It can be easily verified that $p_{01}= p_{14}+p_{12} = p_{23}+ p_{28} = p_{30}+p_{37}= p_{45}= p_{56}= p_{62}= p_{72} = p_{86} = 1$

The mean sojourn times (μ_i) is the state S_i are

$$\mu_0 = \frac{1}{\lambda},\ \mu_1 = \frac{1}{\gamma+\lambda},\ \mu_2 = \frac{1}{\beta+\lambda},\ \mu_3 = \frac{1}{\theta+\lambda},\ \mu_1' = \frac{1}{\gamma},$$
$$\mu_2' = \frac{1}{\beta},\ \mu_3' = \frac{1}{\theta}$$

4. SYSTEM MODEL DESCRIPTION

In this section, the two-unit cold standby redundant system is described. Through semi-Markov assumption, the recurrence equations are obtained for the analysis of state probabilities. The states of the system according semi-Markov process and regenerative point technique are as follows:

State 0: initial state, one unit works, one unit in standby, and the system is working

State 1: operative unit fails and waiting for repair, cold standby unit becomes operative; and the system is working

State 2: failed unit is under first stage repair, other unit is operative and the system is working

State 3: failed unit is under second stage repair, other unit is operative and the system is working

State 4: First failed unit continuously waiting for repair, second failed unit is also waiting for repair, and the system failed

State 5: First failed unit is under first stage repair, second failed unit is continuously waiting for repair, and the system failed

State 6: First failed unit is under second stage repair, second failed unit is continuously waiting for repair, and the system failed

State 7: First failed unit is continuously under second stage repair, second failed unit is waiting for repair, and the system failed

State 8: First failed unit is continuously under first stage repair, second failed unit is waiting for first stage repair, and the system failed

The states S0, S1, S2 and S3 are regenerative states while S4, S5, S6, S7 and S8 are non-regenerative states. Thus E = {S0, S1, S2, S3}.

5. STEADY STATE AVAILABILITY

Let $A_i(t)$ be the probability that the system is in up-state at instant 't' given that the system entered regenerative state i at t = 0. The recursive relations for $A_i(t)$ are given as

$$A_i(t) = M_i(t) + \sum_j q_{i,j}^{(n)} © A_j(t) \quad (3)$$

where *j* is any successive regenerative state to which the regenerative state *i* can transit through n transitions. $M_i(t)$ is

the probability that the system is up initially in state $S_i \in E$ up at time t without visiting to any other regenerative state, we have is

$$M_0(t) = e^{-\lambda t}\ ,\ M_1(t) = e^{-\lambda t}\overline{W(t)},\ M_2(t) = e^{-\lambda t}\overline{H(t)},$$
$$M_3(t) = e^{-\lambda t}\overline{G(t)} \qquad (4)$$

Taking LT of above relations (3) and solving for $A_0^*(s)$. The steady state availability is given by

$$A_0(\infty) = \lim_{s\to 0} s\,A_0^*(s) = \frac{N_1}{D_1}, \text{where} \qquad (5)$$

$N_1 = [(\mu_0+\mu_1\ p_{01})\ (1-p_{22.8,6}-\ p_{23}\ p_{32.7})+ (p_{12} + p_{12.4,5,6})p_{01}(\mu_2+\mu_3\ p_{23})]$

and

$D_1 = [(\mu_0+ \mu_1^{'}\ p_{01})\ (1-p_{22.8,6}-\ p_{23}\ p_{32.7})+ (p_{12} + p_{12.4,5,6})p_{01}(\ \mu_2^{'} + \mu_3^{'} p_{23})]$

6. BUSY PERIOD ANALYSIS FOR SERVER

Let $B_i\ (t)$ be the probability that the server is busy in repairing of the system (unit) at an instant 't' given that the system entered state i at t = 0. The recursive relations for $B_i\ (t)$ are as follows:

$$B_i\ (t) = W_i\ (t) + \sum_j q_{i,j}^{(n)}\ (t) \copyright B_j\ (t) \qquad (6)$$

Where *j* is any successive regenerative state to which the regenerative state *i* can transit through n transitions. $W_i(t)$ be the probability that the server is busy in state S_i due to repairing of the unit up to time t without making any transition to any other regenerative state or returning to the same via one or more non-regenerative states and so

$$W_2 = e^{-\lambda t}\overline{H}(t)\ ,\ W_3 = e^{-\lambda t}\overline{G}(t)$$

Taking LT of above relations (6) and solving for B_0^* (s). The time for which server is busy due to repair is given by

$$B_0(\infty) = \lim_{s\to 0} sB_0^*(s) = \frac{N_2}{D_1}, \text{where}$$

$N_2 = [W_2^*(0) + P_{23}W_3^*(0)]\ [2(p_{12} + p_{12.4,5,6})p_{01}]$ and D_1 is already defined.

7. EXPECTED NUMBER OF VISITS BY THE SERVER

Let $N_i(t)$ be the expected number of visits by the server in (0, t] given that the system entered the regenerative state i at t = 0. The recursive relations for $N_i(t)$ are given as

$$N_i\ (t) = \sum_j Q_{i,j}^{(n)}\ (t) \circledR \left[\ \delta_j + N_j\ (t)\right] \qquad (7)$$

Where j is any regenerative state to which the given regenerative state *i* transits and δj =1, if *j* is the regenerative state where the server does job afresh, otherwise δj = 0. Taking LST of relation (7) and solving for $\tilde{N}_0(s)$. The expected number of visit per unit time by the server are given by

$$N_0(\infty) = \lim_{s\to 0} s\,\tilde{N}_0(s) = \frac{N_3}{D_1}, \text{ where} \qquad (8)$$

$N_3 = [p_{12}\ p_{01}\ (1-p_{22.8,6}-\ p_{23}\ p_{32.7})+ (p_{12} + p_{12.4,5,6})p_{01}p_{23}\ p_{12.4,5,6}]$ and D_1 is already defined.

8. COST-BENEFIT ANALYSIS

The profit incurred to the system model in steady state can be obtained as

$$P = K_0A_0 - K_1B_0 - K_2N \qquad (9)$$

K_0 = Revenue per unit up-time of the system
K_1 = Cost per unit time for which server is busy due repair
K_2 = Cost per unit time visit by the server

9. CONCLUSION

By considering a particular case, $g(t) = \theta e^{-\theta t}$, $h(t) = \beta e^{-\beta t}$ and $w(t) = \gamma e^{-\gamma t}$, the numerical results for some system effectiveness measures are obtained for the system under study. The numerical results for availability and profit are obtained with respect to failure rate (λ) rate for fixed values of parameters as shown respectively in table 1 and 2. It is revealed that Availability and profit increase with the increase of repair rate (θ) and arrival rate of the server (γ). But the value of these measures decrease with the increase of failure rate (λ) and waiting time (β). Thus finally it is concluded that in a cold standby system with arrival time of the server can be made reliable and economical to use

i.) By reducing the waiting time between both stages of repair.
ii. By increasing the repair rate.

REFERENCES

[1] Goel, L.R. and Sharma, S.C., Stochastic analysis of a two-unit standby system with two failure modes and slow switch. Microelectronics and Reliability, 29(4),1989, pp. 493-498.

[2] Khaled, M. El-said and Mohamed, S. El-Sherbeny, Profit analysis of a two unit cold standby system with preventive maintenance and random change in units. *J. Mathematics and Statistics*, 1,2005, 71-77.

[3] Khaled, M. El-Said and Mohamed, S. El-Sherbeny, Stochastic analysis of a two-unit cold standby system with two stage repair and waiting time. Sankhya, 72-B,2010,pp.1-10.

[4] Malik, S.C. and Kumar, A., Reliability modeling of a computer system with priority to s/w replacement over h/w replacement subject to MOT and MRT. *International Journal of Pure and Applied Mathematics*, 80(5),2012,pp. 693-709.

[5] Mokaddis, G., S. and Khaled, M. E., Two models for two-dissimilar unit cold standby redundant system with partial failure and two types of repairs. *Microelectronic Reliability*, 30,1990,pp. 431-451.

[6] Shandrasekhar, P., Natarajan, R. and Yadavalli, S.S.V., A study on a two-unit standby system with Erlangian repair time. *Asia Pacific Journal of Operational Research*, 21,2004, pp. 271-277.

[7] Singh, S.K. and Singh, R.P., Profit evaluation of a two-unit cold standby system with a provision of rest. *Microelectronics and Reliability*, 29(5),1989,pp. 705-709.

[8] Sridharan, V. and Mohanavadivu, P., Stochastic behaviour of a two-unit standby system with two types of repairmen and patience time. *Math. Comput. Modelling*, 28,1998, pp. 6371.

Table: 1. Effect of Arrival Rate of the Server and Various Repair Policies on Availability with respect to Failure Rate (λ)

Λ	γ=.07,θ=.5,β=.8	γ=.07,θ=.5,β=1.0	γ=.07,θ=.7,β=.8	γ=.04,θ=.5,β=.8
0.01	0.998368	0.995592	0.999834	0.968473
0.02	0.964962	0.962194	0.969458	0.891677
0.03	0.91888	0.917306	0.926686	0.811333
0.04	0.869181	0.869196	0.880019	0.73819
0.05	0.820091	0.821728	0.833502	0.674214
0.06	0.773494	0.776633	0.788999	0.61886
0.07	0.73012	0.734587	0.747285	0.570972
0.08	0.690138	0.695753	0.708596	0.52937
0.09	0.653449	0.660043	0.672896	0.49302
0.1	0.619834	0.627259	0.640026	0.461059

Table: 2. Effect of Arrival Rate of the Server and Various Repair Policies on Profit Function with respect to Failure Rate (λ)

Λ	γ=.07,θ=.5,β=.8	γ=.07,θ=.5,β=1.0	γ=.07,θ=.7,β=.8	γ=.04,θ=.5,β=.8
0.01	4983.855	4971.489	4991.219	4835.746
0.02	4811.921	4800.51	4834.476	4449.015
0.03	4578.45	4573.558	4617.588	4046.152
0.04	4328.02	4331.401	4382.349	3680.012
0.05	4081.352	4093.033	4148.566	3360.051
0.06	3847.6	3866.895	3925.301	3083.367
0.07	3630.26	3656.25	3716.285	2844.089
0.08	3430.076	3461.824	3522.585	2636.279
0.09	3246.486	3283.128	3343.967	2454.738
0.1	3078.357	3119.132	3179.583	2295.138

A Study of Exponential Mixture ROC Model

Sudesh Pundir[1], Azharuddin[2]

[1,2]*Department of Statistics, Pondicherry University, Puducherry, India*

Abstract: **In the case of heterogeneity in the data and heavily skewed distribution, we proposed Exponential-Mixture Receiver Operating Characteristic (ROC) model and discussed the properties of this ROC Curve. Area Under the Exponential-mixture ROC Curve (AUC) and its variance are also found. Estimates of the parameters of Exponential-mixture ROC model are derived by using the maximum Likelihood method and method of moments. The proposed model is validated by using the simulation studies**

Keywords: **Exponential-mixture distribution, ROC Curve, Area Under the ROC Curve, Estimates of the Area Under the ROC Curve, Variance of AUC and Monte Carlo simulation.**

1. INTRODUCTION

Mixture distribution arises where a statistical population contains two or more sub-populations. A random variable (X) is said to follow a finite mixture distribution if it has a probability density function of the form

$$f(x) = \sum_{i=1}^{k} p_i f_i(x/\theta_i),\ p_i > 0,\ i = 1,2,...k \quad and \quad \sum_{i=1}^{k} p_i = 1. \tag{1.1}$$

The parameters, $p_i's$ are mixing weights, and $f_i(x/\theta_i)$ is the i^{th} component density of the mixture.

The finite mixture distribution is first introduced by Newcomb in (1886) for outliers. Pearson (1894) also used the mixture distribution for estimating the parameters of two component Normal-mixture distribution by the method of moments. The research work on mixture distribution is growing very fast due to the advent of computers. The first monograph on finite mixture distribution is introduced by Everitt and Hand (1981). Titterington et al. (1985) discussed the finite mixture model in his book. McLachlan and Peel (2000) also discussed the finite mixture model. They discussed the estimation method of finite mixture model.

The mixture distribution have many applications in a large number of areas e.g. Econometrics, Sociology, Engineering, Reliability estimation, Remote sensing, Medical diagnosis and Discriminant analysis.

Schlatmann (2009) discussed the application of mixture model in medical diagnosis. In this paper, we discussed the mixture distribution in medical diagnosis.

Exponential distribution is the only continuous life distribution which has a constant failure rate. The Exponential distribution is also very famous for its memory-less property. Dass and Seong (2011) discussed the multivariate Normal-mixture ROC model. Gonen (2013) also discussed the p-component Normal-mixture ROC model.

He also discussed the Area under the Curve of p-component normal-mixture ROC curve. In this paper we discuss the mixture of two exponential density functions. Exponential distribution is a highly skewed distribution. It is also used in those cases where certain events occur with a constant probability per unit length. Everitt and Hand (1981) discussed the exponential mixture distribution in their comprehensive monograph. Titterington et al. (1985) also discussed the exponential mixture distribution in their book. The probability density function of the Exponential mixture distribution is as follows

$$f(x) = p\frac{1}{\lambda_1}e^{-\left(\frac{x}{\lambda_1}\right)} + (1-p)\frac{1}{\lambda_2}e^{-\left(\frac{x}{\lambda_2}\right)},\ 0 < \lambda_1, \lambda_2 < \infty,\ 0 \le x < \infty. \tag{1.2}$$

The cumulative distribution function of Exponential mixture distribution is as follows

$$F(x) = p\left[1 - e^{\left(-\frac{x}{\lambda_1}\right)}\right] + (1-p)\left[1 - e^{\left(-\frac{x}{\lambda_2}\right)}\right],\ 0 < \lambda_1, \lambda_2 < \infty,\ 0 \le x < \infty\ . \tag{1.3}$$

where p is the weight of the mixture distribution. The sum of the weights of distribution should be equal to 1. The Exponential mixture distribution is very useful in life testing problems.

Receiver Operating Characteristic (ROC) curve is used for the classification of the objects by using the cut-off values. Here Receiver Operating Characteristic curve is defined only for the continuous random variables. The ROC Curve is first introduced by Radar engineer and Electrical engineer 1950's during World War II in Signal detection theory. It is also used in the Psychophysics to classify human detection of weak signals. ROC curve have many applications in Medical as well as Non-Medical fields. ROC curve is also used in the diagnostic accuracy. It classifies the healthy and diseased populations.

The classification of the healthy and diseased population depends on the threshold or cut-off values. Suppose X is a random variable and t is the threshold value in a classification rule, so that an individual belongs to healthy population if classification scores (s) are greater than t otherwise an individual belong to disease population. Suppose that we take healthy population (H) and diseased population (D). There are four classification rates which gives the probability for understanding the discrimination of the patients. True Positive Rate (TPR) is defined as the probability that an individual from disease cases is correctly classified. True Negative Rate (TNR) is defined as the probability that an individual from healthy control is correctly classified. False Positive Rate (FPR) is defined as the probability that an individual from healthy control is misclassified and False Negative Rate (FNR) is defined as the probability that an individual from disease cases is misclassified. The mathematical definitions of TPR, FPR, TNR and FNR is as follows

TPR= $P\left(s > t / D\right)$,

FPR = $P\left(s > t / H\right)$,

TNR = $P\left(s \le t / H\right)$,

FNR = $P\left(s \le t / D\right)$.

Sensitivity and Specificity are statistical terms which are used to evaluate a diagnostic test. These are used to measure the performance of a binary classification test. They are independent of the population of interest subject to the test. Sensitivity is also known as True Positive Rate and Specificity is also known as True Negative Rate. In medical terminology, Sensitivity is defined as the proportion of patients who are suffering from disease and also the test is positive. Specificity is defined as the proportion of patients who are healthy and also the test is negative. Mathematically, Sensitivity and Specificity are defined as follows,

$$Sensitivity = y(t) = \frac{True\ Positive}{True\ Positive + False\ Negative},$$

$$Specificity = x(t) = \frac{True\ Negative}{True\ Negative + false\ Positive}.$$

For getting 100% classification of a test, we need high sensitivity and low 1-Specificity or high True Positive Rate (TPR) and low False Positive Rate (FPR). For the 100% classification, the coordinates of FPR and TPR should be 0 and 1.

ROC Curve is simply a curve between the False Positive Rate (FPR) and True Positive Rate (TPR). The discrimination of the ROC curve varies with the threshold or cut-off values. FPR is also known as 1-Specificity and TPR is also known as Sensitivity. The ROC curve is only a single Curve which tells the information in the cumulative distribution functions of the scores of the two classes. There are three approaches for estimating the ROC curve - Parametric, Non-Parametric and semi-parametric method. In this paper, we discuss only parametric method for estimating the ROC curve. Mathematical definition of ROC curve is given as

$$y\left(t\right) = 1 - G\left[F^{-1}\left(1 - x\left(t\right)\right)\right],\ 0 \le x(t) \le 1. \qquad (1.4)$$

where, F(.) and G(.) denote the cumulative distribution function of healthy observations and the cumulative distribution function of diseased observations.

Properties of ROC Curve

1. The test values of X are smaller than Y.
2. ROC curve is a monotonically increasing function.
3. ROC curve does not change if the classification scores undergo a strictly increasing transformation.
4. The slope of the ROC curve at a threshold value t is given as
$$slope = \frac{p(t)}{q(t)} \qquad 1.5$$
5. For the symmetric properties we use the Kullback-Leibler divergence that gives a critical values of the TPR and FPR. For checking the symmetric property, first we draw the negative chance diagonal about False positive Rate. The ROC curve is called as TPR asymmetric if the curve may adhere to the left edge of the ROC space longer than it does to the top. Similarly, the ROC curve is called as TNR asymmetric if the curve may adhere to the top edge of the ROC space longer than it does to the left edge of the ROC curve (Ref. Hughes and Bhattacharya (2013)). Suppose that X is a continuous random variable, we denote pdfs $f_1(x)$ for diseased cases and $f_2(x)$ for healthy controls. Then the Kullback-Leibler divergence is defined as

$$KL\left(f_1, f_2\right) = \int_D f_1(x) \ln\left[\frac{f_1(x)}{f_2(x)}\right] dx \qquad (1.6)$$

where $f_1(x)$ is the comparison distribution and $f_2(x)$ is the reference distribution. Similarly,

$$KL\left(f_2, f_1\right) = \int_D f_2(x) \ln\left[\frac{f_2(x)}{f_1(x)}\right] dx \qquad (1.7)$$

$f_2(x)$ is the comparison distribution and $f_1(x)$ as the reference distribution and D is the common support range of f_1 and f_2. Here, it should be noted that if $KL\left(f_1, f_2\right)$ and

$KL(f_2, f_1)$ are positive and $KL(f_1, f_2) = KL(f_2, f_1) = 0$, if and only if $f_1(x) = f_2(x)$. These two measure gives the asymmetry of ROC Curve with respect to diagonal. If $KL(f_1, f_2) < KL(f_2, f_1)$, then the ROC Curve is said to be True Positive Rate asymmetric and if $KL(f_1, f_2) > KL(f_2, f_1)$, then the ROC Curve is said to be True Negative Rate asymmetric.

In this paper, there are five sections. In first section, we discussed the review of literature of Mixture distributions, Exponential mixture distribution and ROC curve. In section second, we discussed Exponential mixture ROC model and the properties of the Exponential mixture ROC curve to know the behavior of the ROC curve. In third section, we discussed the Area Under the Curve of Exponential mixture ROC curve to measure its accuracy. The estimates of parameters of exponential mixture ROC model are derived from maximum likelihood method and method of moments. In section four, we derived variance of Area Under the Curve for testing the hypothesis. In the last section, we discussed the simulation studies by taking a numerical example for the validation of the model.

2. EXPONENTIAL MIXTURE ROC MODEL

Suppose that X follows exponential mixture distribution which is coming from healthy controls and Y also follows Exponential mixture distribution which is coming from diseased cases. The probability distribution function of healthy control and diseased cases are

$$f(x) = p\frac{1}{\lambda_1}e^{-\left(\frac{x}{\lambda_1}\right)} + (1-p)e^{-\left(\frac{x}{\lambda_2}\right)}, 0<\lambda_1,\lambda_2<\infty, 0<x\le\infty,\ p>0, \quad (2.1)$$

$$g(y) = p\frac{1}{\lambda_1}e^{\left(\frac{-y}{\lambda_1}\right)} + (1-p)\frac{1}{\lambda_2}e^{\left(\frac{-y}{\lambda_2}\right)}, 0<\lambda_1,\lambda_2<\infty, 0<y\le\infty,\ p>0. \quad (2.2)$$

The cumulative distribution function of healthy control and diseased cases are given as

$$F(x) = p\left[1 - e^{\left(\frac{-x}{\lambda_1}\right)}\right] + (1-p)\left[1 - e^{\left(\frac{-x}{\lambda_2}\right)}\right], \quad (2.3)$$

$$G(y) = p\left[1 - e^{\left(\frac{-y}{\lambda_1}\right)}\right] + (1-p)\left[1 - e^{\left(\frac{-y}{\lambda_2}\right)}\right]. \quad (2.4)$$

The ROC model of two component exponential mixture distribution is as follows

$$y(t) = p\left[x(t)\right]^{\frac{\lambda_{10}}{\lambda_{11}}} + (1-p)\left[x(t)\right]^{\frac{\lambda_{20}}{\lambda_{21}}},\ 0 \le x(t) \le 1. \quad (2.5)$$

$$x(t) = p\,e^{\left(-\frac{t}{\lambda_{10}}\right)} + (1-p)\,e^{\left(-\frac{t}{\lambda_{20}}\right)},$$

and

$p>0,\ 0 < t < \infty,\ 0 < \lambda_{ij} < \infty$ and i=1,2 , j=1,0.

where p is the weight of the mixture distribution and t is the cut-off or threshold value. The first subscript in λ_{ij} shows that density function is from first or second distribution and second subscript shows that it is coming from either healthy controls or diseased cases. Here, second subscript 0 means it is coming from healthy controls and 1 means it is coming from diseased cases.

The Exponential mixture ROC curve should follow the following assumptions.

1. The mean of the diseased distribution should be greater than the mean of the healthy distribution i.e. $\mu_1 > \mu_0$

2. Attach more weight to the population with higher mean.

The Exponential Mixture ROC curve satisfies the following properties:

1. The ROC curve is monotonically increasing function.

Proof: A function is said to be a monotone increasing function, if the first derivative of the function is positive. Differentiating (2.1) with respect to x(t), we get

$$\frac{dy(t)}{dx(t)} = p\left(\frac{\lambda_{10}}{\lambda_{11}}\right)\left[x(t)\right]^{\frac{\lambda_{10}}{\lambda_{11}}-1} + (1-p)\left(\frac{\lambda_{20}}{\lambda_{21}}\right)\left[x(t)\right]^{\frac{\lambda_{20}}{\lambda_{21}}-1} > 0. \quad 2.6$$

As, the first derivative is greater than zero, hence the ROC curve is monotonically increasing function.

2. ROC curve is concave function.

Proof: A function is said to be concave if its second derivative is negative. Differentiating (2.3) with respect to x(t), we get

$$\frac{d^2y(t)}{d\{x(t)\}^2} = p\left(\frac{\lambda_{10}}{\lambda_{11}}\right)\left(\frac{\lambda_{10}}{\lambda_{11}}-1\right)\{x(t)\}^{\frac{\lambda_{10}}{\lambda_{11}}-2} + (1-p)\left(\frac{\lambda_{20}}{\lambda_{21}}\right)\left(\frac{\lambda_{20}}{\lambda_{21}}-1\right)\{x(t)\}^{\frac{\lambda_{20}}{\lambda_{21}}-2} < 0 \quad 2.7$$

Hence, ROC curve is concave in nature.

3. The slope of the ROC curve at the threshold t is given by

$$slope = \frac{f(y/t)}{f(x/t)}$$

$$= \frac{\lambda_{10}\lambda_{20}\left[p\lambda_{21}e^{\left(-\frac{t}{\lambda_{11}}\right)} + (1-p)\lambda_{11}e^{\left(-\frac{t}{\lambda_{21}}\right)}\right]}{\lambda_{21}\lambda_{11}\left[p\lambda_{20}e^{\left(-\frac{t}{\lambda_{10}}\right)} + (1-p)\lambda_{10}e^{\left(-\frac{t}{\lambda_{20}}\right)}\right]}. \qquad (2.8)$$

The slope of the ROC curve also gives the Likelihood-Ratio which is useful in hypothesis testing.

4. ROC curve is invariant with respect to monotone increasing transformation of the test scores.

5. The ROC curve is TPR asymmetric.

Proof: The K-L divergence between the distribution of diseased and healthy group with p(x) as the comparison distribution and q(x) as the reference distribution has been given as

$$KL(p,q) = \left[\ln\lambda_{10} + \ln\lambda_{20} + \ln\left\{p\lambda_{21}e^{\left(\frac{t}{\lambda_{11}}\right)} + (1-p)\lambda_{11}e^{\left(\frac{t}{\lambda_{21}}\right)}\right\} - \ln\lambda_{11} - \ln\lambda_{21} - \ln\left\{\begin{matrix} p\lambda_{20}e^{\left(\frac{t}{\lambda_{10}}\right)} + \\ (1-p)\lambda_{10}e^{\left(\frac{t}{\lambda_{20}}\right)}\end{matrix}\right\}\right] * \left[\frac{p}{\lambda_{11}}e^{\left(\frac{t}{\lambda_{11}}\right)} + \frac{(1-p)}{\lambda_{21}}e^{\left(\frac{t}{\lambda_{21}}\right)}\right] \qquad (2.9)$$

Similarly, the K-L divergence between the distribution of healthy and diseased group with q(x) as the comparison distribution and p(x) as the reference distribution has been given as

$$KL(q,p) = \left[\ln\lambda_{21} + \ln\lambda_{11} + \ln\left\{p\lambda_{20}e^{\left(\frac{t}{\lambda_{10}}\right)} + (1-p)\lambda_{10}e^{\left(\frac{t}{\lambda_{20}}\right)}\right\} - \ln\lambda_{10} - \ln\lambda_{20} - \ln\left\{\begin{matrix} p\lambda_{21}e^{\left(\frac{t}{\lambda_{11}}\right)} \\ +(1-p)\lambda_{11}e^{\left(\frac{t}{\lambda_{21}}\right)}\end{matrix}\right\}\right] * \left[\frac{p}{\lambda_{10}}e^{\left(\frac{t}{\lambda_{10}}\right)} + \frac{(1-p)}{\lambda_{20}}e^{\left(\frac{t}{\lambda_{20}}\right)}\right] \qquad (2.10)$$

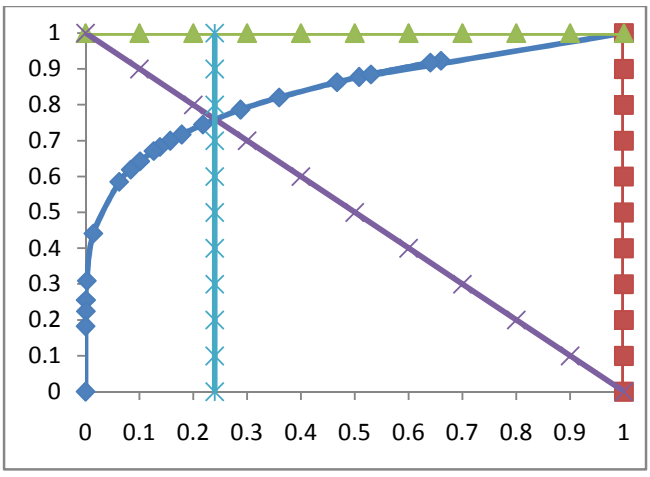


Fig. 2.1: TPR asymmetric Exponential Mixture ROC curve

It was found that KL(q,p) > KL(p,q). These two divergence measures would be zero if the healthy and diseased groups are identical. Hence, we have proved that, the ROC curve is TPR asymmetric. Figure 2.1 shows the asymmetric property of Exponential mixture ROC curve.

3. AREA UNDER THE EXPONENTIAL MIXTURE ROC CURVE

The measure of accuracy of the discrimination between the healthy and diseased distribution is Area Under the ROC curve.The Area Under the ROC curve gives the best measure of accuracy of the classification. Mathematically the Area Under the ROC curve is given as

$$AUC = P(y > x) = \int_0^1 y(t)dt \qquad (3.1)$$

The Area Under the ROC curve lies between 0 and 1. For a perfect diagnostic test, the Area under the ROC curve should be 1 and the curve should lie on the upper left border of the ROC space. For a worthless test, the Area Under the ROC curve will be equal or less than 0.50. Area under the exponential mixture ROC curve is given as

$$AUC = p\left(\frac{\lambda_{11}}{\lambda_{11}+\lambda_{10}}\right) + (1-p)\left(\frac{\lambda_{21}}{\lambda_{21}+\lambda_{20}}\right) \qquad (3.2)$$

The estimates of the parameters of ROC model can be found by using two methods which are discussed below.

(a) Maximum likelihood method

The probability distribution function of exponential mixture distribution which is coming from healthy control is as follows

$$f(x) = pf(x;\lambda_{10}) + (1-p)f(x;\lambda_{20})$$

where

$$f(x;\lambda_{10}) = \frac{1}{\lambda_{10}}e^{-\left(\frac{x}{\lambda_{10}}\right)} \quad and \quad f(x;\lambda_{20}) = \frac{1}{\lambda_{20}}e^{-\left(\frac{x}{\lambda_{20}}\right)}.$$

For estimating the parameter λ_{10}, the likelihood function is given as

$$L(x_{10}, x_{20}, ..., x_{m0} / \lambda_{10}) = \left(\frac{1}{\lambda_{10}}\right)^{m_{10}} e^{-\sum_{i=1}^{m_{10}}\frac{x_i}{\lambda_{10}}}.$$

The log-likelihood of the above equation is

$$\log L(\lambda_{10} / x_{10}, x_{20}, ..., x_{m0}) = m_{10}\log 1 - m_{10}\log\lambda_{10} - \frac{1}{\lambda_{10}}\sum_{i=1}^{m_{10}} x_i.$$

Differentiating above equation with respect to λ_{10} and equating it to zero, we get

$$\hat{\lambda}_{10} = \frac{1}{m_{10}} \sum_{i=1}^{m_{10}} x_i . \tag{3.3}$$

Similarly, we get

$$\hat{\lambda}_{20} = \frac{1}{m_{20}} \sum_{i=1}^{m_{20}} x_i . \tag{3.4}$$

The probability distribution function of Exponential mixture distribution which is coming from diseased cases is written as

$$g(y) = p g(y; \lambda_{11}) + (1 - p) g(y; \lambda_{21}).$$

On the similar lines as done above, the maximum likelihood estimate of $\hat{\lambda}_{11}$ and $\hat{\lambda}_{21}$ are given as

$$\hat{\lambda}_{11} = \frac{1}{n_{11}} \sum_{i=1}^{n_{11}} y_i , \tag{3.5}$$

$$\hat{\lambda}_{21} = \frac{1}{n_{21}} \sum_{i=1}^{n_{21}} y_i . \tag{3.6}$$

Substituting all the estimates from (3.3)-(3.6) in the Area Under the Curve of Exponential mixture ROC curve (3.2), the Estimated AUC is given as

$$\hat{AUC} = p\left(\frac{\frac{1}{n_{11}}\sum_{i=1}^{n_{11}} y_i}{\frac{1}{n_{11}}\sum_{i=1}^{n_{11}} y_i + \frac{1}{m_{10}}\sum_{i=1}^{m_{10}} x_i}\right) + (1-p)\left(\frac{\frac{1}{n_{21}}\sum_{i=1}^{n_{21}} y_i}{\frac{1}{n_{21}}\sum_{i=1}^{n_{21}} y_i + \frac{1}{m_{20}}\sum_{i=1}^{m_{20}} x_i}\right). \tag{3.7}$$

(b) Method of moments

Method of moment is another method for estimating the population parameters. It is a simple method for estimating the parameters. The method of moment is introduced by Pearson (1894) for estimating the parameters of two component normal-mixture distribution. Rider (1961) discussed the method of moment for estimating the parameter of exponential mixture distribution. In the method of moments, first we derive the equation which is based on population moments and these population moments are estimated by drawing the sample observation. These equations are solved by using the sample moments in place of population moment. The rth moment about origin of the exponential mixture distribution is given as

$$\mu_r' = p \int_0^\infty x^r f_1(x) dx + (1 - p) \int_0^\infty x^r f_2(x) dx \tag{3.8}$$

where $f_1(x)$ and $f_2(x)$ are the density functions of the Exponential distribution which have been discussed earlier. Now (3.8) can be written as

$$\mu_r' = p \int_0^\infty x^r \frac{1}{\lambda_1} e^{-\left(\frac{x}{\lambda_1}\right)} dx + (1 - p) \int_0^\infty x^r \frac{1}{\lambda_2} e^{-\left(\frac{x}{\lambda_2}\right)} dx$$

$$\mu_r' = p\Gamma(r+1)(\lambda_1)^r + (1-p)\Gamma(r+1)(\lambda_2)^r \quad for \ r = 1, 2, 3. \tag{3.9}$$

The corresponding sample moment is defined as

$$m_r' = p\Gamma(r+1)(\lambda_1)^r + (1-p)\Gamma(r+1)(\lambda_2)^r, \ for \ r = 1, 2, 3. \tag{3.10}$$

The first three sample moments are given as follows

$$m_1' = p\lambda_1 + (1 - p)\lambda_2 , \tag{3.11}$$

$$m_2' = 2p\lambda_1^2 + 2(1 - p)\lambda_2^2 , \tag{3.12}$$

$$m_3' = 6p\lambda_1^3 + 6(1 - p)\lambda_2^3 . \tag{3.13}$$

Using these equations, we can estimate the parameters λ_1 and λ_2 in terms of sample moments as

$$\hat{\lambda}_1 = \frac{2m_1' - 2(1-p)m_1' \pm \sqrt{-4p(1-p)m_1'^2 + 2p(1-p)m_2'}}{2p} \tag{3.14}$$

$$\hat{\lambda}_2 = \frac{2(1-p)m_1' \pm \sqrt{-4p(1-p)m_1'^2 + 2p(1-p)m_2'}}{2(1-p)} \tag{3.15}$$

4. VARIANCE OF AUC AND CONFIDENCE INTERVAL OF AUC

For finding the variance of AUC of Exponential mixture ROC curve, we will use the delta method. It gives the approximate expression of variance of AUC and it is based on Taylor series expansion.

$$\text{var}iance(AUC) = p\,\text{var}ince\left(\frac{\lambda_{11}}{\lambda_{11}+\lambda_{10}}\right) + (1-p)\,\text{var}iance\left(\frac{\lambda_{21}}{\lambda_{21}+\lambda_{20}}\right) \tag{4.1}$$

$$\text{var}iance(AUC) = p\,\text{var}iance(\delta_1) + (1-p)\,\text{var}iance(\delta_2) \quad (4.2)$$

where, $\delta_1 = \frac{\lambda_{11}}{\lambda_{11} + \lambda_{10}}$ and $\delta_2 = \frac{\lambda_{21}}{\lambda_{21} + \lambda_{20}}$.

First, we find the variance of δ_1 and variance of δ_2 as

$$\text{var}iance(\delta_1) = \left(\frac{\partial \delta_1}{\partial \lambda_{11}}\right)^2 \text{var}iance(\lambda_{11}) + \left(\frac{\partial \delta_{10}}{\partial \lambda_{10}}\right)^2 \text{var}iance(\lambda_{10}) + 2\left(\frac{\partial \delta_1}{\partial \lambda_{11}}\right)\left(\frac{\partial \delta}{\partial \lambda_{10}}\right)\text{cov}ariance(\lambda_{11}, \lambda_{10}) \quad (4.3)$$

$$\text{var}iance(\delta_2) = \left(\frac{\partial \delta_2}{\partial \lambda_{21}}\right)^2 \text{var}iance(\lambda_{21}) + \left(\frac{\partial \delta_2}{\partial \lambda_{20}}\right)^2 \text{var}iance(\lambda_{20}) + 2\left(\frac{\partial \delta_2}{\partial \lambda_{21}}\right)\left(\frac{\partial \delta_2}{\partial \lambda_{20}}\right)\text{cov}ariance(\lambda_{21}, \lambda_{20}) \quad (4.4)$$

For finding the variance of λ_{11}, variance of λ_{10} and also covariance between λ_{11} and λ_{10}, we will use fisher information matrix. The fisher information matrix is given as

$$I(\theta) = -\begin{bmatrix} E\left(\frac{\partial^2 LogL}{\partial \lambda_{11}^2}\right) & E\left(\frac{\partial^2 LogL}{\partial \lambda_{11}\partial \lambda_{10}}\right) \\ E\left(\frac{\partial^2 LogL}{\partial \lambda_{10}\partial \lambda_{11}}\right) & E\left(\frac{\partial^2 LogL}{\partial \lambda_{10}^2}\right) \end{bmatrix}$$

where

$$L = \left(\frac{1}{\lambda_{11}}\right)^{n_{11}} e^{-\sum_{i=1}^{n_{11}}\left(\frac{y_i}{\lambda_{11}}\right)}.$$

Taking log on both sides, we get

$$\log L = n_{11}\log 1 - n_{11}\log \lambda_{11} - \frac{1}{\lambda_{11}}\sum_{i=1}^{n_{11}} y_i. \quad (4.5)$$

Differentiating (4.5), twice with respect to λ_{11}, we get

$$\frac{\partial^2 LogL}{\partial \lambda_{11}^2} = -\frac{n_{11}}{\lambda_{11}^2}.$$

Similarly

$$\frac{\partial^2 LogL}{\partial \lambda_{10}^2} = -\frac{m_{10}}{\lambda_{10}^2}.$$

The covariance terms are zero due to independent identically distributed random variables. Substituting these values in Fisher information matrix, we get

$$I(\theta) = -\begin{bmatrix} E\left(-\frac{n_{11}}{\lambda_{11}^2}\right) & 0 \\ 0 & E\left(-\frac{m_{10}}{\lambda_{10}^2}\right) \end{bmatrix}.$$

The diagonal terms of the inverse of the Fisher information matrix gives

$$variance(\lambda_{11}) = \frac{\lambda_{11}^2}{n_{11}} \text{ and } \text{var}iance(\lambda_{10}) = \frac{\lambda_{10}^2}{m_{10}}.$$

We know that $\delta_1 = \frac{\lambda_{11}}{\lambda_{11} + \lambda_{10}}$. Now differentiating δ_1 with respect to λ_{11} and λ_{10}, we get

$$\frac{\partial \delta_1}{\partial \lambda_{11}} = \frac{\lambda_{10}}{(\lambda_{10} + \lambda_{11})^2} \text{ and } \frac{\partial \delta_1}{\partial \lambda_{10}} = -\frac{\lambda_{11}}{(\lambda_{10} + \lambda_{11})^2}.$$

Substituting all these values in (4.3), we get

$$\text{var}iance(\delta_1) = \left[\frac{\lambda_{10}}{(\lambda_{10}+\lambda_{11})^2}\right]^2 \frac{\lambda_{11}^2}{n_{11}} + \left[-\frac{\lambda_{11}}{(\lambda_{10}+\lambda_{11})^2}\right]^2 \frac{\lambda_{10}^2}{m_{10}}$$

and

$$\text{var}iance(\delta_1) = \frac{\lambda_{11}^2\lambda_{10}^2}{(\lambda_{10} + \lambda_{11})^2}\left[\frac{m_{10} + n_{11}}{m_{10}n_{11}}\right]. \quad (4.6)$$

Similarly, we get

$$\text{var}iance(\delta_2) = \frac{\lambda_{21}^2\lambda_{20}^2}{(\lambda_{21} + \lambda_{20})^2}\left[\frac{m_{20} + n_{21}}{m_{20}n_{21}}\right]. \quad (4.7)$$

Putting the values of $\text{var}iance(\delta_1)$ and $\text{var}iance(\delta_2)$ in (4.2), we get

$$\text{var}iance(AUC) = p\left[\frac{\lambda_{11}^2\lambda_{10}^2}{(\lambda_{11}+\lambda_{10})^2}\left(\frac{m_{10}+n_{11}}{m_{10}n_{11}}\right)\right] + (1-p)\left[\frac{\lambda_{21}^2\lambda_{20}^2}{(\lambda_{21}+\lambda_{20})^2}\left(\frac{m_{20}+n_{21}}{m_{20}n_{21}}\right)\right]. \quad (4.8)$$

For testing the hypothesis,

$$H_0 : AUC = AUC_0 \text{ vs } H_1 : AUC \neq AUC_0,$$

the test statistic of AUC is given as

$$Z = \frac{AUC - \hat{AUC}}{\sqrt{V\left(\hat{AUC}\right)}} \sim N(0,1). \quad (4.9)$$

The 100(1-α)% confidence interval of AUC is given as

$AUC \pm SE\left(\hat{AUC}\right)Z_{\alpha/2}$ (4.10) where α is the level of significance and $Z_{\alpha/2}$ is the critical value of the confidence interval.~

5. SIMULATION STUDIES

In this paper, we use Monte Carlo Simulation technique for validation of our results by taking an example. Monte Carlo Simulation method is very useful when the population is heterogeneous. It is based on the repeated random sampling. The following steps define the Monte Carlo Simulation algorithm

- First define a possible range of unit.
- Second generate random numbers for a given possible distribution over the range.
- Third to execute a deterministic computation from the unit.
- Fourth get the result.

We estimate the population parameters of exponential mixture distribution of six different sample sizes 10, 20, 30, 100, 200, 300. We take the population parameter of exponential mixture distribution viz. $\lambda_{10}=1$, $\lambda_{20}=2$, $\lambda_{11}=5$ and $\lambda_{21}=4$. The sample size of each density function is same $m_{10}=m_{20}=n_{11}=n_{21}=n$. The Area Under the Exponential mixture ROC curve is 78.33% using the population parameters.

The estimated value of the parameters of exponential mixture ROC model using maximum likelihood method and method of moments are given in Tables 5.1 and 5.2. The estimated AUC, its variance for the exponential mixture ROC curve using maximum likelihood method and method of moments are given in the Tables 5.2 and 5.4. The bias of parameters is given in parenthesis.

Table 5.1. The estimated value of parameters of Exponential mixture ROC curve using Maximum Likelihood method

n	$\hat{\lambda}_{10}$	$\hat{\lambda}_{20}$	$\hat{\lambda}_{11}$	$\hat{\lambda}_{21}$
10	0.905 (-0.094)	0.905 (-1.094)	4.058 (-0.941)	4.058 (0.058)
20	0.813 (-0.186)	1.795 (-0.205)	4.258 (-0.741)	0.173 (4.173)
30	1.472 (0.472)	1.472 (-0.528)	4.125 (-0.874)	4.125 (0.125)
100	0.552 (-0.448)	3.60 (1.60)	4.464 (-0.536)	1.683 (-2.317)
200	1.400 (0.400)	1.400 (-0.6)	5.112 (0.112)	5.111 (1.111)
300	0.777 (0.223)	1.477 (-0.522)	6.045 (1.045)	3.656 (-0.344)

Table 5.2. Estimated variance, standard error and confidence interval of AUC of Exponential mixture ROC curve using Maximum Likelihood method

n	$\hat{AUC}$	$v(\hat{AUC})$	$SE(\hat{AUC})$	$\hat{AUC}-Z_{\alpha/2}SE(\hat{AUC})$	$\hat{AUC}+Z_{\alpha/2}SE(\hat{AUC})$
10	0.8175	0.0044	0.0667	0.686	0.9482
20	0.8337	0.0007	0.0271	0.7805	0.8868
30	0.7370	0.0025	0.0500	0.639	0.835
100	0.7185	0.0003	0.0197	0.6798	0.7571
200	0.7850	0.0002	0.0168	0.7520	0.8179
300	0.8339	0.0002	0.0152	0.8041	0.8636

Table 5.3. The estimated value of parameters of Exponential mixture ROC curve using Method of moments

n	$\hat{\lambda}_{10}$	$\hat{\lambda}_{20}$	$\hat{\lambda}_{11}$	$\hat{\lambda}_{21}$
10	0.905 (-0.094)	0.905 (-1.094)	2.847 (-2.153)	3.684 0.316
20	1.194 (0.194)	1.153 (-0.847)	4.782 (-0.218)	14.641 (10.641)
30	1.469 (0.469)	1.472 (-0.528)	3.496 (-1.504)	3.355 (-0.645)
100	1.231 (0.231)	5.984 (3.984)	3.984 (-1.016)	6.125 (2.125)
200	1.399 (0.399)	1.400 (-0.600)	5.112 (0.112)	5.115 (1.115)
300	1.283 (0.283)	4.163 (2.163)	2.905 (-2.095)	5.136 (1.136)

Table 5.4. Estimated variance, standard error and confidence interval of AUC of Exponential mixture ROC curve using Maximum Likelihood method

n	$\hat{AUC}$	$v(\hat{AUC})$	$SE(\hat{AUC})$	$\hat{AUC}-Z_{\alpha/2}SE(\hat{AUC})$	$\hat{AUC}+Z_{\alpha/2}SE(\hat{AUC})$
10	0.771	0.0036	0.6002	0.654	0.889
20	0.838	0.0001	0.0131	0.812	0.864
30	0.701	0.0031	0.0562	0.591	0.811
100	0.682	0.0003	0.0193	0.647	0.725
200	0.785	0.0002	0.0168	0.752	0.818
300	0.651	0.0001	0.0114	0.628	0.673

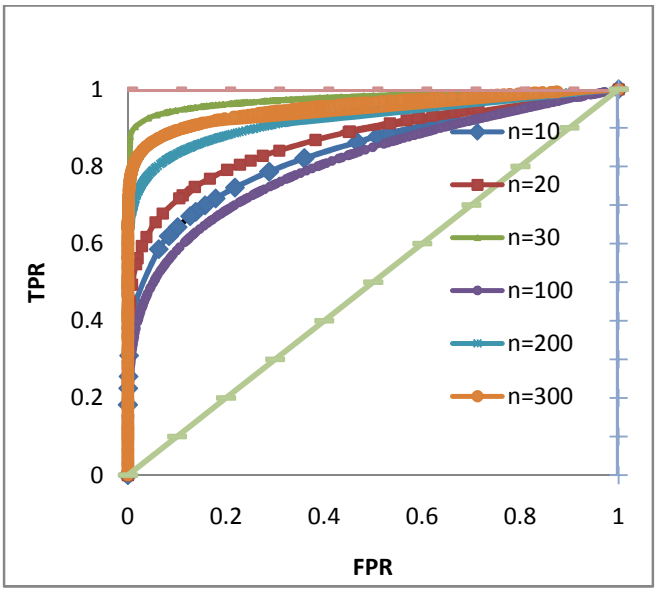


Figure 5.1. Exponential mixture ROC Curves

From Tables 5.1 to 5.4, it is observed that estimate become closer to the parameters with increase in sample size and bias get reduced. It is clear that estimates given by maximum likelihood method are more closer to the true parameter as compared to the estimates by method of moments. It is also observed that the Area under the ROC curve (AUC) is more closer to the true value of AUC using maximum likelihood method as compared to the method of moments.

Figure 5.1 shows Exponential mixture ROC curve for different sample sizes and as the sample size increases the exponential mixture ROC curve is much closer to the perfect ROC curve.

6. CONCLUSION

The Exponential mixture distribution is a very useful distribution in life testing specially in the case of presence of heterogeneity in the population. In this paper, the expression for the Exponential mixture ROC curve is found and its properties are discussed. We also derived the expressions for accuracy, variance and confidence interval of AUC. The

parameters of Exponential mixture ROC model are derived by using the maximum likelihood method and method of moments. It was found that the maximum likelihood method gives better estimates in terms of less bias as compared to the estimates by method of moments. We also observed that the accuracy increased and variance of AUC decreased by increasing the sample size. Hence, when the population have heterogeneity and also follows exponential distribution then one should use Exponential mixture ROC model instead of Exponential ROC model.

REFERENCES

[1] Dass, S.C. and Seong, W.K., "*A Semi-parameteric Approach to Estimation of ROC Curves for Multivariate BinormalMixtures*", 2011, www.stt.msu.edu/Links/Research_Memoranda/RM/RM_683.pdf.

[2] Everitt, B. and Hand, D.J., *Finite Mixture Distributions*, Chapman and Hall, New York, 1981.

[3] Gonen, M., "Mixtures of Receiver Operating Characteristic Curves", *Memorial Sloan-Katter in Cancer,* 2013, http//works.bepress.com/mithat_gonen/23.

[4] Hughes, G. and Bhattacharya B., "*Symmetry properties of Bi-normal and Bi-gamma Receiver operating characteristic curves are described by Kullback-Leibler divergences*", *Entropy*, 15(4), 2013, pp.1342-1356.

[5] McLachlan, G. and Peel D., *Finite Mixture Models*, John Wiley, New York, 2003.

[6] Newcomb, S., "A generalized theory of the combination of observations so as to obtain the best result", *American Journal of Mathematics*, 8, 1886, pp. 343-346.

[7] Pearson, K., "Contribution to the mathematical theory of evolution", *Philosophical Transactions of Royal Society*, *A*, 185, 1894, pp. 71-110.

[8] Rider, Paul R., "Estimating the parameters of mixed Poisson, Binomial and Weibull Distribution by the method of moments", *Bulletin de I'institue International de Statistique,* 1961, part2, 38.

[9] Schlattmann, P., *Medical Application of Finite Mixture Models*, Springer-Verlag, Berlin, Heidelberg, 2009.

[10] Titterington, D.M., Smith, A.F.M. and Makov, U.E., *Statistical Analysis of Finite Mixture Distributions*, John Wiley and Sons Ltd., New York, 1985.

ACKNOWLEDGEMENT

This work was supported by UGC-Major Research Project from University Grants Commission (UGC), New Delhi, INDIA. The authors wish to express their gratitude to UGC for the financial support to carry out this research work.

PROGRAM

In this paper, we did the simulation by using Mathematica 8 software. The commands are as follows:

Dist=MixtureDistribution[{p,1-p},{ExponetialDistribution[1/ λ_1],ExponentialDistribution[1/ λ_2]}]

Data=RandomVariate[Dist,sample size]

FindDistributionParameters[Data,MixtureDistribution[{p,1-p},{ExponentialDistribution[1/ λ_1], ExponentialDistribution[1/ λ_2]}],ParameterEstimator->"MaximumLikelihood"]
FindDistributionParameters[Data,MixtureDistribution[{p,1-p},{ExponentialDistribution[1/ λ_1], ExponentialDistribution[1/ λ_2]}],ParameterEstimator->"MethodOfMoments"]

Assessment of Soil Physico-Chemical Parameter for Sustainable Crop Planning in a Hilly Terrain of Assam

Laxmi Narayan Sethi[1], Bornika Mandal[2], Racktackshree Chelleng[3]

[1]Department of Agricultural Engineering, Assam University (A Central University)
Silchar-788011, Assam, India
[2]Master of Technology in Water Resources Development and Management
Department of Agricultural Engineering, Assam University (A Central University)
Silchar-788011, Assam, India
[3]Bachelor of Technology in Department of Agricultural Engineering
Department of Agricultural Engineering, Assam University (A Central University)
Silchar-788011, Assam, India

Abstract: **Assam state of North Eastern Region of India is surrounded by many hilly terrains which are lying barren throughout the year. In order to achieve sustainable crop production in hilly terrain with humid climate, more appropriate approach is the assessment of soil physico-chemical properties as well as soil fertility. So, the present study describes the details of topographical survey, soil sampling and analysis of physical properties at different soil profiles and find out the status of suitability of land for crop planning in the hilly terrain. The topographical survey revealed the sloppy nature of the top land surface varying the slope from 3 to 7%. And the average depth of soil on the top land was found to be only 60 cm and below which hard pan layer was encountered. So, the soil physico-chemical parameter analysis were carried out at four depth of soil profiles (0-15, 15-30, 30-45 and 45-60 cm). The soil profile analysis revealed that texture of the soils of the study site was sandy loam in nature with average sand, silt and clay percentage of 73, 11 and 17%, respectively. Average bulk density and moisture content was found to be 2g/cc and 9%, respectively. The soil water characteristics analysis revealed that the soil profile of 0-15, 15-30, 30-45 and 45-60 cm confined the field capacity and wilting point water content of 22.42, 23.11, 23.09, 23.51% and 12.44, 11.87, 12.30, 11.91%, respectively. The average pH and EC of the soil samples was found to be 5.3 and 8468.75µS, respectively. The predictive assessment of topographical survey and soil physico-chemical properties at a generic level revealed the scope for growing vegetables and horticultural crops in the hilly terrains.**

Keywords: **Hilly terrain, physical properties, chemical properties and agricultural planning.**

1. INTRODUCTION

Maintenance of soil quality is essential to sustain crop yields even under harsh environments like the humid tropics where high soil erosion, landslides and nutrient losses generally occur. Soil quality assessment has also been suggested as a tool for evaluating sustainability of soil and crop management practices [9]. Soil fertility refers to the ability of the soil to support organic life. It also refers to the inherent capacity of the soil to supply nutrient in adequate amount and in suitable proportions for crop growth and crop yield.

The physical properties of soils determine their adaptability to cultivation and the level of biological activity that can be supported by the soil. Soil physical properties such as texture, bulk density and water content etc. also largely determine the soil's water and air supplying capacity to plants. Soil texture affects the infiltration and retention of water, soil aeration, absorption of nutrients, microbial activities, tillage and irrigation practices [7, 8]. Soil texture is also an indicator of some other related soil features such as type of parent material, homogeneity and heterogeneity within the profile, migration of clay and intensity of weathering of soil material or age of soil [12, 11].

The bulk density of soil (the mass of a unit volume of dry soil) determine the compactness and also considered as a measure of soil structure, for calculating soil pore space and as indicator of aeration status and water content [1]. Bulk density also provides information on the environment available to soil microorganisms. Soil water enhances various soil physicochemical reactions and supplies essential nutrients for plants and animals including micro and macro organisms residing in soils in order that they can carry out their own activities [13, 4]. The portion of stored soil water that can readily be absorbed by plants is said to be available water. The plant available soil water is held within a potential between field capacity (FC) and permanent wilting point (PWP).

Soil reaction (usually expressed as pH value) is the degree of soil acidity or alkalinity, which is caused by particular chemical, mineralogical and/or biological environment. Soil

reaction affects nutrient availability and toxicity, microbial activity, and root growth. Thus, pH is one of the most important chemical characteristics of the soil solution because both higher plants and microorganisms respond so markedly to their chemical environment. Electrical conductivity (EC) is a measure of salinity. In addition to overcoming some of the ambiguities of total dissolved salts measurements, the EC measurement is quicker and sufficiently accurate for most purposes [2].

Since, the soil quality status of the hilly terrain of Assam University, Silchar has not been monitored for sustainable crop planning. So, the present study has been carried out to assess the aforementioned soil physical and chemical properties at different soil profiles of the hilly terrain which is among the non-irrigated land of the Assam state in India.

2. MATERIALS AND METHODS

2.1 Study area

One of the hilly terrains situated in the Assam University, Silchar of Cachar district and in the southern part of the Assam was considered for the study area. The study area hilly terrain of Assam University, Silchar covered total hill top area of about 10000m^2. The climate of the Silchar is warm and humid during summer where average relative humidity is 85% and in winter it is about 78%. The area receives an average of 2196 mm rainfall during the year. Soils of the zone vary from sandy type to clay soil mostly suitable for field crops including horticultural crops. The soil pH ranges from 4.6 to 5.7.

2.2 Topographic survey and soil sampling

In order to assess the suitability of land for agriculture and classification of soils, topographical land survey was carried out using standard surveying instruments such as Global Positioning System (GPS) and Automatic Level. The total area of the hilly terrain was found about 9682.8m^2. Because of dense jungle, it was not possible to make demarcation in to different sections of the land. However, randomly, total of 16 (8 numbers in left side and 8 numbers in right side) observation points were considered for the assessment of soil parameters of the terrain. The topographical view of the study site is shown in Figure1.

The topographic characteristics such as land area, soil depth, slope and elevation of each observation points were determined using standard guidelines of land capability classification [10].

Three main factors such as depth, sampling intensity per unit area of site sampled, and the sampling design are usually considered when developing soil-sampling protocols to monitor change in major soil fertility parameters. It is noted that sampling by fixed depths, rather than by generic horizon, underestimated soil carbon losses due to cultivation [6]. So, the sampling by fixed depth was considered and collected using a soil core cutter and sampler. During collection of samples; dead plants, old manures and areas near trees were excluded.



Figure 1. A topographical view of the hilly terrain

2.3 Analysis of soil physical properties

2.3.1 Soil texture

Soil texture refers to the proportion of the soil “separates” that make up the mineral component of soil. These separates are called sand, silt, and clay. Hydrometer method was used to estimate particle size distribution without any pretreatment, except dispersion with calgon. Hydrometer method and International pipette method are used commonly to determine the particle size of the soil (Both methods are based on principle of sedimentation known as Stocks law) [3]. In the present study, hydrometer method was used to estimate particle size distribution without any pretreatment, except dispersion with calgon.

2.3.2 Bulk density

Bulk density is the proportion of the weight of a soil relative to its volume. It is expressed as a unit of weight per volume, and is commonly measured in units of grams per cubic centimeters (g/cc). Bulk density of soil was estimated by soil corer method (Brady and Weil, 2004) [5] using soil core with a known diameter (d) and height (h).

2.3.3. Moisture content

Soil water enhances various soil physicochemical reactions and supplies essential nutrients for plants and animals including micro and macro organisms residing in soils in order that they can carry out their own activities. The soil

moisture content indicates the amount of water present in the soil. It is commonly expressed as the amount of water (in mm of water depth) present in a depth of one metre of soil. Moisture content of soil was calculated by oven drying method (Soil Survey Standard Test Method) using moisture box, electronic weight machine and soil core. The soil samples were collected and kept in the oven at a temperature of 105˚C for 24 hours.

2.3.4. Soil moisture characteristics

The portion of stored soil water that can readily be absorbed by plants is said to be available water. The plant can avail soil water that is held within a potential between field capacity (FC) of 0.3 bar and permanent wilting point (PWP) of 15 bar. Permanent wilting point (PWP) or wilting point (WP) is defined as the minimal point of soil moisture the plant requires not to wilt. Field capacity (FC) is the amount of soil moisture or water content held in the soil after excess water has drained away and the rate of downward movement has decreased. So, the available soil water characteristics at different potentials (0.3 bar, 1 bar, 5 bar and 15 bar) were determined using the pressure plate apparatus.

2.4 Analysis of soil chemical properties pH

By definition, 'pH' is a measure of the active hydrogen ion (H+) concentration. It is an indication of the acidity or alkalinity of a soil, and also known as "soil reaction". Soil pH was measured by "Electrometric method" using pH meter.

2.4.2 Electrical conductivity

Soil utilizes organic materials for a variety of uses, including providing plants with nutrients, aiding in irrigation, lowering evaporation rates, increasing the nutrient-holding capacity of the soil and providing food for worms, bacteria and other soil organisms. The EC was calculated with the help of a conductivity meter.

3. RESULTS AND DISCUSSION

3.1 Topographic and land characteristics

The topography and land characteristics of the study site are presented in Table 1. The topographical survey revealed that the top land surface is sloppy and undulating.

Table 1. Topography and land characteristics of the study site

Sites	Obser-vation points	Elevation (m) w.r.t. MSL	Slope (%)	Range of soil depth (cm)	Topography and class	Drainage type and class
Left Side	(A)	36.5	2.85		Gently sloping to gently undulating B_2	Moderately well drained C_3
	(B)	36.27	2.04			
	(C)	35.85	4.17			
	(D)	35.77	3.53	25-50		
	(E)	35.72	3.31			
	(F)	35.81	2.60			
	(G)	35.83	2.22			
	(H)	35.84	1.98			
Right Side	(A)	36.32	2.57		Moderately sloping to gently undulating B_3	Moderately well drained C_3
	(B)	35.59	8.67			
	(C)	35.37	7.96			
	(D)	34.87	9.11	50-90		
	(E)	34.24	10.00			
	(F)	34.27	7.91			
	(G)	34.67	5.67			
	(H)	34.59	5.31			

It was observed that left side of terrain has an average land slope of about 3% and so the land is gently sloping to undulating (class B_2 type). However, average land slope of right side of terrain was found to be 7% and which is moderately sloping to gently undulating (Class B_3 type). The drainage systems of both the sides were found to be moderately well drained which indicates that it is a class C_3 type (Land Capability Classification, Agriculture Handbook, United States Department of Agriculture, 1958). The average soil depth in the study area was found 60 cm. So, further sampling and analysis were carried out using the individual samples from four profile depths (0-15, 15-30, 30-45 and 45-60cm).

3.2 Soil physical properties status

Soil samples collected from average 8 locations and 4 depths of profile in the study site were used to determine the soil texture, bulk density, moisture content, soil moisture characteristics.

According to USDA textural classification triangle, it was found that the soils of the study site are sandy loam in nature with average sand, silt and clay percentage of 73%, 11% and 17%, respectively, indicating the coarse nature of the soil and the low water retention characteristics. The depth wise average soil texture status of the study site is presented in Table 2.

Table 2. Depth wise average soil texture status of the study site

Sites	Depth (cm)	Clay (%)	Silt (%)	Sand (%)	Soil Type
Left	0-15	20	10	70	Sandy loam
	15-30	16	6	78	Sandy loam
	30-45	12	12	76	Sandy loam
	45-60	10	12	78	Sandy loam
Right	0-15	16	12	72	Sandy loam
	15-30	20	10	70	Sandy loam
	30-45	20	12	68	Sandy loam
	45-60	20	12	68	Sandy loam

The depth wise wet and dry bulk density, moisture content of the study site are presented in Table 3. The average bulk density was found to be 2g/cc. The average moisture content was found to be 9% which implies available soil water is held within a potential between field capacity (FC) and permanent wilting point (PWP). The moisture content was found in decreasing trend with the increase in the soil depth and vice versa. It was observed that soils with high amount of clay have higher amount of water than soils with low amount of clay content.

The variations of the soil water characteristics are presented in Figure 3. The soil water content at field capacity and wilting points at 0-15, 15-30, 30-45 and 45-60 cm profile were observed to be 22.42, 23.11, 23.09, 23.51% and 12.44, 11.87, 12.30, 11.91% respectively. Soil water content at FC and PWP were found to be increasing with depth for the soil may be due to variation in topography and land use all affect the distribution of soil moisture and different management practice. Soils with high amount of clay have higher amount of water both at 1/3 and 15 bars than soils with low amount of clay content.

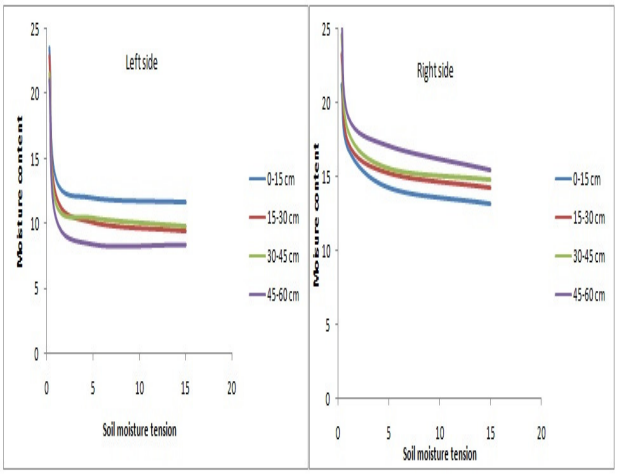


Figure 2. Depth wise soil moisture characteristic in the study site.

3.3. Soil chemical properties status

The observed pH and EC of different soil samples of the study site is also shown in Figure 3 and 4, respectively. The EC of the soil samples were found to be in the range of 4000 to 13600 Micro Siemen (µS). It has been found from the graph that the EC is highest at the soil profile 15-30 cm in left side of terrain and is decreasing with the increase in the depth. The EC of the soil in right side of terrain is almost similar in all the places.

The average pH and EC of all the soil samples were found to be 5.3 and 8468.75µS, respectively which indicate that the soil is strongly acidic in nature and about 50% of applied fertilizer may be available to plants. The pH was found to be more in the upper surface of both the fields as compared to other layers.

Table 3. Depth wise status of bulk density and moisture content the study site.

Observation Points	Depths (cm)	Dry Bulk Density (g/cc)	Wet Bulk Density (g/cc)	Moisture Content (%)	Dry Bulk Density (g/cc)	Wet Bulk Density (g/cc)	Moisture Content (%)
		Left side of terrain			Right side of terrain		
A	0-15	1.83	2.06	12.23	1.59	1.91	20.47
	15-30	1.85	2.02	9.64	1.62	1.83	12.93
	30-45	1.87	2.06	10.50	1.72	1.90	10.17
	45-60	2.17	2.22	2.21	1.84	1.96	6.51
B	0-15	1.35	1.58	16.58	1.42	1.73	21.89
	15-30	1.61	1.72	7.28	1.60	1.81	13.16
	30-45	1.75	1.87	6.69	1.58	1.76	11.38
	45-60	2.32	2.45	5.52	2.14	2.27	5.83
C	0-15	1.58	1.90	19.85	1.59	1.94	22.45
	15-30	1.85	1.96	6.33	1.83	1.96	7.34
	30-45	1.65	1.76	7.04	1.93	1.98	2.96
	45-60	2.26	2.39	5.67	1.96	2.01	2.55
D	0-15	1.66	1.93	16.80	1.53	1.88	22.71
	15-30	1.80	1.92	6.85	1.74	1.85	6.74
	30-45	1.78	1.87	4.71	1.91	1.98	3.61
	45-60	1.89	1.97	4.02	1.99	2.03	2.12
E	0-15	1.78	2.01	12.72	1.57	1.85	17.43
	15-30	1.92	2.05	6.61	1.72	1.84	6.93
	30-45	1.95	2.03	3.94	1.83	1.90	3.95
	45-60	1.99	2.06	3.31	1.95	2.02	3.17
F	0-15	1.58	1.89	19.72	1.59	1.91	20.40
	15-30	1.78	1.90	6.73	1.84	1.96	6.54
	30-45	1.88	1.97	4.57	1.83	1.90	3.55
	45-60	1.95	2.02	3.33	1.98	2.03	2.17
G	0-15	1.63	1.92	17.46	1.59	1.89	18.59
	15-30	1.78	1.89	6.29	1.88	2.00	6.48
	30-45	1.89	1.96	3.33	1.85	1.94	4.48
	45-60	1.93	1.99	3.16	1.95	2.01	2.87
H	0-15	1.49	1.86	24.87	1.57	2.01	20.20
	15-30	1.75	1.87	6.91	1.74	2.01	6.91
	30-45	1.83	1.91	4.37	1.84	2.01	4.02
	45-60	1.87	1.94	3.36	1.93	2.01	2.96

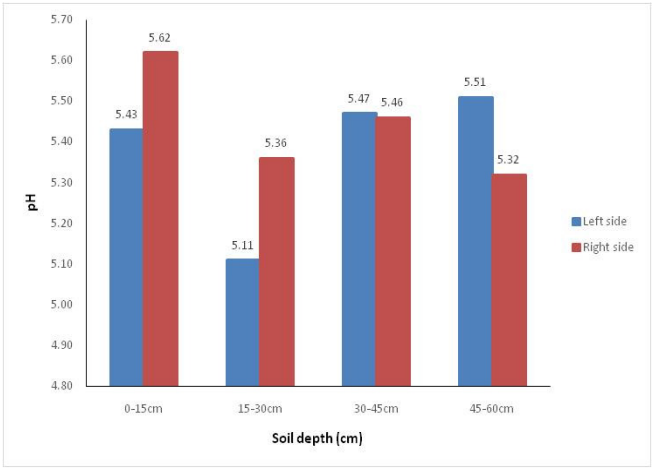


Figure 3. Depth wise average pH status observed in the study site.

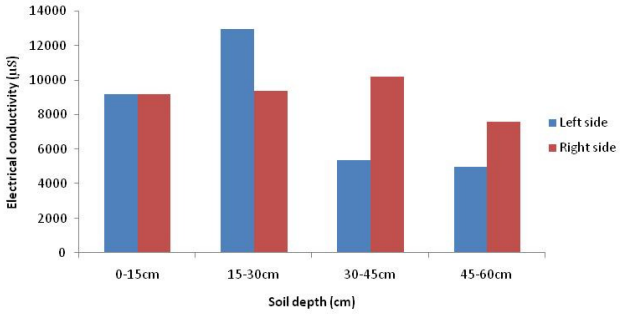


Figure 4. Depth wise average EC status observed in the study site.

4. AGRICULTURAL PLANNING

The development of plants and measures to achieve greater and more efficient output from agriculture; a sound agriculture policy should be able to reconcile three basic needs: the production of food and agricultural products, protection of the environment and the maintenance of the agricultural farm. The hilly terrain is not suitable for the cultivation of rice as it is a well drained land and rice requires lot of water during its plantation period. However, low water requirement crops like carrot, maize, tomato, sweet potato, peas and flowers like roses, cosmos, marigold, hibiscus and calendula are suitable for cultivation. Based on the basic research with the specific parameters of soil, the crop planning for sustainable agriculture in a hilly terrain is proposed and presented in the Table 4.

Table 4. Sustainable agricultural planning of the study site.

Sites	Soil							Crop
	Type	Texture (Avg)	Bulk density (g/cc) (Avg)	MC (%) (Avg)	Soil water Characteristics (Avg)	Soil pH (Avg.)	Soil EC(µS) (Avg.)	
Left side	2-4 % slope, gently sloping to gently undulating, moderately well drained	Sandy loam	1.82	8.52	21.83 (FC) 8.38 (WP)	5.36	8300	Tomato, Maize, Sweet Potatoes, Radish, rose, calendula, cosmos, marigold, pineapple etc.
Right side	3-10 % slope, Moderately sloping to gently undulating well drained	Sandy loam	1.77	9.48	25.98 (FC) 15.43 (WP)	5.33	8637.5	Tomato, Maize, Sweet Potatoes, Radish, rose, calendula, cosmos, marigold, pineapple etc.

Agricultural intensification without adequate restoration of soil fertility may threaten the sustainability of agriculture. Quantitative estimation of plant nutrient depletion from soils is useful for comprehending the state of soil degradation and for devising corrective measures.

5. CONCLUSIONS

Soil physical properties also largely determine the soil's water and air supplying capacity to plants. Many soil physical properties change with changes in land use system and its management such as intensity of cultivation, the instrument used and the nature of the land under cultivation, rendering the soil less permeable and more susceptible to runoff and erosion losses. So, the present study was carried out assess soil physical and chemical properties of a hilly terrain situated in Assam University, Silchar and surrounded by many low hills of Assam state. The physical properties such as soil texture, bulk density, moisture content, soil moisture characteristics and chemical properties such as pH, EC of the soil samples were determined using standard methods.

The land topographical survey and soil characteristics study revealed that the study site is coming under sloppy (3-7%) land. The soil is sandy loam with acidic in nature. Average bulk density and moisture content was found to be 2g/cc and 9%, respectively. The soil water content at field capacity and wilting points at 0-15, 15-30, 30-45 and 45-60 cm profile were observed 22.42, 23.11, 23.09, 23.51% and 12.44, 11.87, 12.30, 11.91% respectively. The findings provide the logistic and basic information for a sustainable agricultural planning in the study site. However, for increasing the yield of the crops to be grown in the hilly terrain a detailed fertility status with available nutrients are also to be studied.

ACKNOWLEDGEMENTS

We are in debt to Krishi Sanskriti for giving us the great opportunity to explore our knowledge.

REFERENCE

[1] Baruah, T.C., and Barthakur, H.P., "A textbook of soil analysis", Viskas Publishing House, New Delhi, India, 1997, pp. 334.

[2] Bohn, H.L., McNeal, B.L., and O'Connor, G.A., "Soil chemistry", 3rd Ed., John Wiley and Sons, Inc., New York, 2001, pp. 307.

[3] Bouyoucos, G .J., "The hydrometer as a new method mechanical analysis of soils", Soil science, 1927, 23, pp. 343-353.

[4] Brady, N.C., and Weil, R.R., "The nature and properties of soils", 13th Ed., Prentice- Hall Inc., New Jersey, USA, 2002, pp. 960.

[5] Brady, N.C., and Weil, R.R., "The nature and properties of soils", 14th Ed., Prentice- Hall Inc., New Jersey, USA, 2004, pp. 960.

[6] Davidson, E.A., and Ackerman, I.L., "Changes in soil carbon inventories following cultivation of previously untilled soils", *Biogeochemistry,* 1993, 20, pp. 161-193.

[7] Foth, H.D., "Fundamentals of soil science', 8th Ed., John Wiley and Sons, Inc., New York, USA, 1990, pp. 360.

[8] Gupta, P.K., "Soil, plant, water and fertilizer Analysis", Shyam Printing Press, Agrobios, India, 2004, pp.438.

[9] Hussain, I., Olson, K.R., Wander, M.M., and Karlen, D.L., "Adaptation of soil quality indices and application to three tillage systems in southern Illinois", Soil and Tillage Research, 1999, 50, pp. 237– 249.

[10] Land Capability Classification, Agriculture Handbook, United States Department of Agriculture, 1958.

[11] Lilienfein, J., Wilcke, W., Ayarza, M.A., Vilela, L., Lima, S.D.C., and Zech, W., "Chemical fractionation of phosphorus, sulphur and molybdenum in Brazilian savannah Oxisols under different land uses", Geoderma, 2000, 96, pp. 31-46.

[12] Miller, R.W., and Donahue, R.L., "Soils in our environment", 7th Ed., Prentice Hall Inc., Englewood Cliffs, New Jersey, 1995, pp. 649.

[13] Tisdale, S.L., Nelson, W.L., Beaton, J.D., and Havlin, J.L., "Soil fertility and fertilizer", 5th Ed., Prentice-Hall of India, New Delhi, 1995, pp. 684.

Changing Role of Consumers in Imminent Smart Grids

Damanjeet Kaur

UIET, Panjab University, Chandigarh
djkb14@rediffmail.com

Abstract: **In this paper, with the change in existing power system, the changing role of consumers in smart grids is discussed. In conventional power system, consumers are only at receiving end and pay tariff for the energy consumed. Consumers are not contributing in power system except the load growth. They are silent in all parts of power system. Only power agencies have monopoly of controlling power. But the power industry is facing major changes these days. Smart grids is a new concept which is changing the existing power system with additional benefits of self healing, high reliability, incorporation of distributed generation and storage options, enable new products and efficient power usage which further causes less carbon emission. These days power sector is divided into three corporations. These are GENCO, TRANSCO AND DISCO and government hold on power industry is decreasing. In smart grids, consumers can play a vital role at generation, transmission and distribution. At generation, consumers can produce energy with the help of distributed generation sources and integrate it with the grid. While at the transmission, consumers can shut down its load during peak hours because of high unit cost, the problem of transmission can be resolved to some extent. Finally as consumers are at distribution side, their load patterns are responsible for power generation. In smart grids, consumers will definitely play an important role by two way communication with power system by smart meters installations, demand response management, efficient usage of energy which causes less pollutants in cities by reducing low carbon emission. In this paper, the changing role of consumers is discussed at generation, transmission and distribution level.**

1. INTRODUCTION

Consumers are the final end of the distribution system. But these days the existing power system is passing through a changing phase for betterment. The existing power grids are upgraded to meet new challenges of self healing, high reliability, resistant to cyber attacks, integrate a variety of distributed generation sources, minimize operation and maintenance cost and optimize asset etc [1-2]. To achieve this, there is need of more automation, communication and control of power grid. In existing power grids, consumers are playing an important role at distribution system while consumers are silent at generation and transmission system. The load growth at consumer side is responsible for up gradation of existing system or installation of new systems to meet load demand. But in these new grids, consumer will play an important role at generation and transmission system also.

In this paper, the changing role of consumers is discussed by contributing to generation, peak load shaving will help to some extent the transmission system. While at the distribution system, consumers will go for two way communication with power utilities by using adapting smart appliances at their places.

2. CHANGING ROLE OF CONSUMERS

In existing power grids, consumers are playing inert role by simply paying for the consumed energy while in upcoming smart grids, the consumers will play an active role by better managing their electricity usage and costs through real-time information exchange. This is possible with the help of smart meters installation at their places. Which would help end users to communicate the power utilities and power utilities would also have more control on individual energy consumption and other functioning. It will motivate customer to participate in the operations of the grid [3-4].

With two way communication with the power utilities, consumers can help the power sector in many ways as given below:

Distributed Generation Integration

These days' governments are emphasizing of use of distributed generation as source of energy. It is expected that consumer can fulfill its own load demand using these sources and whatever is excessive that can be integrated to grid and consumers will get money for the exported power. In addition to this, it will reduce carbon emission and power losses which are otherwise lost in long distance. So it consumers can benefit in terms of money for the transported power which is also reduces the burden on power system.

Postpone of Upgradtion/Installation of New Networks

As consumers have benefits of distributed generation system in terms of energy and money. It will postpone the upgradation/installation of new networks. By placing smart meters at the consumer premises the information of peak or off-peak hours may be conveyed to consumers. As in smart grids, different tariff plans will be introduced for peak and off hours. So consumers will definitely prefer off peak hours for

energy consumption. It will help in reducing peak hours time. Which further cause postpone of new network installation for some years.

Peak Shifting

Peak shifting can help to reduce the need for network reinforcement, as well as reducing the need to build new power stations or run existing ones at low capacity, which is often inefficient and expensive. Electricity networks are designed for peak load conditions. Although peak occurs for short period of time but system is planned for that. Even the size of generators are selected for that peak. If peak demand can be reduced by shifting some usage to off-peak times, then size of network may go small and additional investments can be saved. This will further per unit cost of energy and finally benefits the consumers in terms of money.

Reducing the costs of decarbonisation, and cleaner city air

By shifting peak and using distrusted energy sources. The ash content of conventional power system can be controlled to some extent which further reduces low carbon emission and clean air of city. But this is more real when we go for smart grids and smart meters at the consumer premises.

3. BENEFITS TO CONSUMERS

There is no doubt that smart grids can deliver benefits to the electricity industry, to consumers, and to wider society. Upcoming smary grids will no doubt solve many problem alnong with more monitoring, control and automation. But consumers will benefit in terms of money and environment. The overall unit cost of energy can be reduced by option of selecting peak or off peak hours for using energy. Power utilities will benefit the most as it will benefit in terms of availability of energy, which is the major burden these days. Consumers will help power utilities for reducing their peak demand by using distributed generation. There should be incentives for distributed generation and energy usage during off-peak hours.

It can be expected that there some direct benefits in terms of money while there some social and environment benefits which are indirect benefits for playing an important role in the power sector. These benefits can be achieved by placing smart appliances and smart meters for metering placed at the premises of consumers. These smart appliances need more automation and on-off from remote position. Otherwise the role of consumers can not expect as they can play.

4. AWARENESS TO CONSUMERS REGARDING SMART GRIDS

As consumers can change the scenario of energy usages so it becomes important to make consumers aware about smart grids. They should understand the benefits of technology and how to use them. Otherwise it can be expected that smart grid development is dependent on power sector and consumers relationship. Smart grids will provide consumers with more information about their energy usage, offering them the opportunity to control their usage to save money. Consumers are interested in monetary gains while other indirect gains can be helpful for better living. To make consumers aware it is required awareness workshops and educate them some basic concepts so that they can change behavior to avoid peak conditions.

5. CONCLUSIONS

In this the importance of consumers in proper functioning of smart grids is discussed. In this paper, various areas where active participation of consumers is required is discussed so that effectiveness of smart grids can be understood in a better manner. It is important to make consumers aware about their changing role in power sector in terms of benefits. The benefits may be self sufficient energy generation, monetary gains by using load during off-peak hours which will further reduce burden on the system.

REFERENCES

[1] H. Brown, S. Suryanarayanan and G. Heydt, "Some Characteristics of Emerging Distribution Systems Considering the Smart Grid Initiative," *The Electricity Journal,* vol. 23, Issue 5 pp 65-75, June 2010.

[2] 110th Congress of United States, "Smart Grid," Title XIII, Energy Independence and Security Act of 2007, Washington DC, December 2007.

[3] D. Haughton, G. T. Heydt, "Smart Distribution System Design: Automatic Reconfiguration for Improved Reliability, *Power System Engineering Research Centre*, pp-1-8.

[4] http://www.engage-consulting.co.uk/downloads/pdf/Smart-Grid-A-Great-Consumer-Opportunity.pdf

[5] http://www.consumerfutures.org.uk/files/2013/07/Smart-grids.pdf

Application of Laplace-Differential Transform Method to Solve Non-linear PDEs with Boundary Conditions

Kiranta Kumari[1], Praveen Kumar Gupta[2]

[1,2]*Department of Mathematics & Statistics, Banasthali University, Banasthali-304022, Rajasthan*

Abstract: **In this paper, a novel method called Laplace-differential transform method (LDTM) is presented to obtain an approximate analytical solution for strong nonlinear boundary value problems associated in engineering phenomena. It is determined that the method works very well for the wide range of parameters and an excellent agreement is demonstrated and discussed between the approximate solution and the exact one in three examples. The most significant features of this method are its simplicity and excellent accuracy for the finding. Also, the results reveal that this technique is very effective and convenient for solving complex nonlinearities.**

Keywords: **LDTM, Non-linear PDEs, Boundary conditions.**

1. INTRODUCTION

A nonlinear phenomenon appears in a wide variety of scientific and engineering applications such as chemical physics, fluid dynamics, chemical kinetics, solid state physics and transport in porous medium etc. In the analysis of mathematical models, those techniques are required for providing solutions conforming the physical reality and obtain the exact and approximate solutions. In 1978, a Russian mathematician G.E. Pukhov proposed Differential transform method (DTM) and started from computational structure to solve differential equations by Taylor's transformation. But in 1986, J. K. Zhou [7] has proposed the algorithm and main application of DTM with linear and non-linear initial value problems in electric circuit analysis. Alquran *et* al. [1] have used the combination of Laplace transform method and the DTM for solving non-homogeneous linear PDEs with variable coefficients. The researchers found that the LDTM requires less computational work compared to DTM. Hassan and Erturk [3] have studied the higher order boundary value problems and discussed the higher order series solution for linear and non-linear differential equations. Khan *et* al. [4] have given Laplace decomposition method to obtain the approximate solution of non-linear coupled PDEs and found that the Laplace decomposition method and Adomian decomposition method both can be used alternatively for the solution of higher order initial value problems. Mishra and Nagar [5] have applied a combined form of LTM with Homotopy perturbation method which is called He-Laplace method for solving linear and non-linear PDEs and found that the technique is capable to reduce the volume of computational work as compared to Adomian polynomials. Ravi Kanth and Aruna [6] have extended the DTM to solve the linear and non-linear Klein-Gordon equations and confirmed that the proposed technique provides its computational effectiveness and accuracy.

In this paper, we use a coupling of the Laplace transform method and the DTM for solving nonlinear PDEs with boundary conditions. The goodness of this method is its capability of combining two strongest methods for finding fast convergent series solution of PDEs. To the best of our knowledge no such try has been made to combine LTM and DTM for solving non-linear boundary value problems. This paper considers the effectiveness of the Laplace-differential transform method for solving nonlinear equations. In this paper, the definition of DTM is presented in Section 2. Section 3, contains basic idea of LDTM. Section 4, contains applications of LDTM. The conclusions are included in last Section.

2. DIFFERENTIAL TRANSFORMATION METHOD

The one variable differential transform [2] of a function $u(x,t)$ is defined as

$$U_k(t)=\frac{1}{k!}\left[\frac{\partial^k u(x,t)}{\partial x^k}\right]_{x=x_0} \quad ;k\geq 0 \tag{1}$$

where $u(x,t)$ is the original function and $U_k(t)$ is the transformed function. The inverse of one variable differential transform of $U_k(t)$ is defined as:

$$u(x,t)=\sum_{k=0}^{\infty} U_k(t)(x-x_0)^k, \tag{2}$$

where x_0 is the initial point for the given condition. Then the function $u(x,t)$ can be written as

$$u(x,t)=\sum_{k=0}^{\infty}U_k(t)x^k. \tag{3}$$

3. BASIC IDEA OF LDTM

To illustrate the basic idea of Laplace differential transform method [1], we consider the general form of inhomogeneous PDEs with variable or constant coefficients

$$\pounds[u(x,t)]+\Re[u(x,t)]=f(x,t),\ x\in R,\ t\in R^+, \tag{4}$$

subject to the initial conditions

$$u(x,0)=g_1(x),\quad u_t(x,0)=g_2(x), \tag{5}$$

and the Dirichlet boundary conditions

$$u(0,t)=h_1(t),\ u(1,t)=h_2(t), \tag{6}$$

or the Neumann boundary conditions

$$u(0,t)=h_1(t),\ u_x(1,t)=h_3(t), \tag{7}$$

where $\pounds[.]$ is linear operator w.r.to 't', $\Re$ [.] is remaining operator and *f* is a known analytical function.

First, we take the Laplace transform on both sides of equation (4), w.r.to '*t*', and we get

$$\mathrm{L}[\pounds[u(x,t)]]+\mathrm{L}[\Re[u(x,t)]]=\mathrm{L}[f(x,t)]. \tag{8}$$

By using initial conditions from equation (5), we get

$$\overline{\mathrm{u}}(x,s)+\mathrm{L}[\Re[u(x,t)]]=\bar{f}(x,s), \tag{9}$$

where $\overline{\mathrm{u}}(x,s)$ and $\bar{f}(x,s)$ are the Laplace transform of $\mathrm{u}(x,t)$ and $f(x,t)$ respectively.

Afterwards, we apply differential transform method on the equation (9) w. r. to '*x*', and we get

$$\overline{\mathrm{U}}_{\mathrm{k}}(s)+\mathrm{L}[\Re[U_k(t)]]=\overline{F}_k(s), \tag{10}$$

where $\overline{\mathrm{U}}_{\mathrm{k}}(s)$ and $\overline{\mathrm{F}}_{\mathrm{k}}(s)$ are the differential transform of $\overline{\mathrm{u}}(x,s)$ and $\bar{f}(x,s)$ respectively. In the next step, we apply inverse Laplace transform on both sides of the equation (10) w. r. to '*s*', and then we get

$$\mathrm{L}^{-1}[\overline{U_k}(s)]+\mathrm{L}^{-1}\mathrm{L}[\Re[U_k(t)]]=\mathrm{L}^{-1}[\overline{F_k}(s)],$$

or

$$U_k(t)+\Re[U_k(t)]=F_k(t). \tag{11}$$

Now, apply the differential transform method on the given Dirihlet and Neumann boundary conditions (6) and (7), we get

$$U_0(t)=h_1(t). \tag{12}$$

Let us assume

$$U_1(t)=a\,q(t). \tag{13}$$

By the definition of DTM [3], we take

$$u(1,t)=\sum_{i=0}^{\infty}U_i(t),\ u_x(1,t)=\sum_{i=0}^{\infty}i\,U_i(t). \tag{14}$$

By equation (14), we calculate the value of '*a*'.
Now by the above equations (12) and (13) in (11), the closed form series solution can be written as

$$u(x,t)=\sum_{k=0}^{\infty}U_k(t)x^k.$$

4. NUMERICAL EXAMPLES

To illustrate the applicability of LDTM, we have applied it to non-linear PDEs which are homogeneous as well as non-homogeneous. This method is capable to combine two methods for obtaining exact solutions.

Example 4.1: Consider the following homogeneous non-linear PDE [5]

$$\frac{\partial u}{\partial t}-u\frac{\partial u}{\partial x}-\frac{\partial^2 u}{\partial x^2}=0, \tag{15}$$

subject to the initial conditions

$$u(x,0)=1-x, \tag{16}$$

and the Dirichlet boundary conditions

$$u(0,t)=\frac{1}{1+t},u(1,t)=0. \tag{17}$$

According to the Laplace differential transform method, firstly we applying the Laplace transformation w. r. to 't' on eqn. (15), we get

$$sL[u(x,t)]-u(x,0)=L\left[\frac{\partial^2 u}{\partial x^2}+u\frac{\partial u}{\partial x}\right]. \tag{18}$$

By using initial conditions from equation (16), we get

$$L[u(x,t)]=\frac{1-x}{s}+\frac{1}{s}L\left[\frac{\partial^2 u}{\partial x^2}+u\frac{\partial u}{\partial x}\right]. \tag{19}$$

Here, we applying the inverse Laplace transformation w. r. to '*s*', on both sides:

$$u(x,t)=1-x+L^{-1}\left[\frac{1}{s}L\left[\frac{\partial^2 u}{\partial x^2}+u\frac{\partial u}{\partial x}\right]\right]. \tag{20}$$

Now applying the Differential transformation method on equations (17) and (20) with respect to space variable '*x*', we get

$$U_k(t)=\delta(k,t)-\delta(k-1,t)+L^{-1}\left[\frac{1}{s}L[(k+2)(k+1)U_{k+2}(t)]\right]$$
$$+L^{-1}\left[\frac{1}{s}L\left[\sum_{r=0}^{k}(r+1)U_{r+1}(t)U_{k-r}(t)\right]\right]; \tag{21}$$

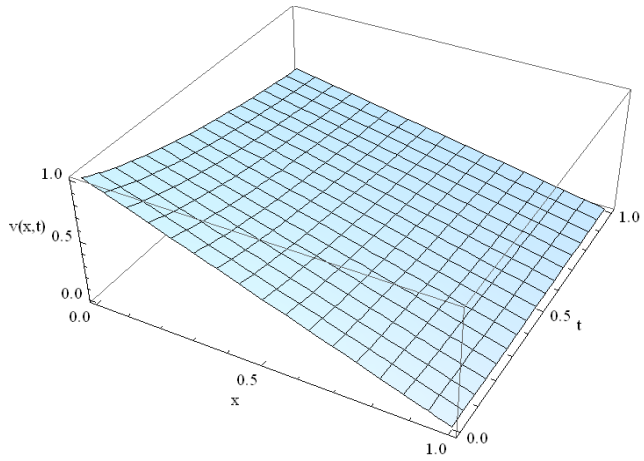
where, $\delta(k,t)=\begin{cases}1;\ k=0\\0;\ k\neq 0\end{cases}$ $U_0(t)=\frac{1}{1+t}.$ (22)

And let us assume

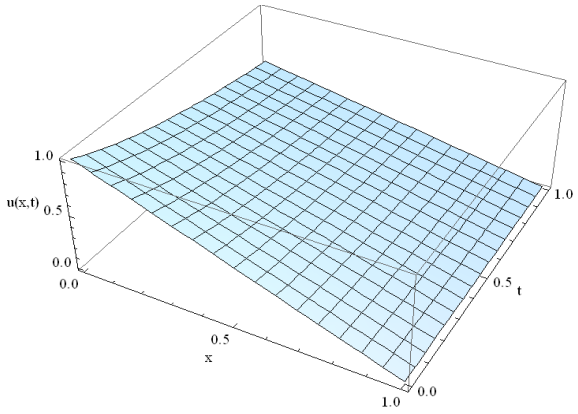
$$U_1(t)=\frac{a}{1+t}. \tag{23}$$

Substituting (22) and (23) into (21) and by straightforward iterative steps, we obtain

$$U_2(t)=-\frac{(a+1)}{2(1+t)^2},\quad U_3(t)=\frac{a+1}{3!(1+t)^2}\left(\frac{1}{1+t}-a\right),$$
$$U_4(t)=\frac{a+1}{4!(1+t)^3}\left[2(2a+1)-\frac{1}{1+t}\right],\ \ldots \tag{24}$$



(a)



(b)

Fig. 1: The behavior of the (a) Exact solution, (b) LDTM solution, w.r.to x and t are obtained for the Example 4.1.

From equation (14), we take

$$u(1,t)=\sum_{i=0}^{\infty}U_i(t), \tag{25}$$

and, we get

$$a=-1.$$

Therefore,

$$U_1(t)=\frac{-1}{1+t}, U_2(t)=0, U_3(t)=0, U_4(t)=0,\ldots \tag{26}$$

Proceeding in this manner the components $U_k(t),\ k\geq 0$ of the DTM can be completely obtained. The differential transformation of $U_k(t)$ will give the series solution

$$u(x,t)=\sum_{k=0}^{\infty}U_k(t)x^k. \tag{27}$$

When we substitute all values of $U_k(t)$ from equation (22) and (26) into equation (27), the series solution can be formed as

$$u(x,t)=\frac{1-x}{1+t}. \tag{28}$$

which is the exact solution.

Example 4.2: The non-homogeneous non-linear PDE [6]

$$\frac{\partial^2 u}{\partial t^2}-\frac{\partial^2 u}{\partial x^2}+u^2=6xt\left(x^2-t^2\right)+x^6t^6, \tag{29}$$

subject to the initial conditions

$$u(x,0)=0,\quad u_t(x,0)=0, \tag{30}$$

and the Neumann boundary conditions

$$u(0,t)=0,\ u_x(1,t)=3t^3. \tag{31}$$

According to the Laplace differential transform method, firstly we applying the Laplace transformation with respect to 't' on eqn. (29), we get

$$s^2L[u(x,t)]-su(x,0)-u_t(x,0)=\frac{6x^3}{s^2}-\frac{36x}{s^4}$$

$$+\frac{6!x^6}{s^7}+L\left[\frac{\partial^2 u(x,t)}{\partial x^2}-u^2(x,t)\right]. \tag{32}$$

By using initial conditions from equation (30), we get

$$L[u(x,t)]=\frac{6x^3}{s^4}-\frac{36x}{s^6}+\frac{6!x^6}{s^9}+L\left[\frac{\partial^2 u(x,t)}{\partial x^2}-u^2(x,t)\right].$$

Here, we applying the Inverse Laplace transformation w.r.t. 's' on both sides, and we get

$$u(x,t)=x^3t^3-\frac{3xt^5}{10}+\frac{x^6t^8}{56}$$

$$+L^{-1}\left[\frac{1}{s^2}L\left[\frac{\partial^2 u(x,t)}{\partial x^2}-u^2(x,t)\right]\right]. \tag{33}$$

Now applying the Differential transformation method on equations (31) and (33) with respect to space variable 'x', we get

$$U_k(t)=t^3\delta(k-3,t)-\frac{3}{10}t^5\delta(k-1,t)+\frac{t^8}{56}\delta(k-6,t)$$

$$+L^{-1}\left[\frac{1}{s^2}L\left[(k+2)(k+1)U_{k+2}(t)-\sum_{r=0}^{k}U_r(t)U_{k-r}(t)\right]\right], \tag{34}$$

$$U_0(t)=0. \tag{35}$$

And let us assume

$$U_1(t)=at^4. \tag{36}$$

Substituting (35) and (36) into (34) and by straightforward iterative steps, we obtain

$$U_2(t)=0,\ U_3(t)=2at^2+t^3,\ U_4(t)=\frac{a^2t^8}{12},$$

$$U_5(t)=\frac{a}{5},\ U_6(t)=\frac{13a^2t^6}{45}+\frac{at^7}{15},\ldots \tag{37}$$

From equation (14), we take

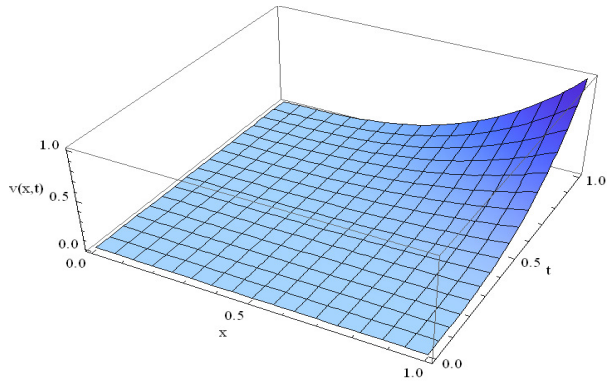
$$u_x(1,t)=\sum_{i=0}^{\infty}iU_i(t).$$

and, we get

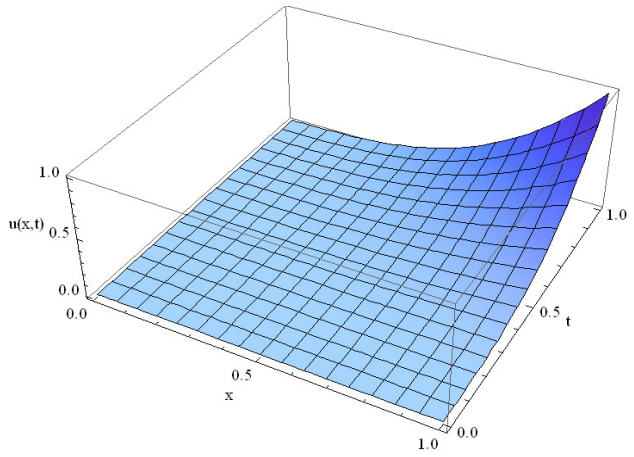
$$a=0.$$

Therefore,

$$U_1(t)=0,U_2(t)=0,U_3(t)=t^3,U_4(t)=0,\ldots \tag{38}$$



(a)



(b)

Fig. 2: The behavior of the (a) Exact solution, (b) LDTM solution, w.r.to x and t are obtained for the Example 4.2.

Proceeding in this manner the components $U_k(t)$, $k \geq 0$ of the DTM can be completely obtained. The differential transformation of $U_k(t)$ will give the series solution

$$u(x,t) = \sum_{k=0}^{\infty} U_k(t) x^k. \tag{39}$$

When we substitute all values of $U_k(t)$ from equation (35) and (38) into equation (39), the series solution can be formed as

$$u(x,t) = x^3 t^3.$$

which is the exact solution.

Example 4.3: Consider the following non-homogeneous non-linear PDE [5]

$$\frac{\partial^2 u}{\partial t^2} + \frac{\partial^2 u}{\partial x^2} + \left(\frac{\partial u}{\partial x}\right)^2 = 2x + t^4, \tag{40}$$

subject to the initial conditions

$$u(x,0) = 0,\ u_t(x,0) = a, \tag{41}$$

and the Neumann boundary conditions

$$u(0,t) = at, u_x(1,t) = t^2. \tag{42}$$

According to the Laplace differential transform method, firstly we applying the Laplace transformation with respect to 't' on eqn. (40), we get

$$s^2 L[u(x,t)] - su(x,0) - u_t(x,0) = \frac{2x}{s}$$

$$+ \frac{4!}{s^5} - L\left[\frac{\partial^2 u}{\partial x^2} + \left(\frac{\partial u}{\partial x}\right)^2\right]. \tag{43}$$

By using initial conditions from equation (41), we get

$$L[u(x,t)] = \frac{a}{s^2} + \frac{2x}{s^3} + \frac{4!}{s^7} - \frac{1}{s^2} L\left[\frac{\partial^2 u}{\partial x^2} + \left(\frac{\partial u}{\partial x}\right)^2\right]. \tag{44}$$

Here, we applying the inverse Laplace transformation with respect to 's', on both sides:

$$u(x,t) = at + xt^2 + \frac{t^6}{30} - L^{-1}\left[\frac{1}{s^2} L\left[\frac{\partial^2 u}{\partial x^2} + \left(\frac{\partial u}{\partial x}\right)^2\right]\right]. \tag{45}$$

Now applying the Differential transformation method on equations (42) and (45) with respect to space variable 'x', we get

$$U_k(t) = at\,\delta(k,t) + t^2\,\delta(k-1,t) + \frac{t^6}{30}\,\delta(k,t)$$

$$- L^{-1}\left[\frac{1}{s^2} L[(k+2)(k+1)U_{k+2}(t)]\right]$$

$$- L^{-1}\left[\frac{1}{s^2} L\left[\sum_{r=0}^{k} (r+1)(k-r+1) U_{r+1}(t) U_{k-r+1}(t)\right]\right], \tag{46}$$

$$U_0(t) = at. \tag{47}$$

And let us assume

$$U_1(t) = bt^2. \tag{48}$$

Substituting (47) and (48) into (46) and by straightforward iterative steps, we obtain

$$U_2(t) = \frac{(1-b^2)t^4}{2},\ U_3(t) = \frac{(1-b)[b(1+b)t^6 - 1]}{3},$$

$$U_4(t) = \frac{(1-b)t^2[6(1+b) + 2b\{1-b(b+1)t^6\} - (1+b)t^6]}{12},$$

… (49)

From equation (14), we take

$$u_x(1,t)=\sum_{i=0}^{\infty} iU_i(t),$$

and, we get

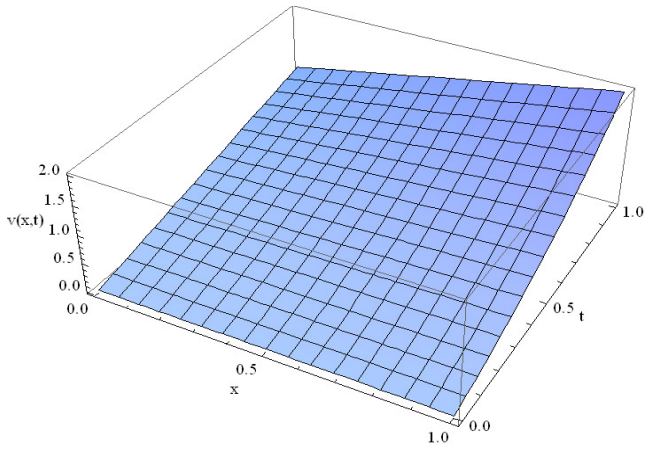
$$b=1.$$

Therefore,

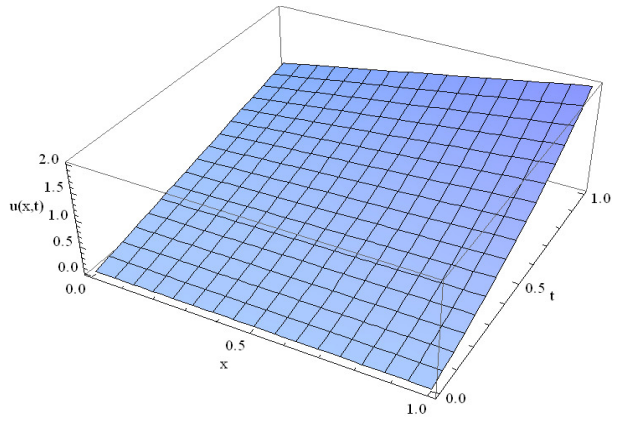
$$U_1(t)=t^2, U_2(t)=0, U_3(t)=0, U_4(t)=0,... \qquad (50)$$

Proceeding in this manner the components $U_k(t)$, $k\geq 0$ of the DTM can be completely obtained. The differential transformation of $U_k(t)$ will give the series solution

$$u(x,t)=\sum_{k=0}^{\infty} U_k(t)x^k. \qquad (51)$$



(a)



(b)

Fig. 3: The behavior of the (a) Exact solution, (b) LDTM solution, w.r.to x and t are obtained for the Example 4.3.

When we substitute all values of $U_k(t)$ from equation (47) and (50) into equation (51), the series solution can be formed as

$$u(x,t)=at+xt^2.$$

which is the exact solution.

5. CONCLUSION

In this paper, the LDTM has been successfully applied to find the exact solution of homogeneous and non-homogeneous non-linear PDEs with boundary conditions. The aim of this paper is to describe that the LDTM is gives more reliable and reasonable solution of non-linear PDEs and it is easy to use. The proposed method requires less computational work compared with the DTM. The LDTM solution can be calculated easily in short time and the graphs were performed by using mathematica-8.

REFERENCES

[1] Alquran, M., Khaled, K.A., Ali, M. and Ta'any, A., "The Combined Laplace Transform- Differential Transformation Method for Solving Linear Non- Homogeneous PDEs", *Journal of Mathematical and Computational Science*, 2, 3, 2012, pp. 690-701.

[2] Gupta, P. K., "Approximate analytical solutions of fractional Benney–Lin equation by reduced differential transform method and the homotopy perturbation method", *Computers & Mathematics with Applications*, 61, 9, May 2011, pp. 2829-2842.

[3] Hassan, H. A. H. and Erturk, V. S., "Solutions of Different Types of the Linear and Non-linear Higher-Order Boundary Value Problems by Differential Transformation Method", *European Journal of Pure and Applied Mathematics*, 2, 3, July 2009, pp. 426-447.

[4] Khan, M., Hussain, M., Jafari, H. and Khan, Y., "Application of Laplace Decomposition Method to Solve Nonlinear Coupled Partial Differential Equations", *World Applied Sciences Journal*, 9, September 2010, pp. 13-19.

[5] Mishra, H. K. and Nagar, A. K., "He-Laplace Method for Linear and Nonlinear Partial Differential Equations", *Journal of Applied Mathematics*, Article ID-180315, January 2012, pp. 1-16.

[6] Ravi Kanth, A. S. V. and Aruna, K., "Differential Transform Method for Solving the Linear and Nonlinear Klein-Gordon Equation", *Computer Physics Commmunications*, 180, 5, May 2009, pp. 708-711.

[7] Zhou, J. K., "*Differential Transformation and its Applications for Electrical Circuits*", in Chinese, *Huarjung University Press*, Wuuhahn, China, 1986.

Inter-Annual and Spatial Rainfall Analysis for Environmental Restoration in Barak Valley of Assam

Laxmi Narayan Sethi[1], Nitin Kumar[2], Doksiri Pegu[3]

[1]Department of Agricultural Engineering, Assam University (A Central University) Silchar-788011, Assam
[2]Department of Agricultural Engineering, Assam University (A Central University) Silchar-788011
[3]Chandini Barman, B. Tech. Student, Department of Agricultural Engineering, Assam University (A Central University) Silchar-788011

Abstract: **Among the climatic elements the rainfall is the first index, ever thought of by farmers and climatic analyzers as it is the most important single factor which determines the cropping pattern of an area in general and the type of crop to be cultivated and its success or failure in particular. In the study area, Barak Valley of Assam (Cachar, Karimganj and Hailakandi), the rainfall is concentrated in a short period during rainy months interspersed with intra-seasonal dry spells. These locations are severely affected by greater inter-annual rainfall variability causing degradation of natural resources in the crop production systems. Therefore, inter annual (month, annual and seasonal) and spatial (station, districts and valley) rainfall analysis has been carried out to presents the rainfall characteristics for environmental restoration in Barak Valley. The average annual rainfall received by the districts Cachar, Karimganj and Hailakandi are 3337.99mm, 2967.03mm, 3321.92mm, respectively. The coefficient of variation of rainfall of Cachar, Karimganj and Hailakandi districts are 30.95, 18.31, 76.08, percent respectively. The average rainfall received by the districts Cachar, Karimganj and Hailakandi during the monsoon season (June-September) is 2208.87, 1967.44and 1182.98mm, respectively. It was found that the mean annual rainfall in Barak valley is 2954.87mm with a standard deviation of 1017.40mm and coefficient of variation of 34.43%. However, average rainfall during the summer, monsoon and winter season was recorded 823.15, 1927.24 and 204.48mm, respectively. The average contribution of mean annual rainfall in Summer (March to May), monsoon season (June-September) and Rabi or Winter (October to February) are found 28, 65, and 7%, respectively. The expected occurrence of rainfall at different probability levels during each season of the three districts were also found so high. Therefore, there is urgent need of special attention for controlling flood, soil erosion with the hydrologic structure design sustainable agricultural planning.**

1. INTRODUCTION

The hydrological behavior of a catchment is a very complex phenomenon which is controlled by a large number of climatic and physiographic factors that vary in time and space. Catchment hydrological models are widely used in climate change impact studies. Analysis of climatic and physiographic data of a particular catchment shall provide the accurate volume of surface runoff, which will be utilize for the designing of water storage, calculation of soil erosion losses etc.

The Barak Valley is located in the southern part of Assam, North East India, and comprises of three districts, (viz., Cachar, Hailakandi and Karimganj) which covers a geographical area of 6922 km^2. Barak Valley experiences humid climate with an annual rainfall ranging between 2500-3300 mm. About 80-85 % of this rainfall occurs during the months of April/May-September/October. The seasonal pattern of rainfall and its variations from year to year govern the flood pulse and determine the extent and duration of inundation of the flood plains by the overflowing river waters. The Barak valley, consisting of highly flood prone area have been ravaged by three major floods—in 1986, followed by the one in 1991, and more recently in 2004. Therefore, a detailed knowledge of rainfall regime is an important prerequisite for controlling flood, soil erosion with the hydrologic structure design sustainable agricultural planning.

Precipitation data is the most important input in hydrological models. In many river basins, records collected in long periods of time contain gaps. This could be due to different circumstances, for instance: absence of observers, problems with the measuring device, loss of records, or maybe the lack of funds to continue the measurements [6]. It is recognized as an essential component of most erosion and catchment water balance models [4] and is a critical factor controlling rill erosion and gully development [7]. Many studies have reported the advantages of working out weekly/monthly/seasonally rainfall probabilities for a station or for an agro-climatic region [1, 2, 3, 5]. However, very few studies have been carried for the North Eastern States of India. So, there is requirement for inter annual (month, annual and seasonal) and spatial (station, districts and valley) rainfall analysis to presents the rainfall characteristics for environmental restoration in Barak *Valley.*

2. MATERIALS AND METHODS

2.1 Study Area

The Barak Valley is situated in the southern part of the Indian state of Assam. The geographical position of Barak valley is N 24^{0}43’34.1"-E 93^o 4’ 21.7" and with altitude of 31.40 m from MSL. Barak Valley is one of the six agro-climatic zone

of Assam. The zone has a geographical area of 6941.2 sq. km (8.84% of state) with three districts, viz. Cachar, Hailakandi and Karimganj.

Soils of the zone vary from sandy type to clay soil mostly suitable for field crops including horticultural crops. The soil pH ranges from 4.6 to 5.7. The climate of Assam is characterized by its extreme humidity. The most distinguishing feature of the climate of Assam is the copious rainfall between March and May at a time. The neighborhood of Cherrapunji and Mawsynram are known to receive the highest rainfall in the whole world. Barak valley receives an average annual rainfall of 3000 mm. Climate of the valley is generally hot and humid with temperature ranges from 10^{o} C to 15^{o}C during winter season and 35^{o}C to 40^{o}C during hot summer season with the relative humidity of 92 to 98 per cent.

Barak Valley zone has 38.58 per cent of total geographical area under forest, 33.08 percent as net sown area and 8.48 per cent as area sown more than once. About 5.47 percent of land is used for plantation crops, miscellaneous trees and other.

Agriculture is the main occupation of the people. Rice is the staple diet of the people and cultivation of rice is the main occupation of those engaged in agriculture. Different pulses, jute, tea and fruit cultivation are the other agricultural crops. Sugarcane, potatoes, cotton, oil seeds, coconut and arecanut cultivation is also practiced on a substantial scale apart from the horticulture. Apart from crops, the zone is suitable for fish and animals rearing throughout the year.

2.2 Spatial and inter annual variability of rainfall



Figure 1. Location of raingauge stations in Barak Valley

The study area is covered by nine raingauge stations installed by the Central Water Commission, India, District Agriculture Office, Cachar, TOCKLAI, Silcoorie. These raingauge stations in the Barak valley are Annapurna Ghat, Lakhipur, Dhalai,Amraghat, Silcoorie located in Cachar district; Karimganj and BadarpurGhat in Karimganj district; and Gharmura and Matijuri located in Hailakandi district.The base map of Barak Valley has been prepared by tracing method and presented the location of all the raingauge station in Figure 1.

The rainfall data are collected on daily basis for nine numbers of raingauge stations in the Barak valley. The spatial variability of rainfall considers the pattern of rainfall in different stations, and districts of the valley. And the inter-annual variability of rainfall considers the long term variation in monthly, seasonally (Summer, Kharif and Rabi) and yearly basis.

2.3 Statistical Analysis

Daily rainfall data were collected for the rainguage stations of Barak Valley for the past 10 years. The daily rainfall data were aggregated to monthly, seasonal and annual totals. The statistical parameters such as mean, standard deviation, variability and expected rainfall at different probability levels were carried out using MS Excel. The details of estimation are explained in the next sections.

2.3.1. Standard deviation

Standard deviation, σ (mm) is calculated using the following formula:

$$\sigma = \sqrt{\frac{\sum_1^m (\mathrm{Pi}-\bar{\mathrm{P}})^2}{\mathrm{m}-1}} \qquad (1)$$

Where, m is the number of raingauge stations, $\bar{P}$ is the mean average annual rainfall values and Pi is the individual rainfall values.

2.3.2. Rainfall variability

"Variability defined as the deviation from mean" or "ratio of the standard deviation to the mean rainfall". In the present study the variability of rainfall for both spatial (station, district and valley) and temporal (seasonal and annual) variability has been analyzed. Co-efficient of variation, Cv (%) is computed using the formula as follows:

$$C_v = \frac{\sigma \times 100}{\bar{\mathrm{P}}} \qquad (2)$$

Where, σ is the standard deviation and $\bar{P}$ is the mean average annual rainfall values.

2.3.3. Probability analysis

The different probability levels were taken up to find out the amount of rainfall anticipated for various categories of cumulative rainfall (monthly, seasonal and annual). Probability analysis was carried out using the SMADA **(Stormwater Management and Design Aid, version 6.0)** software for predicting the probability of amount of rainfall at different probability levels.

3. RESULTS AND DISCUSSION

In order to attain a comprehensive picture of surface rainfall in the Barak Valley, the rainfall pattern, long term (2001-2011) daily rainfall were collected and analyzed from individual raingauge stations. In Barak valley, the rainfall records were collected from the nine raingauge stations. The stations wise, district wise and also for the whole valley, monthly, seasonal and annual analyses of rainfall were carried out in details. The details of the results obtained from the spatio-inter annual rainfall and variability, statistical and probability analysis have been presented in the following sections.

3.1 Station-wise inter-annual rainfall analysis

Inter annual analysis for the different stations of the valley were carried out for determining the trends of variation of total and average monthly, yearly and seasonal rainfall and subsequent rainfall for the year of study. The station-wise daily rainfall data of 11 years (2001 to 2011) were converted to monthly rainfall for the eleven years at each raingauge stations. The average mean monthly rainfall regimes are shown in Figure 2. It was observed that the average monthly rainfall gradually increasing from the January to June and decreasing trend is noticed from July to December. The high intensity trends is noticed in the month of June and July and these months received much more rainfall and then started

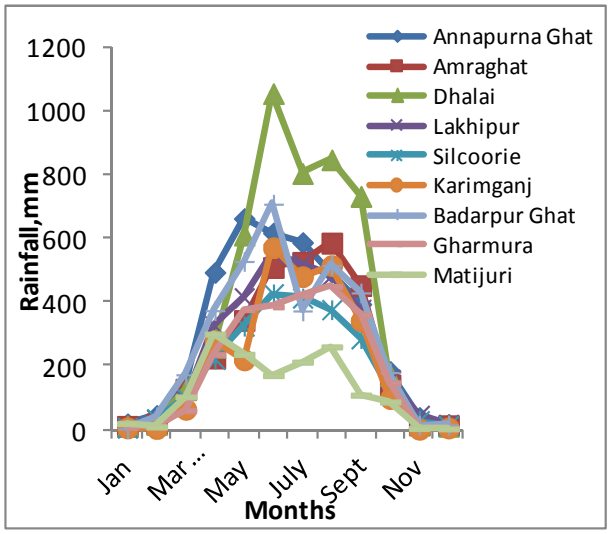


Figure 2. Station-wise variation of monthly rainfall in the Valley.

decreasing from the months of August and lowest of rainfall in the month of December-January. However, among all the nine stations, Dhalai recorded the highest value of rainfall i.e., 1054.85mm in the month of June and the lowest rainfall recorded at Karimganj which is 1.25 mm in the month of November.

3.2 Station-wise seasonal variation of rainfall

The station-wise average seasonal rainfall obtained are presented in Figure 3. During the summer the amount of rainfall gradually increases and however, the amount of rainfall occurrence in this season is largely due to convection effect. The highest amount of rainfall recorded at the Annapurna Ghat was 662.43mm in the month of May and seasonal average was1296.91mm. The lowest rainfall recorded at Gharmura was 59.17mm in March and its seasonal average was 672.1mm.

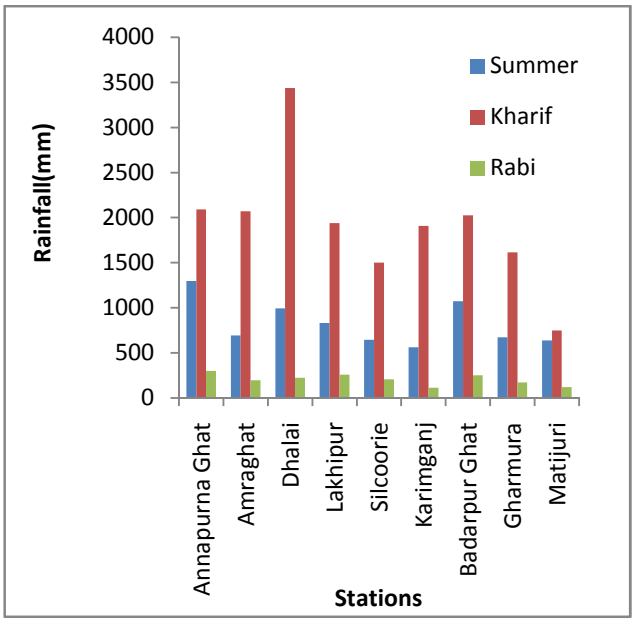


Figure 3. Station-wise variation of mean seasonal rainfall in the Barak Valley.

The kharif season is hot weather season where the amount of rainfall gradually increases, however during this season the valley experiences high rainfall and it is wettest among all the season. The maximum rainfall recorded at Dhalai was1054.85mm in the month of June and lowest recorded at Matijuri was108.1mm in the month of September.

Rabi season is characterized by cold weather season which receives least rainfall throughout the year. It is driest among the all seasons in which maximum rainfall recorded at Annapurna Ghat of 182.29mm in the month of October and lowest rainfall recorded at Karimganj of 1.25mm in the month of November.

3.3 Station-wise annual rainfall analysis

The station-wise annual rainfall variations for the eleven years are presented in Figure 4. Among the stations, the maximum and minimum rainfall was found 4656.13 mm and1509.03mm at the station Dholai and Matijuri, respectively.

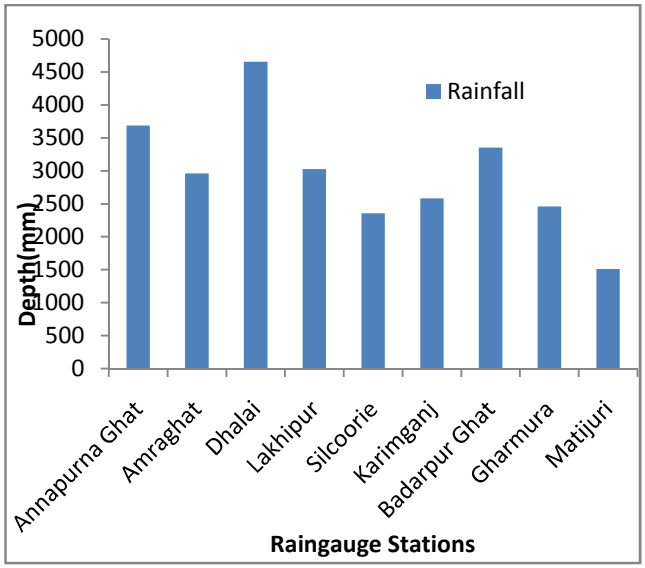


Figure 4. Station-wise annual variation of rainfall in Barak Valley.

The average annual rainfall of the station of Annapurna Ghat, Silchar was found to be 3689.26 mm. While analyzing the long term rainfall, the average annual rainfall for Lakhipur, Cachar was found to be 3028.04 mm. The long term mean annual rainfall of Dhalai, Cachar was found to be 4656.13 mm.

Amraghat climate is mildly sub-tropical with warm, dry summers from April to late May, a strong monsoon from June to September and cool, dry winters from late October to March. It experienced an average annual rainfall of 2962 mm.

3.4 Inter annual rainfall variation in the Valley

The average monthly rainfall of 11 years (2001 to 2011) for nine raingauge station of three districts of Barak Valley inferred that the variation of rainfall were found in every month, and the intensity of rainfall gradually increasing from the January to June and decreasing trend is noticed from July to December. The highly intensity trends is noticed in the month of June and July and these months get highest rainfall which reaches its maximum peak and also it starts to decrease from the months of August and lowest of rainfall in the month of December-January.

The average annual rainfall has been worked out for the entire Barak Valley on the basis of nine rain gauge stations spread uniformly all over the valley for each year of the 11-year period from 2001 to 2011. The long term average annual rainfall of the valley was found to be 3208.98mm. The valley is characterized with unique aerial topography in quantum of rainfall due to the influence of three hills from three sides and its western plane of Bangladesh.

3.5 Spatio-temporal statistics of rainfall

District-wise average monthly, and seasonal and annual variability (%) of rainfall in the valley is shown in Figure 5.

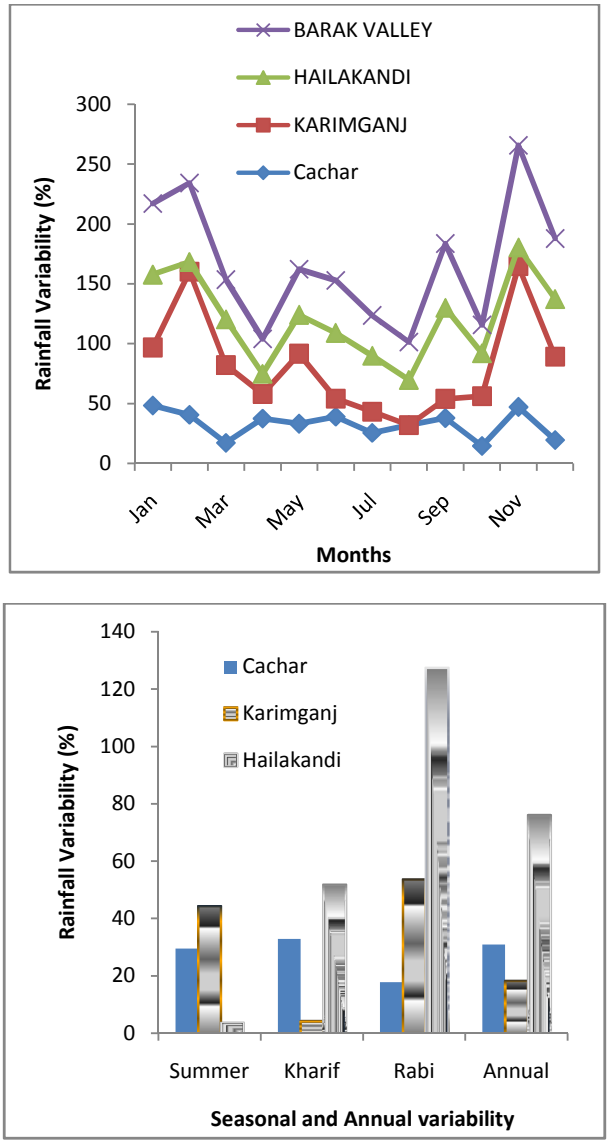


Figure 5. District-wise monthly, seasonal and annual variability of rainfall in the valley.

The mean annual rainfall of Cachar, Karimganj and Hailakandi are 3337.99mm, 2967.02mm and 3321.92mm with the annual co-efficient of variation (C_V) of 30.95, 18.31 and 76.08 percent, respectively. The result indicated that the annual rainfall variability is relatively greater at Cachar than Hailakandi and Karimganj.

Seasonal and annual statistical analyses of rainfall for three districts of Barak Valley are presented in Table 1.

Table 1. Seasonal statistical analysis of rainfall for the districts of Barak Valley.

Parameter	Summer	Kharif	Rabi	Annual
Cachar				
Mean (mm)	892.35	2208.87	236.77	3337.99
% Contribution	26.73	66.17	7.09	100.00
Standard Deviation (mm)	263.43	727.52	42.17	1033.11
CV (%)	29.52	32.94	17.81	30.95
Karimganj				
Mean (mm)	817.86	1967.44	181.73	2967.03
% Contribution	27.57	66.31	6.12	100.00
Standard Deviation (mm)	362.73	82.96	97.51	543.20
CV (%)	44.35	4.22	53.66	18.31
Hailakandi				
Mean (mm)	655.43	1182.98	1483.51	3321.92
% Contribution	19.73	35.61	44.66	100.00
Standard Deviation (mm)	23.58	612.70	1891.16	2527.44
CV (%)	3.60	51.79	127.48	76.08
Barak Valley				
Mean (mm)	823.15	1927.24	204.48	2954.87
% Contribution	27.86	65.22	6.92	100.00
Standard Deviation (mm)	247.48	707.73	62.19	1017.40
CV (%)	30.06	36.72	30.41	34.43

3.6 Expected inter-annual variation of rainfall

In general a Normal distribution is found to be best suitable distribution for rainy season and non-rainy season of monthly rainfall for three districts of Barak Valley. The expected rainfall at different probability levels at different districts and valley are presented in Fig. 6.

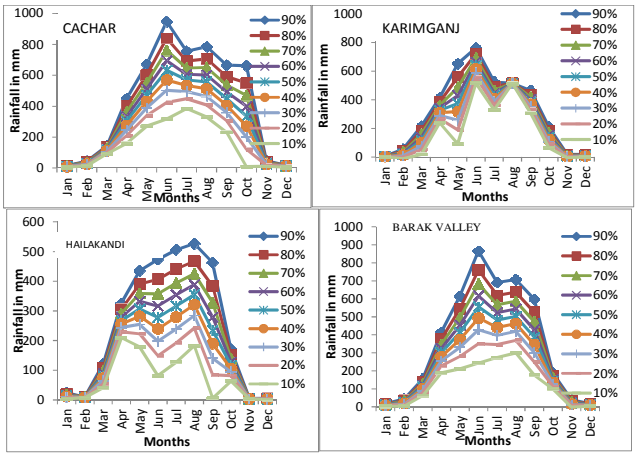


Figure 6. Expected monthly rainfall at different probability levels.

However, the expected seasonal and annual rainfall at different probability levels at different districts and valley are presented in Figure 7. It was found that there is considerable variation of monthly, seasonal and annual rainfall exists from year to year.

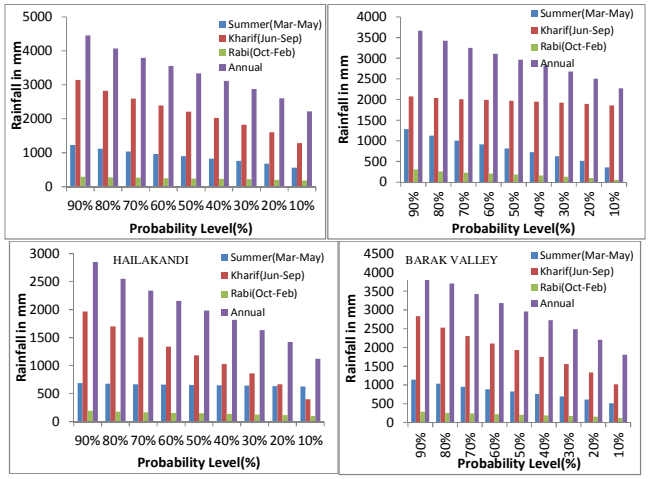


Figure 7. Expected seasonal and annual monthly rainfall at different probability levels.

4. CONCLUSIONS

Barak valley is surrounded by hills from all the three sides except its western plain boundary with Bangladesh and is consisting of highly flood prone area. Normal rainfall of region is 2954.87mm and the valley receives above normal rainfall of Assam state (2818 mm). The heavy rainfall experiences at Cachar district i.e., 3337.99mm followed by Hailakandi (3321.92 mm) and Karimganj (2967.03 mm). During kharif season there is excess rainfall which needs to be harvested and further the total amount runoff generated could be quantified for design of hydrological structure as well as restore environment from soil erosion, landslides and floods and supplemental irrigation for sustainable agriculture in the valley.

ACKNOWLEDGEMENT

The authors are grateful to several staff members of Silcoorie Tea Estate, Silchar, and Water Resources Department and District Agriculture Office, Silchar Assam for provision of unpublished data and numerous useful discussions.

REFERENCES

[1] Agnihotri, Y., Madukar, R. M., and Singh, P., "Weekly rainfall analysis and agricultural droughts at Chandigarh", Vayiimandal, 1986, 16, pp. 54-56.

[2] Deka, S., Borah, M., and Kakaty, S. C, "Distribution of annual maximum rainfall series of North East India", Department of Mathematical sciences, Tezpur University and Department of Statistics, Dibrugarh University, Assam. 2007.

[3] Pegu, D. and Barman,C., "Spatial-Temporal Rainfall and Runoff Analysis for Exploration of Surface Water resources in Barak Valley", Bachelor of Technology Thesis. Department of Agricultural Engineering, Assam University, Silchar, Assam, India, March, 2012.

[4] Van Dijk, A. I. J. M., and Bruijnzeel, L. A., "Modelling rainfall interception by vegetation of variable density using an adapted analytical model. Model description, Journal of Hydrology, 2001, 247, pp. 230-238.

[5] Vennila, G. Subramani, T., and., Elango,L., "Rainfall variation analysis of Vattamalaikarai sub basin, Tamil Nadu", Journal of applied hydrology, 2007, 20(3), pp. 51-60.

[6] Villazon, M. F., and Willems, P. "Filling gaps and daily disaccumulation of precipitation data for rainfall-runoff model of Pirai River basin located in Santa Cruz-Bolivia, tributary of the Amazon river", paper presented in BALWOIS-Ohrid, Republic of Macedonia, 2010, 25, pp.1-9.

[7] Vlek., and Paul, L. G., "Surface runoff and infiltration processes in the Volta Basin, West Africa, observation and modeling", Ecology and Development Series, 2004, No. 18.

Fritz John Type Optimality Criteria for Optimal Solution of Nonlinear Programming Problem

Prashant Chauhan[1], Paras Bhatnagar[2]

[1]*Deptt. of Mathematics, IFTM University, Lodhipur Rajput, Moradabad*
[2]*Deptt. of Mathematics, GLBITM, Greater Noida*

Abstract: **This paper is proposed to study Fritz-John optimality and duality results for nonlinear programming problem. Weir and Mond provided a Fritz John dual for the nonlinear programming problems involving differentiable functions by using the Fritz John optimality conditions instead of Kuhn-Tucker conditions and thus did not require a constraint qualification. Here we associate the Mond Wier type Fritz John dual to the nonlinear programming problem.**

1. INTRODUCTION

Weir and Mond [7] provided a Fritz John dual for the nonlinear programming problems involving differentiable functions by using the Fritz John [4] optimality conditions instead of Kuhn-Tucker [5] conditions and thus did not require a constraint qualification.

Keywords: Nonlinear programming, Convex functions, Fritz-John optimality and duality conditions, Kuhn-Tucker conditions.

1. Introduction

We obtain Fritz John type necessary optimality criteria for the optimal solution of the following nonlinear program:

(P) Min $f(x)$

Subject to $g_j \le 0$, $j = 1,2,3.....,m$, $x \in S$,

Where $S \subseteq R^n$, $f : S \to R$, and

$g_j : S \to R$ $j = 1,2,3.....,m$ are real valued functions. S is a locally connected set such that for each $x^*, x \in S$, there exists a vector value function $H_{x^*,x^{(\lambda)}}$, satisfying:

$$H_{x^*,x^{(\lambda)}} \in S, 0 < \lambda < a \tag{1.1}$$

Let $X^0 = \{x \in S / g_j \le 0, j = 1,2,3.....,m\}$ $H_{x^*,x}$ is continuous in the interval $]0, a(x^*, x)[$ and

$$H_{x^*,x^{(0)}} = x^*, \; H_{x^*,x^{(1)}} = x \tag{1.2}$$

And the right differentials of f and g_j, $j = 1,2,3.....,m$ at x^* exist with respect to the arc $H_{x^*,x^{(\lambda)}}$.

Theorem-1 Let x^*be an optimal solution of (P). If $(df)^+(x^*, H_{x^*,x^{(0+)}})$ and $(dg_I)^+(x^*, H_{x^*,x^{(0+)}})$ are convex functions of x and g_j, $j \in J$ is continuous at $x^*$with S convex or $S = R^n$ then there exist $r_0^* \in R$, $r^* \in R$, Such that

$$r_0^*(df)^+(x^*, H_{x^*,x^{(0+)}}) + (r_0^*)^T (dg_I)^+(x^*, H_{x^*,x^{(0+)}}) \ge 0, \text{ for all } x \in S \tag{1.3}$$

$$(r_0^*)^T g(x^*) = 0 \tag{1.4}$$

$$(r_0^*, r^*) \ge 0 \tag{1.5}$$

Where $I = I(x^*) = \{i / g_i(x^*) = 0\}$

and $J = J(x^*) = \{j / g_j(x^*) < 0\}$.

Proof: First we shall show that the system

$$\left\{ \begin{array}{l} (df)^+(x^*, H_{x^*,x^{(0+)}}) < 0 \\ (dg_I)^+(x^*, H_{x^*,x^{(0+)}}) < 0 \end{array} \right\} \tag{1.6}$$

Has no solution in $x \in S$.

If possible let $x \in S$ be a solution of the system (1.6). Since right differentials of f and g_j, $i \in I$ at x^* exist with respect to the arc $H_{x^*,x^{(\lambda)}}$. Therefore

$$f(H_{x^*,x^{(\lambda)}}) = f(x^*) + \lambda(df)^+(x^*, H_{x^*,x^{(0+)}}) + \lambda\alpha(\lambda) \tag{1.7}$$

and $g_i(H_{x^*,x^{(\lambda)}}) = g_i(x^*) + \lambda(dg_i)^+(x^*, H_{x^*,x^{(0+)}}) + \lambda\alpha_i(\lambda)$ (1.8)

where $\alpha:[0,1]\to R$, $\lim_{\lambda\to 0}\alpha(\lambda)=0$ (1.9)

$\alpha_i:[0,1]\to R$, $\lim_{\lambda\to 0^+}\alpha_i(\lambda)=0$, $i\in I(x^*)$ (1.10)

Using (1.6),(1.9) and (1.10) we get for small enough λ, say $0<\lambda<\lambda_0$ then $(df)^+(x^*, H_{x^*,x^{(0+)}})+\alpha(\lambda)<0$ and

$(dg_i)^+(x^*, H_{x^*,x^{(0+)}})+\alpha_i(\lambda)<0, \quad i\in I(x^*)$

hence it follows by using the relation(1.7) and (1.8) that for $0<\lambda<\lambda_0$,

$f(H_{x^*,x^{(\lambda)}}) - f(x^*) < 0$ (1.11)

$g_i(H_{x^*,x^{(\lambda)}}) - g_i(x^*) < 0, i\in I(x^*)$ (1.12)

Now g_j, $j\in J$ is continuous at x^* and $H_{x^*,x^{(\lambda)}}$ is also a continuous function of λ. Therefore

$\lim_{\lambda\to 0^+} g_j(H_{x^*,x^{(\lambda)}}) = g_j(x^*) < 0$

Which implies that there exist λ_j^*,

$0<\lambda_j^*<a(x^*,x)$, $j\in J$ such that

$g_j(H_{x^*,x^{(\lambda)}})<0$ for $0<\lambda<\lambda_j^*$ (1.13)

Let $\lambda^* = \min(\lambda_0, \lambda_j^*, j\in J)$ then from (1.11) to (1.13) it follows that for $0<\lambda<\lambda_j^*$, $H_{x^*,x^{(\lambda)}}\in X^0$ and $f(H_{x^*,x^{(\lambda)}}) < f(x^*)$, which is a contradiction as x^* is an optimal solution of (P).

Hence the system (1.6) has no solution $x\in S$.

Since $(df)^+(x^*, H_{x^*,x^{(0+)}})$ and $(dg_I)^+(x^*, H_{x^*,x^{(0+)}})$, $i\in I(x^*)$ are convex functions of x therefore there exist $r_0^*\in R, r_i^*\in R, i\in I$ such that

$r_0^*(df)^+(x^*, H_{x^*,x^{(0+)}}) + r_I^{*T}(dg_I)^+(x^*, H_{x^*,x^{(0+)}}) \ge 0$ for all $x\in S$,where $(r_0^*, r_I^*)\ge 0$.

Defining $r_j^* = 0$ we get the required result.

Now we associate the following Mond Wier type Fritz John dual to the problem (P):

(D) Maximize $f(\mu)$

Subject to

$r_0(df)^+(\mu, H_\mu, x^{(0+)}) + r^T(dg)^+(\mu, H_\mu, x^{(0+)}) \ge 0$ for all $x\in X^0$ (1.14)

$\sum_{j=1}^m r_j g_j(\mu) \ge 0$ (1.15)

$\mu\in S$, $(r_0, r)\ge 0$, $r_0\in R$, $r\in R^m$ (1.16)

Theorem-2 (Weak duality) Let x be feasible for (P) and (μ, r_0, r) be feasible for (D). If f is locally P-connected and $\sum_{j=1}^m r_j g_j(\mu)$ is strongly P-connected at μ then $f(x)\ge f(\mu)$.

Proof: If possible let $f(x)<f(\mu)$. Since f is locally P-connected at μ therefore it follows that

$r_0(df)^+(\mu, H_{\mu,x^{(0+)}}) \le 0$ (1.17)

With strict inequality if $r_0>0$.by the feasibility of x and (μ, r_0, r) for (P) and (D) respectively we get

$\sum_{j=1}^m r_j g_j(x) \le \sum_{j=1}^m r_j g_j(\mu),$

Now $\sum_{j=1}^m r_j g_j$ is strongly locally P-connected at μ so,

$d(\sum_{j=1}^m r_j g_j)^+(\mu, H_{\mu,x^{(0+)}}) \le 0$ (1.18)

With strict inequality if some $r_j>0$, $j=1,2,.....,m$. Adding (1.17) ,(1.18) and using (1.16) we get

$r_0(df)^+(\mu, H_{\mu,x^{(0+)}}) + r^T(dg)^+(\mu, H_{\mu,x^{(0+)}}) < 0$

Which is a contradiction to (1.14).

Hence $f(x)\ge f(\mu)$.

Theorem-3: (Strong Duality) Let x^* be an optimal solution of (P), $(df)^+(x^*, H_{x^*,x^{(0+)}})$ and $(dg_I)^+(x^*, H_{x^*,x^{(0+)}})$ be

the convex functions of x and $g_j \quad j \in J$ be continuous at x^* with S convex or $S = R^n$. Then there exist $r_0^* \in R$ and $r_0^* \in R^m$ such that (x^*, r_0, r^*) is feasible for (D) and the values of the objective functions of (P) and (D) are at x^*. Also if for each feasible (μ, r_0, r) for (D), f is locally P-connected and $\sum_{j=1}^{m} r_j g_j$ is strongly locally P-connected at μ then (x^*, r_0^*, r^*) is optimal for (D).

Proof: Since x^* is an optimal solution of (P) therefore by theorem -1, there exist $r_0^* \in R$ and $r_0^* \in R^m$ such that (x^*, r_0^*, r^*) is feasible for (D). Equality of objective functions for (P) and (D) follows trivially. Further if (x^*, r_0^*, r^*) is not optimal for (D) then there exists (μ, r_0, r) ,feasible for (D) such that $f(\mu) > f(x^*)$.which is a contradiction to weak duality.

2. CONCLUSION

In theorem-1, we obtained Fritz John type necessary optimality condition for nonlinear programming problem (P). In theorem-2 and 3, we obtained Mond Wier type duality conditions for nonlinear program by considering a dual (D) of (P).

REFERENCE

[1] Bazaraa, M. S. and Shetty, C.M., Nonlinear Programming, Theory and algorithms, John Wiley and Sons 1979.

[2] Dantzig, G. B., Eisenberg, E. and Cottle, R. W., Symmetric dual of Nonlinear Programs, Pacific J. Math.15, 809-812,(1965).

[3] Faigle, U., Kern K., Still, G., Algorithm Principles to Mathematical Programming, Kluwer Academic publishers, Dordrecht,2002.

[4] John, F., "Extremum Problems with Inequalities as Subsidiary Conditions," in Studies and Essays: Courant Anniversary Volume, K. O. Friedrichs, Neugebauer, O. E., and Stoker, J. J., (Eds.), Wiley-Interscience, N. Y., pp. 187-204, 1948.

[5] Kuhn H. W. and Tucker, A. W., "Nonlinear Programming," Proceedings of second Berkeley Symposium on Mathematical Statistics and Probability, (University of California Press 1951), 481-492

[6] Mond B. and Egudo, R. R., "On strict converse duality in nonlinear programming," J. Inform. Optim. Sci.6 (1985), 113-16.

[7] Mond B. and Weir, T., "Generalized concavity and duality," in Generalized concavity in optimization and economics (eds. S. Schaible and W.T. Ziemba), (Academic Press 1981), 263-279.

On the k-Numbers of Some Generalized Kuratowski Operators in Topology

Ratna Dev Sarma[1], Ankit Gupta[2]

[1,2]*Department of Mathematics,Rajdhani College, University of Delhi, Delhi 110007, India*

Abstract: **If $X$is a topological space and $A \subseteq X$, then the number of distinct setsthat can be obtained from A by using all possible compositions of pre-closure and complement is at most 10. Similarly, this number for $c_\beta, c_\alpha, and\ c_\sigma$is 8,14 and 10 respectively. Explicit expressions for these sets areprovided. An example is also provided where all these different sets are realized.A collection of all the semi groups (monoids) of the monoid generated by c_α, that is$\mathcal{M}_\alpha$ is provided.**

2010 Mathematics Subject Classification: Primary 54A05.

***Keywords and phrases*: Closure operator, monoids, complement operator.**

Corresponding author: Ankit Gupta.

1. INTRODUCTION

The Kuratowski closure-complement Theorem [7], a result of basic point set topology, was first proposed and proved by Kazimierz Kuratowski**.** Since then a lot of research has been carried out on Kuratowski closure operators within and outside the realm of general topology [2,4,12].

In this paper, we investigate the same for some common generalized closure operators, namely, π-, σ-, α-, β-closures. It is found that the maximum number of distinct sets that can be obtained by repeatedly taking closure and complement on a set is 10, 10, 14 and 8 respectively in case of π-closure, σ-closure, α-closure, and β-closure respectively. It is also found that in all these four cases, the generalized Kuratowski operators obtained in the process give rise to a monoids under compositions relation. The generators of these monoids have been obtained and some semi groups contained in these monoids are studied in the paper.

We recall some known definitions:

Definition 1.1 Let (X, τ) be a topological space. Then a subset A of (X, τ) is called

i.)semi-open[8] if $A \subseteq cl\ int(A)$;

ii.)α-open [10] if $A \subseteq int\ cl\ int(A)$;

iii.)pre-open[9] if $A \subseteq int\ cl(A)$;

iv.)β-open[1] if $A \subseteq cl\ int\ cl(A)$.

The complement of a semi-open (resp. α-open, pre-open, β-open) set is known as semi-closed (resp. α-closed, pre-closed, β-closed) set.

Intersection of all the semi-closed (resp. pre-closed, α-closed and β-closed) sets containingthe set A is called the semi-closure (resp. pre-closure, α-closure and β-closure) of A and denoted by $c_\sigma(A)$ $\left(\text{resp. } c_\pi(A), c_\alpha(A) \text{ and} c_\beta(A)\right)$.

Theorem 1.2[3]*In a topological space (X, τ) with $A \subseteq X$,we have*

i.) $c_\pi(A) = A \cup cl\ int\ (A)$;

ii.) $c_\beta(A) = A \cup int\ cl\ int\ (A)$;

iii.) $c_\alpha(A) = A \cup cl\ int\ cl\ (A)$;

iv.) $c_\sigma(A) = A \cup int\ cl\ (A)$;

2. k-NUMBERS OF GENERALIZED CLOSURE OPERATORS

In this section, first we define the$k$-numberin a topology.

Definition 2.1 Let(X, τ)be a topological space. A set$A \subseteq X$and c_j be a generalized closure operator on (X, τ) . Then the maximum number of distinct sets that can be generated from A by successive applications of c_j and the complement operator$c$ is called the$k$*-number* of c_j and is denoted by $k(c_j)$.

Theorem 2.2*Let c_j be a generalized closure operator in (X, τ). Then we have $k(c_j) = 10,8,14\ and\ 10$ for $j= \pi, \beta, \alpha\ and\ \sigma$.*

Proof. *i.)***The case of c_π :**

For $A \subseteq X$, let us use the following notations:

$\pi_0(A) = A$ (the identity) $\quad$ $\pi_4(A) = c.c_\pi(A)$

$\pi_1(A) = c(A)$ (complement) $\quad$ $\pi_5(A) = c.c_\pi.c(A)$(pre-interior)

$\pi_2(A) = c_\pi(A)$(pre-closure) $\quad$ $\pi_6(A) = c_\pi.c.c_\pi(A)$

$\pi_3(A) = c_\pi.c(A)$ $\quad$ $\pi_7(A) = c.c_\pi.c.c_\pi(A)$

$\pi_8(A) = c_\pi.c.c_\pi.c(A)$ $\quad$ $\pi_9(A) = c.c_\pi.c.c_\pi.c(A)$

Here "." denotes the composition operation. For example, $c_\pi.c(A)$denotes the pre-closure of the complement of$A$.

We have

$$\pi_2(A) = A \cup cl\ int(A)$$

$$\begin{aligned}\pi_3(A) = c_\pi.c(A) &= c(A) \cup cl\ int\ \big(c(A)\big) \\ &= c(A) \cup cl.c\big(int(A)\big) \\ &= c(A) \cup c\big(int\ cl(A)\big) = c(A \cap int\ cl(A))\end{aligned}$$

Procedding similarly, we have

$$\pi_4(A) = c\big(A \cup cl\ int\ (A)\big),\ \pi_5(A) = A \cap int\ cl(A)$$

$$\pi_6(A) = c\big([A \cup cl\ int(A)] \cap int\ cl(A)\big)$$

$$\pi_7(A) = [A \cup cl\ int(A)] \cap int\ cl(A)$$

$$\pi_8(A) = [A \cap\ int\ cl(A)] \cup\ cl\ int(A)$$

$$\pi_9(A) = c\big([A \cap\ int\ cl(A)] \cup\ cl\ int(A)\big)$$

Based on the above expressions for $\pi_i(A), i = 0,1, \ldots\ldots,9$, we obtain the following composition table for the operators $\pi_0(A), \pi_1(A), \pi_2(A), \ldots\ldots\ldots, \pi_9(A)$:

o	π_0	π_1	π_2	π_3	π_4	π_5	π_6	π_7	π_8	π_9
π_0	π_0	π_1	π_2	π_3	π_4	π_5	π_6	π_7	π_8	π_9
π_1	π_1	π_0	π_4	π_5	π_2	π_3	π_7	π_6	π_9	π_8
π_2	π_2	π_3	π_2	π_3	π_6	π_8	π_6	π_8	π_8	π_6
π_3	π_3	π_2	π_6	π_8	π_2	π_3	π_8	π_6	π_6	π_8
π_4	π_4	π_5	π_4	π_5	π_7	π_9	π_7	π_9	π_9	π_7
π_5	π_5	π_4	π_7	π_9	π_4	π_5	π_9	π_7	π_7	π_9
π_6	π_6	π_8	π_6	π_8	π_8	π_6	π_8	π_6	π_6	π_8
π_7	π_7	π_9	π_7	π_9	π_9	π_7	π_9	π_7	π_7	π_9
π_8	π_8	π_6	π_8	π_6	π_6	π_8	π_6	π_8	π_8	π_6
π_9	π_9	π_7	π_9	π_7	π_7	π_9	π_7	π_9	π_9	π_7

For the sake of convience, we just write π_i instead of $\pi_i(A)$. The readers may verify the above results for themselves. For example

$$\pi_4 \circ \pi_6(A) = c.c_\pi.c_\pi.c.c_\pi(A) = c.c_\pi.c.c_\pi(A) = \pi_7(A),$$

and so on.

From the above composition table, it is clear that $k(c_\pi) = 10$.

ii.)The Case of c_β:

For $A \subseteq X$, we use the following notations:

$\beta_0(A) = A$ (the identity) $\quad\quad$ $\beta_4(A) = c.c_\beta(A)$

$\beta_1(A) = c(A)$ (the complement) $\quad\quad$ $\beta_5(A) = c.c_\beta.c(A)$ (β-interior)

$\beta_2(A) = c_\beta(A)$ (β-closure) $\quad\quad$ $\beta_6(A) = c_\beta.c.c_\beta(A)$

$\beta_3(A) = c_\beta.c(A)$ $\quad\quad$ $\beta_7(A) = c.c_\beta.c.c_\beta(A)$

The set theoretic expressions for the above expressions are:

$$\begin{aligned}\beta_3(A) = c_\beta.c(A) &= A \cup int\ cl\ int\ \big(c(A)\big) \\ &= A \cup int\ cl\ (c\big(cl(A)\big) \\ &= A \cup int\ c\big(int\ cl(A)\big) \\ = A \cup c\big(cl\ int\ cl(A)\big) &= c(A \cap cl\ int\ cl\ (A))\end{aligned}$$

Procceeding similarly, we have

$\beta_4(A) = c\big(A \cup int\ cl\ int(A)\big)$,

$\beta_5(A) = A \cap cl\ int\ cl(A)$,

$\beta_6(A) = c\big([A \cap cl\ int\ cl(A)] \cup int\ cl\ int\ (A)\big)$,

$\beta_7(A) = [A \cap cl\ int\ cl(A)] \cup int\ cl\ int\ (A)$.

The composition table of $\beta_i, for\ i = 0,1,2\ \ldots\ldots,7$ is the following:

$\circ$	β_0	β_1	β_2	β_3	β_4	β_5	β_6	β_7
β_0	β_0	β_1	β_2	β_3	β_4	β_5	β_6	β_7
β_1	β_1	β_0	β_4	β_5	β_2	β_3	β_7	β_6
β_2	β_2	β_3	β_2	β_3	β_6	β_7	β_6	β_7
β_3	β_3	β_2	β_6	β_7	β_2	β_3	β_7	β_6
β_4	β_4	β_5	β_4	β_5	β_7	β_6	β_7	β_6
β_5	β_5	β_4	β_7	β_6	β_4	β_5	β_6	β_7
β_6	β_6	β_7	β_6	β_7	β_7	β_6	β_7	β_6
β_7	β_7	β_6	β_7	β_6	β_6	β_7	β_6	β_7

From the above table it follows that $k\big(c_\beta\big) = 8$.

iii.) The case of c_α and c_σ:

Proceeding as above, we can see that the number of distinct sets that can be obtained from c_α , c_σ and their complement are 14 and 10 respectively. For $A \subseteq X$, the notations for $c_\alpha$are used:

$\alpha_0(A) = A$ (the identity)	$\alpha_7(A) = c_\alpha.c.c_\alpha.c(A)$
$\alpha_1(A) = c(A)$ (complement)	$\alpha_8(A) = c.c_\alpha.c.c_\alpha(A)$
$\alpha_2(A) = c_\alpha(A)$ (α-closure)	$\alpha_9(A) = c.c_\alpha.c.c_\alpha.c(A)$
$\alpha_3(A) = c_\alpha.c(A)$	$\alpha_{10}(A) = c_\alpha.c.c_\alpha.c.(A)$

$\alpha_4(A) = c.c_\alpha(A)$	$\alpha_{11}(A) = c_\alpha.c.c_\alpha.c.c_\alpha.c(A)$
$\alpha_5(A) = c.c_\alpha.c(A)$ $(\alpha - interior)$	$\alpha_{12}(A) = c.c_\alpha.c.c_\alpha.c_\alpha(A)$
$\alpha_6(A) = c_\alpha.c.c_\alpha(A)$	$\alpha_{13}(A)$ $= c.c_\alpha.c.c_\alpha.c.c_\alpha.c(A)$

The composition table for c_α *is* :

$\circ$	α_0	α_1	α_2	α_3	α_4	α_5	α_6	α_7	α_8	α_9	α_{10}	α_{11}	α_{12}	α_{13}
α_0	α_0	α_1	α_2	α_3	α_4	α_5	α_6	α_7	α_8	α_9	α_{10}	α_{11}	α_{12}	α_{13}
α_1	α_1	α_0	α_4	α_5	α_2	α_3	α_8	α_9	α_6	α_7	α_{12}	α_{13}	α_{10}	α_{11}
α_2	α_2	α_3	α_2	α_3	α_6	α_7	α_6	α_7	α_{10}	α_{11}	α_{10}	α_{11}	α_6	α_7
α_3	α_3	α_2	α_6	α_7	α_2	α_3	α_{10}	α_{11}	α_6	α_7	α_6	α_7	α_{10}	α_{11}
α_4	α_4	α_5	α_4	α_5	α_8	α_9	α_8	α_9	α_{12}	α_{13}	α_{12}	α_{13}	α_8	α_9
α_5	α_5	α_4	α_8	α_9	α_4	α_5	α_{12}	α_{13}	α_8	α_9	α_8	α_9	α_{12}	α_{13}
α_6	α_6	α_7	α_6	α_7	α_{10}	α_{11}	α_{10}	α_{11}	α_6	α_7	α_6	α_7	α_{10}	α_{11}
α_7	α_7	α_6	α_{10}	α_{11}	α_6	α_7	α_6	α_7	α_{10}	α_{11}	α_{10}	α_{11}	α_6	α_7
α_8	α_8	α_9	α_8	α_9	α_{12}	α_{13}	α_{12}	α_{13}	α_8	α_9	α_8	α_9	α_{12}	α_{13}
α_9	α_9	α_8	α_{12}	α_{13}	α_8	α_9	α_6	α_9	α_{12}	α_{13}	α_{12}	α_{13}	α_8	α_9
α_{10}	α_{10}	α_{11}	α_{10}	α_{11}	α_6	α_7	α_{10}	α_7	α_{10}	α_{11}	α_{10}	α_{11}	α_6	α_7
α_{11}	α_{11}	α_{10}	α_6	α_7	α_{10}	α_{11}	α_9	α_{11}	α_6	α_7	α_6	α_7	α_{10}	α_{11}
α_{12}	α_{12}	α_{13}	α_{12}	α_{13}	α_8	α_9	α_8	α_9	α_{12}	α_{13}	α_{12}	α_{13}	α_8	α_9
α_{13}	α_{13}	α_{12}	α_8	α_9	α_{12}	α_{13}	α_{12}	α_{13}	α_8	α_9	α_8	α_9	α_{12}	α_{13}

From the above table it is clear that $k(c_\alpha) = 14$.
In case of c_σ, the notations used for different 10 sets are :

$\sigma_0(A) = A$ $\quad \sigma_4(A) = c.c_\sigma(A)$ $\quad \sigma_8(A) = c_\sigma.c.c_\sigma.c(A)$

$\sigma_1(A) = c(A)$ $\quad \sigma_5(A) = c.c_\sigma.c(A)$ $\quad \sigma_9(A) = c.c_\sigma.c.c_\sigma.c(A)$

$\sigma_2(A) = c_\sigma(A)$ $\quad \sigma_6(A) = c_\sigma.c.c_\sigma(A)$

$\sigma_3(A) = c_\sigma.c(A)$ $\quad \sigma_7(A) = c.c_\sigma.c.c_\sigma(A)$

Like the above three cases, reader can verify that $k(c_\sigma) = 10$.

Below, we provide an example of a topological space for which all these bounds are realized. The elobrate details of the example is available in [6] and hence avoided here.

Example 2.3 Let$X = \mathbf{R}$, the set of real numbers, equipped with the usual topology. Then a subset of $A \subseteq$ X be defined by:

$A = \left\{-\frac{1}{n}, n \in \mathbf{N}\right\} \cup [[1,3]\backslash\{2+\frac{1}{n}, n \in \mathbf{N}\}] \cup [(5,7] \cap \left(\mathbf{Q} \cup \bigcup_{n=1\ to\ \infty}(6+\frac{1}{2n\pi}, 6+\frac{1}{(2n-1)\pi}])\right] \cup (-3,-2]$. For this set, all the sets defined above are different.

If all the above four generalized closure operators and complement operator are taken together, they generate at the most **52**distinct sets under composition of operators. The reader may refer to [6] for further discussion in this regard. Similarly, the sets which satisfiy the property $A = i_\sigma c_\sigma(A)$ have been studiedn in [5] as *PS*-regular sets. In tour above discussion, a set is PS–regular if $A = \sigma_7$(A).

3. MONOIDS OF THE GENERAIZED CLOSURE OPERATORS

Taking composition of operators as the binary operation, we obtain the following monoids of operators:

$$\mathcal{M}_\pi = \{\pi_0, \pi_1, \dots\dots\dots, \pi_8, \pi_9\}$$
$$\mathcal{M}_\alpha = \{\alpha_0, \alpha, \dots\dots\dots, \alpha_{12}, \alpha_{13}\}$$
$$\mathcal{M}_\beta = \{\beta_0, \beta_1, \dots\dots\dots, \beta_6, \beta_7\}$$
$$\mathcal{M}_\sigma = \{\sigma_0, \sigma_1, \dots\dots\dots, \sigma_8, \sigma_9\}$$

This is clear from composition tables provided in the previous section.

Therorem 3.1 The generators of the monoids $\mathcal{M}_\delta, where\ \delta = \pi, \beta, \alpha\ and\ \sigma$ are given by
$i.)$ $\mathcal{M}_\delta = < \delta_1, \delta_i >$, *where* $i = 2,3,4,5$.

Proof. It follows from the fact that $\mathcal{M}_\pi = < \pi_1, \pi_2 >$ and $\pi_2 = \pi_3 \circ \pi_1 = \pi_1 \circ \pi_4 = \pi_1 \circ \pi_5 \circ \pi_1$, to be verified from the composition table.
Same argument is valid for $\mathcal{M}_\alpha, \mathcal{M}_\beta$and$\mathcal{M}_\sigma$.

Theorem 3.2*The total number of distinct semi-groups generated by the members of* $\mathcal{M}_\alpha$ *is 118, under the composition of operators.*

Proof. We enlist all the semi groups contained in $\mathcal{M}_\alpha$ in the following manner. Since the calculation part may be easily verified from the composition table, we leave it to the reader.

i.) Semi-groups with one generator and one element:
$< \alpha_0 > = \{\alpha_0\}, < \alpha_2 > = \{\alpha_2\}, < \alpha_5 > = \{\alpha_5\}$
$< \alpha_5 > = \{\alpha_5\}, < \alpha_8 > = \{\alpha_8\}, < \alpha_{10} > = \{\alpha_{10}\},$
$< \alpha_{13} > = \{\alpha_{13}\}$

ii.) Semi groups with one generator and two elements.

$< \alpha_1 > = \{\alpha_1, \alpha_0\}, < \alpha_6 > = \{\alpha_6, \alpha_{10}\},$

$< \alpha_{11} > = \{\alpha_7, \alpha_{11}\}, < \alpha_9 > = \{\alpha_9, \alpha_{13}\},$

$< \alpha_{12} > = \{\alpha_8, \alpha_{12}\}, < \alpha_{11} > = \{\alpha_7, \alpha_{11}\}$

iii.) Semi groups with one generator and more than two elements:

$$< \alpha_3 > = \{\alpha_3, \alpha_7, \alpha_{11}\}, < \alpha_4 > = \{\alpha_4, \alpha_8, \alpha_{12}\}$$

iii.) Semi groups with one generator and more than two elements:

Now, we provide an exhaustive list of all semi groups with two generators consisting of element of $\mathcal{M}_\alpha$.

$$< \alpha_1, \alpha_2 > = \{\alpha_0, \alpha_1, \alpha_2, \alpha_3, \alpha_4, \dots\dots\dots, \alpha_{13}\}$$
$$< \alpha_1, \alpha_6 > = \{\alpha_0, \alpha_1, \alpha_6, \alpha_7, \alpha_8, \alpha_9, \dots, \alpha_{13}\},$$
$$<\alpha_3, \alpha_4> = \{\alpha_2, \alpha_3, \dots\dots\dots\dots, \alpha_{12}, \alpha_{13}\}$$
$$< \alpha_6, \alpha_9 > = \{\alpha_6, \alpha_7, \dots\dots\dots, \alpha_{12}, \alpha_{13}\}$$

It may be observed that

$$< \alpha_1, \alpha_2 > \supseteq < \alpha_1, \alpha_6 > \supseteq < \alpha_6, \alpha_9 >$$

and$< \alpha_1, \alpha_2 > \supseteq < \alpha_3, \alpha_4 > \supseteq < \alpha_6, \alpha_9 >$.

Further $< \alpha_6, \alpha_9 >$has 9 semi groups each having two generators. They are:

$$< \alpha_7, \alpha_{10} > = \{\alpha_7, \alpha_{10}\}, < \alpha_7, \alpha_{13} > = \{\alpha_7, \alpha_{13}\},$$
$$< \alpha_8, \alpha_{10} > = \{\alpha_8, \alpha_{10}\}, <\alpha_8, \alpha_{13}> = \{\alpha_8, \alpha_{13}\},$$
$$<\alpha_6, \alpha_7> = \{\alpha_6, \alpha_7, \alpha_{10}, \alpha_{11}\},$$
$$<\alpha_8, \alpha_9>= \{\alpha_8, \alpha_9, \alpha_{12}, \alpha_{13}\}$$
$$< \alpha_6, \alpha_8 > = \{\alpha_6, \alpha_8, \alpha_{10}, \alpha_{12}\},$$
$$< \alpha_7, \alpha_9 > = \{\alpha_7, \alpha_9, \alpha_{11}, \alpha_{13}\},$$
$$< \alpha_7, \alpha_8 > = \{\alpha_7, \alpha_8, \alpha_{10}, \alpha_{13}\}$$

Again $< \alpha_6 , \alpha_9 >$ contains 8 semi groups with one generator, namely, $< \alpha_6 >, < \alpha_7 >, < \alpha_8 >, < \alpha_9 >, < \alpha_{10} >, < \alpha_{11} >, < \alpha_{12} >, < \alpha_{13} >$, which are already mentioned in the beginning.

Thus total numbers of semi groups of $< \alpha_6, \alpha_9 >$ are 9+8+1=18 (including itself).

Now, semi groups of$< \alpha_3, \alpha_4 >$, which are not listed above, with two generators are 27 in numbers. They are:

$$< \alpha_2, \alpha_6 > = \{\alpha_2, \alpha_6, \alpha_{10}\}, < \alpha_2, \alpha_{10} > = \{\alpha_2, \alpha_{10}\},$$
$$< \alpha_5, \alpha_{13} > = \{\alpha_5, \alpha_{13}\},$$
$$< \alpha_5, \alpha_9 > = \{\alpha_5, \alpha_9, \alpha_{13}\}$$
$$< \alpha_2, \alpha_7 > = \{\alpha_2, \alpha_7, \alpha_{10}\}, < \alpha_2, \alpha_8 > = \{\alpha_2, \alpha_8, \alpha_{10}\},$$
$$< \alpha_5, \alpha_7 > = \{\alpha_5, \alpha_7, \alpha_{13}\}$$
$$< \alpha_5, \alpha_8 > = \{\alpha_5, \alpha_8, \alpha_{13}\}$$
$$< \alpha_2, \alpha_{11} > = \{\alpha_2, \alpha_6, \alpha_7, \alpha_{10}, \alpha_{11}\},$$
$$< \alpha_2, \alpha_{12} > = \{\alpha_2, \alpha_6, \alpha_8, \alpha_{10}, \alpha_{12}\},$$
$$< \alpha_2, \alpha_{13} > = \{\alpha_2, \alpha_7, \alpha_8, \alpha_{10}, \alpha_{13}\}$$
$$< \alpha_2, \alpha_9 > = \{\alpha_2, \alpha_6, \alpha_7, \dots\dots\dots, \alpha_{12}, \alpha_{13}\},$$
$$< \alpha_5, \alpha_{12} > = \{\alpha_5, \alpha_8, \alpha_9, \alpha_{12}, \alpha_{13}\},$$
$$< \alpha_5, \alpha_{11} > = \{\alpha_5, \alpha_7, \alpha_9, \alpha_{11}, \alpha_{13}\},$$
$$< \alpha_5, \alpha_{10} > = \{\alpha_5, \alpha_7, \alpha_8, \alpha_{10}, \alpha_{13}\}$$
$$< \alpha_5, \alpha_6 > = \{\alpha_5, \alpha_6, \alpha_7, \dots\dots, \alpha_{12}, \alpha_{13}\}$$
$$< \alpha_3, \alpha_6 > = \{\alpha_3, \alpha_6, \alpha_7, \alpha_{10}, \alpha_{11}\}$$
$$< \alpha_3, \alpha_9 > = \{\alpha_3, \alpha_7, \alpha_9, \alpha_{11}, \alpha_{13}\}$$
$$< \alpha_3, \alpha_8 > = \{\alpha_3, \alpha_6, \alpha_7, \dots\dots\dots\dots, \alpha_{12}, \alpha_{13}\}$$
$$<\alpha_4, \alpha_9>=\{\alpha_4, \alpha_8, \alpha_9, \alpha_{12}, \alpha_{13}\}$$
$$< \alpha_4, \alpha_6 > = \{\alpha_4, \alpha_6, \alpha_8, \alpha_{10}, \alpha_{12}\}$$
$$< \alpha_4, \alpha_7 > = \{\alpha_4, \alpha_6, \alpha_7, \dots\dots, \alpha_{12}, \alpha_{13}\}$$
$$< \alpha_2, \alpha_3 > = \{\alpha_2, \alpha_3 , \alpha_6, \alpha_7, \alpha_{10}, \alpha_{11}\}$$
$$< \alpha_4, \alpha_5 > = \{\alpha_4, \alpha_5, \alpha_8, \alpha_9, \alpha_{12}, \alpha_{13}\}$$
$$< \alpha_2, \alpha_4 > = \{\alpha_2, \alpha_4, \alpha_6, \alpha_8, \alpha_{10}, \alpha_{12}\}$$
$$< \alpha_3, \alpha_5 > \{\alpha_3, \alpha_5, \alpha_7, \alpha_9, \alpha_{11}, \alpha_{13}\}$$
$$< \alpha_2, \alpha_5 > = \{ \alpha_2, \alpha_5, \alpha_7, \alpha_8, \alpha_{10}, \alpha_{13}\}$$

Similarly, we get 7 semi groups of $< \alpha_3, \alpha_4 >$ having 3 generators. They are:

$$< \alpha_2, \alpha_3, \alpha_8 > = \{\alpha_2, \alpha_3, \alpha_6, \alpha_7, \dots\dots, \alpha_{12}, \alpha_{13}\}$$
$$< \alpha_4, \alpha_5, \alpha_6 > = \{\alpha_4, \alpha_5, \alpha_7, \alpha_8, \dots\dots, \alpha_{12}, \alpha_{13}\}$$
$$< \alpha_2, \alpha_4, \alpha_7 > = \{\alpha_2, \alpha_4, \alpha_6, \alpha_7, \dots\dots\dots, \alpha_{12}, \alpha_{13}\}$$
$$< \alpha_3, \alpha_5, \alpha_8 > = \{\alpha_3, \alpha_5, \alpha_6, \alpha_7, \dots\dots, \alpha_{12}, \alpha_{13}\}$$
$$< \alpha_2, \alpha_5, \alpha_6 > = \{\alpha_2, \alpha_5, \alpha_6, \alpha_7, \dots\dots\dots, \alpha_{12}, \alpha_{13}\}$$
$$< \alpha_2, \alpha_3, \alpha_5 > = \{\alpha_2, \alpha_3, \alpha_5, \alpha_6, \alpha_7, \dots\dots\dots, \alpha_{12}, \alpha_{13}\}$$
$$< \alpha_2, \alpha_4 , \alpha_5 > = \{\alpha_2, \alpha_4, \alpha_5, \alpha_6, \alpha_7, \dots\dots\dots, \alpha_{12}, \alpha_{13}\}$$

Thus, altogether, total number of distinct semi groups generated by the elements of $\mathcal{M}_\alpha$ without α_0 amounts to 57. One can check that it enumerates four monoids with α_0 and 57 semi groups without α_0.The exhaustive list is provided below:

$$< \alpha_0 >, < \alpha_1 >, < \alpha_2 >, < \alpha_3 >, < \alpha_4 >, < \alpha_5 >, < \alpha_6 >,$$
$$< \alpha_7 >, < \alpha_8 >, < \alpha_9 >, < \alpha_{10} >, < \alpha_{11} >, < \alpha_{12} >,$$
$$< \alpha_{13} >, < \alpha_1, \alpha_2 > , < \alpha_1, \alpha_6 >, <\alpha_3, \alpha_4 >, < \alpha_6, \alpha_9 >, <$$
$$\alpha_7, \alpha_{10} > , < \alpha_7, \alpha_{13} > ,$$
$$< \alpha_8, \alpha_{10} >, <\alpha_8, \alpha_{13}>, <\alpha_6, \alpha_7>, <\alpha_8, \alpha_9>,$$
$$< \alpha_6, \alpha_8 >, < \alpha_7, \alpha_9 > , < \alpha_7, \alpha_8 > , < \alpha_2, \alpha_6 > , < \alpha_2, \alpha_{10}$$
$$> , < \alpha_5, \alpha_{13} > , < \alpha_5, \alpha_9 > , < \alpha_2, \alpha_7 > ,$$
$$< \alpha_2, \alpha_8 > , < \alpha_5, \alpha_7 >, < \alpha_5, \alpha_8 >,$$
$$< \alpha_2, \alpha_{11} >, < \alpha_2, \alpha_{12} > , < \alpha_2, \alpha_{13} > ,$$
$$< \alpha_2, \alpha_9 >, < \alpha_5, \alpha_{12} > , < \alpha_5, \alpha_{11} > ,$$
$$< \alpha_5, \alpha_{10} > , < \alpha_5, \alpha_6 > , < \alpha_3, \alpha_6 > ,$$
$$< \alpha_3, \alpha_9 > , < \alpha_1, \alpha_2 > , < \alpha_1, \alpha_6 > ,$$
$$< \alpha_6, \alpha_9 > , < \alpha_3, \alpha_4 > ,$$
$$< \alpha_3, \alpha_8 >, < \alpha_4, \alpha_9 >, < \alpha_4, \alpha_6 >, < \alpha_4, \alpha_7 >, < \alpha_2, \alpha_3 > ,$$
$$< \alpha_4, \alpha_5 > , < \alpha_2, \alpha_4 > , < \alpha_3, \alpha_5 >,$$
$$< \alpha_2, \alpha_5 >, < \alpha_2, \alpha_3, \alpha_8 >, < \alpha_4, \alpha_5, \alpha_6 >,$$
$$< \alpha_2, \alpha_4, \alpha_7 >, < \alpha_3, \alpha_5, \alpha_8 >, < \alpha_2, \alpha_5, \alpha_6$$
$$>< \alpha_2, \alpha_3, \alpha_5 >, < \alpha_2, \alpha_4, \alpha_5 >$$

Since$\alpha_0$is an identity operator in monoid $\mathcal{M}_\alpha$, therefore by adding $\alpha_0$to each of the semi group not containingα_0,we again get a semi group of $\mathcal{M}_\alpha$, therefore there are $4 + 57.2 = 118$semi groups in $\mathcal{M}_\alpha$.

Similarly, the above study can be carried out for $\mathcal{M}_\pi, \mathcal{M}_\beta$ and $\mathcal{M}_\sigma$ also.

The reader may refer to [11] for similar algebraic treatment of Kuratowski operator.

ACKNOWLEDGEMENT

This work is a part of a research work financed by the University Grant Commission (India).

REFERENCES

[1] Abd EI-Monsef, M. E., Mahmoud, R. A., and El-Deeb, S. N., "β–open sets and β −continuous mappings", *Bull. Fac. Sci. Assiut Univ.*, 12 (1966),pp. 77 – 90.

[2] Brzozowski, J.,Grant, E.,Shallit, J., "Closures in formal languages and Kuratowski's theorem"*Developments in language theory,* 125–144, Lecture Notes in Comp. Sci., 5583,*Springer, Berlin,* 2009.

[3] Császár, Á.,"On γ-Interior and γ-Closure of a Set", *Acta Math. Hungar.*, 80 (1998), pp.89 – 93.

[4] Gardner, B. J.; Jackson, M.,"The Kuratowski closure-complement theorem",*New Zealand J. Math.*38 (2008), 9–44.

[5] Gupta, A., Sarma, R. D., "PS-Regular Sets in Topology and Generalized Topology", *journal of Topology,* 2014, Article Id 274592, 6 pages, 2014. Doi: 10.1155/2014/274592

[6] Gupta, A., Sarma, R. D., "A Note on Some Generalized Closure and Interior Operators in Topology", *Acta Math. Hungar.,* (Communicated)

[7] Kuratowski, K., L'op*é*ration $\bar{A}$ de l'analysis situs, Fund. Math. 3 (1922) 182-199.

[8] Levine,N.,"Semi-open Sets and Semi-Continuity in Topological Spaces", *The American Mathematical monthly*, 70 (1963), pp. 36 – 41.

[9] Mashhour, A. S., Abd EI-Monsef, M. E., and El-Deeb, S. N.,"On Pre continuous and Weak Precontinuous Mappings", *Proc. Math. and Phys. Soc. Egypt*, 51 (1981).

[10] Njăstad, O., "On Some Classes of nearly Open Sets", *Pacific J. Math.*, 15 (1965),pp. 961–970.

[11] Plewik, S.,Walczyńska, M., "The monoid consisting ofKuratowski operations(English summary)" *J. Math.*2013, Art. ID 289854,

[12] Sherman, D., "Variations on Kuratowski's 14-set theorem", *Amer. Math. Monthly*117 (2010), no. 2, 113–123.

Chi Square Divergence Measure and Their Bounds

Ram Naresh Saraswat

Department of Mathematics, Manipal University Jaipur, India

Abstract: **Information and divergence measures are widely used in various applications of pattern recognition, signal processing and statistical applications. In this paper we shall study different methods to find chi-square divergence measures using well known convex functions and their compare to well established results which are well known in the literature of Information Theory. Their Relations are also establishing using some well-known inequalities in this research paper.**

Keywords: - Chi-square divergence, f-divergence measure, Jenson-Shannon's divergenceetc.

AMS Classification 62B-10, 94A-17, 26D15

1. INTRODUCTION

Let

$$\Gamma_n = \left\{ P=(p_1,p_2,.....p_n) \middle| p_i \geq 0, \sum_{i=1}^{n} p_i = 1 \right\}, n \geq 2$$

be the set of all complete finite discrete probability distributions. There are many information and divergence measures exists in the literature on information theory and statistics. Csiszar [2, 3] introduced a generalized measure of information using f-divergence functional

$$I_f(P,Q) = \sum_{i=1}^{n} q_i f\left(\frac{p_i}{q_i}\right) \qquad (1.1)$$

Where $f : \mathbf{R}_+ \to \mathbf{R}_+$ is a convex function and $P, Q \in \Gamma_n$. A class of divergence measures called f-divergences was introduced by Csiszar [2, 3]. Here we shall give some example of divergence measures in the category of Csiszar f-divergence measure.

- Relative Information[10] $D(P,Q) = \sum_{i=1}^{n} p_i \log \frac{p_i}{q_i}$ (1.2)
- Chi-square divergence[6]

$$\chi^2(P,Q) = \sum_{i=1}^{n} \frac{(p_i - q_i)^2}{q_i} = \sum_{i=1}^{n} \frac{p_i^2}{q_i} - 1 \qquad (1.3)$$

- Relative J-S divergence[10]

$$F(P,Q) = \sum_{i=1}^{n} p_i \log\left(\frac{2p_i}{p_i + q_i}\right) \qquad (1.4)$$

- Hellinger discrimination[5]

$$h(P,Q) = 1 - B(P,Q) = \frac{1}{2}\sum_{i=1}^{n}\left(\sqrt{p_i} - \sqrt{q_i}\right)^2 \qquad (1.5)$$

where $B(P,Q) = \sum_{i=1}^{n} \sqrt{p_i q_i}$ is known as Bhattacharya divergence measure [1]

- J-divergence measure [4]

$$J(P,Q) = \sum_{i=1}^{n} (p_i - q_i) \log\left(\frac{p_i}{q_i}\right) \qquad (1.6)$$

- Relative J-divergence measure [4]

$$J_R(P,Q) = \sum_{i=1}^{n} (p_i - q_i) \log\left(\frac{p_i + q_i}{2q_i}\right) \qquad (1.7)$$

2. INFORMATION INEQUALITIES:

The following Inequalities have been established by Taneja [10]. Using their inequalities we have discussed particular cases for chi-square divergence measure.

Theorem: Let $f : \mathbf{R}_+ \to \mathbf{R}$ be the mapping which is normalized i.e. $f(1) = 0$. Suppose that

(i) f is twice differentiable function on (r, R), $0 \leq r \leq 1 \leq R < \infty$ (f' and f'' denote the first and second derivatives of f),

(ii) there exist real constant m, M such that $m < M$ and $m \leq x^{2-s} f''(x) \leq M \quad \forall x \in (r,R),\ s \in \mathbf{R}$

If $P, Q \in \Gamma_n$ are discrete probability distributions with $0 < r \le \frac{p_i}{q_i} \le R < \infty$,

then $m\Phi_s(P,Q) \le I_f(P,Q) \le M\,\Phi_s(P,Q)$ (2.1)

and $m[\eta_s(P,Q) - \Phi_s(P,Q)] \le I_f(P,Q) \le M[\eta_s(P,Q) - \Phi_s(P,Q)]$ (2.2)

and $\eta_s(P,Q) = C_{\Phi's}\left(\frac{P^2}{Q}, P\right) - I_{\Phi's}(P,Q)$ Where

$$\Phi_s(P,Q) = \begin{cases} {}^2K_s(P,Q), & s \ne 0,1 \\ D(Q,P), & s = 0 \\ D(P,Q), & s = 1 \end{cases} \quad (2.3)$$

$$I_\rho(P,Q) = I_{f'}\left(\frac{P^2}{Q}, P\right) - I_{f'}(P,Q) = \sum_{i=1}^{n}(p_i - q_i) f'\left(\frac{p_i}{q_i}\right) \quad (2.4)$$

and

$$\eta_s(P,Q) = C_{\Phi's}\left(\frac{P^2}{Q}, P\right) - I_{\Phi's}(P,Q)$$

$$= \begin{cases} (s-1)^{-1}\sum_{i=1}^{n}(p_i - q_i)\left(\frac{p_i}{q_i}\right)^{s-1}, & s \ne 1 \\ \sum_{i=1}^{n}(p_i - q_i)\log\left(\frac{p_i}{q_i}\right), & s = 1 \end{cases} \quad (2.5)$$

3. CHI-SQUARE DIVERGENCE MEASURE

In this section we shall establish chi-square divergence measure from following convex functions.

Example:1 Let the convex function

$\Phi(t) = t^2 - 1, \forall\ t > 0$ (3.1)

$\Phi(t) = 2t$

$\Phi(t) = 2 \ge 0$

Then we can findout the Csiszar's Φ -divergence measure

$$I_\phi(p,q) = \sum_{i=1}^{n}\frac{p_i^2}{q_i} - 1 = \chi^2(p,q) \quad (3.3)$$

$$I_{\phi'}(p,q) = 2\sum_{i=1} q_i\left(\frac{p_i}{q_i}\right) = 2\sum_{i=1}^{n} p_i = 2$$

$$I_{\phi'}\left(\frac{p^2}{q}, p\right) = 2\sum_{i=1}^{n} p_i\left(\frac{p_i^2}{q_i}.\frac{1}{p_i}\right) = 2\sum_{i=1}^{n}\frac{p_i^2}{q_i} - 2 + 2$$

$$I_{\phi'}\left(\frac{p^2}{q}, p\right) = 2\sum_{i=1}^{n} p_i\left(\frac{p_i^2}{q_i}.\frac{1}{p_i}\right) = 2\left(\sum_{i=1}^{n}\frac{p_i^2}{q_i} - 1\right) + 2$$

$$I_{\phi'}\left(\frac{p^2}{q}, p\right) = 2\chi^2(p,q) + 2$$

From (3.1)

$$\phi'(1)(P_n - Q_n) \le I_\phi(p,q) - Q_n\phi(1) \le I_{\phi'}\left(\frac{p^2}{q}, p\right) - I_{\phi'}(p,q)$$

$$2(P_n - Q_n) \le \chi^2(p,q) - 0 \le 2\chi^2(p,q) + 2 - 2$$

$$2(P_n - Q_n) \le \chi^2(p,q) \le 2\chi^2(p,q)$$

Two cases are created

$2(P_n - Q_n) \le \chi^2(p,q)$ (3.2)

$\chi^2(p,q) \le 2\chi^2(p,q)$

$0 \le \chi^2(p,q)$

From (3.2)

$$0 \le I_\phi(p,q) - Q_n\Phi\left(\frac{P_n}{Q_n}\right) \le I_{\phi'}\left(\frac{p^2}{q}, p\right) - \frac{P_n}{Q_n}I_{\phi'}(p,q)$$

$$0 \le \chi^2(p,q) - Q_n\left(\frac{P_n^2}{Q_n^2} - 1\right) \le 2\chi^2(p,q) + 2 - \frac{2P_n}{Q_n}$$

From (3.3)

$$0 \le I_\phi(p,q) \le I_{\phi'}\left(\frac{p^2}{q}, p\right) - I_{\phi'}(p,q)$$

$$0 \le \chi^2(p,q) \le 2\chi^2(p,q) + 2 - 2$$

$$0 \le \chi^2(p,q) \le 2\chi^2(p,q)$$

$0 \le \chi^2(p,q)$ (3.3)

Example: 3consider a convex function

$$\Phi(t) = t(t-1),\ \forall\ t > 0$$

Function Φ is a convex function from Fig. 3.1and normalized i. e. f(1)=0 Then applying Csiszar's Φ -divergence measure

$$I_{\phi}(p,q) = \sum_{i=1}^{n} \frac{p_i^2}{q_i} - 1 = \chi^2(p,q)$$

$$I_{\phi}(p,q) = \sum_{i=1}^{n} q_i \left(2\frac{p_i}{q_i} - 1 \right)$$

$$I_{\phi}(p,q) = 2\sum_{i=1}^{n} p_i - \sum_{i=1}^{n} q_i$$

$$I_{\phi}(p,q) = 1$$

$$I_{\phi}(\frac{p^2}{q}, p) = 2\chi^2(p,q) + 1$$

From (3.1)

$$\phi'(1)(P_n - Q_n) \le I_{\phi}(p,q) - Q_n\phi(1)$$

$$\le I_{\phi}(\frac{p^2}{q}, p) - I_{\phi}(p,q)$$

$$(P_n - Q_n) \le \chi^2(p,q) - Q_n \le 2\chi^2(p,q) + 1 - 1$$

$$(P_n - Q_n) \le \chi^2(p,q) - Q_n \le 2\chi^2(p,q)$$

From (3.2)

$$0 \le I_{\phi}(p,q) - Q_n\Phi(\frac{P_n}{Q_n})$$

$$\le I_{\phi}(\frac{p^2}{q}, p) - \frac{P_n}{Q_n} I_{\phi}(p,q)$$

$$0 \le \chi^2(p,q) - Q_n \frac{P_n}{Q_n}\left(\frac{P_n}{Q_n^2} - 1 \right)$$

$$\le 2\chi^2(p,q) + 1 - \frac{P_n}{Q_n}$$

$$0 \le \chi^2(p,q) - P_n\left(\frac{P_n}{Q_n^2} - 1 \right) \le 2\chi^2(p,q) + \frac{Q_n - P_n}{Q_n}$$

From (3.3)

$$0 \le \chi^2(p,q) \le 2\chi^2(p,q)$$

$$0 \le \chi^2(p,q)$$

Example: 3considering a convex function

$$\Phi(t) = (t-1)^2,\quad \forall\ t > 1$$

$$\Phi'(t) = 2(t-1),\quad \Phi(1) = 0 = \Phi'(1)$$

$$\Phi''(t) = 2 > 0$$

Then we can find out the Csiszar's Φ -divergence measure

$$I_{\phi}(p,q) = \sum_{i=1}^{n} \frac{p_i^2}{q_i} - 1 = \chi^2(p,q)$$

$$I_{\phi}(p,q) = 2\left[\sum_{i=1}^{n} q_i \left(\frac{p_i}{q_i} - 1 \right) \right]$$

$$I_{\phi}(p,q) = 2\left(\sum_{i=1}^{n} p_i - \sum_{i=1}^{n} q_i \right)$$

$$I_{\phi}(p,q) = 0$$

$$I_{\phi}(\frac{p^2}{q}, p) = 2\sum_{i=1}^{n} p_i \left(\frac{p_i^2}{q_i}.\frac{1}{p_i} - 1 \right) = 2\sum_{i=1}^{n} \frac{p_i^2}{q_i} - 2$$

From (3.1)

$$I_{\phi}(\frac{p^2}{q}, p) = 2\left(\sum_{i=1}^{n} \frac{p_i^2}{q_i} - 1 \right)$$

$$I_{\phi}(\frac{p^2}{q}, p) = 2\chi^2(P,Q)$$

$$\phi'(1)(P_n - Q_n) \le I_{\phi}(P,Q) - Q_n\phi(1)$$

$$\le I_{\phi}(\frac{p^2}{q}, p) - I_{\phi}(P,Q)$$

$$0 \le \chi^2(P,Q) - 0 \le 2\chi^2(P,Q) - 0$$

$$0 \le \chi^2(P,Q) \le 2\chi^2(P,Q)$$

$$0 \le \chi^2(P,Q)$$

From (3.2)

$$0 \le I_{\phi}(P,Q) - Q_n \Phi(\frac{P_n}{Q_n})$$

$$\le I_{\phi'}(\frac{p^2}{q}, p) - \frac{P_n}{Q_n} I_{\phi'}(P,Q)$$

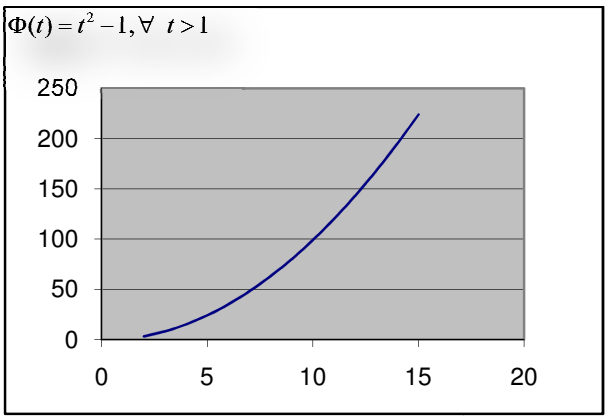


Figure 3.1

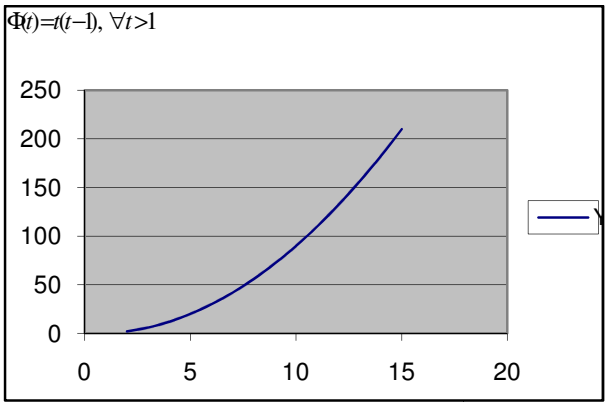


Figure 3.3

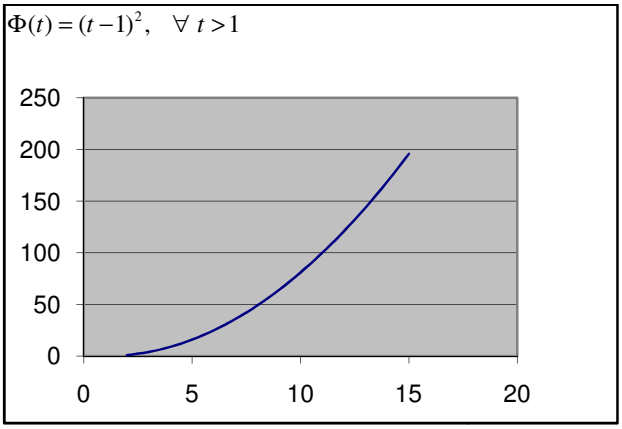


Figure 3.3

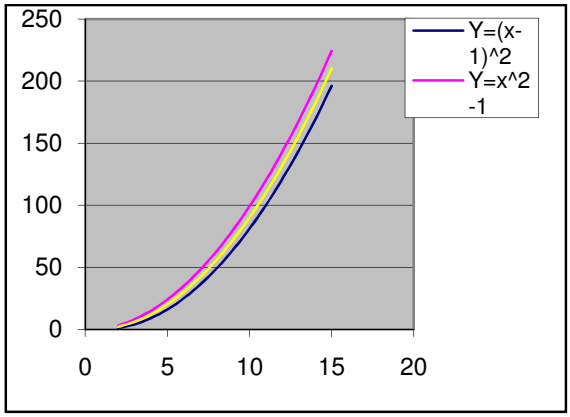


Figure 3.4: Combined graph of following functions

4. BOUNDS OF χ^2 -DIVERGENCE MEASURE:

Proposition: 4.1 Let $P, Q \in \Gamma_n$ be two probability distribution then we have the following relations

$$\chi^2(P,Q) > K(P,Q) \quad (4.1)$$

Proof:-Considering a inequality

$$t^2 - 1 > t \log t, \quad \forall t > 1$$

Putting $t = \frac{p_i}{q_i}$ and applying Csiszar's Φ -divergence measure in above inequality

$$\frac{p_i^2}{q_i^2} - 1 > \frac{p_i}{q_i} \log \frac{p_i}{q_i}$$

$$\sum_{i=1}^{n} q_i \left(\frac{p_i^2}{q_i^2} - 1 \right) > \sum_{i=1}^{n} q_i \left(\frac{p_i}{q_i} \log \frac{p_i}{q_i} \right)$$

$$\sum_{i=1}^{n} \frac{p_i^2}{q_i} - 1 > \sum_{i=1}^{n} p_i \log \frac{p_i}{q_i}$$

$$\chi^2(P,Q) > K(P,Q)$$

where '$K(P,Q)$' is Kullback and Leibler's divergence measure

Proposition: 4.2 Let $P, Q \in \Gamma_n$ be two probability distribution then we have the following relation

$$\chi^2(P,Q) > D(P,Q) \quad (4.2)$$

Proof:-Considering an inequality

$$t^2 - 1 > (t-1)\log\left(\frac{1+t}{2}\right), \ \forall t > 1$$

Putting $t = \frac{p_i}{q_i}$ and applying Csiszar's f -divergence measure in above inequality

$$\frac{p_i^2}{q_i^2} - 1 > \left(\frac{p_i}{q_i} - 1\right)\log\left(\frac{\frac{p_i}{q_i}+1}{2}\right)$$

$$\sum_{i=1}^{n} q_i\left(\frac{p_i^2}{q_i^2} - 1\right) > \sum_{i=1}^{n} q_i\left(\frac{p_i - q_i}{q_i}\right)\log\left(\frac{p_i + q_i}{2q_i}\right)$$

$$\sum_{i=1}^{n} \frac{p_i^2}{q_i} - 1 > \sum_{i=1}^{n} (p_i - q_i)\log\left(\frac{p_i + q_i}{2q_i}\right)$$

$$\chi^2(P,Q) > D(P,Q)$$

Where '$D(P,Q)$' is Relative J-divergence measure

Proposition: 4.3 Let $P, Q \in \Gamma_n$ be two probability distribution then we have the following relation

$$\chi^2(P,Q) > W(P,Q) \quad (4.3)$$

Proof: -Considering a inequality

$$t^2 - 1 > \frac{2t}{1+t}, \ \forall t > 1$$

Putting $t = \frac{p_i}{q_i}$ and using Csiszar's Φ -divergence properties in above inequality

$$\frac{p_i^2}{q_i^2} - 1 > \frac{2\frac{p_i}{q_i}}{1+\frac{p_i}{q_i}}$$

$$\sum_{i=1}^{n} q_i\left(\frac{p_i^2}{q_i^2} - 1\right) > \sum_{i=1}^{n} q_i\left(\frac{2p_i}{p_i + q_i}\right)$$

$$\sum_{i=1}^{n} q_i\left(\frac{p_i^2}{q_i^2} - 1\right) > \sum_{i=1}^{n} \frac{2p_i q_i}{p_i + q_i}$$

$$\sum_{i=1}^{n} \frac{p_i^2}{q_i} - 1 > \sum_{i=1}^{n} \frac{2p_i q_i}{p_i + q_i}$$

$$\chi^2(P,Q) > W(P,Q)$$

Where '$W(P,Q)$, is well known Harmonic mean divergence measure

Proposition: 4.4 Let $P, Q \in \Gamma_n$ be two probability distribution then we have the following relation

$$\chi^2(P,Q) > F(P,Q) \quad (4.4)$$

Proof: Considering a inequality

$$t^2 - 1 > t\log\frac{2t}{1+t}, \ \forall t > 1$$

Putting $t = \frac{p_i}{q_i}$ and applying Csiszar's Φ -divergence measure in above inequality

$$\frac{p_i^2}{q_i^2} - 1 > \frac{p_i}{q_i}\log\frac{2\frac{p_i}{q_i}}{1+\frac{p_i}{q_i}}$$

$$\sum_{i=1}^{n} q_i\left(\frac{p_i^2}{q_i^2} - 1\right) > \sum_{i=1}^{n} q_i\left(\frac{p_i}{q_i}\log\frac{2p_i}{p_i + q_i}\right)$$

$$\sum_{i=1}^{n} q_i\left(\frac{p_i^2}{q_i^2} - 1\right) > \sum_{i=1}^{n} p_i \log\frac{2p_i}{p_i + q_i}$$

$$\sum_{i=1}^{n} \frac{p_i^2}{q_i} - 1 > \sum_{i=1}^{n} p_i \log\frac{2p_i}{p_i + q_i}$$

$$\chi^2(P,Q) > F(P,Q)$$

Where '$F(P,Q)$' is the Relative Jenson-Shannon divergence measure.

Proposition: 4.5 Let $P, Q \in \Gamma_n$ be two probability distribution then we have the following relation

$$\chi^2(P,Q) > J(P,Q) \quad (4.5)$$

Proof: Considering a inequality

$$t^2 - 1 > (t-1)\log t, \ \forall t > 1$$

Putting $t = \frac{p_i}{q_i}$ and applying Csiszar's f -divergence measure

$$\frac{p_i^2}{q_i^2} - 1 > \left(\frac{p_i}{q_i} - 1\right)\log\frac{p_i}{q_i}$$ in above inequality

$$\sum_{i=1}^{n} q_i\left(\frac{p_i^2}{q_i^2} - 1\right) > \sum_{i=1}^{n} q_i\left(\frac{p_i - q_i}{q_i}\right)\log\frac{p_i}{q_i}$$

$$\sum_{i=1}^{n}\frac{p_i^2}{q_i} - 1 > \sum_{i=1}^{n}(p_i - q_i)\log\frac{p_i}{q_i}$$

$$\chi^2(P,Q) > J(P,Q)$$

Where '$J(P,Q)$' is the Jenson divergence measure

Proposition: 4.6 Let $P, Q \in \Gamma_n$ be two probability distribution then we have the following relation

$$\chi^2(P,Q) > B(P,Q) \quad (4.6)$$

Proof: Considering a inequality

$$t^2 - 1 > \sqrt{t}, \ \forall t > 1$$

Putting $t = \frac{p_i}{q_i}$ and applying Csiszar's Φ -divergence measure in above inequality

$$\frac{p_i^2}{q_i^2} - 1 > \sqrt{\frac{p_i}{q_i}}$$

$$\sum_{i=1}^{n} q_i\left(\frac{p_i^2}{q_i^2} - 1\right) > \sum_{i=1}^{n} q_i\sqrt{\frac{p_i}{q_i}}$$

$$\sum_{i=1}^{n}\frac{p_i^2}{q_i} - 1 > \sum_{i=1}^{n}\sqrt{p_i q_i}$$

$$\chi^2(P,Q) > B(P,Q)$$

Where '$B(P,Q)$' be the Bhattacharya Divergence measure

REFERENCES

[1] **Bhattacharya A.,** "Some analogues to amount of information and their uses in statistical estimation" Sankhya 8 (1946) 1-14

[2] **Csiszar I. Information measure,**"A critical servey.Trans.7th prague conf. on info. Th. Statist. Decius. Funct, Random Processes" and 8th European meeting of statist Volume B. Acadmia Prague, 1978, PP-73-86

[3] **Csiszar I.,** "Information-type measures of difference of probability functions and indirect observations" studia Sci.Math.hunger.2 (1961).299-318

[4] **Dragomir S.S., J.Sunde and C.Buse,** "New Inequalities for Jeffreys Divergence measure", Tamusi Oxford Journal of Mathematical Sciences, 16(2) (2000), 295-309

[5] **Hellinger E.,** "NeueBegrundung der Theorie der quadratischen Foemen von unenlichenvielenVeranderlichen" J. Reine Aug. Math., 136 (1909)210-271

[6] **Jeffreys:** "An invariant form for the prior probability in estimation problem", Proc. Roy. Soc. Lon. Ser. A, 186(1946), 453-461

[7] **Kullback S. and R.A Leibler:** "On information and sufficiency". Ann. Nath. Statistics 22(1951), 79-86

[8] **Saraswat R. N.** : Upper and lower bounds on new f-divergence in terms of Relative J-Divergence Measure, Journal of Applied & Computational Mathematics 2(3), 2013, 1-5.

[9] **Sibson R.**, "Information Radius", Z, Wahrs. undverw.geb. (14) (1969), 149-160

[10] **Taneja I.J.,** "New Developments in generalized information measures", Chapter in: Advances in imaging and Electron Physics, Ed. P. W. Hawkes 91 (1995), 37-135.

Mixture of Gompertz Regression Model with Different Frailty Distributions

Richa Sharma[1], David D. Hanagal[2]

[1,2]*Department of Statistics, Panjab University, Chandigarh*

Abstract: **In this article we present a parametric approach to standard mixture model with frailty in the presence of covariates. The problem of analyzing parameters of Gompertz mixture distribution with shared frailty is of interest and the focus of this paper. We propose frailty regression models in Gompertz mixture distributions and assume the distribution of frailty as gamma or inverse Gaussian or positive stable or power variance function distribution. There are some interesting situations like survival times in genetic epidemiology, dental implants of patients and twin births (both monozygotic and dizygotic) where genetic behavior (which is unknown and random) of patients follows a known frailty distribution. These are the situations which motivate to study this particular model. We give estimation procedures and develop test for frailty and the significance of regression parameters. A search of the literature suggests there is currently no work has been done for Gompertz mixture regression model with frailty.**

Keywords: **Frailty, Gamma, Gompertz distribution, Inverse Gaussian, Mixture distribution, Parametric regression, Positive stable, Power variance function, Survival times.**

1. INTRODUCTION

Parametric survival models are regression models in which the distribution of the response is chosen to be consistent with what one would see if the response is time-to failure. In particular, the distribution of the response should have positive support. Examples of such distributions are the exponential, Weibull, log-normal, log-logistic, Gompertz, and the generalized gamma, among others. Here, we consider Gompertz distribution as baseline distribution. The Gompertz distribution is one of the most important growth models. It has many applications in, for example, medical, biological, and actuarial studies. This distribution was first introduced by Gompertz (1825).

Survival models also differ from standard regression models in their ability to account for censoring and truncation. For purposes of interpretability, the distribution of time-to-failure is often times characterized by the hazard function, which is the ratio of the probability density function to one minus the cumulative density function. Hazard functions also provide a convenient means to adjust for regressors, either by assuming that the covariates serve to multiplicatively shift the hazard function (proportional hazards) or by assuming that the covariates serve to accelerate or decelerate the effect of time (accelerated failure time).

A frailty model is a generalization of a survival regression model. In addition to the observed regressors, a frailty model also accounts for the presence of a latent multiplicative effect on the hazard function. This effect, or frailty, is not directly estimated from the data, but instead is assumed to have unit mean and finite variance, which is estimated. In cases where the frailty is greater than one, subjects experience an increased hazard (or risk) of failure and are said to be more frail than their cohorts. In this way, frailty models can provide a useful alternative to a standard survival model when the standard model fails to adequately account for all the variability in the observed failure times.

The notion of frailty provides a convenient way to introduce random effects, association and unobserved heterogeneity into models for survival data. In its simplest form, a frailty model is a random effects model for survival data.

A natural extension of the univariate frailty model would be a multivariate survival model where individuals are allowed to share the same frailty value. The shared frailty model is used with multivariate survival data where the unobserved frailty is shared among groups of individuals, and thus a shared frailty model may be thought of as a random effects model for survival data. In the following, we will restrict our considerations to the bivariate case. Sharing a frailty value also generates dependence between those individuals who share frailties, whereas conditional on the frailty those individuals are independent.

Let a continuous random variable T be the lifetime of an individual and the random variable U be the frailty variable. The conditional hazard function for a given frailty variable $U = u$ at time $t > 0$ is,

$$h(t|u) = uh_0(t)e^{x'\beta} \qquad (1.1)$$

where $h_0(t)$ is a baseline hazard function at time $t > 0$. X is a column vector of covariates and β is a column vector of regression coefficients. The conditional survival function for given frailty at time $t > 0$ is,

$$S(t|u) = e^{-\int_0^t h(y|u)dy} = e^{-uH_0(t)e^{X'\beta}} \quad (1.2)$$

where $H_0(t)$ is cumulative baseline hazard function at time $t > 0$. Integrating over the range of frailty variable U having density $f(u)$, we get marginal survival function as

$$S(t) = \int_0^\infty S(t|u)f(u)du$$
$$= \int_0^\infty e^{-uH_0(t)e^{X'\beta}} f(u)du$$
$$= E\left[e^{-uH_0(t)e^{X'\beta}}\right]$$
$$= L_U(H_0(t)e^{X'\beta}) \quad (1.3)$$

where $L_U(.)$ is a Laplace transformation of the distribution of U.

Once we have survival function at time $t > 0$ of lifetime random variable of an individual one can obtain probability structure and can base their inference on it.

2. GENERAL SHARED FRAILTY MODEL

The shared frailty model is relevant to event time of related individuals, similar organs and repeated measurements for example, if the timing of failure of paired organs like kidneys, lungs, eyes, ears, dental implants etc. are considered. In this model individuals from a group share common covariates. For monozygotic twins, examples are sex and any other genetically based covariates. Both monozygotic and dizygotic twins share date of birth and common pre birth environment. Also for human lifetime, natural disasters and accidents lead to the death of several persons at the same time or in the infectious diseases, two or more family members might visit an infected person and all of them become infected.

The shared gamma frailty model was suggested by Clayton (1978) for the analysis of the correlation between clustered survival times in genetic epidemiology. An advantage is that without covariates its mathematical properties are convenient for estimation (see Oakes, 1982, 1986). However, when adjusting for environment risk factors the analysis of the clustering is more difficult (see Parner, 1998). Until recently, a lack of theory and reliable software had prevented widespread use of this model. In a frailty model, it is absolutely necessary to be able to include explanatory variables. The reason is that the frailty describes the influence of common unknown factors. If some common covariates are included in the model, the variation owing to unknown covariates should be reduced.

Some covariates are indeed common for all members of the group. For monozygotic twins, examples are sex and any other genetically based covariate. Both monozygotic and dizygotic twins share date of birth and common pre-birth environment. By measuring some potentially important covariates, we can examine the influence of the covariates, and we can examine whether they explain the dependence, that is, whether the frailty has no effect (or more correctly, no variation), when the covariate is included in the model. The regression model is derived conditionally on the shared frailty (U).

Suppose n individuals are observed for the study and let a bivariate random variable (T_{i1}, T_{i2}) be the first and second survival times of i^{th} individual ($i = 1,2,3,\ldots n$). Also suppose that there are k observed covariates collected in a vector $X_i = (X_{i1},\ldots..X_{ik})'$ for i^{th} individual where X_{ia} ($a = 1,2,3,\ldots..\ k$) represents the value of a^{th} observed covariate for i^{th} individual. Here, we assume that the first and second survival times for each individual share the same value of the covariates. Let U_i be shared frailty for i^{th} individual. Assuming that the frailties are acting multiplicatively on the baseline hazard function and both the survival times of individuals are conditionally independent for given frailty, the conditional hazard function for i^{th} individual at j^{th} ($i = 1,2$) survival time $t_{ij} > 0$ for given frailty $U_i = u_i$ has the form,

$$h(t_{ij}|u_i, X_i) = u_i h_0(t_{ij}) e^{X_i'\beta} \quad (2.1)$$

where $h_0(t_{ij})$ is baseline hazard at time $t_{ij} > 0$ and β is a column vector of order k of regression coefficients.

The conditional cumulative hazard function for i^{th} individual at j^{th} survival time $t_{ij} > 0$ for given frailty $U_i = u_i$ is,

$$H(t_{ij}|u_i, X_i) = u_i H_0(t_{ij})\eta_i \quad (2.2)$$

where $\eta_i = e^{X_i'\beta}$ and $H_0(t_{ij})$ is cumulative baseline hazard function at time $t_{ij} > 0$.

The conditional survival function for i^{th} individual at j^{th} survival time $t_{ij} > 0$ for given frailty $U_i = u_i$ is,

$$S(t_{ij}|u_i, X_i) = e^{-H(t_{ij}|u_i, X_i)}$$
$$= e^{-u_i H_0(t_{ij})\eta_i} \quad (2.3)$$

Under the assumption of independence, bivariate conditional survival function for given frailty $U_i = u_i$ at time $t_{i1} > 0$ and $t_{i2} > 0$ is,

$$S(t_{i1}, t_{i2}|u_i, X_i) = S(t_{i1}|u_i, X_i)S(t_{i2}|u_i, X_i)$$
$$= e^{-u_i(H_{01}(t_{i1})+H_{02}(t_{i2}))\eta_i} \quad (2.4)$$

Unconditional bivariate survival function at time $t_{i1} > 0$ and $t_{i2} > 0$ can be obtained by integrating over frailty variable U_i having the probability function $f(u_i)$, for i^{th} individual.

$$S(t_{i1}t_{i2}|X_i) = \int_{U_i} S(t_{i1}t_{i2}|u_i)f(u_i)du_i$$

$$= \int_{U_i} e^{-u_i(H_{01}(t_{i1})+H_{02}(t_{i2}))\eta_i} f(u_i)\, du_i$$

$$= L_{U_i}\left[\left(H_{01}(t_{i1}) + H_{02}(t_{i2})\right)\eta_i\right] \quad (2.5)$$

where $L_{U_i}(.)$ is Laplace transform of frailty variable of U_i for i^{th} individual.

Thus, unconditional bivariate survival function for i^{th} individual at time $t_{i1} > 0$ and $t_{i2} > 0$ is,

$$S(t_{i1}t_{i2}|X_i) = L_{U_i}\left[\left(H_{01}(t_{i1}) + H_{02}(t_{i2})\right)\eta_i\right] \quad (2.6)$$

Here onwards we represent $S(t_{i1}t_{i2}|X_i)$ as $S(t_{i1}t_{i2})$.

Once we have unconditional survival function of bivariate random variable (T_{i1}, T_{i2}) we can obtain likelihood function and estimate the parameters of the model.

3. FRAILTY REGRESSION MODEL IN MIXTURE DISTRIBUTION

The mixture distribution in terms of survival function is

$$S(t) = \phi S_1(t) + (1-\phi)S_2(t) = \phi exp[-\lambda_1\gamma_1^{-1}(e^{\gamma_1 t} - 1)] + (1-\phi)exp[-\lambda_2\gamma_2^{-1}(e^{\gamma_2 t} - 1)] \quad (3.1)$$

There are two ways of obtaining frailty models. The first one is

$$S_M(t|U) = \phi S_1(t|U) + (1-\phi)S_2(t|U) = \phi exp[-u\lambda_1\gamma_1^{-1}(e^{\gamma_1 t} - 1)] + (1-\phi)exp[-u\lambda_2\gamma_2^{-1}(e^{\gamma_2 t} - 1)] \quad (3.2)$$

This is called mixture of frailty models or mixture frailty. The second one is

$$S_F(t|U) = exp\left[ulog[\phi exp\{-\lambda_1\gamma_1^{-1}(e^{\gamma_1 t} - 1)\} + (1-\phi)\exp\{-\lambda_2\gamma_2^{-1}(e^{\gamma_2 t} - 1)\}]\right] \quad (3.3)$$

This is called frailty of the mixture distributions in order to make the distinction between the two types. The same technique can be generalized to mixture of more than two distributions. When we integrate with respect to frailty (U), we get survival function of mixture distribution in terms of frailty parameter. The scale parameters λ_1 and λ_2 in the Gompertz mixtures can be expressed in terms of regression parameters in the following way:

$$\lambda_1 = \exp(\beta' X)$$
$$\lambda_2 = \exp(\beta' X) \quad (3.4)$$

where $\beta = (\beta_0, \beta_1, \beta_2, \ldots\ldots, \beta_p)'$ and $X = (1, X_1, \ldots\ldots X_p)'$. If we want to make a distinction between the two scale parameters, one can express λ_1 and λ_2 as

$$\lambda_1 = \theta_1\exp(\beta' X)$$
$$\lambda_2 = \theta_2\exp(\beta' X) \quad (3.5)$$

After substituting λ_1 and λ_2 in (3.2) and (3.3), we get frailty regression models in Gompertz mixtures.

4. GAMMA FRAILTY MODEL

We consider frailty distribution as gamma distribution because the gamma distribution fits well to failure data from a computational and analytical point of view and it is easy to derive the closed form expression of survival and hazard function. Gamma distributions have been used for many years to generate mixtures in exponential and Poisson models. The gamma distribution (we use notation Gamma (α, κ) for the two parameter distribution with shape parameter α and scale parameter κ) is one of the most commonly used distributions to model variables that are necessarily positive.

Let a continuous random variable U follows gamma distribution with shape parameter α and scale parameter κ then density function of U is,

$$f_U(u) = \frac{\kappa^\alpha u^{\alpha-1}\exp(-\kappa u)}{\Gamma(\alpha)}; \quad (4.1)$$

where $\boldsymbol{u} > 0, \alpha > 0, \kappa > 0$

To make the model identifiable, although we consider two parameter gamma distribution, we restrict that expectation of the frailty equal to 1, variance be finite and scale parameter = shape parameter, so that only one parameter needs to be estimated.

Thus the mathematical convenient choice for the distribution of the frailty U is the one parameter ($\alpha = \kappa = \theta^{-1}$) gamma distribution i.e.

$$U \sim \text{Gamma}(\theta^{-1}, \theta^{-1}) \quad (4.2)$$

with the corresponding density function

$$f_U(u) = \frac{u^{\theta^{-1}-1}\exp(-u/\theta)}{\theta^{\frac{1}{\theta}}\Gamma(1/\theta)}\ ;\ u > 0, \theta > 0 \quad (4.3)$$

The Laplace transform of gamma distribution and unconditional survivor function are respectively as follows.

$$L(s) = (1 + s\theta)^{-1/\theta} \quad (4.4)$$

The unconditional bivariate survival function expressed as the Laplace transform of the frailty distribution, evaluated at the cumulative baseline hazard for i^{th} individual at time $t_{i1} > 0$ *and* $t_{i2} > 0$ is,

$$S_\theta(t_1, t_2) = [1 + \theta\{H_1(t_1) + H_2(t_2)\}]^{-1/\theta} \quad (4.5)$$

where $H_i(t_i)$ is cumulative baseline hazard functions of lifetime random variables T_i.

4.1 Gamma Frailty in Gompertz Mixture

Assuming the distribution of frailty variable, *U* as gamma and and integrating Eq. (3.2) over U, we get Gompertz mixture model with gamma mixture frailty, given by

$$S_M(t) = \phi[1 + \theta\lambda_1\gamma_1^{-1}(e^{\gamma_1 t} - 1)]^{-1/\theta} + (1 - \phi)[1 + \theta\lambda_2\gamma_2^{-1}(e^{\gamma_2 t} - 1)]^{-1/\theta} \quad (4.6)$$

The density function corresponding to $S_M(t)$ is

$$f_M(t) = \phi\lambda_1 e^{\gamma_1 t} {S_{M_1}}^{(1+\theta)} + (1 - \phi)\lambda_2 e^{\gamma_2 t} {S_{M_2}}^{(1+\theta)} \quad (4.7)$$

where $S_{M_1}(t) = [1 + \theta\lambda_1\gamma_1^{-1}(e^{\gamma_1 t} - 1)]^{-1/\theta}$

and $S_{M_2}(t) = [1 + \theta\lambda_2\gamma_2^{-1}(e^{\gamma_2 t} - 1)]^{-1/\theta}$ (4.8)

Assuming the distribution of frailty variable, *U* as gamma and and integrating Eq. (3.3) over U, we get Gompertz mixture model with gamma frailty, given by

$$S_F(t) = [1 - \theta\log[\phi exp\{-\lambda_1\gamma_1^{-1}(e^{\gamma_1 t} - 1)\} + (1 - \phi)\exp\{-\lambda_2\gamma_2^{-1}(e^{\gamma_2 t} - 1)\}]]^{-1/\theta} \quad (4.9)$$

The pdf corresponding to above survival function $S_F(t)$ is

$$f_F(t) = \frac{\phi\lambda_1 e^{\gamma_1 t} S_1 + (1-\phi)\lambda_2 e^{\gamma_2 t} S_2}{\phi S_1 + (1-\phi) S_2} S_F^{(1+\theta)} \quad (4.10)$$

where $S_1(t) = \exp[-\lambda_1\gamma_1^{-1}(e^{\gamma_1 t} - 1)]$

$$S_2(t) = \exp[-\lambda_2\gamma_2^{-1}(e^{\gamma_2 t} - 1)] \quad (4.11)$$

Here λ_1 and λ_2 are functions of regression parameters.

5. INVERSE GAUSSIAN FRAILTY MODEL

In shared frailty models gamma distribution is the most commonly used frailty distribution because of its mathematical convenience. However, it has drawbacks (see Kheiri et al. (2007)), for example, it may weaken the effect of covariates. As an alternative to the gamma distribution, the inverse Gaussian (inverse normal) distribution was introduced by Hougaard (1984) and has been used, for example, by Manton et al. (1986), Klein et al. (1992), Keiding et al. (1997), Price and Manatunga (2001), Kheiri et al. (2007) and Duchateau and Janssen (2008).

Hougaard (1984) remarked that survival models with gamma and inverse Gaussian frailties behave very differently, noting that the relative frailty distribution among survivors is independent of age for the gamma, but becomes more homogeneous with time for the inverse Gaussian. The inverse Gaussian distribution has many similarities to standard Gaussian distribution. Furthermore, it provides much flexibility in modeling, when early occurrences of failures are dominant in a lifetime distribution and its failure rate is expected to be non-monotonic. In such situations the inverse Gaussian distribution might provide a suitable choice for the lifetime model. Also inverse Gaussian is almost an increasing failure rate distribution when it is slightly skewed and hence is also applicable to describe lifetime distribution which is not dominated by early failures.

Similar to the gamma frailty model, simple closed-form expressions exist for the unconditional survival and hazard functions, this makes the model attractive. The inverse Gaussian distribution has unimodal density and is the member of exponential family. While its shape resembles the other skewed density functions, such as log-normal and gamma. These properties of inverse Gaussian distribution motivate us to use inverse Gaussian as frailty distribution.

Let a continuous random variable *U* follows inverse Gaussian distribution with parameters μ and α then density function of *U* is,

$$f(u) = \begin{cases} \left[\frac{\alpha}{2\pi}\right]^{\frac{1}{2}} u^{-\frac{3}{2}} e^{-\frac{\alpha(u-\mu)^2}{2u\mu^2}} & ; u > 0, \mu > 0, \alpha > 0 \\ 0 & ; otherwise \end{cases} \quad (5.1)$$

and Laplace transform is,

$$L_U(s) = exp\left[\frac{\alpha}{\mu} - \left(\frac{\alpha^2}{\mu^2} + 2\alpha s\right)^{1/2}\right] \quad (5.2)$$

with expectation and variance

$$E(U) = \mu, Var(U) = \frac{\mu^3}{\alpha}$$

For identifiability, we assume *U* has expected value equal to one i.e. μ = 1.

Now the distribution of the frailty U is the one parameter ($\alpha = \theta^{-1}$) inverse Gaussian distribution i.e.

$$U \sim IG(1, \theta^{-1}) \tag{5.3}$$

Under the restriction, density function and Laplace transformation of inverse Gaussian distribution result in the following simplified form,

$$f(z) = \begin{cases} \left[\frac{1}{2\pi\theta}\right]^{\frac{1}{2}} u^{-3/2} e^{-\frac{(u-1)^2}{2u\theta}} ; u > 0, \theta > 0 \\ 0 \ ; otherwise \end{cases} \tag{5.4}$$

and

$$L_U(s) = exp\left[\frac{1-(1+2\theta s)^{1/2}}{\theta}\right] \tag{5.5}$$

with variance of U is $\theta = 1/\alpha$. Note that there is heterogeneity if $\theta > 0$. The unconditional bivariate survival function expressed as the Laplace transform of the frailty distribution, evaluated at the cumulative baseline hazard for i^{th} individual at time $t_{i1} > 0$ *and* $t_{i2} > 0$ is,

$$S_\theta(t_1, t_2) = exp\left[\frac{1-(1+2\theta\{H_1(t_1)+H_2(t_2)\})^{1/2}}{\theta}\right] \tag{5.6}$$

where $H_i(t_i)$ is cumulative baseline hazard functions of lifetime random variables T_i.

5.1 Inverse Gaussian Frailty in Gompertz Mixture

Assuming the distribution of frailty variable, U as inverse Gaussian and integrating Eq. (3.2) over U, we get Gompertz mixture model with inverse Gaussian mixture frailty, given by

$$S_M(t) = \phi exp\left[\theta^{-1}\left\{1 - \left(1 + 2\theta\lambda_1\gamma_1^{-1}(e^{\gamma_1 t} - 1)\right)^{\frac{1}{2}}\right\}\right] + (1 - \phi)exp\left[\theta^{-1}\left\{1 - (1 + 2\theta\lambda_2\gamma_2^{-1}(e^{\gamma_2 t} - 1))^{1/2}\right\}\right] \tag{5.7}$$

Then pdf corresponding to above survival function $S_M(t)$ is

$$f_M(t) = \frac{\phi\lambda_1 e^{\gamma_1 t} S_{M_1}}{\left[1+2\theta\lambda_1\gamma_1^{-1}(e^{\gamma_1 t}-1)\right]^{\frac{1}{2}}} + \frac{(1-\phi)\lambda_2 e^{\gamma_2 t} S_{M_2}}{\left[(1+2\theta\lambda_2\gamma_2^{-1}(e^{\gamma_2 t}-1)\right]^{1/2}} \tag{5.8}$$

where

$$S_{M_1}(t) = exp\left[\theta^{-1}\left\{1 - \left(1 + 2\theta\lambda_1\gamma_1^{-1}(e^{\gamma_1 t} - 1)\right)^{\frac{1}{2}}\right\}\right]$$

and

$$S_{M_2}(t) == exp\left[\theta^{-1}\left\{1 - (1 + 2\theta\lambda_2\gamma_2^{-1}(e^{\gamma_2 t} - 1))^{\frac{1}{2}}\right\}\right] \tag{5.9}$$

Assuming the distribution of frailty variable, U as inverse Gaussian and integrating Eq. (3.3) over U, we get Gompertz mixture model with inverse Gaussian frailty, given by

$$S_F(t) = exp\left[\theta^{-1}\left[1 - \{1 - 2\theta\log\left[\phi exp\{-\lambda_1\gamma_1^{-1}(e^{\gamma_1 t} - 1)\} + (1 - \phi)\exp\{-\lambda_2\gamma_2^{-1}(e^{\gamma_2 t} - 1)\}\right]\right\}^{1/2}\right]\right] \tag{5.10}$$

The pdf corresponding to above survival function $S_F(t)$ is

$$f_F(t) = S_F[1 - 2\theta\log(\phi S_1 + (1 - \phi)S_2)]^{-1/2} * \frac{\phi\lambda_1 e^{\gamma_1 t} S_1 + (1 - \phi)\lambda_2 e^{\gamma_2 t} S_2}{\phi S_1 + (1 - \phi)S_2} \tag{5.11}$$

where $S_1(t) = \exp\left[-\lambda_1\gamma_1^{-1}(e^{\gamma_1 t} - 1)\right]$

$$S_2(t) = \exp\left[-\lambda_2\gamma_2^{-1}(e^{\gamma_2 t} - 1)\right] \tag{5.12}$$

Here λ_1 and λ_2 are functions of regression parameters.

6. POSITIVE STABLE FRAILTY MODEL

In practice, the gamma frailty specification may not fit well (Shih, 1998; Glidden, 1999; Fan et al., 2000). The positive stable model (Hougaard, 1986) is a useful alternative, in part because it has the attractive feature that predictive hazard ratio decreases to 1 over time (Oakes, 1989). The property is observed in familial associations of the ages of onset of diseases with etiologic heterogeneity, where genetic cases occur early and long-term survivors are weakly correlated. The gamma model has predictive hazard ratios which are time invariant and may not be suitable for these patterns of failures (Fine et al., 2003). Although this replacement helps us to avoid problems induced by the identifiability of the univariate gamma-frailty model i.e. the univariate positive stable-frailty model with observed covariates is non-identifiable.

The positive stable model has the advantage that it fits proportional hazards which means that if the conditional model has proportional hazards, so does the marginal distribution. This is an advantage, when considering the model as a random effects model.

The pdf of positive stable distribution with two parameters α and δ is given by

$$f(u) = \frac{-1}{\pi u}\sum_{n=1}^{\infty}\frac{\Gamma(n\alpha + 1)}{\mathrm{n!}}\left(-u^{-\alpha}\frac{\delta}{\alpha}\right)^n \sin(\alpha n\pi); \quad u > 0, 0 < \alpha < 1 \tag{6.1}$$

with Laplace transform

$$L_U(s) = E[e^{-su}] = exp\left[\frac{-\delta s^\alpha}{\alpha}\right] \tag{6.2}$$

(see Hougaard, 2000, p. 503).

For α=δ, the pdf of positive stable distribution is given by

$$f(u) = \frac{-1}{\pi u}\sum_{n=1}^{\infty}\frac{\Gamma(n\alpha+1)}{\mathrm{n!}}(-u)^{-\alpha n}\sin(\alpha n\pi); \tag{6.3}$$

Thus,

$$f(u) = \frac{-1}{\pi}\sum_{n=1}^{\infty}\frac{\Gamma(n\alpha+1)}{\mathrm{n!}}(-u)^{-(\alpha n+1)}\sin(\alpha n\pi);$$

$$u > 0, 0 < \alpha < 1 \tag{6.4}$$

with Laplace transform

$$L_U(s) = E[e^{-su}] = exp[-s^{\alpha}] \tag{6.5}$$

The unconditional bivariate survival function expressed as the Laplace transform of the frailty distribution, evaluated at the cumulative baseline hazard for i^{th} individual at time $t_{i1} > 0$ *and* $t_{i2} > 0$ is,

$$S_{\alpha}(t_1, t_2) = exp[-\{H_1(t_1) + H_2(t_2)\}^{\alpha}] \tag{6.6}$$

where $H_i(t_i)$ is cumulative baseline hazard functions of lifetime random variables T_i.

6.1 Positive Stable Frailty in Gompertz Mixture

Assuming the distribution of frailty variable, *U* as positive stable and integrating Eq. (3.2) over *U*, we get Gompertz mixture model with positive stable mixture frailty, given by

$$S_M(t) = \phi exp[-\{\lambda_1\gamma_1^{-1}(e^{\gamma_1 t} - 1)\}^{\alpha}] +$$

$$(1-\phi)exp[-\{\lambda_2\gamma_2^{-1}(e^{\gamma_2 t} - 1)\}^{\alpha}] \tag{6.7}$$

Then pdf corresponding to above survival function $S_M(t)$ is

$$f_M(t) = \alpha\big[\phi\lambda_1^{\alpha}\gamma_1^{1-\alpha}e^{\gamma_1 t}(e^{\gamma_1 t}-1)^{\alpha-1}S_{M_1} + (1-\phi)\lambda_2^{\alpha}\gamma_2^{1-\alpha}e^{\gamma_2 t}(e^{\gamma_2 t}-1)^{\alpha-1}S_{M_2}\big] \tag{6.8}$$

where $S_{M_1}(t) = \exp[-\{\lambda_1\gamma_1^{-1}(e^{\gamma_1 t}-1)\}^{\alpha}]$

and $S_{M_2}(t) = \exp[-\{\lambda_2\gamma_2^{-1}(e^{\gamma_2 t}-1)\}^{\alpha}]$ (6.9)

Assuming the distribution of frailty variable, *U* as positive stable and integrating Eq. (3.3) over *U*, we get Gompertz mixture model with positive stable frailty, given by

$$S_F(t) = exp[-[-log\{\phi exp\langle-\lambda_1\gamma_1^{-1}(e^{\gamma_1 t}-1)\rangle + (1-\phi)exp\langle-\lambda_2\gamma_2^{-1}(e^{\gamma_2 t}-1)\rangle\}]^{\alpha}] \tag{6.10}$$

The pdf corresponding to above survival function is

$$f_F(t) = \frac{\alpha[-\log(\phi S_1+(1-\phi)S_2)]^{\alpha-1}[\phi\lambda_1 e^{\gamma_1 t}S_1+(1-\phi)\lambda_2 e^{\gamma_2 t}S_2]}{\phi S_1+(1-\phi)S_2}S_F \tag{6.11}$$

where $S_1(t) = \exp[-\lambda_1\gamma_1^{-1}(e^{\gamma_1 t}-1)]$

$$and\ S_2(t) = \exp[-\lambda_2\gamma_2^{-1}(e^{\gamma_2 t}-1)] \tag{6.12}$$

7. POWER VARIANCE FRAILTY MODEL

This distribution is a three-parameter family uniting gamma and positive stable distributions. The distribution is denoted as PVF(α,δ,θ).

For α = 0, the gamma distributions are obtained with same parametrization.

For α = 1/2, the inverse Gaussian distributions are obtained.

For α = −1, the non-central gamma distribution of shape parameter zero is obtained.

For α = 1, a degenerate distribution is obtained.

For α = 0, the positive stable distributions are obtained.

The parameter set is $(\alpha \le 1, \delta > 0)$, with $(\theta \ge 0\ for\ \alpha > 0)$, and $(\theta > 0\ for\ \alpha \le 0)$. The distribution is concentrated on the positive numbers for $\alpha \ge 0$, and is positive or zero for $\alpha < 0$. In the case $\alpha > 0$, the pdf of PVF is given by (see Hougaard, 2000, p. 504)

$$f(u) = exp\left\{-\theta u + \delta\frac{\theta^{\alpha}}{\alpha}\right\}\frac{1}{\pi}\sum_{n=1}^{\infty}\frac{\Gamma(n+1)}{\mathrm{n!}}$$

$$\left(-\frac{1}{u}\right)^{(\alpha n+1)}\sin(\alpha n\pi);\ u > 0 \tag{7.1}$$

If α<0, the Γ-term in the density is not necessarily defined, and therefore we can use the alternative

expression for pdf of PVF as (see Hougaard, 2000, p. 504)

$$f(u) = exp\left\{-\theta u + \delta\frac{\theta^{\alpha}}{\alpha}\right\}\frac{1}{u}\sum_{n=1}^{\infty}\frac{\left(-\left(\delta\frac{u^{\alpha}}{\alpha}\right)\right)^{n}}{\mathrm{n!}\Gamma(-n\alpha)} \tag{7.2}$$

This expression is valid for all α values, except 0 and 1, with the convention that when the Γ-function in the denominator is undefined (which happens when $n\alpha$ is a positive integer), the whole term in the sum is zero. For $\alpha < 0$, there is

probability $exp(\delta\frac{\theta^{\alpha}}{\alpha})$ of the random variable being zero. For $\alpha \geq 0$, the distribution is unimodal.

If U_1 and U_2 are independent, and U_i follows PVF(α,δ_i,θ); i =1, 2 the distribution of $U_1 + U_2$ is PVF($\alpha,\delta_1 ,\delta_2,\theta$).

So, PVF distribution is infinitely divisible. When $\theta > 0$, all (positive) moments exist, and the mean of Y is $\delta\theta^{\alpha-1}$and its variance is $\delta(1-\alpha)\theta^{\alpha-2}$.

The Laplace transform of PVF distribution is

$$L_U(s) = exp\left[-\frac{\delta\{(\theta+s)^{\alpha}-\theta^{\alpha}\}}{\alpha}\right] \quad (7.3)$$

The unconditional bivariate survival function expressed as the Laplace transform of the frailty distribution, evaluated at the cumulative baseline hazard for i^{th} individual at time $t_{i1} > 0$ *and* $t_{i2} > 0$ is,

$$S_{\alpha,\delta,\theta}(t_1,t_2) = exp\left[\frac{\delta\theta^{\alpha}}{\alpha}\right] exp\left[-\frac{\delta\{(\theta+H_1(t_1)+H_2(t_2))^{\alpha}\}}{\alpha}\right] \quad (7.4)$$

where $H_i(t_i)$ is cumulative baseline hazard functions of lifetime random variables T_i.

7.1 Power Variance Frailty in Gompertz Mixture

Assuming the distribution of frailty variable, U as PVF and integrating Eq. (3.2) over U, we get Gompertz mixture model with PVF mixture frailty, given by

$$S_M(t) = \mu\begin{bmatrix} \phi exp\left[-\frac{\delta\{\theta+\lambda_1\gamma_1^{-1}(e^{\gamma_1 t}-1)\}^{\alpha}}{\alpha}\right] + \\ (1-\phi)exp\left[\frac{-\delta\{\theta+\lambda_2\gamma_2^{-1}(e^{\gamma_2 t}-1)\}^{\alpha}}{\alpha}\right] \end{bmatrix} \quad (7.5)$$

where $\mu = exp\left(\delta\frac{\theta^{\alpha}}{\alpha}\right)$

Then pdf corresponding to above survival function $S_M(t)$ is

$$f_M(t) = \mu\left[\phi\delta\{\theta+\lambda_1\gamma_1^{-1}(e^{\gamma_1 t}-1)\}^{\alpha-1}\lambda_1 e^{\gamma_1 t}S_{M_1} + (1-\phi)\delta\{\theta+\lambda_2\gamma_2^{-1}(e^{\gamma_2 t}-1)\}^{\alpha-1}\lambda_2 e^{\gamma_2 t}S_{M_2}\right] \quad (7.6)$$

where $S_{M_1}(t) = exp\left[-\frac{\delta\{\theta+\lambda_1\gamma_1^{-1}(e^{\gamma_1 t}-1)\}^{\alpha}}{\alpha}\right]$

and $S_{M_2}(t) = exp\left[-\frac{\delta\{\theta+\lambda_2\gamma_2^{-1}(e^{\gamma_2 t}-1)\}^{\alpha}}{\alpha}\right]$ (7.7)

Assuming the distribution of frailty variable, U as PVF and integrating Eq. (3.3) over U, we get Gompertz mixture model with PVF frailty, given by

$$S_F(t) = \mu exp\left[\frac{-\delta}{\alpha}\{\theta - log[\phi exp\{-\lambda_1\gamma_1^{-1}(e^{\gamma_1 t}-1)\} + (1-\phi)exp\{-\lambda_2\gamma_2^{-1}(e^{\gamma_2 t}-1)\}]\}^{\alpha}\right] \quad (7.8)$$

The pdf corresponding to above survival function is

$$f_F(t) = \frac{\delta\mu[\theta-\log\langle\phi S_1+(1-\phi)S_2\rangle]^{\alpha-1}[\phi\lambda_1 e^{\gamma_1 t}S_1+(1-\phi)\lambda_2 e^{\gamma_2 t}S_2]}{\phi S_1+(1-\phi)S_2}S_F \quad (7.9)$$

where $S_1(t) = \exp[-\lambda_1\gamma_1^{-1}(e^{\gamma_1 t}-1)]$

$and\ S_2(t) = \exp[-\lambda_2\gamma_2^{-1}(e^{\gamma_2 t}-1)]$ (7.10)

8. ESTIMATION OF THE PARAMETERS

Some of the lifetimes may be censored, because it is not possible to wait until failure of all individuals in the sample. We consider the censoring time (W) being of the right censoring type which is independent of lifetime (T). We first give estimation procedure for the Gompertz mixture frailty model for different frailty distributions, where a similar estimation procedure holds for frailty model of mixtures. The likelihood based on a sample of size n is given by:

$$L = (\prod_{i=1}^{r} f_M(t_i))(\prod_{i=1}^{n-r} S_M(\omega_i)) \quad (8.1)$$

where r is the number of failed individuals and (n-r) the number of censored individuals in the sample of size n.

We can then maximize the marginal log-likelihood with respect to $\underline{\zeta} = (\gamma_1,\gamma_2,\eta_1,\eta_2,\theta,\beta,\phi)'$ where $\beta = (\beta_0,\beta_1,\beta_2,\ldots\ldots,\beta_p)'$. The likelihood equations can be obtained by taking first order partial derivatives of the log-likelihood and equating them with zero. The likelihood equations are not easy to solve. One may obtain maximum likelihood estimates (MLEs) by applying the Newton-Raphson procedure. The second order partial derivatives of the log-likelihood can also be obtained. The observed information matrix, I is of order (p + 7) x (p + 7) with appropriate second order partial derivatives as follows:

$$I = \begin{bmatrix} \frac{\partial^2 logL}{\partial\gamma_1^2} & \frac{\partial^2 logL}{\partial\gamma_1\partial\gamma_2} & \frac{\partial^2 logL}{\partial\gamma_1\partial\eta_1} & \frac{\partial^2 logL}{\partial\gamma_1\partial\eta_2} & \frac{\partial^2 logL}{\partial\gamma_1\partial\theta} & \frac{\partial^2 logL}{\partial\gamma_1\partial\beta_0} & \frac{\partial^2 logL}{\partial\gamma_1\partial\beta_p} \\ \frac{\partial^2 logL}{\partial\gamma_1\partial\gamma_2} & \frac{\partial^2 logL}{\partial\gamma_2^2} & \frac{\partial^2 logL}{\partial\gamma_2\partial\eta_1} & \frac{\partial^2 logL}{\partial\gamma_2\partial\eta_2} & \frac{\partial^2 logL}{\partial\gamma_2\partial\theta} & \frac{\partial^2 logL}{\partial\gamma_2\partial\beta_0} & \cdots\cdots \frac{\partial^2 logL}{\partial\gamma_2\partial\beta_p} \\ \frac{\partial^2 logL}{\partial\gamma_1\partial\eta_1} & \frac{\partial^2 logL}{\partial\gamma_2\partial\eta_1} & \frac{\partial^2 logL}{\partial\eta_1^2} & \frac{\partial^2 logL}{\partial\eta_1\partial\eta_2} & \frac{\partial^2 logL}{\partial\eta_1\partial\theta} & \frac{\partial^2 logL}{\partial\eta_1\partial\beta_0} & \frac{\partial^2 logL}{\partial\eta_1\partial\beta_p} \\ \frac{\partial^2 logL}{\partial\gamma_1\partial\eta_2} & \frac{\partial^2 logL}{\partial\gamma_2\partial\eta_2} & \frac{\partial^2 logL}{\partial\eta_1\partial\eta_2} & \frac{\partial^2 logL}{\partial\eta_2^2} & \frac{\partial^2 logL}{\partial\eta_2\partial\theta} & \frac{\partial^2 logL}{\partial\eta_2\partial\beta_0} & \frac{\partial^2 logL}{\partial\eta_2\partial\beta_p} \\ \frac{\partial^2 logL}{\partial\gamma_1\partial\theta} & \frac{\partial^2 logL}{\partial\gamma_2\partial\theta} & \frac{\partial^2 logL}{\partial\eta_1\partial\theta} & \frac{\partial^2 logL}{\partial\eta_2\partial\theta} & \frac{\partial^2 logL}{\partial\theta^2} & \frac{\partial^2 logL}{\partial\theta\partial\beta_0} & \cdots\cdots \frac{\partial^2 logL}{\partial\theta\partial\beta_p} \\ \frac{\partial^2 logL}{\partial\gamma_1\partial\beta_0} & \frac{\partial^2 logL}{\partial\gamma_2\partial\beta_0} & \frac{\partial^2 logL}{\partial\eta_1\partial\beta_0} & \frac{\partial^2 logL}{\partial\eta_2\partial\beta_0} & \frac{\partial^2 logL}{\partial\theta\partial\beta_0} & \frac{\partial^2 logL}{\partial\beta_0^2} & \frac{\partial^2 logL}{\partial\beta_0\partial\beta_p} \\ & & \vdots & \vdots & \vdots & \cdots\cdots & \vdots \\ \frac{\partial^2 logL}{\partial\gamma_1\partial\beta_p} & \frac{\partial^2 logL}{\partial\gamma_2\partial\beta_p} & \frac{\partial^2 logL}{\partial\eta_1\partial\beta_p} & \frac{\partial^2 logL}{\partial\eta_2\partial\beta_p} & \frac{\partial^2 logL}{\partial\theta\partial\beta_p} & \frac{\partial^2 logL}{\partial\beta_0\partial\beta_p} & \cdots\cdots \frac{\partial^2 logL}{\partial\beta_p^2} \end{bmatrix} \quad (8.2)$$

The inverse of the observed Fisher information matrix (8.2) is the observed variance-covariance matrix (Σ=I^{-1}) of the MLE

$\underline{\hat{\zeta}} = (\hat{\gamma}_1, \hat{\gamma}_2, \hat{\eta}_1, \hat{\eta}_2, \hat{\theta}, \hat{\beta}, \hat{\phi})'$ of the parameter $\underline{\zeta} = (\gamma_1, \gamma_2, \eta_1, \eta_2, \theta, \beta, \phi)'$ where $\beta = (\beta_0, \beta_1, \beta_2, \ldots\ldots, \beta_p)'$.

Thus, $\sqrt{n}(\hat{\beta} - \beta)$ has an asymptotic multivariate normal distribution with mean vector zero and variance-covariance matrix Σ_{11}, where Σ_{11} is (p+1) x (p+1) variance-covariance matrix of $\beta = (\beta_0, \beta_1, \beta_2, \ldots\ldots, \beta_p)'$.

9. LARGE SAMPLE TESTS

We present test procedure based on large sample which is asymptotically normally distributed.

9.1 Test for Regression Coefficients

The hypotheses about β can be frequently put in the form $H_0 : \beta_{11} = \beta_{11}^0$ with β partitioned as $\beta = (\beta_{11}, \beta_{22})'$ where β_{11} is of dimension k x 1, (k < p + 1) and β_{11}^0 consists of fixed and known values of the corresponding regression parameters of β_{11}. To test H_0 against the alternative that is $H_1 : \beta_{11} \neq \beta_{11}^0$ one can use

$$\Lambda_1 = (\hat{\beta}_{11} - \beta_{11}^0)' \hat{\Sigma}_{22}^{-1} (\hat{\beta}_{11} - \beta_{11}^0) \qquad (9.1)$$

where $\hat{\Sigma}_{22}$ is k x k asymptotic observed variance-covariance matrix of $\hat{\beta}_{11}$. Under H_0, Λ_1 is asymptotically chi-square with *k* d.f.

If $\Lambda_1 > \chi^2_{k,1-\alpha}$, the corresponding regression coefficients are significant at the level of significance α, where $\chi^2_{k,1-\alpha}$ is the chi-square variate with *k* d.f. at level of significance α.

When $\beta_{11}^0 = 0$, it will lead to the test for regression coefficients equal to zero.

REFERENCES

[1] Clayton, D.G., "A model for association in bivariate life tables and its applications to epidemiological studies of familial tendency in chronic disease incidence", *Biometrika*, 65, 1978, pp. 141-51.

[2] Duchateau, L. and Janssen, P., *The Frailty Model*, Springer, Berlin, 2008.

[3] Fan, J.J., Hsu, L. and Prentice, R.L., "Dependence Estimation over a Finite Bivariate Failure Region", *Lifetime Data Analysis*, 6, 2000, pp. 343-55.

[4] Fine, J.P., Glidden, D.V. and Lee, K.E., "A Simple Estimator for a Shared Frailty Regression Model", *J. R. Statist. Soc. B*, 65, 2003, pp. 317-29.

[5] Glidden, D.V., "Checking the adequacy of the Gamma Frailty Model for Multivariate Failure Times", *Biometrika*, 86, 1999, pp. 381-94.

[6] Gompertz, B., "On the Nature of the Function Expressive of the Law of Human Mortality, and on a New Mode of Determining the Value of Life Contingencies", *Philosophical Transactions of the Royal Society of London*, 115, 1825, pp. 513-585.

[7] Hougaard, P., "Life Table Methods for Heterogeneous Populations", *Biometrika,* 71, 1984, pp. 75-83.

[8] Hougaard, P., "A Class of Multivariate Failure Time Distributions", *Biometrika*, 73, 1986, pp. 671-78.

[9] Hougaard, P., *Analysis of Multivariate Survival Data*, Springer-Verlag New York Inc, 2000.

[10] Keiding, N., Andersen, P., and Klein, J., "The Role of Frailty Models and Accelerated Failure Time Models in Describing Heterogeneity due to Omitted Covariates", *Statistics in Medicine*, 16, 1997, pp. 215-224.

[11] Kheiri, S., Kimber, A., and Meshkani, M.R., "Bayesian Analysis of an Inverse Gaussian Correlated Frailty Model", *Computational Statistics and Data analysis*, 51, 2007, pp. 5317-5326.

[12] Klein, J.P., Moeschberger, M., Li, Y.H., and Wang, S.T., "Estimating Random Effects in the Framingham Heart Study", *In: Survival Analysis: State of the Art*, 1992, pp. 99-112.

[13] Manton, K., Stallard, E., and Vaupel, J., "Alternative Models for Heterogeneity of Mortality Risks among the Aged", *Journal of the American Statistical Association*, 81, 1986, pp. 635-644.

[14] Oakes, D., "A Model for Association in Bivariate Survival Data", *J. R. Statist. Soc. B,* 44, 1982, pp. 414-22.

[15] Oakes, D., "Semiparametric Inference in Bivariate Survival Data", *Biometrika*, 73, 1986, pp. 353-61.

[16] Oakes, D., "Bivariate Survival Models Induced by Frailties", *J. Amer. Statist. Assoc.,* 84, 1989, pp. 487-93.

[17] Parner, E., "Asymptotic Theory for Correlated Gamma Frailty Model", *Annals of Statistics,* 26, 1998, pp. 183-214.

[18] Price, D.L. and Manatunga, A.K., "Modeling Survival Data with a Cured Fraction using Frailty Models", *Statistics in Medicine*, 20, 2001, pp. 1515-1527.

[19] Shih, J.H., "A Goodness-of-Fit Test for Association in a Bivariate Survival Model", *Biometrika*, 85, 1998, pp. 189-200.

On Simultaneous Variation of Some Cosmological Parameters

S K J Pacif[1], Abdussattar[2]

[1]*Department of Mathematics, Manipal University, Jaipur, Jaipur, Rajasthan, India*
[2]*Department of mathematics, Faculty of Science, Banaras Hindu University, Varanasi, India*

Abstract: **Einstein field equations with time dependent G and Λ have been considered in such a way which conserves the energy momentum tensor of matter. Coupling of different cosmological parameters is discussed in a general gravitational situation. It is found that the ansatz $\rho \propto \theta^2$, which leads to suitable cosmological models with variable G and Λ in Robertson-Walker geometry with $k = +1$ and in Bianchi type-I space-time, is incompatible in Bianchi type-V space-time.**

Keywords: **Variable cosmic parameters, Anisotropic, homogeneous cosmological models, Einstein field equations with variable Λ and G.**

1. INTRODUCTION

In an evolving universe, the time variation of physically relevant parameters such as the energy density ρ, the volume expansion scalar θ (hence the Hubble parameter $H(=\theta/3)$ and the deceleration parameter $q = -1 - (\dot{H}/H^2)$) and the fluid shear scalar σ are important. In view of the constancy of both, the relative dynamical importance of the energy density and the relative dynamical importance of the rate of fluid shear observed in many special exact cosmological solutions of Einstein's field equations, Collins [1] established a theorem that holds in more general situation. The theorem states that "For any space-time in which the matter content consists of a perfect fluid whose equation of state is $p = (\gamma - 1)\rho$ (where ρ is the energy density, p is the isotropic pressure and γ is a constant) and whose flow vector field forms an expanding geodesic and hypersurface-orthogonal congruence, then, if the cosmological constant is zero,
$\rho \propto \theta^2 \Rightarrow \sigma^2 \propto \theta^2$ and $R^* \propto \theta^2$

where θ and σ are respectively the volume expansion and the rate of shear of the fluid congruence, and R^* is the Ricci scalar curvature of the hypersurfaces orthogonal to the flow. In these space-times, $R^* \leq 0$." A result which however was not noticed by Collins is that, in these space-times the deceleration parameter q comes out to be a constant, but the converse holds only if $\sigma^2 \propto \theta^2$. Another result, which can be seen in this context, is that, when the isotropic pressure p is supplemented by the bulk viscous pressure $-\xi\theta$, where ξ is the bulk viscosity term satisfying $\xi = \xi_0 \rho^{\frac{1}{2}}$ is the coefficient of bulk viscosity, then the above results also hold good.

Einstein's cosmological constant Λ and the Newton's gravitational constant G which were earlier treated as true constants are no longer regarded as constants in cosmology now a days. The existence of Λ is favoured by the recent supernovae Ia observations [2] and which is also consistent with the recent anisotropy measurements of the cosmic microwave background (CMB) made by the WMAP experiment [3]. However, there is a fundamental problem related with the existence of Λ, which has been extensively discussed in the literature. Its value expected from the quantum field theory- calculations is about 120 orders of magnitude higher than that estimated from the observations. A phenomenological solution to this problem is suggested by considering Λ as a function of time, so that it was large in the early universe and got reduced with the expansion of the universe [4], [5]. Variation of Newton's gravitational parameter G was originally suggested by Dirac on the basis of his large numbers hypothesis [6]. As G couples geometry to matter, it is reasonable to consider $G = G(t)$ in an evolving universe when one considers $\Lambda = \Lambda(t)$. Many extensions of general relativity with $G = G(t)$ have been made ever since Dirac first considered the possibility of a variable G, though none of these theories has gained wide acceptance. However a new approach, which has been widely investigated in the past few years [7], [8], is appealing. It assumes the conservation of the energy-momentum tensor which consequently renders G and Λ as coupled field, similar to the case of G in original Brans-Dickie theory. This leaves Einstein's field equations formally unchanged. In this context, an approach is worth mentioning in which the scaling of $G(t)$ and $\Lambda(t)$ arise from an underlying renormalization group flow near an infrared attractive fixed point [9]. The resulting cosmology explains the high redshift SNe Ia and radio sources observations successfully [10]. It also describes the plank era reliably and provides a resolution to the horizon and flatness problems of the standard cosmology without any unnatural fine tuning of the parameters [11]. Gravitational theories with variable G have also been discussed in the context of induced gravity model where G is generated by means of a non-vanishing vacuum expectation value of a scalar field [12]. Different phenomenological cosmological models have been proposed in the past few years, which describe the evolution of these constants (better to call them parameters).

It is believed that the early universe was characterized by a highly irregular expansion mechanism which isotropized later [13]. The level of anisotropy left out by the era of decoupling is only about 10^{-5}, as is revealed by the CMB observations. It could be that whatever mechanism diminished Λ to its present value, could have also rendered the early highly anisotropic universe to the present smoothed out picture. We believe that the variation of all these parameters $\rho, \theta, \sigma, \Lambda$ and G should be linked together. Whatever physical processes are responsible for the evolution of one cosmological parameter should also be responsible for the evolution of others, implying that the different cosmological parameters are coupled together.

We shall keep ourselves limited to Einstein's field equations and to the parameters which appear explicitly therein. It would be worthwhile to mention that models with varying speed of light are recently being promoted. These are supported by claims, based on the measurements of distant quasar absorption spectra that the fine structure constant may have been smaller in the past. However, the speed of light c has a complex character having six different facets which come from many laws of physics that are a priori disconnected from the notion of light itself [14]. If it is the causal speed of which these theories are talking about, then one should not consider a varying c in general relativity unless the structure of the space-time metric is changed and reinterpreted. We consider $c = 1$ throughout our paper and discuss the coupling of the said parameters in a general gravitational situation. It is found that the variation of ρ as θ^2 is incompatible in a Bianchi type-V space-time with variable G and Λ.

2. FIELD EQUATIONS

The universe is assumed to be filled with a distribution of matter represented by the energy-momentum tensor of a perfect fluid

$$T_{ij} = (\rho + p)U_i U_j + p g_{ij} \text{ (in the units with } c = 1), \quad (1)$$

where ρ is the energy density of cosmic matter and p is its isotropic pressure. U_i is the fluid flow vector field which form an expanding geodesic and hypersurface- orthogonal congruence. The Einstein field equations with variable gravitational and cosmological constants are

$$R_{ij} - \frac{1}{2}R_k^k g_{ij} = -8\pi G\left(T_{ij} - \frac{\Lambda}{8\pi G}g_{ij}\right). \quad (2)$$

With the above stated specializations of the fluid, the Raychaudhuri equation [15] reads as

$$\dot{\theta} + \frac{1}{3}\theta^2 + 8\pi G\left\{\frac{1}{2}(\rho + 3p) - \frac{\Lambda}{8\pi G}\right\} + 2\sigma^2 = 0, \quad (3)$$

where $\theta\left(= U^i_{;i}\right)$ is the fluid's volume expansion and $\sigma^2\left(= \frac{1}{2}\sigma_{ij}\sigma^{ij}\right)$ is the fluid shear. In view of the vanishing divergence of the Einstein tensor, equations (1) and (2) give

$$\dot{\rho} + (\rho + p)\theta + \rho\frac{\dot{G}}{G} + \frac{\dot{\Lambda}}{8\pi G} = 0. \quad (4)$$

where an overhead dot $(\cdot)$ denotes differentiation along the fluid flow vector U^i. We now assume as is common in cosmology that, the law of conservation of energy momentum tensor of matter holds $\left(T^{ij}_{;i} = 0\right)$, giving

$$\dot{\rho} + (\rho + p)\theta = 0. \quad (5)$$

By use of which, equation (4) yields

$$8\pi\rho\dot{G} + \dot{\Lambda} = 0, \quad (6)$$

which shows that the variation of ρ, G and Λ are coupled together. We also consider the γ-law equation of state in the form

$$p = (\gamma - 1)\rho, \quad (7)$$

where γ is a constant such that $1 \leq \gamma \leq 2$. Using (7) in (3) and (5) and then eliminating θ between these two, we obtain

$$8\pi G = \left(\frac{2}{3\gamma - 2}\right)\left\{\frac{1}{\gamma}\frac{\ddot{\rho}}{\rho^2} - \left(\frac{3\gamma + 1}{3\gamma^2}\right)\frac{\dot{\rho}^2}{\rho^3} + \left(\frac{\Lambda - 2\sigma^2}{\rho}\right)\right\}. \quad (8)$$

Differentiating (8) and using in (6), we get

$$\frac{\ddot{\rho}}{\rho} - \frac{2}{3}\left(\frac{6\gamma + 1}{\gamma}\right)\frac{\ddot{\rho}\dot{\rho}}{\rho^2} + \left(\frac{3\gamma + 1}{\gamma}\right)\frac{\dot{\rho}^3}{\rho^3} + \frac{3}{2}\gamma^2\dot{\Lambda} - \gamma(\Lambda - 2\sigma^2)\frac{\dot{\rho}}{\rho} - \gamma(2\sigma^2)^{\cdot} = 0. \quad (9)$$

This can be rewritten with the help of (5) and (7) as

$$\frac{d}{dt}\left(\dot{\theta} + \frac{1}{3}\theta^2\right) + \gamma\theta\left(\dot{\theta} + \frac{1}{3}\theta^2\right) - \frac{3}{2}\gamma\dot{\Lambda} + (\Lambda - 2\sigma^2)(-\gamma\theta) + (2\sigma^2)^{\cdot} = 0. \quad (10)$$

A representative length l representing the volume behavior of the cosmic fluid is defined as

$$\frac{\dot{l}}{l} = \frac{1}{3}\theta. \tag{11}$$

Using equation (11) in equation (10) and multiplying l^2; equation (10) can be written as

$$\frac{d}{dt}\left(l^2\frac{\ddot{l}}{l}\right) + \left(\frac{3\gamma-2}{2}\right)\frac{d}{dt}(\dot{l}^2)$$

$$-\frac{\gamma}{2}\frac{d}{dt}(\Lambda l^2) + \frac{1}{3}\frac{d}{dt}(2\sigma^2 l^2)$$

$$+\left(\frac{6\gamma-4}{3}\right)\sigma^2 l\dot{l} = 0. \tag{12}$$

Integrating equation (12) and dividing by l^2; we get

$$\frac{\ddot{l}}{l} + \left(\frac{3\gamma-2}{2}\right)\frac{\dot{l}^2}{l^2} - \frac{\gamma}{2}\Lambda + \frac{1}{3}(2\sigma^2) + \left(\frac{6\gamma-4}{3}\right)\frac{1}{l^2}\int \sigma^2 l\, dl + \frac{\alpha}{l^2} = 0, \tag{13}$$

where α is an arbitrary constant of integration. This gives

$$\Lambda = \left(\frac{2}{\gamma}\right)\frac{\ddot{l}}{l} + \left(\frac{3\gamma-2}{2}\right)\frac{\dot{l}^2}{l^2} + \left(\frac{2\alpha}{\gamma}\right)\frac{1}{l^2} + \frac{4}{3\gamma}(\sigma^2) + \left(\frac{4(3\gamma-2)}{3\gamma}\right)\frac{1}{l^2}\int \sigma^2 l\, dl. \tag{14}$$

Equation (5) can be integrated with the help of (7) and (11) to give

$$\rho = Al^{-3\gamma}, \tag{15}$$

where $A > 0$ is an arbitrary constant of integration. In view of equations (5), (7), (11) and (14), equation (8) can be expressed as

$$G = \frac{1}{8\pi A}\left(\frac{2}{2-3\gamma}\right)$$

$$\left[l^{-3\gamma}\left(3\frac{\ddot{l}}{l} - \Lambda + 2\sigma^2\right)\right]. \tag{16}$$

Raychaudhuri equation (3) can be written in terms of l with the help of (11) as

$$3\frac{\ddot{l}}{l} = -\frac{8\pi G}{2}(\rho + 3p) + \Lambda - 2\sigma^2. \tag{17}$$

Multiplying this equation by $2l\dot{l}$ and making use of equations (5), (6) and (11), we get on integration

$$3\frac{\dot{l}^2}{l^2} + \frac{3k}{l^2} = 8\pi G\rho$$

$$+\Lambda - \frac{4}{l^2}\int \sigma^2 l\, dl, \tag{18}$$

where k is an arbitrary constant of integration, equation (18) is the generalized Friedmann equation in the presence of fluid shear and time dependent G and Λ, which provides the dynamics of the models. The constant k plays the role of curvature parameter in a homogeneous and isotropic FRW space-time ($\sigma = 0$). Equations (11), (14)-(16) describe the coupling of the parameters Λ, G, σ, ρ and θ. It is easy to see that these coupled equations do not form a closed system. However, if supplemented with one more assumption in a given Riemannian space-time representing geometry of the universe, these equations are sufficient to specify the model completely. Several cosmological models with variable G and Λ have been obtained in the last three decades with or without the presence of bulk viscosity in homogeneous isotropic or anisotropic background by assuming one more condition in the form $\rho = \rho_c$ [16], $\rho = constant$ [7]-[8], $(\rho + 3p)l^3 = constant$ [17], $q = constant$ [18]-[21], $H = A(l^{-n} + 1)$ [22]-[23], $\Lambda = \gamma l^{-2}$ [8], $\Lambda = 3\beta H^2$ [24]-[28], $\Lambda = \beta\frac{\ddot{l}}{l} + \frac{\dot{l}^2}{l^2} + 3\gamma l^{-2}$ [29], $G = At^n$ [7], [30]. In the next section we consider the phenomenological ansatz

$$\rho \propto \theta^2 \; or \; \rho = \beta\theta^2, \tag{19}$$

where β is a constant of proportionality.

3. VARIATION OF ρ AS θ^2

Equation (19) with the help of equations (5) and (7) leads to

$$2\frac{\ddot{\rho}}{\rho} - 3\frac{\dot{\rho}^2}{\rho^2} = 0 \tag{20}$$

and

$$\frac{\ddot{\rho}}{\rho} - \frac{2}{3}\left(\frac{6\gamma+1}{\gamma}\right)\frac{\ddot{\rho}\dot{\rho}}{\rho^2}$$

$$+\left(\frac{3\gamma+1}{\gamma}\right)\frac{\dot{\rho}^3}{\rho^3} = 0. \tag{21}$$

The variation of the energy density ρ as given in equation (19) with (5) and (7) gives the time-variation of scale factor as

$$l = mt^{\frac{2}{3\gamma}}, \; m \text{ is a positive constant.} \tag{22}$$

which implies

$$\frac{2}{\gamma}\frac{\ddot{l}}{l} + \left(\frac{3\gamma-2}{\gamma}\right)\frac{\dot{l}^2}{l^2} = 0 \tag{23}$$

and consequently, equation (14) reduces to

$$\Lambda = \left(\frac{2\alpha}{\gamma}\right)\frac{1}{l^2} + \frac{4}{3\gamma}(\sigma^2)$$

$$+\left(\frac{4(3\gamma-2)}{3\gamma}\right)\frac{1}{l^2}\int \sigma^2 l\, dl. \tag{24}$$

The deceleration parameter q in this case comes out to be

$$q = \frac{3\gamma}{2} - 1. \tag{25}$$

It follows that when the cosmological constant Λ and the gravitational coupling constant G are taken to vary with time in space-times in which ρ varies as θ^2, the deceleration parameter q is always constant, but the converse may not be true. Moreover, the condition $\rho \propto \theta^2$ always leads to a big bang origin of the universe.

It may be noted that, though, the recent observations favour accelerating models at present but the possibility of decelerating models with small deceleration parameter are not completely ruled out. It has also been shown that the high redshift supernovae Ia can also be explained successfully in the decelerating models if one takes into account the absorption of light by the intergalactic metallic dust ejected from the supernovae explosions [5], [31].

Taking equation (20) as an additional assumption, Abdussattar and Vishwakarma [8] has obtained a FRW model with variable G and Λ and Vishwakarma [32] has discussed the simultaneous variation of Λ, G and σ^2 in Bianchi type-I space-time with variable G and Λ. In the next section we consider the coupling of these cosmological parameters in a Bianchi type-V space-time employing the ansatz (19).

4. BIANCHI TYPE-V MODEL

We consider a homogeneous and anisotropic Bianchi type-V space-time described by the line-element

$$ds^2 = -dt^2 + X^2(t)dx^2 + e^{2nx}\{Y^2(t)dy^2 + Z^2(t)dz^2\}. \tag{26}$$

For this metric the Einstein's field equations $G_{ij} = -8\pi G T_{ij}$ yield

$$\frac{\ddot{X}}{X} + \frac{\ddot{Y}}{Y} + \frac{\dot{X}\dot{Y}}{XY} - \frac{n^2}{X^2}$$

$$= -8\pi G(t)(\gamma - 1)\rho + \Lambda(t), \tag{27}$$

$$\frac{\ddot{Y}}{Y} + \frac{\ddot{Z}}{Z} + \frac{\dot{Y}\dot{Z}}{YZ} - \frac{n^2}{X^2}$$

$$= -8\pi G(t)(\gamma - 1)\rho + \Lambda(t), \tag{28}$$

$$\frac{\ddot{Z}}{Z} + \frac{\ddot{X}}{X} + \frac{\dot{Z}\dot{X}}{ZX} - \frac{n^2}{X^2}$$

$$= -8\pi G(t)(\gamma - 1)\rho + \Lambda(t), \tag{29}$$

$$\frac{\dot{X}\dot{Y}}{XY} + \frac{\dot{Y}\dot{Z}}{YZ} + \frac{\dot{Z}\dot{X}}{ZX} - 3\frac{n^2}{X^2}$$

$$= 8\pi G(t)\rho + \Lambda(t), \tag{30}$$

$$2\frac{\dot{X}}{X} - \frac{\dot{Y}}{Y} - \frac{\dot{Z}}{Z} = 0. \tag{31}$$

The volume expansion scalar θ and shear σ for the metric (26) are obtained as

$$\theta = \frac{\dot{X}}{X} + \frac{\dot{Y}}{Y} + \frac{\dot{Z}}{Z}, \tag{32}$$

$$\sigma^2 = \frac{1}{3}\left[\frac{\dot{X}^2}{X^2} + \frac{\dot{Y}^2}{Y^2} + \frac{\dot{Z}^2}{Z^2} - \left(\frac{\dot{X}\dot{Y}}{XY} + \frac{\dot{Y}\dot{Z}}{YZ} + \frac{\dot{Z}\dot{X}}{ZX}\right)\right]. \tag{33}$$

An average scale factor is obtained as $l = (XYZ)^{\frac{1}{3}}$. On integration equation (31) yields

$$X^2 = YZ. \tag{34}$$

Equations (27)-(29), with the help of equations (32) and (33) lead to

$$\frac{\dot{X}}{X} = \frac{\dot{l}}{l}, \tag{35}$$

$$\frac{\dot{Y}}{Y} = \frac{\dot{l}}{l} - \frac{k_1}{l^3}, \tag{36}$$

$$\frac{\dot{Z}}{Z} = \frac{\dot{l}}{l} + \frac{k_1}{l^3}, \tag{37}$$

where k_1 is a constants of integration. Equations (35)-(37) can be integrated further to yield

$$X(t) = m_1\, l(t)\,, \tag{38}$$

$$Y(t) = m_2\, l(t)\, exp\left[-k_1 \int \frac{dt}{l^3}\right], \tag{39}$$

$$Z(t) = m_3\, l(t)\, exp\left[k_1 \int \frac{dt}{l^3}\right], \tag{40}$$

where m_1, m_2, m_3 are arbitrary constants of integration satisfying $(m_1.m_2.m_3) = 1$. In view of (34) we get $m_1 = 1$ and $m_2 = m_3^{-1}$. Equation (33) for shear now reads as

$$\sigma^2 = \frac{k_1^2}{l^6}. \tag{41}$$

Equations (38)-(40) with the help of equation (22) give the values of the metric potentials as

$$X(t) = m_1\, mt^{2/3\gamma}, \tag{42}$$

$$Y(t) = m_2\, mt^{\frac{2}{3\gamma}}$$

$$exp\left\{-\frac{k_1}{m^3}\left(\frac{\gamma}{\gamma-2}\right)t^{\frac{\gamma-2}{\gamma}}\right\}, \quad (43)$$

$$Z(t) = m_3\, mt^{\frac{2}{3\gamma}}$$

$$exp\left\{\frac{k_1}{m^3}\left(\frac{\gamma}{\gamma-2}\right)t^{\frac{\gamma-2}{\gamma}}\right\}. \quad (44)$$

So that, with suitable transformation, the metric (26) takes the form

$$ds^2 = -dt^2 + m^2 t^{4/3\gamma}\begin{bmatrix} m_1^2 d\chi_1^2 \\ +m_2^2 e^{2n\chi_1 - 2\left(\frac{k_1}{m^3}\right)\left(\frac{\gamma}{\gamma-2}\right)t^{\frac{\gamma-2}{\gamma}}} d\chi_2^2 \\ +m_3^2 e^{2n\chi_1 + 2\left(\frac{k_1}{m^3}\right)\left(\frac{\gamma}{\gamma-2}\right)t^{\frac{\gamma-2}{\gamma}}} d\chi_3^2 \end{bmatrix}. \quad (45)$$

For the model (45) the different cosmological parameters are obtained as

$$\theta = \frac{2}{\gamma}\frac{1}{t}\ , \quad (46)$$

$$\sigma = \frac{k_1}{m^3}\frac{1}{t^{2/\gamma}}, \quad (47)$$

$$\rho = \frac{A}{m^{3\gamma}}\frac{1}{t^2}, \quad (48)$$

$$\Lambda = \left(\frac{2-\gamma}{\gamma}\right)\left(\frac{k_1^2}{m^6}\right)\frac{1}{t^{\frac{4}{\gamma}}}$$

$$+\left(\frac{2-3\gamma}{\gamma}\right)\left(\frac{n^2}{m_1^2 m^2}\right)\frac{1}{t^{4/3\gamma}}, \quad (49)$$

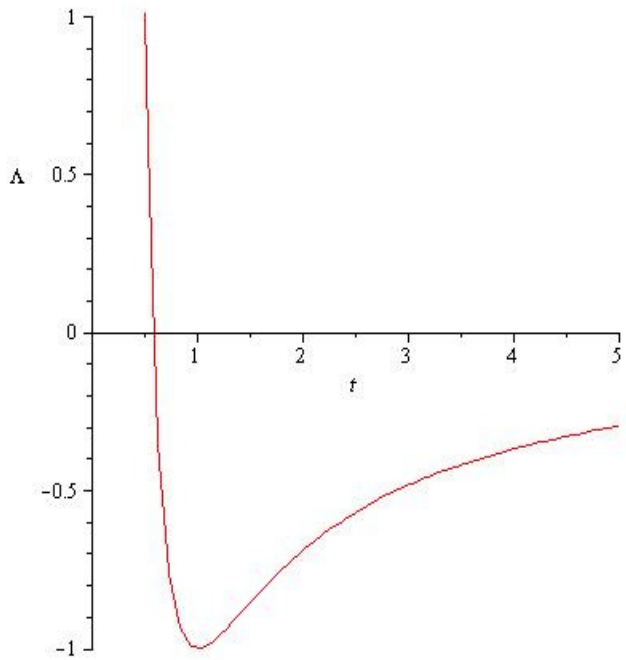
$$G = \left(\frac{m^{3\gamma}}{\pi A\gamma}\right)\left[\frac{1}{6\gamma} - \frac{1}{4}\left(\frac{k_1^2}{m^6}\right)\frac{1}{t^{(4/\gamma)-2}} - \frac{1}{4}\left(\frac{n^2}{m_1^2 m^2}\right)\frac{1}{t^{(4/3\gamma)-2}}\right]. \quad (50)$$

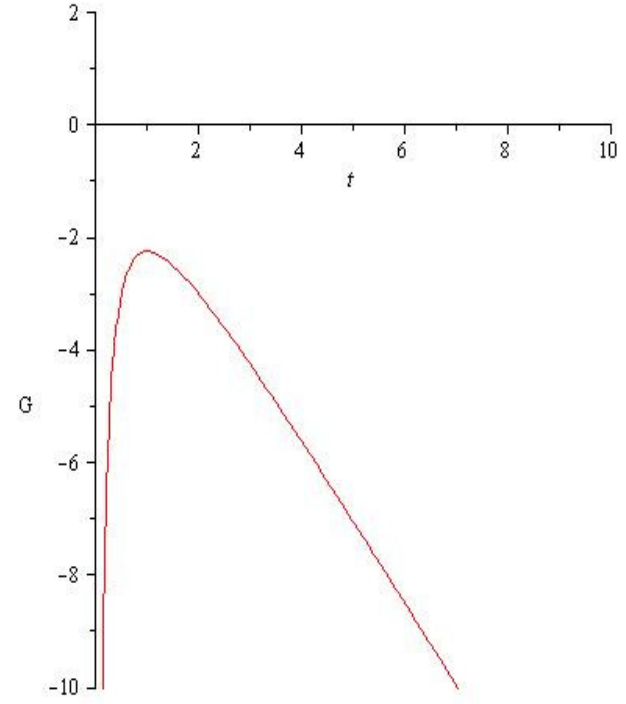
The anisotropy parameter

$\bar{A}\left(=\frac{1}{3}\sum_{i=1}^{3}\left(\frac{H_i - H}{H}\right)^2\right)$, where $H_1 = \frac{\dot{X}}{X}, H_2 = \frac{\dot{Y}}{Y}$, $H_3 = \frac{\dot{Z}}{Z}$ are directional Hubble's factors, is obtained as

$$\bar{A} = \frac{3\gamma^2}{2}\left(\frac{k_1^2}{m^6}\right)\frac{1}{t^{(4/\gamma)-2}} \quad (51)$$

The anisotropy parameter $\bar{A}$ vanishes for large values of t. Therefore at late times, the model represents an isotropic universe. For the obtained model, the variation of Λ and G is depicted in the following figures.





We see that the gravitational coupling constant G remains negative throughout the evolution, whereas the cosmological constant Λ which is initially positive, becomes negative during the course of evolution and ultimately approaches to zero for large values of t. Thus, we conclude that the Bianchi type-V space-time with variable G and Λ is incompatible with the ansatz $\rho \propto \theta^2$.

REFERENCES

[1] Collins, C. B.: Phys. Lett. 60A(5) 397 (1977).

[2] Perlmutter, S. et al.: Astrophys. J. 517 565 (1999); Reiss, A. G. et al.: Astrophys. J. 560 49 (2001); Reiss, A. G. et al.: Astrophys. J. 607 665 (2004).

[3] Bennet, C. L. et al.: Astrophys. J. Suppl. 148 1 (2003).

[4] Abdussattar and Vishwakarma, R. G.: Pramana J. Phys. 47 41 (1996); R G Vishwakarma: Class. Quant. Gravit. 17 3833 (2000); Gen. Relativ. Gravit. 33 1973 (2001); Class. Quant. Gravit. 18 1159 (2001); Class. Quant. Gravit. 19 4747 (2002).

[5] Vishwakarma, R. G.: Mon. Not. R. Astronom. Soc. 331 776 (2002).

[6] Dirac, P. A. M.: Nature 139 323 (1937).

[7] Kalligas, D., Wesson, P. and Everitt, C. W. F.: Gen. Relativ. Gravit. 24 351 (1992).

[8] Abdussattar and Vishwakarma, R. G.: Class. Quant. Gravit. 14 945 (1997).

[9] Bonanno, A. and Reuter, M.: Phys. Lett. B527 9 (2002).

[10] Bentivegna, E., Bonanno, A. and Reuter, M.: JCAP 0401 001 (2004).

[11] Bonanno, A. and Reuter, M.: Phys. Rev. D527 043508 (2002).

[12] Zee, A.: Phys. Rev. Lett. 42 417 (1979); Smolin, L.: Nucl. Phys. B160 253 (1979): Adler, S.: Phys. Rev. Lett. 44 1567 (1980).

[13] Misner, C. W.: Astrophys. J. 151 431 (1968).

[14] Riazuelo, A. and Uzan, J. P.: Phys. Rev. D66 023525 (2002); Ellis, G. F. R. and Uzan, J. P.: Am. J. Phys. 73 240 (2005); Arabab I Arbab: astro-ph/0308068.

[15] Ellis, G. F. R.: R K Sachs, Relativistic Cosmology (Academic Press, New York and London, 1971).

[16] Abdel Rahman, A-M. M.: Gen. Relativ. Gravit. 22(6) 655 (1990).

[17] Abdussattar and Vishwakarma, R. G.: Aust. J. Phys. 50 893 (1997).

[18] Berman, M. S.: Gen. Relativ. Gravit. 23(4) 465 (1991).

[19] Beesham, A.: Phys. Rev. D48(8) 3539 (1993).

[20] Singh, C. P., Suresh Kumar: Int. J. Theorit. Phys. 48 2401 (2009).

[21] Singh, J. P.: Int. J. Theorit. Phys. 48 449 (2009).

[22] Singh, J. P.: Int. J. Theorit. Phys. 48 2041 (2009).

[23] Singh, J. P.: Astrophys. Space Sci. 318 103 (2008).

[24] Arbab I Arbab: Gen. Relativ. Gravit. 29(1) 61 (1997).

[25] Arbab I Arbab: Gen. Relativ. Gravit. 30(9) 1401 (1998).

[26] Arbab I Arbab: Chin. J. Astron. Astrophys. 3(2) 113 (2003).

[27] Singh, T., Beesham, A. and bokazi, W. S.: Gen. Relativ. Gravit. 30(4) 573 (1998).

[28] Singh, C. P., Suresh Kumar and PA.radhan, : Class. Quantum Gravit. 24 455 (2007).

[29] Arbab I Arbab: arxiv: gr-qc/9909044v2.

[30] Beesham, A.: Gen. Relativ. Gravit. 26(2) 159 (1994).

[31] Vishwakarma, R. G.: Mon. Not. R. Astronom. Soc. 361 1382 (2005).

[32] [32] Vishwakarma, R. G.: Gen. Relativ. Gravit. 37(7) 1305 (2005).

Application of Nanotechnology in Food Processing: A Promising Prospective with Considerable Risk

Sanjib K. Paul[1], Sudipto Sarkar[2], Laxmi Narayan Sethi[3], Sujit K. Ghosh[4]

[1,2,3]*Department of Agricultural Engineering, Assam University, Silchar, Assam*
[4]*Department of Chemistry, Assam University, Silchar, Assam*

Abstract: **Nanotechnology is an emerging field of research for every domain of science and technology including food sector. Application of nanotechnology in food industry though still at juvenile stage but outcomes of recent extensive researches has indicated that it can bring revolutionary changes in various area of food domain including post-harvest management, food packaging and storage, biosensors, medicines, nutrient and nutraceutical delivery, additives and ingredients and also bioprocessing of food and effluent in near future. Technology of active and smart or intelligent packaging has received acceleration in its improvement with the incorporation of nanomaterials. Hazardless and edible packaging or coating with nanomaterials has provided a boon in edible packaging and storage sector for preservation and storage of fresh as well as processed food products. For quick detection of pathogenic microorganisms, contaminations, specific nutrient content, adulteration in food products etc., various nanomaterial based biosensors has already developed and some are under experimental trials. Nano-encapsulation of nutrients and nutraceuticals has shown the effectiveness of nanotechnology in maximum delivery of nutrients with minimum destruction. In addition, application of nanotechnology has made the process of food processing more effective with maximum retention of colour, flavor, and nutrient content including various functional components of food products. Researchers also pointed out about the possibility of risk for consumers health and environment with the nanomaterial incorporated food products. Future researches in proper direction to investigate further applicability, potentiality of hazard and establishment of regulations and guidelines for using nanotechnology in food is expected. In this article, current status of various applications nanotechnology in food industry and their potential risk has been discussed.**

Keywords: Nanofood, nutrient delivery, food packaging, nanomaterials

1. INTRODUCTION

Research and development in new materials technology is attracting the attention of researchers all over the globe. Developments are being made to improve the properties of the materials and to find alternative precursors that can give desirable features on the materials. The term *nano* originates etymologically from the Greek, and it means "dwarf." It indicates physical dimensions in the scale called colloquially *nanometer scale*, or also *nanoscale.* Nanotechnology, which is one of the new technologies, refers to the development of devices, structures, and systems whose size varies from 1 to 100 nanometers (nm). The advancement of nanotechnology is fostered with the availability of techniques to examine and visualise things at the atomic scales. Nanoscience and technology explores electrical, optical, and magnetic activity as well as structural behavior at the molecular and submolecular level. Nanoscale structures permit the control of fundamental properties of materials without changing the materials' chemical status. These emergent properties have the potential for great impacts in electronics, medicine, and other fields of science and technology including food processing and preservation.

The last fifteen years has demonstrated advancements in every dimensions of nanotechnology such as nanoparticles and powders, nanolayers and coats, electrical, optical and mechanical nanodevices and nanostructured biological materials [1-5]. This is due to the improvement of mechanical properties, barrier properties, surface biocides, biodegradability and intelligent functionality of nanomaterials [6, 7].

Some nanomaterials occur naturally, but of precise interest are on engineered nanomaterials (EN), which are designed for, and already being used in many products and processes technologies [8]. Engineered nanomaterials are designed at the molecular (nanometer) level to take advantage of their small dimension and novel properties which are generally not observed in their conventional, bulk constituents. The two main reasons why materials at the nano scale can have different properties are increased relative surface area and new quantum effects. Nanomaterials have a much greater surface area to volume ratio than their conventional forms, which can lead to greater chemical reactivity and affect their potentiality. Also at the nano scale, quantum effects can become much more important in determining the materials properties and characteristics leading to novel optical, electrical and magnetic attribute [6, 7]. Nanomaterials are already in commercial use, with some having been available for several years or decades.

Application of nanotechnology in agri-food industry was first pointed out by United States Department of Agriculture (USDA) roadmap published in September 2003 [9]. The main

focus of new applications so far appears to be on food packaging and healthfoods, with only a few known examples in the mainstream food and beverage areas. In the present article, a general overview of the state-of-the-art of nanotechnology, its present scenario, future prospective in the food industry and its considerable risk factors for the consumer health and environment has been discussed. It is expected that the paper will be quite useful for developing the knowledge of present and future researchers in the field of food nanotechnology.

2. PREPARATION OF ENGINEERED NANOMATERIALS AND THEIR PROCESSING

The synthesis of nanomaterials can be achieved in both the 'bottom up' and the 'top down' approaches i.e. either to assemble few atoms together or dissociate (break or dissemble) bulk solids into finer pieces until they are constituted of only a few atoms. This field of technology is a pure example of interdisciplinary activity comprising physics, chemistry, and engineering upto life science and medicine.

There are several different established methods of creating nanostructures but definite structures such as macromolecules, nanoparticles, rods, buckyballs, nanotubes and so on can be synthesized artificially for certain specific materials to fulfill desired purposes. They can also be arranged by methods based on equilibrium or near-equilibrium thermodynamics such as methods of self-organization and self-assembly (sometimes also called bio-mimetic processes). Using these methods, synthesized materials can be arranged into useful shapes so that finally the material can be applied to a certain application.

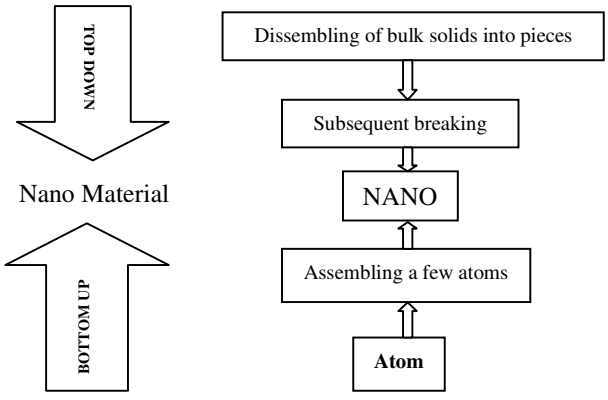


Figure 1. Schematic representation of nano material preparation

3. PRESENT SCENARIO OF APPLICATION OF NANOSYSTEMS IN FOOD TECHNOLOGICAL INNOVATIONS

The term nano-food can be defined as "food which has been cultivated, produced, processed or packaged using nanotechnological techniques or tools or to which manufactured nanomaterials have been added" [10]. In this point of view, it is expected that thousands of food products could emerge based on nanotechnology in the coming decades, though still it is at infancy [11]**.** With realization that nanofood is about the future way of life and is among the most important scientific and technological developments affecting mankind and enterprise, it is important to be better understanding about the applications of nanotechnology in food industry towards economic growth, healthcare and environment which will be eventually determined the priority areas of nanotechnology to be invested. The success in nanofood technology not only can solve the food shortage, but also can improve the health of people by producing healthy foods [11].

Now-a-days, application of nano materials having desired functional characteristics are being analyzing and applying in food processing operations, product development, quality control and analysis such as, post-harvest management and storage, packaging and functional coatings, effective delivery nutrients and nutraceuticals, medicines and therapeutic food, biosensors etc. Nanotechnology is an emerging field, which is expected to have a substantial impact on the modern research and development of science and technology now and in the future. In general, nanotechnology is acknowledged to represent a new frontier area in science and technology of the 21st century. In simple words, nanotechnology is a promising technology seeking to exploit distinct technological advancement of controlling the structure of materials at a reduced dimensional scale approaching individual molecules and their molecular or macromolecular level. In this arena, nanotechnology may provide improved functional and sensory properties to food components. Nano-particles, nano-emulsions, and nano-capsules may be designed to enhance the availability and dispersion of nutrients, antioxidants or nutraceuticals in foods.

3.1 Crop production and post-harvest management of agricultural produce

Drawbacks of the existing techniques like- controlled and modified atmospheric storage (CAP and MAP), cold storage, chemical preservation etc in terms of lacking in desired effectiveness and parallel harmful possessions for health and environment have triggered the researchers towards innovations for the development of alternative packaging and post-harvest management techniques, such as functional edible coatings, disease control of agricultural produce at genetic level with nanotechnology etc. A number of researches have been carrying out their researches to develop coating materials that would coat fruits and vegetables to provide an internal modified atmosphere to them [12]. However, development of an edible coating incorporating nano materials will be an excellent innovation in order to reduce the post-harvest losses of fruits, vegetables and various

other food products. Advancement in nanofabrication and characterization tools have enabled studies of physical, chemical and biological interactions between plant cell organelles and various disease causing pathogens, i.e., plant pathology. A better understanding of plant pathogenic mechanisms such as flagella motility and biofilm formation will lead to improved treatment strategies to control the diseases and protect production [13, 14]. The advancement in nanotechnology-enabled gene sequencing is expected to introduce rapid and cost effective capability within a decade [15], hence leading to more effective identification and utilization of plant gene trait resources.

3.2 Modern food packaging and coating

Nanotechnology has already immerged into packaging industries throughout the world and various extraordinary outcomes have been revealed by various researchers and manufacturers. Various properties of packaging materials like- UV protection, barrier properties to moisture, gasses and volatile components, mechanical strength, thermal resistant and sealability has significantly improved with the ncorporation of nanomaterials into base matrix of packaging materials. Nanotechnology has also shown its potential future in active and smart packaging technology. Reinforcement of nanomaterials having different desired properties into edible films and coatings has brought the attention of researchers into functional and edible nanocoatings.

Examples include plastic polymers with nano clay as gas barrier, nano-silver and nano-zinc oxide for antimicrobial action, nano-titanium dioxide for UV protection, nano-titanium nitride for mechanical strength and as a processing aid, nano-silica for surface coating etc. The use of nano-composite with biopolymers is expected to rise because they offer possibility for carbon-neutral biodegradable materials for packaging [16].This will offer opportunities for developing countries to utilize their agricultural and forestry resources, by-products and wastages or development of biopolymer nano-composites.

Silver nano-particles can be introduced in polymeric materials such as PVC, PE, PET etc while polymerization occurs. Silver Nano particles kill pathogens, bacteria, viruses and fungus and are used as a good and safe packaging material. Such nano based packaging materials are 100 times more secure than the normal one for the storage of juices, milk and other agri-products [17]. Nanotechnological products in packaging food materials thus offer immense potential. Food packaging films in the name of "hybrid system" films have enormous number of silicate nano particles. They massively reduce the entrance of oxygen and other gases, and the exit of moisture and volatiles, thus preventing food from spoiling or drying [10]. Nanotechnology can provide solutions for modifying the permeation behavior of foils, increasing barrier properties and improving mechanical and heat-resistance properties [17]. Other nano tech devices may include developing active antimicrobial and antifungal surfaces and sensing as well as signaling microbiological and biochemical changes.

Nanocomposites or nanoparticles in packaging materials (e.g. silver, TiO_2, SiO_2, nano-clay) can ensure better protection for food, for example by reducing the permeability of foils, deodorizing, blocking UV light, improving mechanical and heat-resistance properties, and acting against bacteria or fungi. Nanoform TiO_2 is transparent, UV resistant, and is sold by several companies as filler particles in foils and plastic containers. Nano-TiO_2 in packaging materials is classified as safe for food, although most of the safety data refers to the larger form of TiO_2. There is no record of any investigations to discover whether packaging materials containing Nano-TiO_2 are just as inert (not generally reactive) as those containing the larger "bulk" form, i.e. it cannot be ruled out that nano-TiO_2 particles migrate from packaging to the food. Nylon nanocomposites are used for food packaging (e.g. in PET bottles for beer and other alcoholic beverages), because they constitute a barrier to oxygen and CO_2, keeping the product fresh and/or preventing nasty smells [17].

Ecology Coatings, Inc. (Auburn Hills, USA) has developed UV-cured coatings specifically to address opportunities within the paper and packaging industry. These coatings offer significant benefits over existing UV-cured coatings, and replace expensive adhesive-plastic lamination used in many label applications. This reduces the cost of materials and simplifies the manufacturing line [18].

Bayer Polymers has developed the Durethan KU2-2601 packaging film, which is transparent, lighter, stronger and more heat resistant than those currently in the market. The primary purpose of food packaging films is to prevent contents from drying out and to protect them from moisture and oxygen. In a different strategy, Kodak is developing antimicrobial films that have the ability to absorb oxygen from the contents of the package, thus impeding food deterioration [10]. Certain other antimicrobial packaging and container products like- BlueMoonGoods™, Fresh Box Silver Nanoparticle, Antibacterial Kitchenware, Sunriver Industrial nanosilver fresh food bag, FresherLonger™ Plastic Storage Bags, Food Storage Containers etc are developed by using silver nanoparticles are also coming into the market commercially [19-21]. Using Zinc oxide a product viz- Nano Plastic Wrap of SongSing Nano Technology Co. Ltd was developed for the purpose of Anti-UV, reflecting IR, sterilizing, better temperature tolerance and fire-proof. In which ZnO uses light to sterilize the surface of the film and hence the food [21].

With the similar strategy 'Voridan' in association with 'Nanocor' has developed nanocomposite containing clay nanoparticles, called Imperm. The resultant bottle is both lighter and stronger than glass and is less likely to shatter. The

nanocomposite structure minimizes loss of carbon dioxide from the beer and the ingress of oxygen to the bottle, keeping the beer fresher and giving it up to a six-month shelf life [10].

Researchers in the Netherlands are going further to develop intelligent packaging that will release a preservative if the food is within the begining of spoilage. This "release on command" preservative packaging operates by using a bio-switch developed through nanotechnology. 'Smart' food packaging will warn when oxygen has got inside, or if food is going off. Such packaging is already in use in brewing and dairy production and consists of nanofilters that can filter out micro-organisms and even viruses [22].

3.3 Nano-biosensors and rapid detection devices

In the recent years the advent of nanotechnology applications in food safety (i.e. detection systems, biosensors, etc) is becoming a key focus of research and development, and the potential benefits of this emerging technology are receiving growing attention from both the public and the private sector. The application of nanobiosensors in food industry could lead to immense improvements in quality control, food safety, and traceability. The advantages of nanobiosensors can lead to their use in various food production processes: from raw material preparation, food processing (quality control), monitoring of storage conditions and use of these devices as cost effective tools for quality & process controls as well as to ensure food safety [17].

In recent years, it has aroused great interest in modifying electrode surfaces with novel nanomaterials so as to achieve a faster electron transfer of biomolecules and a higher specificity and accuracy. This advantage has inspired research in coupling nanomaterial based biosensors with biomolecules. These biosensors have been applied in different areas such as food quality, food safety, clinical analysis and environmental control [17].

Kraft foods, along with researchers at Rutgers University in the US, are developing an "electronic tongue" for inclusion in packaging. This consists of an array of nanosensors which are extremely sensitive to gases released by food as it spoils, causing the sensor strip to change colour as a result, giving a clear visible signal of whether the food is fresh or not [10]. AgroMicron has developed the NanoBioluminescence Detection Spray which contains a luminescent protein that has been engineered to bind to the surface of microbes such as Salmonella and *E. coli*. When bound, it emits a visible glow, the more intense the glow is, the higher the bacterial contamination. The company aims to market the product under the name BioMark and is currently designing new spray techniques to apply in ocean freight containerized shipping as well as to fight bioterrorism [23]. In a similar strategy to ensure food safety, EU researchers in the Good Food Project have developed a portable nanosensor to detect chemicals, pathogens and toxins in food [24]. The project is also developing a device using DNA biochips to detect pathogens. It is a technique that could also be applied to determine the presence of different kinds of harmful bacteria in meat or fish, or fungi affecting fruit. The project also has plans to develop microarray sensors that can be used to identify pesticides on fruit and vegetables as well as those which will monitor environmental conditions at the farm. These have been coined "Good Food sensors" [10].

3.4 Nanotechnology in medicine and therapeutic application

Combination of nanotechnology with medical science has already brought a tremendous changes and advancement in prevention, detection and treatment of various diseases and physiological as well as pathological conditions. The German company Aquanova has developed a new technology which combines two active substances for fat reduction and satiety into a single nano-carrier (micelles of average 30 nm diameter), an innovation said to be a new approach to intelligent weight management. The product is named as NovaSOL Sustain. The NovaSol technology has also been used to create a vitamin-E preparation that does not cloud liquids, called SoluE, and a vitamin C preparation called SoluC. The NovaSOL product can be used to introduce other dietary supplements as it protects contents from stomach acids [25]. Megestrol acetate oral suspension (MAOS) is an appetite stimulant indicated for cachexia in patients with AIDS. It is available in its original formulation, Megace® (MAOS), and as a nanocrystal dispersion, Megace® ES (MA-ES) (Bristol-Myers Squibb, New York, USA). Bioavailability and absorption were found to be greater for MA-ES than MAOS in fasting subjects, thereby, suggesting MA-ES a preferred formulation of megestrol acetate when managing cachectic patients whose caloric intake is reduced [26].

3.5 Nutrient bioavailability and utrient delivery

From the results of the researches on nutrient and nutraceutical delivery with the application of nanotechnological principles, several products are already entered into the market domain. Royal BodyCare, a company utilizing nanotechnology in nutritional sciences, has marketed a new product called NanoCeuticals which is a colloid (or emulsion) of particles of less than 5 nm in diameter. The company claims the product will scavenge free radicals, increase hydration and balance the body's pH. The company has also developed NanoClusters^{TM}, a nanosize powder combined with nutritional supplements. When consumed, it enhances the absorption of nutrients [27].

3.6 Nanobiotechnology

Interdisciplinary research in the application of nanostructures in the field of biotechnology has started addressing so many global problems. Nanobiomaterials are developed utilizing DNA molecules as the basic building units using nucleic acid

engineering. DNA molecules can be modified to develop novel biomaterials such as nanowires and nanomembranes that can be used for nanofiltration processes. It is reported that the expected global production for engineered nanomaterials applied in biotechnology will reach 10 ton per year by 2020 where the present use is 1 ton per year [28, 29].

3.5 Food additives and ingredients

Various nanomaterials are used as additives and/or ingredients to produce various functional food products to achieve certain goals like-low fat absorption on frying,, to supplement and effective delivery of nutrients, to make the process easier and energy efficient etc. In addition to that present day researchers of this domain are concentrated on proper fabrication of nano-sized food components and additives to reduce processing and biological loss. In this context, US based Oilfresh corporation has marketed a new nanoceramic product which reduces oil use in restaurants and fast food shops by half. As a result of its large surface area, the product prevents the oxidation and agglomeration of fats in deep fat fryers, thus extending the useful life span of the oil. An additional benefit is that oil heats up more quickly, reducing the energy required for cooking [30]. Some other products which are designed and developed by using nano-ingredients that are already exist in the market worldwide includes: Fortified Fruit Juice (High Vive. com, USA), Nanoceuticals Slim Shake (assorted flavors, RBC Lifesciences, Irving, USA), NanoSlim beverage (NanoSlim), Oat Nutritional Drink (assorted flavors, Toddler Health, Los Angeles, USA), 'Daily Vitamin Boost' fortified fruit juice (Jamba Juice Hawaii, USA) and nanocapsules containing tuna fish oil (a source of omega 3 fatty acids) in "Tip-Top" Up bread which will break only when it will reach the stomach and will avoid the unpleasant taste (Enfield, Australia) [31]. Nanoparticles of different materials including Silver, gold, copper, platinum, palladium, iridium, titanium and zinc are also used in the production of various food supplements viz-MesoSilver, Mesogold, Mesocopper, Mesoplatinum, Mesopalladium, Mesoiridium, Mesotitanium and Mesozinc respectively [32].

4. THREAT OF NANOTECHNOLOGY IN FOOD PROCESSING

Nano materials offer lots of potential benefits in almost all sectors of technological developments including food processing, preservation, storage, quality assurance, value addition and also food safety and security. It has also proved that this modern technology can become the accelerator in developments of all sectors of human and social need of coming future. But as most of the good inventions has its opposite side of effects also, so the probable harmful aspects of nanotechnology should also be analysed critically and it is the need of present time to conduct extensive researches so that its benificial effects can be utilised to fulfill the global needs by eliminating its hazards.

It is established that products containing natural food nano-structures that are likely to be digested/degraded in the gastro-intestinal (GI) tract (soft nanomaterials) may not require a detailed evaluation compared to products containing insoluble and biopersistent nanomaterials [16]. On this basis the following broad application categories may be considered:

Areas of least concern include food products that contain processed (natural) food nano-structures, which are either digested or solubilised in the GI tract and are not biopersistent. Areas of some concern arise where food products contain encapsulated food/feed additives in nano-sized carriers which may not be biopersistent, but may carry the encapsulated substances across the GI tract. In such condition, tissue distribution of the materials contained in nano-carriers may be different from that of equivalent bulk materials. Also an increased bioavailability of vitamins and minerals may not always be beneficial for consumer health. A greater uptake of food colors or preservatives could take the application outside of the conditions under which the ADI (acceptable daily intake value) was set for the additive [16]. Areas of major concern include when food products contain insoluble, indigestible by the digestion enzyme system, and potentially biopersistent and even non-degradable nano-additives (e.g., metals or metal oxides) or functionalized nanomaterials. Such applications may impart a risk of consumer exposure to hard nanomaterials [16].

Risks of migration of nanomaterials from the packaging into the food and subsequently to the body system are also being advocated [33-35]. This may impact negatively on the use and progress of such packaging materials. But researches has till now showed that the chance of migration of nano particles is very low. It is found that migration can only happen when the size of incorporated nanomaterial is within the lower nm range, have very high dynamic viscosity and if they are not bounded properly with the polymer matrix [36].

Toxicological risk of nanomaterials is also of a major concern but toxicology research and risk assessments in nanotechnology are practically non-existent, especially in the food sector [37] and few have proved to be valuable in terms of their use in assessing toxicity [38]. Some materials exhibit toxicity at the nanoscale and not at the macroscale. For example, Cui et al., (2005) showed that single-walled carbon nanotubes inhibited human embryo kidney cell proliferation and negatively impacted on cell growth and cell turnover[39]. The nanomaterials involved in this study are unlikely to be used in the food industry, however, such toxic effects must be noted at this early stage of technological development and progress must be cautious. It may substantially affect the human and environmental health.

Nano-additives incorporated in foods are readily reactive with the other food compounds, stomach acids as well as enzymes of the GI track, thus will change the internal environment of the digestive system of the individual. This phenomenon may also loss the nano property of the incorporated materials due to agglomeration or aggregation.

Though the risk potentiality of the nanomaterials are under research stage, but another important issue concern to risk is that nanomaterials are extending their range of application in a unexpected progression, but still there are not a single regulation specifically for the application and analysis of nanomaterials in food. General regulatory rules like European Union, Codex Alimentarious, USDA, USFDA, PFA etc. are still following for the purpose, but these regulations concern with general food safety, food contact surface, food hazard, general food adulteration etc. But nanomaterials have certain extraordinary properties than the general bulk materials, so specific regulations are in emergency need for the proper welfare of the society by nano-food technology [40].

The concern aspect regarding nanomaterials differs from country to country. In Taiwan, authority have introduced a quality assurance system viz-'Nano Mark System' for consumers which certifies that a product uses a genuine nanotechnology [41] but food is not included as a category to which this symbol is assigned. In Australia, like Europe, nanotechnologies are regulated by horizontal legislation of European Commission [42]. NICNAS, which regulates chemicals for the protection of human health and the environment, has recently introduced new administrative processes to address nanotechnology [43]. NICNAS monitors changes in industrial usage and can legislate accordingly to ensure legislation remains at the forefront of developments and to ensure emerging challenges in industrial chemical regulation, including the challenge of nanotechnology, are under control [44]. In the United States, multiple federal agencies regulate products associated with nanotechnologies and nanomaterials, but there is no regulatory framework that provides consistent and comprehensive screening and protections for consumers [45]. So, it is transparent that a regulatory gap exists between commercial developments and public expectations about regulatory protections for nanotechnologies [46].

Thus, at present along with the regulatory aspects, a concrete definition of nanomaterials, proper detection and characterization technique, its reactivity with food components, toxicological features, long term effects on human and biological system and risk assessment procedures are the major area of concern issue for utilizing the benefits of nanoscience in a viable way [16]. A number of novel research projects are carrying out worldwide to establish some solution of the above problems.

5. FUTURE EXPECTATIONS AND CONCLUSION

Science and technology of nanomaterials though is at a juvenile stage, but it is already showing a great potentiality in every areas of application**.** Efforts to facilitate international collaboration and information exchange are underway to ensure acceptance and utilization of the many benefits of nanotechnology. All ideas about future applications of nanotechnology in food do not closely resemble with the currently available food and processing technologies. Even though such futuristic speculations are probably not the aim of present-day research, the fact that they are suggested in public media influences the public awareness about food based on nanotechnology. Some of these are that our grandchildren will eat vegetarian "meat" tasting the same as animal meat to guarantee a sustainable food supply for the whole world population or that we need food produced with nanotechnology as a form of preventive medicine. Incorporating many kinds of artificial ingredients in novel chocolate bars with some unforeseen effects for the unsuspecting consumer. This imaginative yet not totally impossible idea keeps popping up in the futuristic speculation about food produced with nanotechnology. Thus, future of nanotechnology in food is expected to be extra-ordinary, which will change the entire scenario of food production, packaging, chemical framework, processing, analysis technique, marketing including consumer safety, but extensive research in this field can only bring the speculations into reality. Continous R&D work is again the only way for the establishment of concrete regulations for the applications of nanotechnology in food industry to ensure the quality, human health and environmental safety thus enhancing the perception of consumers towards nanofoods.

REFERENCES

[1] ObservatoryNANO, "Nanotechnology for Biodegradable and Edible Food Packaging", Working Paper Version, April 2010, available at: *www.observatorynano.eu.* (accessed June, 2011).

[2] deMoura, R.M., Aouada, F.A., Avena-Bustillos, R.J., McHugh, T.J., Krochta, J.M., and Mattoso, L.H.C., "Improved barrier and mechanical properties of novel hydroxypropyl methylcellulose edible films with chitosan/tripolyphosphate nanoparticles", *Journal of Food Engineering,* 92, 2009, pp. 448–453.

[3] Torres-Giner, S., Gimenez, E., and Lagaron, J.M., "Characterization of the morphology and thermal properties of Zein Prolamine nanostructures obtained by electrospinning", *Food Hydrocolloids*, 22, 2008, pp. 601-614.

[4] Yao, C., Li, X., and Song, T., "Electrospinning and crosslinking of zein nanofiber mats", *Journal of Applied Polymer Science*, 103, 2007, pp. 380-385.

[5] Corradini, E.A., Souto, E., Carvalho, A.J.F., Curvelo, A.A.S., and Mattoso, L.H.C., "Mechanical and morphological characterization of starch/zein blends plasticized with glycerol", *Journal of Applied Polymer Science*, 101, 2006, pp. 4133-4139.

[6] Bradley, E.L., Castle, L., and Chaudhry, Q., "Applications of nanomaterials in food packaging with a consideration of

opportunities for developing countries", *Trends in Food Science & Technology*, 22, 2011, pp. 604-610.

[7] Lagaron, J.M., and Lopez-Rubio, A., "Nanotechnology for bioplastics: opportunities, challenges and strategies", *Trends in Food Science & Technology*, 22, 2011, pp. 611-617.

[8] Morris, V.J., and Parker, R., "Natural and designed self-assembled nanostructures in foods", *The World of Food Science: Food Nanotechnology,* 4, 2008, available at: *http:// www. worldfoodscience. org /cms/?pid=1004050* (accessed February, 2010).

[9] Nanoscale Science and Engineering for Agriculture and Food Systems – a report from the USDA workshop, 2003, available at: *www.nseafs.cornell.edu/web.roadmap.pdf* (accessed June, 2012).

[10] Joseph, T., and Morrison, M., "Nanotechnology in Agriculture and Food", 2006, available at. http://www.nanoforum.org/ dateien/temp/nanotechnology%20in%20agricult ure%20and%20 food.pdf?08122006200524 (accessed January, 2008).

[11] Chaudhry Q., Scotter M., Blackburn J., Ross B., Boxall A., and Castle L., "Application and implications of nanotechnologies for the food sector", *Food Additives & Contaminants*, 25(3), 2008, pp. 241-258.

[12] Park, H.J., Chinnan, M.S., and Shewfelt, R.L., "Edible coating effects onstorage life and quality of tomatoes", *Journal of Food Science,* 59(3), 1994, pp. 568-570.

[13] Cursino, L., Li, Y., Zaini, P.A., De La Fuente, L., Hoch, H.C., and Burr, T.J., "Twitching motility and biofilm formation are associated with tonB1 in ***Xylella fastidiosa***", *FEMS Microbiology Letters*, 299, 2009, pp. 193-199.

[14] Zaini, P.A., De La Fuente, L., Hoch, H.C., and Burr, T.J., "Grapevine xylem sap enhances biofilm development by ***Xylella fastidiosa***", *FEMS Microbiology Letters*, 295, 2009, pp. 129-134.

[15] Branton, D., Deamer, D.W., Marziali, A., Bayley, H., Benner, S.A., Butler, T., et al., "The potential and challenges of nanopores sequencing", *Nature Biotechnology*, 26(10), 2008, pp. 1146-1153.

[16] Chaudhry, Q., and Castle, L., "Food applications of nanotechnologies: An overview of opportunities and challenges for developing countries", *Trends in Food Science & Technology,* 22, 2011, pp. 595-603

[17] **Paul, S.K,** Sahu, J.K**.** *Nanotechnology in Food Processing. In: Introduction to Advanced food processing technologies.* Sahu, J.K. (ed.), *CRC press*, ISBN 9781439880715, 2014.

[18] *http://www.nanoid.co.uk/nanofoods.html*, (accessed February, 2010).

[19] Alfadul, S. M., and Elneshwy, A. A., "Use of nanotechnology in food processing, packaging and safety: review", *African Journal of Food, Agriculture, Nutrition and Development*, 10(6), 2010, pp. 2719-2739.

[20] Huang, Y., Chen, S., Bing, X., Gao, C., Wang, T., and Yuan, B., "Nanosilver migrated into food-simulating solutions from commercially available food fresh containers", *Packaging Technology and Science*, 24 (5), 2011, pp. 291-297.

[21] Bouwmeester, H., Dekkers, S., Noordam, M., Hagens,W., Bulder, A., de Heer, C., et al., "Health impact of nanotechnologies in food production", *RIKILT/RIVM Report,* 2007.014, available at: *http://www.rikilt.wur.nl/NR/rdonlyres/BDEEDD31-F58C-47EBA0AA23CB9956CE18/54352/ R20 07014 .pdf* (accessed March 2008).

[22] Bhupinder S.S., "Food nanotechnology-an overview*",* *Nanotechnology, Science and Applications*, 3, 2010, pp. 1-15.

[23] *http://www.agromicron.com/BTP.htm,* (accessed on 22 September 2012).

[24] *http://www.goodfood-project.org/*, (accessed on 22 September 2012).

[25] *http://www.aquanova.de/product-micelle.htm*,(accessed on 22nd September, 2012).

[26] Deschamps, B., Musaji, N., and Gillespie, J.A., "Food effect on the bioavailability of two distinct formulations of megestrol acetate oral suspension", *International Journal of Nanomed*, 4, 2009.

[27] *http://www.smartwoman.royalbodycare.com/ Nanotechnology_ Revolution.aspx* (accessed September, 2012)

[28] Li, X., Zhou, Y., Zheng, Z., Yue, X., Dai, Z., Liu, S., et al., "Glucose biosensor based on nanocomposite films of CdTe quantum dots and glucose oxidase", *Langmuir*, 25(11), 2009, pp. 6580-6586.

[29] Chen, H., and Yada, R., "Nanotechnologies in agriculture: New tools for sustainable development", *Trends in Food Science & Technology*, 22, 2011, pp. 585 – 594.

[30] http://www.oilfresh.com/of1000.html, (accessed September, 2012).

[31] Sabine, G., André, G., Myrtill, S., Michael, N., and Ulrich, F. "Nanoparticles and nanostructured materials in the food industry", *Nano-trust dossiers*, 004, 2010, pp. 1-5.

[32] Food safety authority of Ireland, *The relevance for food safety of applications of nanotechnology in the food and feed industries*, 2008, ISBN 1-904465-59-5, available at. www.fsai.ie (accessed September 2012).

[33] Avella, M., DeVlieger, J.J., Errico, M.E., Fischer, S., Vacca, P., and Volpe, M.G., "Biodegradable starch/clay nanocomposite films for food packaging applications", *Food Chemistry*, 93, 2005, pp. 467-474.

[34] Bradley, E.L., Castle, L., and Chaudhry, Q., "Applications of nanomaterials in food packaging with a consideration of opportunities for developing countries", *Trends in Food Science & Technology*, 22, 2011, pp. 604-610.

[35] EFSA, "21st list of substances for food contact materials, scientific opinion of the panel on food contact materials, enzymes, flavourings and processing aids (CEF) (question No EFSA-Q-2005- 151, EFSA-Q-2006-324, EFSA-Q-2006-323), adopted on 27 November 2008", *The EFSA Journal,* 888-890, 2008, pp. 1-14.

[36] Simon, P., Chaudhry, Q., and Bakos, D., "Migration of engineered nanoparticles from polymer packaging to food e a physicochemical view", *Journal of Food & Nutrition Research*, 47(3), 2008, pp. 105-113.

[37] Tiede, K., Boxall, A. B. A., Tear, S. P., Lewis, J., David, H., and Hassellov, M., "Detection and characterization of engineered nanoparticles in food and the environment", *Food Additives & Contaminants*, 25, 2008, pp. 795-821.

[38] Card, J. W., and Magnuson, B. A., "A method to assess the quality of studies that examine the toxicity of engineered nanomaterials", *International Journal of Toxicology*, 29(4), 2010, pp. 402-410.

[39] Cui, D., Tian, F., Ozkan, C. S., Wang, M., and Gao, H., "Effect of single wall carbon nanotubes on human HEK293 cells", *Toxicology Letters*, 155(1), 2005, pp. 73-85.

[40] Chun, A.L., "Will the public swallow nanofood?" *Natural Nanotechnology*, 4, 2009, pp. 790–791.

[41] Chau, C. F., Wu, S. H., and Yen, G. C., "The development of regulations for food nanotechnology", *Trends in Food Science & Technology*, 18(5), 2007, pp. 269-280.

[42] Lyons, K., and Whelan, J., "Community engagement to facilitate,legitimize and accelerate the advancement of nanotechnologies in Australia", *NanoEthics*, 4(1), 2010, pp. 53-66.

[43] NICNAS, "National industrial chemicals notification and assessment scheme", *Australian Government Gazette*, 2010.

[44] Mittal, A., "Nanotechnology: Nanomaterials are widely used in commerce, but EPA faces challenges in regulating risk", *Washington: United States Government Accountability Office*, 2010.

[45] Corley, E., Scheufele, D., and Hu, Q., "Of risks and regulations: how leading US nanoscientists form policy stances about nanotechnology", *Journal of Nanoparticle Research*, 11(7), 2009, pp. 1573-1585.

[46] Bowman, D. M., and Hodge, G. A., "Nanotechnology: mapping the wild regulatory frontier", *Futures*, 38(9), 2006, pp. 1060-1073.

An Open Loop Method for Time Minimizing Transportation Problem with Mixed Constraints

Swati Agarwal[1], Shambhu Sharma[2]

[1]*Research Scholar, Department of Mathematics, Dayalbagh Educational Institute, Dayalbagh, Agra, India*
[2]*Department of Mathematics, Dayalbagh Educational Institute, Dayalbagh, Agra, India*

Abstract: **In real world situations, different sources and destinations impose different restrictions on supply and demand respectively according to their availability and requirement because of the changing economic and environmental conditions. It is also important that the time required for transportation should be minimum. Keeping this in mind, a time minimizing transportation problem with mixed constraints (TMTP-MC) is investigated in which the objective is to minimize the maximum of the total time that is taken to accomplish the requirements of n demand points using the capacities of m supply points. An open loop method has been developed to improve the initial basic feasible solution by shifting the basic cells to other basic cells or non-basic cells having less time. An algorithm is developed to determine an optimal solution for TMTP-MC. The proposed algorithm is found to be conceptually simple and easy to implement. Finally, a numerical illustration has been presented to demonstrate how this algorithm can be used to obtain optimal solution for TMTP-MC.**

1. INTRODUCTION

The time minimizing transportation problem with mixed constraints (TMTP-MC) we consider in this paper is an extension of a classical time minimizing transportation problem (TMTP). TMTP was originally studied by P. L. Hammer [6]. In 1971, Garfinkel and Rao [5] developed a threshold algorithm for the solution of the TMTP. Szwarc [10] précised Hammer's algorithm and proposed a review of the proof of a result in Hammer's paper. He also provided an extensive survey of the solution of TMTP.

The TMTP focuses attention on determining the quantity of a uniform (homogeneous) commodity transported from a source (i.e. factory where the commodity is manufactured) to the respective destination (i.e. warehouse where the commodity is to be distributed) satisfying the given supply and demand limits so that the transportation work is to be finished in minimum time. This problem actually minimizes the maximum of transportation time needed between a supply point and a demand point such that the distribution between the two points is positive. The aim is to minimize the time of transportation which remains independent of the amount of commodity transported. It is assumed that the carriers have enough capacity to carry goods from an origin to a destination in a single trip and, they start simultaneously from their respective origins. The TMTP is come across in connection with transportation of perishable goods whose shelf life is low, with the delivery of emergency supplies, fire supplies, ambulance services or when military equipment are to be delivered from their bases to fronts where prompt delivery is very necessary.

In literature, a good amount of research [2, 5, 7, 8, 9, 10] is available to obtain an optimal solution for the time minimizing transportation problem with equality constraints but the problem with mixed constraints is still untouched by the researchers. The TMTP-MC is widely useful in many real life situations where different sources and destinations impose different restrictions on supply and demand respectively according to their availability and requirement. Some sources want to supply exactly the fixed amount of goods. However, some other sources do not want to supply the amount less than a fixed amount. This case arises for the big factories, companies etc. Rest other sources are not able to supply more than a fixed amount of goods. This case arises for small factories, companies, etc. Similar conditions occur for the destinations as well. Due to the sources and destinations having mixed nature, the problem is said to be a TMTP-MC.

2. MATHEMATICAL FORMULATION OF THE PROBLEM

The mathematical model for time minimizing transportation problem is to find t_{ij} and x_{ij} which

$$\text{Minimize } Z = \max_{i,j} \left\{ t_{ij} \,/\, x_{ij} > 0 \right\}$$

Subject to the constraints

$$\begin{cases} \sum_{j=1}^{n} x_{ij} \geq a_i, & i \in \alpha_1 \\ \sum_{j=1}^{n} x_{ij} = a_i, & i \in \alpha_2 \\ \sum_{j=1}^{n} x_{ij} \leq a_i, & i \in \alpha_3 \\ \sum_{i=1}^{m} x_{ij} \geq b_j, & j \in \beta_1 \\ \sum_{i=1}^{m} x_{ij} = b_j, & j \in \beta_2 \\ \sum_{i=1}^{m} x_{ij} \leq b_j, & j \in \beta_3 \\ x_{ij} \geq 0 \end{cases}$$

$\alpha_i > 0, \forall i \in I$; $\beta_j > 0, \forall j \in J$

$I = \alpha_1 \cup \alpha_2 \cup \alpha_3 = \{1,2.....m\}$ = set of index of supply points.

$J = \beta_1 \cup \beta_2 \cup \beta_3 = \{1,2.....n\}$ = set of index of demand points.

where

a_i = amount of commodity available at ith supply point

b_j = amount of commodity required at jth demand point

x_{ij} = amount of commodity transporting from ith supply point to jth demand point

m = number of supply points

n = number of demand points

t_{ij} = time required for transporting x_{ij} amount of commodity from ith supply point to jth demand point

3. THEORETICAL DEVELOPMENT

To obtain the optimal solution of the problem it is necessary to search an initial basic feasible solution of the problem.

3.1. Initial Basic Feasible Solution

Let us consider a time minimizing transportation problem with mixed constraints (TMTP-MC) involving *m* origins and *n* destinations. Considering, the carriers have enough capacity to transport goods from an origin to a destination in a single trip. It follows that time t_{ij} does not depend on amount of commodity x_{ij} . In 1974, Brigden [3] gave some necessary and sufficient conditions for the existence of a feasible solution for transportation problem with mixed constraints. These conditions are also applicable to TMTP-MC.
Hence, it is always possible to get an initial basic feasible solution to TMTP-MC if it satisfies one of the following conditions:

3.1.1. Necessary and sufficient conditions for the existence of a feasible solution

(i) $\alpha_1 \neq \phi$ and $\beta_1 \neq \phi$

(ii) $\alpha_1 = \phi$ and $\beta_1 \neq \phi$ with

$$\sum_{j \in \beta_1} b_j + \sum_{j \in \beta_2} b_j \leq \sum_{i=1}^{m} a_i$$

(iii) $\alpha_1 \neq \phi$ and $\beta_1 = \phi$ with

$$\sum_{i \in \alpha_1} a_i + \sum_{i \in \alpha_2} a_i \leq \sum_{j=1}^{n} b_j$$

(iv) $\alpha_1 = \phi$ and $\beta_1 = \phi$ with

$$\sum_{j \in \beta_2} b_j \leq \sum_{i=1}^{m} a_i \ , \ \sum_{i \in \alpha_2} a_i \leq \sum_{j=1}^{n} b_j$$

where, ϕ denotes the null set

The initial basic feasible solution can easily be attained by following a straightforward rule. Initiate the method by subtracting the least element of each row from all the elements of the corresponding row of the given transportation table. The element t_{ij} changes to t'_{ij} as follows:

$$t'_{ij} = t_{ij} - \min_j t_{ij} \qquad \forall \quad i = 1,2.....m$$

and then subtract the least element of each column from all the elements of the corresponding column of the transportation table obtained after row operation. The element t'_{ij} changes to t''_{ij} according as

$$t''_{ij} = t'_{ij} - \min_i t'_{ij} \qquad \forall \quad j = 1,2.....n$$

to get the transformed transportation table.

This will give rise to at least one zero in each row and each column. The least element of each row and each column are detected by these zeros. Now, find out the maximum of non-zero row minima and non-zero column minima.

i.e.

$$\max_{i,j}\{R_i, C_j\} = R_r \text{ or } C_s \qquad r \in \{1,2.....m\} \text{ and } s \in \{1,2.....n\}$$

where,

$$R_i = \min_j (t''_{ij} > 0) \qquad \forall \quad i = 1,2.....m$$

$$C_j = \min_i (t''_{ij} > 0) \qquad \forall \quad j = 1,2.....n$$

If $\max\{R_i, C_j\} = R_r$, then the zero cell of the rth row will be allocated if not, the zero cell of the sth column will be chosen for the allocation.

All allocations are assigned with the help of the table 3.1 which is designed in such a way that only the minimum amount of units is sufficiently assigned to satisfy the whole transportation schedule.

Table 3.1- Assignment of cells

Supply(a_i)	**Demand**(b_j)	**Assign Unit**
$\leq$	$\leq$	0
=	$\geq$	$\min(a_i, b_j)$
$\geq$	$\geq$	$\min(a_i, b_j)$
$\leq$	$\geq$	$\min(a_i, b_j)$
$\geq$	$\leq$	$\min(a_i, b_j)$
=	=	$\min(a_i, b_j)$
=	$\leq$	$\min(a_i, b_j)$
$\leq$	=	$\min(a_i, b_j)$
$\geq$	=	$\min(a_i, b_j)$

Moreover, the row (or column) satisfying the maximum limit of demand and supply will be exhausted. After allocating the first cell, delete the exhausted row or column or both to get the reduced table. In the reduced table, perform the same operation to allocate the second cell. Continuing this process, we will come at the stage where all the demands b_j and supplies a_i corresponding to $i \in \alpha_1 \cup \alpha_2$ and $j \in \beta_1 \cup \beta_2$ are exhausted.

The solution so obtained is our initial basic feasible solution (I.B.F.S.) and the corresponding value of Z is

$Z^{(0)} = \max_{i,j}\{t_{ij} / x_{ij} > 0\} = t_{pq}{}^{(0)}$ where, $Z^{(0)}$ is the maximum time having positive allocations at initial stage. Note that (p,q) cell may or may not be unique.

Remarks

1. In case when $\max\{R_i, C_j\}$ties, try to choose the row or column with maximum value having one zero cell or break tie arbitrarily.
2. In case when two or more zero cells exist in each row or each column, choose the cell arbitrarily for allotment.
3. The basic cells having zero allocation can be reallocated if necessary. As it is known that, zero allocation exhibits no allocation in the cells.

After obtaining I.B.F.S., we will proceed to its improvement.

3.2. Improvement of the Basic Feasible Solution to Optimal Solution

In this section, we have discussed about how the initial basic feasible solution be improved to get the optimal solution.

Here we want to improve the initial basic feasible solution to get the new improved solution. This can be done by vacating the current basic cell having maximum time. In order to vacate that cell, we can shift the allotment of that cell to its corresponding row or column in the cells having time smaller than that basic cell. The cells whose time is greater than the time in (p,q) cell are of no use, so they can be blocked.

During improvisation, the shifting of allotment can be done partially or wholly i.e., the allotment (x_{ij}) in basic cell with maximum time has been shifted partially or wholly to the other basic cell or non-basic cell having less time as compared to the basic cell having maximum time.

Let the amount to be shifted be $\theta \le x_{pq}$. It is known that in the problem with equality constraints, closed loops were formed to shift the basic cell to a non-basic cell and also helps in determining the non-basic cell eligible to enter into the basis. For making closed loops, a basic cell is targeted to become a non-basic cell. In doing so, θ is to be subtracted from the allocation of that basic cell (partially or wholly) and to make supply and demand balanced, the same amount of θ is to be added to the cell eligible to enter into the basis. Iteratively, the closed loop can be completed. θ is taken as long as the solution remains non-negative such that $x_{ij} - \theta \ge 0$ and $x_{ij} + \theta > 0$. It is also known that only the even number of cells can participate in closed loops.

But in the problems with mixed constraints, it is not required to complete the loop to make supply and demand balanced. To deal with such kind of problems open loops have been introduced which are alike closed loops except the following conditions:

i) basic cell having maximum time (initial cell) is not necessarily a terminal cell,

ii) any number of non-basic cells can enter into the basis besides the solution satisfies the non-negativity,

iii) two open loops can be formed simultaneously from same initial cell,

iv) minimum 2 cells are enough to form an open loop.

The criterion for shifting the basic cell is given in table 3.2

Table 3.2- Shifting criterion of basic cells

	Supply(a_p)	**Demand**(b_q)	**No. of units (θ) shifted to Row/Column**
1.	$=/\ge$	$=/\ge$	
(a)	$\sum_{j=1}^{n} x_{pj} - a_p > 0$	$\sum_{i=1}^{m} x_{iq} - b_q > 0$	$\min\left[\left(\sum_{i=1}^{m} x_{iq} - b_q\right), \left(\sum_{j=1}^{n} x_{pj} - a_p\right)\right]$ units to row/column
(b)	$\sum_{j=1}^{n} x_{pj} - a_p = 0$	$\sum_{i=1}^{m} x_{iq} - b_q > 0$	$\min\left[\left(\sum_{i=1}^{m} x_{iq} - b_q\right), x_{pq}\right]$ units to row

(c)	$\sum_{j=1}^{n} x_{pj} - a_p > 0$	$\sum_{i=1}^{m} x_{iq} - b_q = 0$	$\min\left[x_{pq}, \left(\sum_{j=1}^{n} x_{pj} - a_p \right) \right]$ units to column
(d)	$\sum_{j=1}^{n} x_{pj} - a_p = 0$	$\sum_{i=1}^{m} x_{iq} - b_q = 0$	x_{pq} units to row and column both
2.	$=/\geq$	$\leq$	
(a)	$\sum_{j=1}^{n} x_{pj} - a_p > 0$	_	$\left(\sum_{j=1}^{n} x_{pj} - a_p \right)$ units to row/column
(b)	$\sum_{j=1}^{n} x_{pj} - a_p = 0$	_	x_{pq} units to row
3.	$\leq$	$=/\geq$	
(a)	_	$\sum_{i=1}^{m} x_{iq} - b_q > 0$	$\left(\sum_{i=1}^{m} x_{iq} - b_q \right)$ units to row/column
(b)	_	$\sum_{i=1}^{m} x_{iq} - b_q = 0$	x_{pq} units to column
4.	$\leq$	$\leq$	x_{pq} units to row/column

According to the criteria shown in above table, we can shift the amount from the cell (p, q) to the cell in its row or column without affecting the corresponding demand and supply of the cell. But, whether this shifted amount disturbs the demand and supply of the new cell, where it is shifting? In the context of this question, we have the following cases:

i. If the amount does not disturb the demand and supply of the new cell, then that cell will be the terminal cell.

ii. If the amount disturbs the demand and supply of the new cell, then that amount will pass on to the next new cell in a row or column of the current new cell. It means that we have to search a path starting from (p, q) cell connecting the basic or non-basic cell having less time than that of (p, q) cell and reaching to cell where the shifted amount does not disturb the demand and supply of the last cell of the path. That last cell here is defined as terminal cell.

Now, the question arises here is to how we search the terminal cell.

3.3. Selection of terminal cell

In this section, the criterion of selecting the terminal cells has been discussed.

Here, the set of cells where open loop can terminate in order to improve the basic feasible solution is denoted by T_C.

There are two cases arise in selection of the terminal cells which are as follows:

Case 1- If the shifting path goes from $(p,q) \to (p,a) \to (b,a) \ldots\ldots\ldots (h,i)$ i.e. towards p^{th} row.

$$T_C = \left[(i,j) / t_{ij} < t_{pq}, \quad \forall\ j \in \beta_1 \right]$$

In case when β_1 is absent

$$T_C = \left[(i,j) / t_{ij} < t_{pq}, \text{s.t. } b_j - \sum_{i=1}^{m} x_{ij} \geq \theta\ \forall\ j \in \beta_3 \right]$$ but if $b_j - \sum_{i=1}^{m} x_{ij} < \theta\ \forall\ j \in \beta_3$, shift $b_j - \sum_{i=1}^{m} x_{ij}$ units to j^{th} column and search for another $j \in \beta_3$ to shift the remaining $\left[\theta - \left(b_j - \sum_{i=1}^{m} x_{ij} \right) \right]$ units.

Case 2- For the shifting path $(p,q) \to (r,q) \to (r,t) \ldots\ldots\ldots (o,z)$ i.e. towards q^{th} column.

$$T_C = \left[(i,j) / t_{ij} < t_{pq}, \quad \forall\ i \in \alpha_1 \right]$$

In case when α_1 is absent

$$T_C = \left[(i,j) / t_{ij} < t_{pq}, \text{s.t. } a_i - \sum_{j=1}^{n} x_{ij} \geq \theta\ \forall\ i \in \alpha_3 \right]$$ but if

$a_i - \sum_{i=1}^{m} x_{ij} < \theta \ \forall i \in \alpha_3$, shift $a_i - \sum_{i=1}^{m} x_{ij}$ units to i^{th} row

and search for another $i \in \alpha_3$ to shift the remaining $\left[\theta - \left(a_i - \sum_{j=1}^{n} x_{ij}\right)\right]$ units.

Remark- The terminal cells will never exist in i^{th} row/ j^{th} column $\forall$ $i \in \alpha_2$ and $j \in \beta_2$.

After searching for the terminal cell, we shift the amount to the terminal cell to get the improved solution and the corresponding value of Z as $Z^{(1)}$. Repeating the process iteratively, we can obtain $Z^{(2)}$, $Z^{(3)}$ …and so on.

Now question comes here, at what extent we can improve the solution. For this, we need an optimality criterion, which is given below:

3.4. Optimality condition

The solution $t_{pq}{}^{(n)} = \min_{i,j}\{\max t_{ij} / x_{ij} > 0\} = Z^{(n)}$ is said to be optimal to the Time Minimizing Transportation Problem with Mixed Constraints (TMTP-MC), if one of the given conditions holds:

i.) $t_{pj} \geq t_{pq}$ and $t_{iq} \geq t_{pq}$
$j \neq q$ $i \neq p$

ii) $t_{pj} < t_{pq}$, for some $j = 1,2.....n$ and $t_{iq} \geq t_{pq}$, for the shifting path $(p,q) \to (p,a) \to (b,a).....(h,i)$
$j \neq q$ $i \neq p$
$s.t.\ \sum_{i=1}^{m} x_{ia} - b_a = 0$ with $x_{ba} < \theta$ where, $a \in \beta_2 \cup \beta_3$ or, $(h,i) \notin T_C$

and/or, $(p,q) \to (r,q) \to (r,t).....(o,z)$

iii.) $t_{pj} \geq t_{pq}$ and $t_{iq} < t_{pq}$, for some $i = 1,2.....m$, for the shifting path $(p,q) \to (p,a) \to (b,a).....(h,i)$.
$j \neq q$ $i \neq p$

and/or, $(p,q) \to (r,q) \to (r,t).....(o,z)$

iv.) $s.t.\ \sum_{j=1}^{n} x_{rj} - a_r = 0$ with $x_{rt} < \theta$ where,
$r \in \alpha_2 \cup \alpha_3$ or, $(o,z) \notin T_C$.

$t_{pj} < t_{pq}$, for some $j = 1,2.....n$ and $t_{iq} < t_{pq}$, for some $i = 1,2.....m$, for the shifting path
$j \neq q$ $i \neq p$

$(p,q) \to (p,a) \to (b,a).....(h,i)$ $s.t.\ \sum_{i=1}^{m} x_{ia} - b_a = 0$
with $x_{ba} < \theta$ where, $a \in \beta_2 \cup \beta_3$ or, $(h,i) \notin T_C$.

and/or, $(p,q) \to (r,q) \to (r,t).....(o,z)$
$s.t.\ \sum_{j=1}^{n} x_{rj} - a_r = 0$ with $x_{rt} < \theta$ where,
$r \in \alpha_2 \cup \alpha_3$ or, $(o,z) \notin T_C$.

Remark

An open loop algorithm terminates in finite number of steps because the minimum time attained at each iteration corresponds to an extreme point of the set of feasible solutions of TMTP-MC and there is a finite number of extreme points of the feasible set.

Summarizing all the results obtained above, an algorithm to solve TMTP-MC has been developed which is presented in section 4.

4. ALGORITHM

An algorithm of the TMTP-MC to enumerate an optimal solution consists of the following steps:

Step 0: Construct the transportation table for the given problem.

Step 1: Subtract the least element of each row from all the elements of the corresponding row of the given transportation table.

Step 2: Subtract the least element of each column from all the elements of the corresponding column of the transportation table obtained in step 1.

Step 3: Identify the row (or column) with the maximum of non-zero row minima and column minima and allocate the zero cell of that row (or column) using the Table 3.1.

Step 4: Row (or column) satisfying the maximum limit of demand and supply point will be eliminated. Now, go to step 1 to allocate the second cell. Continuing in this way, an initial basic feasible solution is obtained.

Step 5: Starting from the basic cell having maximum time, draw an open-loop to improve the solution by assigning negative sign (-) at the starting point and alternatively assigning positive (+) and negative (-) signs at the nodes of the open-loop.

Step 6: Add the value of θ (the value of θ can be considered with the help of table 3.2.) to all the cells of the open loop marked with positive (+) sign and subtract it from those cells marked with negative (-) sign. In this way, the current solution becomes improved.

Step 7: Repeat steps 5 to 7 until an optimality condition is achieved.

5. NUMERICAL ILLUSTRATION

In this section, we present a detailed example for an illustration of the above algorithm.

Example: Consider a time minimizing transportation problem with three sources O_1, O_2 and O_3 and five destinations D_1, D_2, D_3, D_4 and D_5.

Table- 5.1

	D_1 D_2 D_3 D_4 D_5					
O_1	8	6	8	6	10	≤ 80
O_2	9	8	9	6	7	≥ 120
O_3	11	10	8	13	9	= 140
	= 40 ≥ 40 = 60 ≤ 80 ≥ 80					

Step 1-2: Subtracting the row minima and column minima from all the elements of the corresponding row and corresponding column respectively. We get the following transportation table 5.2.

Table- 5.2

	D_1 D_2 D_3 D_4 D_5					
O_1	0	0	2	0	3	≤ 80
O_2	1	2	3	0	0	≥ 120
O_3	1	2	0	5	0	= 140
	= 40 ≥ 40 = 60 ≤ 80 ≥ 80					

Step 3: The maximum of non-zero row minima and non-zero column minima is 5 corresponding to the column 4 as shown in table 5.4. Now allocate the zero cell of 4th column with 80 units. We get the table as given below:

Table- 5.3

	D_1 D_2 D_3 D_4 D_5						Row Min.
O_1	0	0	2	0	3	≤ 80	2
O_2	1	2	3	80 0	0	$\geq$ ~~120~~ 40	1
O_3	1	2	0	5	0	= 140	1
	= 40 ≥ 40 = 60 ≤ ~~80~~ 0 ≥ 80						
Col. Min.	1 2 2 5 3						

Step 4: 4th column of the above table satisfies the maximum limit of demand (b_4) .Therefore, it will cancelled out and we will continue to allocate the other cells.

Table- 5.4

	D_1 D_2 D_3 D_5					Row Min.
O_1	0	0	2	3	≤ 80	2
O_2	1	2	3	40 0	$\geq$ ~~40~~ 0	1
O_3	1	2	0	0	= 140	1
	= 40 ≥ 40 = 60 ≥ ~~80~~ 40					
Col. Min.	1 2 2 3					

Proceeding in a similar way, we have the following allocations in the given time minimizing transportation table:

Table-5.5

	D_1 D_2 D_3 D_4 D_5					
O_1	8	6	8	6	10	≤ 80
O_2	9	40 8	9	80 6	40 7	≥ 120
O_3	40 11	10	60 8	13	40 9	= 140
	= 40 ≥ 40 = 60 ≤ 80 ≥ 80					

Here, the Initial Basic Feasible Solution has obtained with $Z^{(0)} = 11$: **Step 5-6:** Starting from the (3, 1) cell having maximum time 11, an open loop is formed to vacate that cell. To satisfy the corresponding demand and supply of that cell, two open loops have formed and the cell (3, 4) can be blocked as shown in the following table.

Table-5.6

	D_1 D_2 D_3 D_4 D_5					
O_1	8	6	8	6	10	≤ 80
O_2	9	40 8	9	80 6	40 7	≥ 120
O_3	40 11	10	60 8	13	40 9	= 140
	= 40 ≥ 40 = 60 ≤ 80 ≥ 80					

Now, shifting the allotment of cell (3, 1) to cell (2, 1) and cell (3, 5) as directed in table 5.6 we will get the new improved time i.e., $Z^{(1)} = 9$ with $\sum x_{pq} = 120$

Table-5.7

	D_1 D_2 D_3 D_4 D_5										
O_1	8		6		8		6		10		≤ 80
O_2	40	9	40	8	9		80	6	40	7	≥ 120
O_3	11		10		60	8	13		80	9	= 140
	= 40 ≥ 40 = 60 ≤ 80 ≥ 80										

In the above table, the allotment of cell (2, 1) has been shifted to the cell (1, 1) for further improvement. Here, we get $Z^{(2)} = 9$ with $\sum x_{pq} = 80$. The allotment of cell (3, 5) cannot be shifted to its corresponding row and column, so the solution is optimal by the (iv) optimality criteria.

Table-5.8

	D_1 D_2 D_3 D_4 D_5										
O_1	40	8	6		8		6		10		≤ 80
O_2	9		40	8	9		80	6	40	7	≥ 120
O_3	11		10		60	8	13		80	9	= 140
	= 40 ≥ 40 = 60 ≤ 80 ≥ 80										

Hence, we get the optimal solution for the given TMTP-MC and the corresponding value of $Z^{(2)} = 9$ with $x_{21} = 40, x_{22} = 40, x_{24} = 80, x_{25} = 40, \; x_{33} = 60$ and $x_{35} = 80$

6. CONCLUSION

We have developed a simple algorithm for solving a TMTP-MC. The method presented and discussed above gives us the optimal value in finite number of iterations. The proposed algorithm is easy to understand and apply. It can serve the managers by providing the solution to a variety of distribution problems with mixed constraints. Carriers with limited capacity to carry goods in a single trip also reflect more practical situation in TMTP-MC and are needed for further study.

REFERENCES

[1] Bansal, S., and Puri, M.C., "A min max problem", *Zeitschrift für Operations Research*, 24, 1980, pp. 191-200.

[2] Bhatia, H.L., Swarup, K., and Puri, M.C., "A procedure for time minimization transportation problem", *Indian Journal of Pure and Applied Mathematics*, 8, 1977, pp. 920-929.

[3] Brigden, M.E.B., "A varient of the transportation problem in which the constraints are of mixed type", *Operational Research Quarterly*, 125, 3, 1974, pp. 437-445.

[4] Dantzig, G.B., *Linear programming and extensions*, Princeton University Press, Princeton, NJ.

[5] Garfinkel, R.S., and Rao, M.R., "The bottleneck transportation problem", *Naval Research Logistics Quarterly*, 18, 1971, pp. 465-472.

[6] Hammer, P.L., "Time minimizing transportation problem", *Naval Research Logistics Quarterly*, 16, 1969, pp. 345-357.

[7] Hitchcock, F.L., "The distribution of a product from several sources to numerous localities", *Journal of Mathematics and Physics*, 20, 1941, pp. 224-230.

[8] Pandian, P., and Natarajan, G., "A new method for solving bottleneck-cost transportation problems", *International Mathematical Forum*, 10, 2011, pp. 451-460.

[9] Sharma, J.K., and Swarup, K., "Time minimizing transportation problems", in *Proceedings of Indian Academy of Sciences-Mathematical Sciences*, 86, 1977, pp. 513-518.

[10] Szwarc, W., "Some remarks on the time transportation problem", *Naval Research Logistics Quarterly*, 18, 1971, pp. 473-485.

On Petri Net Generating all the Standard Basis for n-Dimensional Euclidean Space

Gajendra Pratap Singh

(Former Research Scholar)
Department of Applied Mathematics, Delhi Technological University
Shahbad Daulatpur, Main Bawana Road, Delhi-110042, India.
gajendraresearch@gmail.com

Abstract: **Petri nets are the prominent tools of current re- search in branch of discrete mathematics. They are invented by Carl Adam Petri in 1962, a tool for the study of certain discrete dynamical systems. Petri nets form directed bipartite graphs, together with an initial marking. Petri nets have a well known graphical representation in which transitions are represented as boxes and places as circles with directed arcs interconnecting them, to represent the flow relation between them. Petri net can be used as graphical tool to planning and designing such a system with given objectives, more effectively than flowcharts and block diagrams. In this paper, we will discuss a special class of Petri net, called 1-safe Petri net that contains '0', '1' digits as marking vectors in its reachability tree. Here, we will prove that a disconnected 1-safe Petri nets whose reachability tree on the firing of transitions at the $(n-1)_{th}$ stage contain all the standard basis e_i, $1 \leq i \leq n$ for n-dimensional Euclidean Space.**

Keywords: **1-safe Petri nets, directed graph, binary vectors, basis, Euclidean space**

1. INTRODUCTION

Petri nets are a graphical and mathematical tool applicable to model various kinds of dynamic event-driven systems such as computer networks etc. They are invented by Carl Adam Petri [2] in 1962 for describing and studying information processing systems that are characterized as concurrency, parallelism, synchronization etc. As a graphical tool, Petri net can be used for planning and designing a system with given objectives more practically effective than flowchart and block design diagrams. As a mathematical tool, it enables one to setup state equations, algebraic equations and other mathematical models which are govern the behavior of discrete dynamical systems. Petri nets also are useful for both practitioners as well as theoreticians. Practitioners can learn from theoreticians how to make their models more methodical, and theoreticians can learn from practitioners how to make their model more realistic. In this paper, the existence of a disconnected 1-safe Petri net which is isomorphic to n copies of graph $K2$ has been shown and its reachability tree on the firing of transitions at the $(n-1)th$ stage contains all the standard basis ei, $1 \leq i \leq n$ for n-dimensional Euclidean Space. In n-dimensional Euclidean space, the standard basis consists of n-distinct vectors $\{ei : 1 \leq i \leq n\}$, where ei denotes the vector with 1 in the ith coordinate and $0's$ elsewhere. These vectors are a basis in the sense that any other vectors can be expressed uniquely as a linear combination of these.

2. PRELIMINARIES

For standard terminology and notation on Petri nets, we refer the reader to Peterson [3]. In this paper, for the sake of better understanding of proof, we shall adopt the Jenson's matrix[1] form definition, which is as follows:

A *Petri net* is a 5-tuple $C = (P; T; I-; I+; _0)$, where

(a) P is a nonempty set of 'places',
(b) T is a nonempty set of 'transitions',
(c) $P \cap T = \emptyset$,
(d) $I-; I+ : P \times T \longrightarrow N$, where N is the set of nonnegative integers, are called the *negative* and the *positive* 'incidence functions' (or, 'flow functions') respectively,
(e) $\forall p \in P; \exists t \in T : I-(p; t) \neq 0$ or $I+(p; t) \neq 0$ and
$\forall t \in T; \exists p \in P : I-(p; t) \neq 0$ or $I+(p; t) \neq 0$,
(f) $_0 : P \rightarrow N$ is the *initial marking*.

In fact, $I-(p; t)$ and $I+(p; t)$ represent the number of arcs from p to t and t to p respectively. $I-$, $I+$ and $_0$ can be viewed as matrices of size $|P| \times |T|$, $|P| \times |T|$ and $|P| \times 1$, respectively.

As in many standard books (e.g., see [4]), Petri net is a particular kind of directed graph, together with an initial marking $_0$. The underlying graph of a Petri net is a directed, weighted, bipartite graph consisting of two kinds of nodes, called places and transitions, where arcs are either from a place to a transition or from a transition to a place. Hence, Petri nets have a well known graphical representation in which transitions are represented as boxes and places as circles with directed arcs interconnecting places and transitions to represent the flow relation. The initial marking is represented by placing a token in the circle representing a place pi as a black dot whenever $\mu^{O}(pi) = 1$, $1 \leq i \leq n = |P|$. In general, a *marking* $_$ is a mapping μ: $P \rightarrow N$. A marking μ can

hence be represented as a vector $\mu \in Nn$; $n = |P|$, such that the *ith* component of $\mu$is the value $\mu(pi)$.

Let $C = (P; T; I-; I+; \mu)$ be a Petri net. A transition $t \in T$ is said to be *enabled* at μif and only if $I-(p; t) \leq \mu(p)$, $\forall p \in P$. An enabled transition may or may not 'fire' (depending on whether or not the event actually takes place). After firing at μ, the new marking μ' is given by the rule

We say that *t fires at* $\mu$to yield μ' (or, that *t fires* $\mu$to μ'), and we write $\mu - \rightarrow t\ \mu'$, whence μ' is said to be *directly reachable* from μ. Hence, it is clear, what is meant by a sequence like

$$\mu^0 \xrightarrow{t_1} \mu^1 \xrightarrow{t_2} \mu^2 \xrightarrow{t_3} \mu^3 \ldots \xrightarrow{t_k} \mu^k,$$

which simply represents the fact that the transitions $t_1, t_2, t_3, \ldots, t_k$ have been successively fired to transform the marking μ^0 into the marking μ^k. The whole of this sequence of transformations is also written in short as $\mu^0 \xrightarrow{\sigma} \mu^k$, where $\sigma = t_1, t_2, t_3, \cdots, t_k$.

A marking μ is said to be *reachable from* μ^0, if there exists a sequence of transitions which can be successively fired to obtain μ from μ^0. The set of all markings of a Petri net C reachable from a given marking μ is denoted by $M(C, \mu)$ and, together with the arcs of the form $\mu^i \xrightarrow{t_r} \mu^j$, represents what in standard terminology called the *reachability graph* $R(C, \mu)$ of the Petri net C. If the reachability graph has no cycle then it is called *reachability tree* of the Petri net C.

A place in a Petri net is *safe* if the number of tokens in that place never exceeds one. A Petri net is *safe* if all its places are safe.

Let $C = (P,T, I^-, I^+, \mu^0)$ be a Petri net with $|P| = n$ and $|T| = m$, the incidence matrix $I = [a_{ij}]$ is an $n \times m$ matrix of integers, $|P| = n$ and $|T| = m$ and its entries are given by $a_{ij} = a_{ij}^+ - a_{ij}^-$ where $a_{ij}^+ = I^+(p_i, t_j)$ is the number of arcs from transition t_j to its output place p_i, known as positive incidence matrix and $a_{ij}^- = I^-(p_i, t_j)$ is the number of arcs from place p_i to its output transition t_j, known as negative incidence matrix. In other words, $I = I^+ - I^-$

The *preset* of a transition t is the set of all input places to t, i.e., ${}^\bullet t = \{p \in P : I^-(p, t) > 0\}$. The *postset* of t is the set of all output places from t, i.e., $t^\bullet = \{p \in P : I^+(p, t) > 0\}$. Similarly, $p's$ preset and postset are ${}^\bullet p = \{t \in T : I^+(p, t) > 0\}$ and $p^\bullet = \{t \in T : I^-(p, t) > 0\}$, respectively.

The *Hamming distance* between two bit-strings $u = u_1, u_2, \cdots, u_n$, $v = v_1, v_2, \cdots, v_n \in \{0, 1\}^n$ of length n is the number of bit positions in which u and v differ: $d_H^n(u, v) = |\{i \in \{1, 2, \cdots, n\} : u_i \neq v_i\}|$. The Hamming distance between 1011101 and 1001001 is two.

Let x_1, x_2, x_3 $\cdots$, x_n be vectors from n-dimensional Euclidean space and let α_1, α_2, α_3, $\cdots$, α_n be a system of scalars (real numbers). Then the vector

$$X = \alpha_1 x_1 + \alpha_2 x_2 + \alpha_3 x_3 + \cdots + \alpha_n x_n$$

is called a *linear combination* of the vectors x_1, x_2, x_3 $\cdots$, x_n. We also say that X is generated by the vectors x_1, x_2, x_3 $\cdots$, x_n.

If the linear combination $\alpha_1 x_1 \mid \alpha_2 x_2 \mid \alpha_3 x_3 \mid \cdots \mid \alpha_n x_n = 0$ implies that all the $\alpha_i' s - 0$, $\forall n$ then the linear combination is called *linearly independence*.

Let $B - \{x_1, x_2, x_3, \cdots, x_n\}$ be a finite subset of n-dimensional Euclidean space. Then B is called a *basis* if B spans Euclidean space and B is linearly independent.

3. SOME BASIC RESULTS

In this section, we discuss some observational results for 1-safe Petri net whose reachability tree contains standard basis that are the main results for this paper.

Theorem 3.1: Let $C = (P,T, I^-, I^+, \mu^0)$ with $|P| = n$ be a disconnected 1-safe Petri net isomorphic to $nK_2 : \odot \longrightarrow \square$. Then firing of the transitions at the initial marking $\mu^0(p) = 1$, $\forall p \in P$ in the $(n-1)^{th}$ stage generate every standard basis e_i, $1 \leq i \leq n = |P|$, for n-dimensional Euclidean space.

Proof: Let $C = (P,T, I^-, I^+, \mu^0)$ be a disconnected 1-safe Petri net isomorphic to $nK_2 : \odot \longrightarrow \square$.. Since $\mu^0(p) = 1$ $\forall p \in P$, all the transitions are enabled. In the first step of firing of n transitions, we get ${}^nC_1$ distinct binary n-vectors whose Hamming distance is 1 from the initial marking vector. At each of these n marking vectors, $(n - 1)$ transitions are enabled, and after firing give at least ${}^nC_2$ distinct marking vectors each of whose Hamming distance is 2 from the initial marking.

In general at stage $(n \quad 1)$, we get a set of at least ${}^nC_{n-1}$ new distinct binary n-vectors whose Hamming distance is $n-1$ from the initial marking, i.e., these have 1 in the i^{th} position otherwise 0, Hence, they are the required standard basis e_i, $1 \leq i \leq n = |P|$, for n-dimensional Euclidean space.

Theorem 3.2: Let $C = (P,T,I^-,I^+,\mu^0)$, $|P| = n$ be a 1-safe Petri net with $\mu^0(p) = 1$, $\forall p \in P$, then all the standard basis as the marking vectors in its reachability tree can be generated in either first stage of firing or $(n-1)^{th}$ stage of firing.

Proof: Let $C = (P,T,I^-,I^+,\mu^0)$, $|P| = n$ be a 1-safe Petri net with $\mu^0(p) = 1$, $\forall p \in P$. If $|T| < |P|$ then all the standard basis cannot be generated. Suppose $|T| \geq |P|$ then there will be two cases. In case one, all the standard basis will be generate in to the first step of firing of the transitions and in other case, by remark 3.4.2 in [5], which is stated as: In any 1-safe Petri net $C = (P,T,I^-,I^+,\mu^0)$, $|P| = |T| = n$, with $\mu^0(p) = 1$, $\forall p \in P$, at any stage in the dynamics of C when binary n-vectors at Hamming distance k from μ^0 are being generated all the binary n-vectors of Hamming distance less than k have already been generated. In this way at the $(n-1)^{th}$ stage we get the binary vectors whose Hamming distance from the initial marking is $(n-1)$ which are the required standard basis e_i, $1 \leq i \leq n = |P|$, for n-dimensional Euclidean space. ■

Proposition 3.1: If $I^-(p_i,t_j)$=1 $\forall i = j$ otherwise 0 $\forall i \neq j$ and $I^+(p_i,t_j)$=0, $\forall i,j$, then the Petri net C obtained by the incidence matrix $I = I^+ - I^-$ at the $\mu^0(p) = 1$,$\forall p \in P$ in the $(n-1)^{th}$ stage of firing of transitions contain the same number of standard basis as its incidence matrix.

Proof: Since $I^-(p_i,t_j)$=1 $\forall i = j$ otherwise 0 $\forall i \neq j$ and $I^+(p_i,t_j)$=0, $\forall i,j$ imply that $I = I^+ - I^- = -I^-$ which is corresponds to the identity matrix I_n. We know that an identity matrix I_n has n linearly independence columns. If each of the columns consider as the vectors e_i $\forall i$. Further, the Petri net C obtained by the incidence matrix is isomorphic to nK_2 :⊙⟶□. By Theorem 3.1, we get n standard basis e_i, $1 \leq i \leq n = |P|$, for n-dimensional Euclidean space. Therefore, C has the same number of standard basis as its incidence matrix.

Theorem 3.3: Any Petri net C obtained by $|{}^\bullet t| = |t^\bullet| = 1$ and $|{}^\bullet p| = |p^\bullet| = 1$ then at the initial marking $\mu^0(p) = e_i$, i.e., i^{th} component is 1 otherwise 0. Then the reachability tree contains every standard basis e_i, $1 \leq i \leq n = |P|$, for n-dimensional Euclidean space.

Proof: Since $|{}^\bullet t| = |t^\bullet| = 1$ and $|{}^\bullet p| = |p^\bullet| = 1$. Then it will form a cyclic in the Petri net. Further, $\mu^0(p) = e_i$ then the transition t_i is enabled and fire. After firing, we will get $\mu^1(p) = e_{i+1}$, and continuing this process till all the standard basis e_i, $1 \leq i \leq n = |P|$ obtained. ■

4. CONCLUSIONS

In this paper, we have discussed the generation of the standard basis for *n*-dimensional Euclidean space using 1-safe Petri nets. As we know that these standard basis are very much useful in vector space for the linear transformations of vectors.

One think about the characterize those Petri nets which has all the standard basis as the marking vectors. Further, we can also think about which set of vectors are linearly dependence and independence.

REFERENCES

[1] Jensen, K., *Coloured Petri nets*, Lecture notes in Computer Science, 254, Springer-Verlag, Berlin, 1986, 248-299.

[2] Petri, C.A., *Kommunikation mit automaten*, Schriften des Institutes fur Instrumentelle Mathematik, Bonn 1962.

[3] Peterson, J.L., *Petri net Theory and the Modeling of Systems*, Englewood Cliffs, NJ: Prentice-Hall, Inc., 1981.

[4] Reisig, W., *Petri nets*, Springer-Verleg, New York, 1985.

[5] Singh, G.P., *Some Advances in the theory of Petri nets*, a Ph.D. thesis submitted to The Faculty of Technology, University of Delhi, Delhi, India, 2013.

Support Vector Regression (SVR) Model to Predict the Boiling/Non-boiling Length of the Heated Tube in a Vertical Tube Thermosiphon Reboiler

Sadaf Zaidi

Aligarh Muslim University, Aligarh
Department of Chemical Engineering, Aligarh Muslim University, Aligarh-202002 (U.P)

Abstract: **Conventionally, the thermosiphon reboilers are being widely employed in petroleum, chemical and petrochemical industries as vaporizers, evaporators and reboilers. The hydrodynamics and heat transfer in a thermosiphon reboiler interact with each other making the process very complex. Prediction of the rates of heat transfer and thermally induced flow are the primary requirements for the design of thermosiphon reboilers. Some empirical models have been developed and published in literature by a number of workers for the prediction of the length of the boiling/non-boiling section of the heated tube. However, they suffer from critical infirmities. Thus, with the above observation in perspective and given the recent developments in the application of artificial intelligence techniques, the state-of-the-art technique called support vector machine (SVM) or specifically the SVM variant called Support Vector Regression (SVR) was employed for the first time to develop a model for predicting the length of the boiling/non-boiling section of the heated tube in a thermosiphon reboiler, for different single component liquids with wide variation in thermo physical properties and operating parameters. The choice of this technique was prompted by its many attractive features. Moreover, the extensive survey of the literature revealed that very little work had been reported on the application of SVR to chemical engineering problems in general and to heat transfer in particular. No work was found on the application of SVR to model a closed loop vertical tube thermosiphon reboiler.The SVR-based model developed in this study, based on the superior Structural Risk Minimization principle, has been found to be far more superior than any of the published models based on the Empirical Risk Minimization principle. The study has opened new vistas to apply SVR to the problems of chemical engineering in general and heat transfer and boiling heat transfer in particular.**

1. INTRODUCTION

A vertical tube thermosiphon reboiler represents effectively a pump-less system, in which natural, gravity-aided circulation takes place. Thermosiphon reboilers are being used in petroleum, chemical and petrochemical industries as vaporizers, evaporators and reboilers. Apart from this, the device is well adapted for heat transfer in situations prevailing in power plants, cooling systems for nuclear fuel rods in nuclear power reactors, refrigeration systems, pipe stills, and in the electronics industry. It also has relevant for efficiently transferring solar energy with little or no forced flow. The vertical tube thermosiphon reboiler has the advantages of excellent heat transfer rates, cheap manufacturing cost, easy cleaning, little maintenance, simplicity of construction, compactness and low operational costs. The frictional losses in the inlet and outlet piping and the cost of vapor line are minimized as the reboiler can be installed close to the column. The prediction of the rate of liquid circulation (thermally induced flow) and heat transfer is the primary requirement for the design and efficient operation of thermosiphon reboilers. Thermosiphon systems can be used in a wide range of operating temperatures and pressures. In almost all the applications, a subcooled liquid entering the tube gets heated by single phase convection and moves upwards. Depending upon the wall temperature conditions, subcooled boiling may get initiated at the surface. When the liquid attains saturation value, saturated boiling begins with the generation of net vapour, which increases resulting in various flow patterns ranging from bubbly to mist flow. The point at which the two phase begins is known as the incipient point of boiling (IPB) which corresponds to the condition of minimum degree of wall superheat required for the formation and detachment of the vapour bubble from the heated surface. Heat transfer coefficients at the onset of boiling are very high because of the nature of nucleate boiling and the increase in the velocity due to transition from single phase to a two-phase mixture. The IPB effectively divides the tube into two distinct regions; the non-boiling single phase and the two phase with entirely different modes of heat transfer. The prediction of the IPB is thus of paramount importance in the design of various process equipments operating on the thermosiphon reboiler principle. Engineering applications, in which the prediction of incipient boiling is necessary, are numerous. For instance, in some process applications dealing with thin film evaporation, nucleate boiling may not be a desirable phenomenon. However, in boiling water nuclear reactors, it is necessary to be able to predict the location of incipient boiling in the cooling channels, so that the downstream void distribution and the two phase pressure gradient can be determined. Various authors have proposed definitions of boiling incipience.

A number of studies have been conducted to understand the phenomenon of boiling incipience. Models have been proposed based on the semi-empirical approach for predicting the superheat for forced convection boiling in tubes. Important studies on boiling incipience include those by Murphy and Bergles [1], Yin and Messih [2], Hsu and Graham [3], Bergles and Rohsenow [4]. Yin and Abdel Messih [5] determined the liquid superheat during incipient boiling in a uniformly heated forced convection channel, and developed an analytical equation using Freon-11 as the test medium. Agarwal [6], Ali [7], Kamil [8] and Zaidi [9] gave empirical correlations to determine the length of heated tube required for the onset of fully developed boiling (Z_{OB}) in a vertical tube thermosiphon reboiler. Experimentally measured values of Z_{OB} were compared with those predicted by the above equations.

Shamsuzzoha, et al. [10] have carried out a theoretical analysis to develop an analytical equation for the incipient point of boiling, including the effect of submergence. The minimum degree of wall superheat required for the onset of fully developed boiling of liquids was related to their physical properties through the theoretically derived equation. The model was tested using the experimental data available in literature. Shamsuzzoha and Alam [11] have carried out an analysis to predict the boiling incipience in a natural circulation flow reboiler tube taking into consideration the effect of turbulent eddies and submergence. An equation has been proposed to estimate the wall superheat for different types of liquids.

Thus, with the above observations in mind and given the recent developments in the application of artificial intelligence techniques, it was decided to explore the possibility of using one such technique for developing a unified correlation for predicting circulation rate in a thermosiphon reboiler.

Data driven modeling have been finding increasing relevance and acceptability in process industries. Of these, the classical methods such as least-squares methods, the maximum likelihood methods and traditional ANN are based on empirical risk minimization (ERM) principle whereas the support vector machine (SVM) method is based on the structural risk minimization (SRM) principle. This enables the SVM to achieve an optimum network structure by striking a right balance between the complexity of the approximation of the given data and the complexity of the approximating function. SVM is a supervised learning theory from the field of machine learning applicable to both nonlinear classification called support vector classification (SVC) and regression or SVR. The crux of the SVM design is solving a quadratic programming (QP) problem with linear constraints, which depends on the training vectors and the selection of few kernel parameters. The solution of a QP problem provides us the necessary information for choosing the most important vectors known as support vectors (SV) among all the data, and these support vectors will play an important role of defining the discriminant hyperplane or predicting function.

The SVM method has been instrumental in heralding a new era in supervised learning paradigm. It has been successfully applied to many fields; some of which are pattern recognition, phase diagram assessment, molecular and materials design, trace element analysis, cancer diagnosis [12], image analysis, drug design, time series analysis, quality control of food, protein structure/ function and genomics [13]. SVM methods have been applied to regression problems with great success [14, 15]. The applicability of SVR-based models in the field of chemical engineering has been well demonstrated [16,17]. Very little work has been reported in literature on the application of SVR to heat transfer in general and boiling heat transfer in particular. Such studies include those by Gandhi et al. [18]and Zaidi [19]. Besides, to the best of the author's knowledge, no published literature is there on the application of SVR for modeling of the important performance parameters of a thermosiphon reboiler, like the length of heated tube required for the onset of fully developed boiling (Z_{OB}) in a vertical tube thermosiphon reboiler.

In the present study, it is for the first time that SVR-based modeling has been used for predicting the length of heated tube required for the onset of fully developed boiling (Z_{OB}) in a vertical tube thermosiphon reboiler.

The experimental data from literature was first preprocessed. Regression diagnostic tools were used in order to detect outliers. Thereafter, the data was analyzed for the contributions of the influencing variables to the regression and the insignificant variable was dropped. Using this data, a unified SVR-based model was developed. Further, the estimation performance of this model was comprehensively compared and evaluated with the conventional models. In the present work, the experimental data of Ali [7], Kamil [8], Nihaluddin [20] and Zaidi [9] for the boiling of acetone, benzene, ethanol, ethyl acetate, ethylene glycol, propan-2-ol, toluene and distilled water was utilized for the development and validation of the SVR-based models. The regression models used from literature for comparison were those of Ali [7], Nihaluddin [20], Kamil [8], and Zaidi [9].

2. EXPERIMENTATION AND DATA REDUCTION

2.1 Experimentation

The experimental facility employed for the generation of a part of the data (including the author's own work) that was used in the present study, was a single vertical tube thermo siphon reboiler as installed in the Heat Transfer Research Laboratory of the Department of Chemical Engineering, Aligarh Muslim University, Aligarh, India. Agarwal [6] however used a slightly earlier version of the same setup for

the generation of the remaining data. The description of the later setup, operating procedure and data reduction has been necessitated by the fact that to appreciate the models, it was necessary to know these aspects in some detail. The experimental facility consisted of a natural circulation reboiler loop with a condenser and cooling system, power supply system and required instrumentation as shown in the schematic diagram in Fig. 1. The main unit was a U shaped circulation loop made up of two long vertical tubes connected together with the bottom by a short horizontal stainless tube, while the upper ends were connected to a vapor liquid separator and the condenser. One of the vertical tubes was electrically heated and served as the test section. The liquid entered the tube at its bottom end, got heated and rose upwards with subsequent boiling. The vapor liquid mixture entered the separator from where the vapors went to the condenser for total condensation. The condensate and the liquid from the separator were directed towards the top of the other tube serving as down flow cold leg. The entire liquid from the cold leg ultimately entered the test section through a view port. The vapor liquid separator was a cylindrical vessel with a tangential entry of the two phase mixture in the middle. The vapors were condensed by means of two water-cooled condensers used in series. The primary condenser was a spiral coil fitted just below the top cover of the condenser vessel. The condensation took place at the outer surface of the coil and condensed liquid drained down the bottom of the condenser vessel through a vertical tube fitted with a liquid level indicator.

A thermocouple was also inserted in this tube to measure the condensate temperature. The incondensables, if any, from the primary condenser entered the helical coil of the secondary condenser. The exit of the condenser was connected to a glass tube with its free end dipped into a bottle containing the test liquid so as to provide effective.

Visual observation of the removal of traces of dissolved air from the test liquids during initial boil off. A centrifugal pump and storage tank arrangement connected to fresh water supply was used for circulating water in the condensers. To measure the total rise in temperature of the cooling water, thermocouple probes of copper-constantan were located at the inlet of the secondary condenser and the outlet of the primary condenser. In order to control the inlet liquid temperature to the test section, the liquid down flow pipe was jacketted from the lower end up to a height of 1000 mm, using a pipe of 80 mm I.D. in which cooling water was passed as and when needed. The inlet and outlet temperatures of the water in the jacket were measured by means of thermocouple probes fitted therein. The temperature of the test liquid exiting from the down flow pipe and entering the horizontal pipe was measured by another thermocouple probe inserted at the bottom of the down flow pipe. The level of the test liquid in the down flow pipe (submergence) was indicated by a glass tube level indicator. This level acts as the driving force for the circulation of liquid through the loop.

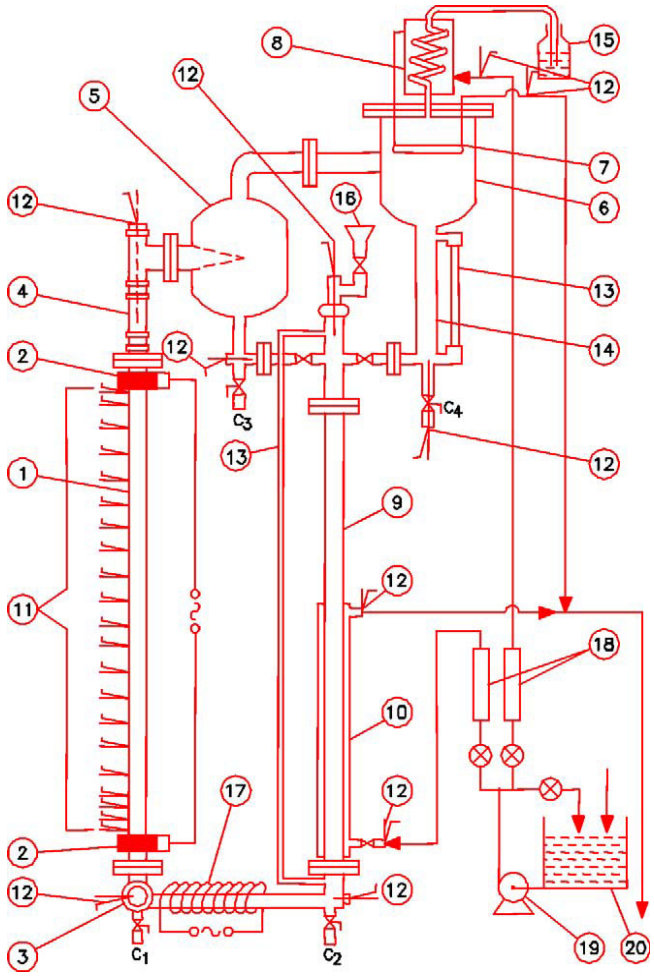
Prior to the start of experimentation the setup was hydraulically tested for leaks. It was flushed with distilled water for through cleaning and finally filled with it up to the top of the test section. The connections to the power supply thermocouple and various measuring instruments were made and checking their calibration ensures the satisfactory performance of these.

Power was supplied to the test section and circulation system. Simultaneously, cooling water supply was activated thereby ensuring adequate amount of cooling water to the condensers. The system was kept running for several hours followed by aging in order to ensure stable tube wall nucleating characteristics. This step was essential for the reproducibility of data. Extreme care was taken that once the tube wall got stabilized; it must remain fully submerged with the liquid as the dry surface was very liable to entrap a thin film of air. This air on heating leaves the surface as tiny bubbles and joins the liquid, thereby setting up micro convection near the surface, resulting in additional extraneous turbulence causing error. During startup for conducting a series of runs, the test liquid was boiled off for about 6-8 hours to remove the last traces of dissolved air that was indicated by the cessation of air bubbles in the bubbler. After this, the desired heat flux was impressed upon the test section by proper adjustment and cooling water flow rate was maintained. Adding or draining the necessary amount of test liquid maintained the liquid level in the down flow pipe. When steady state conditions were established readings of thermocouples, various electrical instruments and rotameters were recorded. The liquid level in the down flow pipe was observed and noted from the glass tube level indicator. While keeping the submergence unchanged, readings were taken for different heat fluxes in increasing order. The horizontal pipe connecting the lower end of the down flow pipe/cold with that of the test section was heated by an electric heater made of 22 SWG nichrome wire wound over a length of 500 mm. It was energized by means of an autotransformer and the power supply was measured by a calibrated wattmeter. This arrangement was used in regulating and maintaining the temperature of the liquid and also in measuring the rate at which it entered the test section (Nihaluddin, 1993).

The test section was a stainless steel tube of 25.56 mm I.D., 28.85 mm O.D and 1900 mm long, tapped between two thick copper clamps designed to provide electrical contact to the tube with negligible contact resistance. The test section was electrically isolated from the rest of the setup by means of specially designed flanges fitted at the lower end and the upper glass tube section leading into the vapor liquid separator. This section gave a visual display of the boiling liquid emerging out of the test section. A view port at the junction of the horizontal tube and the test section enabled a

visual observation of the test liquid to ensure complete absence of any air or vapor bubbles at the entry to the test section. A thermocouple probe at this location was inserted to measure the temperature of the liquid entering the test section. In order to monitor the heat transfer surface temperatures along the tube length, twenty one copper constantan thermocouples were spot welded on the outer surface of the tube at intervals of 50 mm up to a length of 200 mm from the bottom end and of 100 mm over the remaining length.

Data Reduction



1. Test section; 2. Copper clamps; 3. View port for inlet liquid; 4. Glass tube section; 5. Vapor-liquid separator; 6. Primary condenser; 7. Spiral coil; 8. Secondary condenser; 9. Liquid down-flow pipe; 10. Cooling jacket; 11. Wall thermocouple; 12. Liquid thermocouple probes; 13. Liquid level indicator; 14. Condenser down-flow pipe; 15. Bubbler; 16. Feeding funnel; 17. Auxiliary heater; 18. Rotameters; 19. Centrifugal pump; 20. Cold water tank. C_1 to C_4. Drain cock valves

Figure 1. Schematic diagram of the experimental set up

In some experiments, readings from only nineteen such thermocouples have been reported as the other three were probably not working. The energy to the test section was supplied through an automatic voltage stabilizer, autotransformer and low voltage high current transformer. The electrical energy input that got converted to heat in the wall of the test section was quantified by measuring the impressed voltage and current.

The operating parameters taken for investigation with each single component liquid were heat flux and submergence. All the data was generated at atmosphere pressure as prevailing in Aligarh, India. The thermal equilibrium model as suggested by Saha and Zuber [21] , formed the basis of determination of circulation rates and liquid bulk temperature distribution along the heated tube length by making a heat balance on the test section. According to it, as the sub cooled liquid enters the test section of the reboiler loop and because of the uniform heat flux at the heating surface, the liquid bulk temperature starts to increase almost linearly and continues up to the saturation value if all the heat added to the system goes to raise the temperature of the liquid only.

According to it, as the sub cooled liquid enters the test section of the reboiler loop and because of the uniform heat flux at the heating surface, the liquid bulk temperature starts to increase almost linearly and continues up to the saturation value if all the heat added to the system goes to raise the temperature of the liquid only. Thereafter, the liquid bulk temperature would remain constant at the saturation value and all the heat added would go as latent heat to generate vapor. For determining the circulation rate it was necessary to know the effective length of the non-boiling or sensible heating region over which the liquid temperature varied linearly. The lengths of the effective boiling and non-boiling zones over the entire heated tube were determined from the quantity of net vapor generation as obtained from the amount of vapor condensed in the condenser. A heat balance around the condenser gave:

$$M_V = \frac{\left[FC_{LC}(T_{C2} - T_{C1})\right]}{\left[\lambda + C_{L2}(T_{L2} - T_V)\right]} \quad (1)$$

Thus,

$$Z_B = \frac{M_V \lambda}{\pi q d} \quad (2)$$

$$Z_{NB} = L - Z_B \quad (3)$$

The rate of liquid circulation caused by buoyancy-induced flow was evaluated by making a heat balance over the non-boiling section.

$$Q = \pi d Z_{NB} q = m C_L \left(T_{L2} - T_{L1}\right) \quad (4)$$

The liquid temperature distribution along the tube length in the non-boiling zone was calculated assuming a linear relationship as mentioned below.

$$T_L = T_{L1} + \frac{(T_{L2} - T_{L1})Z}{Z_{NB}} \quad (5)$$

where, $Z \le Z_{NB}$

To obtain the correct inside wall temperature, the temperature drop between the thermocouple bead and the inside surface was estimated using the equation of conductive heat transfer with internal heat generation for a cylinder as:

$$\Delta T_W = \frac{q}{2\pi l k_W (D^2 - d^2)}\left[D^2 \ln\left(\frac{D}{d}\right) - \left(\frac{D^2 - d^2}{2}\right)\right] \quad (6)$$

The local heat transfer coefficient at the thermocouple locations was calculated as:

$$h = \frac{q}{(T_W - T_L - \Delta T_W)} \quad (7)$$

The length mean heat transfer coefficient for the entire tube length as well as for the boiling and non boiling sections was calculated as:

$$\overline{h} = \frac{q}{\Delta T_{avg}} \quad (8)$$

where, ΔT_{avg} with proper subscript represents the value for the relevant zone of interest.

3. A BRIEF THEORY OF SVR-BASED MODELING

The detailed theory of SVM can be referred to in several excellent works, for example Vapnik [22] and Smola and Schölkopf [23]. Therefore, in this study only an abridged mention is there of the fundamentals of support vector regression (SVR). Support vector machines (SVMs) are a set of non-parametric machine-learning techniques, whose algorithm aims at a constructive learning procedure based on the statistical learning theory [22]. The crux of the SVM design is solving a quadratic programming (QP) problem with linear constraints, which depends on the training vectors and the selection of few kernel parameters. The solution of a QP problem provides us the necessary information for choosing the most important vectors known as support vectors (SV) among all the data, and these support vectors play an important role of defining the discriminant hyperplane or predicting function. In SVM the basic aim is to map the original data into a feature space F with higher dimensionality via a non linear mapping function ϕ, which is usually unknown, and then carry out linear regression in the feature space. The SVR approximates a function by minimizing the regularized risk function given as:

$$R(C) = C\frac{1}{N}\sum_{i=1}^{N} L_\varepsilon(y, f(x,w)) + \frac{1}{2}\|w\|^2 \quad (9)$$

Where,

$$L_\varepsilon(y, f(\mathbf{x}, w)) = \begin{cases} 0 & \text{if } |y - f(\mathbf{x}, w)| \le \varepsilon \\ |y - f(\mathbf{x}, w)| - \varepsilon & \text{otherwise} \end{cases} \quad (10)$$

and ε is a prescribed parameter.

In Eq. (9), the first term is called the empirical risk or error, which is measured by ε-insensitive loss function given by Eq. (10) and indicates that it does not penalize errors below ε. The parameter ε is the tube size and it is equivalent to the approximation accuracy placed on the data points. It is a user defined value. The second term in Eq. (9), is used as a measurement of function flatness. C is a regularized constant determining the trade-off between the training error and the model flatness. C is also a user defined parameter. When introducing slack variables, the SVR formulation can be expressed mathematically in the form of a convex optimization problem as:

Minimize $\frac{1}{2}\|w^2\| + C\sum_{i=1}^{N} \xi_i + \xi_i^{(*)}$

Subject to

$$(y_i - w \bullet \phi(x) - b) \le \varepsilon + \xi_i,$$

$$(w \bullet \phi(x) + b - y_i) \le \varepsilon + \xi_i^{(*)},\ \xi_i, \xi_i^* \ge 0 \quad (11)$$

The above-mentioned convex optimization problem (Eq.(11)) can be solved by transforming it into its dual form by introducing Lagrange multipliers and exploiting optimality constraints. The final decision function takes the following form:

$$f(x, \alpha_i, \alpha_i^*) = \sum_{i=1}^{N_{sv}} (\alpha_i - \alpha_i^*)(\phi(x_i) \bullet \phi(x_j)) + b \quad (12)$$

where, α and α^* are the introduced Lagrange multipliers. Only the non-zero coefficients, $(\alpha_i - \alpha_i^*)$, and the corresponding input vectors, $\mathbf{x}_i$, are called support vectors (SVs). These SVs are the most informative data points that compress the information content of the training set, thereby representing the entire SVR function. By introducing the radial basis function as the kernel function, all the necessary computations related to ϕ can be performed implicitly in the input space instead of in the feature space. Thus the basic SVR decision function modeling the data takes the following form:

$$f(x, \alpha_i, \alpha_i^*) = \sum_{i=1}^{N_{sv}} (\alpha_i - \alpha_i^*)(K(x_i, x_j) + b \qquad (13)$$

where, $K(x_i, x_j)$ is the kernel function.

The bias parameter, *b*, is computed by applying Karush–Kuhn–Tucker (KKT) conditions, which state that at the optimal solution the product between dual variables and constraints has to vanish.

A fast and efficient algorithm known as Sequential minimal optimization (SMO) has been adopted. The advantage of SMO lies in the fact that solving for the two Lagrange multipliers can be done analytically [24].The computation was carried out on a computer with the following specifications: Lenovo Intel[R], Pentium [R] M processor 1.73 GHz, 795 MHz with 1.24 GB RAM. In order to maintain a similarity in approach so as to facilitate comparison between the results from SVR model and those obtained by literature correlations the same randomly divided data sets were used for training (240 runs) and testing (60 runs). Out of the different kernels, the RBF kernel has been used in this study because of its good general performance and the few parameters to be adjusted. The best values of *C*, epsilon and the kernel parameter γ, were obtained by using the grid search methodology with standard *k*-fold cross-validation procedure on training data set that minimizes the average absolute relative error (AARE) and improves the correlation coefficient (R) values in the direction of unity.

For the statistical analyses of SVR-based model and the models from literature, the following model evaluation parameters were used.

The average absolute relative error (AARE) should be a minimum. It is given as:

$$AARE = \frac{1}{N} \sum_{i=1}^{N} \left| \left[\frac{y_{ipred} - y_{i\exp}}{y_{i\exp}} \right] \right| \qquad (14)$$

2. Correlation coefficient (R) should approach unity for a good fit. It is given as:

$$R = \frac{\sum_{i=1}^{N} (y_{i\exp} - y_{imean}) \times (y_{ipred} - y_{ipredmean})}{\sqrt{\sum_{i=1}^{N} (y_{i\exp} - y_{i\exp mean})^2} \times \sqrt{\sum_{i=1}^{N} (y_{ipred} - y_{ipredmean})^2}} \qquad (15)$$

The root mean square (RMSE) used to evaluate the model should be minimum. Its mathematical expression is given as:

$$RMSE = \sqrt{\frac{\sum_{i=1}^{N} ((y_{i\exp} - y_{ipred}) / y_{ipred})^2}{N}} \qquad (16)$$

The standard measure of how widely values are dispersed from the average value (the mean) is evaluated by the standard deviation (σ). It should be a minimum.

$$\sigma = \sqrt{\sum_{i=1}^{N} \frac{1}{N-1} (\left| (y_{ipred} - y_{i\exp} / y_{i\exp}) \right| - AARE)^2} \qquad (17)$$

The internal predictive capability of the SVR-based model was evaluated by leave-one-out cross validation(Q^2_{LOO}) on the training set, which was calculated by the following equation(Gramatica, 2007):

$$Q^2_{LOO} = 1 - \frac{\sum_{i=1}^{N_{training}} (y_{i\exp} - y_{ipred})^2}{\sum_{i=1}^{N_{training}} (y_{i\exp} - y_{\exp mean})^2} \qquad (18)$$

The external predictive capability of the SVR-based model was evaluated by leave-one-out cross validation(Q^2_{ext}) on the test set, which was calculated by the following equation:

$$Q^2_{ext} = 1 - \frac{\sum_{i=1}^{N_{test}} (y_{i\exp} - y_{ipred})^2}{\sum_{i=1}^{N_{test}} (y_{i\exp} - y_{trmean})^2} \qquad (19)$$

The mean relative error (MRE) for valuating the model should be as low as possible.

$$MRE = \frac{1}{N} \sum_{i=1}^{N} \left| \left[\frac{y_{i\exp} - y_{ipred}}{y_{ipred}} \right] \right| \qquad (20)$$

4. RESULTS AND DISCUSSION

Data preprocessing results

The length of the heated tube (Z_{OB} or Z_{NB}) from the inlet, required for the boiling to be effective has been found to depend upon the wall heat flux (q), submergence (S), inlet liquid sub cooling (ΔT_{sub} or t_{sub}) and ratio of kinematic viscosities of the liquid and the vapor (ν_L/ν_V) [7,8,9]. The data from the sources listed earlier was preprocessed to detect outliers. The data thus obtained consisted of 300 experimental runs involving the boiling of acetone, benzene, ethanol, ethyl acetate, ethylene glycol, propan-2-ol, toluene and distilled water in a thermosiphon reboiler.

All the correlations for predicting the length of the heated tube from the inlet, required for the boiling to be effective, have correlated the experimentally obtained values of Z_{OB} or Z_{NB} with the influencing variables in terms of dimensionless groups. Thus, Z_{OB} or Z_{NB} has been converted to Z_{OB}/Lx100 and q and ΔT_{sub} have been converted to Pe_B and K_{sub} respectively; S and ν_L/ν_V being already dimensionless. The ranges of these dimensionless groups as used in the present study for developing the SVR model are given in Table 1.

In the present study, the RBF kernel was used. For getting a high generalization performance, it was necessary to optimize the model in order to have the right setting of C, ε and γ.

Table 1: Ranges of dimensionless groups used in the present study

Group	Peb	Ksub	S	ν_L/ν_V	Z_{OB}/Lx100
Range	39.3-586.6	1.3-1155	30-100	0.00018-0.23	22-82

For achieving this, grid search methodology with 10-fold cross-validation, was used on the training data by first varying these parameters coarsely in the ranges: C: [2^3, 2^{14}], γ [2^{-12}, 2^{-1}] and ε [2^{-9}, 2^2] and then making a fine search. The optimal values of the model parameters for the SVR-based model are listed in Table 2.

Table 2. Optimal parameters for SVR-based model for length of the non-boiling zone in a vertical tube thermosiphon reboiler.

Model	C	$\gamma = 1/2\sigma^2$	ε	Kernel	Loss function	SVs	training-ng point-s
$Z_{OB/L}$x100	100	0.1	0.32	RBF	ε - insensitive	122	240

After optimization of the SVR parameters, the model output was used to construct the training course curve and the test data course curve as shown in Figure 2 and Figure 3, respectively. It can be seen that the SVR-based model is adequately trained and it predicts the unseen test data well.

Table 3 compares the prediction of the SVR-based model in terms of statistical evaluation parameters using the training data set and the test data set. In terms of the model evaluation parameters, an AARE of 8.98 % and an R of 0.8333 on the training data and corresponding values of 10.08 % AARE and an R of 0.8302 on the test data were obtained. This may be considered as a fairly good prediction and generalization ability, considering the diversity of sources from which the data was obtained. It can be concluded that the model has a good accuracy and generalization ability.

Plots between the actual values of Z_{OB}/Lx100 and those predicted by the SVR model using the training data set and the test data set are shown in Figure 4. The model predicts the experimental data very well. The results demonstrate that the SVR-based model is a robust model. Table 4 illustrates the distribution of predicted data points of Z_{OB}/Lx100 by SVR-based model in terms of absolute deviation for training data.

Table 3. Model evaluation parameters for SVR-based model using the training data and the test data.

SVR Model evaluation parameter	Train data	Test data
AARE (%)	8.98	10.08
R	0.8333	0.8302
RMSE	0.1381	0.1185
SD	0.0918	0.0833
Q^2_{LOO} (Training data), Q^2_{ext}(Test data)	0.6923-	-0.6778
MRE	0.0908	0.0946

Table 4. Percentage distribution of predicted data points of Z_{NB} by SVR-based model in terms of absolute deviation (AD) for training data.

Absolute deviation (AD) (%)	% of SVR model predicted values	Cumulative score
AD< 10	77.91	77.91
10<AD<15	7.5	85.41
15<AD<20	3	88.41
20<AD<25	4.1	92.51
AD>25	7.49	100
Total	100	

It is observed that the SVR-based model predicts nearly 88.41 per cent data points within an absolute deviation of less than 20 % and a total of 92.51 per cent data points within an absolute deviation of less than 25 %. Only 7.49 per cent data points have an AD of more than 25 per cent.

Table 5 depicts the distribution of predicted data points of Z_{OB}/Lx100 by SVR-based model in terms of absolute deviation for the test data set. It can be seen that the SVR-based model predicts nearly 88.33 per cent data points within an absolute deviation of less than 20 % and a total of 93.33 cent data points within an absolute deviation of less than 25 %. Only 6.67 per cent data points have an AD of more than 25 per cent. This shows that the SVR-based model has a good ability to predict the unseen test data set.

Table 5. Percentage distribution of predicted data points of Z_{NB} by SVR-based model in terms of absolute deviation (AD) for test data.

Absolute deviation (AD) (%)	% of SVR model predicted values	Cumulative score
AD< 10	58.33	58.33
10<AD<15	16.67	75
15<AD<20	13.33	88.33
20<AD<25	5	93.33
AD>25	6.67	100
Total	100	

5. COMPARISON OF SVR-BASED MODEL WITH CORRELATIONS AVAILABLE IN LITERATURE

A comparison of the unified SVR-based model for predicting the length of non-boiling section of the heated tube was made against three models from the literature using the test data set. Table 6 depicts the AARE values for each model. It is observed that the SVR-based data-driven model gives an unprecedented lowest AARE value of 10.08 per cent among all the models. The nearest AARE value is 57.19 % exhibited by Kamil [8]. It can therefore be concluded that the prediction performance of the SVR-based model is the best.

Table 6. Performance of different models on test data set to predict the length of the non-boiling zone in a vertical tube thermosiphon reboiler.

Author(s)	AARE (%)
Ali [7]	78.71
Kamil [8]	57.19
Zaidi [9]	77.71
SVR-based model (present work)	10.08

Further, Figure 5 illustrates the prediction performance of the unified SVR-based model vis-à-vis the other three models from literature. It is observed that the SVR-based model gives the most superior performance.

Thus, based on the statistical evaluation parameters, the training and test course curves, the AD values and the comparison with other correlations in literature, the results show that the maiden SVR- based model based on the universal Statistical Learning Theory has very high prediction ability and is very accurate.

6. CONCLUSIONS

In the present study, a model has been developed to predict the length of the boiling/non-boiling section of the heated tube in a thermosiphon reboiler. The SVR-based model is superior to the other models considered in this study as it displays a high degree of accuracy and generalization ability. It shows that the prospects of the application of SVR in chemical engineering in general and heat transfer in particular are very bright.

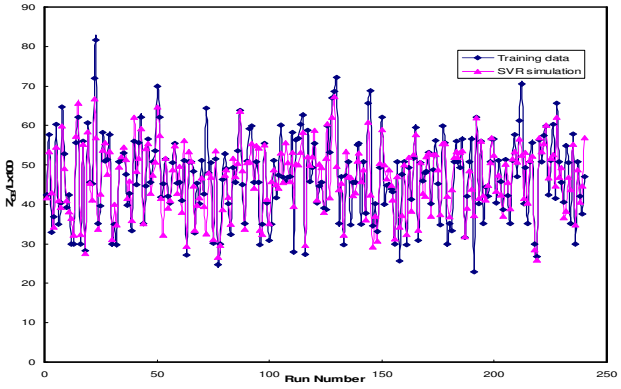


Figure 2. Training course curve for the length of the non-boiling zone.

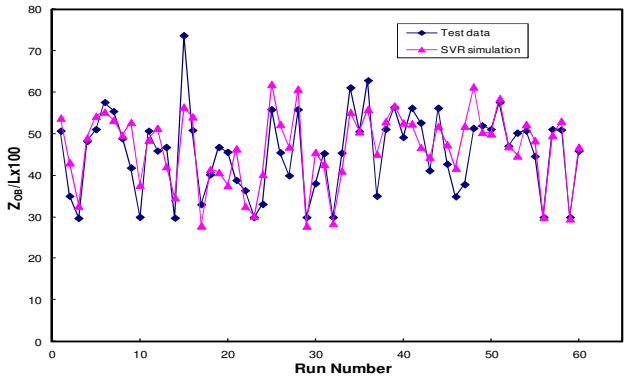


Figure 3. Test course curve for the length of the non-boiling zone.

Notation

A	cross-sectional area of heated tube	
AARE	average absolute relative error	%
b	bias term	b
C_L	heat capacity	J/kg °C
C	cost function	C
d	inside diameter of the tube	m
F	high-dimensional feature space	
f(**x**)	regression function	
k	thermal conductivity	W/m °C
$K(\mathbf{x}_i,\mathbf{x}_j)$	kernel function	
L	Lagrangian function (dual form)	
m	circulation rate	kg/s
N_{sv}	number of support vectors	
Q	heat input	W
q	heat flux	W/m^2
S	submergence	%
T_{L1}	inlet liquid temperature to the tube	°C
T_S	liquid saturation temperature in the tube	°C
T_{sub}	degree of subcooling	°C
w	weight vector	
$\mathbf{x}_i$	ith input vector	
x^o	vapour fraction	
y_i	target output corresponding to the ith vector	
Z_{NB}	length of the non-boiling zone	m

Greek Letters

λ	latent heat of vaporization	J/kg
ρ	density	kg/m^3
μ	dynamic viscosity	$N\ s\ /\ m^2$
σ	width of RBF kernel	
σ_L	surface tension of liquid	N/m
α and α^*	Lagrange multipliers	
γ	regularization parameter	
ε	loss function	
$\varphi(\mathbf{x}_i)$	mapping function to high dimensional feature space for input vector **x**	

Subscripts

exp	experimental
pred	predicted
L	liquid
NB	non- boiling
S	saturation
sub	subcooling
tr	training
V	vapour

Dimensionless Numbers

K_{sub}	subcooling number
Pe_B	Peclet number
Re	Reynolds number
X_{tt}	Lockhart- Martinelli parameter

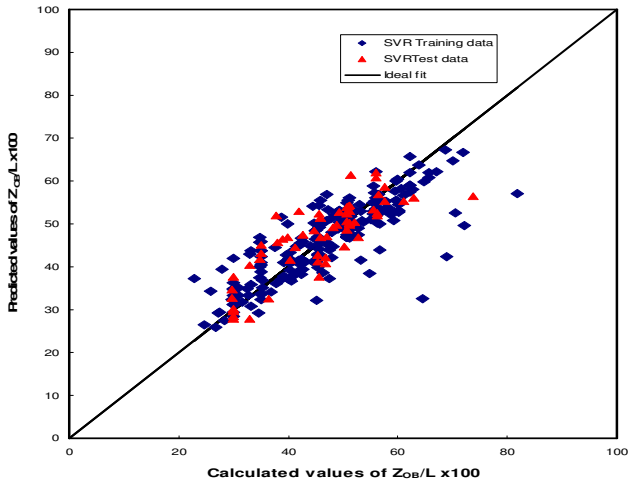


Figure 4. SVR simulation of the length of the non-boiling zone in a vertical tube.

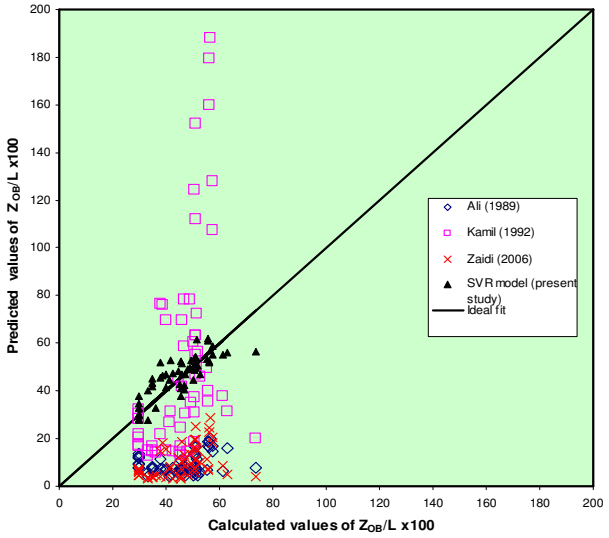


Figure 5. Comparison of SVR simulation of the length of the non-boiling zone with models in literature using test data.

7. ACKNOWLEDGEMENTS

The author wishes to gratefully acknowledge all the authors whose works have been referred to in the paper, Also, the author is grateful to the Aligarh Muslim University for having provided all the facilities for this work.

REFERENCES

[1] Murphy R. W., Bergles, A. E. Subcooled flow boiling of fluro-carbons- hysteresis and dissolved gas effects on heat transfer,

Proceedings of the Heat Transfer and Fluid Mechanics Institute, Stanford Univ. Press, (1972) 400-416.

[2] Yin, S. T., Abdelmessih, A. H. Prediction of incipient flow boiling from a uniformly heated surface, AIChE Symp. Ser.164, 73, (1977) 236-243.

[3] Hsu, Y.Y., Graham, R.W. Transport Processes in Boiling and Two- Phase Systems, Hemisphere Publishing Corporation, Washington (1976).

[4] Bergles, A.E., Rohsenow, W. M. The determination of forced convection surface boiling heat transfer, Trans. ASME. Ser. C, Vol. 86, (1964) 365-372.

[5] Yin, S. T., Abdelmessih, A. H. Measurements of liquid superheat, hysteresis effects and incipient boiling oscillations of Freon-11 in forced convection vertical flow, University of Toronto, Mech. Eng. Tech. Pub. Ser., TP-7401 (1974).

[6] Agarwal, C.P. Heat Transfer Studies in a Vertical Tube of Closed-Loop Thermo siphon, PhD Thesis in Chemical Engineering, University of Roorkee, India (1980).

[7] H. Ali, Studies on Thermosiphon Reboiler, PhD Thesis in Chemical Engineering, Aligarh Muslim University, Aligarh (1989).

[8] M. Kamil, Studies on a vertical tube thermosiphon reboiler, Ph.D. Thesis, Aligarh Muslim University, Aligarh (1992).

[9] Zaidi, S. Studies on Vertical Thermo siphon Reboiler, M. Tech. Chemical Engineering (Petroleum Processing) Thesis, Aligarh Muslim University, Aligarh (2006).

[10] Shamsuzzoha, M., Kamil, M., Alam, S. S. Conditions of Onset of Boiling in a Vertical Thermo siphon Reboiler, Journal of Thermophysics and Heat Transfer, 18 (4) (2004) 448-456.

[11] Shamsuzzoha, M., Alam, S. S. Effect of Bubble Turbulence and Submergence on Boiling Incipience in Vertical Thermosiphon Reboiler, Heat transfer engineering, Vol 29(3) (2008) 306-320.

[12] Chen, N, Lu, W., Yang, J., Li, G., 2004. Support Vector Machine in Chemistry. World Scientific, Singapore.

[13] Li, H., Liang, Y., Xu, Q., 2009. Support vector machines and its applications in chemistry. Chemometrics and Intelligent Laboratory Systems 95, 188-198.

[14] Al-Anazi A.F., Gates I.D., 2010. Support vector regression for porosity prediction in heterogeneous reservoir: A comparative study. Computers & Geosciences 36 1494–1503.

[15] Kavaklioglu, K., 2011. Modeling and prediction of Turkey's electricity consumption using Support Vector Regression. Applied Energy 88, 368–375.

[16] Zhao, B., 2009. Modeling pressure drop coefficient for cyclone separators: a support vector machine approach. Chemical Engineering Science **64**, 4131–4136.

[17] Azamathulla, H. M., Wu, F. C., 2011. Support vector machine approach for longitudinal dispersion coefficients in natural streams. Applied Soft Computing 11, 2902-2905.

[18] Gandhi, A.B., Joshi, J.B., 2010. Estimation of heat transfer coefficient in bubble column reactors using support vector regression. Chemical Engineering Journal 160, 302-310.

[19] Zaidi,S. 2012. Development of support vector regression (SVR)-based model for the prediction of circulation rate in a vertical tube thermosiphon reboiler. Chemical Engineering Science 69, 514-521.

[20] Nihaluddin, 1993. Heat transfer to boiling liquids in a vertical thermosiphon reboiler. M. Sc. Chemical Engineering (Petroleum Processing) Thesis, Aligarh Muslim University, Aligarh, India.

[21] Saha, P., Zuber, N., 1978. An analytical study of the thermally induced two-phase flow instabilities including the effect of thermal non-equilibrium. International Journal of Heat and Mass Transfer 21, 415- 426.

[22] V. N. Vapnik, 1995. The Nature of Statistical Learning Theory, Springer, New York.

[23] A. J. Smola and B. Schölkopf, A tutorial on support vector regression. Statistics and Computing, Vol 14, (2004) 199-222.

[24] Platt, J. (1999). Fast training of support vector machines using sequential minimal optimization. In B. Schölkopf, C. J. C. Burges, & A. J. Smola (Eds.), *Advances in Kernel Methods-Support Vector Learning* (pp. 185-208). Cambridge, MA: The MIT Press.

Temperature Dependent Effective Mass and Scattering Rate for the Heavy Electron System $CeAl_3$

Prajwalit Shikha

Department of Physics, Maitreyi College, Delhi University, New Delhi, India

Abstract: **The present paper reports a temperature dependent calculation of effective mass and scattering rate for the compound CeAl3. It is a heavy electron compound. The calculation uses the Kramers-Konig relations within the model of Millis and Lee. the results are compared with reported experimental data.**

1. INTRODUCTION

The heavy electron systems like $CeAl_3$ and UPt_3 present one of the most fascinating fields of study in condensed matter physics as well as in materials science [1]. The experiments on these compounds have yielded results so surprising as to change our understanding of the behavior of interacting electron systems. The properties of these compounds derive from the partially filled f orbitals of rare-earth or actinide ions [2,3]. The conduction electrons in these metallic compounds have effective masses of 100 to 1,000 times the free-electron mass as opposed to values of about 10 for transition metals. In this paper, we present an evaluation of real and imaginary part of dynamical conductivity $\sigma(\omega)$ frequency and temperature dependent effective mass m^*, and scattering rate Γ at different temperatures in the heavy electron system $CeAl_3$.

The $CeAl_3$ compound has a hexagonal crystal structure. Its resistivity $\rho(T)$ follows the T^2 law viz.

$$\rho(T) = \rho_0 + AT^2 \qquad (1)$$

particularly for $T < 0.3$ K. From experimental measurements, *Awasthi et al.* [4,5] found that the increase in resistivity with temperature at low temperatures at millimeter-wave frequencies is frequency dependent, but at high temperatures (above approximately 10K), the response is almost frequency independent. This implies that in the high temperature regime, the scattering rate $(1/\tau)$ is significantly larger than the millimeter-wave frequencies, and σ_2 is negligible compared to σ_1 , where the optical conductivity is expressed as

$$\sigma(\omega) = \sigma_1(\omega) + i\,\sigma_2(\omega) \qquad (3)$$

2. MODEL AND FORMULATION

Heavy-electron materials can be considered as metals with strongly correlated, yet delocalized electrons. A T^2 - dependence in $\rho(T)$ at low temperatures is usually taken as the criterion for the identification of Fermi-liquid behavior in heavy-electron systems. It is observed in these systems that an enormously large specific-heat coefficient γ implies an effective mass m^* of the quasiparticles, which is several hundred times the free-electron mass. The enhancement of the effective mass is understood due to the presence of localized f electrons in all heavy-electron systems. In $CeAl_3$, these may be Ce ions with 4 f electrons.

The most comprehensive theoretical model for the study of electrodynamical response of the heavy-electron compounds was developed by *Millis and Lee* [6]. As detailed in our earlier paper [7], there are two possible sources of scattering of electrons in these systems. One is the scattering of electrons from the impurities and the other is the scattering from boson fluctuations. Two characteristic plasma frequencies are then expected: the one at high frequency ω_p which identifies the uncorrelated conduction electrons, and the other ϖ_p^* is at low frequency and associated with the heavy plasmons.

A method of estimating m^*/m_b together with the scattering rate Γ is to consider the low-frequency resonance arising from free carriers undergoing frequency dependent scattering. This means that the optical conductivity may be described by a so-called generalized Drude model [8]. Obviously, the frequency dependence of Γ implies, through the Kramers-Kronig relation between σ_1 and σ_2, that m^* is also frequency dependent. The application of the generalized Drude model at different temperatures will permit the evaluation of the temperature dependence of m^* and Γ. Therefore the complex conductivity may be written as [9]

$$\sigma(\omega) = (\omega_p^2/4\pi) / [\Gamma(\omega) - i\omega\{m^*(\omega)/m_b\}] \qquad (3)$$

where ω_p is the unscreened optical plasma frequency. A relationship between σ_1 , σ_2 , and Γ together with m^*/m_b is then obtained as follows:

$$\Gamma(\omega) = (\omega_p^2 / 4\pi)(\sigma_1 / |\sigma|^2) \qquad (4)$$

and

$$m^*(\omega)/m_b = (\omega_p^2 / 4\pi)\,(\sigma_2 / \omega|\sigma|^2) \qquad (5)$$

3. RESULTS AND DISCUSSIONS

The calculated values of σ_1, σ_2, m^*/m_b and Γ for $CeAl_3$ at different temperatures are given in the Tables *1-4* . By taking the experimental values of $\sigma(\omega)$ and calculating $\sigma_1(\omega)$ and $\sigma_2(\omega)$ using Kramers-Konig relations, we have obtained the values of frequency and temperature dependent effective mass $m^*(\omega)/m_b$. Our results for $m^*(\omega)/m_b$ indicates that its value decreases with increase in temperature (at low temperatures) as well as with increase in frequency. For $CeAl_3$, the values of m^*/m_b at $T=1.2K$, $3K$, $5K$ and $10k$ and $\omega = 1x10^2\ m^{-1}$ are found to be *386.53, 284.66, 198.89 and 98.267* and, for the same temperature range but $\omega = 10\ x10^2\ m^{-1}$, are found to be *340.11, 237.58, 121.72* and *31.979*. Experimentally, at *10K* and above in the case of $CeAl_3$, the coherent state does not exist as the surface impedance results suggest, and consequently no mass enhancement is expected.

At low temperatures, m^* in Eq. (*5*) assumes constant values at frequencies below which Γ becomes frequency independent. This crossover frequency [say $\omega_{co}(T)$] is approximately *0.3, 0.9, and 0.7* in units of $10^2 m^{-1}$ *at 1.2, 3.0, and 5.0 K,* respectively. The values of m^*/m_b for $CeAl_3$ *at* ω_{co}*'s are 360, 225, and 160*m_b , which are zero frequency effective masses at these temperatures.

Thus a substantial increase in the effective mass occurs only below *3K (for* $CeAl_3$,$T_K \sim 3$ *K).* The experimental data are taken from the references [8,10]. It is difficult to assign reasons for the quantitative difference with our theoretical results. May be, more rigorous experiments and/or theoretical formulations are needed.

4. ACKNOWLEDGEMENT

This work was carried out at Vinoba Bhave University, Hazaribag.

Table 1 : Evaluation of $\sigma_1(\omega)$ for $CeAl_3$ (in units of $10^6/\Omega m$).

ω (m^{-1})	T = 1.2K	T = 3K	T = 5K	T = 10K
10^0	2.325	1.862	1.629	1.242
10^1	2.356	1.875	1.629	1.242
10^2	2.304	1.889	1.676	1.265
10^3	1.954	1.856	1.604	1.200
10^4	1.862	1.820	1.556	1.186
10^5	1.716	1.803	1.508	1.172

Table 2 : Evaluation of $\sigma_2(\omega)$ for $CeAl_3$ (in units of $10^6/\Omega m$).

ω (m^{-1})	T = 1.2K	T = 3K	T = 5K	T = 10K
10^0	0.934	0.659	0.478	0.259
10^1	0.916	0.642	0.462	0.240
10^2	0.900	0.633	0.455	0.236
10^3	0.895	0.627	0.443	0.228
10^4	0.887	0.610	0.430	0.217
10^5	0.868	0.608	0.428	0.204

Table 3: Evaluation of (m^*/m_b) in $CeAl_3$ [using eq.(5)].

$\omega \times 10^2$ (m^{-1})	T = 1.2K	T = 3K	T = 5K	T = 10K
1	386.53	284.66	198.89	98.267
2	372.86	280.59	190.13	86.538
3	369.12	272.86	178.62	80.499
4	365.89	264.11	170.52	72.539
5	360.86	260.89	161.88	60.869
6	353.43	257.66	143.77	50.478
7	351.74	251.66	143.77	50.478
8	346.08	246.88	134.52	43.349
9	343.58	242.18	127.68	88.862
10	340.11	237.58	121.72	31.979

Table- 4: Evaluation of $h\Gamma(\omega)$ in $CeAl_3$ [using eq.(4)].

$\omega \times 10^2\ m^{-1}$	T =1.2K	T = 3K	T = 5K	T = 10K
1	0.04527	0.07509	0.09518	0.13278
2	0.05153	0.07786	0.09870	0.13395
3	0.05437	0.08059	0.10832	0.13743
4	0.05667	0.08218	0.17053	0.13886
5	0.05908	0.08446	0.11854	0.14033
6	0.06172	0.08872	0.12034	0.14158
7	0.06234	0.09217	0.12649	0.14269
8	0.06417	0.09554	0.13007	0.14355
9	0.06518	0.09771	0.13229	0.14486
10	0.06708	0.10035	0.13658	0.14486

REFERENCES

[1] Demsar,J, Verner,K, Thorsmølle,J, Sarrao,L, and Taylor, A.J., Phys. Rev. Lett. **96** 037401 (2006).

[2] Stewart, G. R.., Rev. Mod. Phys. **56** 755 (1984).

[3] Grewe, N and Steglich, F., Handbook on the Physics and Chemistry of Rare Earth eds K A Gschneider Jr and L Eyring (Elsevier, Amsterdam), **Vol.14** (1991).

[4] Awasthi,A.M., Beyermann,W. P., Carini, J. P. and Grüner,G., Phys. Rev., **B39** 2377 (1989).

[5] Awasthi,A.M., Degiorgi,L. Grüner,G., Dalichaouch Y. and Maple, M.B., Phys. Rev. **B48** 10692 (1993).

[6] Millis, A. J., and Lee, P. A., Phys. Rev., **B35**, 3394(1987).

[7] Shikha, P., Sinha,V. K., and Dubey, J. D., Ind. J. Phys., **82(12)**, 1665(2008).

[8] Sulewski, P. E., Sievers , A. J., Maple, M. B., Torikachvili, M. S., Smith, J. L., and Fisk, Z., Phys. Rev., **B38**, 5338(1988).

[9] Thomas, G., Orenstein, J., Rapkine, D. H., Capizzi, M., Millis, A. J., Bhatt, R. N., Schneemeyer, L. F. and Waszczak, J. W.,, Phys. Rev. Lett. **61**, 1313 (1988).

Experimental Evaporative Coolers for Vegetable Preservation

Ajay Kale[1], Kalyan Sundaram[2]

[1]*Associate Professor, Mechanical Dept, Vishwakarma Institute of Information Technology, Pune, Maharashtra, India*
[2]*Professor, Mechanical Dept, Vishwakarma Institute of Technology, Pune, Maharashtra, India*

Abstract: **Evaporative cooling is a well-known system to be an efficient and economical means for reducing the temperature and increasing the relative humidity in an enclosure. The high cost involved in developing cold storage or controlled atmosphere storage is a pressing problem in several developing countries. Many vegetables need high relative humidity (≥ 70%) with absolutely no exposure to direct heat or sunlight. Annual relative humidity in many parts of India ranges from 35% to 60%. Annual temperatures are also going high in many populated states of India.**

Experiments are conducted on natural and forced updraft evaporative coolers. Coolers are made of G.I sheet of 0.5 mm thick. PUF is used as an insulation and it is placed between the G.I sheets in pressed condition to avoid air gap between G.I sheet and foam. Inner volume of each cooler is one cubic feet with a storing capacity of 1 to 1.5 kg of vegetables only.

Experiments are performed on natural draft and forced updraft evaporative cooler to understand the variations in relative humidity, temperatures and quantity of water evaporated in Pune. Shelf life of few vegetables and their important properties are also measured during experiments.

Observations are also compared with the vegetables kept in open air conditions inside and outside the room. Heat balance for actual quantity of water evaporated and heat transmission in evaporative cooler is made. Sensory evaluation of vegetables is also made after conducting the experiments. It is observed that to avoid the problem of shrinkage, wilting and to retain freshness evaporative cooling is a better option in tropical countries. Shelf life of minimum 4 to 5 days is observed for selected vegetables. Natural evaporative cooler performance *is found better than the performance of forced updraft cooler.*

Experiments are aimed to develop innovative cold storage test rig with the combined use of evaporative cooling, Thermal Energy Storage (TES) concept, ventilation and insulation. These experiments will certainly help to develop low cost cold storages for vegetable preservation at farm end in India.

1. INTRODUCTION

Much of the post-harvest loss of fruits and vegetables in developing countries is due to the lack of proper storage facilities. While refrigerated cool stores are the best method of preserving fruits and vegetables they are expensive to buy and run. Consequently, in developing countries there is an interest in simple low-cost alternatives, many of which depend on evaporative cooling which is simple and does not require any external power supply.

This system is based on the principle that when moist but unsaturated air comes in contact with a wetted surface whose temperature is higher than the dew point temperature of air, some water from the wetted surface evaporates into air. The latent heat of evaporation is taken from water, air or both of them. In this process, the air loses sensible heat but gains latent heat due to transfer of water vapour. Thus the air gets cooled and humidified. The cooled and humidified air can be used for providing thermal comfort. [1]

The efficiency of an evaporative cooler depends on the humidity of the surrounding air. Very dry air can absorb a lot of moisture so greater cooling occurs. In the extreme case of air that is totally saturated with water, no evaporation can take place and no cooling occurs. Evaporative cooling is a well-known economical system for vegetable preservation.

2. EVAPORATIVE COOLER PERFORMANCE PARAMETERS

There are four major factors that affect the rate of evaporation.

2.1 Relative Humidity

When the relative humidity is low, the air is capable of taking on additional moisture, and if other conditions are also met, the rate of evaporation will be higher. On the other hand, when the relative humidity is high, the rate at which water evaporates will be low, and therefore less cooling will occur. Under such conditions, evaporative cooling can be effective if a desiccant (e.g., silica gel) is used to remove moisture from the air before it is cooled.

2.2 Air Temperatures

Air with a relatively high temperature stimulates the evaporation rate and is also capable of holding a relatively great quantity of water vapor. With lower air temperatures, less water vapor can be held, and less evaporation and cooling

will take place. Locations with high temperatures will thus have higher rates of evaporation, and more cooling will occur.

2.3 Air Movement

Air movement influences the rate of evaporation. As water evaporates from a surface it tends to raise the humidity of the air that is closest to the water's surface. If this humid air remains in place, the rate of evaporation will start to slow down as humidity rises. On the other hand, if the humid air near the water's surface is constantly being moved away and replaced with drier air, the rate of evaporation will increase.

2.4 Surface Area

The area of the evaporating surface is another important factor that affects the rate of evaporation. The greater the surface area from which water can evaporate the greater will be the rate of evaporation. A simple example will demonstrate the importance of surface area to evaporation; consider the following two situations. (1) One litre of water placed in a narrow glass container with only about 16 cm2 of surface area exposed to the air; and (2) another litre of water poured into a large shallow pan with about 180 cm2 of surface exposed to the air. If both are left under the same environmental conditions, the large pan of water would dry up much sooner because of the large surface area.

Even though each of these factors has its own separate and significant effect on the rate of evaporation, when combined, their impact is much greater. For example, the first two factors can be discussed together in terms of wet and dry-bulb temperatures. Under conditions where the difference between the wet and dry-bulb temperatures is great, the rate of evaporation will also be great. [3]

The performance of direct and indirect evaporation cooling systems can be assessed on the saturation efficiency (SE), defined as:

$$\varepsilon = \frac{(t_o - t_s)}{(t_o - t_{o,wbt})}$$

Where,

t_o and t_s the dry-bulb temperatures of the air at the inlet and outlet of the system as well as $t_{o,wb}t$, in as the wet-bulb temperature of air at the inlet of the system.

Generally the saturation efficiency of direct evaporative cooling ranges between 60-90%. Typical saturation efficiency values for indirect evaporative cooling systems are in the range of 60-80%. [5, 9]

3. NATURAL DRAFT EVAPORATIVE COOLER

The system is an enclosed system and air is allowed to pass only through the tray containing water. During this process the warm air will come in contact to comparatively large surface of water. Warm room air will exchange sensible heat to water and during evaporation of water part of latent and sensible heat will be taken from surrounding air causing temperature drop of 3°C to 4°C in the enclosure. To enhance effect of adiabatic evaporation of water insulated enclosure with defined height is provided to get the required updraft chimney effect. Increase in relative humidity of 15 to 25% is observed within the enclosure**.** [4]

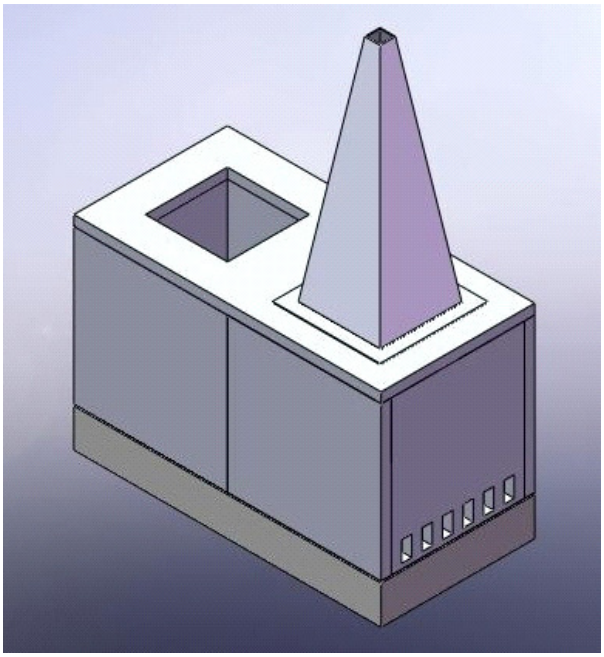


Figure 1. Combined Natural and Forced Updraft Evaporative Cooler

3.1 Thermodynamic Analysis of evaporation of water in Natural Draft Evaporative Cooler

Assumptions made:

1. The system is under steady state and isothermal conditions.
2. The total pressure within the system remains constant.
3. Air as well as water vapour behaves as an ideal gas.
4. There is a slight air movement over the top of tank/tray to remove water vapour which diffuses to that point; however, this movement does not disturb the concentration profile of air in the tank.
5. The water concentration at the surface of water is much more compared to that at the top of the tank (i.e., Cw1> Cw2 or Ca2 > Ca1)

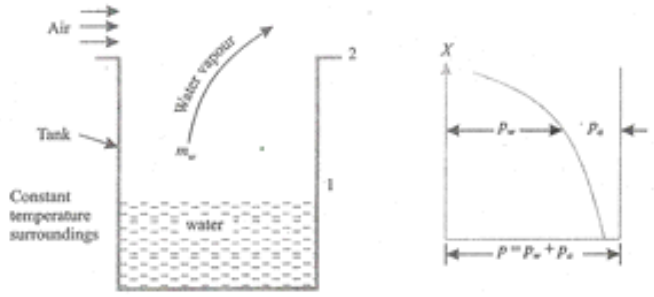


Figure 2. Diffusion of water vapour in air

$$(\dot{m}_w)_{total} = \frac{DAM_w}{G.T} \cdot \frac{p}{(x_2 - x_1)} \ln\left[\frac{p - p_{w2}}{p - p_{w1}}\right]$$

Where,
D= Mass Diffusivity m^2/sec
A= Surface Area in m^2
M_w= Molecular Weight of water
G= Universal Gas Constant
T= Dry Bulb Temperature
P= Atmospheric Pressure
P_{w1}= Partial Pressure of water Vapor at x_1
Pw_2= Partial Pressure of water Vapor at x_2 [8]
$(\dot{m}_w)_{total}$ = Quantity of Water Evaporated in kg/sec

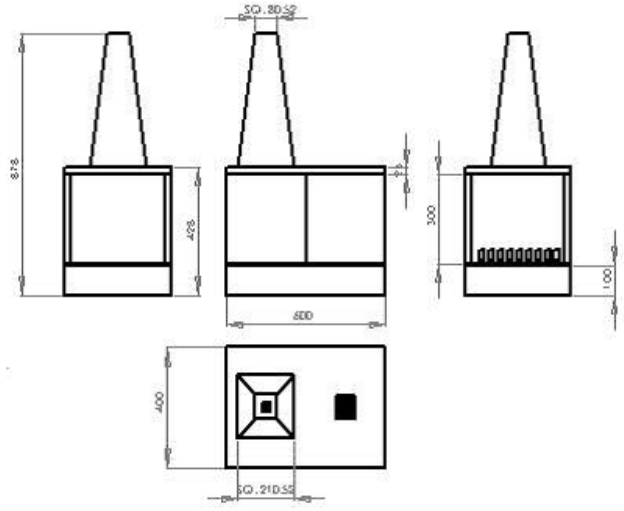


Figure 3. Drawing of combined evaporative cooler

Left Side Chamber: Natural updraft Evaporative Cooler
Right Side Chamber: Forced Updraft Evaporative Cooler
Insulation: PU Foam
Both coolers on mounted on trays containing known quantity of water. MS gauze is placed between trays and coolers to store vegetables on top of it.

Table 1. Experimental results to determine actual quantity of water evaporated in Natural Updraft Evaporative Cooler

Date	Room RH %	RH % inside Cooler	Water Evaporated
24 & 25 Jan 12	56%	72%	110g (300g)
26-28 Jan 12	52%	70%	150g (600g)
29-30 Jan 12	45%	68%	160g (1000g)

3.2 Heat Balance/Thermal analysis

PU Foam = 20 mm thick, G. I Sheets = 0.8 mm thick, Average t_0 = 20°C, Average t_i = 17.5°C, k_{foam}=0.025w/mk, $k_{G.I}$= 55w/mk, ho= 12 w/m^2k, hi= 16 w/m^2k

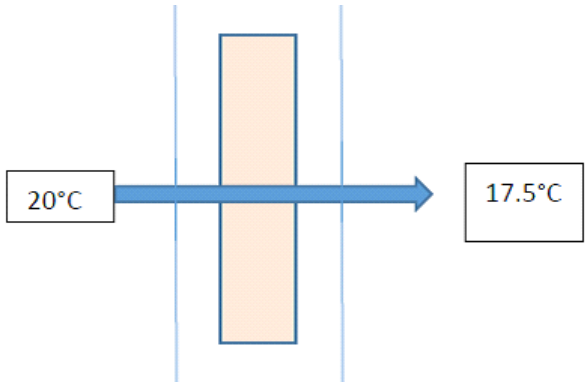


Figure 4. Heat transmission through wall

Q = U. A. (to – ti) .. Watts
Q = 1.058. 0.568. (2.5) = 1.5 ≈ 2 w
Heat penetrated in a day = 2J/s. 24. 3600 = 172.8 kJ
Amount of heat absorbed by evaporating140 gram of water:
1 gm. of water evaporated = 2.466 KJ is absorbed.
Hence, 140 gm. of water = 345 KJ heat is absorbed/Day [6]

Table 2. Heat Balance

Heat Absorbed .. KJ	Heat Removed .. KJ
345 KJ	1) Transmission Heat = 172.8 KJ
	2) m. Cp t = 10KJ (Veg)
	3) m. Cp. t = 12.6KJ (water)
	4) 345 – (1+2+3) = 345 – 195.4 = 149.6 KJ Heat Loss

3.3 Important Observations:

Vegetables kept in Natural Updraft Cooler found better than open room conditions.

Controlled near adiabatic saturation conditions are possible.
Shelf life of 6 to 7 days is observed for Cauliflower and Cabbage.
For cut Cauliflower & Cabbage shelf life is reduced to 3 to 4 days.

4. FORCED UPDRAFT EVAPORATIVE COOLER

The system is an enclosed system with 1 ft^3 volume inside. PU Foam is used as an insulation. Construction is similar to Natural Draft Cooler only the chimney is replaced by fan. Air near the tray containing water is sucked with the help of fan to enhance the effect of adiabatic evaporation. Quantity of water evaporated is increased but increase in relative humidity of 10 to 12% is only observed within the enclosure.



Figure 5. Forced updraft cooler



Figure 6. Vegetable Storage on tray

Gauze is placed above the tray containing known quantity of water. Vegetables are placed over a gauze.

4.1 Thermodynamic Analysis

Assumptions made:

1. The system is under steady state and isothermal conditions.
2. The total pressure within the system remains constant.
3. Air as well as water vapor behaves as an ideal gas.
4. Air flow steadily over water surface at constant velocity.

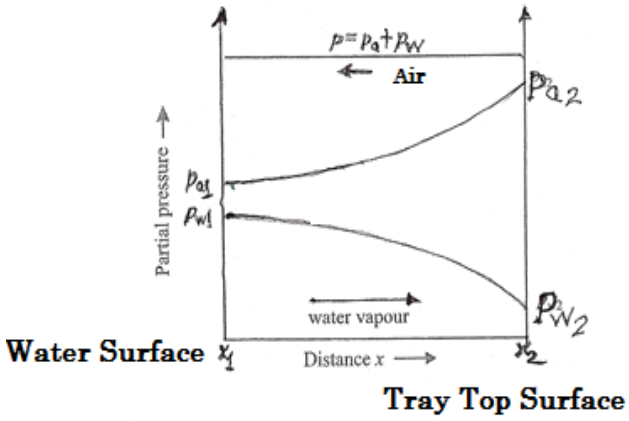


Figure 7. Distribution of partial pressures of water vapor and air

$m_w = h_{mp} . A. (p_{w1} - p_{w2})$ …. Kg/sec
where,
h_{mp} = Mass Transfer Coefficient based on pressure difference.
A= Surface area of water
P_{w1} = Partial Pressure of water vapor at x_1
P_{w2} = Partial Pressure of water vapor at x_2
m_w = Mass of water evaporated in kg/sec [8]

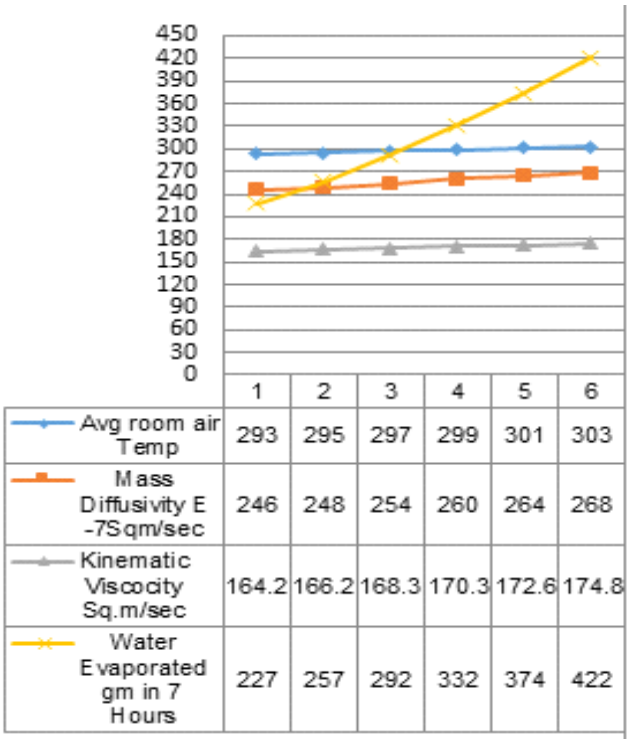
Table 3. Experimental results to determine actual quantity of water evaporated in Forced Updraft evaporative cooler

Date & Time 10 AM	RH % at Room	RH % Inside Cooler	Water Evaporated in 7 Hr
24 & 25 Jan 12	46%	65%	180g (300g)*
26-28 Jan 12	48%	62%	210g (500g)*
29-30 Jan 12	42%	52%	245g (500g)*

- Bracket quantity is the water available in Tray
- Atm. Pr.= 0.93725 bar, Air Velocity = 1m/sec

Forced updraft cooler consumes more power than forced downdraft cooler. Loss of moisture from vegetables is observed in forced updraft cooler. Retainment of relative humidity within the enclosure is difficult in forced updraft evaporative cooler. Continuous non-interrupted power supply is necessary in forced updraft evaporative cooler. But, laminar flow ventilation within enclosure is possible by using forced updraft cooler.

Graph 2. Water evaporated w.r.t average room air temperature and mass diffusivity



	1	2	3	4	5	6
Avg room air Temp	293	295	297	299	301	303
Mass Diffusivity E -7Sqm/sec	246	248	254	260	264	268
Kinematic Viscocity Sq.m/sec	164.2	166.2	168.3	170.3	172.6	174.8
Water Evaporated gm in 7 Hours	227	257	292	332	374	422

Graph 2 indicates that amount of water evaporated will increase with rise in air velocity and average room air temperature. But, increase in absolute humidity within the enclosure is difficult for given air velocity in Forced Updraft Evaporative Cooler. Both, increase in air velocity and average room temperature will enhance the mass diffusivity.

Table 4. Sensory Evaluation after 7 days (5-12 February 2012)

Natural Draft Cooler (Area =0.210 Sq.m)	Forced Draft Cooler Area= 0.095 Sq.m	Open Room	Open Room Cut Vegetables
Water Evapora-ted 150-190 gm in 24 Hours	Water Evaporated 240-310 gm in 7 Hours(v=1 m/sec)	Avg Room Temp Variations 18°C - 22°C	Avg Room RH% 25-45%
Cabbage & Flower more hard, Better	Cabbage & Flower became Soft, Separation, Not O.K	Blackening Spots 20% on Flower & Soft, Cabbage 10% Yellowish	Moisture Loss More, 70% Wastage or Loss, No Fres-hness





Condition of Vegetables after 7 Days in Coolers
Figure 8. a) Natural Updraft b) Forced Updraft





Figure 9. Conditions of vegetables in open room

5. CONCLUSION

Lower RH% & Higher Temp lead to more moisture loss in vegetables. It will result into shrinkage, wilting and loss of freshness. Higher RH% and higher temperature lead to rottening of vegetables. It will make vegetables more susceptible to the attack of micro-organisms. For given conditions performance of Natural draft Cooler is found better than Forced Draft Cooler. Experimental results ascertain the fact that keeping low temperature of 15°C +/- 2°C and RH 70 – 80% will definitely enhance the shelf life of vegetables for all seasons. Findings are useful to construct innovative low cost cold storage for vegetable preservation with combined concepts of evaporative cooling, thermal energy storage and passive insulation.

REFERENCES

[1] "Evaporative Cooling Practical Action", Indian Agricultural Research Institute, Pusa Campus, New Delhi - 110 012, India

[2] Taye S. Mogaji and Olorunisola P. Fapetu "Development of an evaporative cooling system for the preservation of fresh vegetables." African Journal of Food Science Vol. 5(4), pp. 255 – 266, April 2011

[3] J.T Liberty, W.I Okonkwo and E.A Echiegu "Evaporative Cooling: A Postharvest Technology for Fruits and Vegetables Preservation." International Journal of Scientific & Engineering Research, Volume 4, Issue 8, August-2013

[4] Nader V. Chalfoun, "Design and Application of Natural Down-draft Evaporative Cooling Devices." Academy of Scientific Research and Technology, CAIRO, EGYPT, 1990.

[5] J.T. Libertya, B.O. Ugwuishiwua, S.A Pukumab AND C.E Odoc, "Principles and Application of Evaporative Cooling Systems for Fruits and Vegetables Preservation." INTERNATIONAL JOURNAL OF CURRENT ENGINEERING AND TECHNOLOGY ISSN 2277 – 4106

[6] T.Jagadeesh, DR.K.Subba Reddy, "Performance Analysis of the Natural Draft Cooling Tower in Different Seasons." IOSR JOURNAL OF MECHANICAL AND CIVIL ENGINEERING (IOSR-JMCE), VOLUME 7, ISSUE 5 (JUL. - AUG. 2013), PP 19-23

[7] Isaac F. Odesola, and Onwunka Onyebuchi, "A Review of Porous Evaporative Cooling for the Preservation of Fruits and Vegetables." THE PACIFIC JOURNAL OF SCIENCE AND TECHNOLOGY, VOLUME 10. NUMBER 2. NOVEMBER 2009

[8] R. K. Rajput "HEAT AND MASS TRANSFER" S. CHAND & COMPANY, NEW DELHI

[9] Evaporative Cooling Course from NPTEL SITE, INDIA

Application of Virtual Reality in Assessment and Enhancement of Cognitive Abilities of Military Personnel

Khushboo Bhargava[1], Kusum Gupta[2], Sushil Chandra[3], Ahsan Z Rizvi[4]

[1]Banasthali Vidyapith, Jaipur
[2]Institute of Nuclear Medicine and Allied Sciences, Delhi
[3]Indian Institute of Technology, Indore[3]
bhargava.0711@gmail.com

Abstract: **Virtual Reality has been adopted by military for training soldiers for combat situations or other dangerous settings where they have to learn how to react in appropriate manner. Simulated environments such as battlefield scenarios are created which are similar to those faced by the military personnel in real warfare. The subjects are immersed in these situations which have visual and auditory experiences to see their real actions and to demonstrate what their subconscious tactical decisions might be when confronted in a similar manner. As rewinding and repeating are not possible in real environments, through simulations we can re-enact a particular scenario which is safe and less costly.**

To help the soldiers when in real war the cognitive abilities which will be assessed and enhanced are: attention, working memory, stress and focus through the various shooting tasks under various situations performed in VR environment. The neurocognitive tests performed will be: Virtual environment tests and psychological tests. The virtual environment tests are the tasks performed in VR Environment. The psychological tests are D2 attention for focus, BVMT for working memory, TOVA for attention and ECG for stress. They will be judged in cognitive abilities on results of tasks performed. Recorded result will be analyzed through SPSS software. It will give the correlation between various tests based on parameter i.e. Response Time. Thus through the repeated immersion of subject in VR Environment we can enhance the cognitive abilities of military personnel in war situations without actual damage to life.

1. VIRTUAL REALITY

Virtual reality is a computer-simulated environment that makes physical presence in places that are prototype of real world. The environment makes us feel as if we are in a real world. For these environments to be immersive, highly visual and 3D equipments used are head mounted displays, data gloves, VR glasses etc.

1.1 VR in military

- Flight simulation
- Battlefield simulation
- Medic training
- Vehicle simulation
- Virtual boot camp

Using VR we can create an environment through which training can be provided without damage to life. Soldiers are trained in a controlled environment where they perform various tasks similar to those faced by them in the battlefield. Repeated training by performing the tasks can also be done in VR environment in a shorter time. Training through these tasks will help them to perform better when they face the real war.

2. PURPOSE OF THIS REVIEW

This review will focus on various psychological tests and VR environment tests that could be performed to assess and enhance the cognitive abilities of military personnel. The VR environment test will include various shooting task under different conditions and psychological tests include ECG, BVMT, TOVA, and D2 attention. Finally SPSS software will be used to find correlation between various tests based on response time.

3. RECENT FINDINGS

Currently VR is being used for training military personnel for combat situations. Creating simulators for various military operations.

4. VIRTUAL REALITY AND COGNITION

VR is now being used to create environments focused on cognitive processes like: attention, working memory, stress, and focus. Through VR we can create environments which are dynamic, immersive, and three dimensional in which all cognitive abilities are assessed and enhanced. Virtual reality can be defined as a computer controlled multisensory multi

sensor based communication technologies that allow better interactions with data and involve human senses in new ways. This technology enables the people to deal with information more easily. VR provides a different way to see and experience information, one that is dynamic and immediate. The virtual world is interactive; it responds to the user's action. Thus the virtual environments can help a lot in dealing with the actual situations faced by soldiers when in real war.

5. DEVELOPMENT OF VIRTUAL ENVIRONMENT

The VR environment can be developed using various game engines like unity, cry engine, unreal etc. Game engine is a software framework designed for the development of video games. The functionality provided by game engine includes 2D or 3D graphics, collision detection, sound, scripting, animation, artificial intelligence, networking etc. Game engines can be written in any programming languages like C, C++, and java though each language is structurally different and may provide different levels of access to specific functions.

6. VR ENVIRONMENT TESTS

This will include some tasks similar to those faced by soldiers when in a battlefield. Some of the tasks are shooting enemies, keeping track of changing position of enemy and your peers, your prevention, keeping yourself focused and stress free.

7. PSYCHOLOGICAL TESTS

7.1 Paper and pencil tests

Questionnaires which include statements which have to be answered in yes or no. They are easy to take.

7.1.1 D2 Attention test

This test is done to measure the focus of subject. It asks participants to cross out any letter'd' with two marks above it or below it in any order. The surrounding distractors are usually similar to the target stimulus, for example a 'p' with two marks or a'd' with one or three marks. Thus it measures processing speed, rule compliance, and quality of performance, allowing an estimation of individual attention and concentration performance.

7.1.2 Brief visuospatial memory test (BVMT)

This test is done to measure working memory of subject. Six geometric figures are printed in a 2 x 3 array on separate pages.

Test structure

The subject performs three trials in which he views the stimulus page for 10 seconds and is asked to draw as many of the figures as possible in their correct location on a page in the response booklet. A delayed recall trial is administered after a 25-minute delay. Last, a recognition trial, in which the respondent is asked to identify which of 12 figures were included among the original geometric figures, is administered.

8. COMPUTERIZED TEST

8.1 Test of variables of attention (T.O.V.A.)

The test is used to measure a number of variables involving the test takers response to either a visual or auditory stimulus. For individuals between the ages of 4-5, the T.O.V.A test is 10.9 minutes long, while for older individuals the test lasts 21.6 minutes. During the first section of the test, the objective is to measure attention during a boring task. For adults, this section is 10.8 minutes long and the non-target is presented 3.5 times for every 1 time a target is presented. The second section of the test is a measure of attention where target is presented frequently. This section is also 10.8 minutes long and the target is presented 3.5 times for every 1 time a non-target is presented. The T.O.V.A. measures a set of different variables to determine whether or not response times and attention is at the normal range for the sex and age of the test take.

9. CONCLUSION

The Virtual reality technology is widely used in clinical research, battlefield training and many other fields. The objective is to measure the cognitive functions through virtual reality and to validate with psychological tests, as well as provide it as a training and assessment module. If we compare the VR environment with computerized test battery and paper pencil test then we will get the better results. Virtual Environment should be highly immersive because it will increase the possibility of better feel of environment and score. This could be the limitation of experiment. The age factor, environment parameters becomes limitation to get better results. Environment gives better results as comparison to psychological test at a certain level.

10. FUTURE SCOPE

After the experiment though there is an improvement in cognitive functions of subjects but only few results are significant. As the frontal lobe of our brain is mainly responsible for the attention related tasks and occipital lobe is also i.e. related to vision do not shows significant improvement for all the channels. We can also consider other parameters while considering the SPSS software to find the correlations. Other psychological tests could also be used to give better results. We can also try to make the VR environment more immersive.

REFERENCES

[1] Parsons, T.D., and Albert, R., "Neuropsychological Assessment of Attention Processing using Virtual Reality", *Annual Review of Cyber Therapy and Telemedicine* vol. 6, November 1, 2008 pp. 01-10.

[2] Rene, H., "Virtual Reality in the Military: Present and Future", *Student Conference on IT* vol. 2, April 13, 2010

[3] Parsons, T.D., and Albert, R., "Initial Validation of a Virtual Environment for Assessment of Memory Functioning: Virtual Reality Cognitive Performance assessment", *CYBERPSYCHOLOGY & BEHAVIOR* vol. 11, November 1, 2008.

[4] Parsons, T.D., McPherson S., Victoria S.P., "Enhancing Neurocognitive Assessment Using Immersive Virtual Reality", *IEEE Conference* vol.5, December 2008

[5] S. L. Anna, H. L.Robert, G. P. David, "The impact of secondary tasks on multitasking in a Virtual environment", 22 November 2005.

[6] Parsons T.D., Courtney C., Albert A. Rizzo, Armstrong Christina, Edwards Joseph, and Reger Gregory," Virtual Reality Paced Serial Assessment Test for Neuropsychological Assessment of Military Cohort", *Medicine Meets Virtual Reality 19 J.D. Westwood et al. (Eds.) IOS Press, 2012.*

[7] Gobbetti Enrico and Scateni Riccardo., "Virtual Reality: Past, Present, and Future", *13th International Conference on Multimodal Interaction - ICMI 2011,* June 3, 2010.

[8] Antonio Yuri, Vilas Boas Gonçalves, "Overview of Virtual Reality Technologies", March 8, 2014.

[9] Sebastian T.K., Crucian G.P., Dünser Andreas, Bartneck Christoph, John C Dalrymple-Alford , "Validity evaluation of a spatial memory task in Virtual environments", *CYBERPSYCHOLOGY & BEHAVIOR* vol.12, March 2, 2009.

Data Science – A Statistical Modelling in Health Science

Sarojini G. Deshmukh[1], U. B. Aithal[2]

[1,2] *Jagdishprasad Jhabarmal Tiberewala, University, Rajasthan*

Abstract: **In the developmental stage of fields of Science, Technology, Social Science, Business and management, Health Science etc., there is problem of dealing of Big Data which is one of the most promising trends and which has led to the development of a new interdisciplinary area called Data Science. Data science includes high performance computing, data processing, development and management of databases, data warehousing, mathematical representations, statistical modeling and analysis, and visualization with the goal of extracting information from the data collected for domain-specific applications. With a major Big Data objective of turning data into knowledge, statistics is an essential scientific discipline because of its sophisticated methods for statistical inference, prediction, quantification of uncertainty, and experimental design. The facts collected during enquiry are made flawless for the scientific decisions by using statistical modeling techniques and inferences. Statistical thinking helps to make scientific discoveries, quantifies the reliability, reproducibility and general uncertainty associated with the big data.**

In the health sciences most studies are concerned with the possible causes, remedies, determinants, related factors of a set of observations related to socio-economic-cultural, health, environmental status of a person facing any disease. Healthcare Scientists appeal to statistical modeling to confirm their hypotheses about possible causal relationships among the characteristics they consider, by taking the controlling relevant covariates and especially possible confounding factors to what extent can a statistical model performs about causal relationships among characteristics.

Keywords: **data science, big data, statistical modeling, health care analysis.**

1. INTRODUCTION

The new era of statistics is observing, exciting developments and new trends in statistical modeling and its applications in various fields of Science, Technology, Social Science, Business and Management, Health Science etc. In such developmental stage, there is problem of dealing of Big Data which is one of the most promising trends and which has led to the development of a new interdisciplinary area called Data Science. In the field of statistics, Cleveland [5] introduced this term as a new direction for the statistical area in 2001. It is used in the prominence of sagacity of statistical methods at large for collecting, analyzing and modeling of it. Data science includes high performance computing, data processing, development and management of databases, data warehousing, mathematical representations, statistical modelling and analysis, and visualization with the goal of extracting information from the data collected for domain-specific applications. One of the most active areas of data science research is related to very large data sets, or big data, which pose computational and statistical challenges to the investigator. [11] One of the examples of how big data have changed statistical inference is multiple testing, a tool of testing which include a wide variety of people, allowing interdisciplinary areas to be contained in multiple field having multiple hypothesis testing is a fundamental problem in statistical inference where the primary goal is to consider a set of hypothesis tests simultaneously. [8] For instance, health study incorporates concepts from both statistics and health science and it is possible for an individual working in this area to be both a statistician and a health scientist.

Health Science data tries to sense out of observations, the selection of what one observes depends upon underlying thrust of study and theoretical constructs. The facts thus collected are however often far from flawless for the scientific decisions. Statistical thinking not only helps make scientific discoveries, but it quantifies the reliability, reproducibility and general uncertainty associated with these big data. Statistical thinking will be vital to Big Data challenges. With a major Big Data objective of turning data into knowledge, statistics is an essential scientific discipline because of its sophisticated methods for statistical inference, prediction, quantification of uncertainty, and experimental design. Such methods have helped and will continue to enable researchers to make discoveries in science, government, and industry. The Big Data Research and Development Initiative announced in USA in March, 2012 to help accelerate the pace of discovery in science and engineering, strengthen the national security, and transform teaching and learning. Since the launch of the initiative, the National Science Foundation (NSF), the National Institutes of Health (NIH), and the Defense Advanced Research Projects Agency (DARPA) of USA have launched major Big Data programs. [2]

2. RESEARCH METHODOLOGY

A model is not personal mental image of some reality but is inter subjective constructions which can be applied with the

aim of providing a simplified form of complex reality. A statistical model is based on stochastic representation of real world. It is made up of a set of assumptions under which the data are to be analyzed and interpreted.

Typical assumptions of statistical models are: whether the observed random variables follow identical distribution; the observations are independent; the basic sampling distributions are continuous and may pertain to a family characterized by a finite number of parameters.

In this research paper researcher is trying to highlight the key points of data science and the applications of statistical modelling related to health research. The information is searched and gathered by the researcher using secondary sources like published journals, online journals, published books, online books, etc. And the primary data of anaemic condition of the females of reproductive and non-reproductive age groups is collected from the Kolhapur city. This primary data is analysed using fitting of model to the data and testing its goodness using chi - square test.

3. OBJECTIVITY OF THE PROBLEM

In this paper an attempt has been made to find out different aspects of data of health and hence to fit a suitable model for the observed data of anaemic condition of women of different age groups and its inter-relations.

4. HEALTH SCIENCE SCENARIO

Data in Health science are massive, can vary from patient to patient in a very significant way. In the health sciences most studies are concerned with the possible causes, remedies, determinants, related factors etc. of a set of observations related to socio-economic-cultural, health, environmental status of a person facing any disease. In this field in particular, for policy or planning reasons, it is important to know what causes which effects and its inferences for future prophecy. The raw data of health are produced by complicated measurement technologies that introduce bias and variation that must be removed before the measurements represent biological quantities of interest. Similarly, to produce results that will replicate in future studies, it is critical to account for the biological variability between individuals and within an individual. Models are often characterized in terms of parameters—numerical characteristics of the model.

Health care Scientists appeal to statistical modeling to confirm or disconfirm their hypotheses about possible causal relationships among the variables they consider, taking controlling for relevant covariates and especially for possible confounding factors to what extent can a statistical model say something about causal relationships among variables. Finding a model that adequately describes the main features of the medical data is a process consisting of initial data analysis, graphical checks, parameter estimation and assessment of goodness of fit. [3]

In health research it is essential to use various multivariable modeling techniques. Multiple linear regression models, logistic regression analysis and proportional hazards regression models are mostly applicable in health research. Linear regression is used with interval outcomes (such as level of hemoglobin). With interval variables, equally sized differences on all parts of the scale are equal. Hemoglobin level is an interval variable. Logistic regression is used with dichotomous outcomes (yes or no; for example, severity of anaemia). Proportional hazards regression is used when the outcome is the length of time to reach a discrete event such as end point of disease or death.

There is a special class of statistical model called as structural model or causal model for describing multivariate data modelling. Structural equation modeling is a multivariate statistical analysis technique that is used to analyze structural relationships. Structural equation modeling technique is the combination of factor analysis and multiple regression analysis, and it is used to analyze the structural relationship between measured variables and latent constructs. Structural equation modeling is preferred by the researcher because it estimates the multiple and interrelated dependence in a single analysis. [8] In structural equation modeling, two types of variables are used endogenous variables and exogenous variables. In structural equation modeling, endogenous variables are equivalent to dependent variables. In structural equation modeling, exogenous variables are equal to the independent variable.

In structural equation modeling, theory can be thought of as a set of relationships providing consistency and comprehensive explanations of the actual phenomena. It is also termed as causal modeling.

Causal models

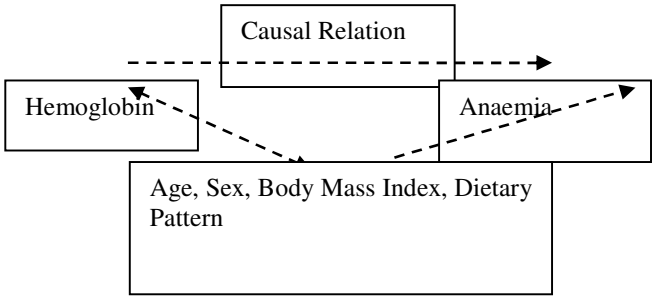
If the analyst wants to draw causal inferences, then the approach has to move from a descriptive one to a modeling approach. Causal relationships can arise through a number of pathways. Models and estimators vary in sophistication with the degree of detail of the causal relationship the analyst is aiming to uncover. [10] For example, maternal education can affect child health either directly, through knowledge of healthy behavior, or indirectly, through preferences for child health. If the analyst is interested simply in whether educating women is an effective means of raising child health, irrespective of the mechanism through which it works, then the statistical model, and estimator, can be quite simple.

Constructs are defined at different levels, and the hypothesized relations between these constructs operate

across different levels. These types of "multilevel" theoretical constructs require specialized analytic tools to properly evaluate. [8]

The medical model takes a reductionist view of health: Disease is seen simply as a defect in the person that is corrected by medical intervention. We can see how this plays out, for example, in how modern epidemiologists identify risk factors for disease. Epidemiology has constructed a number of authoritative design approaches (e.g. disease-control studies) and analytic tools (e.g. logistic regression that produces relative risk estimates) that are used to identify significant risk factors for development of, say, anaemia disease in women. Important risk factors for anaemia include genetic tendency; biology (low level of hemoglobin); dietary pattern (malnutrition); culture (background); and environment (access to health care). However, even though these factors clearly are operating at different levels, they are almost always measured at the individual-level.

Causal Relation between the variables Age, Sex, Body Mass Index, Dietary Pattern and hemoglobin.



5. USE OF COMPUTATIONAL STATISTICS WHILE DEALING WITH BIG DATA

Here the term "computational statistics" is used somewhat more broadly to include not only the methods of statistical computing, but also statistical methods like modelling that are computationally intensive. Thus, to some extent, "computational statistics" refers to a large class of modern statistical methods. [14]

While comparing between computational statistics and statistical computing the emergence of the field of computational statistics becomes coincidental with that of statistical computing, and would not have been possible without the developments in statistical computing. [7]

Predictive analytics, involves searching for meaningful relationships among variables and representing those relationships in models. There are response variables—things we are trying to predict. There are explanatory variables or predictors—things we observe, manipulate, or control that could relate to the response. Consider three general approaches to research and modeling as employed in predictive analytics: traditional, data-adaptive, and model-dependent. The traditional approach to research and modeling begins with the specification of a theory or model. Traditional methods, such as linear regression and logistic regression, estimate parameters for linear predictors. [4] Model building involves fitting models to data. After we have fitted a model, we can check it using model validity techniques for its future prophecy. In general, statistical analysis involves the prescribed expression of uncertainty in terms of probabilities. The reality that statistical analysis generates probabilities that there are relationships should not be seen in itself as an argument against the use of statistical evidence. [9]

Table showing age wise distribution of women having anaemia:

Age Groups	Number of women having anaemia	pi (proportion)
15-19	12	0.03428571
20-24	23	0.06571429
25-29	12	0.03428571
30-34	20	0.05714286
35-39	29	0.08285714
40-44	45	0.12857143
45-49	62	0.17714286
50-54	67	0.19142857
55-59	80	0.22857143
Total	350	1.0000000

A single predictor Poisson Regression model is fitted to the observed data to test the research hypothesis regarding the relationship between the age and anaemia.

$p_i = e^{(-\alpha + \beta x)}$

where p_i: probability of outcome of anaemia in different age groups,

β : regression coefficient

α: intercept

e = 2.7183 is the base of the system of natural logarithms.

X = can be categorical or continuous.

The analysis is carried out and the result showed that, Predicted p_i of Anemia = $e^{(-4.35 + 0.0512* \text{Age})}$

The Chi-square goodness of fit test is used to check the effectiveness of the model that yielded a calculated value 11.62. At 5% level of significance the critical value is $\chi^2_{0.05}(8) = 15.507$ and is insignificant ($p > 0.05$). It shows that the model defined above is good for the data corresponding to anemia.

6. CONCLUSION

In this paper, we demonstrate that the Poisson regression modelling technique can be a powerful analytical technique for use when outcome variable is dichotomous. The effectiveness of the model was checked by predicted probabilities and inferential goodness of fit test.

REFERENCES

[1] Ahalt, S., et al. (2014), "Data to Discovery: Genomes to Health", A White Paper from the National Consortium for Data Science. RENCI, University of North Carolina at Chapel Hill. http://dx.doi.org/10.7921/G03X84K4

[2] A Working Group of the American Statistical Association, (July 2, 2014), "Discovery with Data: Leveraging Statistics with Computer Science to Transform Science and Society", ASA.

[3] Bender R., Grouven. U. (1997), ''Ordinal Logistic Regression in Medical Research'', Journal of the Royal college of Physicians of London, Vol. 31 No.5.

[4] Chao-Ying J P, et al. (September/October 2002), ''An Introduction to Logistic Regression Analysis and Reporting'', The Journal of Educational Research, [Vol 96(No. 1)]

[5] Cleveland W. (2001). "Data science: An action plan for expanding the technical areas of the field of statistics", Int. Statist. Rev, 69: 21-26.

[6] Douglas A. Luke, (2005), Luke Fina pdf, Book of Multilevel modelling, Saint Louis University School of Public Health.

[7] James E. Gentle, et al, (2012), "How Computational Statistics Became the Backbone of Modern Data Science", http://sfb649.wiwi.hu-berlin.de ISSN 1860-5664

[8] J.D. Storey, (2002) "A direct approach to false discovery rates", Journal of the Royal Statistical Society: Statistical Methodology 64 479–498.

[9] Naser A. Rashwan and Maie M. Kamel, (2011), "Using Generalized Poisson Log Linear Regression Models in Analyzing Two-Way Contingency Tables", Applied Mathematical Sciences, Vol. 5, no. 5, 213 – 222

[10] Pearl J. (2000), Causality. Models, Reasoning, and Inference, Cambridge University Press, Cambridge.

[11] Tze Leung Lai (2013), "Data Science, Statistical Modeling, and Financial and Health Care Reforms", Department of Statistics, Stanford University, Stanford, CA 94305-4065, USA.

ABSTRACTS

Recent Developments and Future Role of Hydropower, Solar and Wind Energy Resources in India

Aditya Chauhan[1], Ganesh Panday[2], Sachin Chauhan[3], Jagdish Singh Mehta[4]

[1,3,4]Department of Mechanical Engineering, Graphic Era Hill University, Bhimtal Campus, Nainital, Uttarakhand, India
[2]Department of Chemistry, Graphic Era Hill University, Bhimtal Campus, Nainital, Uttarakhand, India

ABSTRACT

Energy is the primary and most universal measure of all kinds of work by human beings and nature. Non-conventional sources of energy is one of the areas of emerging technologies which have higher prioprity with reference to national needs.The present review article deals with the study of developments in hydropower, solar and wind energy and their role as alternative energy resources. Renewable energy sources currently supply somewhere between 15 to 20 percent of world's total energy demand. New renewable energy sources (solar energy, wind energy, modern bio-energy, geothermal energy, and small hydropower) are currently contributing about two percent. The most important application for new alternative energy resources, such as wind, solar, hydro electric power, is in the area of electric power generation. Wind power can be generated from the energy potential of on-shore wind flow on a cost-competitive basis, but only at a low-load factor of about 20%. Solar thermal energy, on the other hand, is an economically feasible option mainly for water heating. Hydro power is developed by allowing water to fall under the force of gravity. Infact the generation of Hydro power on a large scale became possible around the beginning of the twenieth century only with the development of electric power transmission.

Key words: Renewable energy resources, Hydro, Wind, Solar, Electric power

*****

Construction of PBIB Designs through Chosen Lines and Triangles of Graphs

Davinder Kumar Garg[1], Syed Aadil Farooq[2]

[1]Department of Statistics, Punjabi University, Patiala-147002 (India)
[2]Research Scholar, Department of Statistics, Punjabi University, Patiala-147002 (India)

ABSTRACT

In this paper, we have constructed partially balanced incomplete block (PBIB) designs with two and three associate classes by establishing a link between PBIB designs and graphs through the chosen lines and the number of triangles. We have considered six configurations for this purpose and constructed four two associate class PBIB designs and two three associate class PBIB designs.

Keywords: *PBIB designs, Graphs, paths, points, lines, triangles*

*****

Comparative Study of Various Evapo Transpiration Methods

(A case study with special reference to Jodhpur Region)

Er. Daria Singh, Jodhpur

ABSTRACT

Water is the prime need for the survival of all living things, whether it belongs to flora kingdom or fauna kingdom and industrial development. The demand on water for domestic, commercial, industrial and agricultural purposes is increasing significantly in the recent past. The situation is exacerbated by the growing population and urbanization, thereby there is an increased pressure on agriculture.

In the practice of sustainable water resources management, knowledge of evapo-transpiration (ET) over a range of spatial and temporal scale is essential. During the past several decades, ET estimates have widely been used in water resources management, hydrological modeling and irrigation scheduling to define crop water requirements. Such estimation of crop water requirements is one the principle steps in planning, designing and operation of irrigation and water resources system. These crop water requirements vary with crop characteristics and local agro-hydro-meteorological conditions. A number of methods for its evaluation are available but they all have their own limitations.

The evaporation and evapo-transpiration are closely simulated by the evaporation pan. The processes, in turn, depend upon the various climatological factors. Temperature, Relative Humidity, Sunshine hours, Wind velocity and Rainfall are the major hydro-meteorological parameters, which influence the pan evaporation.

Since, Kharif Crop Season (Week No. 26–44) and Rabi Crop Season (Week No. 45 – 10) are the two main agricultural seasons in Jodhpur region of Rajasthan, hence these two seasons have been selected for the present study.

FAO–24 Penman (Modified) Method has been chosen as reference method for estimation of evapo-transpiration for Jodhpur Region due to its wide applicability all over the world. Different methods for estimating monthly evapo-transpiration have also been used. They are compared and correlated with FAO–24 Penman method for increasing the applicability of these methods in Jodhpur region of Rajasthan.

*****

Impedance and Dielectric Spectroscopy of Nano-Graphite Reinforced Silicon Elastomer Nanocomposites

Janita. Saji[1], A. Khare[2], S.P. Mahapatra[2]

[2]Department of Physics, National Institute of Technology, Raipur 492010 India
[3]Department of Chemistry, National Institute of Technology, Raipur 492010 India

ABSTRACT

Impedance and dielectric spectra of silicone elastomer nanocomposites were used to study their secondary (α* or β) relaxation behavior as a function of nano-graphite loadings in the frequency range of 10^{-1} to 10^{6} Hz. The effect of nano-graphite loadings on real and imaginary parts of complex impedance was distinctly visible and explained on the basis of interfacial polarization of filler and relaxation dynamics of polymer chains. The effects of nano-graphite loadings on loss tangent, dielectric permittivity, complex dielectric modulus and electrical conductivity have also been studied. The dielectric permittivity of the composites strongly depends up on the extent of nano-graphite concentration and temperature. The conductivity and relaxation phenomenon have been investigated through dielectric modulus formalism. Nyquist plots, Cole-Cole plots and Argand diagram confirm the existence of non-debye relationship. The frequency dependence of ac conductivity has been investigated by using Percolation theory. The percolation phenomenon has been discussed from electrical conductivity and dielectric permittivity. The percolation threshold was found to be at 6 phr nano-graphite loading. SEM photomicrographs shows well dispersion of nano-graphite.

Keywords: Elastomer; nano-graphite; impedance; dielectric; relaxation; conductivity; percolation.

****

Moments of Order Statistics from Lindley Distribution in the Presence of Multiple Outliers

Mahesh Kumar Panda

Centre for Statistics, Central University of Orissa, Koraput (764020), Odisha
mahesh2123ster@gmail.com

ABSTRACT

In this article, exact expressions for the single and product moments of order statistics from Lindley distribution under the contamination model have been derived. Contamination model is an outlier model where one considers the possibility that some of the observations come from altered form of the originally anticipated distribution. The most commonly studied contamination model, and the one which we have considered is called the slippage model. Generally, in literature most of the works have considered the single outlier model with regard to slippage model due to the fact that; the algebraic and computational difficulties arise when the number of outliers increases. Suppose be n random variables then we assume that $X_1, X_2, ..., X_{n-k}$ are independently distributed with probability density function (p.d.f.) f(x) while the remaining k (i.e. Outliers) $X_{n-k+1}, ..., X_n$ are assumed to be independent with p.d.f. arises from some modified version of f(x), which is called g(x), in which the location and/or scale parameters have been shifted in value. Next, we have obtained the effect of the outliers on the Best Linear Unbiased Estimator (BLUE) of the scale parameter.

Keywords: Lindley distribution, Contamination model, Outlier model, Slippage model, BLUE.

*****

Vapor Phase Alkylation of Aniline Over Ferrite Nanoparticles

Malvika Kadian[1], R.K Gupta[2]

Guru Jambheshwar University of Science and Technology, Hisar-125001
malvikadian@gmail.com

ABSTRACT

Various ferrospinels of Copper and Cobalt viz. $CuFe2O_4$ (CF-1), $Cu_{0.75}Co_{0.25}$ $Fe2O_4$ (CF-2), $Cu_{0.5}Co_{0.5}$ $Fe2O_4$ (CF-3), $Cu_{0.25}Co_{0.75}$ $Fe2O_4$ (CF-4), $CoFe_2O_4$ (CF-5) were prepared by low temperature co-precipitation method.They were characterised by various techniques.On scanning by I.R, they showed two strong bands, one at 700 cm^{-1} due to stretching vibration of tetrahadral M-O group and the other at 500 cm^{-1} due to stretching vibration of octahedral M-O group. XRD analysis showed the single phase spinel structure for all the compositions. Their particle size calculated using XRD was found to be at nanometer scale. Surface morphology of the $Cu_{1-x}Co_xFe_2O_4$ (x=0, 0.25, 0.5, 0.75 and 1) nanoparticles was investigated by scanning electron microscopy. The vapor phase alkylation of aniline with methanol was carried out in a fixed-bed down-flow reactor. The composition of the product mixture was analysed by using high performance liquid chromatography (HPLC). Among the different composition of the system, ferrospinels possessing low ´ x ' values were found to be highly active and selective for NMA at temperature 350˚C, WHSV $0.5h^{-1}$ and molar ratio of methanol to aniline 5. The surface area and acidity of the ferrospinels follow the order CF-1 < CF-2 < CF-3 < CF-4< CF-5.

*****

Sequential Testing Procedures in a Family of Lifetime Distributions with Applications

Md. Wasi Alam

Indian Agricultural Statistics Research Institute, New Delhi-12
wasi@iasri.res.in

ABSTRACT

A family of distributions has been considered. Sequential testing procedures have been developed for the family when the known parameter is assumed to be constant. Sequential testing procedures have also been developed for the family under the situation when known parameter has undergone a change and the robustness of the developed testing procedures have been examined. The developed sequential testing procedures have been applied on real data set on mortality rate of white fly (*Bemissia tabaci*) after spray of the Imidacloprid at the concentration of 0.2%.

Keywords: Sequential probability ratio test; family of distributions; robustness, white fly.

*****

Chaos in Science and Engineering

Mohammad Sajid

College of Engineering, Qassim University, Buraidah, AlQassim, Saudi Arabia
msajid@qec.edu.sa

ABSTRACT

Chaos is new scientific tool developed over recent years that is utilized for solving advanced scientific and technological research problems. It brings science and technology on advance level in many disciplines and it is increasingly being used in all many research areas, due to its wide-ranging applications. For development and modernization of science and technology, it is necessary to include chaos theory in the fundamental research as well as its applications. Some advantageous thought on chaos from current applicable researches are extracted. It attracts mathematicians, scientists and technologists toward chaos theory in any field of their researches. The goal of this presentation is to demonstrate some advancement in mathematics, science and technology using chaos theory followed by its basic introduction.

Keywords: Bifurcation, chaos, iteration, fixed points, periodic points.

*****

Axisymmetric Deformation in Transversely Isotropic Thermoelastic Media

Nidhi Sharma, Parveen Lata

ABSTRACT

The present investigation deals with the axisymmetric deformation in anisotropic thermoelastic solid due to thermomechanical sources. Laplace and hankel transform techniques are employed to solve the problem. The integral transform have been inverted by using a numerical technique to obtain the displacement, stresses, conductive temperature. Effect of anisotropy at the various temperatures is depicted graphically. Concentrated normal force and normal force over the circular region have been taken as an application of the approach.some special cases of interest are deduced.

*****

Impact of two Temperature in Thermoelastic Media

Nidhi Sharma[1], Parveen Lata[2]

ABSTRACT

In this paper,the effect of angle of inclination at the interface of a transversely isotropic thermoelastic media due to inclined load is investigated. Effect of two temperature on the various inclinations is analysed.Result is derived and analysed on the components of displacement, stresses and conductive temperature.Laplace transform with respect to time variable and fourier transform with respect to space variable are applied to solve the problem.Expressions of stresses,conductive temperature in the transformed domain are obtained.The numerical inversion technique is used to obtain the solution in physical domain.Graphic representations due to response of two temperature and changes of inclination are shown.Some particular cases are also discussed.

******

Schiff Bases of Heterocycles and their Metal Complexes: Synthesis, Spectral, Thermo- analytical and Biological Applications

Sangamesh A. Patil[1], Bhimashankar M. Halasangi[2], Prema S. Badami[3]

[1,2]P.G. Dept. of Studies in Chemistry, Karnatak University, Dharwad- 580003, India.
[3]Department of Chemistry, Sharanabasaveshwar College of Science, Gulbarga- 585102, India
[1]patil1956@ rediffmail.com

ABSTRACT

Series of Co(II), Ni(II) and Cu(II) metal complexes of newly synthesized Schiff bases derived from 2-hydrazino-4-(coumarin-3-yl)thiazole and isatin/ 5-chloroisatin have been studied. Schiff bases have been characterized by NMR, IR and mass spectral data. The bonding of Schiff bases to the metal ions through donor atoms has been confirmed on the basis of IR spectral study. The elemental analyses of metal complexes indicate the stoichiometry of the type $MLCl_2$. Further, this has been supported by the mass spectral data. The molar conductance values of metal complexes reveal that, all the metal complexes are non- electrolytic in nature. The thermo- analytical data indicates that, the synthesized metal complexes underwent three step decomposition. The magnetic moment values of all the metal complexes are well in agreement with the paramagnetic nature. The UV-vis spectral data along with the magnetic property confirm the octahedral geometry for all the metal complexes.

Most of the metal complexes exhibited better anti-microbial activities compared to the corresponding Schiff bases. The DNA cleavage study of metal complexes indicates that, all the metal complexes potentially cleaved the DNA of *E. Coli*.

The analytical, magnetic, spectral and thermo- analytical data indicate that, all the Co(II), Ni(II) and Cu(II) complexes exhibit co-ordination number six.

*****

Application of Electro-chromic Tungsten Oxide Nano Wires to Determine Bioelectrogenesis in Microbial Fuel Cells

Sharma I.[1], Ghangrekar M.M.[2]

[1]P.K.Sinha Center for Bioenergy, Department of Civil Engineering
Indian Institute of Technology, Kharagpur (W.B.)-721302
[1]itisharma@atdc.iitkgp.ernet.in, [2]ghangrekar@civil.iitkgp.ernet.in

ABSTRACT

The production of wastewater and energy requirement will never be discontinued till the human being is on earth. Microbial fuel cells (MFC), furnished with different electrode materials and bacterial inoculum are the advance technology for biological conversion of chemical energy of the waste organic matter in to electricity. The electrogenic microbial populations, those are capable of moving electrons to solid phase materials like electrodes, are the key research subject of above technology. Thus MFC, having this population have been shown to be effective for solid/liquid waste remediation with the added benefit of generating electricity. Domestic wastewater or sludge is the most popular inoculums for MFCs. Apart from sludge, various other sources like soil, cow dung, pure cultures, sand, mining soil etc. are used in MFCs to make microbial biofilm. However, there is no existing method to check whether the electrogenic microbes are present in the MFCs system even after their inoculation in the reactor.

The MFCs required 0–8 days for current generation depending on the inoculum source. Technologies related to sensing electrochemically active bacteria can make it easy to select proper inoculum for Anodic chamber of MFC, thus it can enhances reliability and sustainability of the MFC start-up and operation. In this study, WO_3 nano fibers are synthesized by the hydrothermal method to evaluate electrochemical property of microbial population by way of chromatic changes. Sodium tungstate dihydrate and sodium chloride treated with hydrochloric acid were used to synthesize crystalline nano WO_3, using Teflon autoclave at 180 degree for 16 hours.

The structural and morphological characterization of tungsten oxide nano fibers was done using XRD and FESEM, respectively. The chromatic changes in the inoculated sample after addition of electro-chromic nano WO_3, produced significant blue color due to extracellular electron transfer of electrogenic bacteria. Therefore, this is the rapid detection technique which can be accomplished in a test tube to determine electrogenic property of microbial populations in the inoculum used in MFCs. This kind of rapid identification of electrogenic microorganism will make selection of suitable inoculum for MFC to expedite its start-up and harvest more power in terms of direct electricity using organic wastewater or waste slurries as fuel. This is the first effort of external identification of electrogenic activity and further efforts are on for standardization of this test protocol.

*****

Evaluation of Selected Medicinal Plants to judge their Confirmation as Anti-Diabetic Using Mathematical and Statistical Techniques

Sonia Sharma[1], Rachit Kumar[1], Hemlatha Vasishtha[2], Deepankar Sharma[4]

[1,2]Sai Nath University, Ranchi - India
[3]IIMT Institute of Engineering & Technology, Meerut IIMT, Meerut - India
[4]D.J. College of Phamacy, Modinagar – India, [1]s29sonia@gmail.com

ABSTRACT

The present study based on the statistical and mathematical studies of three selected plant. Keeping in view the comprehensive statistical analysis of selected potential extracts were carried out to evaluate and statistically signify their efficacy data in the treatment of diabetes mellitus. The efficacy data of the selected medicinal plants were applied to critical statistical tools for their antioxidant, anti-diabetic and anti-hyperlipidemic activities. The statistical and mathematical analysis were carried out for the herbal antidiabetic selected medicinal plants. The given plants may exert their activity throughout different and sometimes combined pathways targeting most organ tissues implicated in the pathophysiology of diabetes mellitus such as pancreas, liver, intestine, kidney and peripheral tissues. These plants devotee special attention for their multi and unexpected mechanisms of action through the pharmacological studies with the help of statistical and mathematical tools. All the extract of all three plants were standardized with detailed pharmacological studies by various tools. All extract were found to be safe and useful in diabetes and its complication. This paper will enhance the possible mechanism of action of the phytoprinciples for their pharmacological response with help of statistical and mathematical tools. These tools will provide safety, efficacy and toxicity data for the selected medicinal plants and the rationale behind their use as anti-diabetic drugs. These tools will enhance their claim to be used as regular anti-diabetic drugs.

Keywords: medicinal plants, diabetes, mathematical tools, statistical tools, biological activity.

*****

Probabilistic Analysis of a Standby System with Provision of Priority of Repair

Upasana Sharma[1], Jaswinder Kaur[2]

[1]Department of Statistics, Punjabi University, Patiala
[1]usharma@pbi.ac.in, [2]jassusidhu7@yahoo.in

ABSTRACT

The present study deals with a standby system consisting of two compressor units. Initially one unit is operative and the other is standby. For the system to be in operating state only one unit is needed. The operative unit can fail due to due to various types of failures which can be categorized as- serviceable type, repairable type and replaceable type. In case of any type of failure the priority of service, repair or replacement is given on FCFS basis. Real data on failure and repair rates of such units collected from milk plant, have been used for present study. Mean time to system failure and availability has been computed graphically as well as numerically by using semi-Markov process and regenerative point technique for the present system.

Keywords: *Compressor unit, Regenerative point technique, Refrigeration system, semi-Markov process.*

*****

Synthesis and Characterization of Porous Coordination Complex/Polymer from Cashew Nut Shell Liquid (CNSL): A Sustainable Development

Fahmina Zafar[1], Hina Zafar[2], Eram Sharmin[3], Nahid Nishat[4]

[1,4]Inorganic Materials Research Laboratory, Department of Chemistry, Jamia Millia Islamia, New Delhi 110025, India
[2] Division of Inorganic Chemistry, Department of Chemistry, Aligarh Muslim University Aligarh 202002, India
[3]Department of Pharmaceutical Chemistry, College of Pharmacy, Umm Al-Qura University, Makkah Al-Mukarramah
fahmzafar@gmail.com

ABSTRACT

Sustainable resources have been attracted considerable attention in the development of different kind of materials for versatile field of applications due to their non toxic nature, various functionality, environmental concerns as well as depletion of petroleum feed stock. Later problem reflects a global requirement for sustainability without resource exhaustion. Cashew nut shell liquid (CNSL), is an agro byproduct, associated with anacardic acid, cardol, 2- methyl cardol and cardanol. It is a versatile and valuable raw material for wide applications and considered as an alternative resource for the petroleum derived materials. In present work an attempt has been taken to synthesize porous coordination complexe/polymer from technical Cashew nut shell liquid (TCNSL, contains 62.86 % Cardanol) with divalent Manganese ions (Mn^{2+}) via "solid- state in situ" approach with conventional and microwave-irradiation techniques. The synthesized materials have been characterized by FTIR and UV-Vissible spectral techniques. Hydrophilic and hydrophobic behavior of the synthesized coordination complex / polymer has been determined by contact angle measurement. Morphology of the materials has been tested by Optical microscopy, Scanning Electron Microscopy (SEM) and High-resolution transmission electron microscopy (HRTEM) while amorphous or crystalline behaviour determined by XRD techniques. The aforementioned studies reveal that the synthesized complex/polymer is hydrophilic and porous in nature that can increase their application as eco-friendly materials in the field of catalysis, gases and dyes adsorption, targeted drug release etc.

ACKNOWLEDGEMENTS

Dr Fahmina Zafar is thankful to UGC (New Delhi, India) for Dr D S Kothari fellowship, ref # F.4/2006(BSR)/13-986/2013(BSR) and the Head, Dept of Chemistry, Jamia Millia Islamia, for providing facilities to carry out their research work

REFERENCES

[1] C. Voirin, S. Caillol, N. V. Sadavarte, B. V. Tawade, B. Boutevin and P. P. Wadgaonkar. *Polym. Chem,* (2013), DOI: 10.1039/c3py01194a
[2] J. H. Jung, J. H. Lee, J. R. Silverman and G. John. *Chem. Soc. Rev.* 42, 924-936 (2013).
[3] R.l L. Quirino, T. F. Garrison and M. R. Kessler, Green Chem., 16, 1700-1715 (2014)

*****

Use of Adomian and Restarted Adomian Methods for Solving Algebraic Equations

Mohammad Danish

Department of Chemical Engineering, Aligarh Muslim University, Aligarh-202002, UP, India

ABSTRACT

Nonlinear algebraic equations arise frequently in the modeling of many engineering systems. More specifically, these equations appear while mathematically representing the steady state model of a lumped parameter system, e.g. a continuous stirred tank reactor, single or multiple effect evaporators, flash drum etc. In this study, the application of two efficient methods namely, Adomian Decomposition Method (ADM) and one of its variant namely, Restarted ADM (RADM) has been demonstrated by solving an algebraic equation. Some peculiar characteristics of the obtained solutions, depicting the advantages and limitations of these methods, are shown and discussed, which may be followed while solving nonlinear algebraic equations.

Keywords: Adomian decomposition, Algebraic equations, Numerical Solution

*****

Biologically Active and Thermally Stable Polymeric Schiff Base and Its Coordination Polymers with Some Divalent Transition Metals Ions

Raza Rasool[1], Nahid Nishat[2]

[1,2]Inorganic Materials Research Laboratory, Department of Chemistry, Jamia Millia Islamia, New Delhi 110025

ABSTRACT

Developments of coordination polymers by linking transition metal ions with the polydentate ligands such as polymeric Schiff base have been constantly growing interest over the past years. The polymeric Schiff base based coordination polymers have attractive chemical, physical and biological properties and they have been found applications such as aqueous thickeners, impregnates, textile seizers, adhesives, additives, resins, catalysts and biomedical. In present work an attempt have been taken to synthesize new polymeric Schiff base of anthranilic acid, glutaraldehyde, barbituric acid and formaldehyde, and their coordination polymers with divalent metals [Mn(II), Ni(II), Co(II), Cu(II) and Zn(II)]. The newly synthesised Schiff base coordination polymers have been characterized by IR, ^{1}H-NMR and UV-visible spectral techniques. The elemental analysis, magnetic moment measurement and thermal behaviour of the synthesized materials along with geometry of the central metal ions have also been discussed. All the coordination polymers have been screened for their antibacterial activity against *S. aureus*, *E. coli, S. typhi* and antifungal activity against *A. niger* and *C. albicans* by agar well diffusion method. The results of electronic specral studies show that Cu (II) polymer is square planar, while Mn(II) and Co(II) polymers have octahedral geometry. The biological and thermal studies reveal that Cu(II) and Zn(II) based polymeric Schiff base coordination polymers show higher antibacterial activity and thermal stability than the other coordination polymers due to its higher stability constant, and they may be used as antifungal and antifouling agents for various projects.

*****

Homogeneous CO_2 Emission using Fuzzy Clustering

K. Ranganathan[1], Manish Kumar Goyal[2]

[1,2]Dept of Civil Engineering, Indian Institute of Technology, Guwahati, Guwahati-781039, India

ABSTRACT

Top of Form

Carbon dioxide level in the atmosphere had reached its historic peak in the mid of 2014 due to anthropogenic activities .The primary cause of the climate change is because of fossil fuel based energy production. Even though, there were several policies made by the Indian Government in collaborations with the scientific community, the problem still prevails. To mitigate the carbon dioxide emissions, it is necessary to formulate intensification policies that would be implemented at the regional level rather than deriving national level policies. National level inventories are not accurate as like as the inventories made in regional level. To support the robust policy's, this paper deals with an application of fuzzy clustering algorithm to identify homogeneous CO_2 emission regions in India. Major findings of this study were (1) Maharashtra stands at first position in a single class as largest carbon dioxide emitter due to usage of fossil fuels in energy production (2) States like Gujarat and West Bengal hold second position. Similarly Tamil Nadu, Andhra Pradesh, Uttar Pradesh, Rajasthan and Madhya Pradesh were in the top third position in country energy based carbon dioxide emissions.

Keywords: Carbon dioxide emissions; Fuzzy Clustering; Fossil fuel.

*****

Application of Nanotechnology in Medical Sciences Specially for Treating Cancer and Tumor

Vineeta Jain

Department of Physics, JNCT BHOPAL

ABSTRACT

Nanotechnology has recently become one of the most active research fields in the area of Medical science. The most profound impact of nanomaterials will be in medicine, where nanoparticles and other nanomaterials will create new classes of drugs and medical devices. For example, nanoparticles are needed for targeted delivery of small molecule cancer drugs and nucleic acids. Nanocrystalline silicon carbide is a candidate material for artificial heart valve due to its low weight, high strength extreme hardness and high corrosion resistance. Many researcher attach Ethylene glycol molecules this nanoparticle drugs are useful for cancer tumor.

Using bio-resources, scientists from the Indian Institute of Chemical Technology (IICT), Hyderabad They have synthesized eco-friendly gold nanoparticles can be used as carriers for delivering anti-cancer drugs and also for diagnosing the disease The biocompatible nanoparticles developed from leaf extracts, shown promising results and to remove cancer cells for lung and breast cancer cell lines.

*****

Sensors and Actuators B 206 (2015) 443–448

Contents lists available at ScienceDirect

Sensors and Actuators B: Chemical

journal homepage: www.elsevier.com/locate/snb

On the performance of Tamm-plasmon and surface-plasmon hybrid-mode refractive-index sensor in metallo-dielectric heterostructure configuration

Ritwick Das [a,*], Triranjita Srivastava [b], Rajan Jha [c]

[a] School of Physical Sciences, National Institute of Science Education and Research, Bhubaneswar 751005, India
[b] Department of Physics, Kalindi College, University of Delhi, New Delhi 110008, India
[c] Nanophotonics and Plasmonics laboratory, School of Basic Sciences, Indian Institute of Technology Bhubaneswar, Bhubaneswar 751007, India

ARTICLE INFO

Article history:
Received 30 April 2014
Received in revised form 9 September 2014
Accepted 11 September 2014
Available online 28 September 2014

Keywords:
Photonic bandgap
Surface plasmons
Dispersion

ABSTRACT

Hybrid modes formed as a consequence of coupling between Tamm-plasmon polariton (TPP) mode and surface plasmon polariton (SPP) mode in a metallo-dielectric heterostructure geometry exhibit interesting dispersive features which can be employed for realizing highly sensitive and accurate surface-plasmon-resonance (SPR) sensor. The transverse magnetically (TM) polarized TPP modes (TM-TPP), formed at the interface of distributed-Bragg reflector (DBR) and metal, are strongly dispersive as compared to SPP modes at optical frequencies that forms the basis of narrow interaction bandwidth which, in turn, results in improved accuracy of sensing. By deploying a nano/micro-fabrication compatible TiO_2/SiO_2-based DBR architecture in combination with different plasmon-active metals such as gold (Au), silver (Ag) and aluminum (Al), we propose a TM-TPP and SPP hybrid-mode sensor which exhibit high sensitivity $\geq$ 900 nm/RIU for analyte refractive indices varying between 1.330 and 1.345. The investigation also revealed that the hybrid-mode sensor is most accurate in case of Al-based configuration amongst Au, Ag and Al which is primarily due to weaker dispersion characteristics exhibited by Al at visible frequencies. Since, the dispersive behavior of TM-TPP modes could be tailored appropriately in any spectral band, the sensing configuration could be immensely useful for designing sensors at those wavelength where optical sources are readily available.

© 2014 Elsevier B.V. All rights reserved.

1. Introduction

Biochemical sensing using optical surface modes such as surface-plasmon-polaritons (SPP), Bloch surface modes, etc. have gained overwhelming prominence over the last two decades due to design simplicity and label-free detection mechanism [1–4]. The obvious advantage is derived from the mode-field distribution of surface modes which are characterized by decaying field envelope in the constituent layers (one of them being sensing medium) with field-amplitude reaching maximum at the interface. Therefore, any change taking place at the surface due to biomolecular as well as biochemical interactions leads to change in SPP-mode dispersion which is quantified in terms of transmission or reflection spectra [1]. Here, it is important to appreciate that the sensor performance is primarily determined by the dispersion characteristics of SPP-mode which, in turn, depends on (*i*) material dispersion of constituents and (*ii*) the dispersion due to surface guidance mechanism [5,6]. Since, the interface is usually formed by two homogeneous semi-infinite media in case of SPP based sensors, the possibility to tailor the dispersion by altering the surface guidance mechanism (2nd route) is impractical. So, the emphasis is mainly laid on improving material dispersive features to enhance the sensitivity of such sensors [1,7] or by employing amplitude or phase modulation of incident beam [8,9]. In this context, TM-polarized surface modes formed at the interface of a metal and a periodically-stratified medium, also called optical Tamm-plasmon-polariton (TPP) modes [10,11], are potential candidates from the perspective of sensing refractive index changes in an homogeneous medium. Photonic bandgap (PBG) guided TM-TPP modes exhibit far less absorptive losses as compared to SPP modes which ensures an improved *Q*-factor of resonance [12,13]. This particular feature promises to improve the detection accuracy of sensing and hence, the configuration is expected to exhibit better signal-to-noise ratio. Previously, the sharp-resonance feature of TPP-modes have been investigated for developing compact slow-light devices and optical absorbers [14,15], realizing efficient magneto-photonic

* Corresponding author. Tel.: +91 6742304106.
E-mail address: ritwick.das@niser.ac.in (R. Das).

http://dx.doi.org/10.1016/j.snb.2014.09.032
0925-4005/© 2014 Elsevier B.V. All rights reserved.

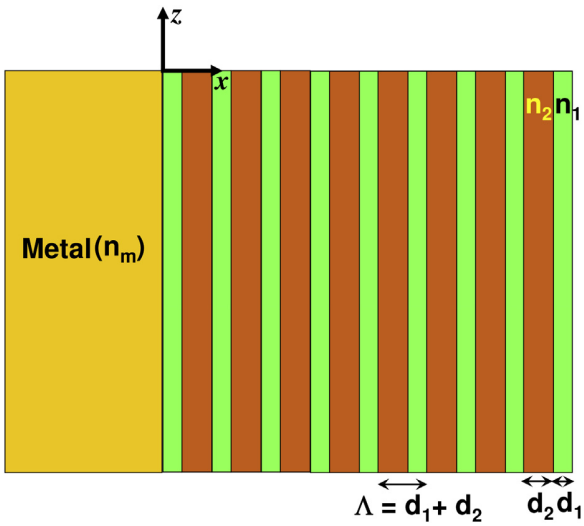


Fig. 1. Schematic of Metal/TiO_2/SiO_2 DBR based configuration supporting TM-TPP modes; propagation direction: *z*-axis.

devices [16], enhancing $\chi^{(3)}$ nonlinearity for devising low threshold bistable optical switches [17], efficient third harmonic generation [18], realizing tunable plasmon polaritons [19] and a few more [20,21]. Here, we present a nano-micro fabrication compatible, simple TiO_2/SiO_2 distributed-Bragg-reflector (DBR) configuration for realizing TPP–SPP hybrid-mode based refractometer which exhibit high sensitivity to changes in analyte index. We show that the sensitivity and accuracy of refractive index measurement of analyte medium are inherently functions of dispersion for TM-TPP mode as well as SPP mode which can be significantly tailored by appropriate choice of metal layer. It is worthwhile to note that the sensor performance could also be improved by tailoring the dispersion characteristics of TM-TPP mode but this would require shifting the point of operation closer to the band-edges of photonic bandgap. This would inevitably add more number of bilayers in DBR geometry for containing the field thereby, resulting in escalation of experimental challenges. Therefore, we analyze the TPP–SPP hybrid-mode refractive-index sensor performance in configurations involving widely used plasmon-active metals, namely gold (Au), silver (Ag) and aluminum (Al) in order to devise a practical sensor.

2. Optical Tamm modes

We consider a geometry shown in Fig. 1 where the boundary at $x=0$ is shared by a semi-infinite DBR-section (refractive indices n_1 and n_2 and thicknesses d_1 and d_2, respectively) with a semi-infinite metal layer (refractive index $\equiv n_m$). The periodicity (Λ) is given by $\Lambda = d_1 + d_2$. Without any loss of generality, we assume $\partial/\partial y = 0$ and the surface-modes propagate along *z*-direction. Since, we are primarily interested in TM-polarized modes, the magnetic field could be written as,

$$H_y(x, y, z, t) = H_y(x)e^{i(\omega t - \beta z)} \tag{1}$$

where $\beta = \frac{2\pi}{\lambda} n_{eff}$ is the mode propagation constant, n_{eff} is the mode-effective index and $\omega = ((2\pi c)/\lambda)$ is the angular frequency. Here, $H_y(x)$ is the transverse mode-field satisfying the scalar-wave equation $n^2(x)(d/dx)[(1)/(n^2(x))(dH_y(x))/(dx)] + k_x^2(x)H_y(x) = 0$. For guided modes, the transverse components of wavevector (k_x) takes different values in each layer in Fig. 1 and it is given by $k_{ix}^2 = (k_0^2 n_i^2 - \beta^2)$ where $i = 1, 2$. Here $k_0 = (2\pi)/(\lambda)$ and the mode-propagation constant β remains constant across each interface. It is well-known that the other non-zero components of TM-polarized field are E_x and E_z which can be ascertained using the Maxwell's curl equations. The H_y field in different regions of Fig. 1 can be mentioned as [22–24],

$$H_y(x) = C_0 e^{k_m x} \qquad x \le 0 \tag{2}$$

$$\begin{aligned} H_y(x) &= C_1[a_0 e^{ik_{1x}(x-N\Lambda)} + b_0 e^{-ik_{1x}(x-N\Lambda)}]e^{iNK_{TM}\Lambda} \quad N\Lambda \le x \le N\Lambda + d_1 \\ H_y(x) &= C_1[c_0 e^{ik_{2x}(x-N\Lambda-d_1)} + d_0 e^{-ik_{2x}(x-N\Lambda-d_1)}]e^{iNK_{TM}\Lambda} \quad N\Lambda + d_1 \le x \le (N+1)\Lambda \end{aligned} \tag{3}$$

where $K_{TM}\left(=\frac{1}{\Lambda}\cos^{-1}[Re(A_{TM})]\right)$ is the Bloch wavevector, $a_0 = B_{TM}$ and $b_0 = e^{iK_{TM}\Lambda} - A_{TM}$ are the complex amplitudes of forward and backward propagating waves in n_1 layer. Here, $N = 0, 1, 2, 3, \ldots$ corresponds to the unit-cell number. We define $A_{TM} = e^{ik_{1x}d_1}[\cos(k_{2x}d_2) + (i/2)((n_1^2/n_2^2)(k_{2x}/k_{1x}) + (n_2^2/n_1^2)(k_{1x}/k_{2x}))\sin(k_{2x}d_2)]$ and $B_{TM} = e^{-ik_{1x}d_1}[(i/2)((n_2^2/n_1^2)(k_{1x}/k_{2x}) - (n_1^2/n_2^2)(k_{2x}/k_{1x}))\sin(k_{2x}d_2)]$ [22,24]. Here, it is worthwhile to point out that K_{TM} is complex within the photonic stop-band and its imaginary component determines the field decay in DBR region [22,24]. On the other hand, the decay of mode-field in metal is governed by $k_m = (\beta^2 - k_0^2 n_m^2)^{(1/2)}$. In this case, the complex amplitudes of forward (c_0) and backward (d_0) propagating-wave in n_2 layer are related to that in n_1 layer (i.e. a_0 & b_0 respectively) as

$$\begin{pmatrix} c_0 \\ d_0 \end{pmatrix} = \frac{1}{2}\alpha \begin{pmatrix} e^{ik_{1x}d_1}\left(1+\gamma\frac{k_{2x}}{k_{1x}}\right) & e^{-ik_{1x}d_1}\left(1-\gamma\frac{k_{2x}}{k_{1x}}\right) \\ e^{ik_{1x}d_1}\left(1-\gamma\frac{k_{2x}}{k_{1x}}\right) & e^{-ik_{1x}d_1}\left(1+\gamma\frac{k_{2x}}{k_{1x}}\right) \end{pmatrix} \begin{pmatrix} a_0 \\ b_0 \end{pmatrix} \tag{4}$$

where $\alpha = (n_2 k_{1x}/n_1 k_{2x})$ and $\gamma = (n_1^2/n_2^2)$. By imposing the continuity condition for TM-polarized field (Eq. (2) and (3)) i.e. H_y and $\left(\frac{1}{n_1^2}\right)(\partial H_y/\partial x)$ to be continuous at $x = 0$, we obtain the following mode-dispersion equation [25],

$$\frac{e^{iK_{TM}\Lambda} - A_{TM} - B_{TM}}{e^{iK_{TM}\Lambda} - A_{TM} + B_{TM}} = i\frac{n_1^2}{n_m^2}\frac{k_m}{k_{1x}} \tag{5}$$

The constants C_0 and C_1 in Eq. (2) and (3) respectively, are related as $C_1 = \frac{C_0}{(a_0+b_0)}$. The TPP-modes are obtained by solving the mode-dispersion relation (Eq. (5)) with $n_{\text{eff}} < n_2$ for a given geometry. It is important to note that the use of quarter-wave stack (QWS) condition, proposed by West et al. [24], cannot be employed here to obtain suitable values of d_1 and d_2. The QWS condition is given by $k_{1x}d_1 = k_{2x}d_2 = (\pi/2)$ which leads to $e^{iK_{TE}\Lambda} - A_{TM} - B_{TM} = 0$ [24]. When this happens, Eq. (5) results into $n_{\text{eff}} = n_m$ which is a trivial solution. It is essentially a consequence of the fact that the field (H_y) goes to *zero* at $x = 0$ (metal-DBR boundary) when the QWS condition is satisfied. Since, the field would always be decaying in the metal, there cannot be any field in the metal when $H_y = 0$ at $x = 0$. Therefore, it implies that the mode field will always be *zero* (for all $x < 0$) in the metal when QWS condition is satisfied.

3. Design of multilayer DBR section

For designing the metal-DBR section, we consider a DBR geometry comprising bilayers of TiO_2 (n_1) and SiO_2 (n_2) which share the boundary ($x = 0$) with semi-infinite metal layer. In order to draw comparison of refractometer performance with respect to widely employed plasmon-active metals, we carry out analysis with gold (Au), silver (Ag) and aluminum (Al) layers separately. At an operating wavelength of $\lambda = 632.8$ nm, the $(n_{\text{eff}})_{TPP}$ of TM-TPP mode is obtained by solving Eq. (5) for various values of d_1 and d_2 of DBR and plotted in Fig. 2. Fig. 2a corresponds to Au/TiO_2/SiO_2 based geometry whereas Fig. 2b and c represents n_{eff} variation for Ag/TiO_2/SiO_2 and Al/TiO_2/SiO_2 based configurations respectively. The refractive

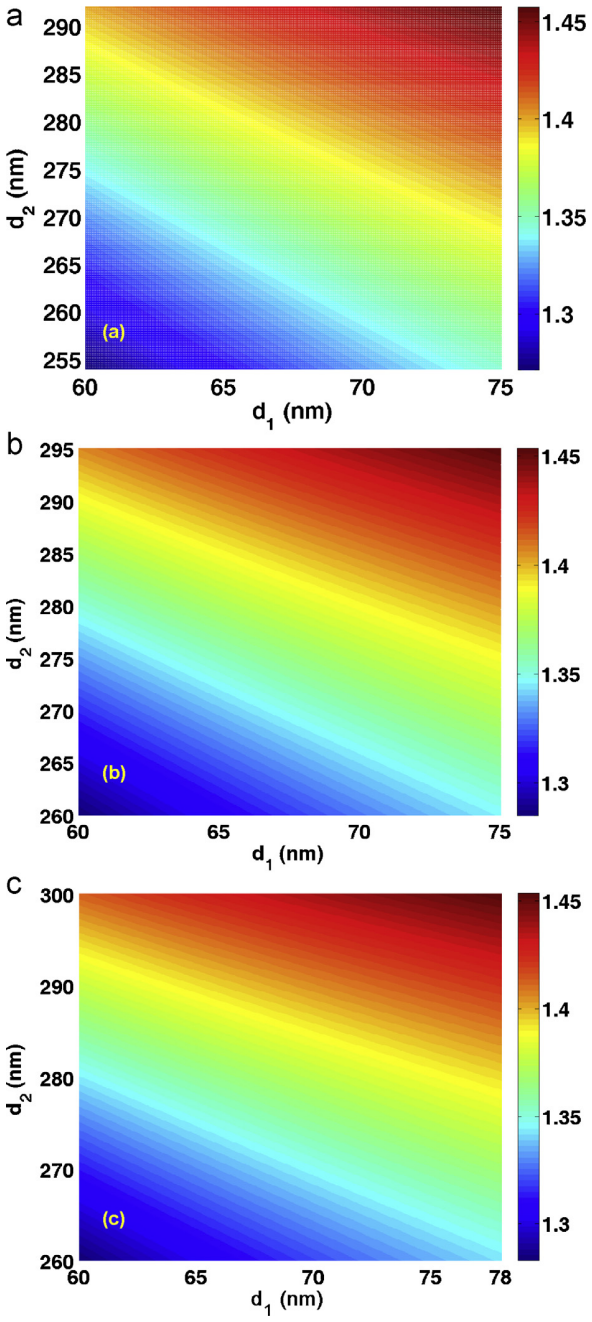


Fig. 2. Variation of real part of mode-effective index (n_{eff}) of TM-TPP modes in Metal/TiO_2/SiO_2 DBR configuration shown in Fig. 1 as a function of d_1 and d_2 for $\lambda = 632.8$ nm (color-bar corresponds to n_{eff}). (a) Au/TiO_2/SiO_2 DBR, (b) Ag/TiO_2/SiO_2 DBR and (c) Al/TiO_2/SiO_2 DBR.

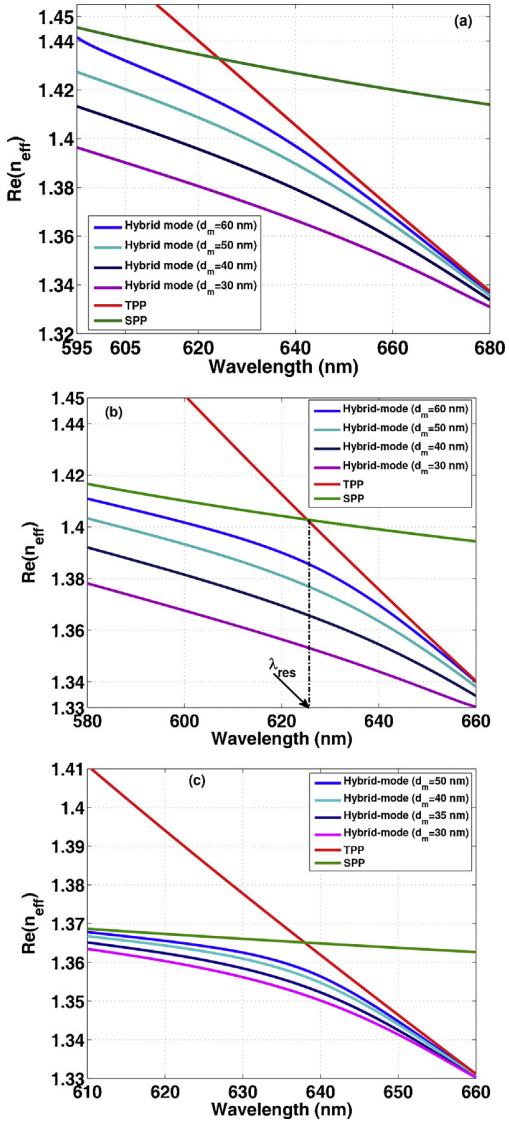


Fig. 3. Variation of real part of mode-effective index ($Re(n_{eff})$) of TM-TPP mode, SPP mode and hybrid mode as a function of wavelength in (a) Analyte/Au/TiO_2/SiO_2 ($d_1 = 72$ nm, $d_2 = 285$ nm), (b) Analyte/Ag/TiO_2/SiO_2 ($d_1 = 75$ nm, $d_2 = 280$ nm); λ_{res} is the wavelength at which TM-TPP and SPP modes intersect and (c) Analyte/Al/TiO_2/SiO_2 ($d_1 = 75$ nm, $d_2 = 275$ nm) based DBR configuration.

indices of Au, Ag and Al has been taken from Palik [26] and that for TiO_2 and SiO_2 layers are taken from the values given by Toyoda et al. [27] and Ghosh et al. [28] respectively. Since, the idea is to devise a TM-TPP/SPP hybrid-mode sensor, d_1 and d_2 is chosen such that the $(n_{eff})_{TPP}$ lie close to n_{eff} of SPP mode formed at metal-analyte interface. For simplicity, the analyte refractive index is considered to be 1.33 here. As an example, $(n_{eff})_{SPP} \sim 1.43$ for SPP mode at Au-analyte interface when $\lambda = 632.8$ nm. In order to have $(n_{eff})_{TPP} \sim 1.42 - 1.44$, Fig. 2a shows that $70\,\text{nm} \le d_1 \le 75$ nm and $280\,\text{nm} \le d_2 \le 290$ nm. Similarly, $(n_{eff})_{SPP} \sim 1.40$ for SPP mode at Ag-analyte interface at $\lambda = 632.8$ nm which gives an idea that d_1 and d_2 should be in the range of 70 –75 nm and 275 –285 nm, respectively. In case of Al-analyte interface, $(n_{eff})_{SPP}$ lies close to 1.36 when $\lambda = 632.8$ nm which indicates that $70\,\text{nm} \le d_1 \le 75$ nm and $270\,\text{nm} \le d_2 \le 280$ nm.

In view of the observations made above, we choose $d_1 = 72$ nm, $d_2 = 285$ nm for Au/TiO_2/SiO_2 configuration, $d_1 = 75$ nm, $d_2 = 280$ nm for Ag/TiO_2/SiO_2 configuration and $d_1 = 75$ nm, $d_2 = 275$ nm for Al/TiO_2/SiO_2 configuration for designing the DBR section. With these thicknesses, the variation of n_{eff} of TM-TPP modes for the Au/DBR, Ag/DBR and Al/DBR configurations, as a function of wavelength, is shown in Fig. 3a–c respectively. In addition, we have shown the variation of n_{eff} for SPP modes supported at Au/analyte, Ag/analyte and Al/analyte interface. The analyte refractive index is taken to be $n_a = 1.33$ and it is assumed to be negligibly dispersive as compared to metal. From Fig. 3a–c, it is apparent that the dispersion curves for TM-TPP and SPP modes intersect at $\lambda_{res} \approx 625$ nm for Au and Ag based configuration whereas the curves intersect at $\lambda_{res} = 638$ nm in case of Al. When the analyte index (n_a) change, the SPP dispersion curve would shift which would eventually lead to a

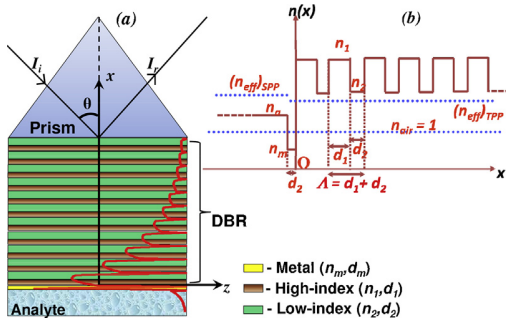


Fig. 4. (a) Schematic of Analyte/Metal/TiO_2/SiO_2 geometry for studying the TM-TPP/SPP hybrid-mode based sensing configuration. Prism is employed to facilitate excitation of TM-TPP modes. Qualitative mode-field plot for Analyte/Au/TiO_2/SiO_2 configuration is superimposed on the structure and (b) refractive-index-profile of the geometry for qualitatively describing the location of $n_{\text{eff(TPP)}}$ and $n_{\text{eff(SPP)}}$ as compared to material refractive indices.

different point of intersection for TM-TPP and SPP curves. This shift in dispersion curve intersection point could be quantified in terms of change in wavelength. Hence, this idea could be employed for realizing an SPR sensor where a thin metal (d_m) shares one boundary with DBR section and the other boundary with analyte. Here, it is important to note that the accuracy of detection of such system would be determined by the bandwidth of interaction ($\Delta\lambda$) for TM-TPP and SPP modes which, in turn, is decided by the difference in dispersion curve slope for interacting modes.

4. Optimum metal thickness

In order to achieve efficient TM-TPP and SPP mode-coupling, the choice of metal thickness (d_m) is crucial. An ultra-thin (<10 nm) metal layer would lead to suppression of individual modal characteristics of TM-TPP and SPP modes, thereby affecting the device performance adversely. On the other hand, a thick metal layer (≈100 nm) would inhibit any possibility of intermodal interaction. In this case, we would optimize the metal thickness as dictated by the SPR sensor performance parameters. We consider a geometry shown in Fig. 4a with finite metal layer thickness. The metal shares the boundary with an analyte layer (n_a) at $x = -d_m$. Refractive index profile of the structure indicating the location of $n_{\text{eff(TPP)}}$ and $n_{\text{eff(SPP)}}$ with respect to n_1, n_2, n_m and n_a is shown in Fig. 4b. Light is launched on the geometry using the prism as shown in Fig. 4. Since, the idea is to identify the wavelength at which coupling between TM-TPP and SPP mode is realized, we would assume that light is incident on the face of prism such that 'θ' remains same for all the wavelengths. Following an identical recipe described in previous section, we write the solution (H_y) of scalar-wave equation as,

$$H_y(x) = C_2 e^{k_a(x+d_m)} \qquad x \le -d_m \tag{6}$$

$$H_y(x) = C_3 e^{k_m x} + C_4 e^{-k_m x}; \qquad -d_m \le x \le 0 \tag{7}$$

$$\begin{aligned} H_y(x) &= C_5[a_0 e^{ik_{1x}(x-N\Lambda)} + b_0 e^{-ik_{1x}(x-N\Lambda)}]\, e^{iNK_{TM}\Lambda} \quad N\Lambda \le x \le N\Lambda + d_1 \\ H_y(x) &= C_5[c_0 e^{ik_{2x}(x-N\Lambda-d_1)} + d_0 e^{-ik_{2x}(x-N\Lambda-d_1)}]e^{iNK_{TM}\Lambda} \quad N\Lambda + d_1 \le x \le (N+1)\Lambda \end{aligned} \tag{8}$$

Here, $k_a = \left(\beta^2 - k_0^2 n_a^2\right)^{1/2}$ determines the mode-field penetration in analyte and the complex amplitudes C_2, C_3, C_4, C_5 could be evaluated after imposing appropriate boundary conditions. In order to appreciate the TM-TPP and SPP mode-coupling, we impose continuity of H_y and $(1/n^2(x))(dH_y/dx)$ at $x = -d_m$ and $x = 0$ which leads to hybrid-mode dispersion relation mentioned below [29].

$$\eta \frac{e^{iK_{TM}\Lambda} - A_{TM} - B_{TM}}{e^{iK_{TM}\Lambda} - A_{TM} + B_{TM}} = \frac{\tanh(k_m d_m) + \xi}{1 + \xi \tanh(k_m d_m)} \tag{9}$$

where $\eta = -i(k_{1x}/k_m)(n_m^2/n_1^2)$ and $\xi = (k_a/k_m)(n_m^2/n_a^2)$. We would like to point out that Eq. (9) is a general equation for such geometries which can be used to obtain Eq. (5) when $d_m \to \infty$. For complex K_{TM} a qualitative plot of $|H_y|^2$ for Analyte/Au/TiO_2/SiO_2 is superimposed on the structure (red-curve). We solve Eq. (9) to obtain the variation of n_{eff} of the hybrid-mode in case of Au, Ag and Al as a function of wavelength for different values of d_m in Fig. 3a–c, respectively. In all the three cases, n_{eff} of the hybrid-mode dispersion curves exhibits an anti-crossing behavior around λ_{res}. The curves asymptotically converge to SPP mode at shorter wavelength and to TM-TPP mode at longer wavelengths. It could also be observed that the hybrid-mode dispersion curve drifts away from the intersection point (λ_{res}) for smaller metal thickness (d_m). From the normal-mode analysis, the hybrid-mode propagation constant $\beta_{hy} = ((\beta_{TPP} + \beta_{SPP})/2) - \kappa$ where κ is the coupling constant that could be alternately estimated by spatial overlap of mode-fields for TM-TPP and SPP mode [30]. Therefore, the dispersion of hybrid-mode in Fig. 3a–c clearly suggests that κ would be small when d_m is large. This can also be appreciated by noting the fact that a thick metal layer (large d_m) would weaken the intermodal interaction. Hence, it is physically expected that κ would become smaller for thicker d_m and vice-versa [30].

In order to obtain appropriate metal thickness, we note that the accuracy of detecting changes in refractive index of an analyte primarily depends on the spectral linewidth ($\Delta\lambda$) for response function of refractometer configuration. A narrower linewidth improves the accuracy of measurement and vice-versa. In fact, the detection accuracy (DA) is mathematically represented as,

$$DA = \frac{1}{\Delta\lambda} = \frac{0.784\pi}{\lambda_{res}^2} \frac{|N_{g(TPP)} - N_{g(SPP)}|}{\kappa} \tag{10}$$

where $N_{g(TPP)}$ and $N_{g(SPP)}$ are the respective group-indices of TM-TPP and SPP modes when $d_m \to \infty$. According to Eq. (10), the DA improves when the TM-TPP and SPP modes are weakly coupled (small κ) and hence, this observation advocates a choice of thicker d_m. However, it is also to be noted that an extremely thick metal would inhibit any intermodal coupling between TM-TPP and SPP modes, thereby ceasing the existence of hybrid-mode. Such a situation occurs when $d_m \ge 75$ nm for Au as well as Ag and $d_m \ge 60$ nm for Al. Hence, we choose $d_m = 60$ nm for Au and Ag in order to investigate the refractometer performance whereas $d_m = 50$ nm in case of Al for studying the same.

5. Performance of refractive-index sensor

In view of the fact that the TM-TPP mode-indices are lower than the constituent material-indices, it is easier to excite such modes using $N-BK7$ or fused-silica glass prisms. Therefore, we study the TM-TPP/SPP hybrid-mode sensor performance by analyzing the reflectivity of a tunable laser beam from the DBR-section $((I_r(\lambda)/I_i(\lambda)))$ as shown in Fig. 4. We define the spectral sensitivity as

$$S_n = \frac{|\delta\lambda_{res}|}{\delta n_a} \tag{11}$$

where λ_{res} is the wavelength at which modal-dispersion curves for TM-TPP and SPP modes intersect in Fig. 3 and $\delta\lambda_{res}$ is the change in λ_{res} when analyte index changes by δn_a. Fig. 5 shows the variation of spectral sensitivity (S_n) for hybrid-mode sensor as a function of analyte index (n_a) for Au, Ag and Al based configuration. Here, it can be seen that S_n of Au based configuration monotonically increases from ≈890 nm/RIU to ≈970 nm/RIU when n_a changes from 1.329 to 1.345. The S_n values are significantly higher and comparable to the practical SPR sensors reported earlier [31–34]. In case of Analyte/Ag/TiO_2/SiO_2 geometry, it is interesting to observe that S_n exhibits a negligible change over an identical range of n_a as compared to Au-based configuration. In fact, S_n remains constant for n_a varying between 1.331 and 1.332. On the other hand, the

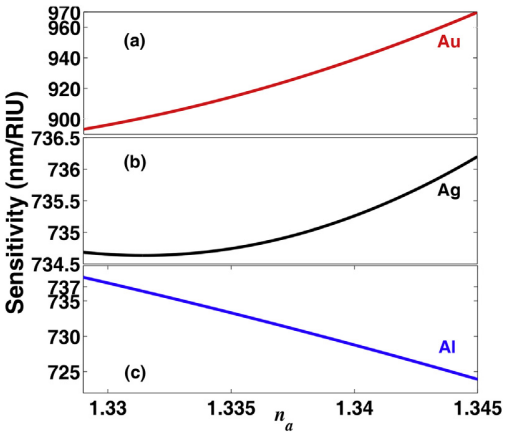


Fig. 5. Variation of sensitivity (S_n) of TM-TPP/SPP hybrid-mode refractometer in (a) Analyte/Au/TiO_2/SiO_2 geometry, (b) Analyte/Ag/TiO_2/SiO_2 geometry and (c) Analyte/Al/TiO_2/SiO_2 geometry as a function of analyte index (n_a). For (a) $d_1 = 72$ nm, $d_2 = 285$ nm and $d_m = 60$ nm, for (b) $d_1 = 75$ nm, $d_2 = 280$ nm and $d_m = 60$ nm and for (c) $d_1 = 75$ nm, $d_2 = 275$ nm and $d_m = 50$ nm.

Al-based configuration decreases monotonically from ≈738 nm/RIU to ≈724 nm/RIU when n_a goes from 1.329 to 1.345. It is worthwhile to note that the dielectric sensors such as ring-resonator based sensors, interferometric sensors and photonic crystal based sensors exhibit smaller spectral sensitivity ($\leq 100 - 200$ nm/RIU) [35].

The variation of *DA* for Au, Ag and Al based geometries as a function of analyte index is shown in Fig. 6. The *DA* of *Al*-based configuration varies from 76 μm^{-1} to 80 μm^{-1} for $1.329 \leq n_a \leq 1.345$ and hence, it is the most accurate amongst the three configurations under study. On the other hand, *DA* for Au based geometry is smallest and remains almost constant ≈20 μm^{-1} for an identical change in n_a. The Ag based configuration exhibits moderate *DA* values which varies between 47 μm^{-1} and 49 μm^{-1} when n_a changes from $1.329 \leq n_a \leq 1.345$.

The observations with regard to S_n and *DA* could be understood by noting the dispersion of Au, Ag and Al in Fig. 3a–c respectively. It can be seen that the contrast in dispersion slopes of TM-TPP and SPP modes in Fig. 3a (Au) is smaller as compared to that in Fig. 3b and c (Ag & Al). This is essentially due to stronger dispersion of SPP mode in case of Au which reduces the difference in slopes of dispersion curves for SPP mode and TM-TPP mode. On the other hand, the dispersion of SPP mode in Al based configuration is weakest which results in maximum difference in slopes for SPP mode and TM-TPP mode. Also, it is worthwhile to note that the TM-TPP

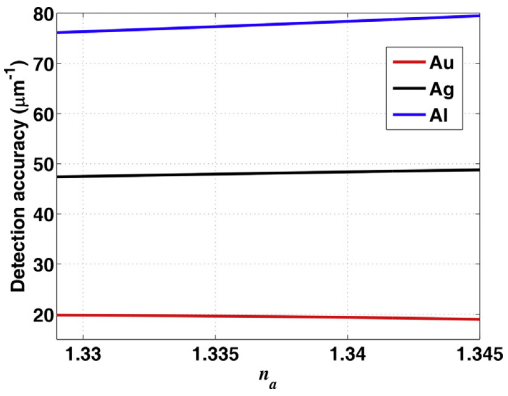


Fig. 6. Variation of detection accuracy (DA) of TM-TPP/SPP hybrid-mode refractometer in Analyte/Au/TiO_2/SiO_2 geometry, Analyte/Ag/TiO_2/SiO_2 geometry and Analyte/Al/TiO_2/SiO_2 geometry as a function of analyte index (n_a).

mode dispersion slopes are almost same for all the three metals. This observation has a direct impact on S_n which is determined by the shift in wavelength at which the dispersion curves intersect i.e. λ_{res}. A small increase in n_a would move the n_{eff} curve of SPP mode upwards and λ_{res} would be blue-shifted. The magnitude of blue-shift in λ_{res} would essentially be determined by difference of dispersion curve slopes for individual SPP and TM-TPP modes. If the difference in dispersion slope is less, the blue-shift will be more and vice-versa. Therefore, according to Fig. 3, we expect S_n to be maximum for Au based configuration for which the contrast in dispersion slopes of SPP and TM-TPP modes is least. This feature is confirmed by S_n values in Fig. 5. By virtue of weaker SPP-mode dispersion at Al-analyte interface, the shift $|\delta\lambda_{res}|$ decreases with increasing n_a which manifests into smaller S_n for higher analyte indices (Fig. 5). On the other hand, $DA \propto (|N_{g(TPP)} - N_{g(SPP)}|/\kappa)$ where the group-index $N_g = n(\lambda) - \lambda(dn/d\lambda)|_{\lambda=\lambda_{res}}$. Hence, *DA* would be more in situations where the interacting modes exhibit more contrasting dispersion slopes and weaker coupling (small κ). Although the values of κ for Au, Ag and Al based configuration remain almost same, the difference in dispersion slope is maximum for Analyte/Al/TiO_2/SiO_2 geometry and hence, it exhibits the largest *DA* amongst the configurations under study (see Fig. 6).

6. Conclusion

We have presented a comprehensive analysis for designing TM-TPP & SPP hybrid-mode refractometer configuration which exhibits high sensitivity towards changes in analyte refractive index. We obtain the mode-dispersion relation for TM-TPP mode by using Bloch-modes in the periodically stratified region and solve the dispersion relation to estimate d_1 and d_2 for TiO_2/SiO_2 based DBR geometry. The metal thickness (d_m) is determined by considering its impact on accuracy of detection scheme. A comparison is drawn for refractometer performance with different plasmon-active metals such as Au, Ag and Al. It is found that Au based TM-TPP/SPP hybrid-mode sensor exhibits maximum sensitivity (∼900 nm/RIU) but worse *DA* (≈20 μm^{-1}) whereas Al based configuration is most accurate ($DA \approx 80\ \mu m^{-1}$) with moderate sensitivity ($S_n \sim 730$ nm/RIU). Both the components (S_n & *DA*) which describe the refractometer performance, are mainly functions of dispersion characteristics of interacting TM-TPP mode, SPP mode as well as the hybrid mode. We have shown that the *DA* improves when the interacting modes have more contrast in dispersion slopes. Using this observation, it is expected that the *DA* would substantially improve for all the plasmon active metals (Au, Ag, Al) in the near-infrared and mid-infrared regime such as in communication band ($\lambda \approx 1.55\ \mu m$) where SPP modes are much less dispersive. In addition, the dispersive features of DBR geometry could be tailored appropriately to design the refractometer with desirable characteristics in any spectral band, thereby facilitating sensor designing based on the availability of optical sources.

References

[1] M. Pillarik, J. Homola, Surface plasmon resonance (SPR) sensors: approaching their limits? Opt. Express 17 (16505) (2009) 16505–16517.
[2] J. Homola, S.S. Yee, G. Gauglitz, Surface plasmon resonance sensors: review, Sens. Actuators B 54 (1999) 3–15.
[3] A. Farmer, A.C. Friedli, S.M. Wright, W.M. Robertson, Biosensing using surface electromagnetic waves in photonic band gap multilayers, Sens. Actuators B 173 (2012) 79–84.
[4] F. Villa, L.E. Regalado, F.R. Mendieta, J.G. Armenta, Photonic crystal sensor based on surface waves for thin-film characterization, Opt. Lett. 27 (2002) 646–648.
[5] G.G. Nenningera, P. Tobiškab, J. Homola, S.S. Yee, Long-range surface plasmons for high-resolution surface plasmon resonance sensors, Sens. Actuators B 74 (2001) 145–151.
[6] J. Ctroký, J. Homola, P.V. Lambeck, S. Musa, H.J.W.M. Hoekstra, R.D. Harris, J.S. Wilkinson, B. Usievich, N.M. Lyndin, Theory and modelling of optical waveguide sensors utilising surface plasmon resonance, Sens. Actuators B 54 (1999) 66–73.

[7] H. Matsui, W. Badalawa, A. Ikehata, H. Tabata, Oxide surface plasmon resonance for a new sensing platform in the near-infrared region, Adv. Opt. Mater. 1 (2013) 397–403.
[8] Z. Yu, S. Fan, Extraordinarily high spectral sensitivity in refractive index sensors using multiple optical modes, Opt. Express 19 (2011) 10029–10040.
[9] J. Dostálek, H. Vaisocherová, J. Homola, Multichannel surface plasmon resonance biosensor with wavelength division multiplexing, Sens. Actuators B 108 (2005) 758–764.
[10] M. Kaliteevski, I. Iorsh, S. Brand, R. Abram, J. Chamberlain, A.V. Kavokin, I. Shelykh, Tamm plasmon-polaritons: possible electromagnetic states at the interface of a metal and a dielectric Bragg mirror, Phys. Rev. B 76 (2007) 165415.
[11] S. Brand, M. Kaliteevski, R. Abram, Optical Tamm states above the bulk plasma frequency at a Bragg stack/metal interface, Phys. Rev. B 79 (2009) 085416.
[12] A.P. Vinogradov, A.V. Dorofeenko, S.G. Erokhin, M. Inoue, A.A. Lisyansky, A.M. Merzlikin, A.B. Granovsky, Surface state peculiarities in one-dimensional photonic crystal interfaces, Phys. Rev. B 74 (2006) 045128.
[13] N. Malkova, C.Z. Ning, Tamm surface states in a finite chain of defects in a photonic crystal, J. Phys.: Condens. Matter 19 (2007) 056004.
[14] M.E. Sasin, R.P. Seisyan, M.A. Kalitteevski, S. Brand, R.A. Abram, J.M. Chamberlain, A.Yu. Egorov, A.P. Vasilév, V.S. Mikhrin, A.V. Kavokin, Tamm plasmon polaritons: slow and spatially compact light, Appl. Phys. Lett. 92 (2008) 251112.
[15] G. Du, H. Jiang, Z. Wang, Y. Yang, Z. Wang, Heterostructure-based optical absorbers, J. Opt. Soc. Am. B 27 (2010) 1757–1762.
[16] T. Goto, A.V. Dorofeenko, A.M. Merzlikin, A.V. Baryshev, A.P. Vinogradov, M. Inoue, A.A. Lisyansky, A.B. Granovsky, Optical Tamm states in one-dimensional magnetophotonic structures, Phys. Rev. Lett. 101 (2008) 113902.
[17] W.L. Zhang, Y. Jiang, Y. Zhu, F. Wang, Y.J. Rao, All-optical bistable logic control based on coupled Tamm plasmons, Opt. Lett. 38 (2013) 4092–4095.
[18] C. Xue, H. Jiang, H. Lu, G. Du, H. Chen, Efficient third-harmonic generation based on Tamm plasmon polaritons, Opt. Lett. 38 (2013) 959–961.
[19] C. Grossmann, C. Coulson, G. Christmann, I. Farrer, H.E. Beere, D. Ritchie, J.J. Baumberg, Tunable polaritonics at room temperature with strongly coupled Tamm Plasmon polaritons in metal/air-gap microcavities, Appl. Phys. Lett. 98 (2011) 231105.
[20] Y. Wan, Z. Zheng, W. Kong, X. Zhao, Y. Liu, Y. Bian, J. Liu, Nearly three orders of magnitude enhancement of Goos-Hanchen shift by exciting Bloch surface wave, Opt. Express 20 (2012) 8998–9003.
[21] H. Zhou, G. Yang, K. Wang, H. Long, Multiple optical Tamm states at a metal-dielectric mirror interface, Opt. Lett. 35 (4112) (2010) 4112–4114.
[22] P. Yeh, A. Yariv, C.S. Hong, Electromagnetic propagation in periodic stratified media. I. General theory, J. Opt. Soc. Am. 67 (1977) 423–438.
[23] S.R.A. Dods, Bragg reflection waveguide, J. Opt. Soc. Am. A 6 (1989) 1465–1476.
[24] B.R. West, A.S. Helmy, Properties of the quarter-wave Bragg reflection waveguide: theory, J. Opt. Soc. Am. B 23 (2006) 1207–1220.
[25] R. Das, T. Srivastava, R. Jha, Guided-mode analysis of Tamm-plasmon polariton at metal-heterostructure dielectric interface, J. Lightwave Technol. 32 (2014) 1221–1227.
[26] E.D. Palik (Ed.), Handbook of Optical Constants of Solids, 1st ed., Academic Press, New York, 1985.
[27] T. Toyoda, M. Yabe, The temperature dependence of the refractive indices of $SrTiO_3$ and TiO_2, J. Phys. D: Appl. Phys. 16 (1983) L251.
[28] G. Ghosh, M. Endo, T. Iwasaki, Temperature-dependent Sellmeier coefficients and chromatic dispersions for some optical fiber glasses, IEEE J. Lightwave Technol. 12 (1994) 1338–1342.
[29] R. Das, T. Srivastava, R. Jha, Tamm-plasmon and surface plasmon hybrid-mode based refractometry in photonic bandgap structures, Opt. Lett. 39 (2014) 896–899.
[30] M.N. Weiss, R. Srivastava, Spectral characteristics of asymmetric directional couplers in graded index channel waveguides analyzed by coupled-mode and normal-mode techniques, Appl. Opt. 34 (1995) 1029–1040.
[31] R. Jha, J. Villatoro, G. Badènes, V. Pruneri, Refractometry based on photonic crystal fiber interferometer, Opt. Lett. 34 (2009) 617–619.
[32] R. Jha, A.K. Sharma, High performance sensor based on surface plasmon resonance with chalcogenide prism and aluminum for detection in infrared, Opt. Lett. 34 (2009) 749–751.
[33] R. Verma, B.D. Gupta, R. Jha, Sensitivity Enhancement of a surface plasmon resonance based biomolecules sensor using graphene and silicon layers, Sens. Actuators B 160 (2011) 623–631.
[34] P. Bhatia, B.D. Gupta, Surface plasmon resonance based fiber optic refractive index sensor: sensitivity enhancement, Appl. Opt. 50 (2011) 2032–2036.
[35] I.M. White, X. Fan, On the performance quantification of resonant refractive index sensors, Opt. Express 16 (2008) 1020–1028.

Biographies

Ritwick Das received his M.Sc. and Ph.D. degrees from Indian Institute of Technology, Delhi, India in 2004 and 2008, respectively. From October 2008 to March 2010, he was a Postdoctoral Researcher at ICFO-The Institute of Photonics Sciences, Barcelona, Spain. He is currently working as Assistant Professor at School of Physical Sciences at National Institute of Science Education and Research (NISER) Bhubaneswar, India. His areas of research are optical waveguides, nanophotonics, optical sensors and nonlinear optics. He has published more than 30 research articles in international journals of repute.

Triranjita Srivastava received her M.Sc. degree from DDU Gorakhpur University, Gorakhpur, U.P., India in 2005 and Ph.D degree from Indian Institute of Technology Delhi, India in 2010. From April 2011 to May 2012, she was an Assistant professor in department of Applied Physics at Delhi Technological University, Delhi, India. Currently, she is working as Assistant Professor in department of Physics, Kalindi College (University of Delhi), New Delhi, India. Her areas of research are plasmonics, integrated optics and optical sensors. She has published more than 20 research papers in different international journals of repute

Rajan Jha received his M.Sc. and Ph.D. degree from Indian Institute of Technology Delhi, India in 2001 and 2007 respectively. From early 2008 to July 2009, he was a post doctoral researcher at ICFO - The Institute of Photonics Sciences, Barcelona, Spain. He was awarded JSPS (Japanese Society for Promotion of Science) fellowship in 2009 and DAAD fellowship in 2013. He is currently working as Assistant Professor of Physics in School of Basic Sciences at Indian Institute of Technology Bhubaneswar, India. He is a regular member of Optical Society of America (OSA) and is a life member of Optical Society of India (OSI). His areas of research are optical fiber sensors, nano & bio-photonics, waveguide & interferometer. He has published more than 35 research articles including a review article in international journals of repute.

International Journal of Emerging Technology and Advanced Engineering
Website: www.ijetae.com (ISSN 2250-2459, ISO 9001:2008 Certified Journal, Volume 4, Issue 10, October 2014)

Optimization of Process Parameters in Turning Operation Using Response Surface Methodology: A Review

Ranganath M S[1], Vipin[2], Harshit[3]
[1]Associate Professor, [2]Professor, [3]Student
[1, 2]Production and Industrial Engineering, [3]Mechanical Engineering, Delhi Technological University, Delhi, India

***Abstract*— The parameters affecting the roughness of surfaces produced in the turning process for various materials have been studied by many researchers. Design of experiments were conducted for the analysis of the influence of the turning parameters such as cutting speed, feed rate and depth of cut on the surface roughness. The results of the machining experiments were used to characterize the main factors affecting surface roughness by the DOE techniques like Taguchi, Full factorial, Response Surface Methodology and other methods. The key element for achieving high quality at low cost is Design of Experiments (DOE). Response surface methodology (RSM) is an effective tool for robust design, it offers a simple and systematic qualitative optimal design to a relatively low cost. In this paper RSM, an approach of DOE used by various researchers to analyze the effect of process parameters like cutting speed, feed, and depth of cut on Surface Roughness of work material while machining with various tools and to obtain an optimal setting of these parameters that may result in good surface finish have been discussed.**

***Keywords*—DOE, Response surface methodology, ANOVA, Surface Roughness, Turning.**

I. INTRODUCTION

The need for selecting and implementing optimal machining conditions and most suitable cutting tools has been felt very important over few decades.Surface roughness has become the most significant technical requirement and it is an index of product quality. In order to develop a surface roughness model and optimize, it is essential to understand the current status of work in this area. A good surface finish is desired in order to improve the properties, fatigue strength, corrosion resistance and aesthetic appeal of the product. The manufacturing industries specially are focusing their attention on dimensional accuracy and surface finish. In order to obtain optimal cutting parameters to achieve the best possible surface finish, manufacturing industries have resorted to the use of handbook based information and operators experience. This traditional practice leads to improper surface finish and decrease in the productivity due to sub-optimal use of machining capability.

This causes high manufacturing cost and low product quality .Surface roughness is mainly a result of process parameters such as tool geometry (i.e. nose radius, edge geometry, rake angle) and cutting conditions (feed rate, cutting speed, depth of cut) [8].Surface roughness is harder to attain and track than physical dimensions are, because relatively many factors affect surface roughness. Some of these factors can be controlled and some cannot. Controllable process parameters include feed, cutting speed, tool geometry, and tool setup. Other factors, such as tool, work piece and machine vibration, tool wear and degradation, and work piece and tool material variability cannot be controlled as easily [13]. The important cutting parameters considered for discussion here are cutting speed, feed and depth of cut. It is found in most of the cases surface roughness decreases with increase in cutting speed and decrease in feed and depth of cut. Since these cutting parameters will decide about the type of chips which we expect at the time of machining of a single constant material thus we have to analyze them for no such built-up edge chips formation.

Response Surface Methodology

RSM is a collection of mathematical and statistical techniques that are useful for modeling and analysis of problems in which a response of interest is influenced by several variables and the objective is to optimize this response [10].RSM can be defined as a statistical method that uses quantitative data from appropriate experiments to determine and simultaneously solve multi-variable equations correlating the dependent parameters(response) such as cutting force, power consumption, surface roughness, tool life with independent parameters (input variables). cutting speed, feed rate and depth of cut, in a turning process. The graphical representations of these equations are called response surfaces, which can be used to describe the individual and cumulative effect of the input variables on the response and to determine the mutual interactions between the input variables and their subsequent effect on the response.

International Journal of Emerging Technology and Advanced Engineering
Website: www.ijetae.com (ISSN 2250-2459, ISO 9001:2008 Certified Journal, Volume 4, Issue 10, October 2014)

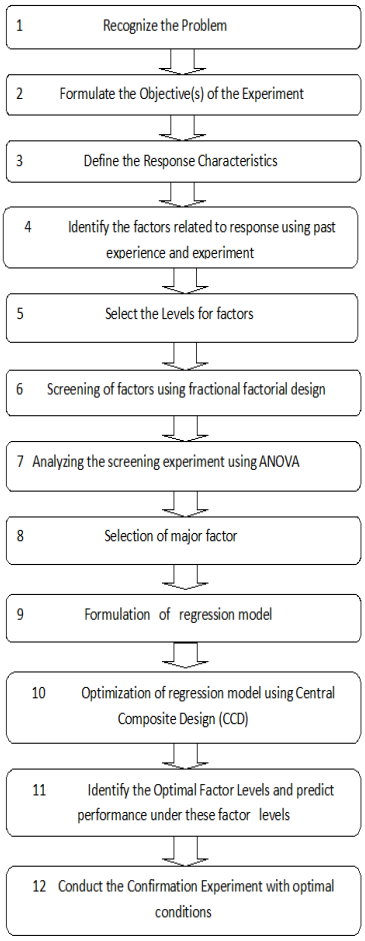


Figure 1.Steps in Response Surface Methodology (RSM).

In design optimization using RSM, the first task is to determine the optimization model, such as the identification of the interested system measures and the selection of the factors that influence the system measures significantly. To do this, an understanding of the physical meaning of the problem and some experience are both useful. After this, the important issues are the design of experiments and how to improve the fitting accuracy of the response surface models. DOE techniques are employed before, during, and after the regression analysis to evaluate the accuracy of the model.RSM also quantifies relationships among one or more measured responses and the vital input factors.

The work which initially generated interest in the package of technique was by box and Wilson in 1951.RSM can be used in the following ways [20]:

1) To determine the factor levels that will simultaneously satisfy a set of desired specifications,
2) To determine the optimum combination of factors that yields a desired response and describes the response near the optimum,
3) To determine how a specific response is affected by changes in the level of the factors over the Specified levels of interest,
4) To achieve a quantitative understanding of the system behavior over the region tested,
5) To predict product properties throughout the region, even for a factor combinations not actually run,
6) To find the conditions necessary for process stability (insensitive spot).

To generate contour surface [5]

Response surface methodology, or RSM, is a collection of mathematical and statistical techniques in which a response of interest is influenced by several variables and the objective is to optimize this response. For example, suppose that a chemical engineer wishes to find the levels of temperature (x_1) and pressure (x_2) that maximize the yield (y) of a process. The process yield is a function of the levels of temperature and pressure, $y = f(x_1, x_2) + e$

Where e represents the noise or error observed in the response y. Then the surface represented by $h = f(x_1, x_2)$, which is called a Response surface. We usually represent the response surface graphically, where h is plotted versus the levels of x_1 and x_2. To help visualize the shape of a response surface, we often plot the contours of the response surface as well. In the contour plot, lines of constant response are drawn in the x_1, x_2 planes. Each contour corresponds to a particular height of the response surface. Objective is to optimize the response. In RSM, polynomial equations, which explain the relations between input variables and response variables, are constructed from experiments or simulations and the equations are used to find optimal conditions of input variables in order to improve response variables. For the design of RSM, many researchers have used central composite design (CCD) for their experiments. CCD is widely used for fitting a second-order response surface. CCD consists of cube point runs, plus center point runs, and plus axial point runs.

International Journal of Emerging Technology and Advanced Engineering
Website: www.ijetae.com (ISSN 2250-2459, ISO 9001:2008 Certified Journal, Volume 4, Issue 10, October 2014)

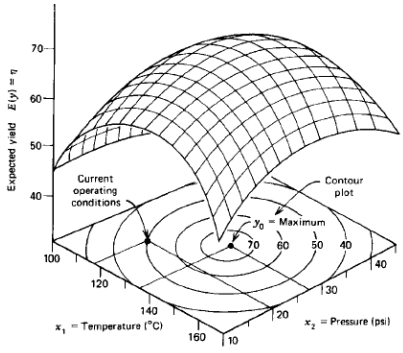


Fig2: To generate contour surface

The three factors speed, feed rate, depth of cut, selected in the screening experiment, will be used in CCD. The process can be studied with a standard RSM design called a Central composite design (CCD). The factorial portion is a full factorial design with all factors at three levels, the star points are at the face of the cube portion on the design which correspond to value of -1. This is commonly referred to as a face centered CCD. The center points, as implied by the name, are points with all levels set to coded level 0, the midpoint of each factor range, and this is repeated six times. Twenty experiments to be performed. For each experimental trial, a new cutting edge to be used. The latest version of the Minitab or Design Expert may be used to develop the experimental plan for response surface methodology. The same software can also be used to analyze the data collected.

II. Literature Review

Vipin and Harish Kumar [24] used Response surface methodology for their investigations. The surface roughness models were developed for turning leaded gun metal under dry conditions. The models were developed in terms of cutting speed, feed rate and depth of cut obtained experimentally. The effects of cutting variables (cutting speed, feed and depth of cut) on surface roughness had been investigated by Central composite Design. The first-order model was developed by an experimental design consisting of 12 experiments. Twelve experiments constitute Eight experiments (23 factorial designs) and Four experiments (an added centre point repeated four times) as shown in Fig.2. This was done to predict the 'b' parameters as used in the Equation. The blocks provide the confidence interval of the parameters and help in the analysis of variance. A second-order model was developed by adding six augment points to the factorial design.

Depending on the capacity of the machine, an augment length of ±1 was chosen. The augment points consist of three levels for each of the independent variables denoted by -1, 0, 1. These six experiments were repeated twice to develop the second-order model. The resulting 12 or 24 experiments form the central composite design with 23 designs. Regression analysis was successfully used to develop the surface roughness model. The surface roughness equation showed that the feed is the main influencing factor on the surface roughness, followed by cutting speed and depth of cut in the operation model. Increasing any of these three cutting variables increases the surface roughness. Dual-response contours provided useful information about the maximum attainable surface roughness for a given metal removal rate as a function of all three independent cutting variables.

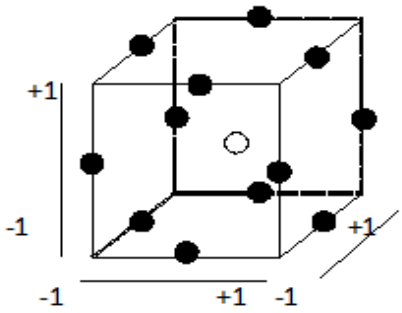


Fig3: Representation of a CCD

Alexandru STANIMIR.et.al.,[22] have presented a paper where in order to find out a mathematical relation of polynomial second degree type which describe, in finish turning of hardened 205 Cr115 steel, the roughness parameter Ra dependence on cutting edge wear, depth of cut, feed rate and cutting speed, a factorial design methodology was used. The experimental tests were done according to a composed, central, four-factor five-level factorial program. The established second degree polynomial relationship for the Ra calculus as a function of the cutting conditions and the flank wear approximate in a satisfactory way the studied phenomena. The main influence on the surface roughness was exerted by the feed rate and flank wear.The interactions of some parameters as feed rate and flank wear had a great influence on the roughness values of the machined surface. Karin Kandananond [7] used Design of Experiment for the determination of Empirical Model for Surface Roughness in Turning Process.

International Journal of Emerging Technology and Advanced Engineering
Website: www.ijetae.com (ISSN 2250-2459, ISO 9001:2008 Certified Journal, Volume 4, Issue 10, October 2014)

This process was performed in the final assembly department at a manufacturing company which supplies fluid dynamic bearing (FDB) spindle motors for hard disk drives (HDDs). The work pieces used were the sleeves of FDB motors made of ferritic stainless steel, grade AISI 12L14. A 2k factorial experiment was used to characterize the effects of machining factors, depth of cut, spindle speed and feed rate on the surface roughness of the sleeve. The results show that the surface roughness was minimized when the spindle speed and feed rate were set to the highest levels while the depth of cut was set to the lowest level. Even though the results from this research were process specific, the methodology deployed can be readily applied to different turning processes. As a result, practitioners have guidelines for achieving the highest possible performance potential. The purpose of this research is to quantify the effect of depth of cut, spindle speed and feed rate on surface roughness of the FDB sleeve in HDD. The factorial design was utilized to obtain the best cutting condition which leads to the minimization of the surface roughness. The half normal plot and ANOVA indicate that the feed rate (C) is the most significant factor followed by spindle speed (B) and feed rate (A). Moreover, it was interesting to note that there are interactions among these three factors with the highest order term, ABC. Regarding the model validation, the regression model developed proves accuracy and has the capability to predict the value of response within the limits of factors investigated. After the optimal cutting condition is implemented, the surface roughness was significantly reduced about 8 percent. In addition to the factorial design experiment, the RSM and Taguchi design were proved to be potential methodologies to develop an empirical model and optimize the surface roughness of the metal work pieces.

M. Aruna and V. Dhanalaksmi [3] used Inconel 718, a nickel based super-alloy accounting for about 50% by weight of materials used in an aerospace engine, mainly in the gas turbine compartment. This is owing to their outstanding strength and oxidation resistance at elevated temperatures in excess of 5500 C. machiningis a requisite operation in the aircraft industries for the manufacture of the components especially for gas turbines. This paper is concerned with optimization of the surface roughness when turning Inconel 718 with cermet inserts. Optimization of turning operation is very useful to reduce cost and time for machining. The approach was based on Response Surface Method (RSM). In their work, second-order quadratic models were developed for surface roughness, considering the cutting speed, feed rate and depth of cut as the cutting parameters, using central composite design.

The developed models were used to determine the optimum machining parameters. These optimized machining parameters were validated experimentally, and it was observed that the response values were in reasonable agreement with the predicted values. The experiment was performed by using a PMT –TNS-25 CNC lathe. Inconel 718 cylindrical rod is considered as the work piece material. Titanium carbide based cermet inserts (Triangular) were used as the cutting tool. The consequences of the experimental data is used for predicting the outcome of assorted input machining parameters such as cutting speed, feed and depth of cut on the surface roughness when machining Inconel 718 using cermet inserts. A non-linear regression equation was developed and projected. Cutting speed has the strongest effect on the surface roughness among the selected parameters; it was inversely proportional to the response. It was found that the surface roughness could be controlled in the design stage which was the most effective and inexpensive way.

Y. Sahin, A.R. Motorcu [17] presented a paper in which the surface roughness model was developed in terms of main cutting parameters such as cutting speed, feed rate and depth of cut, using response surface methodology. Machining tests were carried out in turning AISI 1050 hardened steels by cubic boron nitride (CBN) cutting tools under different conditions. The model predicting equations for surface roughness of Ra, Rz and Rmax were developed using an experimental data when machining steels. The results indicate that the feed rate was found out to be dominant factor on the surface roughness, but it decreased with decreasing cutting speed, feed rate, and depth of cut for these tools. In addition, average surface finish of Ra value produced by CBN cutting tool was about 0.823 µm when machining hardened steels. However, the Ra value decreased about 0.55 µm in terms of trial conditions. Moreover, a good agreement between the predicted and experimental surface roughness was observed within reasonable limit. To develop a second-order model, a design consisting of 18 experiments was conducted. Eight experiments constitute 23 factorial designs with an added center point repeated four times, the added center point being used to estimate pure error. An augment length of 2 was chosen depending on the capacity of the center lathe. The augments point consists of three levels for each of the independent variables denoted by -2,-1, 0, +1, +2. The following conclusions were drawn from the cutting conditions in machining hardened AISI 1050 steels using CBN/TiC cutting tools.

International Journal of Emerging Technology and Advanced Engineering
Website: www.ijetae.com (ISSN 2250-2459, ISO 9001:2008 Certified Journal, Volume 4, Issue 10, October 2014)

The result clearly showed that feed rate was the most powerful factor on surface roughness for all tools. In general, surface roughness of Ra, Rz and Rmax parameters decreased with decreasing main cutting parameters of V (cutting speed), f (feed rate), d (depth of cut) for CBN cutting tools. Furthermore, the average surface finish values of Ra produced by CBN/TiC cutting tools was about 0.823 µm for machining the hardened carbon steel. However, this Ra value even reduced about 0.55 µm depending upon cutting parameters. Moreover, the regression model showed that the predicted values had been very close to experimental values of surface roughness when machining hardened steels.

M. Naga PhaniSastry and. K. Devaki Devi [17] have presented a paper which was concerned with the effect of turning process parameters (cutting speed, feed rate, and depth of cut) on the metal removal rate and surface roughness as responses or output parameters. Response surface methodology (R.S.M), determine and present the cause and effect of the relationship between true mean response and input control variables influencing the response as a two or three dimensional surface. R.S.M had been used for designing a three factor with three level central composite factors design in order to construct statistical models capable of accurate prediction of responses. The results obtained shows that the application of R.S.M can predict the effect of machining parameters on MRR and surface roughness. A case of straight CNC turning of aluminum bar using HSS tool was being considered. The predicted optimal setting ensured minimization of surface roughness and maximization of MRR (Material Removal Rate). Optimal result was verified through confirmatory test. The roughness is measured by surface roughness meter (Stylus Type) and the force is measured by dynamometer .The results were then recorded to analyze the effect of different parameters and their levels on surface roughness and MRR. The model for three different parameters namely speed, feed and depth of cut for turning process in CNC LATHE on aluminium material were developed using response surface method(RSM).The second order models had been validated with the analysis of variance. It was found that the feed and depth of cut had more significant effect while speed had less significant effect on MRR and feed and depth of cut had equal significance on surface roughness (Ra).

LB Abhang and M Hameedullah [1] have published a paper in which experimental investigations had been conducted to determine the effect of the tool geometry (effective tool nose radius) and metal cutting conditions (cutting speed, feed rate and depth of cut) on surface finish during the turning of EN-31 steel. First and second order mathematical models were developed in terms of machining parameters by using the response surface methodology on the basis of the experimental results. The surface roughness prediction model had been optimized to obtain the surface roughness values by using LINGO solver programs. LINGO is a mathematical modeling language which is used in linear and nonlinear optimization to formulate large problems concisely, solve them, and analyze the solution in engineering sciences, operation research. It gives minimum values of surface roughness and their respective optimal conditions. The factorial design with eight added centre points (24 + 8) used in this work is a composite design. A reliable surface roughness model for steel turning was developed using RSM and incorporated cutting speed, feed rate, depth of cut, and the tool nose radius. The study was optimized by the LINGO-solver approach, which is a global optimization technique. This has resulted in a fairly useful method of obtaining process parameters in order to attain the required surface quality. The optimal parameter combination of the turning process corresponded to a cutting speed of 189 m/minute, a feed rate of 0.06 mm/revolution, a depth of cut of 0.2 mm, and a tool nose radius of 1.2 mm by the Lingo-solver approach. This had validated the trends available in the literature and extended the data range to the present operating conditions, apart from improving the accuracy and modeling by involving the most recent modeling method. The application of LINGO-solver optimization to obtain optimal machining conditions will be quite useful at the computational planning stage in the production of high quality goods with tight tolerances by a variety of machining operations, and in the adaptive control of automated machine tools.

Srinivasan, A. et al [21] published a paper in which an attempt has been made to model the machinability evaluation through the response surface methodology in machining of homogenized 10% micron Al2O3 LM25 Al MMC manufactured through stir casting method. Results:

International Journal of Emerging Technology and Advanced Engineering
Website: www.ijetae.com (ISSN 2250-2459, ISO 9001:2008 Certified Journal, Volume 4, Issue 10, October 2014)

The combined effects of three machining parameters including cutting speed (s), feed rate (f) and depth of cut (d) on the basis of three performance characteristics of tool wear (VB), surface Roughness (Ra) and cutting Force (Fz) were investigated. The contour plots were generated to study the effect of process parameters as well as their interactions. The process parameters were optimized using desirability-based approach response surface methodology. RSM model have been developed for predicting tool life, surface roughness and cutting force. The optimized cutting condition that gives lower surface finish and cutting force when machining micron MMCs had been identified: Cutting speed 'V' 100 m/min, Feed 'f' 0.1 mm/rev and Depth of cut 'a' 0.10 mm. The surface roughness improves with increase of the cutting speed whilst increasing feed adversely affects the surface roughness. The tool wear increases with increase of the cutting speed, the feed and the depth of cut. Among the machining parameters cutting speed had the most dominant effect on tool wear. The cutting force almost linearly varies with feed. At low cutting speed the cutting force was higher and the interactions of cutting speed with feed and depth of cut with feed dominantly affects the cutting forces. The machining parameters for turning process were optimized using Taguchi's technique for minimizing the tool wear, surface roughness and cutting force. The developed model had been validated experimentally and exhibit low values of error.

Ranganath. M. S. et al. [16], presented the findings of an experimental investigation into the effects of speed, feed rate and depth of cut on surface roughness in CNC turning of Aluminium (KS 1275).

Table 1:
Design Table [16]

Run	Blk	A	B	C
1	1	0	0	0
2	1	0	0	-1
3	1	-1	1	1
4	1	0	0	0
5	1	0	1	0
6	1	-1	-1	1
7	1	-1	-1	-1
8	1	0	0	0
9	1	-1	1	-1
10	1	1	1	1
11	1	0	0	1
12	1	1	1	-1
13	1	-1	0	0
14	1	0	0	0
15	1	0	-1	0
16	1	1	-1	-1
17	1	0	0	0
18	1	1	-1	1
19	1	1	0	0
20	1	0	0	0

Response surface methodology and Taguchi techniques were used to accomplish the objective of the experimental study. L27 orthogonal array design was used for conducting the experiments. RSM as well as Taguchi's techniques revealed that Feed is the most significant factor in minimizing surface roughness followed by speed and depth of cut. RSM technique predicted results better than the Taguchi's technique.

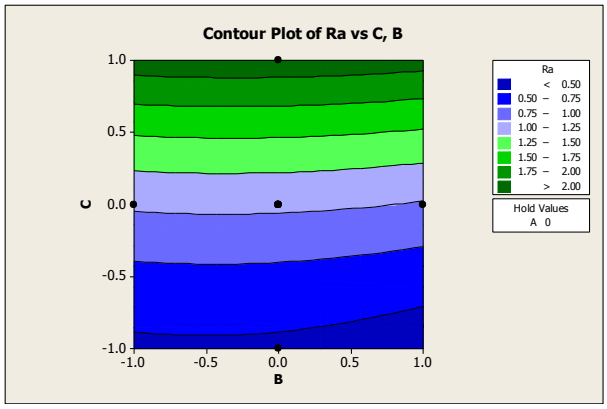


Figure 4: Contour Plot of Ra vs C, B [16]

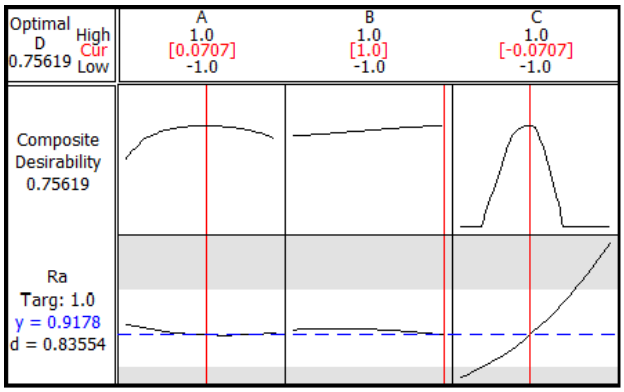


Figure 5: Optimization Plot [16]

Young Kug Hwang and Choon Man Lee [6] paper presents an investigation into the MQL (minimum quantity lubrication) and wet turning processes of AISI 1045 work material with the objective of suggesting the experimental model in order to predict the cutting force and surface roughness, to select the optimal cutting parameters, and to analyze the effects of cutting parameters on machinability. Fractional factorial design and central composite design were used for the experiment plan.

International Journal of Emerging Technology and Advanced Engineering
Website: www.ijetae.com (ISSN 2250-2459, ISO 9001:2008 Certified Journal, Volume 4, Issue 10, October 2014)

Cutting force and surface roughness according to cutting parameters were measured through the external cylindrical turning based on the experiment plan. The measured data were analyzed by regression analysis and verification experiments were conducted to confirm the results. From the experimental results and regression analysis, this research project suggested the experimental equations, proposed the optimal cutting parameters, and analyzed the effects of cutting parameters on surface roughness and cutting force in the MQL and wet turning processes., a number of experiments should be done to confirm results. A two-level fractional factorial design with resolution V, was used for screening experiments. The reason for the usage of resolution V was to analyze the main effect and two-factor interactions. Generally, in resolution V,the main effects are confounded with four-factor interactions, and two-factor interactions are confounded with three-factor interactions. If interactions higher than three-factor interactions can be ignored, the main effect and two-factor interactions can be analyzed. In this paper, in order to select the optimal cutting parameters and to analyze the effect of cutting parameters on surface roughness and cutting force, experimental equations were suggested. Within the range of cutting parameters used in this study, we were able to draw the following conclusions. Using fractional factorial design, nozzle diameter, cutting speed, feed rate, and depth of cut were found as the parameters affecting the surface roughness of the MQL turning. Experimental equations, which can estimate the surface roughness and cutting force in the MQL and wet turning processes of AISI 1045 work material, were suggested with RSM. From the verification experiment, the cutting force equations confirmed the validity in the MQL and wet turning processes, but the surface roughness equations were not appropriate for accurate prediction. When considering surface roughness and cutting force at the same time in the MQL turning process, the optimal combination of cutting parameters to maximize the machinability was as follows: nozzle diameter of 6mm, cutting velocity of 361m/min, feed rate of 0.01mm/rev, and depth of cut of 0.1mm. In the case of the wet turning process, the optimal combination of cutting parameters consisted of nozzle diameter of 6mm, cutting speed of 394m/min, feed rate of 0.02mm/rev, and depth of cut of 0.1mm. According to the experiment results, cutting speed and depth of cut showed opposite effects on cutting force and surface roughness. Therefore, cutting conditions should be set under a clear standard because the optimal combination of cutting conditions could be different depending on machinability.

If we consider only surface roughness and cutting force, MQL turning has more advantages than wet turning.

Ali riza motorcu [11] uses the response surface methodology to investigate the effects of main cutting parameters such as cutting speed, feed rate, and depth of cut on the surface roughness when turning AISI 1050 carbon steel. Machining tests were carried out with uncoated ceramic (KY1615) and coated ceramic cutting tools (KY4400). Optimal machining conditions for the desired surface finish were determined. The adequacy of the second order developed model was analyzed by using analysis of variance. The experimental results indicated that the feed rate was the dominant factor, followed by the depth of cut. The cutting speed showed the minimal effect on the surface roughness. It could be seen that the KY1615 tool produced a better surface roughness than the KY4400 tool. It was shown that average surface roughness' of Ra values were about 2.515 μm, 2.984 μm for the KY1615, KY4400 cutting tools, respectively. Furthermore, the analysis of variance for the second-order model indicated that squares terms were significant on the roughness, but interaction terms of cutting parameters were insignificant for both cutting tools. To develop a second-order model, a design consisting of 18 experiments was conducted. Details of the model and design are given elsewhere (Sahin and Motorcu, 2004; Motorcu, 2006). 18 experiments constitute 23 factorial designs with an added center point repeated four times, the added center point being used to estimate pure error. An augment length of 2 was chosen depending on the capacity of the center lathe. The augments point consists of three levels for each of the independent variables denoted by -2, -1, 0, +1, +2. The RSM was adopted to investigate the effects of machining factors such as cutting speed, feed rate, and depth of cut on the surface roughness when turning the AISI 1050 carbon steel. The feed rate was the dominant factor, followed by the depth of cut. The cutting speed showed the minimum effect on the surface roughness. Furthermore, it could be seen that the KY1615 cutting tool produced a better surface roughness than that of the KY4400 tool. The average surface roughness, Ra values were about 2.515 μm, 2.984 μm for the KY1615, KY4400 cutting tools, respectively. It was found that it was appropriate when machining the mild steel with ceramic based cutting tools under high speed conditions. Moreover, the ANOVA showed that the quadratic effects were significant on the roughness while the interactions terms of cutting parameters were statistically insignificant for both cutting tools.

International Journal of Emerging Technology and Advanced Engineering
Website: www.ijetae.com (ISSN 2250-2459, ISO 9001:2008 Certified Journal, Volume 4, Issue 10, October 2014)

Alagarsamy S.V, Rajakumar N.[2] used an effective approach for the optimization of turning parameters based on the Taguchi's method with Response surface methodology (RSM) .The paper discusses the use of Taguchi's technique for minimizing required surface roughness and maximizing the material removal rate in machining Aluminium Alloy 7075 using TNMG 115 100 tungsten carbide tool. Experiments were conducted based on the established Taguchi's technique L27orthogonal array and Minitab-16 statistical software was used to generate the array. Three machining parameters were chosen as process parameters: Cutting Speed, Feed rate and Depth of Cut. The orthogonal array, signal to noise ratio and analysis of variance were employed to study the performance characteristics in CNC turning operation. Optimal values of process parameters for desired performance characteristics were obtained by Taguchi design of experiment. A second order mathematical model in terms of cutting parameters was also developed using response surface model. the Taguchi method and Response surface methodology was applied for analysing to get a minimum surface roughness and maximum material removal rate for turning process of Aluminium Alloy 7075 using CNC machine via considering three influencing input parameters- Speed, Feed and Depth of Cut. The optimize results for Surface Roughness indicate that the input parameter feed had most influencing to the quality characteristics of surface roughness. Best parameters found for surface finish machining were-Cutting Speed: 500 m/min; Feed: 0.10 mm/rev; Depth of Cut: 0.3mm. For depth of cut being most affecting parameter .Whenever the MRR increases feed and depth of cut were gradually increases. Finally found the best parameters of MRR were-Cutting Speed: 1500 m/min; Feed: 0.20 mm/rev; Depth of Cut: 0.8mm. The equations obtained from Response Surface Methodology for Surface Roughness, MRR were having R-sq. values as 98.85%, and 97.56% respectively. Predicted response values were calculated from Taguchi Analysis and Response Surface Methodology were very similar.

Wasif G. M. & Safiulla M. [25] have presented a paper to find the effects of the various machining (turning) process parameters on the machining quality of NICROFER C263 ALLOY and to obtain the optimal sets of process parameters so that the quality of machined parts can be optimized. The working ranges and levels of the machining process (turning) parameters were found using three factors. Cutting speed (V- m/min), feed rate (f – mm/rev) and depth of cut (d - mm).

The Design-Expert software had been used to investigate the effects of the Machining process parameters and subsequently to predict sets of optimal parameters for optimum quality characteristics. The response surface methodology (RSM) in conjunction with second order central composite rotatable design had been used to develop the empirical models for response characteristics. Desirability functions had been used for simultaneous optimization of performance measure. Confirmation experiments was further conducted to validate the results. Conclusion: Quadratic model was fitted for surface roughness. The results show that the surface roughness did not vary much with experimental depth of cut in the range of 0.1 to 0.15 mm. Feed rate was the dominant contributor, accounting for 69.06% of the variation in surface roughness whereas cutting speed accounts for 3.30% and depth of cut 2.41%. Secondary contributions of interaction effect between speed and depth of cut (3.90%), second order (quadratic) effect of cutting speed (17.11%) and feed (4.2 %). The values of feed, speed, depth of cut had been found for best surface finish (lowest surface roughness). These were 0.14 mm/rev .76.10 m/min and 0.102 mm respectively. The value of surface roughness at these setting is predicted as 0.626558 μm.

Basha N.Z.,Vivek S.[4] presented a paper that investigates the effect of process parameter in turning operation to predict surface roughness of Aluminium 6061, by optimizing the input parameters such as spindle speed, feed rate and depth of cut by using coated carbide tool. A second order mathematical model was developed using regression technique and optimization was carried out using Box-Behnken of response surface methodology. The application of response surface methodology for optimizing the input parameters such as spindle speed (rpm), feed rate (mm/min) and depth of cut (mm), the output parameter surface roughness can also be optimized for economical production. Therefore, this study attempts the application of response surface methodology to find the optimal solution of the cutting conditions for giving the minimum value of surface roughness using design- expert 8.0 software. The confirmatory test was conducted and found that the percentage of error within ±1.5%. Conclusions obtained from experimental data were used to predict the surface roughness 'Ra' by developing the regression model using DoE. A good surface roughness was obtained at the feed rate (0.04-0.05 mm/min) and spindle speed (1700-2000 rpm). The change in feed rate (0.04-0.08 mm/min) had a significant effect on surface roughness (0.72-0.66μm) at higher spindle speed (2000rpm).

International Journal of Emerging Technology and Advanced Engineering
Website: www.ijetae.com (ISSN 2250-2459, ISO 9001:2008 Certified Journal, Volume 4, Issue 10, October 2014)

The change in feed rate (0.04-0.08 mm/min) had no significant effect on surface roughness (0.71-0.72µm) at lower spindle speed (1000 rpm). A feed rate less than 0.06 and depth of cut less than 0.70 had been preferred for obtaining good surface finish.

Sahoo P. [18] presents an experimental study of roughness characteristics of surface profile generated in CNC turning of AISI 1040 mild steel and optimization of machining parameters based on genetic algorithm. The three level rotatable central composite designs were employed for developing mathematical models for predicting surface roughness parameters. Response surface methodology was applied successfully in analyzing the effect of process parameters on different surface roughness parameters. The second order mathematical models in terms of machining parameters were developed based on experimental results. The experimentation was carried out considering three machining parameters depth of cut, spindle speed and feed rate as independent variables and three different roughness parameters Centre line average roughness, root mean square roughness and mean line peak spacing as response variables. It was seen that the surface roughness parameters decrease with increase in depth of cut and spindle speed but increase with increase in feed rate. The models selected for optimization had been validated with F-test. The adequacy of the models of surface roughness has been established with Analysis of Variance (ANOVA). Genetic Algorithm was used to determine the optimum machining parameters in order to obtain the best possible surface quality. The confirmatory tests conducted with the optimum parameter combinations show good agreement with the predictions.

Subramanian M. et al [23] used RSM and GA to Predict Surface Roughness Based on Process Parameters in CNC Turning of AL7075-T6" that deals with the study and development of a regression model to predict surface roughness in terms of geometrical parameter, nose radius of cutting tool TNMG insert and machining parameters, cutting speed and cutting feed rate for machining AL7075-T6, using Response Surface Methodology (RSM). The surface roughness of machined surface was measured by Mitutoyo Surftest SJ201. The second order mathematical model in terms of machining parameters was developed for predicting surface roughness. The adequacy of the model was checked by employing ANOVA. The direct and interaction effects were graphically plotted which helps to study the significance of these parameters on surface roughness. Also the mathematical model is optimized using Genetic Algorithm to attain minimum surface roughness.

The predicted values of roughness were found to match closely with the observed values. The optimum values of input parameters were identified as nose radius = 1mm, cutting speed = 3500rpm and feed = 0.1mm.

III. CONCLUSIONS

On the basis of the experimental results and derived analysis by earlier researchers the studies may be concluded as below:

- The surface roughness is continuously improved with the increase in cutting speed, but increase in feed rate and depth of cut causes a significant deterioration of surface roughness.
- The results obtained using the Response Surface Methodology provides a systematic, efficient and easy-to-use approach for the cutting process optimization.
- Significance of interactions and square terms of parameters is more clearly predicted in Response surface methodology.
- The Response surface methodology shows significance of all possible combinations of interactions and square terms.
- Response surface methodology technique requires almost double Time for conducting experiments as that needed for Taguchi technique.
- Response surface methodology technique can model the response in terms of significant parameters, their interactions and square terms which is not provided by other technique.
- 3D surfaces generated by Response surface methodology can help in visualizing the effect of parameters on response in the entire range specified
- Optimization plot is a special feature which can be obtained from Response surface methodology. Thus Response surface methodology is a better tool for optimization and can better predict the effect of parameters on response.

REFERENCES

[1] Abhang. L. B and Hameedullah. M, Optimal Machining Parameters for Achieving the Desired Surface Roughness in Turning of Steel,TJER, Vol. 9, No. 1,2012,pp. 37-45

[2] Alagarsamy S.V, Rajakumar N.Analysis of Influence of Turning Process Parameters on MRR & Surface Roughness Of AA7075 Using Taguchi's Method and Rsm"International Journal of Applied Research and Studies (iJARS) ,Volume 3, Issue 4, 2014.

[3] Aruna. M and Dhanalaksmi. V, Design Optimization of Cutting Parameters when Turning Inconel 718 with Cermet Inserts, World Academy of Science, Engineering and Technology ,vol. 61, 2012.

[4] Basha N.Z., Vivek S. Optimization of CNC Turning Process Parameters on Aluminium 6061 Using response surface methodology IRACST – Engineering Science and Technology: An International Journal (ESTIJ), vol. xxx, no. xxx, 2013.

[5] Hae-Jin C., Response Surface Methodology (Ch.10.RegressionModeling Ch.11.ResponseSurfaceMethodology) School of Mechanical Engineering, Chung-Ang University.

[6] Hwang. Y. K and Lee. C. M, Surface roughness and cutting force prediction in MQL and wet turning process of AISI 1045 using design of experiments, Journal of Mechanical Science and Technology,vol. 24,issue. 8 ,2010,pp.1669~1677

[7] Kandananond. K , The Determination Of Empirical Model For Surface Roughness In Turning Process Using Design Of Experiment, vol., 8,issue. 10, 2009

[8] Kumar H, Mohd. Abbas, Aas Mohammad, Hasan Zakir Jafri, Optimization of cutting parameters in CNC Turning, International Journal of Engineering Research and Applications (IJERA), Vol. 3, Issue 3, 2013,pp. 331-334,

[9] Lin W.S., Lee B.Y., Wu C.L., Modeling the surface roughness and cutting force for turning. J. Mater. Process. Technol.vol. 108, 2001, pp. 286–293.

[10] Montgomery, D.C., . Design and Analysis of Experiments, Wi1ey, New York, 4th ed.,1997

[11] Motorcu, A. R.: Surface Roughness Evaluation When Machining Carbon Steel With Ceramic Cutting Tools, Uludağ Üniversitesi Mühendislik- Mimarlık Fakültesi Dergisi, Cilt 14, Sayı 1, 2009

[12] Noordin MY, Venkatesh VC, Sharif S, Elting S, Abdullah A. Application of response surface methodology in describing the performance of coated carbide tools when turning AISI 1045 steel. *Journal of Materials Processing Technology*. Vol. 1 issue 1, 2004,pp 46-58.

[13] Rafai N. H. and Islam M. N, An Investigation Into Dimensional Accuracy And Surface Finish Achievable In Dry Turning, Machining Science and Technology, Volume 13, Issue 4, 2009,pp 571-589,

[14] Ranganath M S and Vipin, Effect of Machining Parameters on Surface Roughness with Turning Process- Literature Review, International Journal of Advance Research and Innovation, Volume 2, 2014,pp 531-536,

[15] Ranganath M S and Vipin, Optimization of Process Parameters in Turning Operation Using Taguchi Method and Anova: A Review, International Journal of Advance Research and Innovation, Volume 1, 2013,pp 31-45

[16] Ranganath M S, Vipin, Nand Kumar and R. Srivastava Surface Finish Monitoring in CNC Turning Using RSM and Taguchi Techniques International Journal of Emerging Technology and Advanced Engineering Website: www.ijetae.com, ISO 9001:2008 Certified Journal, Volume 4, Issue 9, 2014.

[17] Sahin. Y, Motorcu. A. R , Surface roughness model in machining hardened steel with cubic boron nitride cutting tool International Journal of Refractory Metals & Hard Materials vol.26 ,2008,pp.84–90

[18] Sahoo P., Optimization Of Turning Parameters For Surface Roughness Using RSM and GA, Advances in Production Engineering & Management vol.6 ,2011,pp.197-208

[19] Sastry. M N P and. Devi. K D, Optimization of Performance Measures in CNC Turning using Design of Experiments(RSM) , Science Insights: An International Journal vol. 1 (1),2011,pp.1-5

[20] Sharma. A.V.N.L. Parametric Analysis And Multi Objective Optimization Of Cutting Parameters In Turning Operation Of EN353 – With CVD Cutting Tool Using Response Surface Methodology Journal Of Engineering And Innovative Technology (IJEIT) Volume 2,2013

[21] Srinivasan, A.,R.M. Arunachalam, S. Ramesh and J.S. Senthilkumaar, Machining Performance Study on Metal Matrix Composites-A Response Surface Methodology Approach, American Journal of Applied Sciences vol. 9 issue 4,2012,pp.478-483

[22] Stanimir. A, Regressions Modeling Of Surface Roughness In Finish Turning Of Hardened 205cr115 Steel Using Factorial Design Methodology Fiabilitate Si Durabilitate - Fiability& Durability No 1(7),2011, Editura "Academica Brâncuşi" , Târgu Jiu

[23] Subramanian M. et ellUsing RSM and GA to Predict Surface Roughness Based on Process Parameters in CNC Turning of AL7075-T6. International Journal of Innovative Research in Science, Engineering and Technology Volume 3, Special Issue 3, 2014

[24] Vipin and Kumar. H, Surface Roughness Prediction Model by Design of Experiments for Turning Leaded Gun Metal, International Journal of Applied Engineering Research,Volume 4 Number 12,2012 pp. 2621–2628,

[25] Wasif M. G., Safiulla. M, Evaluation Of Optimal Machining Parameters Of Nicrofer C263 Alloy Using Response Surface Methodology While Turning On Cnc Lathe Machine , International Journal of Mechanical and Industrial Engineering (IJMIE), Vol-2,Iss-4,2012

ISSN:0975-9646

Performance Analysis of A Novel Scheduling Algorithm for Different Traffics in LTE Networks

*Vallari Sharma, **Prof. P.K Chopra

*M.Tech - student, Department of ECE, Ajay Kumar Garg Engineering College, Ghaziabad, India
**HoD, Department of ECE, Ajay Kumar Garg Engineering College, Ghaziabad, India

***Abstract*-As the demand for Packet based mobile broadband system is increasing day by day .So, to meet the needs of future mobile communication requirements, 3GPP (3rd Generation Partnership Project) has standardized a new technology which is the next step of current 3G mobile network i.e. LTE(Long Term Evolution) The main objective of LTE is to achieve high data rate, low latency radio access technology and to serve the challenges arising from the growing demand of network services like VoIP, video streaming, web browsing with constraints on delays and bandwidth requirements. LTE is an emerging and promising technology for the improvement in the performance which is achieved through streamlining the system for packet services as long term evolution is an all Internet protocol based network. Traffic scheduling plays an important role in LTE technology by assigning the shared resources among users in the most efficient manner. This paper presents there is a scheduling mechanism which is studied and its performance is analyzed for the different traffic flows like video, voice and text traffic with fixed user equipments and number of packets in queue in terms of the different parameter metrics such as the Average Goodput, Average Delay time, Invalid Packet rate, Packet loss ratio and Spectral efficiency.**

Keywords:Long term evolution (LTE), Channel Quality Indicator (CQI), User Equipment UE), Quality of Service (QoS).

I. INTRODUCTION

As LTE is all IP network technology, the requirements like high speed data rate, low latency, increased spectral efficiency, scalable bandwidth etc. can be fulfilled by selecting several key technologies for LTE radio interface. Of which, the most important technologies are multiple access through SCFDMA (Single Carrier Frequency Division Multiple Access) in uplink, OFDMA (Orthogonal Frequency Division Multiple Access) in downlink and multiple antenna technology. For high flexibility of LTE, variable bandwidth feature is included which gives freedom to network operator to use bandwidth between 1.4MHz and 20MHz. The 20MHz bandwidth can provide up to
150Mbps downlink user data rate with 2X2 MIMO and 300 Mbps with 4x4 MIMO. The most important feature introduced by LTE specifications is enhanced Quality of Service (QoS) support by means of new RRM technique [1]. An extension in the system capacity and improvement in the performance as compared to the high speed packet access is expected from LTE. The objective of LTE was to develop a framework for the evolution of the 3GPP radio-access technology towards a high-data-rate, spectral efficiency, low value of latency and packet optimized radio-access technology. The need for this system is to have data rates of high speed, low latency, increased spectral efficiency, scalable bandwidths, flat all-IP network architecture etc [4]. The main objective of the LTE network is to increase the data-rate to fulfill the demand of services. The Radio resources are divided and shared efficiently among different active users while maintaining a satisfied level of QoS to all active users. To fulfill the requirements, the LTE system uses orthogonal frequency division multiple access (OFDMA) technology in the downlink. In this, a single multiplexer is used and the data is divided into its different sub-carriers. The Filter banks are replaced by Inverse Fast Fourier Transform in case of higher number of sub carriers. In LTE, for both FDD and TDD modes, the downlink modulation technique used is OFDM [1] SC-FDMA (Single Carrier Frequency Division Multiple Access) in uplink in which different users are provided with different non overlapping sub-carriers and multi-antenna technology [3]. The Key characteristics of LTE are Resource allocation in the frequency domain takes place with the resolution of 180MHz resource blocks both in uplink and in downlink [2]. The scheduling mechanism, implemented in the evolved base station (eNodeB) and distributing radio resources among users according to the channel quality indication it get from the user equipment according to the channel condition

II. LTE ARCHITECTURE

The LTE architecture is given in Fig 1 in which there are two layers Evolved Packet Core and Evolved UTRAN. The EPC consists of MME (Mobility Management Entity) and different gateways for the communication with the outside world and E-UTRAN consists of evolved base stations (eNBs).The main feature of LTE systems is Multi user scheduling because it is responsible for allocating different resources to different active users in order to satisfy the QoS needs. The Packet Scheduler are deployed at the eNodeB (for both uplink and downlink).A Physical Resource Block (PRBs) consists of 7symbols x 12 subcarriers. With QoS, different applications meet different requirements. Different

scheduling strategies are used for the services like Proportional Fair, Round Robin, Modified Largest Weighted Delay First, Exponential-Proportional Fair, Logarithmic Rule etc. and all these algorithms comes under different categories of LTE scheduling strategies.

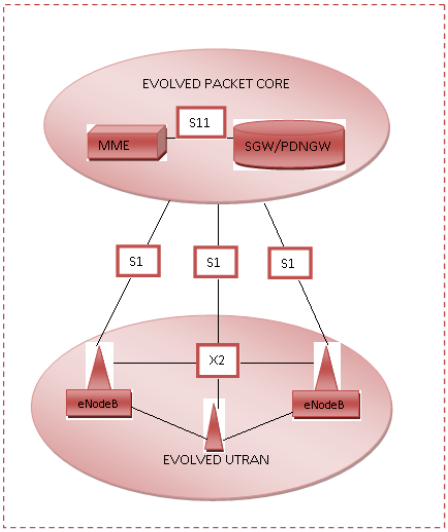


Fig 1.LTE Architecture

They are classified as- Channel unaware, Channel aware/ QoS unaware, Channel aware/QoS aware and Semi Persistent scheduling for VoIP support. The most important objective of LTE scheduling is to fulfill the requirements of Quality of Service. A key feature of LTE is the inclusion of advanced Radio Resource Management (RRM) procedures in order to increase the performance of the system up to the Shannon limit. Packet scheduling mechanisms plays an important role, because they are responsible for selecting, with fine time and frequency resolutions, distribution of radio resources among different stations, considering the channel condition and QoS requirements. This goal should be accomplished by providing an optimal trade-off between spectral efficiency and fairness. The downlink channel under frequency division duplex configuration is considered as an object of our study, but they are valid for other configurations also. A survey was also provided for complementing the above concepts on recent technique. Thus, this survey would be useful for the readers interested in learning the basic concepts. Performance comparison of the already available scheduling schemes with focus on QoS is done.

III. PACKET SCHEDULING

Multi-user scheduling is one of the main features in LTE systems because it is in charge of distribution of available resources among active users to satisfy their QoS needs. Packet schedulers (for both the downlink and the uplink) are deployed at the eNodeB, and OFDMA provides no inter-channel interference. They work with one TTI and one Resource Block in the time and frequency domain respectively. The LTE may operate as a pure packet switching system and all the traffic including delay sensitive services need to be scheduled. Therefore, the scheduling mechanism implemented in the network base station (BS) and distribution of radio resources among users should be considered as a significant part of the system design. The purpose of Packet Scheduling is to distribute the resources among users in a fair and efficient way to maximize the system throughput along with. The scheduler is basically very important part of the LTE system as it is very beneficial for determining the performance of the system.

Fig 2 represents that the main Radio Resource Management modules that interact with the downlink packet scheduler. The process of packet scheduling is divided into number of sequences per TTI:

(a) Each UE decodes the reference signals, computes the Channel quality indicator, and sends it back to the eNodeB.

(b) The eNodeB uses the CQI information for the allocation decisions and fills up a RB “allocation mask”.

(c) The AMC module selects the best MCS that should be used for the data transmission by scheduled users.

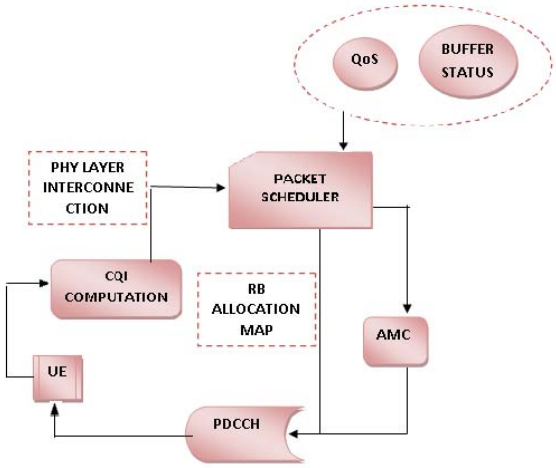


Fig 2.Packet Scheduler

(d) The information about these users, the allocated RBs, and the selected MCS are sent to the UEs on the PDCCH.

(e) Each UE reads the PDCCH payload and, in case it has been scheduled, accesses to the proper PDSCH payload

IV. SCHEDULING MECHANISM

In this scheduling mechanism, the results are analyzed for the video traffic only and for fixed number of packets in queue of user equipments i.e. 120. For achieving QoS requirements of LTE netwoks, the most important parameters are many QoS parameters i.e. time delays, error rates and goodputs. There are basically three phases for designing PPM and in this the first phase works in frequency domain and rest of the two phases work in time domain.

1. Initial Scheduling for Physical Resource Blocks (PRBs).

2. Managing queues and predication of packets for delays.
3. Cut in process.

a. Initial Scheduling for PRBs

First consider the frequency domain. In this phase, focus is on the system performance. PRBs are allocated to users with best CQI's. In each TTI, the CQI values of different users are compared. The design goal of the first phase is to have good throughputs.

b. Managing Queues and predication of packets for delays

In the second phase the performance of those users are considered whose CQI values are not good. Those users may be located at the cell edges relative to base station. Their packets are not transmitted to the destination on time. There will be out of date packets present which are discarded at the destinations if we only consider the throughputs

c. Cut in process

For attaining maximum throughput, the resource block y is allocated to user x but in case, when there is no cut in process. From all the available users, a cut in user z is chosen such that,

$$C_{z,y} = \min (ET_{x,y} - ET_{z,y})$$

Of all the available users let that cut in user z will generate minimum decrease in the value of throughput for the utilization of resource block y. This process is repeated until all the resource blocks are allocated to the users properly or all the cut in users are properly handled. If, initially all the cut in users are handled then the users with highest throughput are allocated with the remaining of the resource blocks. If, in the second case all resource blocks are allocated then this indicates that there is need for more resource blocks for the cut in users

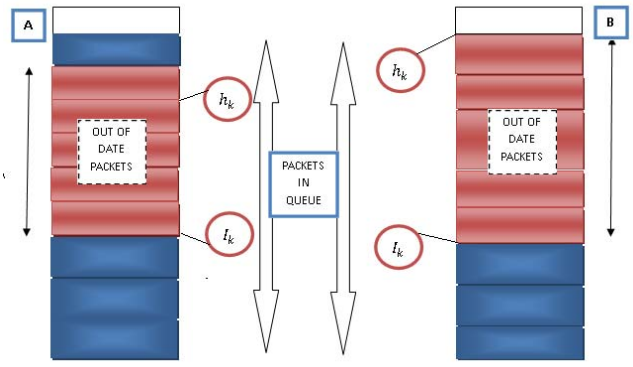


Fig 3 Scenario of Continuous out of date packets

V. Results And Discussion

Fig 4(a) shows the average cell goodput for video, voice and text flows with fixed user equipments and the average cell goodput for the video flow is maximum while for the text flow is minimum.

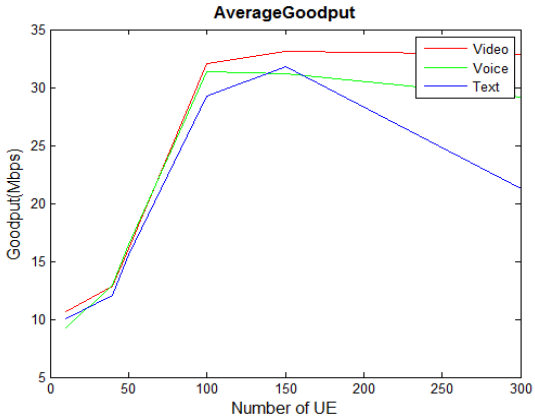


Fig 4(a) Average Cell Goodput

Fig 4(b) shows the Average Delay time for the three different flows and it shows that the delay time in text traffic is very high as compared to other two traffic flows.

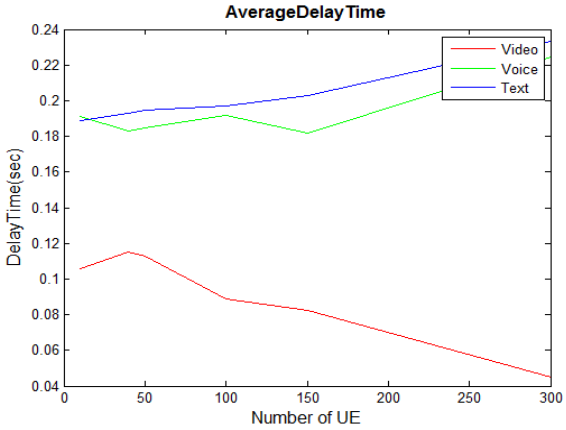


Fig 4(b) Average Delay Time

Fig 4(c) shows the invalid packet rate for the different traffics and the video traffic is having minimum invalid packet rate while it is maximum for text traffic.

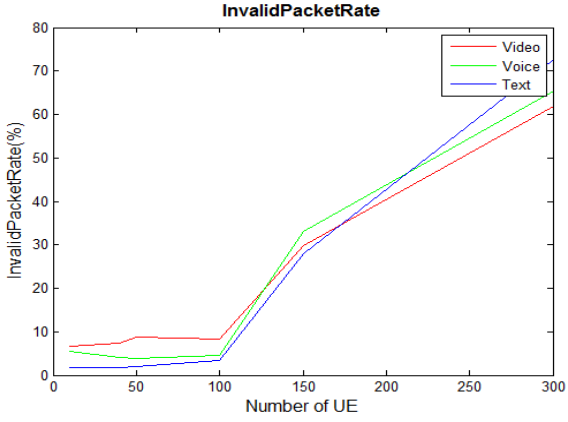


Fig 4(c) Invalid Packet Rate

Fig 4(d) shows the packet loss ratio and its very is high in case of text traffic and minimum value in case of video traffic as more number of packets are transmitted in this case. Fig 4(e) shows the spectral efficiency, video traffic is having highest spectral efficiency among all the three traffic flows.

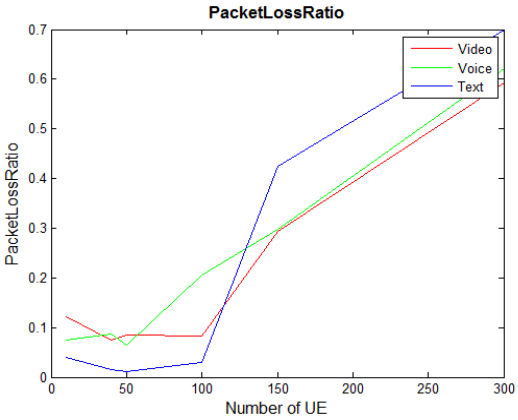


Fig 4(d) Packet Loss Ratio

VI. CONCLUSION

In this paper, a scheduling mechanism is studied for downlink video traffic for different flows like video, voice and text traffics with fixed user equipments in terms of Average goodput, Average Delay time, Invalid Packet rate, Spectral Efficiency and Packet loss ratio. Future research will focus on more challenging problems of scheduling, considering both the uplink and downlink directions.

ACKNOWLEDGMENT

We sincerely thank Ajay Kumar Garg Engineering College for providing the framework to accomplish our work

REFERENCES

[1] B. Sahoo, 2011"Performance Comparison of Packet Scheduling Algorithms for Video Traffic in LTE Cellular Network", *IJMNCT, Vol.3 , No.3, pp 1307.*

[2] F. Capozzi, G. Piro, Student Member, IEEE, L.A.Grieco, Member, IEEE, G. Boggia, Senior Member, IEEE, and P. Camarda, 2013 "Downlink Packet Scheduling in LTE Cellular Networks: Key Design Issues and a Survey", *IEEE Communication surveys and tutorialsVol.15, No.2, pp 678-700.*

[3] O.Iosif, I. Banica, 2013 " Performance Analysis of Downlink LTE using System level Simulator" , *U.P.B.Sci.Bull.,Series C, Vol.75, Iss 1, pp 815-820.*

[4] .Biernacki, K.Tutschku, 2013 "Comparative Performance Study of LTE Downlink Schedulers", *Springer, Vol.74, No.2, pp 585-599.*

[5] M.H Habaebi, J.Chebil, A.G Al-Sakkaf and T.H Dahawi, "Comparison Between Scheduling Techniques In Long Term Evolution",IIUM Engineering Journal,Vol.14, No. 1, 2013.

[6] G. Aiyetoro, G. Giambene and F. Takawira, 2012 "Performance Analysis of M-LWDF and EXP-PF Schedulers for Real TimeTraffic in Satellite LTE Networks", *University of Siena, Italy, Vol.12, No.4, pp 1512-1523.*

[7] J. Huang, V.G. Subramanian, R. Agrawal, R. Berry, Downlink scheduling and resource allocation for OFDM systems, IEEE Trans. Wireless Commun. 8 (1) (2009) 288–296.

[8] D.Keke, W.bin, G.Hui, W.Wennai, 2013 "Energy saving scheduling for the LTE Multicast services", Journal of Engineering(China), *Vol.30, No.5, pp 423-429.*

[9] W.Kuang Lai, C.LTang,2013 "QoS-aware downlink packet scheduling for LTE networks", Elsevier, Vol.57, No.7, pp 1689-1698.

[10] G. Piro, L. Grieco, G. Boggia, R. Fortuna, P. Camarda, Two-level downlink scheduling for real-time multimedia services in LTE networks, IEEE Trans. Multimedia 13 (5) (2011) 1052–1065

AUTHORS



Vallari Sharma received her B.Tech degree from Uttar PradeshTechnical University, Lucknow. Now, She is pursuing M.Tech (ECE) from Ajay Kumar Garg Engineering College, Ghaziabad. Her area of interest is mobile and wireless communication.



Prof. Pradeep Kumar Chopra entered the field of education in the year 2004 after 24 years of exemplary service in the technical branch of the Indian Air Force, He earned his Bachelor's degree in Engineering (Electronics) from Delhi college of Engineering in the year 1979 and Masters in Technology from IIT Delhi in the year 1985. He also has a Masters degree in Defense Studies from Madras University. While he was in the Indian Air Force he was part of and headed a number of important technical projects. For his exemplary services he was awarded "Vishist Seva Medal" by the President of India in the year 1993.He took premature retirement from the IAF in the year 2004 and entered the field of education. He is the Head of Dept. (Electronics and Communication) in Ajay Kumar Garg Engineering College in Ghaziabad.

International Journal of Electronic and Electrical Engineering.
ISSN 0974-2174, Volume 7, Number 3 (2014), pp. 321-326
© International Research Publication House
http://www.irphouse.com

Performance Analysis of Brushless DC Motor Using Intelligent Controllers and Minimization of Torque Ripples

Vishal Srivastava[1], Ashish Chourasia[2] and Shaba Anjum[3]

[1,2,3]*Electrical Engineering Department, Delhi Technological University, Delhi*

Abstract

Brushless DC motor (BLDCM) is a high performance, low maintenance cost, adequate torque, high speed, high reliability motor and widely used in industries having several advantages over other type of motors. The reason of popularity is due to its simpler speed control with enhanced performance by the use of electronic commutation. The above mentioned characteristics and properties of BLDC motor provide a large research domain in Electrical drives. This paper presents a simulation study of Speed Control of BLDC motor for performance analysis and comparison using intelligent controller (ANFIS) with conventional controller (PI, PID). The further study will be used for minimizing the ripples in Torque and Speed along with admissible current control. The simulation study and analysis of results will form the basis of the conclusion.

Keywords: Brushless DC motor (BLDCM), Electronic commutation, Speed Control, ANFIS (intelligent controller), PI, PID (Conventional Controller), Ripples.

1. Introduction

The Permanent Magnet Brushless DC (BLDC) motor is the ideal choice for applications that require high power-to volume ratio, high reliability, and high efficiency. BLDC motor is considered to be a high performance motor and is capable of providing large amounts of torque over a vast speed range. BLDC motors are a derivative of the most commonly used DC motor and they share the same torque and speed performance curve characteristics.[5]. A BLDC motor requires an inverter and a rotor position sensor to perform commutation process because a permanent magnet synchronous motor does not have brushes and commentators in DC motors [5].

Consumers now demand for lower energy costs, better performance, reduced acoustic noise, and more convenient features [4]. These BLDC motors are not limited to household applications, but these are suitable for other applications such as medical equipment's, transportation, HVAC, motion control and many industrial tools [6]. ANFIS controller provides feasibility and easy in accessing the controllers in terms of linguistic variables .Schemes based Adaptive Neuro-Fuzzy Controller Based on Emotional Learning Algorithm [2-4] meant for speed control of brush less direct current (BLDC) drives have been implemented. The modeling and simulation analysis for BLDCM which provides a good foundation and method for system design and verifying intelligent control strategy. The performance is observed with Conventional Speed controller and ANFIS speed controller and comparison is done to know which gives the better results. The drive system is dependent on the position and current sensors for control.

2. Control Schemes for Speed Control of BLDC motor drive system

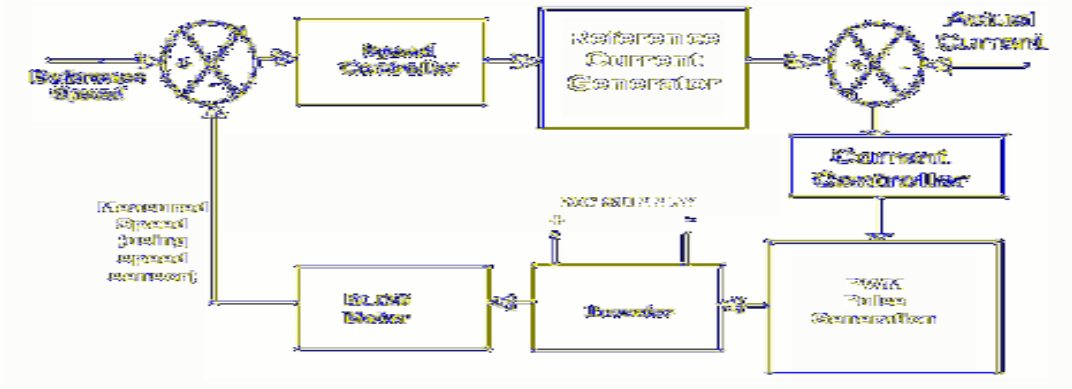


Fig. 1

Conventional Speed Controller- The actual speed of BLDC motor is obtained using the speed/position encoder and is compared with the set value and the error is processed by the Conventional speed controller as shown in Fig.1 to get the reference torque.

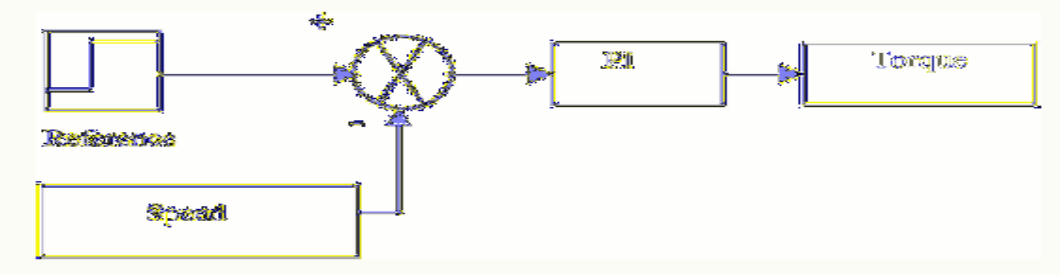


Fig. 2

ANFIS Speed Controller- The ANFIS Controller does not require a mathematical model of the system and it works on a structure prepared from the knowledge base. In ANFIS Speed controller the inputs used are the speed error and rate of change of speed error.

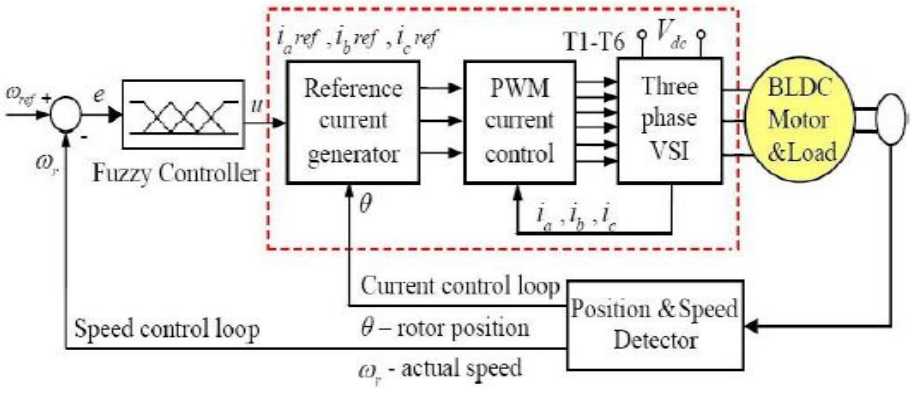


Fig. 3

3. Implementation of Simulation Model in MATLAB/ SIMULINK

According to the mathematical model given above, the complete motor drive is simulated in MATLAB/ SIMULINK environment. A double-loop control scheme is used in this system, where the outer loop is speed loop with PI controller and the inner loop is current loop with hysteresis controller. The entire drive is divided into several functional blocks, which includes BLDCM body block, speed PI controller block, current hysteresis controller block, current reference block, inverter block and commutation logic block. By the logical combination of these blocks, the simulation model of BLDCM drive is implemented.

4. Simulink Model of Speed Control of Brushless DC using Conventional Controllers

4.1 With Conventional Controller

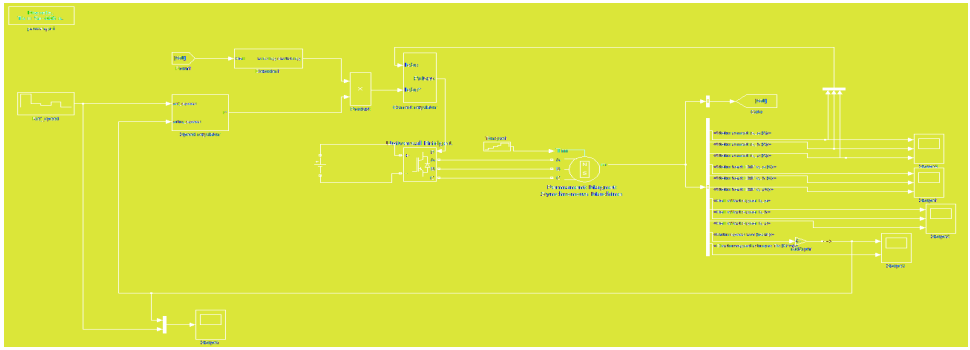


Fig. 4

4.2 With ANFIS Controller

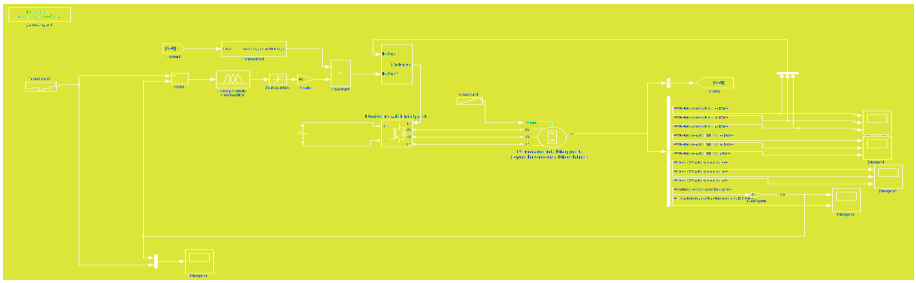
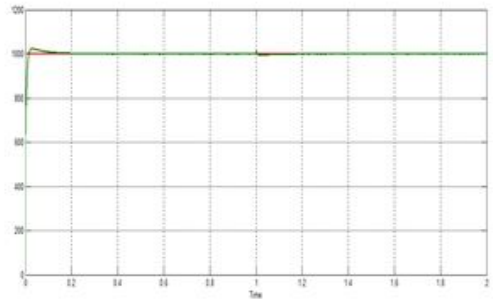


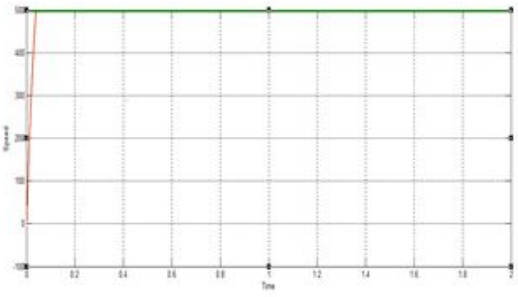
Fig. 5

5. Simulation Results

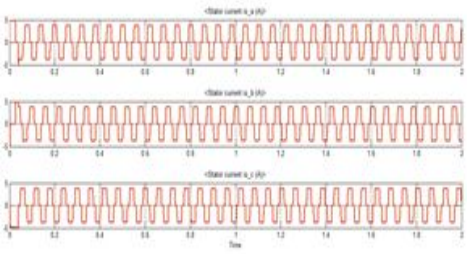
Modeling and simulation of a 3 phase, 4 poles, and 6.2 Nm PMBLDC motor is carried out using MATLABI SIMULINK. The performance characteristics are presented. The purpose of the simulation is to evaluate the performance of the PMBLDC drive system when Conventional speed controller is used and comparing its performance when ANFIS speed controller is used. By using ANFIS controller the speed is improved and current as well as Torque come in admissible value and ripples is also minimized.



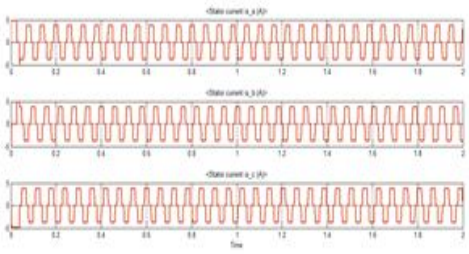
Speed



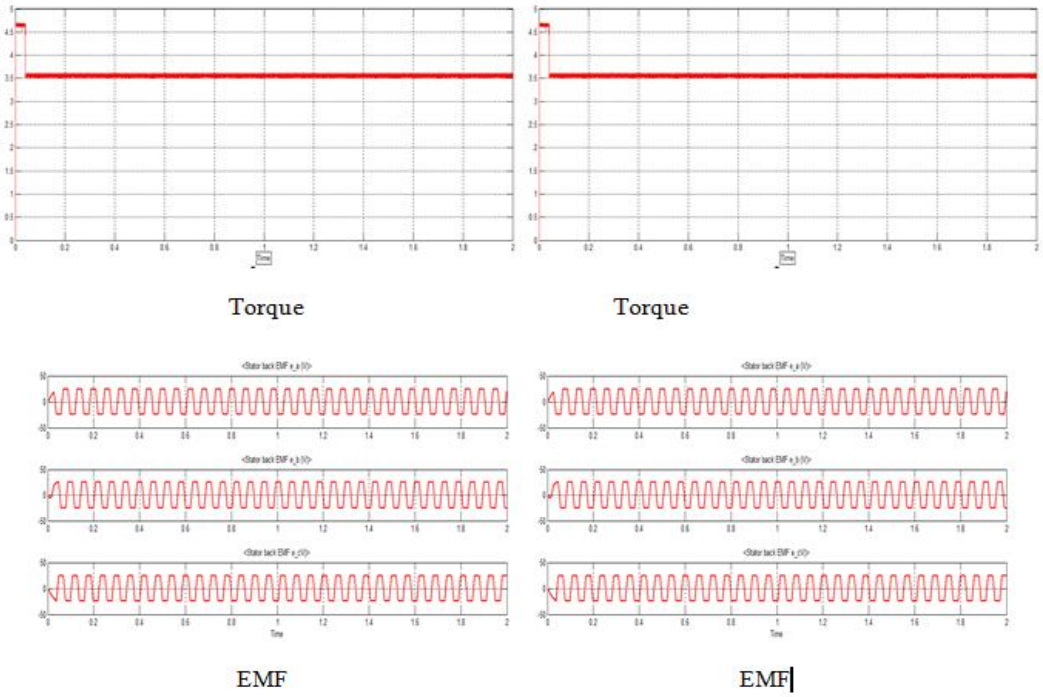
Speed



Current



Current



(a) With Conventional Controller (b) With ANFIS Controller

References

[1] Pragasan Pillay and R. Krishnan,"Modeling Simulation and Analysis of Permanent Magnet Motor Drives, Part II: The Brushless DC Motor Drives", in IEEE Trans. on Industrial Applications, vol. 25, no. 2, pp. 274-279, MarchiApril 1989.

[2] Pragasan Pillay and R. Krishnan,"Modeling of Permanent Magnet Motor Drives", in IEEE Trans. On Industrial Electronics, vol. 35, no. 4, pp. 537-541, November 1988.

[3] R. Krishna, “electric motor drives” (modeling, analysis and control), low price Edition.

[4] A. Halvaei Niasar, A. Vahedi, H. Moghbelli "Speed Control of a Brushless DC Motor Drive via Adaptive Neuro-Fuzzy Controller Based on Emotional Learning Algorithm," International Conference on Electrical Machines and Systems (ICEMS), vol. 3, pp 230-234, 2005.

[5] Chung-Jin Kwon, Woo-Yong Han, Sung-Joong Kim and Chang-Goo Lee "Speed Controller with Adaptive Fuzzy Tuning For BLDC Motor Drive Under Load Variations" at SICE Annual Conference in Fukui, pp 311S-3121,2003.

[6] Chang Liang Xia, *Permanent Magnet Brushless DC Motor Drives and Controls*, Wiley Press, Beijing, 2012

[7] . Moreno, M. E. Ortuzar and J.W. Dixon, "Energy-management system for a hybrid electric vehicle, using ultracapacitors and neural networks," *IEEE Trans. Ind. Electron.*, vol.53, no.2, pp. 614- 623, April 2006.

[8] A. Rubai, A. Ofoli, and M. Castro, dSPACE DSP-Based Rapid Prototyping of Fuzzy PID Controls for High Performance Brushless Servo Drives, *IEEE Industry* Applications Conference, 41st IAS Annual Meeting, page(s):1360–1364, 2006.

International Journal of Electronic and Electrical Engineering.
ISSN 0974-2174, Volume 7, Number 1 (2014), pp. 1-6
© International Research Publication House
http://www.irphouse.com

Performance Analysis of Three Phase Induction Motor Controlled Via Indirect Vector Control Using D Space 1104 R&D Controller Board

Abhishek Choudhary[1], Ashish Chourasia[2] and Vishal Srivastava[3]

[1,2,3]*Electrical Engineering Department, Delhi Technological University, Delhi*

Abstract

Electrical Drives today have become an important part of the modern industry. The motor drivesare used in very wide power range. In various applications where speed and position control is of great significance, the drives are controlled via a power electronic converter, an interface between the input power and the motor. Power consumption of the drive and the harmonics that it injects in the supply plays an important role in the overall performance of the drive. In this paper, a comparison of the power consumed in a 3 HP induction motor drive when controlled via PWM invertor is made with an uncontrolled motor running at same speed under same loading conditions and THD calculations for the both is done.

Keywords: Drives, PWM, harmonics, THD (Total Harmonic Distortion).

1. Introduction

The control and estimation of induction motor [7] drives constitute a vast subject, and the technology has further advanced in recent years. Induction motor drives with cage type machines have been the workhouse in the industry for variable speed application in a wide power range that covers from fractional kilowatts power to multi megawatts. These applications include pumps and fans, paper and textile mills, subway and locomotive propulsions, electric and hybrid vehicles, machine tools and robotics, home appliances, heat pumps and air conditioners, rolling mills, wind generation systems etc. The energy saving aspect of variable frequency drives is getting a lot of attention now days.

The control and estimation of AC drives [7] in general are considerable more complex than those of DC drives, and this complexity increases substantially if high performance are demanded. The main reason of this complexity is need of variable frequency, harmonically optimum convertor power suppliers, the complex dynamics of AC machines, machines parameter variations[8], and difficulties of processing feedback signals in the presence of harmonics.

2. Types of Induction Motor Drives

The induction motor drives are broadly classified in two category i.e. Scalar control and Vector control.

2.1 Scalar control

Scalar control methods are basically simple and less accurate, and only the magnitude of control variable is altered. These methods are basically slow due to coupling effect of flux and torque.

2.2 Vector control or Field Oriented Control

At the present time, the field oriented control (FOC) technique or Vector control has widespread use in high performance induction motor drives. It allows, by means of co-ordinate transformation, to de couple the electromagnetic torque control from the rotor flux, and hence induction motor acts as a DC motor. In this technique, the variables are transformed into a reference frame in which the dynamic variables are like DC quantities. The decoupling control between the flux and torque allows induction motor to achieve fast transient response. Therefore, it is preferably used in high performance motor applications. Field Oriented control uses a vector model of the drive which is valid during transient operational so, which facilitates faster control of the drive.

2.3 Indirect Vector control

There are essentially two general methods of vector control. One, called the direct or feed- back method, was invented by Blaschke [1], and the other, known as the indirect or feed forward method was invented by Hasse [2, 4].The two methods differ in the way the rotor angle is determined. In direct FOC the angle is obtained by the terminal voltages and currents, while as in indirect FOC, the angle is obtained by using rotor position measurement and machine parameter's estimation.

Field orientation has emerged as a powerful tool for controlling ac machines such as inverter-supplied induction motors/synchronous motors. The dynamic performance of such drives is comparable to that of a converter fed four quadrant dc drives. The complex functions required by field oriented control are executed by intelligent controllers using microcontrollers or digital signal processors (DSP), thus greatly reducing the necessary control hardware [3, 6].

An important requirement to obtain good control performance is to make the motor parameters in the field-oriented controller coincide with the actual parameters of the motor. The ability to inject currents into the motor with a current source opened up

new possibilities for parameter determination. It was Takayoshi [4] who described a new identification technique utilizing injected negative sequence components. It is shown that the stator as well as rotor resistance and leakage inductance can be determined on line while the motor is driving the load. The theory is verified with a full-scale hybrid computer simulation of a field-oriented controlled PWM inverter based induction motor drive.

2.4 Direct Vector Control

In direct FOC [5] the rotor angle or control vector is obtained by the terminal voltages & currents directly by using flux estimators. The direct vector control is also known as feedback vector control scheme. Similar to Indirect Vector Control, various controllers have been implemented on direct vector controlled induction motor drives also to improve the performance of the drive.

While the direct method is inherently the most desirable control scheme, it suffers from high cost and the unreliability of the flux measurement. Although the indirect method can approach the performance of the direct measurement scheme, the major weakness of this approach is centered upon the accuracy of the control gains which, in turn, depend heavily on the motor parameters assumed in the feed forward control algorithm.

3. Mathematical equations governing IMFOC

Axis transformation is governed by following set of equations [7]

$$I_{dq0} = TI_{abc} = \frac{2}{3}\begin{bmatrix} Cos\theta & Cos\left(\theta - \frac{2\pi}{3}\right) & Cos\left(\theta + \frac{2\pi}{3}\right) \\ -Sin\theta & -Sin\left(\theta - \frac{2\pi}{3}\right) & -Sin\left(\theta + \frac{2\pi}{3}\right) \\ \frac{1}{2} & \frac{1}{2} & \frac{1}{2} \end{bmatrix}\begin{bmatrix} I_a \\ I_b \\ I_c \end{bmatrix} \quad \text{eq. 1}$$

$$I_{abc} = Te^{-1}I_{dq0} = \frac{2}{3}\begin{bmatrix} Cos\theta & -Sin\theta & 1 \\ Cos\left(\theta - \frac{2\pi}{3}\right) & -Sin\left(\theta - \frac{2\pi}{3}\right) & 1 \\ Cos\left(\theta + \frac{2\pi}{3}\right) & -Sin\left(\theta + \frac{2\pi}{3}\right) & 1 \end{bmatrix}\begin{bmatrix} I_d \\ I_q \\ I_o \end{bmatrix} \quad \text{eq. 2}$$

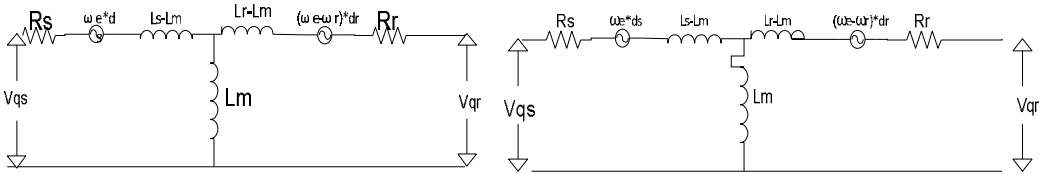


Fig. 1: Circuit diagram of induction motor after axis transformation.

Voltage Equations are $V_{qs} = R_s * i_{qs} + \frac{d\psi_{qs}}{dt} + \omega_e\psi_{ds}$ **eq.** 3

$$V_{ds} = R_s * i_{ds} + \frac{d\psi_{ds}}{dt} + \omega_e \psi_{qs} \quad \text{eq.4}$$

$$V_{qr} = R_r * i_{qr} + \frac{d\psi_{qr}}{dt} + (\omega_e - \omega_r)\psi_{dr} \quad \text{eq.5}$$

$$V_{dr} = R_r * i_{dr} + \frac{d\psi_{dr}}{dt} - (\omega_e - \omega_r)\psi_{qr} \quad \text{eq.6}$$

Flux Equations are

$$\psi_{qs} = L_{ls} * i_{qs} + (i_{qs} + i_{qr})L_m \quad \text{eq.7}$$

$$\psi_{qr} = L_{lr} * i_{qr} + (i_{qs} + i_{qr})L_m \quad \text{eq.8}$$

$$\psi_{ds} = L_{ls} * i_{ds} + (i_{ds} + i_{dr})L_m \quad \text{eq.9}$$

$$\psi_{dr} = L_{lr} * i_{dr} + (i_{ds} + i_{dr})L_m \quad \text{eq.10}$$

4. Simulation & Hardware Implementation

Above schemes are implemented on a 3HP, 415 volt Induction motor drive which is controlled by IMFOC (indirect vector control) [4] using D space R&D controller board.

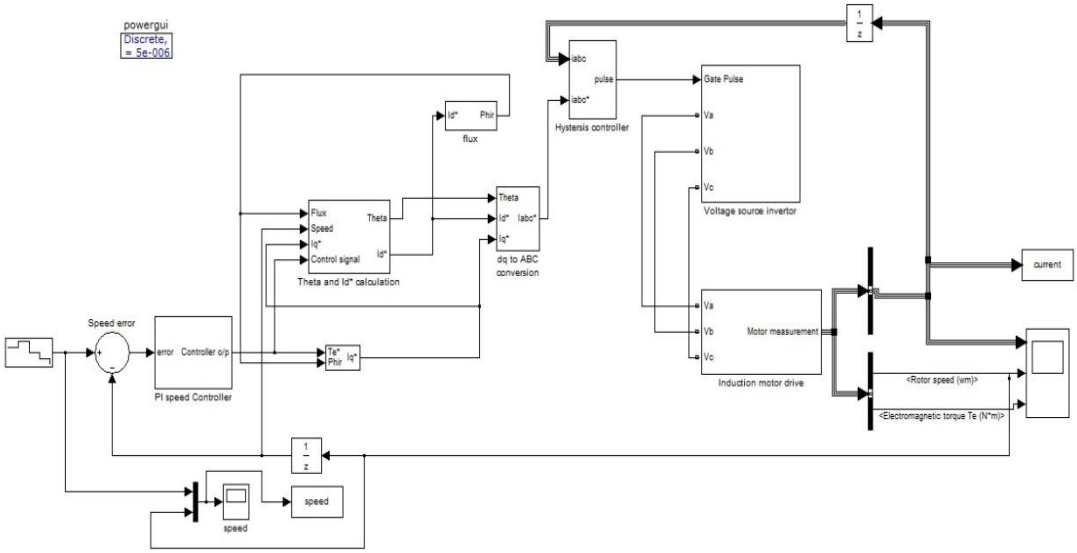


Fig. 2: Simulation model of 3HP, indirect vector controlled drive.

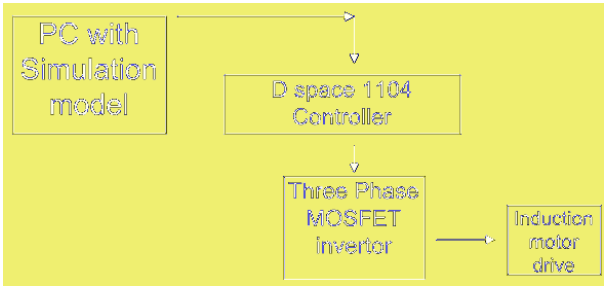


Fig. 3: Block diagram showing layout of Hardware Implementation.

5. Results

The simulation of the indirect vector controlled drive is presented below. The THD content in the current when motor was run with rated load is 34% and when motor was run without load is 9.009%. The higher percentage of THD is acceptable as FOC is variable frequency drive and hence THD calculated at base frequency of 50 Hz would always have a high value. In the Speed Vs. time characteristics, Dotted green line shows reference speed and darkens green line show actual speed of the motor.

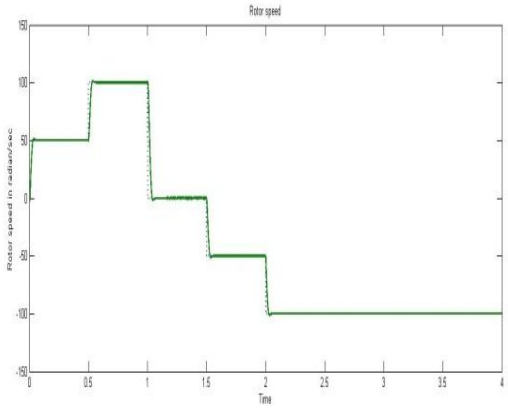


Fig. 2: Variation of Speed

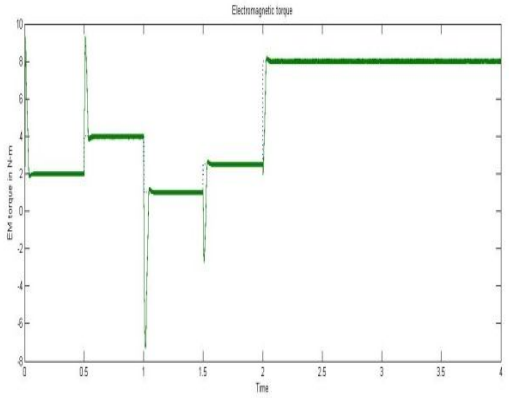


Fig. 3: Variation of Torque.

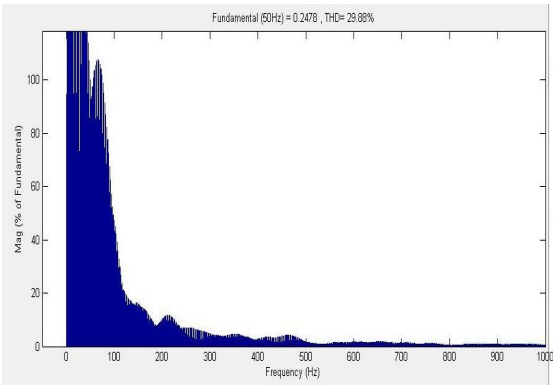


Fig. 4: THD when rated load is applied on motor

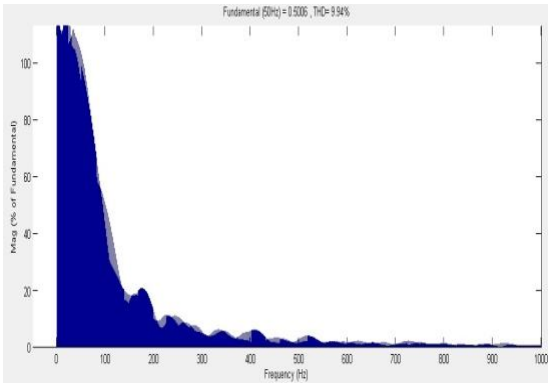


Fig. 5: THD when motor is run at No load.

References

[1] F. Blaschke, "Das VerfahrenDer Feld orientierung Zur Regelung Der Asynchronous machine", Siemens Forschungs-undEntwicklungsberichte1, 1972.

[2] K. Hasse, "Zur dynamik drehzahlgeregelter antriebe mit stromrichtergespeisten asynchrony-kurzschlublaufenn- aschinen", Darmstadt, Techn. Hochsch., Diss., 1969.

[3] Rupprecht Gabriel. Werner Leonhard, and Craig J. Nord by, “Field-Oriented Control of a Standard AC Motor Using Microprocessors”, IEEE Transactions On IndustrialApplicationsVol.IA-16,No.2,March/April1980

[4] Takayoshi Matsuo and Thomas A. Lipo, “A Rotor Parameter Identification Scheme for Vector-Controlled Induction Motor Drives”, IEEE Transactions On IndustryApplications,Vol.IA-21,No.4,May/June1985

[5] David M. Brod, and Donald W. Novotny, “Current Control of VSI-PWM Inverters”, IEEE Transactions On Industry Applications,Vol.IA-21. No. 4, May/June1985

[6] Masato Koyama, Masao Yano, Isao Kamiyama, And Sadanari Yano, “Microprocessor-Based Vector Control System For Induction Motor Drives With Rotor Time Constant Identification Function”, IEEE Transactions on Industry Applications,Vol.Ia-22,No.3,May/June1986.

[7] Bimal. K.Bose–“Modern Power Electronics & AC Drives”, Prentice Hall.

[8] Shoeb Hossien–“Vector Control of Induction Motor using Fuzzy Controller”, Dissertation year 2013, Delhi Technological University, New Delhi.

[9] Bimal K. Bose, Nitin R. Patel, and Kaushik Rajashekara “A Neuro–Fuzzy-Based On-Line Efficiency Optimization Control of a Stator Flux-Oriented Direct Vector-Controlled Induction Motor Drive”, IEEE Transactions On Industrial Electronics, Vol. 44, No. 2, April 1997

[10] S.Williamson, R.C. Healey, “Space Vector Representation Of Advanced Motor Models For Vector Controlled Induction Motors”, IEE Proc-Electr, Power Appl., Vol. 143, No. I, January 1996

Realization of DVCCTA Based Versatile Modulator

Neeta Pandey[1],Rajeshwari Pandey[2], Aseem Sayal[3], Manan Tripathi[4]
[1,2] Dept. of Electronics & Communication Engineering, Delhi Technological University, Delhi, India
[3,4] Dept. of Electrical Engineering, Delhi Technological University, Delhi, India
n66pandey@rediffmail.com, rajeshwaripandey@gmail.com, aseem.sayal@gmail.com, manantripathi1990@gmail.com

Abstract

In this paper, a Differential Voltage Current Conveyor Transconductance Amplifier (DVCCTA) based versatile modulator is proposed which can work as an amplitude modulator, frequency modulator, delta modulator and sigma delta modulator. The modulator operational scheme uses pulse generator as a core and its output is used as carrier signal. A DVCCTA based pulse generator is proposed first and subsequently configured as different modulators. Compact realization is the key feature of the proposed circuit as it uses two DVCCTA, a grounded resistor and a grounded capacitor hence is appropriate for IC realization. The functionality of the proposed circuit is verified through SPICE simulations using TSMC 0.25µm CMOS process model parameters. The performance parameters such as power dissipation and noise for various modulator schemes are also obtained.

Keywords

Differential voltage current conveyor transconductance amplifier (DVCCTA),Amplitude Modulation (AM), Frequency Modulation (FM), Delta Modulation, Sigma Delta Modulation.

1. Introduction

Modulation is a process of modifying some characteristic of a carrier signal according to the instantaneous value of modulating signal and is a fundamental requirement of any communication system. Analog and digital modulations are two representative classes of modulation techniques. Amplitude and frequency modulation fall under analog modulation schemes wherein amplitude and frequency of the carrier signal respectively are varied according to the instantaneous value of the modulating signal while keeping other parameters constant. Delta and sigma delta modulation belong to digital modulation and are widely used in digital communication, digital signal processing and analog to digital converters.

Mobile communication systems and portable electronic equipments demand low-power circuitry to enable longer battery operation. The current-mode (CM) processing has emerged as a promising solution for such circuits as CM circuits are designed for lower voltage swings. Exploiting this virtue of CM processing the researchers have reported a large number of modulator circuits using different CM active building blocks (ABB) such as Current conveyor II (CCII) [1], operational transconductance amplifier (OTA) [2]-[4], current controlled current difference transconductance amplifier (CCCDTA) [5],multiple output current controlled current difference transconductance amplifier (MOCCCDTA)[6] and operational transresistance amplifier (OTRA) [7]. The pulse width of the carrier signal is modulated in accordance with input modulating signal in circuits proposed in [1]-[7]. Sigma delta modulators are the other class of modulators available in literature [4], [8]-[15].These modulators can be classified as designs based on (i) switched capacitor technique [8]-[11] (ii) switched current technique [12] (iii) Loop filter and quantizer method [13]-[15] and (iv) ABB [4]. A detailed comparison of these structures is given in Table 1.It is evident from Table 1 that a large number of modulator circuits are available in literature but only the modulator structure of [4] can provide amplitude, frequency, delta and sigma delta modulated outputs. In this paper, a DVCCTA based versatile modulator is presented which employs two ABBs and two grounded passive elements only as against the three ABBs and three passive elements used in [4].

The paper is organized as follows. Section 2 describes the port relation of DVCCTA and its CMOS based implementation. Operational scheme of the proposed modulator is elaborated in Section 3 wherein a DVCCTA based pulse generator core is described first followed by it's applications as amplitude, frequency, delta and sigma delta modulators. The proposed work is concluded in section 6.

Table 1. Comparison of exiting Modulator topologies.

Ref. No.	Implementation Scheme	Active Element Used	Modulation Type
[1]	Schmitt triggerfollowed byintegrator	CCII, Opamps	PWM
[2]- [3]	Schmitt trigger followed by integrator	OTAs	PWM
[4]	Schmitt trigger followed by integrator	OTAs	AM, FM, delta and Sigma delta
[5]	Schmitt trigger followed by integrator	CCCDTA	PWM
[6]	Schmitt trigger followed by integrator	MOCCCDTA	PWM
[7]	Schmitt trigger followed by integrator	OTRA	PWM
[8]	Switched capacitor	Opamps	Sigma delta
[9]	Comparator based switched capacitors	Dynamic Comparator OTA	Sigma delta
[10]	Class-C inverterSwitched capacitor	Class-C inverter	Sigma delta
[11]	Comparator based switched capacitors	Opamps	Sigma delta
[12]	Switched current CMOS	None	Sigma delta
[13]- [15]	Loop filter+Quantizer	Opamps	Sigma delta
Proposed	Schmitt trigger followed by integrator	DVCCTA	AM, FM, delta and sigma delta

2. DVCCTA

The DVCCTA [16], a relatively new ABB, employs DVCC [17] as input block which is followed by a TA. The circuit symbol of DVCCTA is shown in Fig. 1 and its terminal characteristics in matrix form are given by (1).

$$\begin{bmatrix} I_{Y1} \\ I_{Y2} \\ V_X \\ I_Z \\ I_{O-} \end{bmatrix} = \begin{bmatrix} 0 & 0 & 0 & 0 & 0 \\ 0 & 0 & 0 & 0 & 0 \\ 1 & -1 & 0 & 0 & 0 \\ 0 & 0 & 1 & 0 & 0 \\ 0 & 0 & 0 & -g & 0 \end{bmatrix} \begin{bmatrix} V_{Y1} \\ V_{Y2} \\ I_X \\ V_Z \\ V_{O-} \end{bmatrix} \quad (1)$$

where g is transconductance of the DVCCTA. The CMOS implementation of DVCCTA [16] is given in Fig. 2. It comprises of a DVCC block (Md1–Md12) [16] which is followed by transconductance amplifier (Md13–Md20). The value of transconductance (g) is expressed by (2) which can be adjusted by varying current I_{Bias} thereby making it electronically tunable.

$$g = \sqrt{2\mu C_{ox}(W/L)_{15,16} I_{Bias}} \quad (2)$$

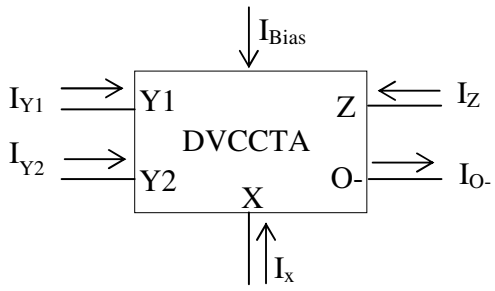


Fig. 1. Symbol of proposed DVCCTA.

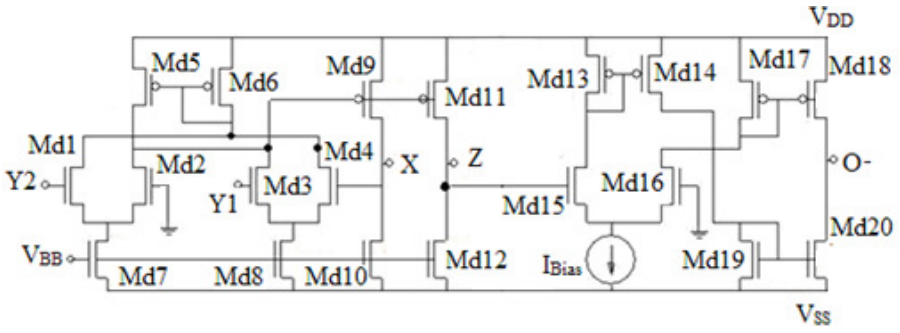


Fig. 2. CMOS Implementation of DVCCTA[16].

3. Modulator Operational Scheme

The modulator operational scheme uses pulse generator as a core and its output is used as carrier signal. The pulse generator can be constructed using the well-known scheme of placing an integrator in a feedback loop with Schmitt trigger [18] as shown in Fig. 3 and has been implemented using DVCCTA in this work. The DVCCTA based realization of pulse generator is depicted in Fig. 4. The first DVCCTA with capacitor *C* forms an integrator whereas the second DVCCTA work as Schmitt trigger with resistor *R*.

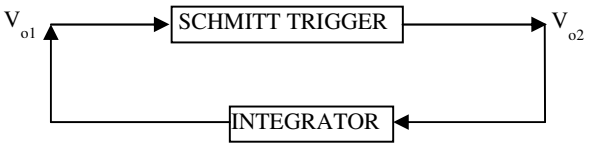


Fig. 3. Pulse generator Scheme [18].

The operation of the circuit is as follows. Both DVCCTA operate in saturation mode irrespective of the bias currents and voltages at the input terminals as their Z ports are left open. The voltage of Z port would approach to V_{DD} or V_{SS} depending upon the current flowing into X (I_{in}) terminal.

$$V_z = \begin{cases} V_{DD} & for\ I_{in} \geq 0 \\ V_{SS} & for\ I_{in} < 0 \end{cases} \tag{3}$$

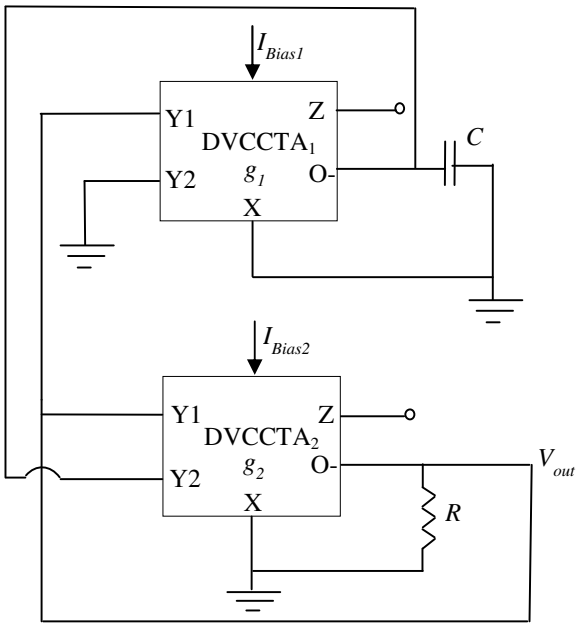


Fig. 4. Proposed DVCCTA based pulse generator.

It may be noted that the amplitude of current would be positive if voltage of Y1 terminal is larger than Y2 terminal voltage. The amplitude of current flowing through O- port would remain constant and equal to bias current (I_{Bias}) and the exact values would be given by (4).

$$I_{O-} = \begin{cases} -I_{Bias} & for\ I_{in} \geq 0 \\ I_{Bias} & for\ I_{in} < 0 \end{cases} \tag{4}$$

The maximum and minimmum output voltages of the schmitt trigger are given by (5).

$$V_{\max} = I_{Bias2} R \tag{5(a)}$$

$$V_{\min} = -I_{Bias2} R \tag{5(b)}$$

The upper and lower threshold values for the schmitt trigger are given by (6).

$$V_{TH} = V_{\max} = I_{Bias2} R \tag{6(a)}$$

$$V_{TL} = V_{\min} = -I_{Bias2} R \tag{6(b)}$$

The frequency of the output signal can be obtained by calculating the charging (to V_{TH}) and discharging (to V_{TL}) time of the capacitor. The time taken by the capacitor to charge to V_{TL} from level V_{TH} is given by (7).

$$t_1 = \frac{C(V_{TH} - V_{TL})}{I_{Bias1}} \tag{7}$$

The time taken by the capacitor to discharge from V_{TH} to V_{TL} is given by (8).

$$t_2 = \frac{C(V_{TL} - V_{TH})}{-I_{Bias1}} \tag{8}$$

The frequency of the output signal is expressed as

$$f = \frac{1}{t_1 + t_2} \tag{9}$$

As V_{TL} and V_{TH} are equal in magnitude, using (6) to (9), the frequency is computed by (10) which can be adjusted electronically via bias currents of DVCCTAs.

$$f = \frac{I_{Bias1}}{4RCI_{Bias2}} \tag{10}$$

In the following subsections, analog (AM and FM) and digital (Delta and Sigma-Delta modulation) modulator circuits based on pulse generator circuit of Fig.4 are presented.

3.1 Amplitude Modulator

In amplitude modulation, the amplitude of the carrier signal is varied according to the instantaneous value of the modulating signal. According to (5), the output amplitude of the pulse generator circuit of Fig. 4 depends on bias current $I_{Bias2.}$ Therefore, the pulse generator circuit can work as amplitude modulator if the bias currents $I_{Bias1}$and I_{Bias2} are taken as sinusoidal modulating signal ($I_m(t)$) superposed on the dc offset signal (I_{offset}). The condition on the amplitude of modulating signal and offset current is given by (11).

$$I_{Bias2} = I_{offset} + I_m(t)\ for\ all\ t \tag{11}$$

Using (5), the maximum and minimum output voltages are expressed by (12)

$$V_{\max} = (I_{offset} + I_m(t))R \quad 12(a)$$

$$V_{\min} = -(I_{offset} + I_m(t))R \quad 12(b)$$

Thus peak to peak output voltage is given by (13).

$$V_{out} = 2(I_{offset} + I_m(t))R \quad (13)$$

The output voltage amplitude is proportional to modulating signal if a sufficiently large offset current is chosen. Since the output frequency is function of ratio of bias currents I_{Bias1}/I_{Bias2} as shown by (10), the output frequency remains unaltered if the ratio of bias currents I_{Bias1} and I_{Bias2} are kept equal. Thus the circuit of Fig. 5 works as an amplitude modulator.

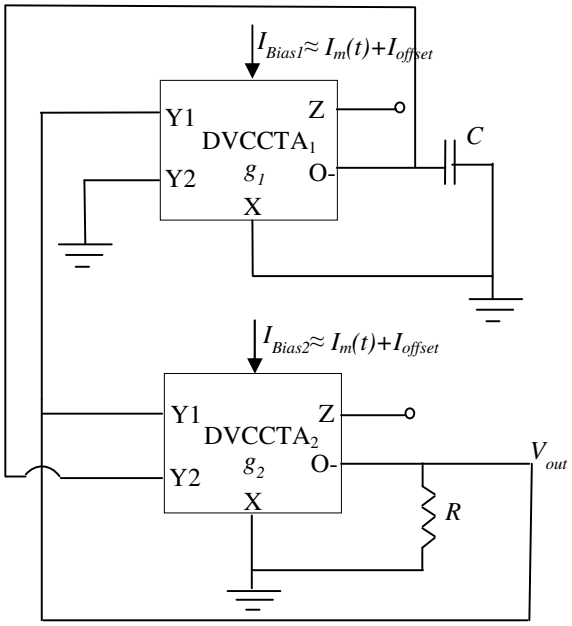


Fig. 5. Proposed AM Modulator.

3.2 Frequency Modulator

In frequency modulation, the frequency of the carrier signal is varied according to the instantaneous value of the modulating signal. According to (10), the frequency of pulse generator is function of ratio of bias currents I_{Bias1}/I_{Bias2}whereas the output amplitude depends solely on bias current $I_{Bias2.}$ Therefore, the pulse generator circuit can work as frequency modulator if a sinusoidal modulating signal ($I_m(t)$) superimposed on the dc offset signal (I_{offset}) is applied as bias currents I_{Bias1} while keeping bias current I_{Bias2} constant. This selection of bias currents causes the output to toggles between $I_{Bias2}R$ and $-I_{Bias2}R$ whose frequency varies with the instantaneous value of the modulating current. Fig. 6 shows the DVCCTA based frequency modulator.

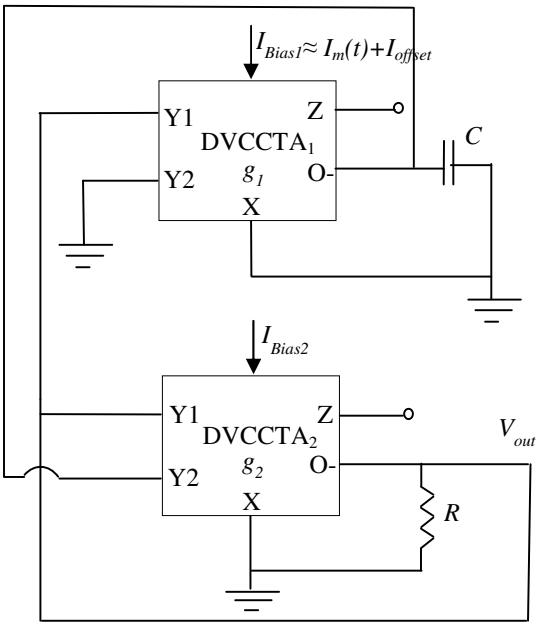


Fig. 6. Proposed FM Modulator.

3.3 Delta Modulator

The pulse code modulation (PCM) is fundamental technique for digital modulation. It, however, has drawback of data redundancy in digitally encoded data. The differential pulse code modulation (DPCM) eliminates this problem by encoding difference between successive samples. Delta modulation is a special case of DPCM where the output is one bit encoded. The schematic of Delta modulation is shown in Fig. 7 wherein the difference of the input and integrated output signal is applied to limiter and sampler. The 1st DVCCTA of Fig. 4 gives integrated output as capacitor voltage. The 2nd DVCCTAprovides functionality of both limiter and sampler as it generates output voltage $I_{Bias2}R$ or $-I_{Bias2}R$ by comparing the output voltage with the capacitor voltage. If the modulatinginput signal is connected to Y1 terminal of 2nd DVCCTA as shown in Fig. 8 then the comparison is performed between modulating and integrated output signals which is desired in delta modulator.

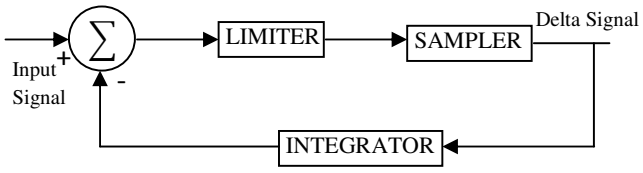


Fig. 7 Delta Modulator Scheme.

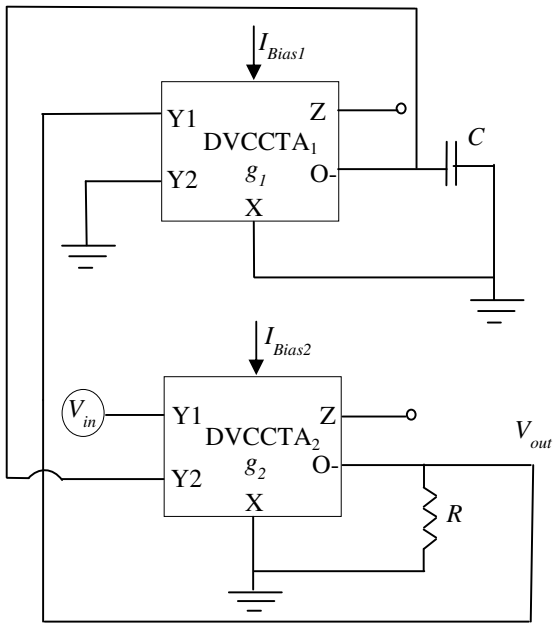


Fig. 8. Proposed Delta Modulator.

3.4 Sigma Delta Modulator

Sigma delta modulation is another scheme, as shown in Fig. 9, which can be considered as smoothed version of delta modulation [19]. The name sigma delta modulator comes from the fact that a sigma which means integrator is put in front of delta modulator. A close observation of the schematic of Fig. 7 and Fig. 9 indicates that the only difference in the implementation scheme of the delta and sigma delta modulator lies in the way input is fed to a limiter and a sampler blocks. The limiter and sampler blocks as shown in Fig. 7 and Fig. 9 can be realized with DVCCTA based pulse generator circuit implemented in Fig. 4.For sigma delta modulation, the difference between output and modulating signal need be integrated. This can be easily achieved by the voltage differencing property of the DVCCTA (building block employed in pulse generator circuit), i.e. by simply connecting modulating signal to Y2 terminal of first DVCCTA block in Fig. 4.The resulting DVCCTA based schematic of sigma delta modulator is shown in Fig. 10.

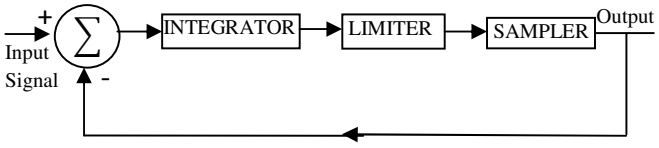


Fig. 9. Sigma Delta Modulator Scheme.

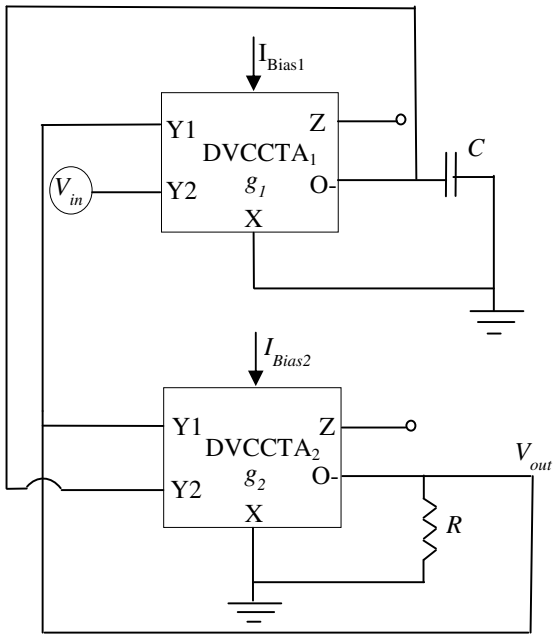


Fig. 10. Proposed Sigma Delta Modulator.

4. Simulation Results

The theoretical propositions have been verified through SPICE simulations using TSMC 0.25µm CMOS process model parameters. The CMOS schematic of Fig. 2 is used for DVCCTA implementation. Aspect ratio used for various transistors is given in Table 2. Supply voltages of V_{DD} = -V_{SS} = 1.25 V and V_{BB} = -0.8V are used and the passive components are chosen as C = 100 pF and R = 4 KΩ. The voltage V_z and current I_{O-} responses of proposed pulse generator are plotted in Figs. 11 and 12 respectively for I_{Bias1} = I_{Bias2} = 20µA. It may be noted that V_z and I_{O-} saturate to supply voltages and bias current respectively thus verifying the theoretical propositions of (3) and (4). The pulse generator output and the voltage across the capacitor are depicted in Fig. 13. The transient responses of the pulse generator by simultaneous variation of I_{Bias1} and I_{Bias2} from 20µA to 50µA in step of 10µA are shown in Figs. 14(a) – (d) respectively. The analytical and simulated pulse generator output amplitude curves with respect to bias currents, for different capacitance values (50pF, 100pF and 200pF) are plotted in Fig. 15. It is observed from Fig.15 that the output amplitude is dependent on bias currents irrespective of capacitance value which is in tune with the proposed theory. It may also be noted that the analytical and simulated responses are in close agreement. The transient responses of the pulse generator, showing frequency variation with I_{Bias1}, have been depicted in Figs. 16 (a) – (d) wherein I_{Bias1} is varied from 10µA to 50µA in step of 10µA keeping I_{Bias2} fixed at 20 µA. Figure17 shows the analytical and simulated frequency versus I_{Bias1} curves, for different capacitor values, depicting the frequency controllability through I_{Bias1}. Both analytical and simulated frequency curves are found to be in synchronization.

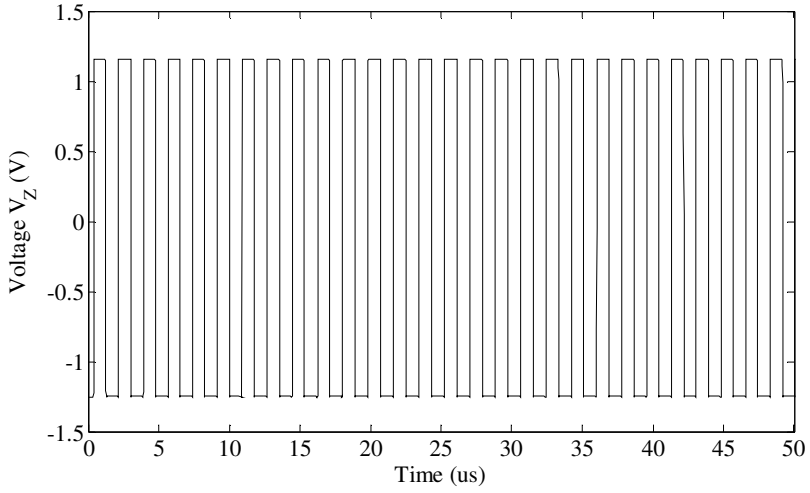


Fig. 11. Voltage V_z of pulse generator.

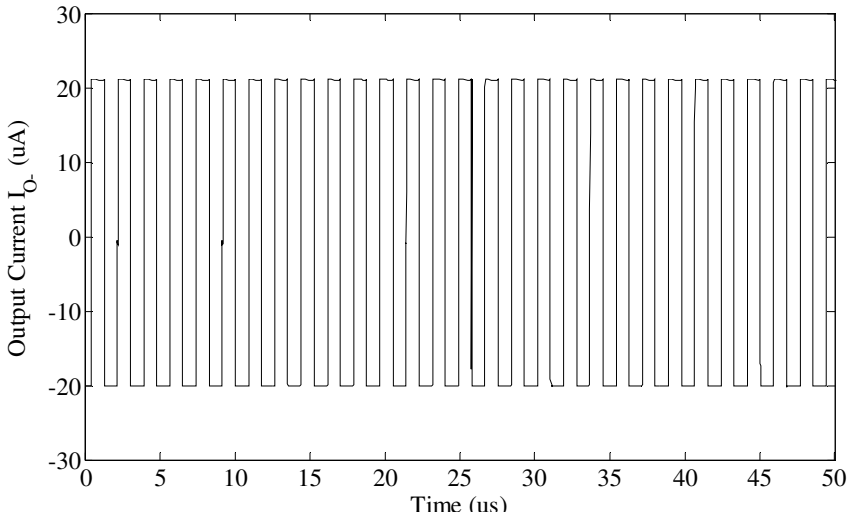


Fig. 12. CurrentI_{O-} of pulse generator.

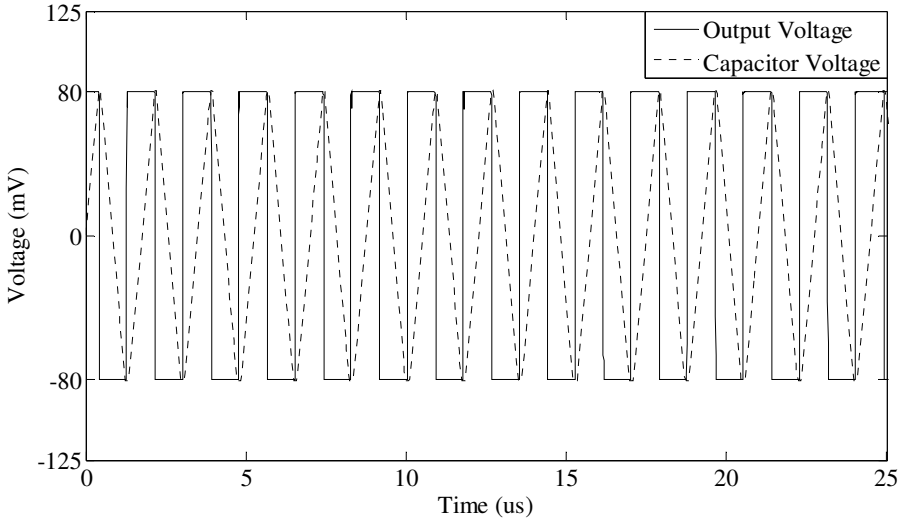


Fig. 13. Output and Capacitor's voltage waveform of pulse generator.

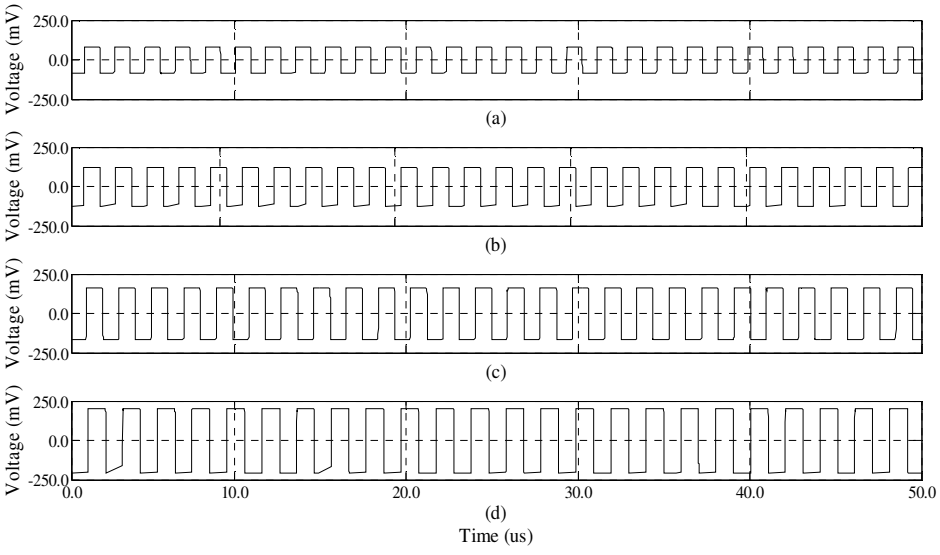


Fig. 14. Output voltage with (a) $I_{Bias1} = I_{Bias2}$ =20μA, (b) $I_{Bias1} = I_{Bias2}$ =30μA, (c) $I_{Bias1} = I_{Bias2}$ = 40μA and (d) $I_{Bias1} = I_{Bias2}$ = 50μA.

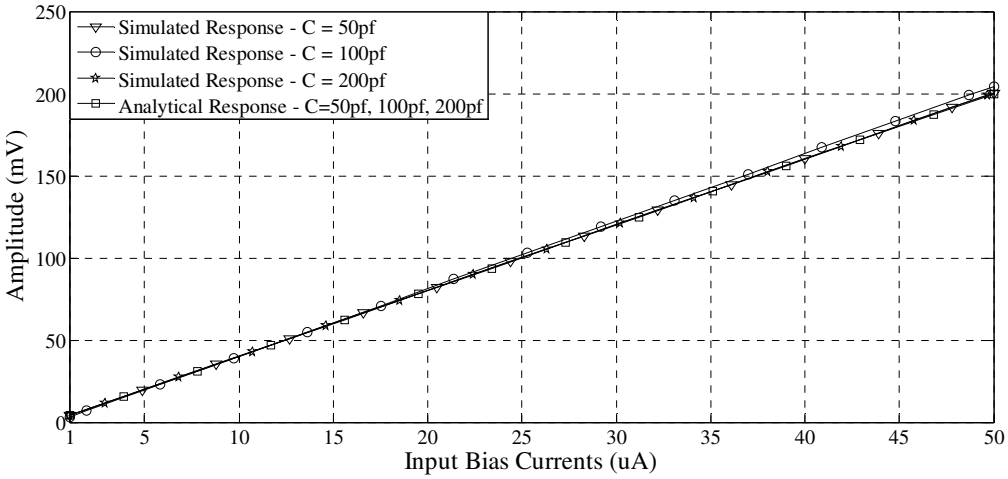


Fig. 15. Amplitude Vs bias current of pulse generator.

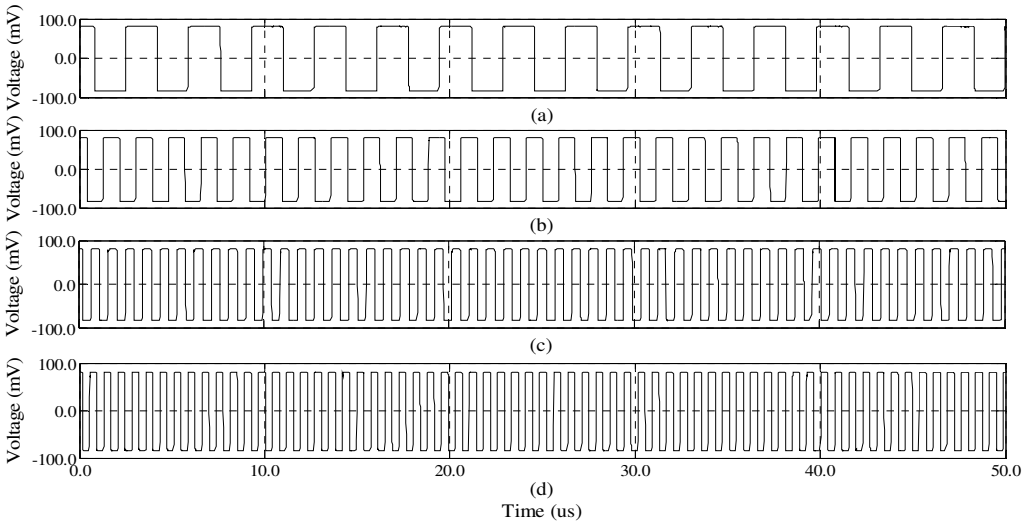


Fig. 16. Output voltage with I_{Bias2} = 20μA and I_{Bias1} = (a) 10μA, (b) 20μA, (c) 40μA and (d) 50μA

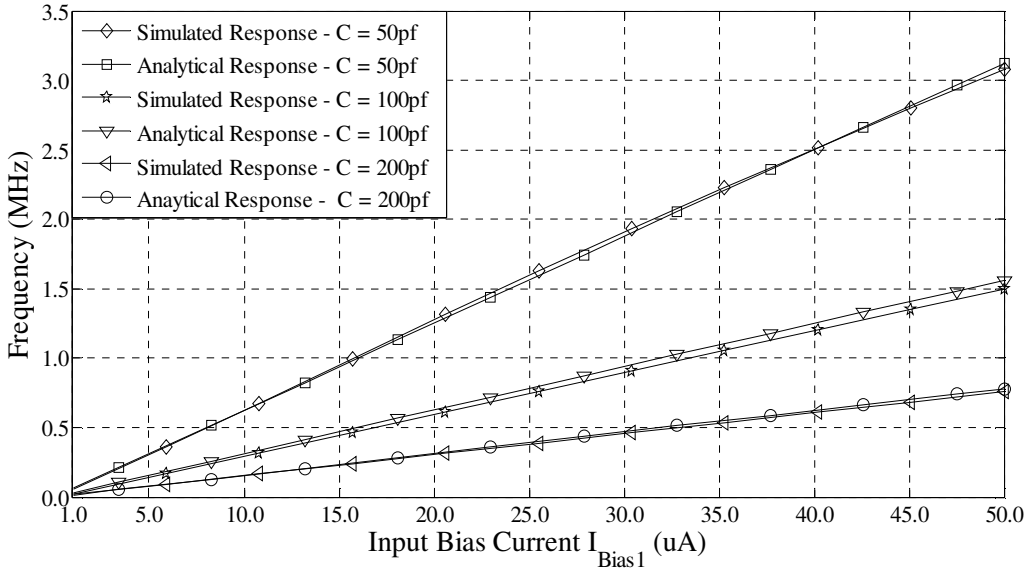


Fig. 17. Frequency Control of pulse generator.

Table 2. Aspect ratio of transistors.

DVCCTA	
MOSFETs	**W(µm)/L(µm)**
Md5,Md6,Md13,Md14,Md17-Md20	5/0.5
Md9,Md11	8.5/0.5
Md1,Md2,Md3,Md4	10/0.5
Md15,Md16	27/0.5
Md7,Md8	27.25/0.5
Md10,Md12	44/0.5

In order to obtain amplitude modulated output a 10µA, 10 KHz sinusoidal modulating signal is superimposed on the bias currents I_{Bias1} and I_{Bias2} keeping DC offset to be 20µA. The modulating current signal and amplitude modulated output voltage are shown in Fig. 18 (a) and (b) respectively. The workability of pulse generator as frequency modulator is verified by applying $I_{Bias1}(t)$ as a 20µA, 10 KHz sinusoidal modulating signal with a DC

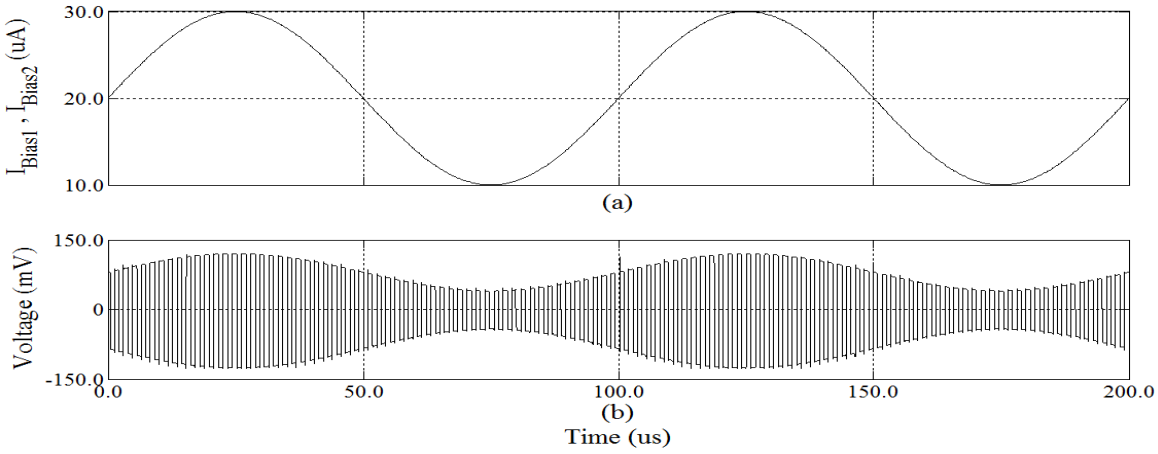


Fig. 18.(a) Modulating signal and (b) Amplitude Modulated signal.

offset of 30µA and keeping I_{Bias2} constant at 20µA. The modulating and the modulated output signals are shown in Fig. 19(a) and (b) respectively. The performance of the delta and sigma delta modulators is verified for two different modulating signals; a triangular and a sinusoidal each one represented as 50 KHz, 150mV signal. The bias currents I_{Bias1} and I_{Bias2} are respectively set as 20µA and 40µA. The outputs of delta modulator for triangular and sinusoidal modulating signals are shown in Figs. 20 and 21 respectively and that for sigma delta modulators are given in Figs. 22 and 23 respectively.

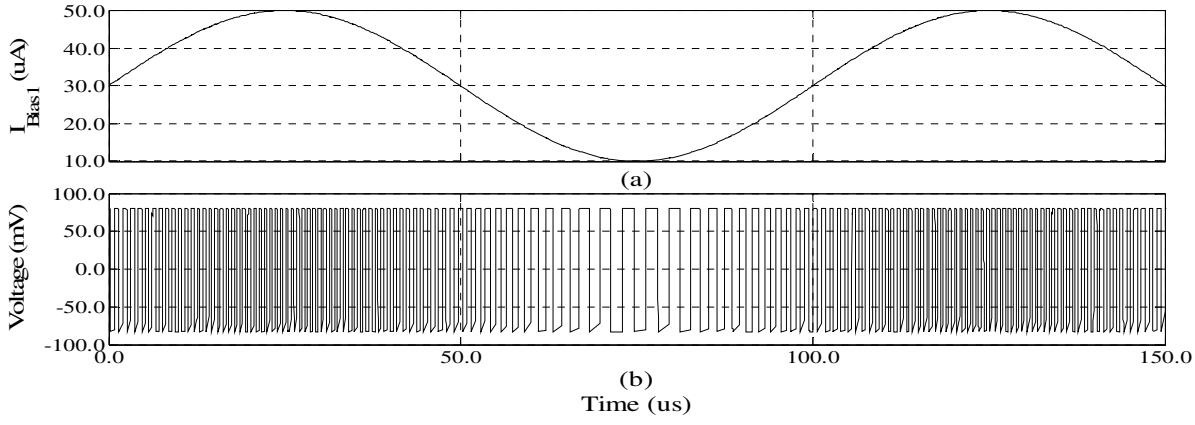


Fig. 19. (a) Modulating signal and (b) Frequency Modulated signal.

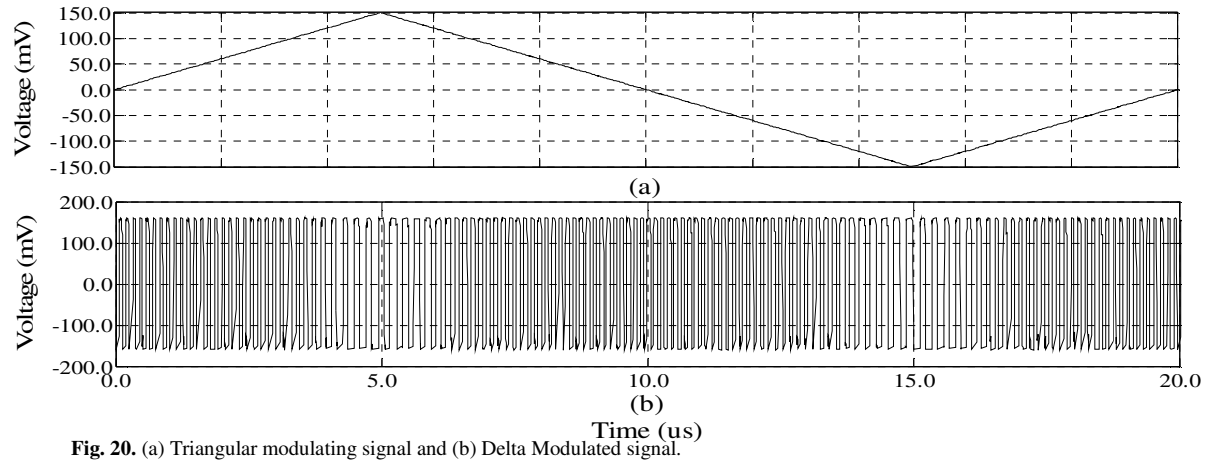


Fig. 20. (a) Triangular modulating signal and (b) Delta Modulated signal.

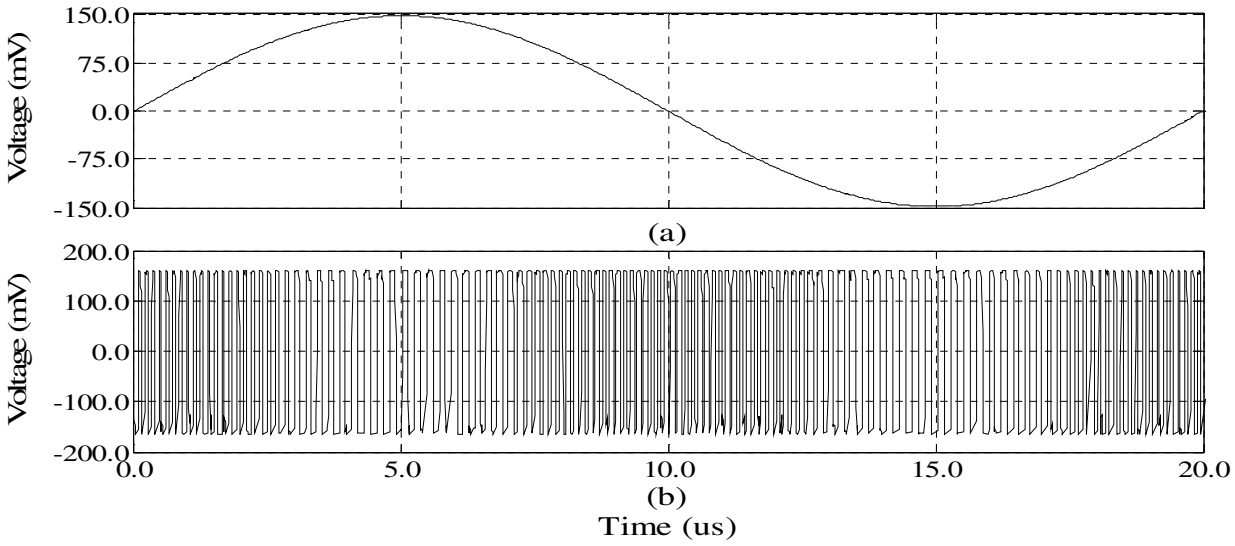


Fig. 21.(a) Sinusoidal modulating signal and (b) Delta Modulated signal.

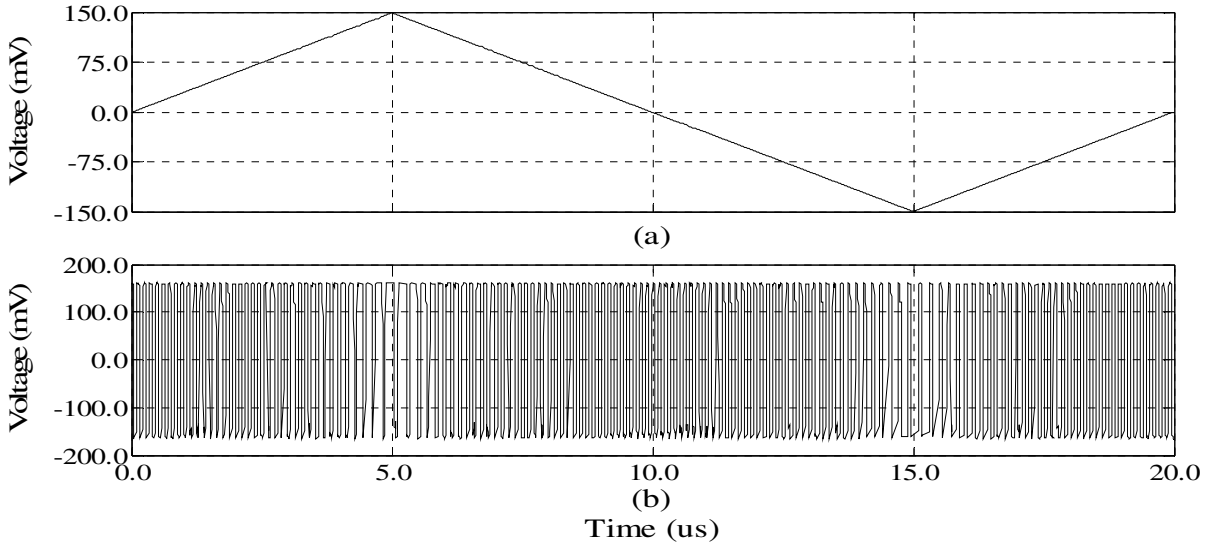


Fig. 22.(a) Triangular modulating signal and (b) Sigma Delta Modulated signal.

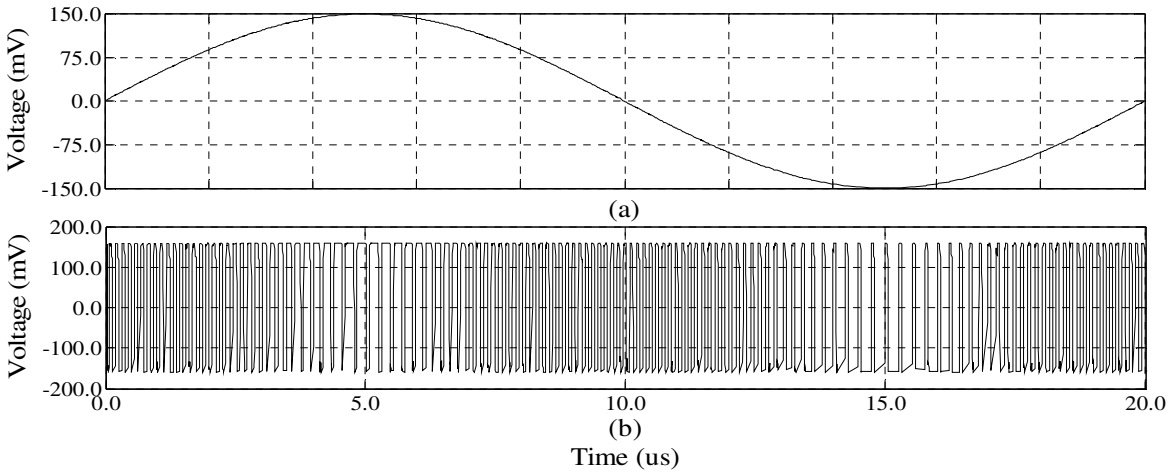


Fig. 23.(a) Sinusoidal modulating signal and (b) Sigma Delta Modulated signal.

5. Performance Evaluation

The performance of proposed DVCCTA based modulator circuits is studied in terms of power dissipation. The overall performance characteristics of DVCCTA based modulators are summarized in Table 3. The performance of proposed DVCCTA based modulator circuits is studied in terms of power dissipation and output noise voltage. The power dissipation of the versatile modulator circuit when I_{Bias1} and $I_{Bias2}$are set to 1μA each is 0.418mW. The minimum cut-off value of the input bias current, $I_{Bias2}$for proper functioning of circuit as an amplitude modulator is 0.5μA. The modulating signal with maximum frequency of 3.84MHz can be applied to FM Modulator when I_{Bias1} is set to 0.01μA. On increasing the magnitude of I_{Bias1}, the frequency of modulating signal can be increased to maximum value of carrier signal frequency.

Table 3. Performance Characteristics of DVCCTA based modulators.

Modulator Type	Power Dissipation (mW)	Output Noise Voltage (nV)
AM Modulator	0.55mW	15.64nV
FM Modulator	0.36mW	4.50nV
Delta Modulator	1.69mW	5.79nV
Sigma Delta Modulator	0.63mW	15.64nV

6. Conclusion

A differential voltage current conveyor transconductance amplifier (DVCCTA) based modulator configuration is presented in this paper. A pulse generator based on DVCCTA has been is proposed and later configured as AM, FM, Delta and Sigma Delta Modulator. The topology uses grounded capacitor and is suitable from integration viewpoint. The simulation results are included to demonstrate the workability of the pulse generator scheme and different modulation schemes. The performance of modulation schemes are studied in terms of power dissipation and noise.

References

[1] Siripruchyanun M, Wardkein P, Sangpisit W., "A simple pulse width modulator using current conveyor", *Proceedings of TENCON IEEE Region 10 Conference*, Kuala Lampur, 2000, 452-57.

[2] Kim H, Kim Hee-Jun, Chung Won-Sup., "Pulsewidth Modulation Circuits Using CMOS OTAs", *IEEE Transactions on circuits and systems*, 2007; 54:1869-78.

[3] Siripruchyanun M, Wardkein P., "A fully independently adjustable, integrable simple current-controlled oscillator and derivative PWM signal generator", *IEICE Transactions Fundamentals*, 2003; E86-A: 3119-26.

[4] Tuwanut P, Koseeyaporn J, Wardkein P, "A novel versatile modulator circuit", *AEU - International Journal of Electronics and Communications*,2009; 63: 387-97.

[5] Siripruchyanun M, JaiklaW, "Current-controlled current differencing transconductance amplifier and applications in continuous-time signal processing circuits", *Analog Integrated Circuits and Signal Processing*, 2009; 61: 247-57.

[6] Silapan P, Siripruchyanun M, "Fully and electronically controllable current-mode Schmitt triggers employing only single MO-CCCDTA and their applications", *Analog Integrated Circuits and Signal Processing*, 2011; 68: 111-28.

[7] Pandey R, Pandey N, Paul SK.,"Voltage Mode Pulse Width Modulator Using Single Operational Transresistance Amplifier", *Journal of Engineering*, 2013, 2013, doi:10.1155/2013/309124.

[8] Bourdopoulos G, Pneumatikakis A, Deliyannis T, "Second order Sigma-Delta modulator realization", *Proceedings of IEEE International Conference on Electronics, Circuits and Systems*, Greece, 1996, 85-8.

[9] Yamamoto K, Carusone AC, "A 1-1-1-1 MASH Delta-Sigma modulator with dynamic comparator- based OTAs", *IEEE Journal of Solid-State Circuits*, 2012; 47: 1866-83.

[10] ChaeY, Kwon M, Han G., "A 0.8-μW switched-capacitor Sigma-Delta modulator using a class-C inverter", *Proceedings of IEEE International Symposium on Circuits and Systems*, Canada, 2004, I-1152-5.

[11] Momeni M, Basinchi PB, Glesner M, "Comparison of Opamp-based and comparator-based Delta-Sigma modulation", *Proceedings of Design Automation and Test*, Munich, 2008,.688-93.

[12] Tan N, Eriksson S, "A fully differential switched-current Delta-Sigma modulator using a single 3.3-V power-supply voltage", *Proceedings of IEEE International International Symposium on Circuits and Systems*, London, 1994, 485 - 88.

[13] Farshidi E.,"A new current-mode Sigma Delta modulator",*International Journal of Electronics and Electrical Engineering*, 2012, 2: 1-9.

[14] Farshidi E, Ahmadpoor N, "A continuous time Sigma Delta modulators using CMOS Current Conveyors", *World Academy Of Science, Engineering and Technology*, 2011; 54: 231-4.

[15] Zanbaghi R, Hanumoluand PK, Fiez TS, "An 80db DR, 7.2 MHz bandwidth single Opampbiquad based ΔΣ modulator dissipating 13.7 mW", *IEEE Journal of Solid-State Circuits*, 2013; 48: 487-501.

[16] Jantakun A, Pisutthipong N, Siripruchyanun M,"A Synthesis of Temperature Insensitive/Electronically Controllable floating simulators based on DV-CCTAs", *Proceedings of International Conference Electrical, Electronics, Computer, Telecommunications, and Information Technology*, Chonburi, 2009. 560-3.

[17] Elwan HO, Soliman AM, "Novel CMOS differential voltage current conveyor and its applications", *IEE Proceedings of Circuits Devices Sysems*, 1997; 144: 195-200.

[18] Sedra A, Smith K, Microelectronic Circuits, *Oxford University Press*, 2004.

[19] Pui-in Mak, Seng-Pan U, Martins RP, "Analog-Baseband architectures and circuits for multistandard and low voltage wireless transceivers", *Springer*, 2007.

International Journal of Advanced Science and Technology
Vol.70 (2014), pp.55-64
http://dx.doi.org/10.14257/ijast.2014.70.06

Reconfigurable Inverted Circular Patch Antenna for Wireless Applications

Preet Kaur[1], S. K. aggarwal[2] and Asok De[3]

[1,2]*YMCA universityElectronics Department, Faridabad, India*
[3]*Director, NIT Patna, Bihar, India*
[1]*preetmoar@gmail.com,*[2] *sa_3264@yahoomail.com,*[3]*asok.de@gmail.com*

Abstract

This paper presents a frequency reconfigurable inverted circular patch antenna with U-slot. The incorporation of U-slot in the circular patch provides a wide impedance bandwidth than conventional patch antenna. By introducing shorts at appropriate position on U-slot and on feed, antenna can be made resonant at two frequency bands (1.80GHz-1.98GHz) and (2.10GHz-2.68GHz) in two modes. The proposed antenna not only avoid the interference problem faced in fixed dual band antenna but at the same time provides a good gain of nearly 8 dB in both mode of operation. The prototype of optimized antenna is fabricated and experimental results are in close agreement with the simulated one. This antenna can be used for different wireless application like Personal Communication System (PCS) and Bluetooth/WLAN.

Keywords: *Aperture coupling, Inverted circular patch antenna, Multiband, Reconfigurable antenna*

1. Introduction

With the growth of wireless industry, the demand for miniaturization in antenna size has gained popularity in recent past. A number of approaches have been proposed by researchers to reduce the size of antenna. One approach that has evolved in the recent past is the usage of multiband antennas. These antennas use multiple frequency bands to support two or more applications (*e.g.,* PCS and WLAN/Bluetooth). Therefore in-place of using individual antenna for each wireless application; one antenna could easily perform the same task. These antennas though effective in terms of cost and has low profile but suffer from serious drawback of interference.

To resolve this issue reconfiguration concept has been proposed in literature as they provide selectivity in frequency, polarization, bandwidth and gain. Hence for different wireless application like PCS (1.85GHz-1.99GHz), WLAN (2.4 GHz-2.483GHz), Bluetooth (2.4 GHz-2.5GHz) need of low profile, low cost and high gain reconfigurable antenna is in demand. Reconfiguration in antenna performance is usually achieved by incorporating pin diode, FET, transistor switches, variable capacitors, varactor diodes or MEMS switches in design of the antenna. A number of papers are available in literature that discusses the usage of reconfiguration concept in dual band antennas for wireless application [8-14] as follows:

An electronically tuneable dual band slot antenna has been proposed in [8-9]. The two resonant frequencies are due to the $\lambda/2$ and λ modes, which impose some complications to obtain similar radiation patterns at both bands. Also, the maximum realized gain at the lower band is 0.6 dBi and the higher band is 2 dBi.

ISSN: 2005-4238 IJAST
Copyright ⓒ 2014 SERSC

In [10], a reconfigurable multiband Planar Inverted-F Antenna (PIFA) for wireless application was presented. This antenna works at 900, 1800, 1900 and 2400 MHz with gain values of -3.9, -1.98, -1.98 and -1.75 dBi respectively.

In [11], a dual-band reconfigurable antenna using varactor and inductor was proposed. This antenna has tuning range from 2100-2900 MHz.

In [12], a coplanar waveguide fed microstrip slot antenna was presented. This antenna operates at two frequency ranges with almost same radiation pattern with maximum gain of nearly 2dB in both the modes of operation. In [13], a frequency reconfigurable square ring slot antenna for operation in GSM and WLAN frequency bands was presented. The gain of antenna was not taken into consideration as one of the performance metric while designing the antenna.

A varactor tuned dual band slot antenna with was proposed in [14].This antenna has similar radiation pattern with low cross-polarization and .5dB and 1.8dB gain in two mode of operation. In [18], areconfigurable fractal antenna for multiband application is presented. It works in four modes and can be used for different wireless applications.

In all of the above proposals the gain that is an essential parameter for antenna is either not considered or not good in all the reconfiguration modes. Therefore this paper presents a high gain frequency reconfigurable inverted circular patch antenna. The Proposed antenna operates at two frequency bands i.e. (1.8GHz-1.98GHz), when switches are on and (2.10GHz-2.68GHz), when switches are off. Both the simulation and experimental results of return loss, gain and radiation pattern are presented.

The rest of the paper is organized as follows. In Section II, design and optimization of antenna is explained. In Section III, frequency reconfiguration procedure, simulation and measured results of the proposed antenna in two modes is presented and discussed. Finally, the paper is concluded in Section IV, followed by references.

2. Antenna Design

The proposed reconfigurable inverted circular patch antenna consists of two substrate layer separated by air gap. The substrate material used is low cost Arlon 25N with Relative permittivity (ε_r) = 3.38, Thickness (h) =1.52mm and loss tangent (δ) =0.0025. The upper layer consists of a circular patch of Radius (a) = 28mm with U-shape slot as shown in Figure 1. Lower layer consists of Microstrip line which is used to feed the antenna using aperture coupling as shown in Figure 2 and Figure 3.

Circular patch radius is first calculated mathematically [1-2] for resonant frequency (f_r) =1.6 GHz as given below.

$$f_r = \frac{8.794}{a_e\sqrt{\varepsilon_r}}$$

$$a_e = a\left[1 + \frac{2h}{\pi\varepsilon_r a}\left\{ln\left(\frac{a}{2h}\right) + (1.41\varepsilon_r + 1.77) + \frac{h}{a}(.268\varepsilon_r + 1.65)\right\}\right]^{1/2}$$

$a_e$is the effective radius and
$a$is physical radius of circular patch.

Due to fringing fields [2] at the periphery of the patch conductor, a circular patch with physical radius a has an effective radius a_e such that $a_e > a$. Circular patch antenna having the aperture coupling is designed in Zealand IE3D software.

 Copyright ⓒ 2014 SERSC

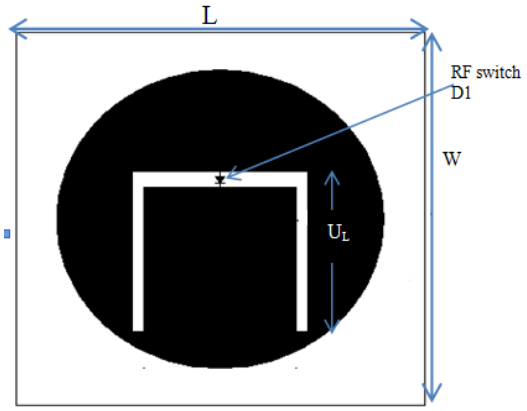


Figure 1. Bottom Surface of Top Layer of Antenna

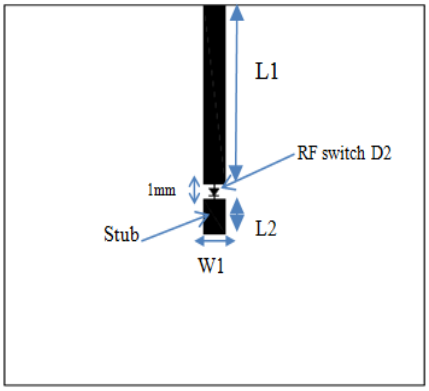


Figure 2. Bottom Surface of Bottom Layer of Antenna

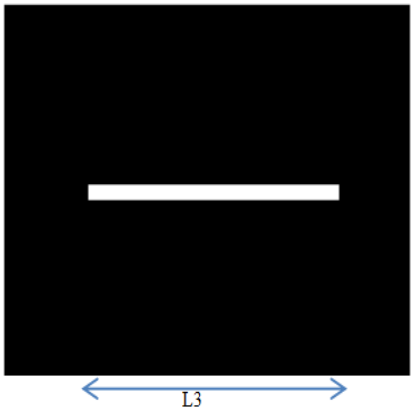


Figure 3. Top Surface of Bottom Layer of Antenna

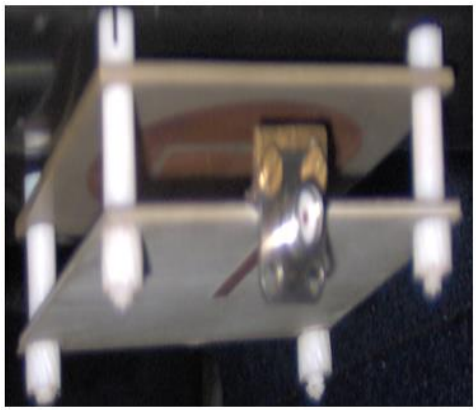


Figure 4. Photograph of Fabricated Antenna

By using thick air substrate and with proper slot loading good impedance bandwidth and high gain can be achieved [6] [15].Air gap introduced between two layer of antenna has an effect of lowering the effective permittivity of patch antenna, thus resonant frequency get shifted to upper side and impedance bandwidth gets improved. U-slot is etched in circular patch antenna to further increase the bandwidth [16-17]. Air gap between two layers, position, length and width of U-slot is optimized using IE3D software so that antenna resonates nearly at 2.4GHz with wide impedance bandwidth and good gain.

Two switches are used to make the antenna reconfigurable as shown in Figure 1 and Figure 2. The critical design parameter of the inverted circular patch antenna is shown in Table 1. The optimized antenna prototype is built as shown in Figure 4.

Copyright ⓒ 2014 SERSC

Table 1. Critical Antenna Design Parameters

Antenna Parameter	Dimension(mm)	Antenna Parameter	Dimension(mm)
Radius of circular patch	28	L1	40.2
L	70	L2	1.8
W	70	L3	42.1
Air gap between two layers	10	W1	3.616
Length of U-slot($U_{L)}$	30	Width of U-slot	2

3. Results and Discussion

The antenna is simulated and analyzed using Zealand IE3d software. This proposed antenna works in two modes, U-slot mode and L-slot mode. Relationship between the operation modes and the states of switches is shown in Table 2.

Table 2. Relationship between Various Modes and Switch Positions

Mode	Switch Position
U-slot Mode	D1=off , D2=off
L-slot Mode	D1=on , D2=on

For modeling of RF switch, a common way is that when switch is on, it is represented by metal tape ($1\times1mm^2$) and when switch is off, no metal tape is used. In simulation and measurement this modeling is used to get the results.

U-slot Mode: - In this mode diode D1 and D2 are in off position. Simulated and measured return loss of antenna is shown in Figure 5. The experimental return loss of fabricated antenna is taken using HP8720B network analyzer. Simulated and measured gain of antenna is shown in Figure 6. Gain and radiation pattern of fabricated antenna is measured in anechoic chamber. A calibrated horn antenna is used to measure the gain of this antenna. Simulated radiation pattern of antenna in U-slot mode at 2.05 GHz and 2.5 GHz is shown in Figure 7 and Figure 8 respectively. Measured radiation pattern is shown in Figure 9 and Figure 10. Following points can be concluded for this mode.

- The proposed antenna resonates at 2.3 GHz in this mode and covers the frequency band of 2.10 GHz-2.68 GHz as shown in Figure 5.
- The circular patch has U-slot which provides the wide impedance bandwidth of 24.2%.
- From Figure 5, it clear that measured return loss is in good agreement with simulated one.
- Simulated and Measured gain of antenna in U-slot mode is approximately 8dB.

 Copyright ⓒ 2014 SERSC

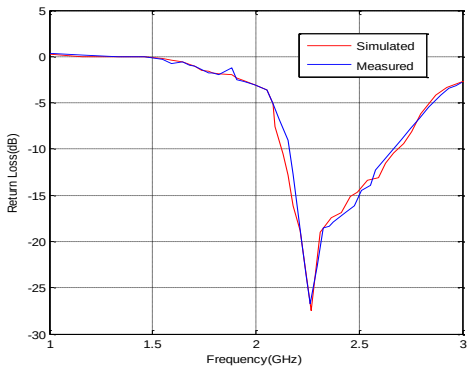


Figure 5. Return Loss of U-slot Mode

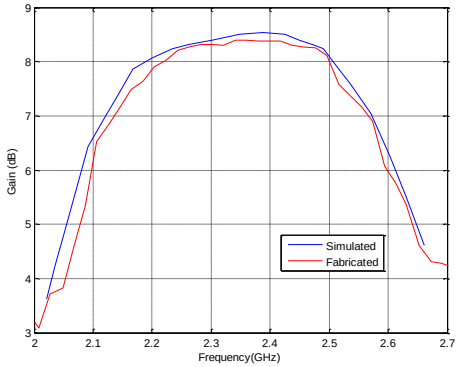


Figure 6. Gain of U-slot Mode

- Due aperture coupling back lobe appears in radiation pattern, but it is 16-20dB down to the main lobe.
- Experimental results in Figure 9 and Figure 10 shows more back lobe level in comparison to simulated results due to finite ground plane effect and losses.

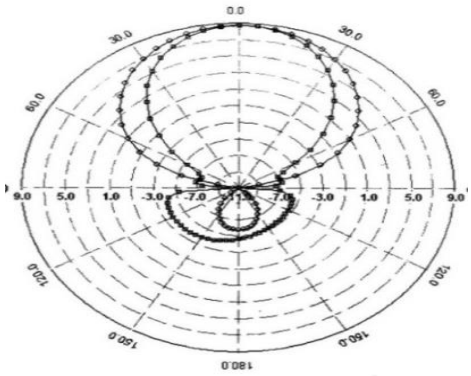


Figure 7. Simulated Radiation Pattern of U-slot Mode at 2.05 GHz for φ = 0^0 and φ = 90^0

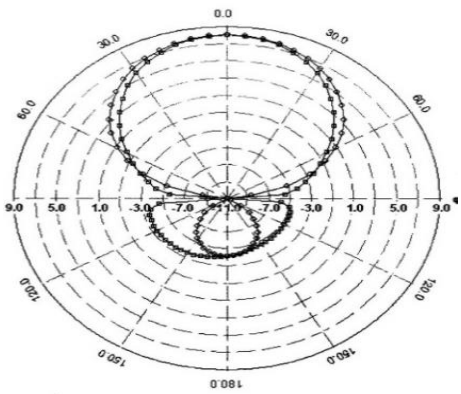


Figure 8. Simulated Radiation Pattern of U-Slot Mode at 2.5 GHzfor φ = 0^0 and φ = 90^0

Copyright ⓒ 2014 SERSC

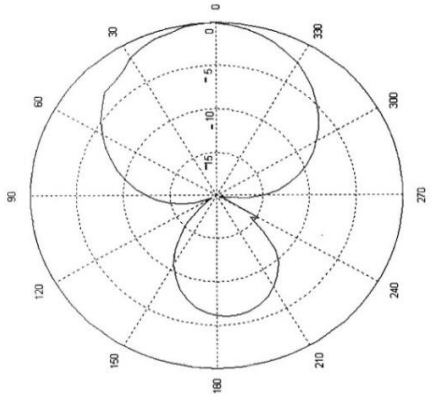


Figure 9. Measured Radiation Pattern of U-Slot Mode at 2.05GHzfor φ = 0^0

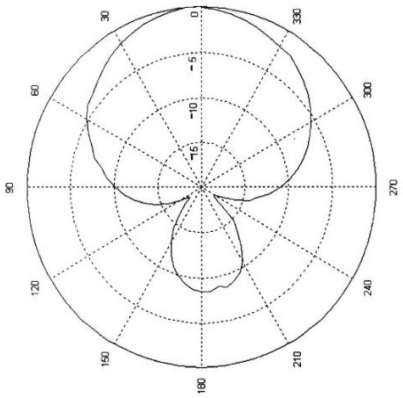


Figure 10. Measured Radiation Pattern of U-Slot Mode at 2.5 GHz for φ = 0^0

L-SLOT MODE: -When both the switch D1 and D2 are in on position, antenna works in L-slot mode. Simulation is done by leaving a copper gap of 1mm at the middle of U-slot. Current flow through this copper gap at the center of U-slot and it seems that circular patch antenna has two L-slot. Due to change in current distribution resonant frequency gets changed. For proper matching in L-slot mode length of microstrip line is changed using diode D2.

Simulated and experimental return loss of antenna is shown in Figure 11. For testing a copper strip of $1 \times 1mm^2$ is connected at center of u-slot to convert it into L-slot and copper strip of $1 \times 1mm^2$ is also connected to feed to connect it to the stub. Gain of antenna is shown in Figure 12. Simulated and measured radiation pattern of antenna in L-slot mode is shown in Figure 13 and Figure 14 respectively. Following points can be concluded for this mode.

- In this mode antenna resonates at frequency of 1.88 GHz and covers the frequency band of 1.80 GHz-1.98GHz.
- Measured return loss as shown in Figure 11 is in close agreement with simulated one.
- In L-slot mode antenna has impedance bandwidth of 9.5%.
- At resonant frequency antenna has gain of 7.8dB as shown in Figure 12.

 Copyright ⓒ 2014 SERSC

- Back lobe appears in radiation pattern due to aperture coupling, but it is 16-20dB down to the main lobe. In Experimental results back lobe level is more as compared to simulated results due to finite ground plane effect.

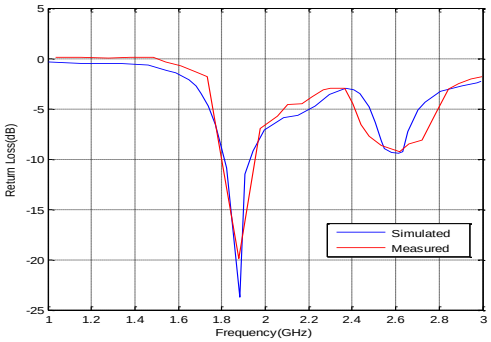


Figure 11. Return Loss of Antenna in L-Slot Mode

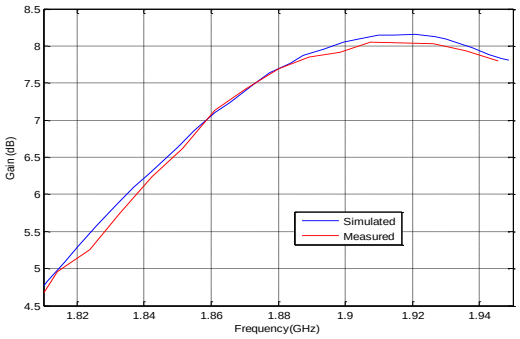


Figure 12. Gain of Antenna in L-Slot Mode

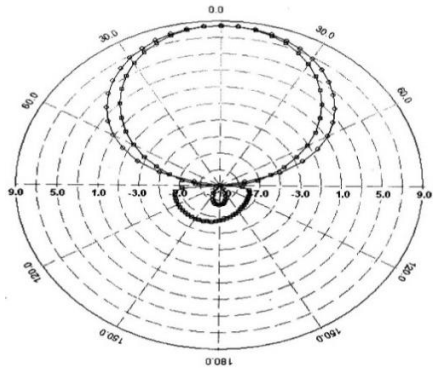


Figure 13. Simulated Radiation Pattern of Antenna in L-Slot Mode at 1.88 GHzφ = 0^0 & φ = 90^0

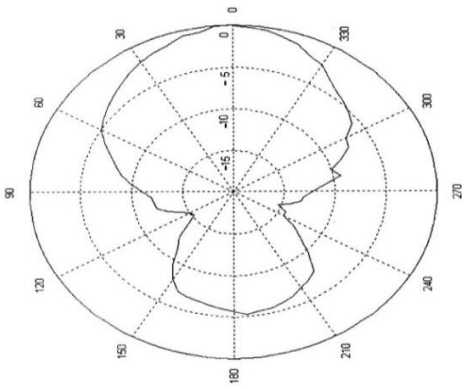


Figure 14. Measured Radiation Pattern of Antenna in L-Slot Mode at 1.88 GHz for φ = 0^0

Copyright ⓒ 2014 SERSC

Radiation pattern and gain of antenna in both the modes are approximately same, only frequency bands changes as antennas switches from one mode to another, which is desired characteristic of reconfigurable antenna.

4. Conclusion

A high gain frequency reconfigurable inverted circular patch antenna fed by microstrip line using aperture coupling is presented. Frequency reconfiguration is achieved by changing the current distribution in circular patch. Antenna operates in two modes and cover the frequency bands (1.80GHz-1.98GHz) and (2.10GHz-2.68GHz). The proposed antenna has a good gain of approximately 8 dB in both the modes and covers a wide impedance bandwidth of 24.2% in U-slot mode and 9.5% in L-slot mode. Back lobe appears in radiation pattern of antenna due to aperture coupling which can be further reduced by using a reflector. In U-slot mode antenna can be used for Bluetooth and WLAN application and in L-slot mode it can be used for PCS application.

References

[1] C. A. Balanis, "Antenna Theory: Analysis and Design", New York: Wiley, **(1997)**.
[2] R. Garg, P. Bhartia, I. Bahl and A. Ittipiboon, "Micro strip antenna design handbook", Artech House Inc., **(2001)**.
[3] J. Anguera, E. Martínez, C. Puente, C. Borja and J. Soler, "Broadband Dual-Frequency Microstrip Patch Antenna With Modified Sierpinski Fractal Geometry", IEEE Transactions on Antennas and Propagation, vol. 52, no. 1, **(2004),** pp. 66-73.
[4] S. Maci and G. B. Gentili, "Dual-frequency patch antennas", IEEE Antennas and Propagation Magazine, vol. 39, no. 6, **(1997),** pp. 13-20.
[5] S. Maci, B. B. Gentili, P. Piazzesi and C. Salvador, "Dual band slot loaded patch antenna," IEEE Antennas and Propagation Magazine, vol. 39, no. 6, **(1997),** pp. 13-20.
[6] D. D. Krishna, M. Gopikrishna, C. K. Aanandan, P. Mohanan and K. Vasudevan, "Design of a compact dual band slot loaded circular microstrip antenna with a superstrate", Progress in Electromagnetics Research, vol. 83, **(2008),** pp. 245-255.
[7] D. Llorens, P. Otero and C. C. Penalosa, "Dual-band, single CPW port, planar slot antenna," IEEE International Antennas and Propagation Symposium Digest, **(2003)**, pp. 137–139.
[8] N. Behdad and K. Sarabandi, "A varactor tuned dual-band slot antenna," IEEE Transaction on Antennas and propagation, vol. 54, no. 1, **(2006)** pp. 401–408.
[9] N. Behdad and K. Sarabandi, "Dual-Band Reconfigurable Antenna With a Very Wide Tunability Range," IEEE Transaction on Antennas and Propagation, vol. 54, no. 2, **(2006),** pp. 406–419.
[10] Y. K. Park and Y. Sung, "A reconfigurable antenna for quad-band mobile handset applications", IEEE Transactions on Antennas and Propagation, vol. 60, no. 6, **(2012),** pp. 3003-3006.
[11] C. T. P. Song, Z. H. Hu, J. Kelly and P. Gardner, "Wide tuneable dual-band reconfigurable antenna for future wireless devices", Loughborough Antenna and Propagation Conference, UK, **(2009)** September 16-17, pp. 601-604.
[12] L. Xiaowu, Z. Min, C. Linji and Y. Feiqun, "Design of a on board dual frequency reconfigurable antenna", 6th IEEE International Conference on ITS Telecommunications Proceedings, **(2006)**, pp. 394-396.
[13] Preetkaur, "A reconfigurable square ring slot antenna for operation in GSM and WLAN frequency bands", International Journal of Microwave and Optical technology, vol. 7, no. 1, **(2012)** pp. 49-54.
[14] N. Behdad and K. Sarabandhi, "A varactor tuned dual band slot antenna", IEEE Transactions on Antennas and Propagation, vol. 54, no. 2, **(2006),** pp. 401-407.
[15] W. H. Hsu and K. L. Wong, "A wideband circular patch antenna", Microwave and Optical Technology Letters, vol. 25, **(2008),** pp. 327- 328.
[16] K. L. Wong and H. C. Tung, "A compact patch antenna with an inverted U-shaped radiating patch," IEEE Antennas Propagation Society International Symposium Digest, **(2001)**, pp. 728–731.
[17] S.–L. S. Yang, A. A. Kishk and K.-F. Lee, "Frequency reconfigurable U-slot microstrip patch antenna", IEEE antennas and wireless propagation letters, vol. 7, **(2008),** pp. 127-129.
[18] P. Kaur, A. De, S. K. Aggarwal, "Design of A Novel Reconfigurable Fractal Antenna for Multi-Band Application", International Journal of Advanced Science and Technology, vol. 62, **(2014),** pp. 103-112.

 Copyright ⓒ 2014 SERSC

Authors

Preet Kaur is B. tech (Electronics & communication Engr.) from DCRUST, Murthal and M. tech (RF& Microwave Engr.) from IIT Roorkee and currently pursuing her Ph. D from YMCA University of Science and Technology, Faridabad. Her academic interests include metamaterials, antenna design and electromagnetic wave theory. She is working as Assistant professor (Electronics Engr.) with YMCA University, Faridabad since 2008.

Dr.S.K.Aggarwal is B. tech (Electrical Engr.) from NIT, Calicut (Kerala) and M. tech from Delhi College of Engineering and Ph. D from JamiaMillaIslamiya University, Delhi. He is currently the Professor and Chairman of electronics department with YMCA University of Science and Technology.

Dr. Asok Dereceived the B.E and M.E degree from Jadavpuruniversity, Kolkata and Ph.D. degrees from IIT Kharagpur in 1986.He is currently the Director of National Institute of Technology, Patna (Bihar). His research interest includes microwave Engr., metamaterials, EM-wave propagation, and antenna miniaturization.

Copyright ⓒ 2014 SERSC

Copyright ⓒ 2014 SERSC

Accepted Manuscript



Red light emitting $BaNb_2O_6$: Eu^{3+} phosphor for solid state lighting applications

Amit K. Vishwakarma, Kaushal Jha, M. Jayasimhadri, A.S. Rao, Kiwan Jang, B. Sivaiah, D. Haranath

PII: S0925-8388(14)02426-8
DOI: http://dx.doi.org/10.1016/j.jallcom.2014.10.016
Reference: JALCOM 32361

To appear in: *Journal of Alloys and Compounds*

Received Date: 19 August 2014
Revised Date: 27 September 2014
Accepted Date: 2 October 2014

Please cite this article as: A.K. Vishwakarma, K. Jha, M. Jayasimhadri, A.S. Rao, K. Jang, B. Sivaiah, D. Haranath, Red light emitting $BaNb_2O_6$: Eu^{3+} phosphor for solid state lighting applications, *Journal of Alloys and Compounds* (2014), doi: http://dx.doi.org/10.1016/j.jallcom.2014.10.016

This is a PDF file of an unedited manuscript that has been accepted for publication. As a service to our customers we are providing this early version of the manuscript. The manuscript will undergo copyediting, typesetting, and review of the resulting proof before it is published in its final form. Please note that during the production process errors may be discovered which could affect the content, and all legal disclaimers that apply to the journal pertain.

ACCEPTED MANUSCRIPT

Red light emitting $BaNb_2O_6$: Eu^{3+} phosphor for solid state lighting applications

Amit K. Vishwakarma[1], Kaushal Jha[1], M. Jayasimhadri[1,*], A.S. Rao[1], Kiwan Jang[2], B. Sivaiah[1,3], D. Haranath[3]

[1]*Luminescent Materials Research Lab, Department of Applied Physics, Delhi Technological University, Delhi 110 042, India*

[2]*Department of Physics, Changwon National University, Changwon 641-773, Republic of Korea*

[3]*CSIR-National Physical Laboratory, Dr. K.S. Krishnan Road, New Delhi 110 012, India*

Abstract:

Europium doped barium niobate (Eu^{3+}:$BaNb_2O_6$) phosphors were successfully synthesized by conventional solid state reaction method. Thermogravimetric analysis-differential scanning calorimetry (TGA-DSC), x-ray diffraction (XRD) and scanning electron microscopy (SEM) characterization techniques have been used to disclose thermal, structural and morphological properties of the synthesized phosphors. X-ray diffraction pattern for the synthesized phosphor calcined at 1200 ^oC confirms the formation of pure orthorhombic phase for $BaNb_2O_6$. In addition to the above mentioned characterizations, photoluminescence properties were also investigated for the $BaNb_2O_6$ phosphor under near-UV/blue excitations. Intense red emission observed at 611 nm due to $^5D_0 \rightarrow {}^7F_2$ transitions of Eu^{3+} under the excitations of both 394 nm ($^7F_0 \rightarrow {}^5L_6$) and 466 nm ($^7F_0 \rightarrow {}^5D_2$). The CIE chromaticity coordinates evaluated from the emission spectra are falling in the pure red region of the CIE 1931 diagram, which are very much close to the commercial red phosphor (Y_2O_2S :Eu^{3+}). The above results indicate that Eu^{3+} doped $BaNb_2O_6$ phosphors may be potential candidates to use in white LEDs in which tricolor (red/green/blue) phosphors are excited by near ultraviolet light.

****Corresponding author:*** *Tel.:* +91-9013553360

E-mail: jayaphysics@yahoo.com (M. Jayasimhadri)

ACCEPTED MANUSCRIPT

1. Introduction

Inorganic compounds doped with rare earth ions form an important class of phosphor materials, which have been utilized for developing efficient white light emitting diodes, emission display devices such as field emission displays (FED), plasma display panels (PDP), bio and medical applications [1-4]. Due to low energy consumption, longer lifetime and environmental friendliness, solid state lighting has been received much attention to replace the traditional lighting sources such as incandescent and fluorescent lamps [5-7]. The phosphor converted (pc) emission is one of the important approaches to produce efficient commercial white LEDs with the combination of blue LED and yellow phosphor ($Y_3Al_5O_{12}:Ce^{3+}$). Such type of phosphors consists of poor color rendering index (CRI) due to lack of red component in white light emission [8-11]. Moreover, near-UV phosphor converted LEDs have many potential advantages due to their excellent color rendering index, light color tolerance and high conversion efficiency into visible light. Pondering on the aforementioned points, we made an effort to prepare and investigate near-UV excited efficient germane red phosphors aptly suitable for white light emitting diodes. Among different rare earth ions, Eu^{3+} ion is one of the most promising and extensively used ions for the preparation of optoelectronic devices, which essentially requires red light component [11, 12].

Niobate group materials are attractive for good electro-optic, pyroelectric, piezoelectric and non-linear properties and have technological applications in the field of photonics, frequency doubler, holographic storage and microwave dielectric materials. According to Watchel [13] and Blasse *et al.* [14], the luminescence properties of inorganic compounds containing niobium-oxygen complex (NbO_6) are structurally sensitive as the absorption edge of the niobates is due to the charge transfer within this complex. However, niobate compounds containing rare earth ions

ACCEPTED MANUSCRIPT

have received much attention for the application as luminescent materials although few pure niobate compounds do not exhibit luminescence. Up to now, various pure and rare earth doped niobates such as $KNbO_3$ [15-16], $LiNbO_3$ [17-19], $KLaNb_2O_7$ [20], $Sr_xBa_{1-x}Nb_2O_6$ [21-22], $LnNbO_4$ (Ln= Pr, La, Ga and Y) [23-24], $Ba_5Nb_4O_{15}$ [25] have been extensively studied for the applications in lasers, holographic image recording, photo catalytic, optical data storage, switching, optical computing etc. due to their excellent optical properties. Among all the intrinsic alkaline earth metaniobate compounds (ANb_2O_6, where A = Ca, Sr and Ba), the charge generation in $BaNb_2O_6$ under UV light irradiation may be anticipated higher due to smaller energy gap compared to the other metaniobate powders [26]. On the other hand, photo catalytic activities and microwave dielectric properties of barium niobates have been intensively focused in recent years [27-30]. However, to the best of our knowledge, the study of the optical/luminescent properties of europium doped barium niobates has not been reported so far.

In the present study, we have synthesized $BaNb_2O_6$ powders by solid state reaction method and explored its potential as phosphor host material by doping europium. Thermal, structural and morphological properties were analysed. Emission spectra measured as a function of Eu^{3+} concentration and investigated the luminescence properties in detail for $BaNb_2O_6$ phosphor. The results mainly reveal the calcination temperature and Eu^{3+} concentration required to obtain optimized red emitting single phase $BaNb_2O_6$ phosphor for the application of near-UV based white light emitting diodes.

2. Experimental Procedure

Powder samples of $BaNb_2O_6$:xEu^{3+} (where x = 1, 4, 10, 12, 14 and 16 mol %) were prepared by conventional solid state reaction method from the starting materials with AR grade

ACCEPTED MANUSCRIPT

$BaCO_3$ (99%), Nb_2O_5 (99.9%) and Eu_2O_3 (99.9%). The required stoichiometric amounts of starting materials were thoroughly mixed in an agate mortar pestle for an hour with an appropriate amount of acetone and then sintered in a programmable muffle furnace by keeping the mixture in an alumina crucible. The powder is heated up to a temperature of 625 °C for one hour and then sintered at 1200 °C with the heating rate of 6 $^oC\ min^{-1}$ for 5 h in an ambient atmosphere.

The crystalline phase of synthesized samples was identified with Rigaku Corp. X-ray diffractometer (Model-Mini flex-II), in the 2θ range from 20 to 60° using nickel-filtered Cu Kα radiation with the accelerating voltage 30 kV and tube current 15 mA. Thermal analysis of $BaNb_2O_6$ powder was carried out by Mettler Toledo, thermogravimetric analysis (TGA) - differential scanning calorimetric (DSC) equipment (Model: Star-e System) under N_2 atmosphere at heating rate of 10 °C/min from room temperature to 1200 °C. The morphology and microstructure were characterized with SEM (Hitachi, Model- S-3700N) for the synthesized alkaline earth niobate samples. The photoluminescence properties were measured for all the samples using an Edinburgh Luminescence spectrometer (Model: F900) fitted with Xenon flash lamp at room temperature.

3. Results and Discussion

3.1. Thermal and structural properties

The thermal behaviour of $BaNb_2O_6$ was investigated by utilizing TGA and DSC profiles as shown in Fig.1. There are two major stages of weight loss observed in TGA curve. At first stage of weight loss about 16.52 % between 100-600 ^oC accompanying their corresponding

ACCEPTED MANUSCRIPT

endothermic broad peak at 455 ^{o}C in DSC attributed due to removal of moisture and acetone. In the second stage, slight weight loss about 9.34 % observed between 600-785 ^{o}C attributed due to release of CO_2 gas. In addition to that one exothermic peak observed at 1050 ^{o}C, which could be due to the formation of main $BaNb_2O_6$ phase. Based on the TGA profile, it is noticed that total weight loss in the process of forming $BaNb_2O_6$ up to the calcination temperature 1200 ^{o}C is about 25.86 %. DSC profile exhibits crystallization temperature (T_c) at 1050 ^{o}C for the $BaNb_2O_6$ powder sample. Hence, the samples calcined at 1100 and 1200 ^{o}C were characterized by using XRD to optimize the calcination temperature and phase purity as shown in Fig. 2 (b & c). Based on the XRD profiles shown in Fig. 2 (b), it may be revealed that the pure phase of $BaNb_2O_6$ is not observed at 1100 ^{o}C. The diffraction pattern observed for the sample calcined at 1200 ^{o}C shown in Fig. 2 (c) is purely due to $BaNb_2O_6$ and all the lines are matching with the reported values of orthorhombic $BaNb_2O_6$ (JCPDS:14-0027). No other impurity phase was detected, which indicate the formation of pure orthorhombic $BaNb_2O_6$ phase at the calcination temperature 1200 ^{o}C. The crystallite size (D) and strain (ε) of $BaNb_2O_6$ were calculated by most reliable Williamson - Hall (W-H) equation [$\beta\, Cos\, \theta + \left(\frac{K\lambda}{D}\right) + 4\varepsilon\, Sin\theta$], where D is average crystallite size, K= shape factor (0.94), β = full width half maxima (FWHM) , θ = the Braggs angle , λ = x-ray wavelength and ε is strain[31, 32]. The average crystallite size and strain are found to be ~50-55 nm and strain 0.08%, respectively. Further the average crystallite size calculated by conventional Debye- Scherer's equation [33] [$D = K\lambda/\beta Cos\theta$] is in good agreement with the crystallite size calculated from W-H method. The calculated lattice parameters are a = 12.168 Å, b =10.253 Å and c =7.845 Å which belongs to space group *47:pmmm* and volume (V)= 977.012 $Å^3$.

ACCEPTED MANUSCRIPT

Fig. 3 represents the SEM micrograph for the optimized $BaNb_2O_6$:12 mol % Eu^{3+} sample sintered at 1200 °C. It was clearly seen from the figure that the particles are agglomerated with irregular morphology in the µm range. The typical crystalline grain size is in the range of 3-5 µm in dimension. The micrometre crystalline powder would be suitable to obtain high efficient phosphor and very much useful for solid state lighting applications [34].

3.2. Luminescence properties

Excitation spectrum of 12 mol% Eu^{3+} doped $BaNb_2O_6$ phosphor sintered at 1200 °C is shown in Fig. 4. The spectrum exhibits five bands due to intra 4f transitions of the Eu^{3+} ions and assigned as $^7F_0 \rightarrow {}^5D_4$, $^7F_0 \rightarrow {}^5L_7$, $^7F_0 \rightarrow {}^5L_6$, $^7F_0 \rightarrow {}^5D_3$ and $^7F_0 \rightarrow {}^5D_2$ at wavelengths 362, 383, 395, 417 and 466 nm, respectively. The broad excitation band 300-400 nm may be attributed to the charge transfer band, which may be originated from an electron transfer from 2p orbital of an oxygen ligand to an empty 4f orbital of europium ion and the host charge transfer band occurs from an oxygen atom to the empty 4d orbital of the central niobium atoms within NbO_6 group [35]. The intense bands $^7F_0 \rightarrow {}^5L_6$ (395 nm) and $^7F_0 \rightarrow {}^5D_2$ (466 nm) observed in near-UV and blue regions, which confirms the existence of Eu^{3+} state in Eu^{3+} doped $BaNb_2O_6$ phosphor. Moreover, this phosphor is suitable to efficiently excite in near-UV and blue regions, which is one of the prerequisite properties to use this phosphor for preparation of white light emitting devices.

Figs. 5 and 6 show the emission spectra of Eu^{3+} doped $BaNb_2O_6$ phosphor for different concentrations of europium measured under 395 and 466 nm excitation wavelengths, respectively. The emission peak centred at 592 nm ($^5D_0 \rightarrow {}^7F_1$) is attributed to magnetic dipole (MD) transition and intense emission peak at 611 nm ($^5D_0 \rightarrow {}^7F_2$) is ascribed to electric dipole

ACCEPTED MANUSCRIPT

(ED) transition. In general, magnetic dipole transition is allowed and electric dipole transition is forbidden as per the selection rule. But, forbidden electric dipole transition ($^5D_0 \rightarrow {}^7F_2$) became partially allowed due to odd parity component of the crystal field in $BaNb_2O_6:Eu^{3+}$. Two weak emission bands observed at 654 and 703 nm are assigned as ($^5D_0 \rightarrow {}^7F_3$) and ($^5D_0 \rightarrow {}^7F_4$), respectively. According to Judd-Ofelt theory intensity distribution of $^5D_0 \rightarrow {}^7F_j$ (where j=0, 1, 2, 3 and 4) transitions depends only on the symmetry of local environment around activator ions. Owing this property, few transitions are hypersensitive to the crystal environment and their intensity extremely influenced by the ligand ions in the host are called as hypersensitive transitions [36]. Here, ED transition $^5D_0 \rightarrow {}^7F_2$ is hypersensitive whereas MD transition $^5D_0 \rightarrow {}^7F_1$ is insensitive. The emission intensity of the observed bands is changing with Eu^{3+} ion concentrations whereas the shape of the emission band is not changing. It is well known that the trivalent lanthanides energy levels are weakly affected by ligand ions in crystals because the 4f electrons are shielded by the external electric fields of the outer $5s^2$ $5p^6$ electrons. Therefore, the shape of the optical spectra for most of the phosphors with the same lanthanide doping are similar to those expected for free ions [37]. Fig. 7 shows the variation of emission intensity with Eu^{3+} concentration in the range from 1 to 16 mol% under the excitation of 395 nm. The intensity of all the observed emission bands increases with Eu^{3+} concentration by reason of energy migration among the activators up to 12 mol% and beyond this finally reached at killer site due to quenching mechanism associated with exchange interaction**.** Such exchange of energy between the Eu^{3+} ions is obvious as the distance between them decreases with increasing Eu^{3+} ion concentrations [38, 39].

In the present work, the emission intensity of $^5D_0 \rightarrow {}^7F_2$ (ED) transition is more intense than the $^5D_0 \rightarrow {}^7F_1$ (MD) transition in $BaNb_2O_6:Eu^{3+}$. Therefore, the activator Eu^{3+} (0.95 Å)

ACCEPTED MANUSCRIPT

occupies the Ba^{2+} (1.42 Å) site without an inversion symmetry, which helps to improve the purity of red color [40]. Hence, Eu^{3+} can act as a good luminescent activator for red phosphor due to intense $^5D_0 \rightarrow {}^7F_2$ transition centred at 611 nm based on the fact that red emission constituted by very narrow emission band appears brighter than the broad red emission to human eye though the phosphor exhibiting same red chromaticity and emission energy [38]**.** The integrated emission intensity ratio between electric (red) and magnetic (orange) dipole transitions [I ($^5D_0 \rightarrow {}^7F_2$) /I ($^5D_0 \rightarrow {}^7F_1$)] has been calculated and is called as asymmetric ratio. This obtained Red (R)/Orange (O) ratio are found to be increase with Eu^{3+} concentration up to 12 mol% and considered that 12 mol % of Eu^{3+} as optimum R/O ratio (5.556) achieved for $BaNb_2O_6$:Eu^{3+} phosphor [41]**.** The simplified energy level diagram is plotted in Fig. 8 to demonstrate the mechanism involved in the emission and excitation processes for Eu^{3+} doped $BaNb_2O_6$ phosphor. When the Eu^{3+} ions were excited with 395 nm (to $^5L_6$ level) and 466 nm (to $^5D_2$ level) light, the population relaxes finally to the $^5D_0$ level through non-radiatively and then exhibit four emission bands in the visible region from $^5D_0$ level (shown as downward arrow) [42].

The color purity of the material can be estimated in terms of mathematically driven coordinates called Commission International De I'Eclairage (CIE) chromaticity coordinates. Fig. 9 shows the CIE chromaticity diagram for optimized sample of 12 mol% Eu^{3+} doped $BaNb_2O_6$ phosphor sintered at 1200 °C in ambient atmosphere under 395 nm excitation. The calculated color coordinates were found to be (x=0.628 and y=0.365), which falls in the pure red region suggests that the investigated phosphor may be used as red emitting phosphor for RGB composed white light emitting diodes (LEDs). In addition to that, the calculated CIE chromaticity coordinates for $BaNb_2O_6$:Eu^{3+} are closer to the commercial red phosphor of

ACCEPTED MANUSCRIPT

$Y_2O_2S:Eu^{3+}$ (x= 0.622, y= 0.351) and also close to the National Television Standard Committee (NTSC) standard value of red phosphor (x= 0.67, y= 0.33) [43].

4. Conclusions:

Various molar concentrations of Eu^{3+} (1, 4, 8, 10, 12, 14 and 16 mol %) doped $BaNb_2O_6$ phosphors have been synthesized by high temperature solid state reaction technique and the thermal, structural, morphological and photoluminescence properties were analyzed. The particle size in the order of 3-5 µm observed for the sample synthesized at 1200 °C. The obtained phosphors exhibit strong red emission under near-UV and blue excitations at 395 and 466 nm, respectively. Eu^{3+} doped $BaNb_2O_6$ phosphor exhibit concentration quenching at beyond 12 mol% of Eu^{3+} ion concentration due to energy transfer processes. The CIE chromaticity coordinates for the present phosphor are very much closer to the commercial red phosphor ($Y_2O_2S:Eu^{3+}$). The obtained results for $BaNb_2O_6 : Eu^{3+}$ phosphor indicate that this phosphor can be used as a red component phosphor for the fabrication of near-UV/blue GaN-based white LEDs.

Acknowledgements:

The authors are grateful to DAE-BRNS, Govt. of India for the sanction of a research project (No. 2011/34/2/BRNS/130. dt. 21/04/2011). This work also has been partially supported by Priority Research Centers Program through the National Research Foundation of Korea (NRF) funded by the Ministry of Education, Science and Technology (2010-0029634)

ACCEPTED MANUSCRIPT

References

[1] M. Leskela, J. Alloys Comp. 275-277 (1998) 702-708.

[2] A.N. Belsky, J. C. Krupa, Displays 19 (1999) 185-196.

[3] C.R. Ronda, T. Justel, H. Nikol, J. Alloys Comp. 275-277 (1998) 669-676.

[4] J.H. Oh, S.J. Yang, Y.R. Do, Light Sci. Appl. 3 (2014) e141

[5] J.M. Phillips, M.E. Coltrin, M.H. Crawford, A.J. Fischer, M.R. Krames, R.M. Mach, G.O. Mueller, Y. Ohno, L.E.S. Rohwer, J.A. Simmons, J.Y. Tsao, Laser & Photon. Rev. 1 (2007) 307-333.

[6] M. Nyman, M.A. Rodriguez, L.E. Shea-Rohwer, J.E. Martin, P.P. Provencio, J. Am. Chem. Soc. 131 (2009) 11652-53.

[7] A.A. Setlur, J.J. Shiang, U. Happek, Appl. Phys. Lett. 92 (2008) 081104.

[8] T. Justel in: C. Ronda (Edited), Luminescence From Theory to Applications, WILEY-VCH Verlag GmbH & Co. KGaA Weinheim 2008 pp. 179-190.

[9] J. Silver, R. Withnall, in : A. Kitai (Ed) Luminescent Material and Applications, John Wiley & Sons ltd, Chichester, 2008 pp 75-109.

[10] H. Daicho, T. Iwasaki, K. Enomoto, Y. Sasaki, Y. Maeno, Y. Shinomiya, S. Aoyagi, E. Nishibori, M. Sakata, H. Sawa, S. Matsuishi, H. Hosono, Nat. Commun. 3 (2012) 1132.

[11] X. Li, J.D. Budai, F. Liu, J.Y. Howe, J. Zhang, X.J. Wang, Z. Gu, C. Sun, R.S. Meltzer, Z. Pan, Light Sci. Appl. 2 (2013) e50.

[12] D. Uma Maheswari, J.S. Kumar, L.R. Moorthy, K. Jang, M. Jayasimhadri, Physica B 403 (2008) 1690-1694.

[13] A. Wachtel, J. Electrochem. Soc. 111(5) (1964) 534.

ACCEPTED MANUSCRIPT

ACCEPTED MANUSCRIPT

[14] G. Blasse, M.G.J. vanLeur, Mater. Res. Bull. 20 (1985) 1037-1045.

[15] C.H. Wen, S.Y. Chu, C.K. Wen, J. Cryst. Growth 269 (2004) 479-483.

[16] T.H. Fang, Y.J. Hsiao, Y.S. Chang, Y.H. Chang, Mater. Chem. Phys. 100 (2006) 418-422.

[17] D. Hreniak, A. Speghini, M. Bettinelli, W. Strek, J. Lumin. 119-120 (2006) 219-223.

[18] J.H. Yao, B.X. Yan, Y.H. Chen, J.J. Xu, G.Y. Zhang, Y.F. Ruan, W.R. Li, Opt. Mater. 27 (2004) 373-376.

[19] C. Koepke, K. Wisniewski, D. Dyl, M. Grinberg, M. Malinowski, Opt. Mater. 28 (2006) 137-142.

[20] A. Kudo, Chem. Mater. 9 (1997) 664-669.

[21] T.P.J. Han, F. Jaque, D. Jaque, L. Ivleva, Chem. Phys. Lett. 417 (2006) 196-199.

[22] M.O. Ramirez, L.E. Bausa´, A. Speghini, M. Bettinelli, L. Ivleva, J. Garı´ Sole´, Phys. Rev. B 73 (2006) 35119.

[23] S.K. Misra, S.I. Andronenko, J. Phys. Chem. B 108 (2004) 9397-9402.

[24] X. Xiao, B. Yan, J. Alloys Comp. 421 (2006) 252-257.

[25] A.M. Srivastava, J.F. Ackerman, W.W. Beers, J. Solid State Chem. 134 (1997) 187-191.

[26] I.S. Cho, S.T. Bae, D.H. Kim, K.S. Hong, Int. J. Hydrogen Energy 35 (2010) 12954 - 12960.

[27] S.P. Gaikwad, V. Samuel, R. Pasricha, V. Ravi, Bull. Mater. Sci. 28 (2005) 121-123.

[28] M.D. Ewbank, R.R. Neurgaonkar, W.K. Cory, J. Feinberg, J. Appl. Phys. 62 (1987) 374-380.

[29] D.W. Kim, K.S. Hong, C.H. Kim, K. Char, Appl. Phys. A 79 (2004) 677–680.

ACCEPTED MANUSCRIPT

ACCEPTED MANUSCRIPT

[30] D.W. Kim, H.B. Hong, K.S. Hong, C.K. Kim, D.J. Kim, Jpn. J. Appl. Phys. 41(2002) 6045-6048.

[31] B.D. Cullity, S.R. Stock, Elements of X-ray Diffraction 3rd ed., Prentice-Hall Inc, 2001, pp 167-171.

[32] S. Bathula, R.C. Anandani, A. Dhar, A.K. Srivastava, Mater. Sci. Eng. A 545 (2012) 97-102.

[33] G. Swati, S. Mishra, D. Yadav, R.K. Sharma, D. Dwivedi, N. Vijayan, J.S. Tawale, V. Shanker, D. Haranath, J. Alloys Comp. 571 (2013) 1-5.

[34] X. Z. Xiao, B. Yang, J. Alloys Comp. 433 (2007) 246-250.

[35] J. Hou, P. Chen, G. Zhang, Y. Fang, W. Jiang, F. Huang, Z. Ma, J. Lumin. 146 (2014) 97-101.

[36] U. Rambabu, S.D. Han, RSC Adv. 3 (2013) 1368-1379.

[37] Y.C. Chang, C.H .Liang, S.A. Yan, Y.S Chang, J. Phys. Chem. C 114 (2010) 3645-3652.

[38] X. Zhao, J. Wang, L. Fan, Y. Ding, Z. Li, T. Yu, Z. Zou, Dalton Trans. 42 (2013) 13502-13508.

[39] V.R. Bandi, M. Jayasimhadri, J. Jeong, K. Jang, H.S. Lee, S.S. Yi, J.H. Jeong, J. Phys. D: Appl. Phys. 43 (2010) 395103-395110.

[40] G.S.R. Raju, R. Pavitra, J.S. Yu, Phys. Chem. Chem. Phys. 16(2014) 18124-18140.

[41] L. Li, H.K. Yang, B.K. Moon, Z. Fu, C. Guo, J.H. Jeong, S.S. Yi, K. Jang, H.S. Lee, J. Phys. Chem. C 113(2013) 610-617.

[42] W.T. Carnall, P.R. Fields, K. Rajnak, J. Chem. Phys. 49 (1968) 4450.

ACCEPTED MANUSCRIPT

ACCEPTED MANUSCRIPT

[43] S. Qi, D. Wei, Y. Huang, S. Kim, Y.M. Yu, H.J. Seo, J. Am. Ceram. Soc. 97 (2014) 501-506.

Figure Captions:

Fig.1: TGA-DSC curves for $BaNb_2O_6$ powder.

Fig.2: X-ray diffraction patterns of $BaNb_2O_6$ powder (a) standard data for $BaNb_2O_6$ (JCPDS no. 14-0027) (b) calcined at 1100 °C and (c) calcined at 1200 °C for 5 h.

Fig.3: Scanning electron micrograph of $BaNb_2O_6:Eu^{3+}$ (x = 12mol %) sintered at 1200 °C

Fig. 4: Room temperature photoluminescence excitation spectra (λ_{em}=611 nm) of $BaNb_2O_6:Eu^{3+}$ at 12 mol%

Fig. 5: Room temperature photoluminescence emission spectra (λ_{ex}=395 nm) of $BaNb_2O_6:Eu^{3+}$ at different concentrations

Fig. 6: Room temperature photoluminescence emission spectra (λ_{ex}=466 nm) of $BaNb_2O_6:Eu^{3+}$ at different concentrations

Fig.7: Variation of emission intensity with the Eu^{3+} concentration in $BaNb_2O_6$ phosphor.

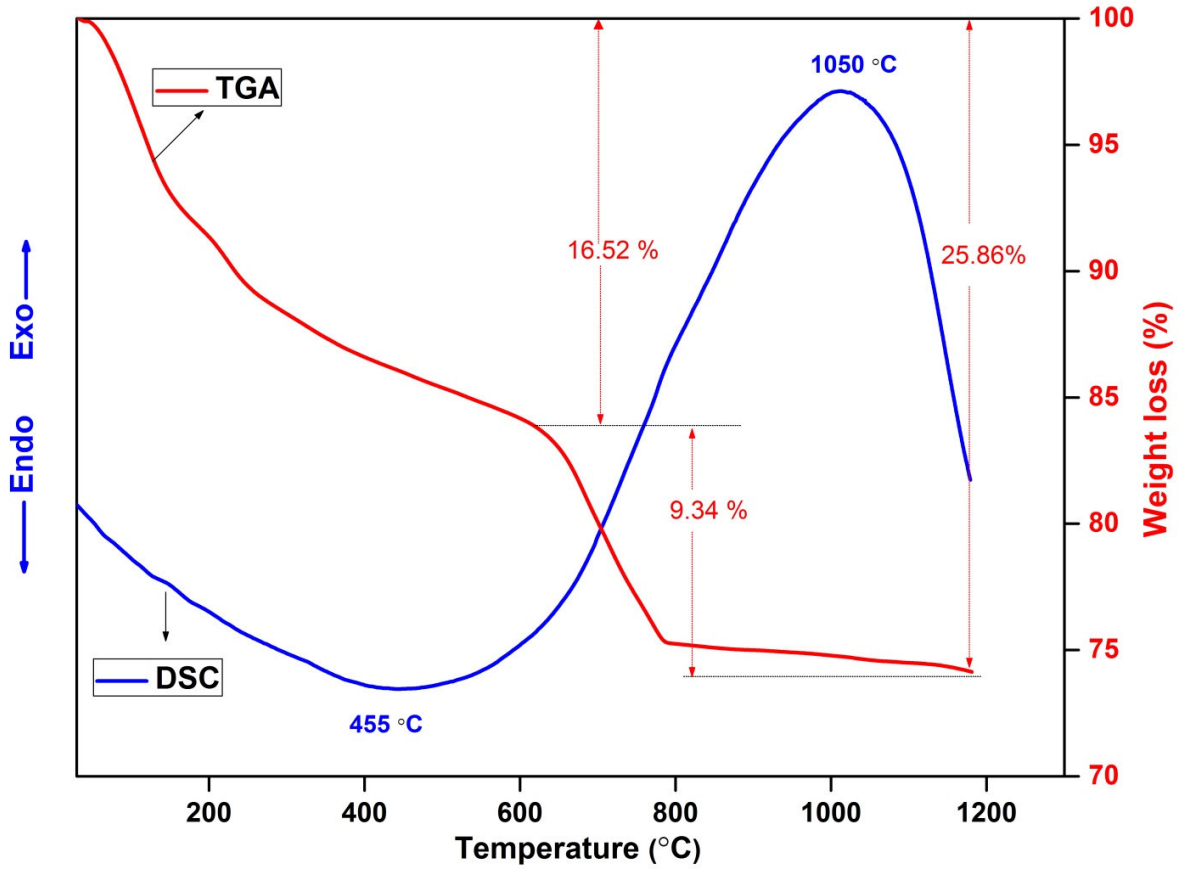
Fig.8: Simple model illustrating the energy transfer from $BaNb_2O_6$ to Eu^{3+} and the emission process of Eu^{3+} in $BaNb_2O_6$.

Fig. 9: CIE chromaticity diagram for 12 mol% Eu^{3+} doped $BaNb_2O_6$ phosphor.

ACCEPTED MANUSCRIPT

ACCEPTED MANUSCRIPT

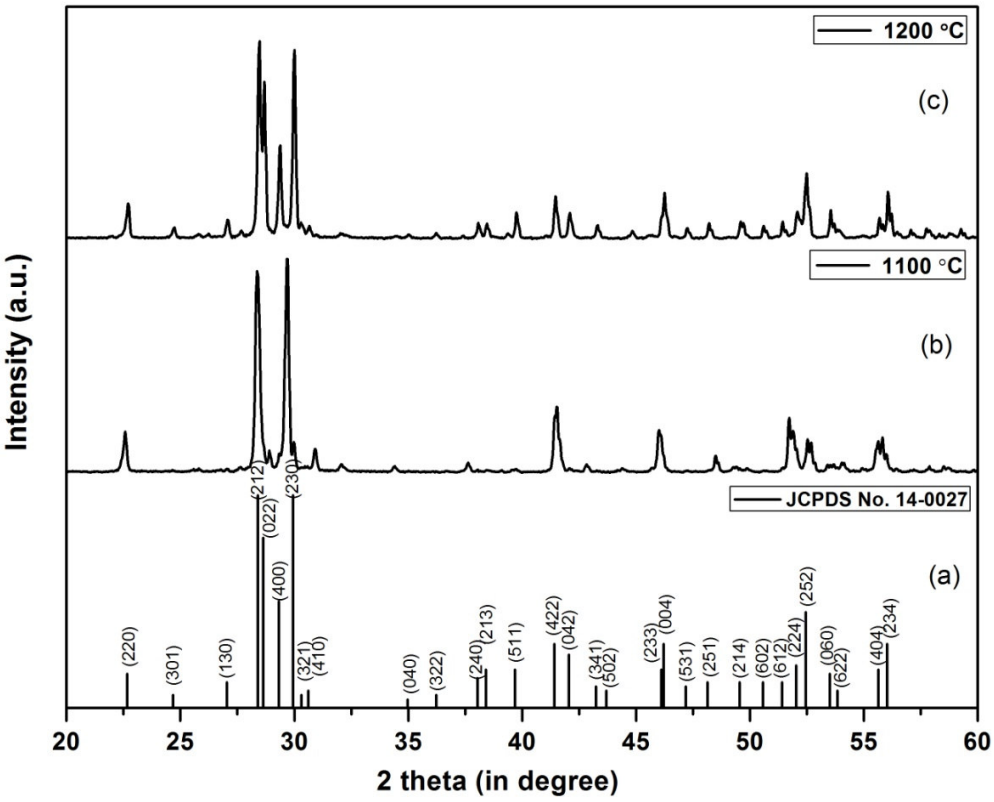
Fig. 1.



ACCEPTED

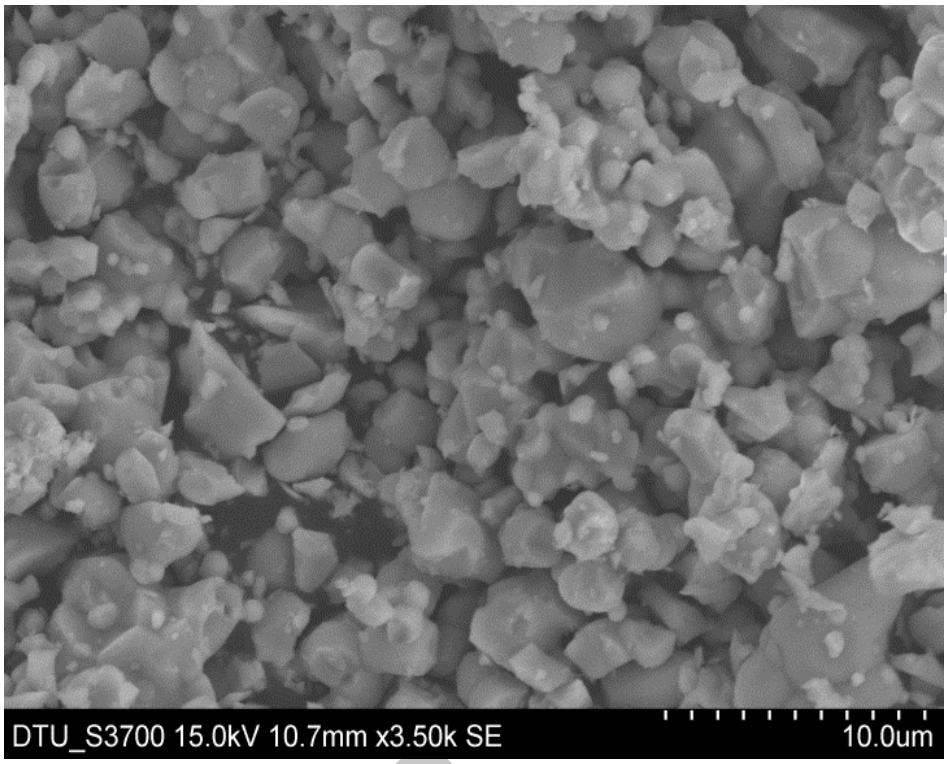
ACCEPTED MANUSCRIPT

Fig. 2.



ACCEPTED MANUSCRIPT

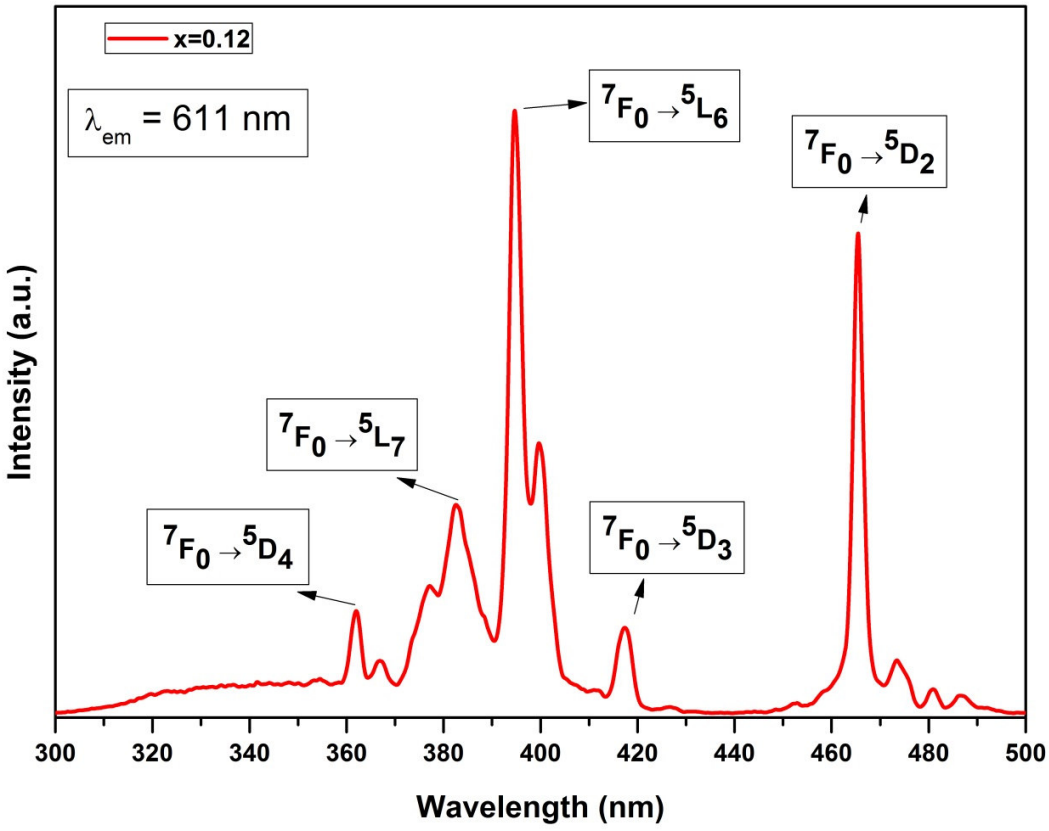
Fig. 3.



ACCEPTED MANUSCRIPT

ACCEPTED MANUSCRIPT

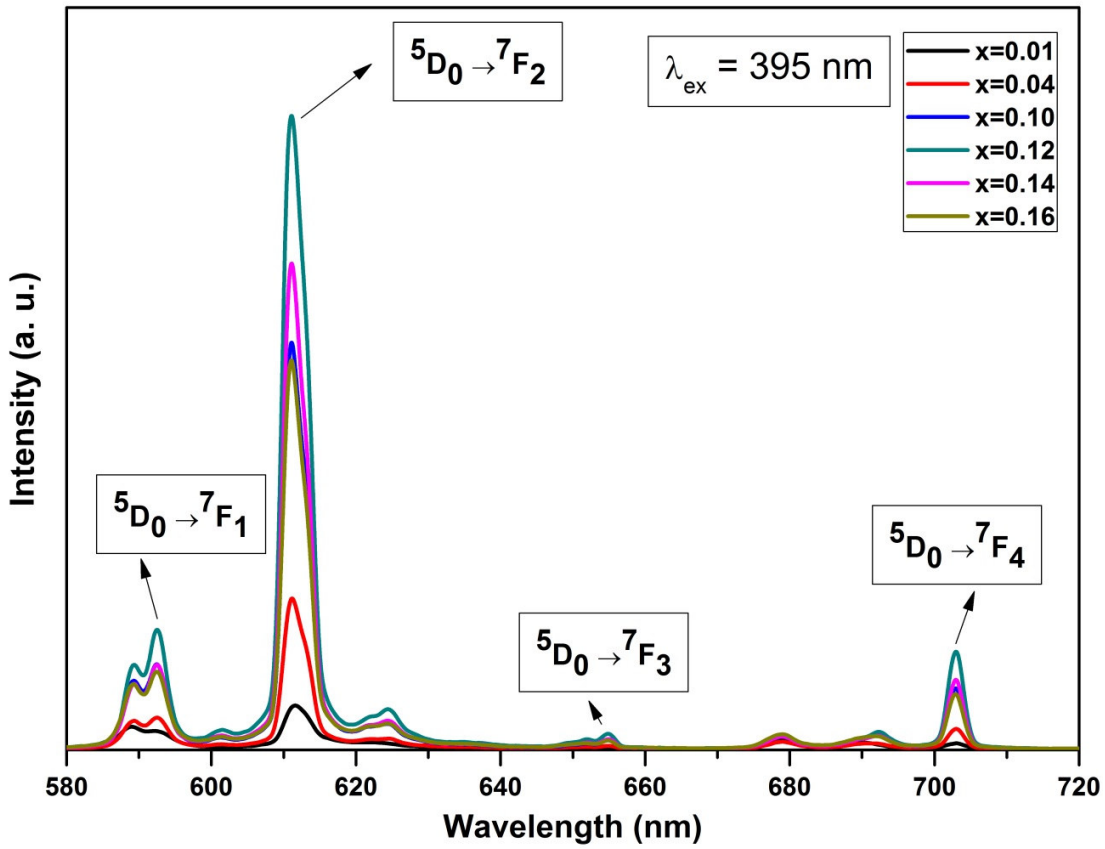
Fig. 4.



ACCEPTED

ACCEPTED MANUSCRIPT

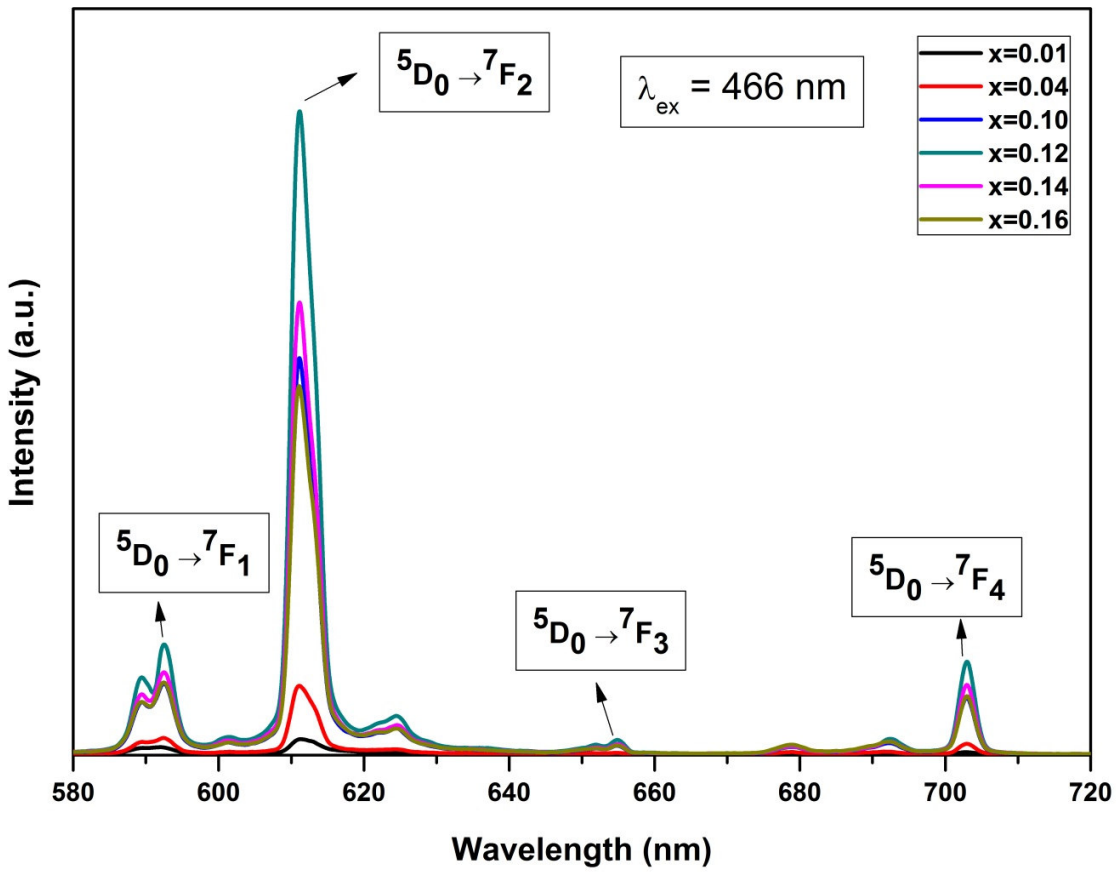
Fig. 5.



ACCEPT

ACCEPTED MANUSCRIPT

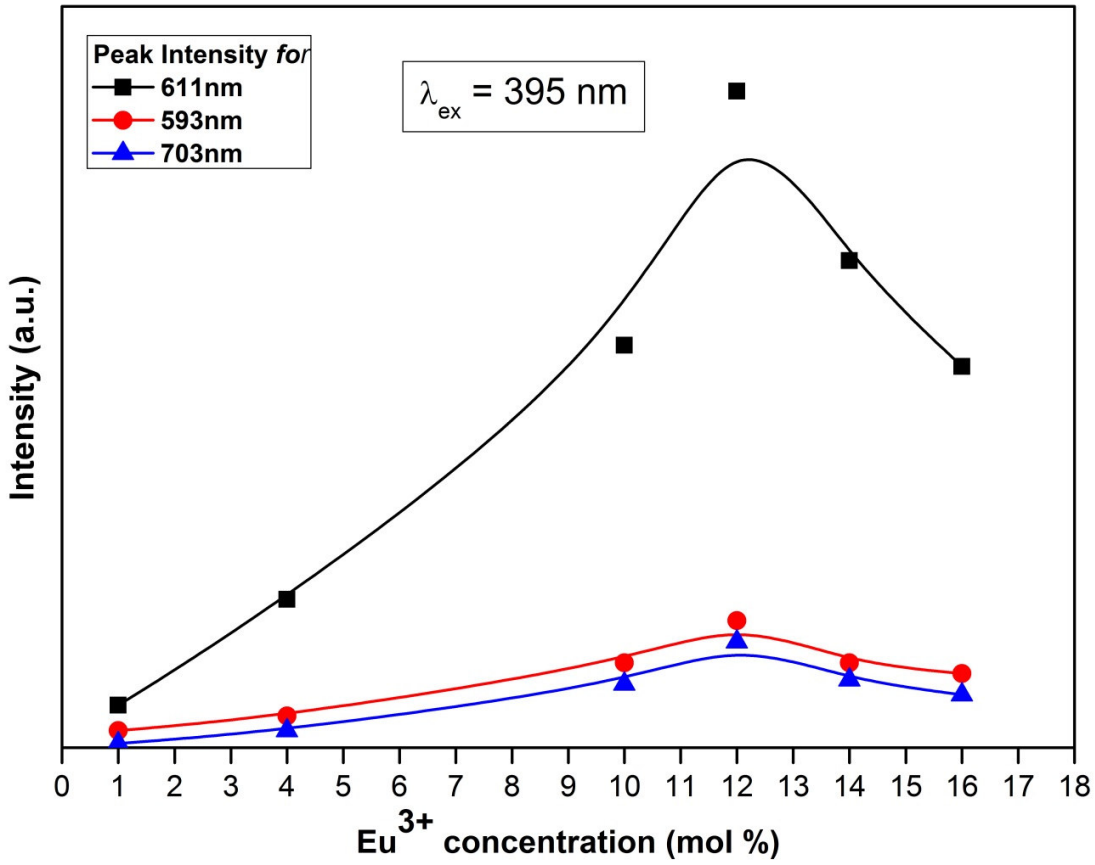
Fig. 6.



ACCEPT

ACCEPTED MANUSCRIPT

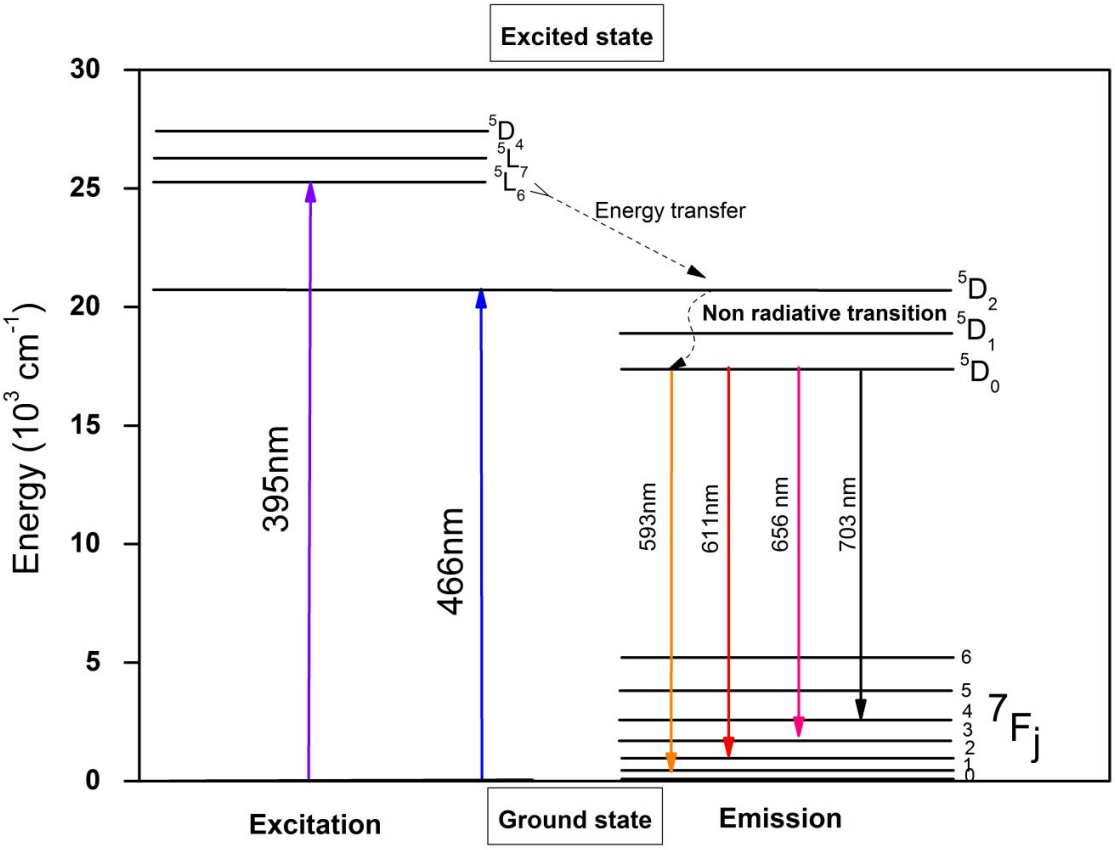
Fig. 7.



ACCEP

ACCEPTED MANUSCRIPT

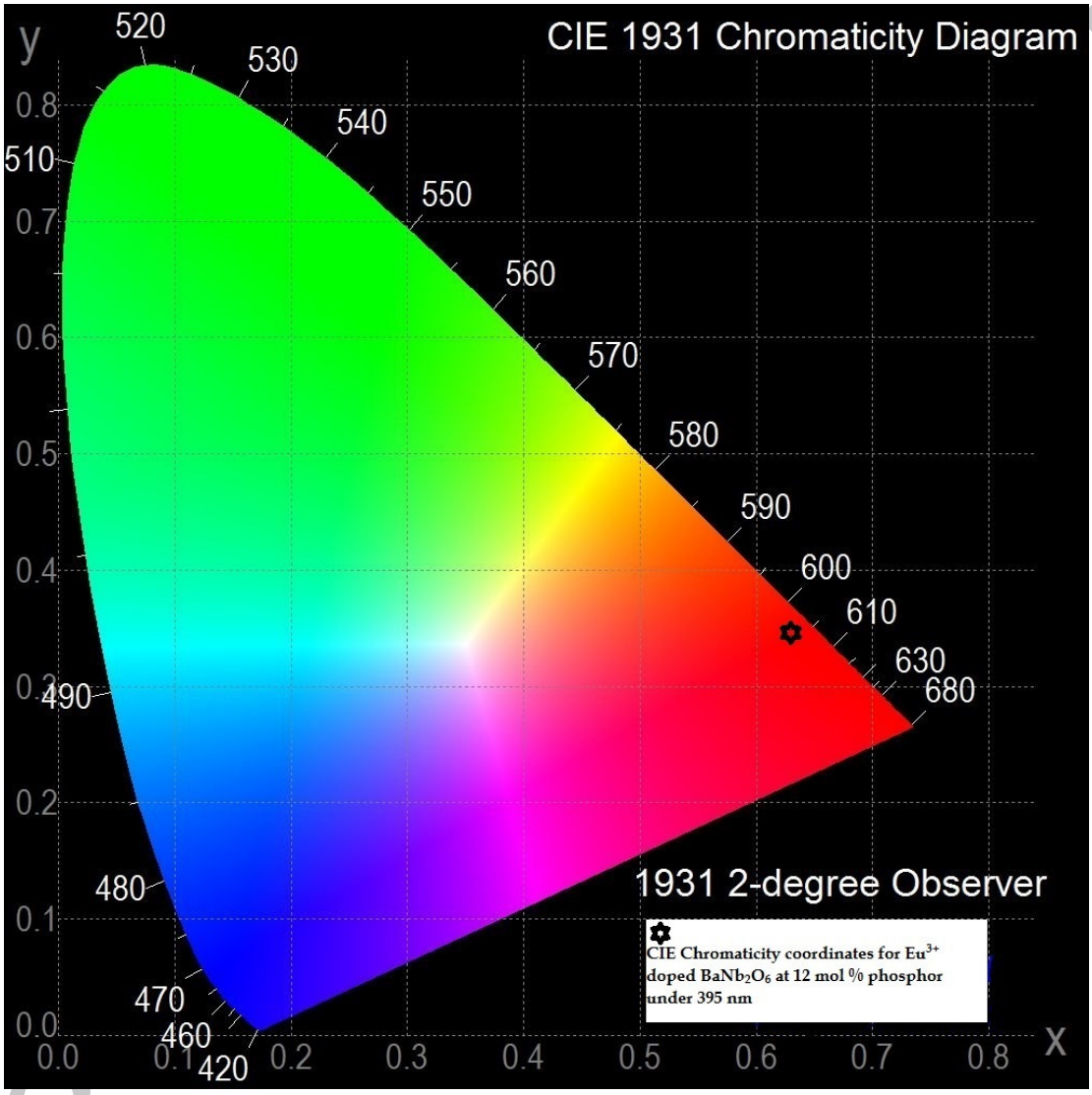
Fig. 8.



ACCEPTED

ACCEPTED MANUSCRIPT

Fig. 9.



ACCEPTED MANUSCRIPT

Highlights

- Successfully synthesized new orthorhombic phase Eu^{3+}:$BaNb_2O_6$ red phosphors
- Thermal and Luminescent properties have been explored for the first time.
- Strongest excitation peaks observed at 395 nm (near UV) and 466 nm (blue)
- Eu^{3+} concentration was optimized to obtain efficient phosphor
- CIE coordinates are very much closer to the commercial red phosphor (Y_2O_2S:Eu^{3+})
- The results indicate that Eu^{3+} doped $BaNb_2O_6$ is suitable for n-UV based white LEDs

ACCEPTED MANUSCRIPT

Volume 2, Issue 3 (2014) 564-567 ISSN 2347 - 3258
International Journal of Advance Research and Innovation

Study of Designing a Solar Concentrator for Crematorium using Solar Energy

A. C. Kashyap *, J. P. Kesari, A. K. Rai, Hukam Singh
Department of Mechanical Engineering, Delhi Technological University, New Delhi, India

Article Info

Article history:
Received 20 July 2014
Received in revised form
10 August 2014
Accepted 20 August 2014
Available online 15 September 2014

Keywords

Scheffler reflector,
Concentration Ratio,
Solar Tracking

Abstract

While cremation is an established Hindu ritual practice since ancient times and the Hindu religion permits the cremation of dead body in day-time only, there is much more scope of solar crematorium in this ritual; as solar power is also available in day-time only. Between 500 and 600 kg of wood are used to cremate a dead body. Many trees are felled to meet this requirement. As a result we are significantly contributing in global warming and polluting the atmospheric air much more. Therefore today, world is moving towards the sustainable energy sources which are renewable and biodegradable in nature. One of most sustainable energy source is sunlight that too is inexhaustible and available free of cost. The heat (energy) produced is very clean with no pollutants. So above environmental problems can be the addressed very well by using solar crematorium. Therefore anyone can be a firm believer of world powered by solar energy. In this paper, a special concentrator has been designed to supply required sufficient heat energy to the crematorium by concentrating solar energy. Its speciality is a flexible surface curvature and simultaneously with a non-moving focal area.

1. Introduction

India is facing the twin problems of fast depletion of conventional fuels and environmental degradation. There is an urgent need to reduce dependence on petroleum and other conventional fuels for better economy and environment. Utilization of solar energy can address both these issues. Nearly the sun is the source of all the energies on earth.

When one thinks of the word "solar", photovoltaic modules and panels automatically come to mind, which converts the sunlight into electricity but that is not the case here. Since the sunlight has very little part, only 10% of its energy as lighting effect and large portion, 90% as thermal effect. So energy of solar radiation can be utilized more in solar thermal power generation than in solar photo-voltaic (which utilizes only lighting effect of sunlight) for power generation. A crematorium too requires very large amount of heat energy which can be harnessed by directly by solar concentrator. On the other hand, I will never suggest using of solar photo-voltaic panels to obtain such a large amount of heat indirectly for cremating a corpse. As firstly, PV panels convert only 10% (lighting effect) of solar energy into electricity, and then this electricity is converted into heat by allowing passing through very high amount of resistance. This conversion of electricity into the heat is too associated with several losses. So employing solar PV panels will not be feasible for cremating a corpse. Although these PV panels can be used to get electricity for running the accessories like tubes, fans in office/cabins and necessary motors installed in tracking system.

Since combustion chamber of crematorium is stationary and not movable but solar concentrators require tracking the Sun, as a result a movable focus is obtained. This is major problem in designing a solar concentrator for the crematorium. This problem was shorted out by Wolfgang Scheffler who invented a new concentrator (scheffler reflector) tracking the Sun without changing it focus. In this paper, scheffler reflector is redesigned to determine required size (Aperture Area) of the concentrator to obtain sufficient heat energy for cremating a corpse.

Corresponding Author,
E-mail address: ackashyap@hotmail.com
All rights reserved: http://www.ijari.org

2. Literature Review

Not much extensive and dedicated work is seen after studying a lot of different popular journals available. Few works has been reported and added in this paper for solar furnaces and cost estimation of solar equipments.

The largest solar furnace is located in Font-Romeu-Odeillo-Via, high in the Pyrenees Mountains in the Basque region of the French/Spanish border. It has been operational since 1970. This is the same area in which the world's first solar furnace was built; this solar furnace was put in place at Mont-Louis in 1949 by Professor Felix Trombe. Odeillo and Mont-Louis are within 15km of each other. The furnace makes use of an array of 10000 mirrors to reflect sunlight into a gigantic concave hemisphere which then focuses the energy onto an area roughly the size of a cooking pot. The flat mirrors track the sun in unison and redirect the solar thermal energy towards the crucible which is being used for melting steel.

World's first solar crematorium is being developed in our country of Goraj village (30 km East of Baroda) in Gujarat state by Muni Seva Ashram with the help of Ronnie Sabawalla of Rashron Energy and Auto limited. In 1998 they started with a specially designed Scheffler reflector with 50m² mirror surfaces. But its initial concentration-factor of about

C = 100 turned out to be by no means enough to allow proper cremation.

3. Cremation Process

A crematorium is a furnace that is able to generate temperatures of 760–1150°C to ensure disintegration of the corpse. Cremation is the process of burning a dead body at very high temperatures until there are only brittle, calcified bones left, which are then pulverized into "ashes." These ashes can be kept in an urn, buried, scattered or even incorporated into objects as part of the last rites of death.

As per Hindu ritual practice, there is an established sentimental fact of cremating the dead body completely at one goes. And there must not be left any un-burnt portion of the body. Otherwise the soul of that person will remain unsatisfied, and it will be converted into the devil or imp which will victimize or terrorize the concerned relatives for his/her satisfaction.

4. The Concept of Solar Crematorium

The basic concept of solar crematorium is to ignite the dead body locally anywhere and anyhow with the help of a huge concentrating reflector having very high CR and to maintain the combustion of dead body by supplying the fresh atmospheric air with the help of blower. Once combustion of dead body starts within the cremation chamber, it also releases heat which automatically in combination with solar energy obtained from concentrating reflector maintains continuous burning of dead body until complete dead body gets converted into ash. See figure:1. A system of solar crematorium can be divided into following components:

- Solar Concentrator
- Tracking System
- Cremation Chamber

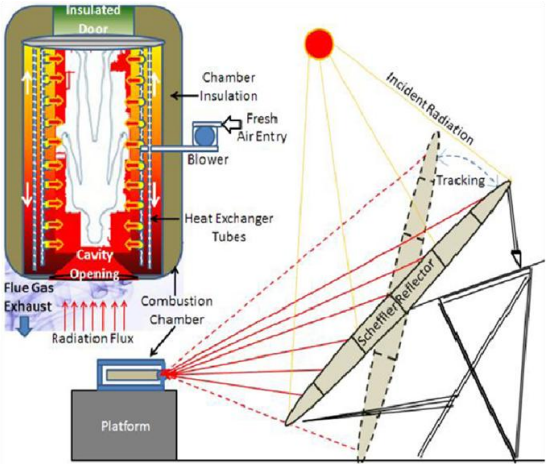


Fig: 1. Block Diagram of Solar Crematorium

5. Solar Concentrator

Parabolic Scheffler Reflectors can provide (you with) high temperature heat. Their speciality is a flexible surface curvature and a nonmoving focal area. Therefore their use is now becoming increasingly popular in many parts of the world, especially in India.

5.1. Designing the Solar Concentrator

The size (Aperture Area) of concentrator (Scheffler reflector) is determined by reverse design procedure. Which is described step by step as following:

First of all "**E**" (total energy) required to burn completely a single dead body is calculated. Since a traditional Hindu funeral pyre takes 2-3 hours and consumes 500–600kg of open wood pile to burn completely a corpse. But considering 100% efficiency of combustion chamber, if all the energy released from wood is utilized, only 22 kg of wood will be sufficient to completely burn down a body. Considering 80% efficient cremation chamber, 100kg of wood will be sufficient for cremating a single corpse in 1 to 2Hrs if heat loss is optimized to minimum value by effective insulation of combustion chamber. Since calorific value of wood is 19700kJ/kg. Therefore

$$E = 100kg \times \frac{19700kJ}{kg} = 1970000kJ = 1970MJ$$

Now "**P**" power (in MJ/hr) required to burn completely the body in combustion chamber is determined. If we design a reflector to cremate a dead body in 2hrs then this (total energy) "**E**" required to burn completely the dead body must be obtained/captured by the reflector within 2hrs. Therefore

$$P = \frac{1970MJ}{2Hrs} = 985MJ/Hrs$$

Finally "**A**", **size** (Aperture Area) of Scheffler reflector is determined. Since DNI (Direct Normal Irradiance) is $5MJ/m^2hr$ ($\approx 4.9212\ MJ/m^2hr = 1367W/m^2$ X 3600sec). So Aperture Area "**A**" is obtained by dividing "**P**" (power) with DNI. i.e.

$$A = \frac{P}{DNI} = \frac{985MJ/Hr}{5MJ/m^2\,Hr} = 197\,m^2$$

5.2. Material of the Concentrator

The concentrators (Scheffler reflector) are made up of several small double sided (two plane mirrors are joined on their each other silver coating sides) plane mirrors. Theoretically single sided mirror is sufficient for the Scheffler reflector, but double sided mirror is used to protect the silver material which is coated on the almost completely transparent glass. Because of intense heat and temperature of solar energy there is possibility of silver coatings to melt away from the rear surface of the glass. Therefore the rear side mirror protects the silver coating to melt away by reflecting back the sunlight if any from rear side, and simultaneously by avoiding the erosion and corrosion. This rear side mirror also provides the additional strength to the front mirror.

The efficiency/reflectivity of several plane mirrors in the Scheffler reflector ranges 90-95% when new. Though it is not important much more, because efficiency is greatly considered where we pay money for energy/fuels which (solar energy) is free here. Here efficiency/reflectivity of mirror is only considered to determine size (aperture area) of the Scheffler reflector.

6. Tracking System

Since the speciality of Scheffler reflector is flexible surface curvature and a nonmoving focal area. Their use is now becoming increasingly popular in many parts of the world, especially in India. Almost all concentrators have a

rigid structure and the focus, the hot area where all light is concentrated, moves along with the direction of the sun. This makes its use a little bit impractical.

This is a paraboloidal mirror which is rotated about axes that pass through its centre of mass, but this does not coincide with the focus, which is outside the dish. If the reflector were a rigid paraboloid, the focus would move as the dish turns. To avoid this, the reflector is made flexible, so it is bents as it rotates so as to keep the focus stationary. Ideally, the reflector would be exactly paraboloidal at all times. In practice, this cannot be achieved exactly, so the Scheffler reflector is not suitable for purposes that require high accuracy.

6.1. Stopping the Sun

The sun gives us the impression of movement basically because the earth is revolving under our feet. One way to stop moving while rotating is to locate yourself in the center or axis of the rotation. Imagine a carousel. When you go to its center, you will still rotate, but will not move sideways any longer. The same way, the hot focus of the Scheffler Reflector is placed in the axis of rotation of the reflector. Thus it remains in a fixed place, giving maximum convenience.

6.2. Moving with the Sun

Just as the earth spins around an axis through the North Pole and the South Pole, the Scheffler Reflector spins around an axis parallel to that, just in the opposite direction. (It counteracts the earth's rotation, cancel it out.)

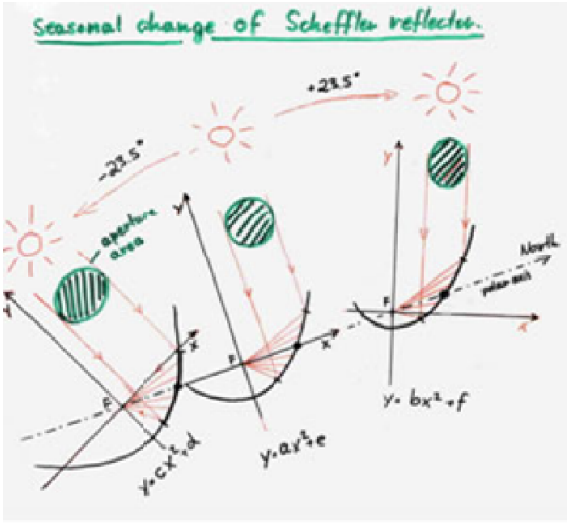
This is called polar mounting or mounting on a polar axis. The speed is one revolution per day, or, better, half a revolution in half a day, since we do not use at night. This way the reflector keeps facing the sun in a constant manner. The constant speed is controlled with mechanical clockwork. For practical reasons, the shape of the reflector is such that the hot focus is outside of the reflector, either on the north side or the south side. This way the hot focus can be even inside a building while the reflector remains outside.

6.3. Bending and Flexing, the Most Unique Feature of the Scheffler Reflectors

This is the most important point of the design of the Scheffler reflector, and is normally completely overlooked by people who see the reflector. In winter, the sun is low above the horizon, while in summer it moves high up into the sky. Under these changing conditions, having a different angle of the sunlight every day, it is difficult to maintain a small and hot focus in a fixed place during all the four seasons. The design of the Scheffler Reflectors provides the only widespread solution to this demanding situation. First it sounds almost unbelievable, but the reflector is made to change the shape of its entire surface to adapt itself to the different angles of the sunlight.

This way, a small and hot focus is achieved during all seasons. This sounds very complicated to make and to handle, but it turns out not to be so.

If you take a round or elliptical piece of orange peel and slightly squeeze it in your hand, you get a similar change of shape as it is required for the reflector. When you squeeze it, in one direction it will become more curved, while in the other direction it flattens out a bit. When you pull it apart instead, it will flatten out in this direction and curve in the other one. This gives you the basic idea on what type of shape change is required for the reflector to achieve a small focus at all seasons. For the real reflector all these shapes are of course calculated first. A scientific pocket calculator and your school math are sufficient to do this job. It's all based on the equations of a parabola and straight lines and calculating their intersection points.



Different parabolas focus the sunlight at different seasons. The incident light has to be parallel to their y-axis. Note the seasonal change in the aperture area, focus "F" and the center of the Scheffler reflector (black dot) remain stationary

It also uses the fact that whenever you cut a paraboloid with a plane, you get an ellipse; in school we used to learn this only for a cone. That is why the Scheffler reflectors have this typical elliptical shape.

The small straight section of the frame near the focus improves the flexing behavior in that section. This is found by trial and error method. Reflectors like the SK-14 (used for cooking or, steam generation) are circular. This is because their plane of cutting is perpendicular to the paraboloid. In that special case the short and the long diameters of the ellipse become of the same length and we get a circle. After a lot of observation done on Scheffler reflector it is found that five points are sufficient to support the reflector frame. And, very important, only two of them needed to be adjusted in order to create all different shapes required during the whole year. These two are adjusted manually after every few days, just pushing or pulling them until all light enters the hot focus again properly.

It is very important to keep the number of adjustments to this minimum; otherwise it is felt that handling would be too cumbersome for the user. Actually a third adjustment in the center of the dish would have been necessary, but after studying the geometry for some time, it is found that it could be designed this adjustment as an automatic lever. The lever pushes the center of the reflector forward or retracts it automatically when the reflector is set for the seasonally lower or higher sun. At that time, the angle of the reflector towards its mounting along the polar axis changes, and the lever is activated. The whole structure is well balanced and easy to turn. It is made from light iron tubes and bars, which are softer in the places which require more

bending (like near the focus) and stiffer where less bending is appropriate (the areas far from the focus).



Fig: 3. Automatic tracking Stand for small Scheffler reflector



Fig: 4. Crematorium tracking stand aligned with back crane and reflector frame

The power output varies with the season (Fig: 2). The Sun which shines more from the front into the reflector sees a larger reflector (large aperture), and thus more power is collected. In the same way, a sun shining more from behind sees a smaller reflector and less power is collected. A 2.7 m² reflector can typically bring 1.2 lts of water to boiling point within 10 minutes. The circle (see figure 5) at the center highlights the position of the lever for the seasonal shape change.



Manual changing of length of the reflector's rear support for seasonal adjustment

7. Application

Parabolic Scheffler Reflectors can provide (you with) high temperature heat. So it can be used besides solar crematorium, for all types of cooking, steam generation and many other applications.

8. Conclusion

In conclusion, it is established that a well-designed and maintained system is capable of solar cremation. Utmost care should be taken in maintaining such a system and operating at appropriate weather conditions. It is finally recommended that such systems should be highly promoted to conserve energy and foster a cleaner environment.

References

[1] J. P. Kesari, Krishen, P B Sharma, Solar Power is a Panacea for Changing Rural India, The role of CSP under Indo-Japan Collaboration, 2nd International Symposium –collaborative research project of CSP for India and Japan, 2012, Tokyo Institute of Technology, Tokyo, Japan

[2] J. P. Kesari, P. B. Sharma, Empowering India with Solar Energy Technology: A Roadmap at International Conference on Climate Change and Sustainable management of rural Resources, 2012, ITM University Gwalior

[3] J. P. Kesari, Jaspreet Singh, Sushant Kr. Singh, Rohit Gupta, P B Sharma, Development of Solar Electric Hybrid Vehicle, paper accepted for publication in SAE International, 2012, SIIMC

[4] Report on Solar Radiant energy Over India, India Meteorological Department, Ministry of Earth Sciences, New Delhi, 2009

[5] R. Patil, et al.: Experimental Analysis of Scheffler Reflector Water Heater Thermal Science, 2011, 15(3), 599-604

[6] M. Reuss, Solar District Heating in Germany – Findings and Prospects, Proceedings of the ISES Solar World Congress, 2011, Kassel, Germany.

[7] http://www.hcasia.safan.com/mag/hcajanmar13/r06.pdf

[8] Solar Fix Focus Reflectors; Projects; Technical explanations: www.solare-bruecke.org

[9] www.globosol.ch/gs/.../Report_08_Scheffler_Solar_Crematorium1.p.

International Journal of Electronic and Electrical Engineering.
ISSN 0974-2174, Volume 7, Number 3 (2014), pp. 287-292
© International Research Publication House
http://www.irphouse.com

Synthesis of Nano-structured p-type Higher Manganese Silicide

Govind Ram Gurjar[1], Purnima Swarup Khare[1], Saravanan Muthiah[2,3], B.D. Pathak[3] and Ajay Dhar[2]

[1]Department of Nanotechnology, Rajiv Gandhi Proudhyogiki Vishwavidhyalaya, Bhopal-462001
[2]Materials Physics & Engineering Division, CSIR-National Physical Laboratory, New Delhi
[3]Department of Mechanical Engineering, Delhi Technological University, Delhi-110042
E-mail: msaravanan04@gmail.com

Abstract

The abundance and economic route synthesis materials are excellent potential thermoelectric material and such type of materials have much attention compared to other thermoelectric materials. The higher manganese silicide (HMS) is a best thermoelectric material in view of its abundance, non-toxic and chemical stability. To increase the figure-of-merit of such useful higher manganese silicide, we adopt nano-structuring approach which involves large interfaces between the nano-grained structures, significantly lower the thermal conductivity. High purity Mn (99.95 %) powders, Si (99.95 %) powders were weighed and mixed in high energy ball mill. The mixed powders were vacuum sealed in quartz tube and kept in furnace at 900 K for 48 hours. Then, the powders were milled in high energy ball mill with 15:1 ball to powder ratio for 50 hours. The stainless steel jars and bowl is used for this purpose and milling is carried out at argon atmosphere. The milled powders were synthesized via rapid sintering process employing spark plasma sintering (SPS). In the present study, we report the synthesis of nano-structured higher manganese silicide employing ball milling followed by SPS and its micro-structural features.

Keywords: Nanomaterials, Higher manganese silicide, Spark plasma sintering.

1. Introduction

Thermoelectric technology is a solid state energy conversion technology and best for both ways of, heat to be converted into electricity and electricity to be converted into refrigeration [1-7]. The efficiency of a thermoelectric material is determined by the dimensionless figure-of-merit, $ZT = \alpha^2\sigma/\kappa$, where α is the Seebeck coefficient, σ is the electrical conductivity, κ is the thermal conductivity, and T is the temperature. To maximize *ZT*, α & σ must be large and κ must be small. Maximizing *ZT* is a challenging task, as optimizing one of this physical parameter affects the other. Nanotechnology provides the solution of large phonon scattering without the interruption of carrier flow across the matrix. Spark plasma sintering (SPS) is the one of the most successful techniques for consolidation and sintering of nanostructured materials for obtaining near theoretical densification while retaining the nano-grained structure[8,9]. This technique works mainly based on the electric spark discharge, where a high energy pulse current momentarily generate spark plasma between the particles resulting in highly localized temperatures[10]. The rapid heating rates and shorter sintering cycles during SPS with simultaneous application of load avoids grain growth in nano-structured materials. In the present study, we report the synthesis of nano-structured p-type higher manganese silicide thermoelectric materials employing ball milling followed by spark plasma sintering technique.

2. Experiment Details

High purity Mn (99.95 %) powders, Si (99.95 %) powders were weighed and mixed in high energy ball mill. The stainless steel jars and bowl is used for this purpose and milling is carried out at argon atmosphere. The mixed powders were vacuum sealed in quartz tube and kept in furnace at 900 K for 48 hours. Then, the powders were milled in high energy ball mill with 15:1 ball to powder ratio for 50 hours. X-ray diffraction analysis was carried out using monochromatic Cu Kα radiation using RigaKu X-ray diffractometer. Crystallite size measurements were carried out using X-ray diffractometer and crystallite size was calculated using Debye-Scherrer's formula. The loading & unloading of powder materials handled in glove box (Mbraun Inert Gas System, GmBH, Germany) to minimize oxidation and other atmospheric contamination. The material is sintered by spark plasma sintering process, heated at 1173 K for 3 minutes at 60 MPa in a graphite die in vacuum. The surface morphology of sintered pellets was studied using field emission scanning electron microscope (SUPRA V40, Carl Zeiss, Germany).

3. Results & Discussions

Fig. 1a & b shows the XRD patterns of vacuum sealed followed by furnace reacted HMS powders and 50 hours milled HMS powders respectively. The XRD peak profile shown in Fig. 1(d) indicates an increase in peak broadening with a sharp decrease in peak intensity after 50 h of ball milling, due to the formation of nanostructure and the generation of crystalline defects created by impact and shear forces of stainless steel

jars & balls. The average crystallite size of 50 hours milled powder was found to be ~25 nm, from ~50 nm initial HMS powder. Ball milled powders were subsequently consolidated and sintered employing SPS technique (Fig. 2), which resulted nano-structured fully dense HMS pellet.

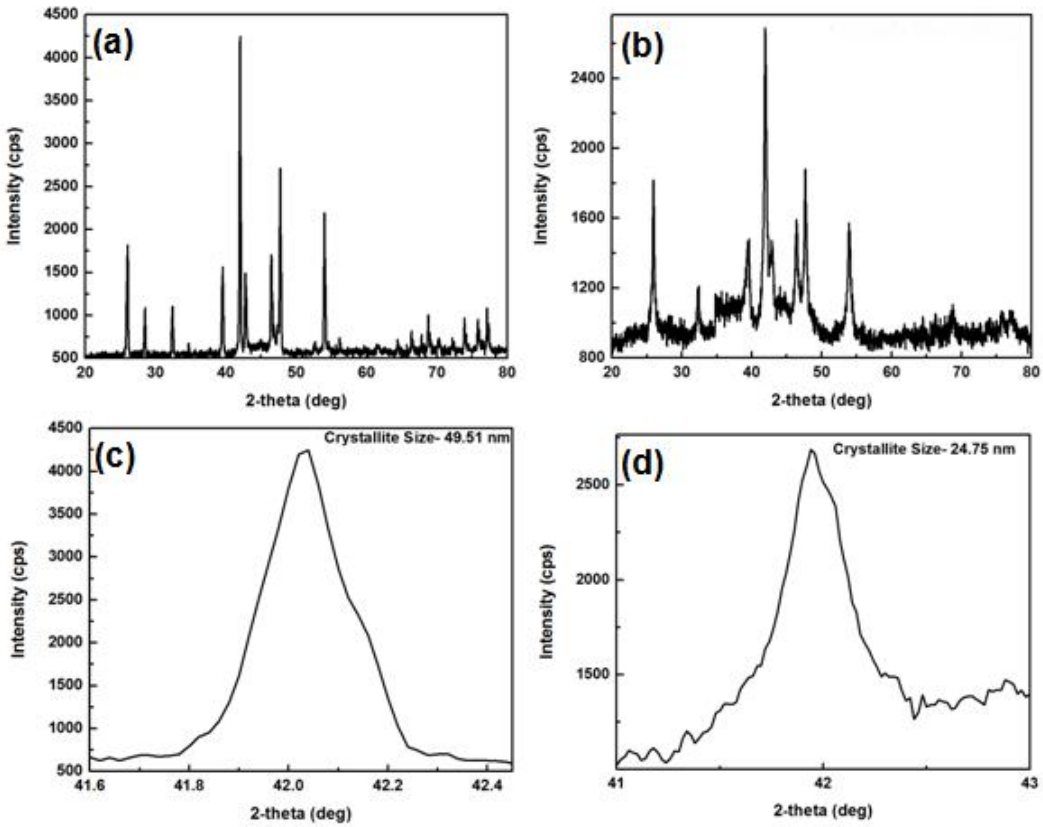


Fig. 1: XRD patterns of HMS: (a) & (c) Vacuum sealed followed by furnace reaction, (b) & (d) ball milled after 50 hours



Fig. 2: Spark Plasma Sintering Machine.

Fig. 3 shows the electron microscopy images of spark plasma sintered HMS pellets (a) after Vacuum sealed followed by furnace reaction, (b) after 50 hours of ball milled. The surface morphology of the balled milled HMS pellets shows evidence of sub-grains and nano-grains with non uniform grain boundaries. The microstructure of vaccum sealed followed by furnace reacted HMS pellet has no evidence of distinct grains with grain boundaries.

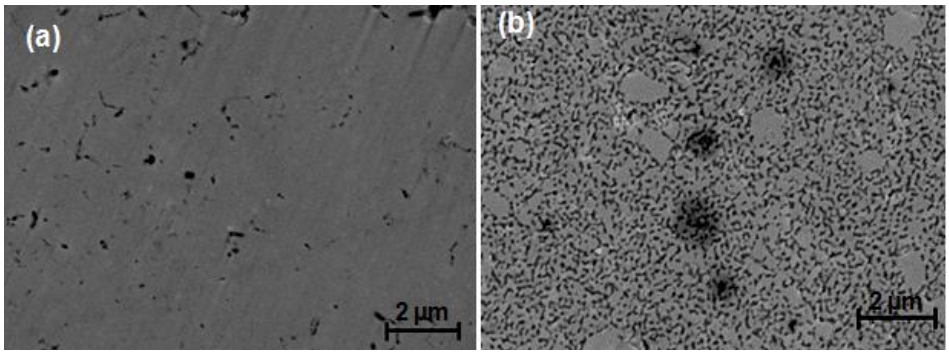


Fig. 3: SEM images of SPSed HMS pellet (a) Vacuum sealed followed by furnace reaction, (b) ball milled after 50 hours.

However, furnace reacted SPSed HMS pellet shows the evidence of second phases at sub-micron level. The present study revealed that ball milled followed by SPS technique promoted the formation of ultra-fine grains accompanied with non-uniform grain boundaries. From the micro-structural analysis (Fig. 3b), it can be inferred that SPS technique retain the nanoscale features of the p-type higher manganese silicides with near theoretical density. The anticipated lower thermal conductivity could be achieved by these types of microstructures. However, the obstacle of carrier/hole movement around the grain boundaries should be tuned for practical applications.

4. Conclusions

To summarize, we synthesized the nano-structured p-type higher manganese silicide thermoelectric material employing ball milling followed by spark plasma sintering technique. The average crystallite size ~ 25 nm has been achieved after 50 hours of ball milling. SPS synthesized Higher Manganese Silicide material shows the evidence of sub-grains and nano-grains with non uniform grain boundaries. These micro-structural features would enhance the thermoelectric properties of p-type TE material. The transport properties measurement of these nano-structured HMS pellet are the future avenues.

5. Acknowledgements

The authors thank the Director, CSIR-National Physical Laboratory, New Delhi, for the encouragement of this work. The technical support rendered by Thermoelectrics group, CSIR-NPL is gratefully acknowledged.

References

[1] Vining C B. CRC Handbook of Thermoelectrics, CRC Press, Boca Raton, Fla, USA, 1995.
[2] Ioffe A F. Semiconductor Thermoelements and Thermoelectric Cooling (Inforsearch, London, 1957).
[3] Wood C. Rep. Prog. Phys. 1988; 51: 459.
[4] Snyder G J and Toberer E S. Nat. Mater. 2008; 7:105
[5] Kraemer D, Poudel B, Feng H P, Caylor J C, Yu B, Yan X, Ma Y, Wang X, Wang D, Muto A, McEnaney K, Chiesa M, Ren Z, and Chen G. Nat. Mater. 2011; 10:532
[6] Pulikkotil J J, Singh D J, Auluck S, Saravanan M, Misra D K, Dhar A, and Budhani R C, Phys. Rev. 2012; B86: 155204
[7] Muthiah S, Pulikkotil J, Srivastava A K, Kumar A, Pathak B D, Dhar A, and Budhani R C, Appl. Phys. Lett.2013;103: 053901 .
[8] Roberto Orru, Roberta Licheri, Antonio Mario Locci, Alberto Cincotti, Giacomo Cao, Materials Science and Engineering R. 2003; 63:127- 288.
[9] Guo-Dong Zhan, Joshua Kuntz, Julin Wan, Javier Garay, Amiya K Mukherjee, Scripta Materialia. 2002; 47:737- 741.
[10] Hansang Kwon, Mehdi Estili, Kenta Takagi, Takamichi Miyazaki, Akira Kawasaki, Carbon. 2009; 47: 570-577.

Volume 2, Issue 3 (2014) 568-573 ISSN 2347 - 3258
International Journal of Advance Research and Innovation

Thermodynamic analysis of a Solar Thermal Syphon Pump

Kaushalendra K. Dubey [*, a], R. S. Mishra [a], Gopal P. Sinha [b]
[a] Department of Industrial & Automobile Engineering, Delhi Technological University, New Delhi, India
[b] Department of Mechanical Engineering, Sharda University, Gr. Noida, Uttar Pradesh, India

Article Info

Article history:
Received 12 July 2014
Received in revised form
2 August 2014
Accepted 30 August 2014
Available online 15 September 2014

Keywords

Solar Thermal Energy,
Siphon Pump,
Overall Efficiency,
Exergetic Efficiency

Abstract

This paper describes the idea of the development of a solar thermal energy driven pump for lifting of ground water for irrigation as well as for meeting urban supply system. The principles are equally applicable for lifting any liquid, the head being dependent on density of the liquid. This has the potential of saving over 93billion kWh of electrical energy and 3.3 billion litres of diesel (fossil fuel) per year, for India. The invention has been patented. The most attractive feature of the pump is the absence of any moving part, which makes it almost maintenance-free. Syphon action created by water vapour picked-up from the source, lifts the water from the reservoir through the delivery head. This is being demonstrated for the first time. The efficiency of the entire system is also high on account of no moving parts. Solar thermal energy is used to create a pressure higher than the atmospheric pressure, over the surface of liquid to be pumped to height H. The pressure lifts the liquid through a tube dipped below its surface and delivers to head H, determined by additional pressure created through thermal energy and the mass-density of the liquid.

Nomenclature

Aa = aperture area of PTC in m^2
Sc = solar constant in KW/m^2
Pc = pressure created by solar energy in Pascal,
P_A = Atmospheric pressure in Pascal
Υ = Mass density of liquid in kg /m^3.
g = acceleration due to gravity in m/s^2.
h = Enthalpy of steam.
H = Discharge height.
m_w = mass flow rate of water in m^3/s.
m_s = mass flow of steam in m^3/s.
V = flow velocity of water in m/s
Hs = friction loss in pipe.
ϕ = Latitude angle of location where system is installed in degree
β = Inclination angle of PTC system from horizontal in degree.
r_r = Rim Radius in meter.
ϕ_r = Rim Angle in degree
f = Focal Distance in meter.
h_p = Parabolic Height in meter.
D = Receiver or Boiler Diameter in meter.
C_R = Concentration Ratio
Θ = Incidence Angle in degree.
ω = Hour angle
γ = System Azimuth angle in degree
δ = Solar Incidence angle in degree.
Ψ = Flow exergy of fluid.
$\tau\alpha$ = Effective Transmission.
Ib = SolarRadiation.(W/m^2)
n = Total no of day in month measured from 1st January.
$\eta_{opto\text{-}thermal}$ = Opto-Thermal efficiency of Siphon system
Rk = Thermal Resistance of Receiver or Boiler Tube
Acond = Effective area of conduction in m^2
ϵr = Non selective absorber parameter.
Qgen = Heat generated from PTC.
Qreq = Required Heat for steam generation.
$\eta_{thermo\text{-}siphon}$ = Thermal Efficiency of system.
ηo = Overall Efficiency.
η_{SPV} =Solar Photovoltaic panel Efficiency.
η_{pump} = Irrigation pump Efficiency.
η_{CC} = Charge-Controller Efficiency.
η_B = Battery Efficiency.
l = Length
b = Width
t = Thickness
PTC=Parabolic Through Collector.
STSP= Solar Thermal Siphon Pump.
SPVP= Solar Photovoltaic Pump System.

Corresponding Author,
E-mail address: Professor_rsmishra@yahoo.co.in
All rights reserved: http://www.ijari.org

1. Introduction

Most of the developing countries have large needs of irrigation for meeting their agricultural requirements for food-security. The drinking water requirement also necessitates lifting of ground water to a height ranging from 50 to 200 feet. This requires huge amount of energy which is currently supplied through electricity and fossil fuel based engines. For a country like India the energy consumed for lift irrigation has been 93225.28MU, (in the year 2011), 1MU= 1M kWhr [6].In most of the cases the developing countries are endowed with rich solar energy. Some of it has been used for lift irrigation using photovoltaic panels electrically coupled to a conventional motor pump system, or Stirling cycle based engine coupled through a conventional pump. The potential number of SPV pumps is estimated at 70 million, with extending irrigation support to untapped markets [7]. This work reports the use of direct solar thermal energy for creating pumping action. The uniqueness of this development is that the pumping action requires no moving parts-reciprocating, rotating or expander action. Therefore there is no possibility of wear and tear or lubrication requirement or loss of energy due to friction between moving parts. Siphon action created by water vapour picked-up from the source, lifts the water from the reservoir through the delivery head. This is being

demonstrated for the first time. The efficiency of the entire system is also high on account of no moving parts. The flow chart in fig-1 summarises various attempts of using solar energy for pumping action under three broad heads- (i) through generation of electrical energy which is used to drive a conventional motor coupled to rotary or reciprocating pump, (ii) thermal engine using solar energy driving a conventional pump and (iii) utilisation of solar energy for thermo siphon action. An excellent review of the development of solar energy based pumps have been carried out by Y.Wong et al [11].The proposed thermo-siphon pump is a high pressure steam forced pump where there is no limitation of a suction head of less than 34 feet of water, the delivery head is unlimited based on the concentration of solar energy and the aperture area requirement of the solar collector has been worked out in subsequent paragraphs.

A model has been fabricated for proving the concept. This model demonstrates lifting of water through a head of nearly 5 to 10 feet Fig 3, shows a sketch of the parabolic trough collector (PTC) used for concentrating the solar thermal energy.

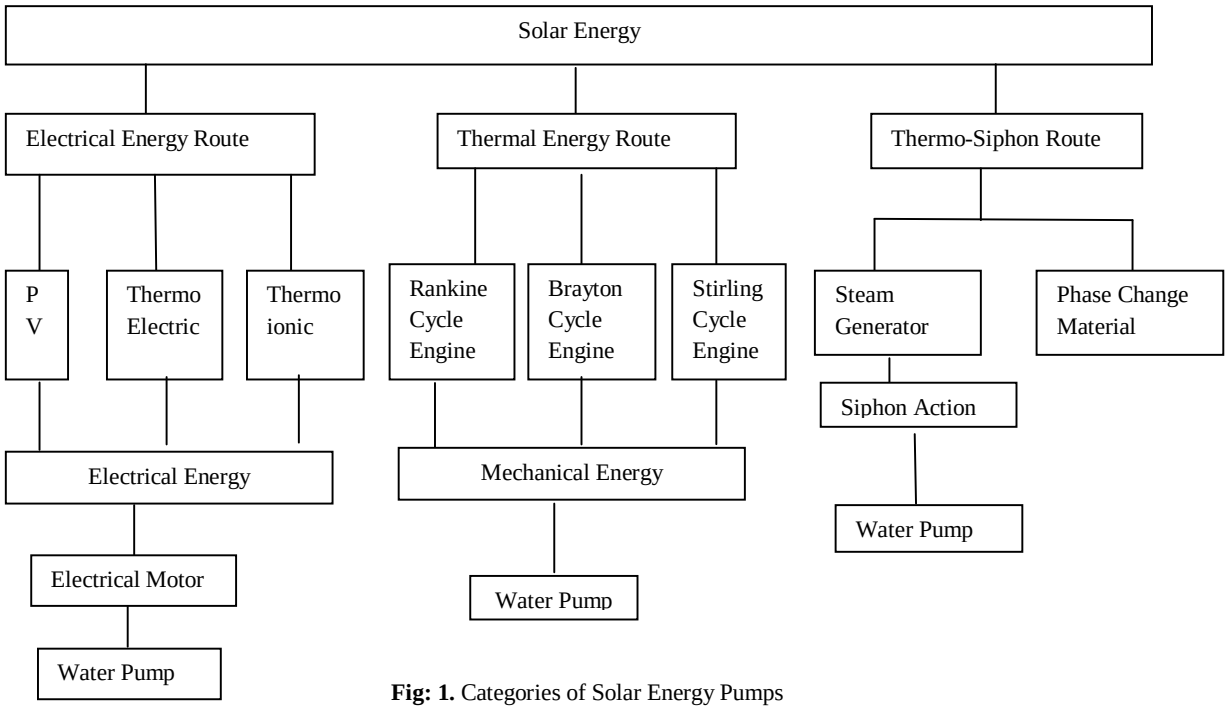


Fig: 1. Categories of Solar Energy Pumps

In most of the developing countries are endowed with rich solar energy. Some of it has been used for lift irrigation using photovoltaic panels electrically coupled to a conventional pump, or Stirling cycle based engine coupled through a conventional pump. The potential number of SPV pumps is estimated at 70 million, with extending irrigation support to untapped markets [7]. Total cost (before subsidy) for installation and commissioning of SPV water pump system varies from Rs. 190,000 to 290,000 or even Rs. 450,000/-[8][9].Capital cost of a 1.8 kWp solar PV pump is about Rs. 0.3 million. The payback period of solar PV pump (without subsidy) replacing a diesel pump is about 9 years (at a cost of diesel is Rs. 32/litre) [10].Purohit evaluated the financial attractiveness of different renewable energy technologies for irrigation water pumping in India. He calculated the following unit costs for water for SVP pumping systems [10].Diesel engine pump sets and Photovoltaic based electric motor pump sets capacities given in Table-1.

Table: 1. SPV based and diesel base irrigation pumping capacities in India [6]

Technology	**Capacity**	**Unit**	**Unit cost for water (without capital subsidy) Rs./m³**	**Unit cost for water (with capital subsidy for S) Rs./m³**
1. SPV pump				
PV pump (surface)	900	Wp	0.85	0.37
PV pump (surface)	1800	Wp	0.83	0.34
PV pump (submersible)	1200	Wp	1.25	0.77
PV pump (submersible)	1680	Wp	1.13	0.65
PV pump (submersible)	1800	Wp	1.17	0.69

2. Electric motor pump				
(Surface)	5	hp	0.38	0.38
(Surface)	10	hp	0.30	0.30
(Submersible)	5	hp	0.39	0.39
(Submersible)	10	hp	0.31	0.31
3. Diesel engine pump set				
(Surface)	5	hp	1.13	1.13
(Submersible)	10	hp	1.02	1.02
Technology	**Capacity**	**Unit**	**Unit cost for water (without capital subsidy) Rs./m³**	**unit cost for water (with capital subsidy for S) Rs./m³**
1. SPV pump				
PV pump (surface)	900	Wp	0.85	0.37

In this context the current work reports about using direct solar thermal energy for creating pumping action. The unique part of this development is that the pumping action requires no moving parts, reciprocating or rotating and therefore there is no possibility of wear and tear or lubrication requirement. A model has been fabricated for proving the concept as shown in Fig 1. This model demonstrates lifting of water through a head of nearly 5 to 10 feet.

2. Working of Solar Thermal Siphon Pump

Solar Thermal Siphon pumping system (STSP) may be used to lift water from the ground or any liquid to a height without using any moving mechanical-part by pressurized steam through siphon action. The steam is generated by solar energy concentrator on a tube filled with the liquid. The concentration of solar energy can be achieved by parabolic trough collector (PTC) / concave / plane mrors type solar concentrator or through Fresnel lenses based solar thermal system.

Water liquid enters into a boiler cell, through an inlet regulated by a float valve action, for maintaining a uniform level. Steam generated in the boiler flows through a perfectly insulated and sealed pipe into an enclosure connected to ground water to be pumped. The discharge pipe is dipped below the ground water. The pressurized steam lifts the water to the delivery head H, through a siphon action. The conversion of water in to steam at boiling temperature of water depends upon the thermal energy obtained from the area of PTC (Aperture Area of concentrator).The heat raise the temperature of boiler and water gets converts into steam. The water feeding pipe use some amount of steam pressure feeding water to the boiler [8]. Fig-2a and Fig-2b show the model and working set up of the thermo-syphon pump. Dimension of all parts of STSP listed in Table-2.

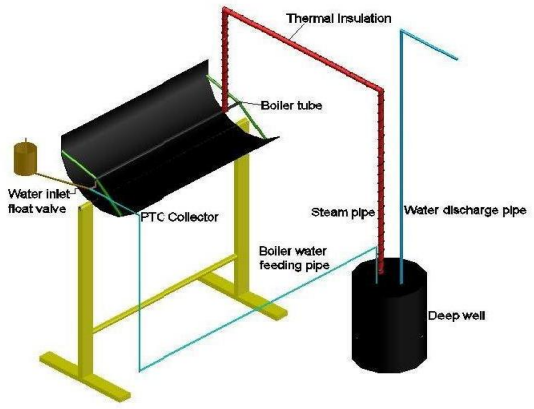


Fig: 2a. Schematic of Solar thermal Siphon Pump



Fig: 2b. Working set up of solar thermal Siphon Pump at Sharda Univ Greater Noida campus

3. Principles of the Solar Thermal Syphon System

The solar thermal siphon pump derives its pumping action by putting additional pressure on the surface of the liquid, to be lifted. This additional pressure is obtained using solar thermal energy in concentrated form.

The concentrated solar thermal energy obtained by a parabolic trough collector (PTC) is given by [2]

Q_{gen} = Aa Ib W ……. (1)

The useful solar gain by the collector = Qu = Aa (τα) Ib W

τα = Effective Transmission

The head of lifted water or liquid is given by

H = (Pc - P_A)/ βg meters .Where Pc is pressure created by solar energy in Pascal, P_A is Atmospheric pressure in Pascal, β is Mass density of liquid in kg /m^3 and g is acceleration due to gravity in m/s^2.

3.1 Collection and Concentration of Solar Thermal Energy using PTC.

For generating steam, whose pressure is used for pumping of liquid to a height, we require concentrated solar thermal energy for super heated high pressure steam at a high pressure. This is achieved by a PTC or a Fresnel lens or a combination of the two. The concentrated thermal energy obtained through PTC is given by Heat required for steam generation [4],

$Q_{reqired} = m_{water} [Cp_{water} (T_{boiling} - T_{ambient}) + LHwater] + m_{steam} [Cp_{steam} (T_{sup} - T_{boiling}) + LH_{vaporisation}]$ KJ ….. (2)

For system to work continuously

Qgen >. Qreq ……. (3)

Boiling Temperature of water for the exerting the required steam pressure ($T_{boiling}$) is directly taken from steam table corresponding to the pressure Pc. This heat can generate steam at a pressure Pc is given by

Pressure required on water table for achieving the discharge head

Pc = $10^5 + 10^4$ H Pa ……. (4)

This pressure on the surface of the liquid can lift it by 'H' meter through siphon action is given by

H = (Pc - Pa)/ βg meter ……. (5)

3.2 Estimation of specified head H and flow rate Q

Heat from PTC is mainly required to meet the heat loss occurring due to imperfect insulation and the temperature difference between the superheated steam and the ambient. It is given by,

Total energy in steam = Energy given to discharge

$m_s h = m_w g H + ½ m_w v^2 + hs$ ……. (6)

Conduction loss in pipe = Effective surface area for conduction (Acond) / thermal resistance (R_k). [1]

$[\frac{(Tr-Ta)}{Rk} \times \frac{Acond}{Aa}]$ ……. (7)

3.3 Design parameters of PTC.

Parabolic through collector (PTC) are preferred for solar steam generation because high temperature can be obtained without any degradation of collector efficiency. The specifications of PTC shown in figure-2 of PTC design for steam generation. All design calculations provide by equations below.

Projected area for heat require = Aperture area of PTC = Aa m^2

Solar Constant [2] = 1000W/m^2 (Standard for India)

For a designer (including losses), solar constant taken as = 550W/m^2.

Parabolic Aperture area of PTC = Aa m^2 = 550 W / Q_{gen}.

Solar radiation (Ib) = 750W/m^2. (Taken average value for month of April-May)

But area of PTC plate sheet = 1.5 × Aa m^2 (Assume).

Dimensions of PTC on the basis of aperture area, Aa = b × h

Rim Angle [5] = $\phi_r = Sin^{-1} (Aa / 2 r_r)$ ……. (8)

Focal Distance [5] = $f = \frac{Aa}{4 \tan\frac{\phi r}{2}}$ ……. (9)

Parabolic Height [5] = h_p = f

Receiver or Boiler Diameter [5] = D = $\sqrt{\frac{4}{1000\ \pi\ b}}$ m … (10)

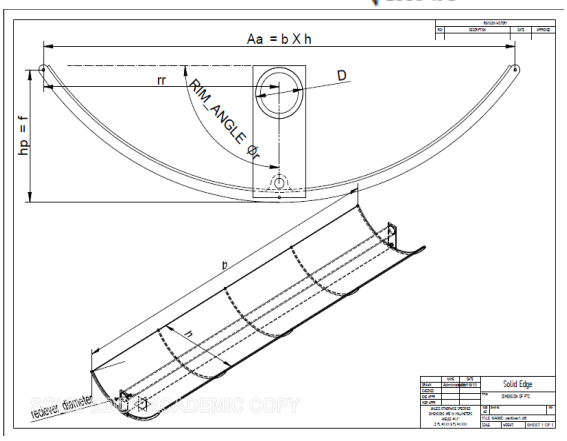


Fig: 3. Schematic of parabolic through collector.

Concentration Ratio [5] = $C_R = \frac{Aa-D}{\pi D}$ ……. (11)

Incidence Angle (Θ) [2] = Cos Θ = Sin ϕ (Sin δ * Cos β + Cos δ* Cos γ * Cos ω * Sin β) + Cos ϕ (Cos δ * Cos ω * Cosβ –Sin δ * Cos γ * Sin β) + Cos δ * Sin γ * Sin ω * Sin ……. (12)

ω = Hour angle [2] = (Solar Time – 12:00)15^0.

(Afternoon solar time taken as +ve hour angle, whereas forenoon solar time taken as –ve solar time.)

δ = Solar Incidence angle [2] = 23.45 × Sin $[\frac{360}{365}(n + 284)]$ ……. (13)

3.4 Dimensions of STSP parts

Table: 2. Dimensions of STSP parts

STSP Parts	Dimensions
Reflector	l = 2.44 m, b= 1.25 m, t= 0.4 m. Aperture Area = 2.44 m^2
G.I Sheet for reflector support.	l = 2.44 m, b= 1.25 m, t= 0.36 m.
Copper Water Tube	L = 2.44m,Diameter = 20mm, Volume = 7.6 ×10^{-5} m^3
PVC Steam Tube	Diameter =14mm, Thermally insulated with glass wool.
Supporting Iron Frame **Arc** **Rods** **Rivets** **Mounting Nut**	No. Of Arc = 5, No of Rods = 3 t = 3 mm, Arc length = 1.25 m t = 3mm, l = 2.44 m 10 (Aluminium with head), l = 10mm, diameter = 4mm. Diameter = 9mm (5mm from top and each side)
Iron Stand	l = 1.17 m, t = 5mm.

4. Efficiency involved

4.1 Opto-Thermal Efficiency ($\eta_{opto-thermal}$)

$\eta_{opto-thermal}$ =qu / Ib Aa = $\eta_O - \frac{1}{Ib}[\frac{(Tr-Ta)}{Rk} \times \frac{Acond}{Aa}] + \epsilon r [\frac{Tr4-Tc4}{CR}]$ ……..(14)

Rate of use full energy = $q_u = \eta o\ I_b\ Aa - U_L (Tr - Ta) Aa$ …….. (15)

Rk = Thermal Resistance of Receiver or Boiler Tube =

$$\frac{\text{Distence Travel by conductive heat in boiler tube or recevier } (x)}{\text{Thermal conductivity of recevier metal } (K) \times \text{Condution Area } (A)}$$

4.2 Thermal Efficiency ($\eta_{\text{thermo-syphon}}$)

$\eta_{\text{thermo-syphon}}$ or $\eta_I = Q_{required} / Q_{gen}$ … (16)

4.3 Over All Efficiency (ηo)

$\eta o = \eta_{\text{opto-thermal}} \times \eta_{\text{thermo-syphon}}$ … (17)

5. Exergy Balance of solar thermal syphon system

Exergy of a Flow Stream per unit mass

A flowing fluid has flow energy; that is the energy needed to maintain flow in a pipe or line;

$w_{flow} = Pv$ ……..…… (18)

The flow work is the boundary work done by a fluid on the fluid downstream. The exergy associated with flow energy can be written as

$\Psi_{flow} = PV – P0V = (P – P0) V$ ……..…….. (19)

The exergy of a flow stream can be found from:

The general energy and exergy balance can be expressed in the rate form [12]-

$\sum \dot{\Psi} in - \sum \dot{\Psi} out = \sum \dot{\Psi}$ dest ……..…….. (20)

$\Psi_{heat} - \Psi_{work} + \Psi_{mass\ in} - \Psi_{mass\ out} = \Psi_{Dest}$ …….. (21)

Using above equation 20 and 21 therate form of the general exergy balance can be expressed as follows:

$$\sum \left(1 - \frac{\dot{T}o}{Ts}\right) Qu - \dot{W} + \sum \Psi mass\ in - \sum \Psi\ mass\ out = \Psi_{D\ est}$$

…….. (22)

Where $\Psi_{in} = \dot{m}\ [((h_1 – h0) – T0\ (s_1 – s0) + \mathbf{V_1}^2/2 + gz_1)]$

…… (23)

$\psi_{out} = \dot{m}\ [((h_2 – h0) – T0(s_2 – s0) + \mathbf{V_2}^2/2 + gz_2)]$…..… (24)

Due to same elevation of inlet-outlet of flowing fluid = Z_1 = Z_2.

$$(1-\frac{To}{Ts})Q_u - \dot{m}[(h_{out} - h_{in}) - To\ (S_{out} - S_{in}) + (\frac{\mathbf{V2^2 - V1^2}}{2})] = \psi_{Dest}$$

…….. (25)

The change in the enthalpy and entropy of water in the copper water tube is expressed as

$\Delta h = h_{out} - h_{in}$ ……..…… (26)

$\Delta S = S_{out} - S_{in}$ ……..…… (27)

The exergy efficiency of a solar thermal siphon system can be calculated in terms of the net output exergy of the system or exergy destructions in the system.

$\psi_{Dest} = To\ (S_{out} - S_{in})$ ……..…… (28)

$$\eta_{II} = \frac{\dot{m}[(h\ out - h\ in) - To\ (S\ out - S\ in)]}{(1-\frac{To}{Ts})Qu}$$ ……..…….(29)

6. Estimation of STSP efficiency with Photovoltaic pump efficiency.

Efficiency of Solar Photovoltaic Pump (η_{SPVP})

$\eta_{SPVP} = \eta_{SPV} * \eta_B * \eta_{CC} * \eta_{pump}$ ……..…… (30)

$\eta_{SPV} = 15\%$

Above equations taken from ref no [2]

$\eta_{pump} = 50\%$

$\eta_{CC} = 90\%$

$\eta_B = 85\%$

Lead-acid batteries typically have columbic efficiency of 85% and energy efficiencies in order of 70 % [9]. Columbic efficiency is the ratio of number of charges that enter the battery during charging compared to the number that can be extracted from the battery during discharging [9].

η_{CC} depend on the input-output level of voltage-current. DC-AC conversion efficiency as 100% but practically it is not possible because some account of heat dissipated by the passive components. Therefore, there is no way to simulate 100% charge-controller efficiency. We can assume more than 90%.Farm irrigation pumping is around 70 to 80% of total farm electricity usage [10].

$\eta_{overall\ SPVP} = 15\% * 85\% * 90\% * 70\% = 8.08\ \%$

7. Results and Discussion.

An experiment with the fabricated model was carried out in the month of April-May. In a mid day when the sun rays were focused on the copper boiler, the pump lifted the water from the down reservoir and sprayed a stream up to a required height. The concept was clearly demonstrated.

The result of energy and exergy analysis of STSP shown in table no 3:

Table: 3. STSP Efficiency results

System/Efficiency (%) ↓	$\eta_{optical}$ →	$\eta_{thermal}$ or η_I	$\eta_{overall} = \eta_{optical} \times \eta_{thermal}$	$\eta_{exrgetic}$ or η_{II}
STSP	75	46.6	34.9	10.1

8. Conclusion

It is possible to use direct solar thermal energy for pumping action instead of going through the photovoltaic electrical route, where the overall efficiency of SPV based pumping system comes to 8% against 35-36% of solar thermal siphon pump system. Thus there is a gain of almost 450% in the utilisation of solar energy. Apart from this significant gain in utilisation of solar energy, there is further indirect savings in energy required for production of solar photovoltaic panel. STSP exergetic efficiency is more than $\eta_{overall\ SPVP}$, it conducted that the proposed solar thermal siphon pump would be a significant environment friendly attempt for harnessing solar energy compare to photovoltaic based solar system. The unique part of this development is that the solar thermal siphon pump has no moving parts and it is thus maintenance free.

References

[1] Frank Kreith, Jan F. Kreider, McGraw-Hill, Principles of solar engineering, 1981

[2] S. P. Sukhatme, Solar Energy: Principles of Thermal Collection and Storage, Tata McGraw-Hill, 2008

[3] John Wiley & Sons, Introduction to Fluid Mechanics by Fox & McDonald, 2008

[4] P. K. Nag, Basic and applied Thermodynamics, Tata McGraw-Hill, 2004

[5] S. Kalogirou, S. Lloyd, Use of solar parabolic trough collectors for hot water production in Cyprus. A feasibility study. Renewable Energy 2(2): 117-124. 1992

[6] State-wise Electricity Consumption & Conservation Potential in India. Bureau of Energy Efficiency (BEE) Ministry of Power, Government of India, Report, 2009, www.emtindia.net/eca2009/14Dec2009/CombinedSummaryReport.pdf
[7] HWWI, CDM potential of SPV pumps India. http://www.hwwi.org/uploads/tx_wilpubdb/HWWI_Research_Paper_4.pdf, 2005
[8] Gopal P Sinha, Kaushalendra Kr Dubey, Solar Thermal Siphon pump System for Irrigation, India Patent, Patent Docket No- 9684, Application No-1626/DEL/2013,Reference No- E-2/5773/2013-DEL, E-3/5571/2013-DEL, E-5/5240/2013-DEL, Date of Patent filied-30/05/2013.
[9] Cral John Rydh, Bjorn A. Sanden, Energy Analysis of batteries in photovoltaic syste,Part-ll, Energy return factors and overall efficiencies, Journal of energy conversion and management, Elsevier, 46, 2005, 1980-2000
[10] Jamse Curaan, Agricultural Resource Management. Irrigation Pump Efficiency, www.farmpoint.tas.gov.au.
[11] Y. W. Wong, K. Sumathy, Solar thermal water pumping systems-a review Department of Mechanical Engineering\ University of Hong Kong\ Hong Kong, 1998
[12] Ebru Kavak Akpinar, Fatih Kocyigit, Energy and exergy analysis of a new flat-plate solar air heater having different obstacles on absorber plates, Journal of Applied Energy, Elsevier, 87, 2010, 3438-3450

WIRELESS CONTROL OF DC GEARED MOTOR AND HOME APPLIANCES FROM COMPUTER USING MICROCONTROLLER

J.N.Rai[1], Rohit Devdhar[2], Utkarsh Sareen[3]

[1, 2, 3] *Department Of Electrical Engineering, Delhi Technological University, (India)*

ABSTRACT

In the present article we have focused for the development of working model on wireless control of dc geared motor and home appliances from computer using AT MEGA 16 microcontroller. Microcontroller is connected to computer using RS232 protocol. A USB to serial convertor (DB9 connector) is used for the connection between computer port and MAX232 [1].COUNTER0 of the microcontroller is used to generate PWM signal. Motor is connected in CHOPPER TYPE-A configuration. Duty cycle of chopper is varied by varying the PWM of the counter generated wave. The speed of the dc geared motor is directly proportional to the duty cycle. Thus by varying duty cycle speed can be varied. PWM generation is controlled by the keys of the computer. For home automation by pressing the key on keyboard of a computer relay status is changed from NO to NC or vice versa. Relays control the home appliances. Through programming it is possible to control both dc geared motor and home appliances simultaneously. Further the attempt has been made to develop this control into a cost effective model.

Keywords: Chopper, Counters, Dutycycle, PWM, Uart.

1. INTRODUCTION

Now a day's every system is automated in order to face new challenges in the present day situation. Automated systems have lessmanual operations, so that the flexibility, reliabilities are high and accurate. Hence every field prefers automation and wireless control systems. Wireless home automation has several advantages over control of home appliances through wire and two-way switches. If we want to control the appliances at a distance of some meter to several kilometres then cost of wire and losses increases with increase in length. If wireless home automation is used in place of conventional methods for the control of home appliances then cost of wire and losses can be reduced. Home automation is necessary to control home appliances wirelessly and accurately. By using the techniques illustrated in this project we can control the appliances wirelessly and the appliances of a group of network can be controlled. Motion control plays a vital role in industrial automation. Different types of motors AC, DC, SERVO or stepper are used depending upon the application. Out of these,Dc geared motors are widely used because they are easily controllable. Among the different control methods for controlling the speed of Dc geared motor. Armature voltage control method using pulse width modulation (PWM) is best one [2]. The

IJATES

speed of Dc geared motor is directly proportional to the voltage applied to its armature winding. The average voltage across the armature can be controlled by controlling the pulse width [3]. The motor is connected in chopper type-A configuration. The output voltage is controlled by varying the duty cycle which is controlled through pulse width modulation.

2. EXPERIMENT COMPONENT

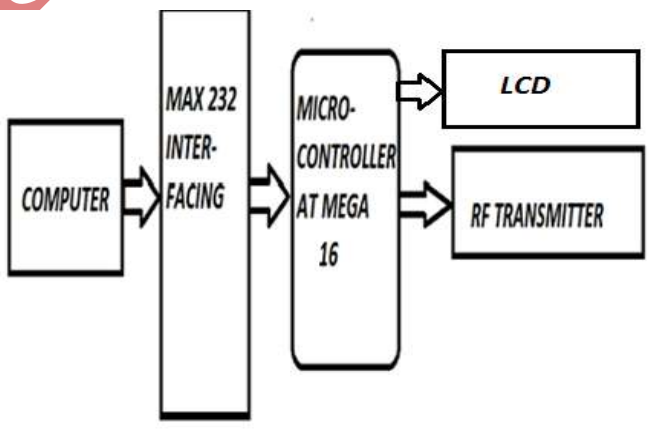
2.1 HARDWARE

1. AT MEGA16 MICROCONTROLLER.
2. COMPUTER.
3. DB9 CONNECTOR
4. MAX232
5. RF MODULE
6. RELAY
7. ULN2803
8. LCD
9. OPTOCOUPLER 4N35
10. MOSFET
11. DC GEARED MOTOR
12. TRANSFORMER (230/12V)
13. IC 7805
14. IC 7812
15. RESISTORS
16. CAPACITORS
17. POTENTIOMETERS.

2.2 SOFTWARE

1. PROTEUS.
2. AVR DUDE
3. EMBEDDED C
4. AVR STUDIO

3. BLOCK DIAGRAM



IJATES

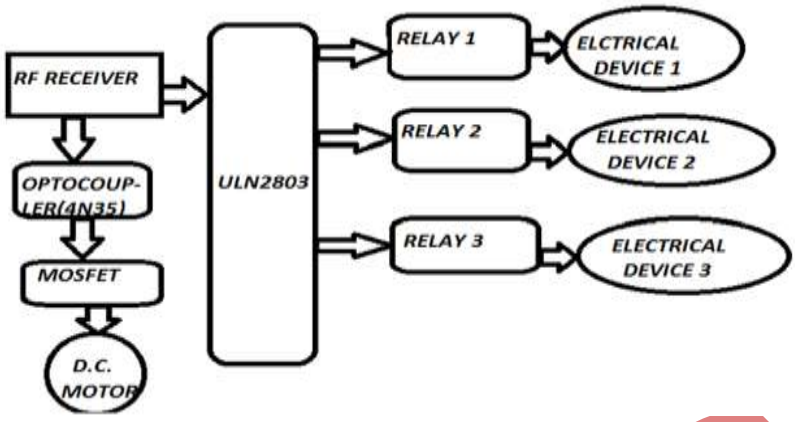


Fig.1 Block Diagram Of Hardware Module.

IV. HARDWARE DESCRIPTION

1.AT MEGA 16 MICROCONTROLLER: There is a whole wide range of microcontroller available in the market. But this particular project is developed using AVR series of microcontroller (ATMEGA16). Because of its inbuilt timer and counter qualities. PWM is generated through TIMER0/COUNTER0 of the microcontroller. [5]

2. DB9 CONNECTOR: It is 9 pin male/female connector. In DB9 9 represent total number of pins and D represents the two parallel rows of pins that are in the shape of D alphabet.

3.16*2 LCD: (16*2) have 16 columns and 2 rows. To show the device status whether the appliances are off or on and to show the dc geared motor speed lcd is used.Lcd may be used in 8-bit mode or 4-bit mode. By using 4-bit mode 4pins of the microcontroller can be saved. Therefore in this project 4-bit mode is used.

4. SPDT RELAY: To control the home appliances SPDT relay is used. The rating of relays are(250V, 10A) for a.c. supply. Relay are controlled by IC ULN2803 which provides 12V signal to relays.

5. ULN2803:The ULN2803A is a high-voltage, high-current Darlington transistor array. The device consists of eight npn Darlington pairs that feature high-voltage outputs with common-cathode clamp diodes for switching inductive loads. The collector-current rating of each Darlington pair is 500 mA.

6. OPTOCOUPLER (4N35): an opto-isolator, also called an optocoupler, photo coupler, or optical isolator, is a component that transfers electrical signals between two isolated circuits by using light. Opto-isolators prevent high voltage from affecting the system receiving the signal. Optocoupler withstand input-to-output voltages up to 3.5kVand speed of switching is 7us.

7. MAX232:The MAX232 is a dual driver/receiver that includes a capacitive voltage generator to supply TIA/EIA-232-F voltage levels from a single 5V supply. Each receiver converts TIA/EIA-232-F inputs to 5-V TTL/CMOS levels. These receivers have a typical threshold of 1.3 V, a typical hysteresis of 0.5 V, and can accept ±30-V inputs. Each driver converts TTL/CMOS input levels into TIA/EIA-232-F levels.

8. PMDC: A PMDC GEARED MOTOR of ratings(24V, 2A, 500RPM) is used in this project. Field excitation is fixed (due to permanent magnet) and the armature voltage is controlled by varying the duty cycle in chopper type A configuration.

9. RF MODULE (435Mz): An RF module (radio frequency module) is a usually small electronic circuit used to transmit and receive radio signals on a number of carrier frequencies. Data from the microcontroller is transmitted to receiving end via RF module.

10. TRANSISTOR (MJE3055T): In this project Transistor is used as a switch. When base signal is high (5V) then the transistor becomes ON otherwise it remains OFF.

11. POWER SUPLLY:

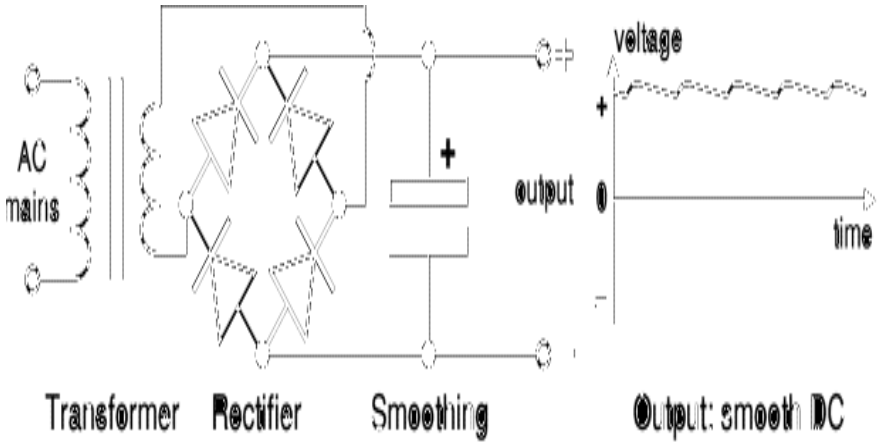


Fig.2 Circuit For Power Supply

V. SOFTWARE DESCRIPTION

1. AVR STUDIO4: This software is used to generate the hex file from programming. It provides a environment to write the program and generate the hex file.

2. X-CTU: this software is used to send data to microcontroller through the RS232 communication. We can also changethe Baud rate through this software.

3. ISIS PROFESSION 7(PROTEUS): Simulation is completed using proteus software.

4. AVRDUDE: It is used to burn program in the microcontroller.

VI. DESIGNING OF HARDWARE MODULE



Fig. 3 DC Geared Motor Connection Transistor And Optocoupler



Fig.4 Relay Connection with IC ULN2803 And RF Receiver.

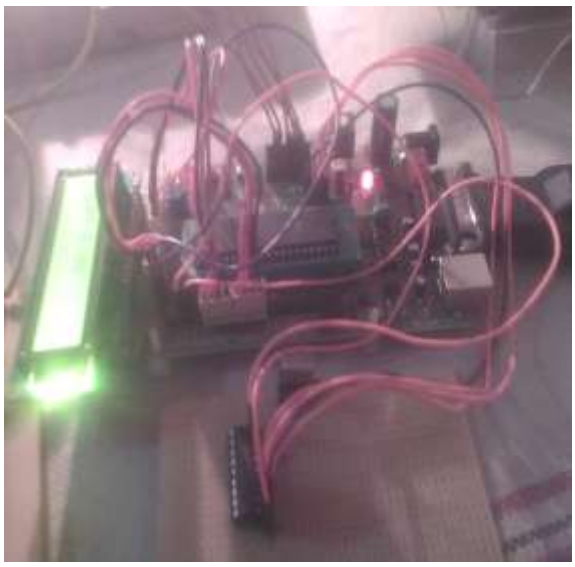


Fig.5 Microcontroller Connection With RF Receiver, LCD and DB9 Connector



Fig.6 View Of Complete Hardware Module

VII. SIMULATION DIAGRAM OF THE CIRCUIT

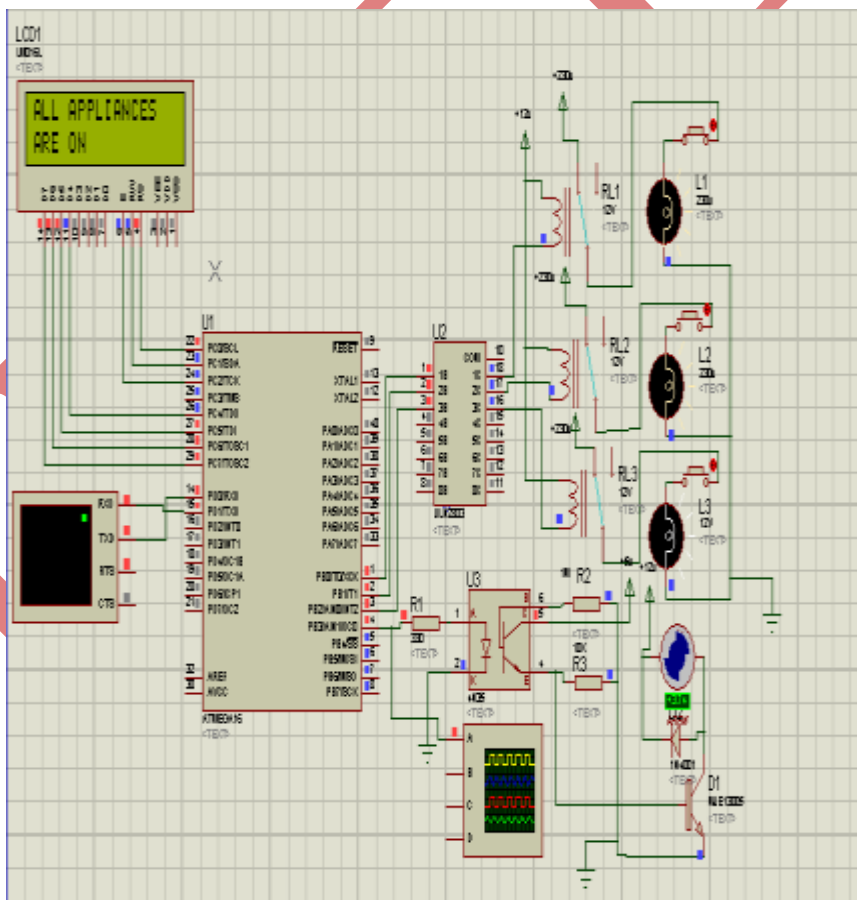


Fig.7 Simulation Diagram Showing All Appliances Are On

VIII. PROGRAM

8.1 LCD Operation

8.1.1 TO INITIALIZE THE LCD:

```
voidlcd_init();
{
// This function Initializes the lcd moduleand  must be called before calling lcd related functions Arguments:
}
```

8.1.2. TO SEND COMMAND TO LCD:

```
voidlcd_command(unsigned char);
{
// This function is used to send command to the lcd.
}
```

8.1.3. TO SEND DATA TO LCD:

```
voidlcd_data(unsigned char);
{
// This function is used to send data to lcd.
}
```

8.1.4. TO SEND STRINGS TO LCD:

```
voidlcd_string(unsigned char *str);
{
//this function is used to send string of words to lcd.
}
```

8.1.5. TO SEND A NUMBER TO LCD:

```
voidlcd_number(unsigned int);
{
// this function is used to send a number to lcd.
}
```

8.2 UART Operation

8.2.1 TO INITIALIZE THE UART:

```
voiduart_init();
{
```

//This function is used to initialize the uart. Baud rate is defined in this function by defining the UBRRH AND UBRRL registers. Receiving and Transmitting is enabled and mode of operation is also defined in this function. In this project we are using 8 Bit mode operation.

```
}
```

8.2.2 TO RECEIVE A CHARACTER THROUGH UART:

IJATES

```
unsigned char uart_rec();
```

8.2.3 TO SEND A CHARACTER:

```
voiduart_sendch(unsigned char data);
```

8.2.4 TO SEND A STRING:

```
voiduart_sendstr(char *send);
```

IX. MAIN PROGRAM

```
#include<avr/io.h>
#define F_CPU 1000000UL
#include<util/delay.h>
#define Baud_Rate 4800UL
#define ubbr_value ((F_CPU/(16UL*Baud_Rate)) - 1)
#include<avr/lcd.h>
#include<avr/uart.h>

int main()
{
TCCR0 |= (1<<WGM00)|(0<<WGM01)|(1<<COM01)|(1<<CS00)|(0<<CS01)|(1<<CS02)|(0<<COM00);
DDRB  =0xff;
DDRC=0xff;
unsigned char x;
unsignedint a=0;
DDRC = 0XFF;
lcd_init();
uart_init();

OCR0=0x00;

while(1)
{
x=uart_rec();

if((x=='a')||(x=='A'))
{
lcd_clear();
lcd_command(0x80);
lcd_string("RELAY 1 ON");
PORTB=0X01;
```

IJATES

```
}

if((x=='b')||(x=='B'))
{
lcd_clear();
lcd_command(0x80);
lcd_string("RELAY 2 ON");
PORTB=0X02;
}

if((x=='e')||(x=='E'))
{

if(a>=0xfa)
{
a=0xff;
lcd_clear();
lcd_command(0x80);
lcd_string("MOTOR IS RUNNING");
lcd_command(0xc0);
lcd_string("AT FULL SPEED");
}
else
{
a +=0x2a;
lcd_clear();
lcd_command(0x80);
lcd_string("MOTOR SPEED IS");
lcd_command(0xc0);
lcd_string("INCREASING");
}
OCR0=a;

}

return 0;
}
```

X. WORKING

IJATES

When a key is pressed by the operator on the computer keyboard then using the X-CTU or HYPERTERMINAL software, binary code corresponding to the key pressed can be send to microcontroller through USB to serial convertor and IC MAX-232. The output of MAX232 is connected to the microcontroller.

10.1 FOR APPLIANCES CONTROL

When a key is pressed then microcontroller compares the data received at the receiving pin to the condition given in the programming. On the basis of this condition microcontroller takes a decision. For example if a key 'a' is pressed the microcontroller enables the pin PB1. In this way microcontroller remains in the loop or it may do any other task (interrupt control). As soon as a key is pressed it compares it according to the programming and if the condition come out to be true then it give a high signal at PB1. The status of the microcontroller output can be transmitted through RF transmitter. RF receiver receives the signal and its output is connected to the ULN2803 which is further connected to the RELAY. IC ULN2803 outputis low when its input is high.One end of relay is connected to the power supply the second end is connected to the output of ULN2803. When input to the ULN2803 is high then its output become low thus the circuit is completed and current starts flowing through the relay. Thus normally open (NO) contacts become normally closed (NC). Thus device connected to the relay become on.

10.2FOR MOTOR CONTROL

The operation of DC geared motor is basically controlled through the pulse width modulation technique. Motor is connected in chopper type 'A' configuration [3]. The motor speed is directly proportional to the voltage applied to the armature. The average output voltage across the armature depends on the on-off time of the switch [2]. As key 'e' is pressed the motor speed increases because the counter shifts upwards every time,the key 'e' is pressed. When key 'f' is pressed the motor speed decreases because the counter shifts downwards every time the key 'f' is pressed.

XI. CHOPPER TYPE-A CONFIGURATION

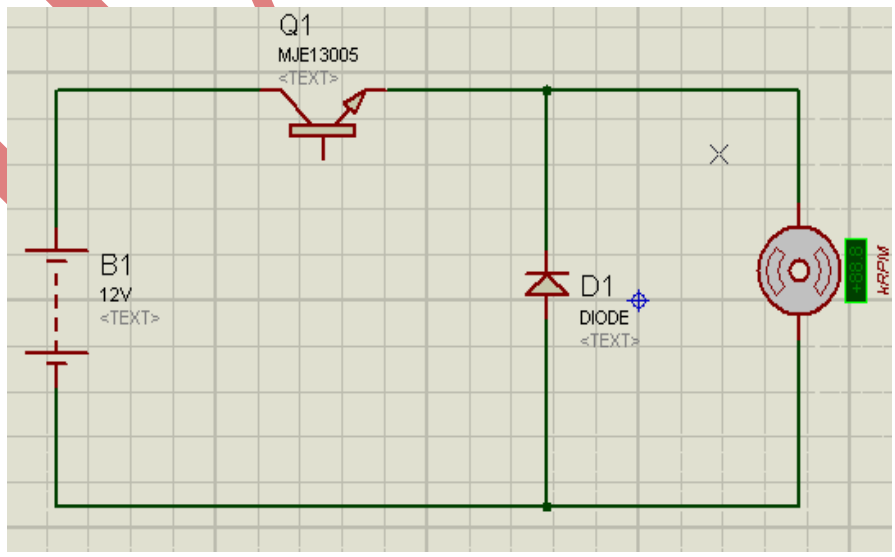


Fig.8 Chopper Type-A Configuration [2].

Output voltage= $a*V_s$ ……(1)

Where duty cycle(a) = T_{on}/T_{off}…(2)

T_{on} is the on time of the switch when a gate pulse is applied. When gate pulse is not applied it remains off. The gate pulse is given by the microcontroller. By using the counters of microcontroller pulse width can be controlled. Counters are controlled through programming. Depending upon the key pressed counter will increment or decrement its value.

XII. OBSERVATIONS

When key 'E' or 'e' is pressed then pulse width decreases.

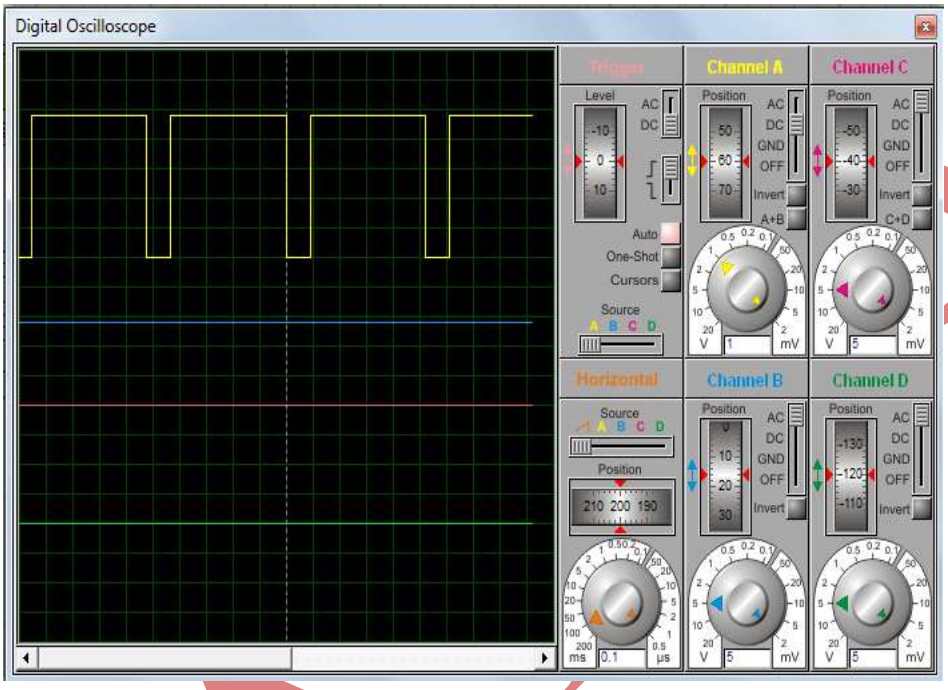


Fig.9when Key 'E' Or 'E' Is Pressed Then Motor Speed Increase As Pulse Width Increases.

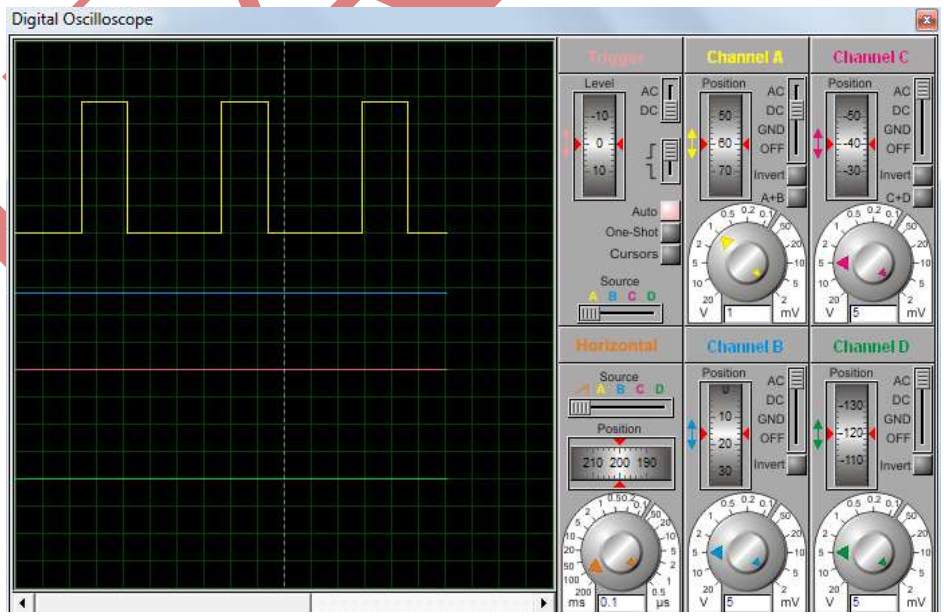


Fig.10 When Key 'F' Or 'F' Is Pressed Then Motor Speed Decrease As Pulse Width Decreases.

'A' or 'a' ----Relay 1 On.

'B' or 'b'----Relay 2 On.

'C' or 'c' ----Relay 1 and 2 are On.

'D' or 'd'----both Relay1 and Relay 2 are Off.

'E' or 'e' ----Motor speed increases .

'F' or 'f'----Motor speed decreases.

'G' or 'g' ----Motor runs at full speed.

'J' or 'j'----Motor stops.

'I' or 'i' ----Relay 3 On.

'J' or 'j'----Relay 1and 3 are On.

'K' or 'k' ----Relay 2 and Relay 3 are On.

'L' or 'l'----All Relay are On.

'Y' or 'y' ----All appliances are On.

'Z' or 'z'----All appliances are Off.

XIII. RESULT

In our working model we have observed that the speed increases on increase in the pulse width and decrease with decrease in pulse width applied to the gate of switch (as can be seen in simulation). Further by burning the programme in the microcontroller we have successfully come in a situation to control the width of pulse by using keyboard. So that by pressing a proper key as per the programme the pulse width can be varied.Hence we have controlled the speed and direction of dc geared motor via computer using at mega 16 microcontroller. Secondly we have also successfully controlled home appliances through computer.

XIV. CONCLUSION

The designing of a sustainable system to control the speed and orientation of a Dc geared motor and to control the home appliances wirelessly was successfully implemented in this paper.Dc geared motors have speed control capabilities which means that speed, torque and even direction of rotation can be changed at any time to meet the new conditions. By using wireless control of home appliances both energy and investment can be saved. This is a cost effective model also as we can control the dc geared motor and home appliances both from one microcontroller simultaneously. The paper provides a platform for further advancement in the field of industrial use of DC geared motors and home automation.

REFERENCES

[1] **J**eetender Singh Chauhan, Sunil Semwal / International Journal of Engineering Research and Applications (IJERA) ISSN: 2248-9622 www.ijera.com Vol. 3, Issue 1, January -February 2013, pp.778-783.

[2] Bimbhra, P.S., Power Electronics. New Delhi, Khanna Publishers, 2006.

[3] Dubey, G.K., Fundamentals of Electrical Drives. New Delhi, Narosa Publishing House, 2009.

[4] M.H.rashid, Power Electronics, Pearson education.

[5] Embedded C programming & the Atmel AVR (By Richard Barnett, Larry O'Cull, Sarah Cox).

IJATES